Modelling of Ultraviolet and Visible Emissions in Comets

Thesis submitted to
Cochin University of Science and Technology

In partial fulfillment of the requirements
for the award of

Doctor of Philosophy
in
Physics

UNDER THE FACULTY OF SCIENCES

by
Susarla Raghuram

Space Physics Laboratory
Vikram Sarabhai Space Centre
Indian Space Research Organisation
Thiruvananthapuram
INDIA

July 2013

Declaration

This is to declare that the work presented in this thesis was carried out at the Space Physics Laboratory (SPL), Vikram Sarabhai Space Centre (VSSC), Thiruvananthapuram for the award of the degree of Doctor of Philosophy in the Faculty of Sciences from the Cochin University of Science and Technology, Cochin, Kerala, India. This Thesis is the outcome of the original work done by me and the work did not form part of any dissertation submitted for the award of any degree, diploma, associateship or any other title or recognition from any University/Institution.

July 2013 **Susarla Raghuram**

भारत सरकार
अंतरिक्ष विभाग
विक्रम साराभाई अंतरिक्ष केन्द्र
तिरुवनन्तपुरम-695 022
केरल, भारत.
फोन : (0471) 2562330
फैक्स : (0471) 2706535
तार/Gram: SPACE

Government of India
Department of Space
Vikram Sarabhai Space Centre
Thiruvananthapuram-695 022
Kerala, INDIA.
Telephone : (0471) 2562330
Fax : (0471) 2706535
e-mail: anil_bhardwaj@vssc.gov.in

SPACE PHYSICS LABORATORY

Dr. Anil Bhardwaj, FNA, FASc
Scientist-G & Head, PSB

CERTIFICATE

Certified that the thesis entitled “**Modelling of Ultraviolet and Vissible Emissions in Comets**” submitted by Mr. **Susarla Raghuram**, to Cochin University of Science and Technology, Cochin, embodies the original results of the investigations carried out at the Space Physics Laboratory, Vikram Sarabhai Space Centre, Thiruvananthapuram, under my guidance. The work presented in this thesis has not been submitted for the award of any other degree or diploma to any other university or institution.

July 2013

Dr. Anil Bhardwaj
(Thesis Supervisor)

Countersigned

Dr. K. Krishnamoorthy
Director
Space Physics Laboratory

भारतीय अंतरिक्ष अनुसंधान संगठन   Indian Space Research Organisation

भारत सरकार
अंतरिक्ष विभाग
विक्रम साराभाई अंतरिक्ष केन्द्र
तिरुवनन्तपुरम-695 022
केरल, भारत.
फोन : (0471) 2562330
फैक्स : (0471) 2706535
तार/Gram: SPACE

सत्यमेव जयते

Government of India
Department of Space
Vikram Sarabhai Space Centre
Thiruvananthapuram-695 022
Kerala, INDIA.
Telephone : (0471) 2562330
Fax : (0471) 2706535
e-mail: anil_bhardwaj@vssc.gov.in

SPACE PHYSICS LABORATORY

Dr. Anil Bhardwaj, FNA, FASc
Scientist-G & Head, PSB

CERTIFICATE

This is to certify that all the relevant corrections and modifications suggested by the audience during the Pre-synopsis seminar and recommended by the Doctoral committee of **Mr. Susarla Raghuram** (Ph.D. Reg. No. 3794) have been incorporated in the thesis.

July 2013

Dr. Anil Bhardwaj
(Thesis Supervisor)

Countersigned

Dr. K. Krishnamoorthy
Director
Space Physics Laboratory

परमेस्वरार्पणमस्तु

Acknowledgments

I believe – whenever, wherever, and whatever we learn, somewhere, somewhat, and somehow will come into use once in the life. I am sure that time that spent in my research career was useful to understand several things, not only about cometary science and more importantly in building my character. I was bestowed with a highly positive and constructive environment about which I always feel great. My sincere acknowledgments to the association of several nice people who made my life happier during this Ph.D. period.

After several successes and failures I understood that the path that has been chosen mostly can decide the result. I am so glad to have such a guide, Dr. Anil Bhardwaj, who has shown me the right path and constantly supported me with his great patience. I owe him a great debt of gratitude for his invaluable guidance and support. His suggestions and discussions are always very useful in my research.

I sincerely thank Dr. K. Krishna Murthy, Director Space Physics Laboratory, for his encouragement in my research work and provided me excellent facilities in the Laboratory. His positive comments are helpful to improve my presentation skills and also in evaluating my work.

Thanks to Prof. R. Sridharan, former Director of Space Physics Laboratory, who motivated me to pursue this research.

I would like to the SPL staff, Ms. P. R. Suseela, Mrs. C. Geetha, Ms. Shishira, Ms. Shalini, Mr. Watson, Mr. Ashokan, Mr. T. K. Vijayan, Mr. Jihas, Ms. Prameela, to mention a few for taking care my administrative works. Thanks to CUSAT office staff for helping me in all academic procedures.

I should thank the Academic committee of Space Physics Laboratory, Dr. Anil Bhardwaj, Dr. K. Parameswaran, Dr. M. Mohan, Dr. K. Rajeev, Dr. Prabha R. Nair, Dr. Geetha Ramkumar, Dr. Tarun Pant, Dr. R. K. Choudhary, Dr. Suresh Raju, Dr. K. Kishore Kumar Dr. S.Suresh Babu, Dr. Sunil Kumar, Dr. D. B. Subramanyam, Dr. Satheesh Thampi, Dr. G. Manju, Dr. N. V. P. Kiran Kumar, Dr. Siji Kumar and Dr. S. S. Das, for evaluating my work every year with positive criticism. I appreciate the scientific discussions with Vipin, Dhanya, Supriya and Abhinaw which were very enlightening.

During this research period, I am lucky to have a good companion and friend Mr. Sonal Kumar Jain. My acknowledgments for his support in all aspects. I wish we could maintain this forever.

I thank the CUSAT Research committee members, Prof. Anatharaman, Dr. Mohan Kumar, Prof. Santosh, and Prof. Ramesh Babu for critically evaluating my work every year and helping me with their suggestions.

I am happy to have nice batch mates, Anish, Sumod, Sherine, and Prijith during this research period. I thank them for their good company.

There are several happy moments with my senior friends Jai, Lijo, Veena, and Liji. I thank them for being a part of my research career. Thanks also to my SPL friends, Ambili, Anu, Asha, Tinu, Arun, Arya, Manoj, Madhav, Renju, Neethu, Ajesh, Ashok, Lakshmi, and Sreedevi for providing a good ambiance.

I would like to thank Dr. Sandhya, Dr. Mukunda, Dr. Hossain, Dr. Vineeth, Dr. Vijayakumar, Dr. Nizy, Dr. P. Hegde, Dr. Uma, Mr. Tirtha Prathim Das, Mrs. Neha, Mr. Manoj Mishra, Mr. Imran, Mr. Sobhan, Mr. K. Subrahmanyam, Mrs. Mridula, , Mr. Manoj Mishra, Dr. Korak saha for their support and encouragement.

My sincere thanks to Vikram Sarabhai Space Centre, for supporting me with ISRO fellowship along with several facilities. My sincere regards to my lecturers Dr. M. Ramakrishna, S. Symasunder, Dr. Ravibabu for intensifying my interest in Physics

During this period I was blessed to have such lovable roommates, Kiran, Kiran pinumalla, and Ashok, who brightened my life. "Thanks" is a small word to convey my gratitude to them. I owe to them for their caring and support during this Ph.D. period. There are several joyful moments that brought me because of good family friends, Nagesh & Sowmya, Tushar & Shweta, Rajkumar & Manjula, Baluragi & Chaitanya, Anil & Anusha, Ashok & Mukta and Kiran & Sucharita. I enjoyed playing with sweet kids, Tushar, Diya, Soujanya, Chinmayi, Ananth, Ananya, Akshith. Thanks to them for providing me a happy life with their great presence.

I would like to thank my family Sri. Gowri devi (mother), Sri. Saibabu (Father), Kalyani (sister), and Somasekhar (brother-in-law) and aunt Sri. Uma rani for their support.

I am very happy to have close friends Mr. Lakshmi Kiran & Mrs. Sivaranjani, Mr. Ramanjulu, Mr. Udaya chaitanya. My sincere acknowledgments to them.

My personal life became livelier when I found my soul partner. I must thank my lovely wife Himabindu for her great support during the real rough times. I am looking forward to have a great time with her forever.

Contents

Preface . . . xvii
Publications and Conference presentations . . . xix
List of Figures . . . xxi
List of Tables . . . xxv
List of Acronyms . . . 1

1 Introduction 1
1.1 Cometary reservoirs and dynamical taxonomy . . . 3
1.2 Physical properties of comets . . . 7
  1.2.1 Nucleus . . . 7
  1.2.2 Cometary coma . . . 9
  1.2.3 Tails . . . 13
1.3 An overview of spectroscopic emissions from comets . . . 14
  1.3.1 Ultraviolet emissions . . . 14
  1.3.2 Visible emissions . . . 16
  1.3.3 X-ray, Infrared, and Radio wave emissions . . . 17
  1.3.4 Modelling studies of cometary emissions . . . 18
1.4 Motivation of this study . . . 20
1.5 Outline of thesis . . . 20

2 Description of model and input parameters 23
2.1 Introduction . . . 24
2.2 Model . . . 24
  2.2.1 Photoattenuation . . . 25
  2.2.2 Electron degradation: Analytical yield spectrum approach . . . 26
  2.2.3 Coupled Chemistry of gas phase reactions . . . 28
2.3 Input parameters for model . . . 29
2.4 Solar ultraviolet radiation flux . . . 29
  2.4.1 EUVAC model . . . 30
  2.4.2 SOLAR2000 (S2K) model . . . 30
2.5 Cometary coma . . . 30
  2.5.1 Haser's model . . . 31
2.6 Photon impact cross sections . . . 32
  2.6.1 H_2O and OH . . . 32
  2.6.2 CO_2 . . . 35
  2.6.3 CO . . . 36
2.7 Electron impact cross sections . . . 37

2.7.1 H_2O . . . 38
2.7.2 CO_2 and CO . . . 38
2.8 Dissociative recombination of ions . . . 39
2.8.1 H_3O^+ and H_2O^+ . . . 40
2.8.2 CO_2^+ and CO^+ . . . 42
2.9 Summary . . . 42

3 CO Cameron band emission 43
3.1 Introduction . . . 43
3.2 Model . . . 45
3.3 Calculations on comet 103P/Hartley 2 . . . 47
3.4 Results for 103P/Hartley 2 . . . 48
3.4.1 Production and loss of $CO(a^3\Pi)$ . . . 48
3.4.2 Intensity of Cameron band of CO molecule . . . 49
3.5 Calculations on comet 1P/Halley . . . 52
3.6 Results for comet 1P/Halley . . . 54
3.6.1 Production and loss of $CO(a^3\Pi)$ . . . 54
3.6.2 Intensity of CO Cameron bands . . . 55
3.7 Discussion . . . 61
3.7.1 Effect of model parameters on the calculations . . . 62
3.7.1.1 Electron impact cross sections . . . 62
3.7.1.2 Solar EUV-UV flux . . . 63
3.8 Summary . . . 64

4 Red and green emissions in comets at heliocentric distance of 1 AU 65
4.1 Introduction . . . 66
4.2 Model . . . 69
4.3 Calculations on comet C/1996 B2 Hyakutake . . . 72
4.4 Results for comet C/1996 B2 Hyakutake . . . 72
4.4.1 Production and loss of $O(^1S)$ . . . 72
4.4.2 Production and loss of $O(^1D)$ . . . 74
4.4.3 Green and red-doublet emission intensities . . . 77
4.5 Calculations on comet C/1995 O1 Hale-Bopp . . . 84
4.6 Results for comet C/1995 O1 Hale-Bopp . . . 86
4.6.1 Production and loss of $O(^1S)$ . . . 86
4.6.2 Production and loss of $O(^1D)$ . . . 87
4.6.3 Green and Red-doublet emission intensities . . . 92
4.6.4 Radiative efficiencies of $O(^1S)$ and $O(^1D)$ atoms . . . 96
4.6.5 Excess velocities of $O(^1S)$ and $O(^1D)$ . . . 98
4.7 Discussion . . . 100
4.7.1 Comparison of model calculations with observations . . . 102
4.7.1.1 Atomic oxygen emission lines on comet C/1996 B2 Hyakutake . . . 102
4.7.1.2 Atomic oxygen [OI] 6300 Å emission line on comet Hale-Bopp . . . 105
4.7.1.3 Width of green and red-doublet emission lines . . . 108
4.7.2 Effect of model parameters on the calculated intensities . . . 109
4.7.2.1 Expansion velocity of neutrals . . . 109
4.7.2.2 Relative abundances of neutral species . . . 110

4.7.2.3 Effect of slit dimension on the derived O(^{1}D) production rate . . . 112
4.8 Summary and Conclusions . . . 112

5 Red and Green emissions of atomic oxygen at large heliocentric distances 117
5.1 Introduction . . . 117
5.2 Model . . . 118
5.3 Results . . . 122
5.3.1 Production processes of O(^{1}S) and O(^{1}D) . . . 122
5.3.2 Loss processes of O(^{1}S) and O(^{1}D) . . . 122
5.3.3 [OI] green to red-doublet emission intensity ratio and line widths . 123
5.4 Discussion . . . 131
5.4.1 Impact of CO on the G/R ratio . . . 133
5.4.2 Impact of CO_2 on the G/R ratio . . . 134
5.4.3 Impact of collisional quenching of O(^{1}S) and O(^{1}D) on the G/R ratio . . . 135
5.4.4 Green and red-doublet emission line widths . . . 136
5.5 Summary and conclusion . . . 137

6 Summary, Limitations, and Future scope 139

Appendix A Additional Tables 143

Appendix B Publications 167

References 219

Thesis advisor
Anil Bhardwaj

Author
Susarla Raghuram

Modelling of Ultraviolet and Visible Emissions in Comets

Preface

Comets are the spectacular objects in the night sky since the dawn of mankind. Due to their giant apparitions and enigmatic behavior, followed by coincidental calamities, they were termed as notorious and called as 'bad omens'. With a systematic study of these objects modern scientific community understood that these objects are part of our solar system. Comets are believed to be remnant bodies of at the end of evolution of solar system and possess the material of solar nebula. Hence, these are considered as most pristine objects which can provide the information about the conditions of solar nebula. These are small bodies of our solar system, with a typical size of about a kilometer to a few tens of kilometers orbiting the Sun in highly elliptical orbits. The solid body of a comet is nucleus which is a conglomerated mixture of water ice, dust and some other gases. When the cometary nucleus advances towards the Sun in its orbit the ices sublimates and produces the gaseous envelope around the nucleus which is called coma. The gravity of cometary nucleus is very small and hence can not influence the motion of gases in the cometary coma. Though the cometary nucleus is a few kilometers in size they can produce a transient, extensive, and expanding atmosphere with size several orders of magnitude larger in space. By ejecting gas and dust into space comets became the most active members of the solar system. The solar radiation and the solar wind influences the motion of dust and ions and produces dust and ion tails, respectively.

Comets have been observed in different spectral regions from rocket, ground and space borne optical instruments. The observed emission intensities are used to quantify the chemical abundances of different species in the comets. The study of various physical and chemical processes that govern these emissions is essential before estimating chemical abundances in the coma. Cameron band emission of CO molecule has been used to derive CO_2 abundance in the comets based on the assumption that photodissociation of CO_2 mainly produces these emissions. Similarly, the atomic oxygen visible emissions have been used to probe H_2O in the cometary coma. The observed green ([OI] 5577 Å) to red-doublet emission ([OI] 6300 and 6364Å) ratio has been used to confirm H_2O as the parent species of these emissions. In this thesis a model is developed to understand the photochemistry of these emissions and applied to several comets. The model calculated emission intensities are compared with the observations done by space borne instruments like International Ultraviolet Explorer (IUE) and Hubble Space Telescope (HST) and also by various ground based telescopes.

Introduction to comets and various emission observed as well as motivation for the present thesis are explained in Chapter 1. The details of input parameters (viz., solar photon flux, photon and electron impact cross sections of different species, rate coefficients of various reactions) required to model these emissions and the model are presented in Chapter 2. The model developed to understand the physical processes governing CO Cameron band emission is described in Chapter 3. This model is applied to two comets, viz., Halley and Hartley, on which this emission is observed. Using chemical reactions that produces atomic oxygen green and red-doublet emissions a model is developed to understand the photochemistry of these visible emissions. This model is described in Chapter 4, whereas the model calculations are compared with the observations on comets Hyakutake and Hale-Bopp at 1 AU. These atomic oxygen emissions are also observed on several comets at large heliocentric distances (>2 AU) where CO and CO_2 are dominant O-bearing species. This model is applied on comets observed at large heliocentric distances to study the photochemistry of atomic oxygen green and red-doublet emissions. The results of this model and comparison with the observations are presented in Chapter 5. The results of this work are summarized in Chapter 6 along with limitations and future scope of the study.

Publications:

1. Anil Bhardwaj and **Susarla Raghuram** (2011), Model for Cameron-band emission in comets: a case for the EPOXI mission target comet 103P/Hartley 2, Monthly Notices of Royal Astronomical Society 412(1):L25.

2. **Susarla Raghuram** and Anil Bhardwaj (2012), Model for the production of CO Cameron band emission in comet 1P/Halley, Planetary and Space Science 63–64, 139–149.

3. Anil Bhardwaj and **Susarla Raghuram** (2012), A coupled chemistry-emission model for atomic oxygen green and red-doublet emissions in the comet C/1996 B2 Hyakutake. The Astrophysical Journal 748, 13.

4. **Susarla Raghuram** and Anil Bhardwaj (2013), Model for atomic oxygen visible line emissions in comet C/1995 O1 Hale-Bopp. Icarus, 223, 91-104.

5. **Susarla Raghuram** and Anil Bhardwaj (2013), Photochemistry of atomic oxygen green and red-doublet emissions in comets at large heliocentric distances (Revised and Submitted).

Conference presentations:

1. **Raghuram, S.** and A. Bhardwaj (2010), Model of Cameron Band Emission in Comet P/Hartley 2, Seventh AOGS Annual Meeting, Hyderabad, India, July 5–9.

2. **Raghuram, S.** and A. Bhardwaj (2010), Model of Cameron Band Emission in Comet P/Hartley 2, International workshop on Advances in Planetary Atmospheres and Exploration at PRL, Ahmedabad, July 12 - 13.

3. **Raghuram, S.** and A. Bhardwaj, Cameron Band Emission in Comet 1P/Hartley, 16th National Space Science Symposium, Saurashtra University, Rajkot, Feb. 24–27, 2010.

4. **Raghuram, S.** and A. Bhardwaj (2012), Coupled chemistry emission model on comet C/1996 B2 Hyakutake, National Space Science Symposium (NSSS) at S. V. University. Tirupathi.

5. **Raghuram, S.** and A. Bhardwaj (2012), Coupled chemistry emission model for green (5577 Å) and red-doublet (6300, 6364 Å) emissions of Atomic Oxygen in Comets, 39^{th} COSPAR Scientific Assembly, Mysore, India, 14–22 July, 2012.

6. **Raghuram, S.** and A. Bhardwaj (2012), Model for the Cameron band emission of CO molecule in comets, 39^{th} COSPAR Scientific Assembly, Mysore, India, 14–22 July, 2012.

7. **Raghuram, S.** and A. Bhardwaj (2012), Forbidden atomic oxygen line emissions in Comets at large heliocentric distances, International Symposium on Atmospheres of Terrestrial Planets: Observations & Modeling at PRL, Ahmedabad, July 23 - 24.

List of Figures

1.1 A graphical representation of comet's orbit and physical changes occurring in a comet at different heliocentric distances. 2
1.2 The schematic diagram showing the location of cometary reservoirs and planets in the solar system. 4
1.3 The classification of comets based on Tisserad parameter (T). 6
1.4 Various space missions targeted to comets and the corresponding solar activity. 8
1.5 The observed cometary nuclei from different space missions and their physical dimensions. 9
1.6 The SOHO SWAN hydrogen Ly-α image of comet Hale-Bopp's coma during its perihelion 1 April 1997 along with the visible image showing dust and plasma tails. 11
1.7 Schematic diagram representing different physical processes occurs in the cometary coma at 1 AU and having minimum gas production rate of 10^{26} s^{-1}. 12
1.8 The photograph of comet Hale-Bopp showing spectacular dust and ion tails at its last perihelion on 1 April 1997 around 0.3 AU from the Sun. . 13
1.9 The UV and optical spectrum of comet 103P/Hartley 2 obtained using Field object spectrograph on Hubble space telescope. 16

2.1 The schematic representation of model calculation. 24
2.2 The calculated photoelectron production rate at 1000 km cometocentric distance for different gas production rate comets. 26
2.3 The calculated photoelectron flux at 1000 km cometocentric distance for different gas production rate comets. 28
2.4 The intensities are integrated along the line of sight to calculate surface brightness profile. 29
2.5 Neutral density distribution in a comet of H_2O production rate 1×10^{30} s^{-1}. 33
2.6 Photon cross sections of H_2O for different dissociation and ionization channels. 34
2.7 Photon cross sections of CO_2 for different dissociation and ionization channels. 36
2.8 Photon cross sections of CO for different dissociation and ionization channels. 37
2.9 The electron impact collision cross sections of H_2O. 39

2.10 The electron impact collision cross sections of CO_2. 40
2.11 The electron impact collision cross sections of CO. 41

3.1 Schematic energy level diagram of carbon monoxide molecule showing different electronic different transitions. 44
3.2 Electron impact cross sections of CO and CO_2 producing CO($a^3\Pi$) . . . 47
3.3 Solar fluxes taken from EUVAC and S2K models for the day 13 March 1986. 48
3.4 Calculated radial production rate profiles for CO($a^3\Pi$) in comet 103P/Hartley 2. 49
3.5 Calculated radial loss rate profiles of CO($a^3\Pi$) in comet 103P/Hartley 2. 50
3.6 Calculated brightness profile for Cameron band emission of CO in comet 103P/Hartley 2 along the projected distances. 51
3.7 Calculated radial profiles of various production mechanisms of CO($a^3\Pi$) in comet 1P/Halley 54
3.8 Radial profiles of various loss mechanisms of CO($a^3\Pi$) in comet 1P/Halley for 4% CO_2 and 7% CO relative abundances using EUVAC solar flux. . . 57
3.9 The calculated radial profiles of number density CO($a^3\Pi$) in comet 1P/Halley. 58
3.10 The integrated Cameron band brightness profiles as a function of projected distance from nucleus in comet 1P/Halley. 60
3.11 The calculated (1-0) Cameron band emission brightness in the IUE projected field of view on 13 March 1986 in comet 1P/Halley. 61

4.1 Schematic energy level diagram of atomic oxygen showing different spectroscopic transitions related to ^{1}S and ^{1}D metastable states. 67
4.2 Calculated radial profiles on comet C/1996 B2 Hyakutake for major production mechanisms of O(^{1}S) 74
4.3 Calculated radial profiles on comet C/1996 B2 Hyakutake for the photodissociation of CO_2 producing O(^{1}S) at different wavelength bands. . . 75
4.4 Calculated radial profiles on comet C/1996 B2 Hyakutake for the major loss mechanisms of O(^{1}S). 75
4.5 Calculated radial profiles on comet C/1996 B2 Hyakutake for the major production mechanisms of O(^{1}D). 76
4.6 Calculated radial profiles on comet C/1996 B2 Hyakutake for the photodissociation of H_2O producing O(^{1}D) at different wavelength bands . . 77
4.7 Calculated radial profiles on comet C/1996 B2 Hyakutake for the photodissociation of CO_2 producing O(^{1}D) at different wavelength bands . . 78
4.8 Calculated radial profiles on comet C/1996 B2 Hyakutake for major loss mechanisms of O(^{1}D) 79
4.9 Calculated number density profiles of O(^{1}S), O(^{1}D), O(^{3}P), and OH, along with those of H_2O, CO, and CO_2 on comet C/1996 B2 Hyakutake. 79
4.10 Calculated emission brightness profiles on comet C/1996 B2 Hyakutake along projected distances for 5577 Å and 6300 Å line emissions for different CO_2 relative abundance and yield for O(^{1}S) production in photodissociation of H_2O 80
4.11 Calculated radial profiles on comet C/1995 O1 Hale-Bopp for major production mechanisms of O(^{1}S). 87
4.12 Calculated radial profiles on comet C/1995 O1 Hale-Bopp for the photodissociation of CO_2 producing O(^{1}S) at different wavelength bands . . 88

4.13 Calculated radial profiles on comet C/1995 O1 Hale-Bopp for the major loss mechanisms of the O(^{1}S) . . . 88
4.14 Calculated radial profiles on comet C/1995 O1 Hale-Bopp for the major production mechanisms of O(^{1}D) . . . 89
4.15 Calculated radial profiles on comet C/1995 O1 Hale-Bopp for the photodissociation of H_2O producing O(^{1}D) at different wavelength bands . . 90
4.16 Calculated radial profiles on comet C/1995 O1 Hale-Bopp for the photodissociation of CO producing O(^{1}D) at different wavelength bands . . . 90
4.17 Calculated radial profiles on comet C/1995 O1 Hale-Bopp for the photodissociation of CO_2 producing O(^{1}D) at different wavelength bands . . 91
4.18 Calculated radial profiles on comet C/1995 O1 Hale-Bopp for major loss mechanisms of the O(^{1}D) . . . 92
4.19 Calculated number density profiles of O(^{1}S), O(^{1}D), O(^{3}P), and OH, along with those of H_2O, CO, and CO_2 on comet C/1995 O1 Hale-Bopp 93
4.20 Calculated atomic oxygen 6300, 5577, and 2972 Å emission lines brightness profiles on comet C/1995 O1 Hale-Bopp as a function of the projected distance . . . 94
4.21 Calculated green to red-doublet intensity ratio along projected distances in comet C/1995 O1 Hale-Bopp for different CO_2 relative abundances and with 0.5% yield for O(^{1}S) production in the photodissociation of H_2O. . . 97
4.22 Calculated radiative efficiency profiles of O(^{1}S) and O(^{1}D) on comets C/1995 O1 Hale-Bopp and C/1996 B2 Hyakutake. . . . 98
4.23 Calculated excess energy profiles of O(^{1}D) in photodissociation of H_2O, CO, and CO_2 and that of O(^{1}S) in photodissociation of CO_2 on comets C/1995 O1 Hale-Bopp and C/1996 B2 Hyakutake. . . . 99
4.24 Calculated green to red-doublet intensity ratio along projected distance in comet C/1996 B2 Hyakutake for different CO_2 relative abundance and yield for O(^{1}S) production in photodissociation of H_2O. . . . 103

5.1 Calculated radial O(^{1}S) production rate profiles for major production mechanisms in comet C/2006 W3 Christensen. . . . 123
5.2 Calculated radial O(^{1}D) production rate profiles for major production mechanisms in comet C/2006 W3 Christensen. . . . 124
5.3 Calculated radial loss rate profiles for major loss mechanisms of the O(^{1}D) and O(^{1}S) in comet C/2006 W3 Christensen. . . . 125
5.4 Calculated number density profiles of O(^{1}S), O(^{1}D), and OH, along with those of H_2O, CO, and CO_2 in comet C/2006 W3 Christensen 127
5.5 Calculated atomic oxygen red-doublet and green line brightness profiles along the cometocentric projected distances on comet C/2006 W3 Christensen. . . . 129
5.6 The calculated G/R ratio profiles along the projected distance in six different comets. . . . 130
5.7 The calculated radiative efficiency profiles of O(^{1}S) and O(^{1}D) in comets for different gas production rates . . . 131
5.8 The calculated G/R ratio as a function CO_2 abundance in comets for different water production rates . . . 132

List of Tables

1.1 The important properties of the cometary reservoirs of our solar system taken from *Stern* [2003]. 4
1.2 List of space missions targeted to study comets. 6
1.3 Principle emissions of atoms, molecules and ions observed in cometary ultraviolet and visible spectra. 15

3.1 Reactions for the production and loss of CO($a^3\Pi$). 46
3.2 The calculated CO($a^3\Pi$) production frequency (s^{-1}) for three different processes at 1 AU. 52
3.3 The Calculated CO Cameron band brightness of comet 103P/Hartley 2 for different conditions 53
3.4 The Calculated brightness of the CO Cameron band at comet 1P/Halley for different conditions on 13 March 1986. 56
3.5 The Calculated CO Cameron band brightness of comet 1P/Halley on different days of IUE observation. 59

4.1 Reactions accounted for the production and loss of O(^{1}S) in the model. . 71
4.2 Reactions accounted for the production and loss of O(^{1}D) in the model. . 73
4.3 Calculated percentage contribution for major production processes of O(^{1}S) and O(^{1}D) atoms in comet C/1996 B2 Hyakutake with varying relative abundance of CO_2 and O(^{1}S) yield. 81
4.4 Calculated percentage contribution for the major production processes of the green (red-doublet) emission in the slit projected field of view on comet C/1996 B2 Hyakutake. 82
4.5 Calculated percentage contributions for the major production processes of O(^{1}S) and O(^{1}D) in comet C/1995 O1 Hale-Bopp with varying relative abundance of CO_2 for 0.5 % O(^{1}S) yield. 95
4.6 Calculated percentage contributions for the major production processes of green and red-doublet emissions in the total observed projected field of view (2.4 × 10^5 km) on comet C/1995 O1 Hale-Bopp with varying relative abundance of CO_2. 96
4.7 Calculated green to red-doublet emission brightness ratio averaged over 5″ × 5″ slit, at different geocentric distances of comet C/1996 B2 Hyakutake and by varying CO_2 abundance. 104
4.8 Calculated intensities of green and red-doublet emissions and the G/R ratio in comet C/1996 B2 Hyakutake on different days of observation in March 1996. 105

4.9 The model calculated intensities of forbidden atomic oxygen emission lines on comet Hale-Bopp and the comparison of atomic oxygen 6300 Å line with the observation . . . 106
4.10 The model calculated green and red-doublet emission intensities on comet Hale-Bopp and the derived O(^{1}D) and H_2O production rates for different slit dimensions. . . . 107

5.1 Observational conditions of various comets along with corresponding H_2O production rates and CO_2 and CO relative abundances relative to H_2O and comparison of calculated green to red-doublet emission intensity ratios with the observations. . . . 119
5.2 Calculated percentage contributions for major production processes of O(^{1}S) and O(^{1}D) in six different comets. . . . 126
5.3 Calculated percentage contributions for major production processes of green and red-doublet emissions in the slit projected field of view on different comets and the comparison of the calculated and observed line widths. . . . 128

A.1 List of gas-phase ion-chemistry reactions accounted for the coupled chemistry model. . . . 143
A.2 Parameters for the EUVAC solar flux model. . . . 147
A.3 Photon cross section of H_2O for different dissociation and ionization channels 148
A.4 Photon cross section of CO_2 for different dissociation and ionization channels . . . 154
A.5 Photon cross section of CO for different dissociation and ionization channels. 160
A.6 Jackman's analytical fitting parameters for electron impact cross sections of different excited states of H_2O. . . . 164
A.7 Jackman's analytical fitting parameters for electron impact cross sections of different excited states of CO_2. . . . 165
A.8 Jackman's analytical fitting parameters for electron impact cross sections of different excited states of CO. . . . 166

Chapter 1

Introduction

Contents

1.1 Cometary reservoirs and dynamical taxonomy 3

1.2 Physical properties of comets 7

1.2.1 Nucleus 7

1.2.2 Cometary coma 9

1.2.3 Tails 13

1.3 An overview of spectroscopic emissions from comets 14

1.3.1 Ultraviolet emissions 14

1.3.2 Visible emissions 16

1.3.3 X-ray, Infrared, and Radio wave emissions 17

1.3.4 Modelling studies of cometary emissions 18

1.4 Motivation of this study 20

1.5 Outline of thesis 20

Since the dawn of mankind night sky remained as a mysterious platform for various heavenly bodies and puzzling events. Comets are always spectacular and were appalling objects for humans in the pre-scientific history. Ancestors witnessed several giant ghost like comet apparitions in the night sky which were followed by coincidental calamities making comets notoriously as "bad omens". The spectacular apparition and enigmatic behavior of the comets in the night sky introduced several myths in the history. The quest for understanding these apparitions lead to a systematic study of comets. The modern scientific community identified these objects as a part of our solar system. Comets are classified as small bodies of the solar system which are orbiting around the Sun in highly elliptical orbits. Since most of the time in their orbit is spent far away from the Sun, the amount of heat received by the comet from the Sun is not enough for their physical evolution, which is not the case for the planets. Unlike planets, comets do not have internal active heat source that can cause any physical evolution. Hence, comets are believed as least evolved objects since the formation of the solar system. These objects remained as leftovers during the end of the formation of the solar system and may contain pristine material which belongs to solar nebula.

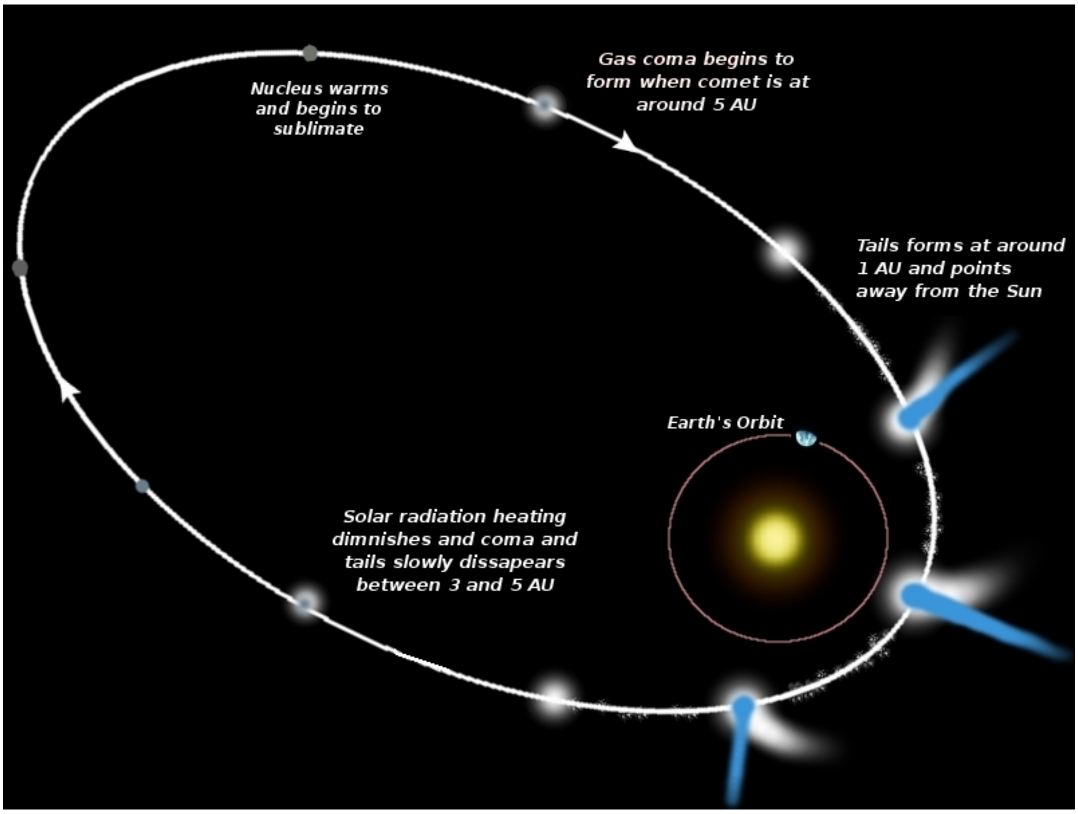

Figure 1.1: A graphical representation of comet's orbit and physical changes occurring in a comet at different heliocentric distances. The blue tail which points radially away from the Sun is ion tail whereas the curved white tail is dust tail. Objects and features shown in this figure are not to the scale.

The solid body of the comet is the nucleus orbiting around the Sun in a highly elliptical orbit. Nucleus is a conglomerated mixture of essentially water ice and dust with a size of around one to few tens of kilometer. When this icy body advances toward the Sun in its orbit, the solar radiation sublimates the ices present in the nucleus. The sublimated gases rush into the surrounding vacuum and produces a gaseous envelope around the cometary nucleus. This transient gaseous atmosphere around the cometary nucleus is called as cometary coma. A typical cometary orbit and the physical changes a comet undergoes during its orbital motion is graphically presented in Figure 1.1. When comet is far away from the Sun (>10 AU) the heat received from the Sun is not sufficient to sublimate ices and to produce visible cometary coma, hence it is very difficult to observe the comets at large heliocentric distances. As the comet start approaching the Sun, the solar radiation received by the nucleus starts increasing resulting in the formation of coma. The dust released during sublimation scatters the solar visible light and produce visible cometary coma. As the comet reaches near the Sun the sublimation rates of ices increases producing more gas and dust. During this active state the solar radiation and solar wind strongly interacts with the cometary coma and produces two tails: dust tail and ion tail. The large non-refractory materials, which are separated during sublimation, unaffected by both solar radiation and solar wind follows the cometary orbit as a meteor trail. Solar radiation exerts pressure on the dust grains in the cometary coma. Due to cometary motion and inertia the dust particles follow a curved path, whereas electromagnetic interaction of solar wind with cometary ionized coma keeps the ion tail straight pointing radially away from the Sun. The observation that the ion tail in comets always point radially away from the Sun led to the discovery of solar wind [*Biermann*, 1951]. Around the perihelion distance the complete cometary activity turns to its maximum phase. When comet recedes from the Sun the solar heating of nucleus diminishes causing coma and tails to gradually start reducing in size and finally disappear altogether and the comet attains idle condition. A few meters of cometary surface is lost due to solar heating in each revolution. Thus, a typical comet of mass 10^{14} kg can revolve around the Sun about 10^{6} times in its lifetime provided no other forces disintegrate it or disturb its orbit.

1.1 Cometary reservoirs and dynamical taxonomy

The modern scientific community suggest that our solar system is formed after gravitational collapse of a giant molecular cloud. Comets formed in the outer region of our solar nebula where different ices could survive against the radiation from the young Sun. The water vapor condensed over the dust grains constituted the cometary nucleus. During the evolution of solar system comets underwent several collisions with planets and some of them were scattered to large heliocentric distances.

The observations of several comets and their orbital motion have been recorded historically which have been used to classify them. Based on the revolution period (T_p) comets have been broadly divided into two groups: long period comets ($T_p > 200$ years) and short period comets ($T_p < 200$ years). Our current scientific understanding is that there are two main cometary reservoirs in the solar system: one is Kuiper belt and the other is Oort cloud. The studies of these sources are mainly linked to origin and evolution of the solar system. A schematic diagram which represents the location of cometary reservoirs with respect to solar system bodies taken from *Stern* [2003] is shown in Figure 1.2. The major properties of these cometary sources are tabulated in Table 1.1

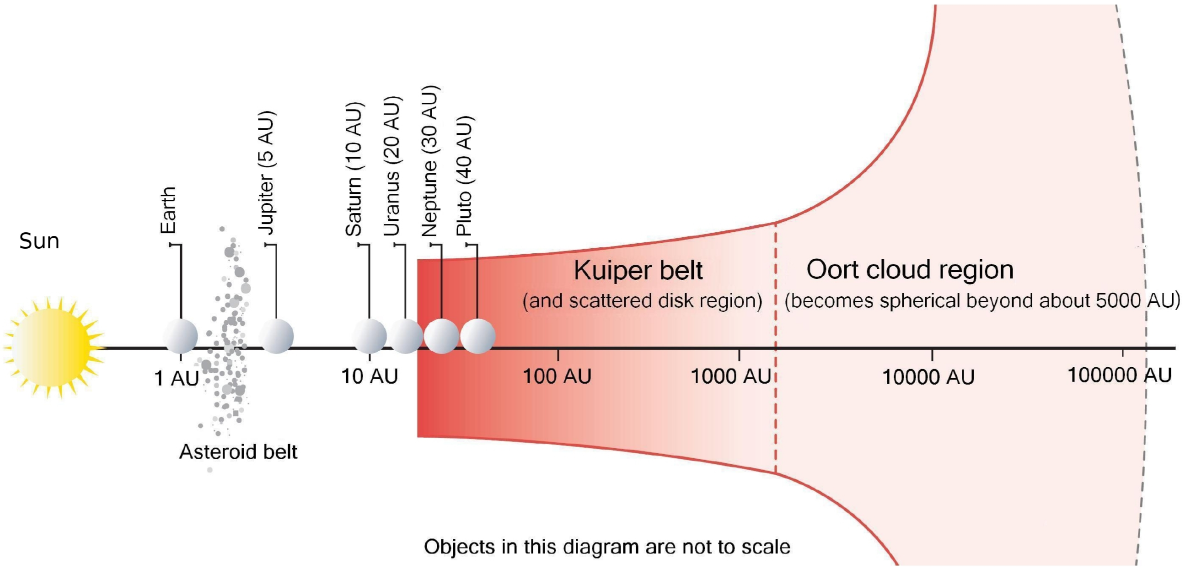

Figure 1.2: The schematic diagram showing the location of cometary reservoirs and planets in the solar system [Image credits to *Stern*, 2003].

Table 1.1: The important properties of the cometary reservoirs of our solar system taken from *Stern* [2003].

	Kuiper belt	Oort cloud
Shape	disk-like	Spheroidal
Distance range	30 – 1000 AU	$1 \times 10^3 - 1 \times 10^5$ AU
Comet population	$\sim 5 - 10 \times 10^9$	$1 \times 10^{11} - 5 \times 10^{12}$
Estimated mass (including smaller debris)	$\sim 0.1\ M_\oplus{}^*$	$\sim 1 - 50\ M_\oplus$
Ambient surface temperatures	30 – 60 K	5 – 6 K
Origin	Largely in-situ	Ejected material from the Kuiper belt and outer-planets zone
Return mechanism from the reservoir	Dynamical chaos due to planetary perturbations and collisions	Perturbations due to passing stars, galactic tides and molecular clouds

$^*M_\oplus$ denotes the mass of the Earth.

The Oort cloud:

Considering various recorded observations *Oort* [1950] systematically studied the cometary orbital parameters for different comets. He proposed that there should be essentially a spherical isotropic reservoir of comets surrounding the Sun at large heliocentric distances. This reservoir is now known as Oort cloud. The stars passing near to this Oort cloud perturbs their motion and pushes the comets into inner solar system [see *Stern*, 2003, and references there in]. The typical distances of this Oort cloud lies around 10^5 AU. Several models have shown that the formation of Oort cloud is a natural by-product of cleaning and ejection of debris from the giant planets [eg., *Safronov*, 1987].

The Kuiper belt:

Not all comets have very elongated orbits indicating the Oort's cloud origin. Comets having shorter orbital period display shallow, prograde orbital inclinations relative to the ecliptic plane. This gives a clue about another source of comets which lies in or near the ecliptic plane suggested by several workers. The existence of such a disk like material was hypothesized by *Kuiper* [1951]. The present ground based observation techniques detected such moderate sized bodies confirming the Kuiper belt [*Jewitt and Luu*, 1993]. Many theoretical studies suggest that most of the comets present in Kuiper belt originated locally. The present understanding of the location of Kuiper belt is beyond 30 AU. The outer Kuiper belt smoothly merges with inner Oort cloud.

The population of Oort cloud and Kuiper belt comets is dynamically classified according to Tisserand parameter (T_j), a quasi-constant in three body problem Sun-Jupiter-Comet,

$$T_j = \frac{a_j}{a} + 2\,\sqrt{\frac{a_j}{a}(1-e^2)}\;\cos i$$

where a is semi-major axis, e is eccentricity, and i is inclination of comet's orbit with respect to the Jupiter's orbit having semi-major axis a_j. The dynamical classification of comets based on the Tisserand parameter is shown in Figure 1.3. The comets having Tisserand parameter value greater than two are classified as ecliptic because most of these comets have low inclined orbital paths. These comets are again classified into three groups. The comets having Tisserand parameter between two and three are Jupiter family whose orbit is completely dominated by Jupiter's gravitational field. The two other groups having Tisserand parameter greater than three and having semi-major axis internal and beyond the Jupiter's orbit are Encke family ($a < a_j$) and Chiron family ($a > a_j$), respectively.

The comets having Tisserand parameter smaller than two belongs to nearly isotropic family and most of them are arriving from the Oort cloud. Generally these comets enter into the inner solar system because of gravitational perturbations of passing stars. The comets injected into inner planetary system are grouped into two categories. The comets having semi major axis less than 10,000 AU are categorized as returning comets, whereas those with semi-major axis greater than 10,000 AU as dynamically new comets. The new comets generally enter the solar system for the first time. The returning comets having semi major axis less than 40 AU are called Halley-type and the rest are categorized as isotropically distributed external comets.

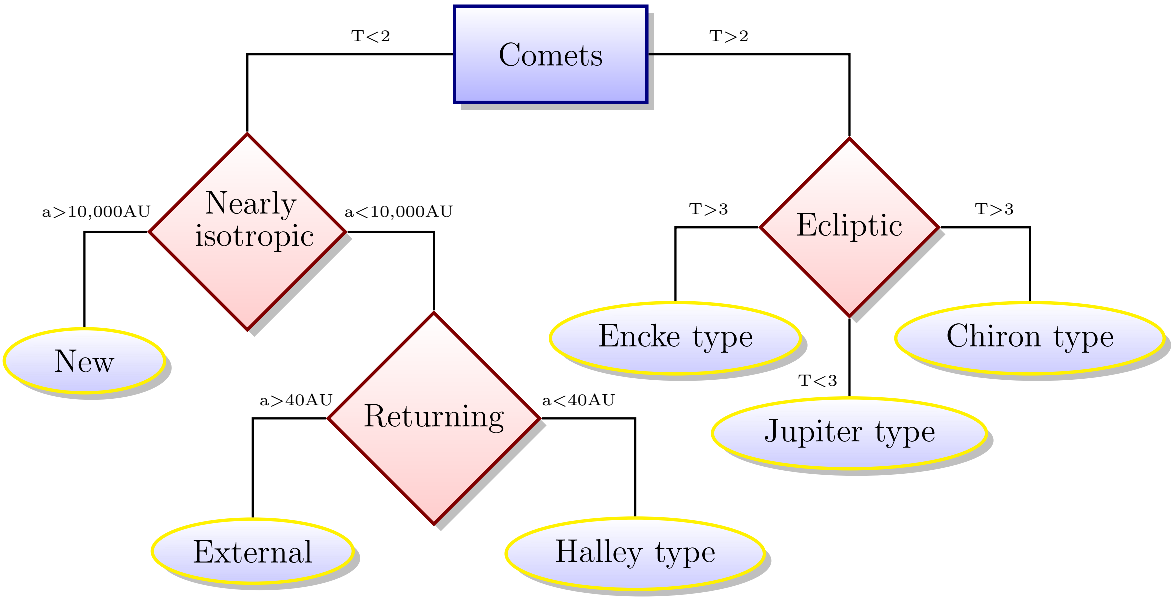

Figure 1.3: The classification of comets based on Tisserad parameter (T).

Table 1.2: List of space missions targeted to study comets.

Spacecraft	Comet name	Encounter date
International Cometary Explorer (ICE)	21P/Giacobini–Zinner	11 September 1985
VEGA 1	1P/Halley	6 March 1986
Suisei	1P/Halley	8 March 1986
VEGA-2	1P/Halley	9 March 1986
Sakigake	1P/Halley	11 March 1986
Giotto	1P/Halley	14 March 1986
ICE	1P/Halley	25 March 1986
Giotto Extended Mission (GEM)	26P/Grigg–Skjellerup	10 July 1992
Deep Space 1	19P/Borrelly	22 September 2001
Stardust	81P/Wild 2	2 January 2004
Deep Impact	9P/Tempel 1	4 July 2005
EPOXI**	103P/Hartley 2	4 November 2010
Stardust-NExT	9P/Temple 1	14 February 2011
Rosetta	67P/Churyumov–Gerasimenko	August 2014*

**EPOXI is an acronym for two other acronyms (Extrasolar Planet Observation and Characterization (EpOCh) and Deep Impact eXtended Investigation (DIXI), *Expected encounter period.

1.2 Physical properties of comets

Comets are the most active objects of our solar system. Though the solid body is a few kilometers in size, comets can create extensive and unique atmospheres in the interplanetary space by ejecting neutral gas and dust into surrounding vacuum during their active period. The space missions that encountered the comets are tabulated in Table 1.2.

The five space missions which explored comet 1P/Halley during 1986 have changed the perspective of cometary science dramatically. These encounters also changed our understanding about the physics of the comets. More recent successful missions, Deep Impact and Stardust-Next that encountered comet 9P/Temple 1 at different locations of its revolution period have supplied new information about the cometary nucleus. The EPOXI (Extra solar Planet Observation and Characterization (EpOCh) and Deep Impact eXtended Investigation (DIXI)) mission targeted to comet 103P/Hartley 2 explored several morphological features of cometary nucleus. The upcoming ESA's Rosetta space mission will encounter comet 67P/Churyumov-Gerasimenko in 2014. This mission is going to land on the cometary nucleus and study various physical properties of the cometary nucleus. Various space missions that encountered comets and corresponding solar activity during the encounter period are plotted in Figure 1.4. Except the Deep Space 1 mission all the cometary missions flybys during low or moderate solar active conditions. The salient physical features of the comets are described below.

1.2.1 Nucleus

Nucleus is the main source for different physical processes occurring in the comets during cometary orbital motion around the Sun. A typical near-Earth comet occupies a few degrees of solid angle in the night sky whereas the source for the total cometary activity is only a maximum of a few tens of kilometers in size. Due to dense blanketing of gas and dust coma it is difficult to observe the cometary nucleus using ground based observations. Till now only five cometary nuclei have been observed directly by space missions. Cometary nuclei observed from different space missions along with their physical dimensions are shown in Figure 1.5. The total active region on comet 1P/Halley nucleus surface is about 10% with average density of about $0.6 - 1$ g cm^{-3}. Different physical properties of cometary nuclei are reviewed by *Lamy et al.* [2004]. During revolution around the Sun the cometary nucleus absorbs most of the incident solar radiation and rest is reflected back. The amount of energy reflected from the surface depends on the albedo of the nucleus which mainly depends on the composition and surface properties. The observed albedo of comet Halley nucleus is around 4% [*Lamy et al.*, 2004]. The absorbed energy increases the temperature of the nucleus and subsequently increase the sublimation rates of the ices. Since ice is a bad conductor of

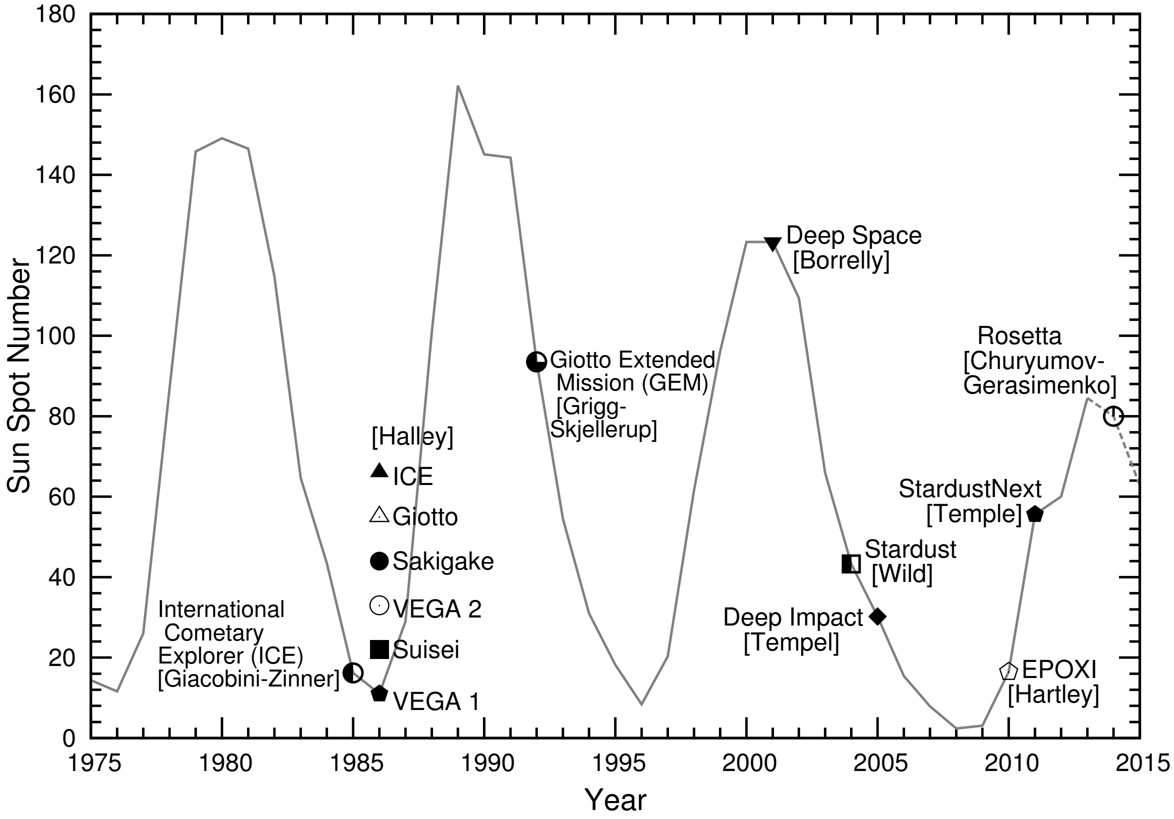

Figure 1.4: Various space missions targeted to comets and the corresponding solar activity.

heat, the penetration of heat is up to a few meters from the surface and also these ices are conglomerated with dust grains which can influence evaporation of volatile components. At a given heliocentric distance the temperature of the cometary nucleus depends on balance between the incoming energy and the radiated energy. The energy balance at the cometary nucleus can be written as

$$\frac{F_{\odot}(1-A_v)}{4\pi r^2}\cos z = (1-A_{IR})\sigma T^4 + Z(T)L(T) \tag{1.1}$$

$F_{\odot}$ is the incident total solar radiation intensity at 1 AU. A_v and A_{IR} are the bond albedo of the nucleus in the visible and infrared region, respectively, and r is heliocentric distance. $Z(T)$ and $L(T)$ represent the vaporization rate of the gas (in molecule cm^2 sec^{-1}) and the latent heat (in ergs molecule^{-1}) for sublimation, respectively. T is the temperature and z is solar zenith angle. The first model for nucleus suggested by *Whipple* [1950]. It was a single, small, and solid body of agglomerated compound of ices and dust and named them as "dirty icy balls". This cometary nucleus model is widely accepted after the observation of 1P/Halley by Halley Multicolor Camera (HMC) onboard Giotto mission. The sublimation temperatures of conglomerated ices are different and sublimation rates changes the composition of coma with heliocentric distance based on the available heat content [*Meech and Svoreň*, 2004].

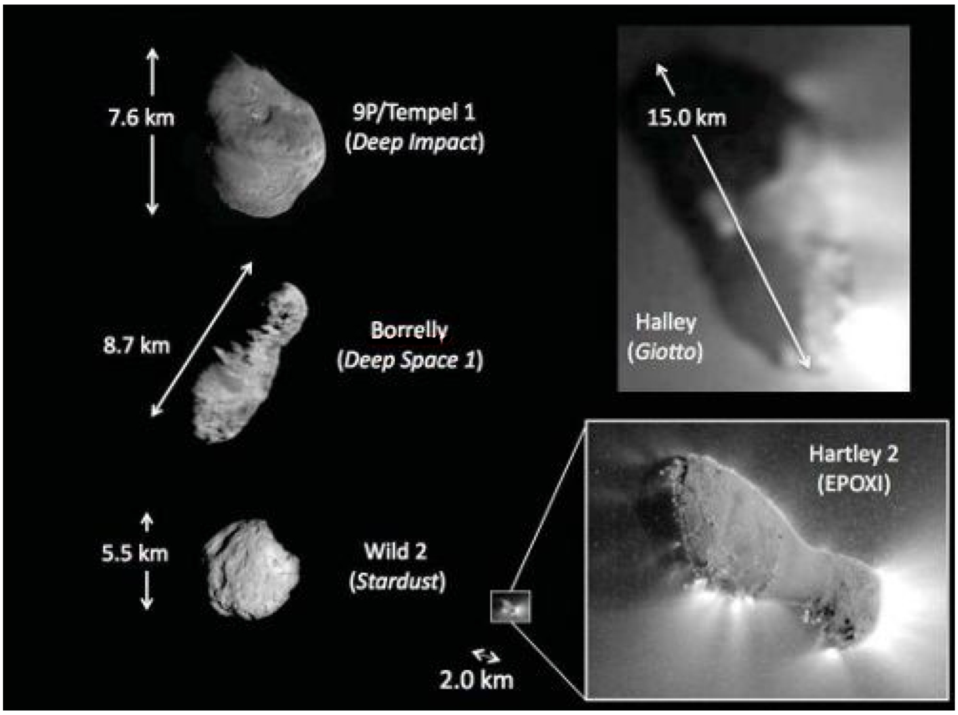

Figure 1.5: The observed cometary nuclei from different space missions and their physical dimensions. Images taken from different space missions presented at the same scale. Credit: Science/AAAS.

There are three sources of energy available for the comets : solar radiation, radioactivity, crystallization. The radioactive source (^{26}Al) is important source when comet is far away from the Sun. As the comet approaches the Sun the solar radiation mainly determines the cometary activity. When comet is around 100 AU from the Sun the amount of heat received is sufficient to sublimate the CO ices (sublimation temperature is 25 K) in the nucleus. Hence CO is the major species in the cometary coma at larger heliocentric distances. When comet approaches around 12 AU, CO_2 ice also sublimates and hence CO and CO_2 become the major species in the cometary coma. When cometary nucleus temperature rises to 90 K (around 5 AU) the amorphous ice changes to crystalline. This phase change is additional source of energy. Around 3 AU the cometary nucleus attains the temperature of 180 K and water ice sublimates, making H_2O as the major species in the cometary coma.

1.2.2 Cometary coma

The sublimation of cometary icy clathrate produces gases which diffuse into space due to their thermal energy acquired by solar heating and also due to large pressure difference. The dust separated from the icy mantle during sublimation process is dragged radially outwards by ejecting gases. The gravitational field of cometary nucleus is weak and can not influence the motion of the gas. Only large dust particles will be attracted by nucleus and forms a fraction to few meters thick layer of dust on the nucleus surface called “Knudsen layer”. The gas molecules perforated through this layer drag dust along with them. The gases and dust diffuse into space and expand spherically from the source of origin to several orders of magnitude distance. This giant dusty gaseous envelope around the nucleus is called as cometary coma. The cometary atmosphere is transient and responds quickly to space environment conditions. Under no gravitational influence and best vacuum, cometary atmosphere is unique environment to study atomic and molecular properties. The gases oozes out from the cometary nucleus surface with a typical velocity of 1 km s^{-1} at 1 AU heliocentric distance.

In a active comet, the species that are produced directly from nucleus due to ice sublimation are called parent species, which collide among themselves and with dust grains. For a typical moderately active comet, the decoupling of collisional interaction between dust and gas occurs at around 100 km from the nucleus. Below 100 km radial distances, the adiabatic expansion and IR cooling of these gases results in decrease in temperature upto <30 K while at larger radial distances the solar UV photodissociation heats the gas faster than the rate at which it cools and increases its temperature. The gas molecules colliding with each other forms a collision-dominated coma in the expanding atmosphere. In planetary atmospheres the height of exobase is defined as the region in which local collisional mean free path becomes equal to atmospheric scale height of that molecule. Similarly, in comets the boundary of the spherical collisional coma is taken as the distance where local mean-free-path is equal to the distance from the center of the nucleus. For a typical comet having a coma with gas production rate of Q (s^{-1}) and expanding with velocity v (~1 km s^{-1}) the radius of collisional zone R_{col}, according to *Whipple and Huebner* [1976], is given by

$$R_{col} = \sigma \frac{Q}{4\pi v} \tag{1.2}$$

where σ is the collisional cross section of water molecule (the dominant species at 1 AU) which is about 3×10^{-15} cm^{-2} and v is the expanding velocity of cometary species in km s^{-1}. For a typically bright comet, like Halley, having gas production rate Q = 10^{29} s^{-1}, the collisional zone is around 20,000 km, whereas in case of a very bright comet, like Hale-Bopp (~10^{30} s^{-1}), it is around 10^5 km. Based on the water molecular collisions the radius of the collisional coma serves as a theoretical boundary to separate the cometary coma into two regions: inner and outer cometary coma.

The solar radiation before reaching the cometary nucleus must pass through an extensive, absorbing, and dusty atmosphere. The radiation reaching the cometary nucleus sublimates the ices. Any change in the dust and/or gas production rates would affect the optical characteristics of the coma and results in change in nucleus ice sublimation rate. A fraction of incident solar UV radiation interacts with the species prevailing in the cometary coma and drives photochemical reactions, like dissociation, ionization, excitation, dissociative ionization and dissociative excitation. The higher

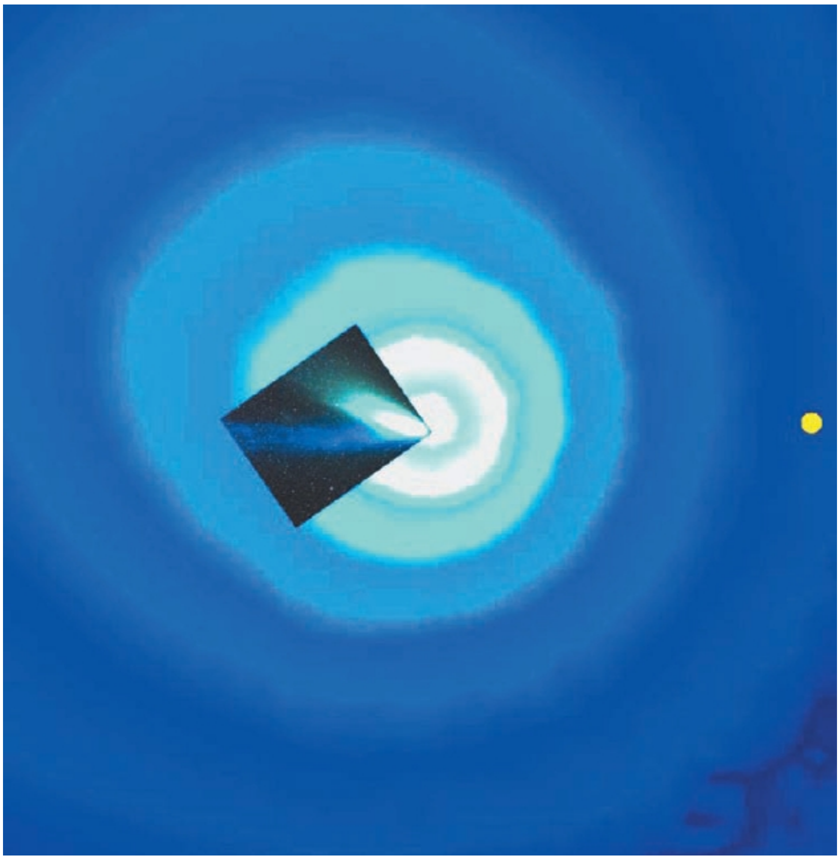

Figure 1.6: The SOHO SWAN hydrogen Ly-α image of comet Hale-Bopp's coma during its perihelion 1 April 1997 along with the visible image showing dust and plasma tails. The image is approximately 40^0 on a side and small yellow disk shows the angular size of the Sun and solar direction. Image credits to *Combi et al.* [2000].

energy photons in EUV solar radiation ionize the cometary species and produce energetic photoelectrons, which further interact with the ambient cometary species and play an important role in the photochemistry. At large radial distances the interaction of solar radiation turns the neutral cometary molecular coma into atomic coma with products such as O, H, C, and N. The Hydrogen cometary coma of Hale-Bopp, which is largest atomic coma, is imaged by SOHO SWAN instrument, shown in Figure 1.6, occupies a sphere of radius around 10^7 km in space. Hence, based on the composition the cometary coma can be divided into molecular coma and atomic coma. In the outer coma the chemical lifetime of each species depends on the flux of solar wind, solar photons flux and the interacting cross sectional area offered by the species. The species having smaller lifetime can prevail in the space to a few hundreds to thousands kilometer distance in the coma, whereas the species having larger lifetime can spread to several orders of magnitude than the size of nucleus. The average distance traveled by a cometary species is called scale length which is a product of initial velocity of species and chemical lifetime of the species. Since atomic scale lengths are larger than that of molecules the outer coma is mostly dominated by atomic species. As the comet moves in the orbit, the amount of solar photon flux changes, which results in the change in the scale lengths of the cometary species.

The composition of cometary coma changes with the nature of cometary nucleus and also with the heliocentric distance. The observed emission spectra of several comets at 1 AU are very similar except the changes in peak intensity. The typical composition of inner cometary coma at 1 AU is ∼80% H_2O, ∼15% CO, and ∼5% CO_2 as major species and remaining all other species such as H_2CO, CH_3OH, and HCO are less than 1% [*Rodgers et al.*, 2004; *Combi et al.*, 2004].

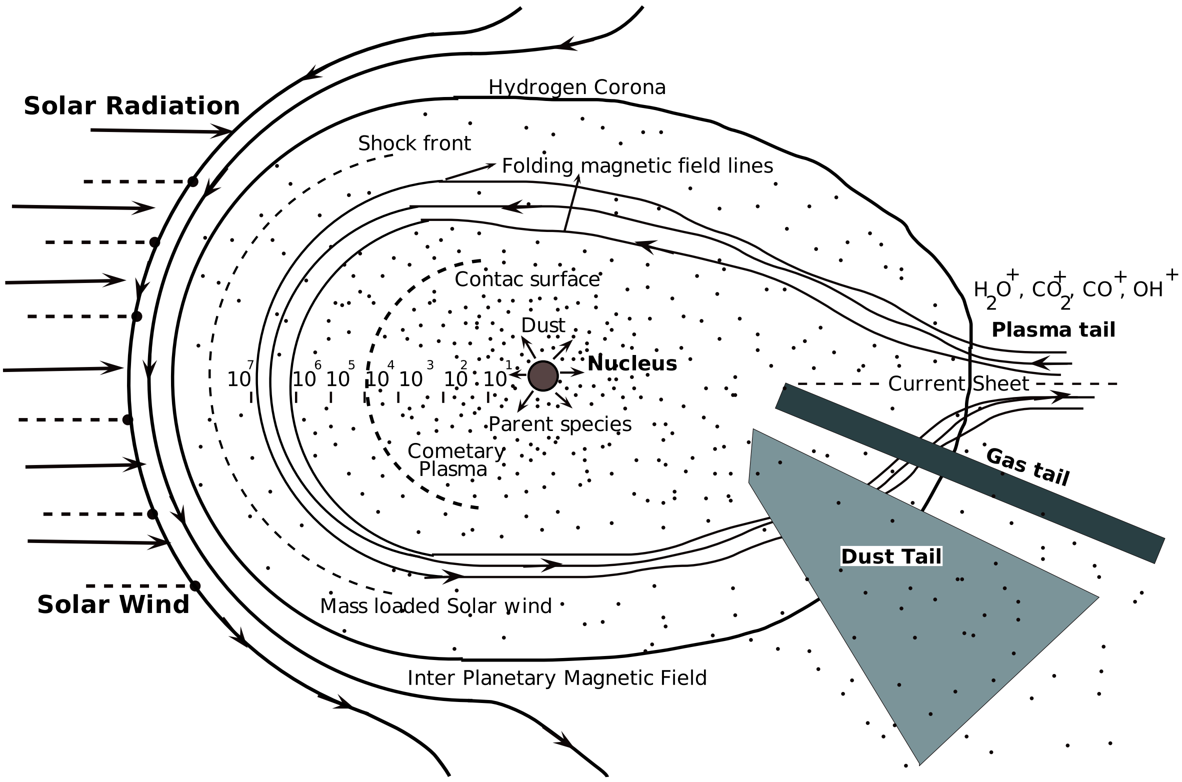

Figure 1.7: Schematic diagram representing different physical processes occurs in the cometary coma at 1 AU and having minimum gas production rate of 10^{26} s^{-1}. In this figure the location of the Sun is on left hand side.

The UV photons ionize cometary species and produce cometary ionosphere on scales of around 10^3–10^4 km. Besides photons, Sun also emitting charged particle, called solar wind, which are blowing into the interplanetary space. The solar wind, carries the interplanetary magnetic field, interacts with the cometary coma. Various physical processes occurs at different cometocentric radial distances are shown in Figure 1.7. When the solar wind flows from day side of outer cometary coma, the ions feel the interplanetary magnetic field and they are picked up by the solar wind. This process is called mass loading. Solar wind can not assimilate more number of cometary ions during its flow. When solar wind is loaded with heavier cometary species, the speed of solar wind reduces drastically to subsonic level due to conservation of momentum which results in the bow shock formation. For a typical active comet the distance of bow shock occurs at around 10^7 km from the cometary nucleus. The mass loaded solar wind further moves towards the cometary nucleus and at 10^4 km distance the incoming ram pressure of the mass-loaded solar wind is balanced by kinetic pressure of cometary ions. The cometary neutrals and solar wind separated through a boundary called contact surface, which is typically forms at around 10^4 km, below which the solar radiation created cometary ions exits and above which the mass loaded solar wind flows. Above the contact surface the interplanetary magnetic field piles up into magnetic barrier and forms a diamagnetic cavity. The interplanetary magnetic field lines drapes around the diamagnetic cavity and ions will be directed towards night side of the comet forming the ion tail. More information about the interaction of solar wind with cometary coma can be found in *Ip* [2004].

Figure 1.8: Comet Hale-Bopp is a long period comet reached its last perihelion on 1 April 1997 around 0.3 AU from the Sun. It was one of the brightest comets seen in recent times. It had a highly elongated orbit with high inclination, almost perpendicular to the ecliptic. The orbital period as it approached perihelion was 4200 years. The dust (White) and ion tails (Blue) of comet Hale-Bopp are shown in this Figure and position of the Sun is on left bottom side. Image courtesy: John Laborde.

1.2.3 Tails

The cometary tails are the extended cometary coma due to interaction of solar radiation and solar wind with cometary species. The solar radiation exerts a constant pressure on the dust grains of typical size 1 μm and drag them along the line joining Sun-comet. Due to inertia and cometary motion these dust particles follow a curved path. The trail of these dust particles appears as a tail. Due to scattering of visible solar photons by dust grains these dust tails appears generally in white colour.

The solar wind interaction with cometary plasma manifests the ion tail which is very dynamic compared to dust tail. The solar wind which is blowing towards the comet assimilates the cold cometary plasma. The cometary ions experience the Lorentz force due to incoming interplanetary magnetic field which is frozen in solar wind and follow the draped magnetic field lines resulting the formation of ion tail [see *Ip*, 2004, and references there in]. The ion tails appears blue in color due to CO^+ ion emission. Ion tails are always straight and pointing away from the Sun. Since comets can have orbit above and below the ecliptic plane the observed ion tails can be used to understand conditions of the solar wind at different solar latitudes, hence comets are considered as natural probes of solar wind [*Lisse et al.*, 2004]. The spectacular dust and ion tails of comet Hale-Bopp are shown in Figure 1.8.

1.3 An overview of spectroscopic emissions from comets

The light coming from the comets is the key that provide information about comets through remote observations. The observation of comets in different spectral region gives the information about composition and physical processes occurring in the comets. Using rocket, ground, and space-based optical instruments the comets have been observed in different spectral regimes. Comets provides an astrophysical laboratory to study the atomic and molecular processes in the best vacuum environment. In-situ observations are concerned to a particular comet, whereas there are many remote observations which are useful to understand the global picture of the comets in different spectral regions using ground-based and space-based optical instruments. Using the observed intensities of emissions, the relative abundances of species have been derived in comets. However, the derived abundances are based on certain assumptions. For the ground-based observatories terrestrial atmosphere is a strong absorbing medium for the ultraviolet and infrared photons coming from the comets. Recent advances in the optical instruments have made possible for the observation of comets in the infrared region from ground based observatories. Since comets are moving, there is a Doppler shift between the terrestrial and cometary emission lines. Using very high resolution optical instruments the terrestrial emission can be separated from the cometary emission.

1.3.1 Ultraviolet emissions

The cosmically abundant atoms H, C, N, O, and S do have their principle transition in vacuum ultraviolet region which can be determined from spectroscopic observations. The ultraviolet and visible spectrum of comet 103P/Hartley 2 is shown in Figure 1.9. H

Table 1.3: Principle emissions of atoms, molecules and ions observed in cometary ultraviolet and visible spectra.

Species	Transition	Wavelength (Å)	System name
		Molecules	
OH	$A^2\Sigma^+$–$X^2\Pi_i$ (0,0)	3080	
CN	$B^2\Sigma^+$–$X^2\Sigma^+$ (0,0)	3883	Violet
	$A^2\Pi$–$X^2\Sigma^+$ (2,0)	7873	Red
C_2	$d^3\Pi_g$–$a^3\Pi_u$ (0,0)	5165	Swan
	$A^1\Pi_u$–$X^1\Sigma_g^+$ (3,0)	7715	Philips
	$D^1\Sigma_u^+$–$X^1\Sigma_g^+$ (0,0)	2313	Mulliken
CH	$A^2\Delta$–$X^2\Pi$ (0,0)	4314	
	$B^2\Sigma^-$–$X^2\Pi$ (0,0)	3871, 3889	
CS	$A^1\Pi$–$X^1\Sigma^+$ (0,0)	2576	
NH	$A^3\Pi_i$–$X^3\Sigma^-$ (0,0)	3360	
CO	$A^1\Pi$–$X^1\Sigma$	1200–2800	Fourth positive
	$a^3\Pi$–$X^1\Sigma$	1900–2700	Cameron band
	$E^1\Pi$–$X^1\Sigma^+$ (0,0)	1076	Hopfield Brige
	$C^1\Sigma^+$–$X^1\Sigma^+$ (0,0)	1087	Hopfield Brige
	$B^1\Sigma^+$–$X^1\Sigma^+$ (0,0)	1150	Hopfield Brige
S_2	$B^3\Sigma_u$–$X^3\Sigma_g$	2800–3050	
H_2	$B^1\Sigma^1$–$X^1\Sigma_g^+$ (6,1) & (6,3)	1071.6 & 1166.8	
NH_2	$\tilde{A}^2A_1$–$\tilde{X}^2B_1$	4500–7350	
C_3	$\tilde{A}^1\Pi_u$–$X^1\Sigma_g^+$	3440–4100	Comet Head group
		Atoms	
H I	$^2P^0$–^2S	1216	
O I	$^3S^0$–^3P	1302-1306	
O I ^1D	^1D–^3P	6300, 6364	Red-doublet
O I ^1S	^1S–^3P	2972	
O I ^1S	^1S–^1D	5577	Green
C I	$^3D^0$–^3P	1561	
	$^3P^0$–^3P	1657	
N I	^4P–$^4S^0$	1134	
	^4P–$^4S^0$	1200	
S I	^3P–$^3S^0$	1807-1826	
		Ions	
CO^+	$B^2\Sigma^+$–$X^2\Sigma^+$ (0,0)	2190	First Negative
	$A^2\Pi$–$X^2\Sigma^+$ (2,0)	4273	Comet Tail
CH^+	$A^1\Pi$–$X^1\Sigma^+$ (0,0)	4225, 4237	Douglas-Herzberg
OH^+	$A^3\Pi$–$X^3\Sigma^-$ (0,0)	3565	
N_2^+	$B^2\Sigma^+$–$X\Sigma^+$ (0,0)	3914	First Negative
CO_2^+	$\tilde{B}^2\Sigma_u$–$\tilde{X}^2\Pi_g$	2883, 2896	
	$\tilde{A}^2\Pi_u$–$\tilde{X}^2\Pi_g$	2800–5000	
H_2O^+	$\tilde{A}^2A_1$–$\tilde{X}^2B_1$	4270–7540	

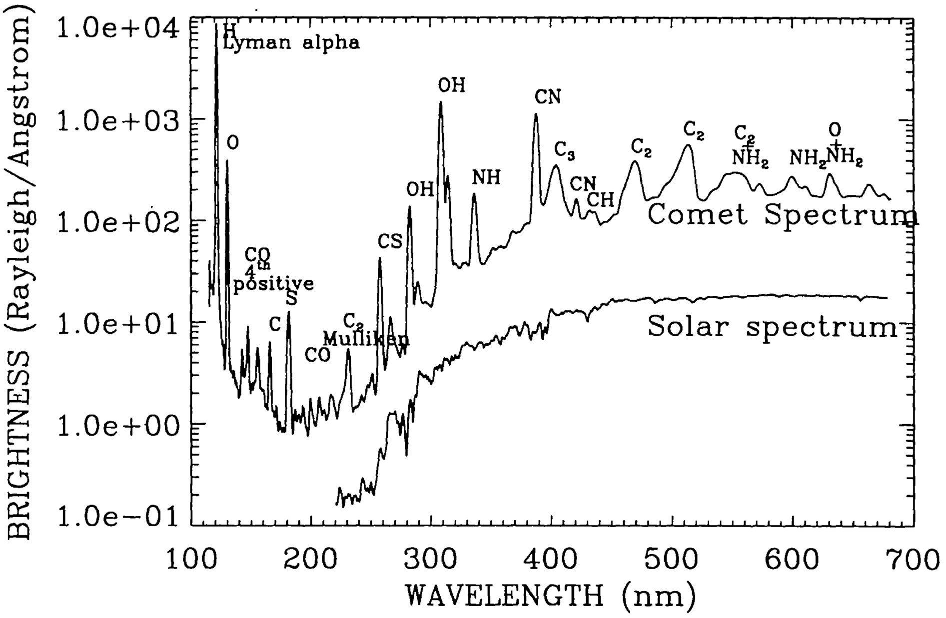

Figure 1.9: The UV and optical spectrum of comet 103P/Hartley 2 obtained using Field object spectrograph on Hubble space telescope [*Weaver and Feldman*, 1992].

and OH emissions are strongest in the cometary ultraviolet spectrum due to their large abundances and fluorescent scattering of solar photons. Studying comets in ultraviolet region provides information about the solar radiation deposition in the cometary coma. The space-based spectroscopic observations of comets in the UV region provide the information about composition, abundance, and spatial distribution of neutral species in the cometary coma [e.g., *Feldman et al.*, 2004].

Ultraviolet observations of comets have been made by using various sounding rockets, orbiting astronomical observatories like IUE, HST, and Far Ultraviolet Spectroscopic Explorer (FUSE). The slit width of the space based observatories are small to cover the entire cometary coma of a typical comet at 1 AU. The entire cometary coma can be covered either by using long slit observations or by repositioning the telescope to image different directions of cometary coma or both. The important UV emissions of cometary coma are tabulated in Table 1.3

1.3.2 Visible emissions

Cometary dust grains scatter most of the solar visible radiation which makes comets as spectacular objects in the night sky for the naked eye observers. Several atomic, molecular, and ionic emissions are also present in the visible cometary spectrum. To study morphological and compositional studies of comets and to isolate the light reflected by dust grain from the emissions by gas species narrow band filters have been used by observers [*Schleicher and Farnham*, 2004].

Mainly there are five important neutral species, viz., OH, NH, CN, C_3 and C_2, which produces emissions in the visible region [*Feldman et al.*, 2004]. None of these are assumed to exist in the cometary nucleus. They are mainly produced due to photodissociation of short-lived parent species which emanate during sublimation of cometary ices or by photochemistry. Emissions from H_2O^+ and CO^+ have also been observed in the visible cometary coma. There are other emissions, like NH_2 and atomic oxygen (5577, 6300, and 6364 Å), present in the visible cometary spectrum. Several ground-based optical telescopes have been used to study the visible emissions from comets.

1.3.3 X-ray, Infrared, and Radio wave emissions

The first detection of X-ray emissions in comet Hyakutake by satellite ROSAT [*Lisse et al.*, 1996] was a big surprise. Normally, X-ray emissions are expected from very hot plasma environments, like stars, supernova remnants, accretion disks around neutron stars, and black holes, which possess several million degree hot gaseous environments. After several observations in different comets it is well established that comets emit X-rays continuously [*Lisse et al.*, 2004]. Several emission mechanisms have been proposed to explain the observed X-rays from the cold cometary coma. The charge exchange between highly ionized solar wind ions (like, O^{5+}, O^{6+}, O^{7+}, C^{4+}, O^{5+}, N^{4+}, N^{5+}, He^+, and Mg^{7+}) and cometary neutrals is the accepted mechanism which explain the different features of the observed cometary X-ray spectra [see reviews of *Krasnopolsky et al.*, 2004; *Bhardwaj et al.*, 2007; *Bodewits et al.*, 2008; *Dennerl et al.*, 2012; *Lisse et al.*, 2004]. The peak emission of X-rays is found on sun-ward side of cometary coma. The temporal variation in the X-ray emission intensities is useful in understanding the solar wind composition variability using comets as the probes.

H_2O and CO_2 molecules can be observed directly in the infrared and radio wavelengths of electromagnetic spectrum. Earth's atmosphere absorbs these cometary emissions strongly and it is difficult to separate the faint doppler shifted cometary emissions from terrestrial emissions. But the recent advances in near-infrared ($\sim$1–5 μm) spectroscopic instruments have made direct detection of H_2O possible from ground based observatories [*Dello Russo et al.*, 2000]. The detection of several molecules in infrared wavelength by various instruments in different comets have been reviewed by *Bockelée-Morvan et al.* [2004]. The main excitation mechanism for infrared emissions is resonance fluorescence by solar photons. The infrared emissions of parent molecules are optical thick in the inner cometary coma, hence careful treatment of radiative transfer modelling is required to convert the observed column densities to production rates. The OH 18-cm emission line is an important cometary emission feature in sub-millimeter observations. Several new molecules have been found in comets Hyakutake and Hale-Bopp at radio wavelengths. A review of infrared and sub-millimeter observations is presented in *Bockelée-Morvan et al.* [2004] and *Feldman et al.* [2004].

1.3.4 Modelling studies of cometary emissions

Observing different spectroscopic emissions is important to understand composition and spatial distribution of cometary species. Modelling of these emissions is the only way to study the underlying physical and chemical processes which are governing these emissions. There are several atomic and molecular emissions in the ultraviolet and visible cometary spectra as shown in Figure 1.9. Most of the emissions in the ultraviolet and visible spectrum are due to resonance fluorescence of solar photons by atoms, molecules and ions in the cometary coma. In visible region [OI] forbidden emissions at 5577, 6300, 6364 Å are the only known atomic emissions. Several atomic emissions like H Ly-α at 1216 Å, CI 1356 and 1931 Å, SI 1807 Å, and OI 1304, 2972 Å have been observed in ultraviolet spectrum.

In order to model these emissions the knowledge about the distribution of neutral species in the coma is an essential requirement. Several models have been developed to study the spatial distribution of cometary species considering various physical and chemical processes [eg., some of the earlier models are *Whipple*, 1950; *Oppenheimer*, 1975; *Giguere and Huebner*, 1978; *Huebner and Giguere*, 1980; *Mitchell et al.*, 1981; *Biermann et al.*, 1982]. But most of these models had many simplified assumptions, like constant gas temperature and expansion velocity. The number density in the inner coma is large enough that the gaseous motion can be described by fluid dynamics. Cometary coma is a mixture of different fluids containing various species, like neutrals, ions, electrons, and dust grains of different sizes. The gas coma interacts with the entrained dust and decelerates the outflowing gas speed. *Marconi and Mendis* [1983] have shown that the gas velocity reduces to subsonic speed due to dust and gas drag using a hydrodynamic model.

At larger radial distances in the coma since hardly collisions occurs the fluid description of coma is unrealistic [*Rodgers et al.*, 2004]. The number densities of secondary products and their expansion velocities are linked to the photochemical lifetimes of parent molecules and the production mechanisms. Non-radial ejection of daughter species is also possible in the outer cometary coma. *Haser* [1957] modelled number densities of secondary products does not account the former mentioned processes. *Festou* [1981] and *Combi and Delsemme* [1980] addressed this problem in two different ways. *Festou* [1981] developed vectorial model which is a numerical approach to solve the density and column density distribution of parent and daughter species. *Combi and Delsemme* [1980] developed a model based on Monte Carlo technique to simulate the expansion velocities of the cometary species. The Monte Carlo models can be applicable directly to general cometary problems, like variable outflow velocity, asymmetric coma, and radiation pressure accelerating daughter species.

The earlier photochemical models mainly considered only photon initiated reactions and suggested that the inner cometary coma is opaque to solar UV photons and also concluded that ion-molecular reactions are important in the inner coma. Later models included additional reactions, like electron impact ionization, dissociation, excitation, recombination of ions and studied different energy sources in the inner coma [*Schmidt et al.*, 1988; *Cravens and Green*, 1978; *Ip*, 1985; *Boice et al.*, 1986; *Körösmezey et al.*, 1987; *Bhardwaj et al.*, 1990, 1996; *Bhardwaj*, 1999, 2003; *Weaver et al.*, 1994; *Haider and Bhardwaj*, 2005].

Several physics based models like *Gombosi et al.* [1986] also have been developed to explain the conditions of cometary coma for different gas production rate comets using conservation laws of mass continuity, momentum, and energy. The first fully kinetic model for the water-dominated cometary coma that included a fairly complete description of the physics was presented by *Hodges* [1990]. A very useful application of Direct simulation of Monte Carlo (DSMC) to an expanding comet atmosphere was to understand the time-dependent effects of the dynamics of the expanding atmosphere of Comet 1P/Halley [*Combi*, 1996]. *Biver et al.* [1999] found that the coma of Comet Hale-Bopp underwent a transition from CO-dominated to H_2O-dominated at a heliocentric distance of about 3 AU both before and after perihelion. *Ip* [1983] computed a photochemical/hydrodynamic model for a CO-dominated comet at a heliocentric distance of 1 AU. More details of modelling and photochemistry are presented in the extensive reviews of *Combi et al.* [2004] and *Rodgers et al.* [2004]. The photochemistry of different dissociative products in H_2O-dominated cometary coma has been studied by several investigators [*Huebner and Carpenter*, 1979; *Oppenheimer and Downey*, 1980; *Festou and Feldman*, 1981; *Festou*, 1981; *Huebner*, 1985; *Krankowsky et al.*, 1986; *Allen et al.*, 1987; *Crovisier*, 1989; *Huebner et al.*, 1992; *Wu and Chen*, 1993; *Cochran and Schleicher*, 1993; *Budzien et al.*, 1994].

The five space missions that encountered comet 1P/Halley have changed significantly the perspective of cometary science. The measurements of dust grains in comet Halley encounter shown that significant fraction of elementary dust composition consist of organic matter (CHON) [*Kissel et al.*, 1986]. A model with a variety of complex reactions have been developed by *Huebner and Boice* [1997]. Models have also been developed to account for extended sources of CO and H_2CO following the breakup of polyoxymethylene (POM) molecules [*Boice et al.*, 1990; *Cottin et al.*, 2001]. The conditions in the cometary coma are explained by developing various hydrodynamic-chemical models by different workers [*Huebner*, 1985; *Körösmezey et al.*, 1987; *Wegmann et al.*, 1987; *Rodgers and Charnley*, 2002].

The solar wind plays a minor role in the destruction of water compared to photochemistry, but plays an important role in the ion chemistry of the coma, which also involves many other atomic and molecular ions [*Häberli et al.*, 1996]. During passage of cometary coma of Halley, the plasma spectrometer PLASMAG on board VEGA 2 spacecraft registered a sudden increase in solar wind plasma density [*Gringauz et al.*, 1986]. At a cometocentric distance of ∼40,000 km highly enhanced suprathermal (keV) electrons have been recorded in VEGA 2 data. *Mendis* [1987] proposed that the high energy portion of the electron spectrum is due to cometary aurora which is similar to terrestrial-type auroral spectra in the inverted V-events. *Mendis* [1987] also suggested that due to draped interplanetary magnetic field around the cometary coma, and under disturbed solar wind condition, the solar wind electrons originating from comet tail accelerate towards day side and precipitate in the cometary coma. Using *Green et al.* [1985] three-dimensional yield spectra function, *Bhardwaj et al.* [1990] degraded the solar wind electron flux measured by PLASMAG at 25 eV, 100 eV, 2 keV, and 5 keV in the coma. The degraded solar wind electrons in the cometary are called as auroral electrons. Several studies have shown that these auroral electrons are the potential energy sources for dissociating, ionizing, and exciting the cometary species [*Bhardwaj et al.*, 1990; *Haider et al.*, 1993; *Bhardwaj et al.*, 1996; *Haider and Bhardwaj*, 1997, 2005].

1.4 Motivation of this study

Theoretical modelling of ultraviolet and visible emissions is essential to estimate the abundances of species in the cometary coma and subsequently the composition of the nucleus. As discussed in the previous section several excitation mechanisms have been proposed. A quantitative study is required to study the role of each mechanism in producing different emissions in cometary spectrum. In this thesis CO Cameron band and atomic oxygen visible forbidden emissions have been studied by accounting for important excitation mechanisms and the contribution of each production process is quantified. Quantification of different production processes in producing these emissions is the main objective the current study. In this study updated atomic and molecular parameters, viz., photon and electron impact cross sections, Einstein coefficients, Frank-Condon factors of different species have been used.

1.5 Outline of thesis

In this thesis a coupled-chemistry model is developed to study CO Cameron band emission and atomic oxygen forbidden visible emissions on various comets having different gas production rates and abundances. This model is applied on comets in which these emissions are observed and results are compared with the observations. The work presented in this thesis is important to understand the photochemistry of cometary coma that govern CO Cameron band and atomic oxygen visible emission lines (viz., 5577, 2972, 6300, and 6364 Å) and for better interpretation of composition of comets and have implications for different observations of comets using ground and space based instruments. The organization of thesis is as follows.

The model calculations and input parameters are described in Chapter 2. In this work the model atmosphere is calculated using from Haser's formula by inputing gas production rates, relative abundances, and gas expansion velocities from different observations. The comet dependent inputs are presented in the appropriate sections in the following chapters. Essentially the major composition of cometary coma is H_2O, CO_2 and CO, so these gases only are considered in the model atmosphere. The chemical lifetimes of these species and production of various dissociative products are calculated using solar flux taken from two popular solar models, viz., EUV flux model for Aeronomic Calculation (EUVAC) and SOLAR2000 (S2K). The photon and electron impact cross sections are taken from different experimental studies to incorporate the photon and photoelectron reactions. The attenuation of solar photons in cometary atmosphere is calculated using Lambert-Beer's law whereas the UV-EUV generated photoelectrons are degraded using Analytical Yield Spectrum (AYS) approach. Several ion-neutral chemical reactions are also incorporated in the model. The photochemical processes considered in the model are discussed in subsequent chapters.

- **Chapter 3: CO Cameron band emission.**
  In Chapter 3 a model is developed to understand the photochemistry of CO Cameron band emission in comets and it is applied to comets 1P/Halley and 103P/Hartley 2. The major production and loss processes for the exited state CO($a^3\Pi$) of CO Cameron band emission are discussed. The calculations suggest that photoelectron impact excitation is more important process of CO($a^3\Pi$) production than the photodissociation of CO_2. Since this emission is shown to be controlled mainly by electron impact reactions it is suggested that the observed CO Cameron band emission intensity can be used to calculated the photoelectron density rather than CO_2 relative abundance in comets.

- **Chapter 4: Atomic oxygen green and red-doublet emissions at heliocentric distance of 1 AU.**
  A coupled chemistry model developed to study the forbidden atomic oxygen green (5577 Å) and red-doublet (6300 & 6364 Å) emissions is presented in Chapter 4. The red-doublet emission has been used to quantify the H_2O production rate while intensity ratio of green and red-doublet emissions (G/R ratio) is used to examine whether these forbidden emissions originated from H_2O and/or CO_2 and CO. In several comets, the observations made near heliocentric distance of 1 AU found the G/R ratio value of 0.1 which has been used as an indicator to confirm H_2O as the parent source for these emissions by referring to the theoretical calculations of *Festou and Feldman* [1981]. The higher observed value of the G/R ratio is ascribed to larger relative abundances of CO_2 and CO. We applied our model to two different comets viz., C/1996 B2 Hyakutake and C/1995 O1 Hale-Bopp, which

have different H_2O production rates and observed nearly at 1 AU. It is found that besides CO_2 relative abundance, the G/R ratio depends on the observed projected area on the comet which depends on slit-dimension used for the observation and geocentric distance of the comet. The model calculations suggest that the G/R ratio value of 0.1 can not be used as a benchmark to confirm H_2O as the parent source for forbidden atomic oxygen visible emissions.

- **Chapter 5: Atomic oxygen green and red-doublet emissions at larger heliocentric distances.**
  At larger heliocentric distances (>2 AU), due to low sublimation temperatures the relative abundances of CO_2 and CO starts increasing. The forbidden atomic oxygen emission lines are observed on several comets at larger (2 to 5 AU) heliocentric distances. We present our model calculations on six comets (viz., C/2006 W3 Christensen, C/2007 Q3 Siding Spring, C/2002 K4 (LINEAR), 116P/Wild 4, C/2009 P1 (Garradd), C/2001 Q4 (NEAT)) in Chapter 5 where the G/R ratio, and green and red-doublet emission line widths are observed at heliocentric distances of 2 to 4 AU. Our study suggest that the photodissociation of CO does not have any role in producing green and red-doublet emissions and consequently on the G/R ratio. The photodissociation of CO_2 produces the $O(^1S)$ atoms with larger kinetic energy which manifests in the green line being wider than the red-doublet emissions. We have shown that the collisional quenching can alter the G/R ratio value by an order of magnitude whereas the effect of CO_2 relative abundance is smaller. The model calculations suggest that the observed G/R ratio can be used to probe CO_2 relative abundances provided the cometary coma is observed over a large projected distances. If a comet has equal abundances of CO_2 and H_2O, then the red-doublet emission is significantly ($\sim$50%) controlled by CO_2 photodissociation and thus the G/R ratio is not suitable to estimate CO_2 relative abundance.

- **Chapter 6: Summary, limitations, and Future scope**
  The summary, conclusion and future scope of the present work is discussed in Chapter 6. The limitations of the model is also presented in this chapter. The model developed in this thesis work can provide a quantitative information about different physical and chemical processes causing the emissions in the inner coma which can be used to interpret the composition of various comets.

Chapter 2

Description of model and input parameters

Contents

2.1 Introduction **24**

2.2 Model **24**

2.2.1 Photoattenuation 25

2.2.2 Electron degradation: Analytical yield spectrum approach . . 26

2.2.3 Coupled Chemistry of gas phase reactions 28

2.3 Input parameters for model **29**

2.4 Solar ultraviolet radiation flux **29**

2.4.1 EUVAC model 30

2.4.2 SOLAR2000 (S2K) model 30

2.5 Cometary coma **30**

2.5.1 Haser's model 31

2.6 Photon impact cross sections **32**

2.6.1 H_2O and OH 32

2.6.2 CO_2 35

2.6.3 CO 36

2.7 Electron impact cross sections **37**

2.7.1 H_2O 38

2.7.2 CO_2 and CO 38

2.8 Dissociative recombination of ions **39**

2.8.1 H_3O^+ and H_2O^+ 40

2.8.2 CO_2^+ and CO^+ 42

2.9 Summary **42**

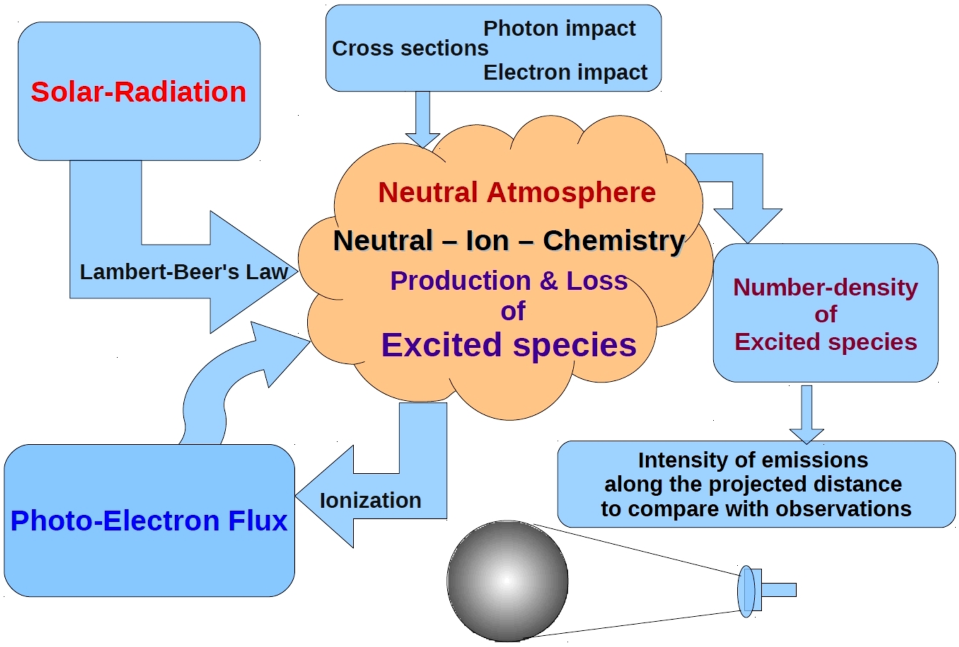

Figure 2.1: The schematic representation of model calculation.

2.1 Introduction

Modelling studies are essential to study various physical and chemical processes involved in producing different emissions in the cometary coma. I developed a model to quantify contributions of various physical processes that governs the intensities of CO Cameron band and atomic oxygen visible emissions on different comets and compared with the observations.

2.2 Model

This is a photochemical model that accounts for a network of reactions, like production and loss processes of different excited and ionized species in the coma. The main energy sources (like UV-EUV photons and photoelectrons) and potential sinks (like collisions and radiative decay) that govern emission intensities are accounted. All important collisional processes that determine the number densities of the cometary species are coupled with different production and loss processes by solving one dimensional continuity equation. The schematic representation of the model is presented in Figure 2.1. First I discuss the attenuation of UV-EUV photons in cometary coma followed by generation of photoelectrons flux. I also explain the production and destruction mechanisms of ions and excited species that are accounted in the cometary coma to calculate the net number density profiles of different species. The calculated number density profiles of these excited species are used to calculate emission profiles. The emission rate profiles are integrated along the line of sight to calculate surface brightness over the observed projected field of view.

2.2.1 Photoattenuation

The attenuation of photons in the cometary atmosphere is calculated using Lambert-Beer law and the attenuated solar flux $I(r,\lambda)$ of wavelength λ at a cometocentric distance r is

$$I(r,\lambda) = I(\infty,\lambda)\ exp[-\tau(r,\theta,\lambda)] \tag{2.1}$$

Here $I(\infty,\lambda)$ is unattenuated solar UV photon flux of wavelength λ at the top of the atmosphere and $\tau(r,\theta,\lambda)$ is the optical depth of the medium at cometocentric distance r, for solar zenith angle θ, and for wavelength λ. The optical depth of the medium is calculated using the following equation.

$$\tau(r,\theta,\lambda) = \sum_i \sigma_i^A(\lambda) \int_r^\infty n_i(r') f(r',\theta) dr' \tag{2.2}$$

Here $\sigma_i^A(\lambda)$ is the absorption cross section at wavelength λ, and $n_i(r')$ is the neutral number density of ith species at r' radial distance. The value of function $f(r',\theta)$ is given by *Green and Martin* [1966] as

$$f(r',\theta) = \frac{1}{\left[1 - \left(\frac{R+r}{R+r'}\right)^2 sin^2\theta\right]^{1/2}} \tag{2.3}$$

Here R is the radius of the nucleus of the comet which depends on the comet. The integration of above equation gives
for $\theta \leq 90°$,

$$\tau = \sigma\ n(d)\ d\ \frac{1}{sin\theta}\left(\frac{\pi}{2} - cos^{-1} sin\theta\right) \tag{2.4}$$

and for $\theta > 90°$,

$$\tau = \sigma\ n(d)\ d\ \frac{1}{sin\theta}\left(\frac{\pi}{2} + cos^{-1} sin\theta\right) \tag{2.5}$$

where d = R + r.

The primary photoelectron production rate $Q(E,r,\theta)$ having energy E at radial distance r and for solar zenith angle θ is calculated by degrading solar radiation in the neutral atmosphere using

$$Q(E,r,\theta) = \sum_i \int_\lambda n_i(r)\ \sigma_i^I(\lambda)\ \ [I_\infty(\lambda)\ exp(-\tau(r,\theta,\lambda))]\ \ d\lambda \tag{2.6}$$

Here $\sigma_i^I(\lambda)$ is ionization cross section of the i^{th} species at the wavelength λ, $n_i(r)$ is its neutral gas density and $\tau(r,\theta,\lambda)$ is the optical depth of the medium at a solar zenith angle θ. All calculations are done at solar zenith angle θ of 0^0. The calculated photoelectron production rate for different gas production rates is shown in Figure 2.2.

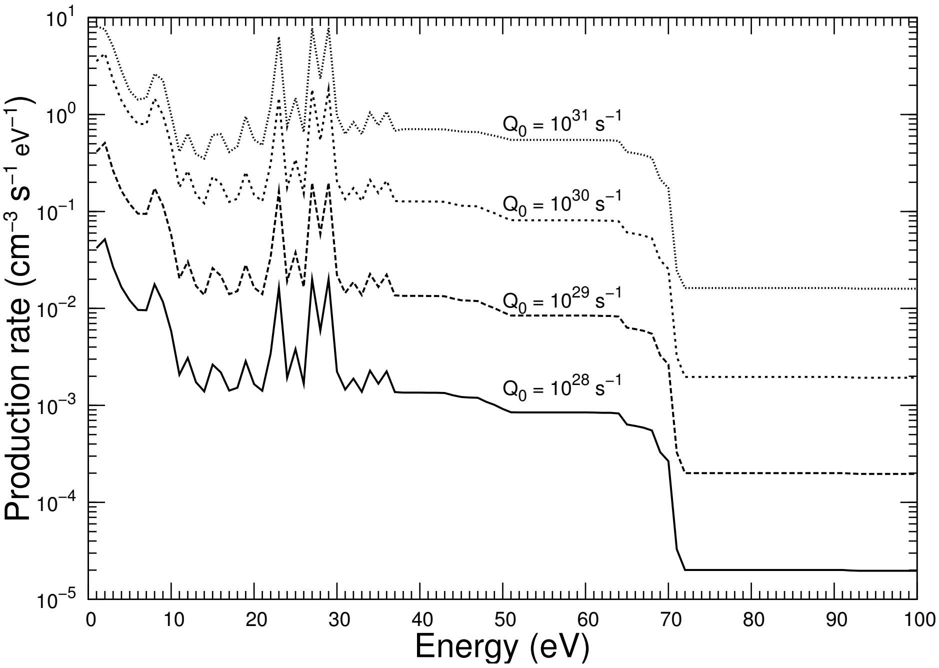

Figure 2.2: The calculated photoelectron production rate at 1000 km cometocentric distance for different gas production rate comets.

2.2.2 Electron degradation: Analytical yield spectrum approach

The solar EUV radiation ionizes the cometary species and produces electrons of various energies which are called photoelectrons. Such EUV-generated photoelectrons interact with the cometary species and redistribute their energy in the cometary coma via various collisions. When photoelectrons interact with the atmospheric species they do not get destroyed like photons during their passage through cometary atmosphere. The photoelectrons having sufficient energy can also dissociate, ionize, and excite the cometary neutral species. The photoelectrons finally become indistinguishable from the ambient thermal electron population by loosing their energy via various inelastic collisions with different cometary species. In order to calculate the net photoelectron flux in the cometary coma, the EUV-generated photoelectrons should be degraded by accounting all possible collisional processes (both elastic and inelastic) with different species. There are different theoretical approaches to address this problem. I used Analytical Yield Spectra (AYS) method to calculate the steady state photoelectron flux in H_2O-dominated cometary atmosphere which is based on Monte Carlo technique developed by *Green et al.* [1985].

The AYS method of degrading electrons in the neutral cometary atmosphere can be explained briefly in the following manner. Monoenergetic electrons incident along the Z-axis in an infinite medium are degraded in a collision-by-collision manner using Monte Carlo technique. The energy and position of the primary electron and its secondary or tertiary electrons are recorded at the instant of each inelastic collision. The total number of inelastic events in the spatial and energy bins, after the incident electron and all its secondaries and tertiaries have been completely degraded, is used to generate numerical yield spectra. These yield spectra contain the information regarding the electron degradation process and can be employed to calculate the yield for any inelastic event. The numerical yield spectra generated in this way can be represented analytically, which contains the information about all possible collisional events based on the input electron impact cross sections, resulting in the AYS. This yield spectrum can be used to calculate the steady state photoelectron flux. More details of the AYS approach and the method of photoelectron flux computation are given in several previous papers [*Singhal and Haider*, 1984; *Bhardwaj et al.*, 1990, 1996; *Singhal and Bhardwaj*, 1991; *Bhardwaj*, 1999, 2003; *Bhardwaj and Michael*, 1999; *Haider and Bhardwaj*, 2005; *Bhardwaj and Jain*, 2009; *Bhardwaj and Raghuram*, 2012; *Raghuram and Bhardwaj*, 2012].

The expression for water vapour two-dimensional yield spectra is generated by *Green et al.* [1985]. The analytical yield spectra of water vapour as a function of the spectral energy E for the incident electron of energy E_k is calculated using the following expression.

$$U^c(E, E_k) = C_o + C_1 \left[\frac{(E_k + K)}{(E - M)^2 + L^2} \right] \tag{2.7}$$

Where $E_k = E_o/1000$ in keV, and other constants are $C_o = 0.028$, $C_1 = 726$, $K = 0.0154$ keV, $M = 1.43$ eV, $L = 3.11$ eV.

The Volume Excitation Rate (VER) for a given excited state of the ith species can be calculated using following equation

$$VER = \int_{W_{ki}}^{100} Q(E_o, r, \theta)\ dE_o \int_{W_{ki}}^{E_o} U^c(E, E_o)\ p_{ki}(E)\ dE \tag{2.8}$$

Where $Q(E_o, r, \theta)$ is the primary photoelectron production rate calculated using the equation 2.6 and $U^c(E, E_o)$ is the yield spectra which contains information of all electron impact collisional processes calculated using equation 2.7. $p_{ki}(E)$ is the probability of formation of the excited state due to interaction of photoelectron energy E and it can be calculated as

$$p_{ki}(E) = \frac{n_i \sigma_{ki}(E)}{\sum_j n_j \sigma_j(E)} \tag{2.9}$$

Where σ_j is the inelastic cross section and σ_{ki} is the cross section for the excited state k of ith species.

The volume excitation rate of a given state using photoelectron flux spectrum $\phi(r, E)$ can also be calculated as

$$VER = n_i \int_{W_{ki}}^{100} \phi(r, E) \sigma_{ki}(E) dE \tag{2.10}$$

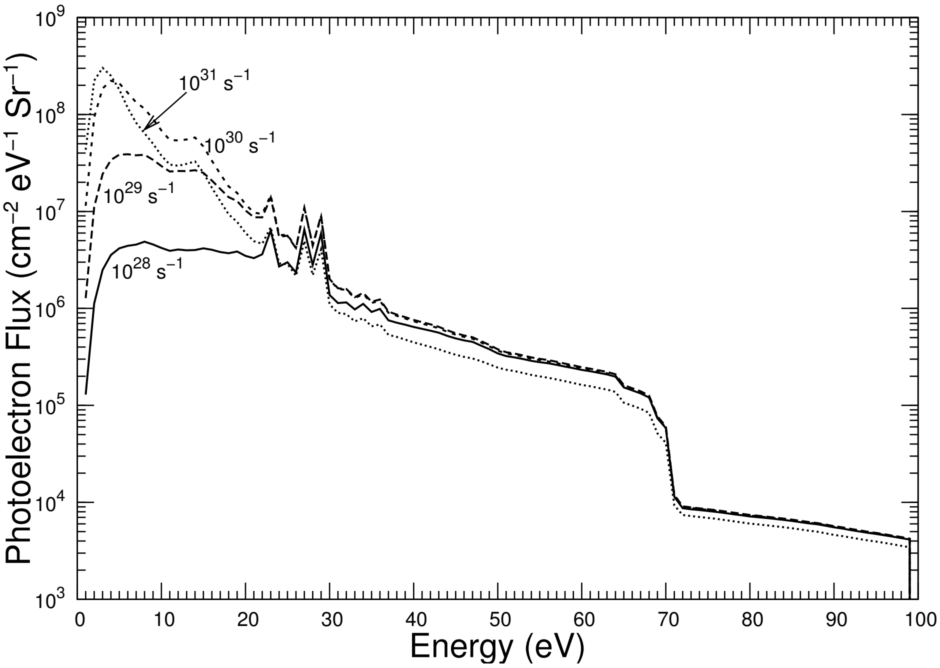

Figure 2.3: The calculated photoelectron flux at 1000 km cometocentric distance for different gas production rate comets.

By comparing the equations 2.8 and 2.10 the photoelectron flux can be calculated using the following equation

$$\phi(E,r) = \int_{W_{ki}}^{100} \frac{Q(E,r,\theta)U^c(E,E_o)}{\sum n_i(r)\sigma_j(E)} \tag{2.11}$$

The calculated photoelectron flux spectrum in comets for different neutral gas production rates is presented in Figure 2.3.

2.2.3 Coupled Chemistry of gas phase reactions

Having calculated production rate profiles of different excited state species and ions, I have accounted for a network of chemical reactions which incorporate all possible ion-ion, ion-neutral, and neutral-neutral collisions in the cometary coma. The total reactions considered in the model are tabulated in Table A.1. This chemical network of reactions contains the source processes for some species which are destruction channels for other species. Hence all these reactions are coupled to find the net density profile of various species in the cometary coma.

The calculated densities of the species are converted into emission rates using transition probabilities, Franck-Condon factors of the transitions. Assuming spherical symmetry of the coma, these emission rates integrated along the line of sight and the surface brightness profiles are calculated to compare with the observation. The schematic representation of line of sight integration is shown in Figure 2.4

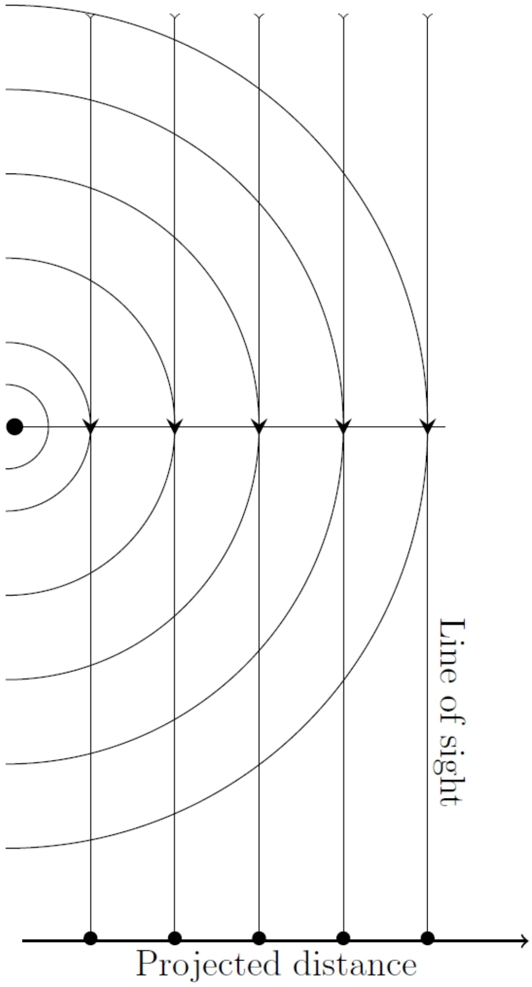

Figure 2.4: The intensities are integrated along the line of sight to calculate surface brightness profile.

2.3 Input parameters for model

The basic inputs that are required to model the emissions are described in the following sections and the comet dependent input parameters will be presented later in the appropriate sections.

2.4 Solar ultraviolet radiation flux

The solar ultraviolet radiation essentially determines the chemical lifetime of the neutral species and drives several photochemical processes, like dissociation, ionization, and electronic, vibrational, and rotational excitation in the cometary coma. The photorates of cometary species depends on the solar flux and the corresponding cross section at different wavelengths. The continuous measurement of solar UV flux is generally not available and also there are several discrepancies in the measured fluxes. Hence, generally planetary and cometary aeronomy calculations depend on the empirical solar irradiation modelled fluxes. These empirical models uses different proxies to predict the solar radiation flux, like F10.7 cm radio wave flux, Sunspot number, H Ly-α, etc. There are several other proxies also used to forecast the solar radiation. In the present model calculations I have used two popular solar flux models: EUVAC of *Richards et al.* [1994] and S2K of *Tobiska* [2004]. Using these two model fluxes, the observed aeronomical emissions of terrestrial and other planetary upper atmospheres were successfully explained in different works.

2.4.1 EUVAC model

Richards et al. [1994] developed a solar EUV flux model for aeronomical calculations (EUVAC) using solar radio 10.7 cm flux and its 81-day average value as proxies. This model can predict the solar flux in the wavelength region 0 to 1050 Å in 37 bins with 50 Å bin width and at a few important solar emission lines. Rocket-borne spectrometer measured solar UV flux on 23 April 1974 [F74113 flux, *Heroux and Higgins*, 1977; *Torr et al.*, 1979] is the reference spectrum for this model. *Richards et al.* modified the reference F74113 flux in a few wavelength bins to match with the measured photoelectron fluxes in Earth's atmosphere. The empirical relation for this model is

$$F_i = F74113_i \left[1 + A_i \left(\frac{F10.7A + F10.7}{2} - 80 \right) \right] \tag{2.12}$$

Where F74113$_i$ is the measured input solar EUV flux measured on 23 April 1974 by rocket flight and A$_i$ is the scaling factor for the ith bin. F10.7A is the 81-day average of the daily F10.7 index. The input F74113 solar flux is presented in Table A.2

2.4.2 SOLAR2000 (S2K) model

This model is developed in different phases by adding new proxies into the model. I used SOLAR2000 S2K version 2.36 to calculate the emission intensities in the cometary coma. SC#21REFW is the reference solar flux for this model. This model provides solar flux in bins of width 50 Å up to 1050 Å wavelength and also in bins of width 10 Å upto radio wavelengths. For more details refer *Tobiska* [2004].

2.5 Cometary coma

The density distribution of neutral species in the cometary coma is required for modelling the emission intensities and subsequently to compare the calculated intensities with the observations. The sublimation of ices produces gases that radially expand out into the vacuum to distances many orders of magnitude larger than the size of cometary nucleus. Historically, in comets, because of its simplicity in calculation, Haser's neutral gas expansion model [*Haser*, 1957] has been used in modelling the emission intensities and to determine the relative abundances of cometary species. However, there are other models, like vectorial model [*Festou*, 1981] and Monte Carlo method based spatial distribution model [*Combi et al.*, 1998] of cometary species, that have been used in modelling the spectroscopic emissions in comets. The calculated number densities by all these models closely agree in the inner coma. In the thesis I have used Haser's formulation in calculating the number density profiles of parent species for all comets.

2.5.1 Haser's model

The Haser's model [*Haser*, 1957] assumes a spherical distribution of gases around the nucleus which are radially expanding into the vacuum with a constant velocity. This model does not account for the collisions between cometary species.

Parent species distribution:

When cometary nucleus approaches the Sun, the solar radiation heats the ices and gases are ejected due to sublimation process. The gaseous species which are directly released from the nucleus are called parent species. Due to large pressure difference between gaseous coma and surrounding, these gases will expand radially out into the vacuum with a typically speed of 1 km s^{-1}. If E is evaporation rate (cm^{-2} s^{-1}) of nucleus of radius R_o due to solar heating, the number of neutral species (Q) ejected radially into space per second is given by

$$Q = 4\pi R_o^2 E$$

Let us assume that $N(r)$ particles are crossing a spherical shell of radius r per second with speed v. During course of passage if no species are lost due to photodissociation, then $N(r) = Q$. Assuming a spherical shell of thickness dr, the loss rate of the species per unit length due to solar radiation is β, then the net number of species crossing the spherical shell dr is

$$N(r + dr) = N(r) - \beta N(r) dr$$

differentiating the above equation both sides we get

$$\frac{dN(r)}{dr} = -\beta N(r)$$

The general solution for the above equation is

$$N(r) = Ae^{-\beta r}$$

Applying boundary conditions N(r=0) = Q then A = Q

$$N(r) = Qe^{-\beta r} \tag{2.13}$$

The total number of species crossing the spherical surface can be obtained by integrating the total number density $n(r)$ over spherical shell of radius r

$$N(r) = \int_0^{2\pi} \int_{\pi}^{\pi} n(r)\ v\ r\ d\theta\ r\ cos\theta\ d\phi$$

$$N(r) = 4\pi r^2\ v\ n(r)$$

by comparing the equation 2.13 with the above equation

$$Qe^{-\beta r} = 4\pi r^2\ v\ n(r)$$
$$n(r) = \frac{Q}{4\pi r^2 v} e^{-\beta r}$$

which is Haser's formula for parent species in cometary coma.

The number density $n_i(r)$ of ith species in the coma at a cometocentric distance r is given by

$$n_i(r) = \frac{f_i Q}{4\pi v_i r^2}(e^{-\beta_i/r}) \tag{2.14}$$

Here v_i is the average velocity of neutral species taken as 1 km s^{-1}, β_i is the scale length ($\beta_{H_2O} = 8.2 \times 10^4$ km, $\beta_{CO_2} = 5.0 \times 10^5$ km, and $\beta_{CO} = 1.4 \times 10^6$ km at 1 AU heliocentric distance) and f_i is the fractional abundance of the ith species.

Daughter species distribution:

Several species observed in the cometary coma do not originated directly from the sublimation of nucleus. They are produced due to solar radiation interaction with the parent species. The number density of water dissociative product OH at a given cometocentric distance r is calculated using Haser's two parameter coma model

$$n_{OH}(r) = \frac{Q_P}{4\pi v r^2} \frac{\beta_P}{\beta_R - \beta_P}(e^{-\beta_P r} - e^{-\beta_R r}) \tag{2.15}$$

Here v is the average velocity of daughter species taken as 1 km s^{-1}, and β_P and β_R are the destruction scale lengths of the parent (H_2O, 8.2 × 10^4 km) and daughter (OH, 1.32 × 10^5 km) species, respectively [*Huebner et al.*, 1992]. The neutral O-bearing parent species density profiles using the equations 2.14 and 2.15 are presented in Figure 2.5.

2.6 Photon impact cross sections

2.6.1 H_2O and OH

The absorption, ionization, dissociation, dissociative excitation and dissociative ionization cross sections of H_2O molecule averaged over 1 nm bin are presented in Table A.3. These cross sections are shown graphically in Figure 2.6. The dissociation of H_2O molecule starts at wavelengths less than 2424 Å and the primary products are H and

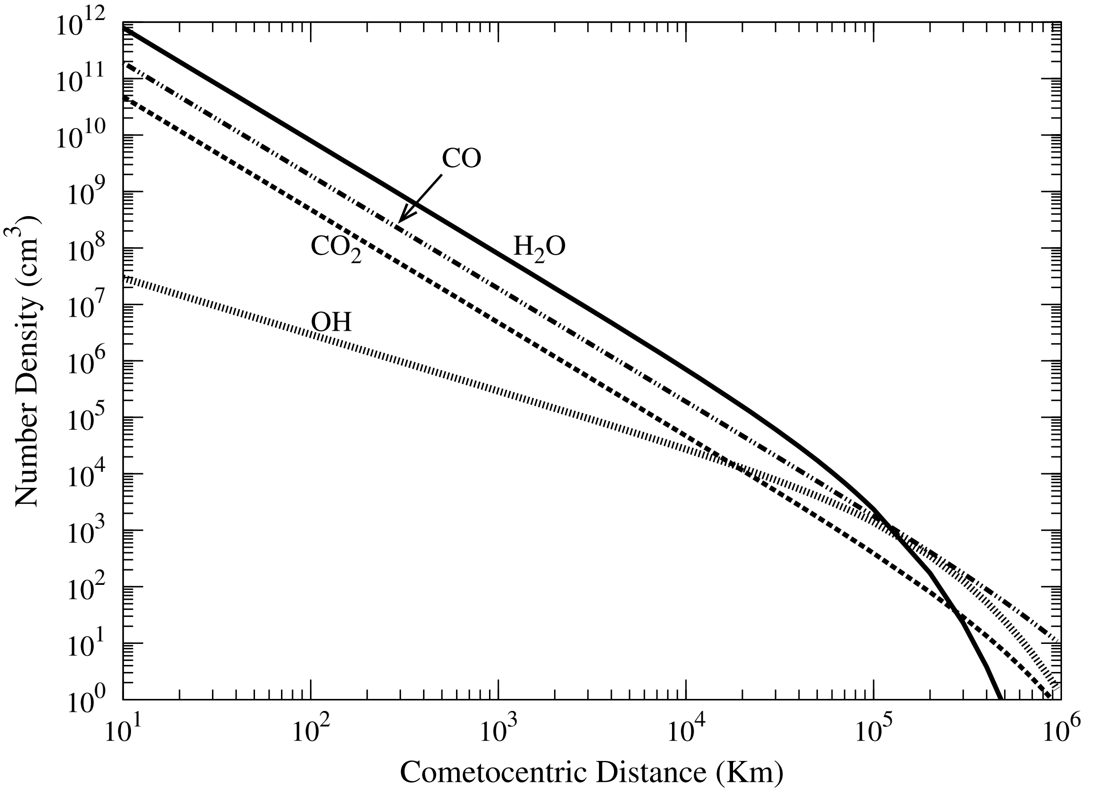

Figure 2.5: Neutral density profiles for a comet with H_2O production rate of 10^{30} s^{-1} and with relative abundances of 25% CO and 6% CO_2. Densities of H_2O, CO_2, CO are calculated using Haser's formula, whereas OH density profile is calculated using Haser's two parameter model.

OH. But the pre-dissociation process mainly starts from 1860 Å [*Watanabe and Zelikoff*, 1953]. The threshold wavelength for the photoionization of H_2O is 984 Å. Hence, solar UV photons in the wavelength region 1860 to 984 Å can dissociate H_2O and produce different daughter products. *Festou* [1981] discussed various dissociation channels for H_2O in the wavelength region less than 1860 Å. Solar photons in the wavelength region 1357 to 1860 Å dissociates around 72% of H_2O molecules into ground states of H and OH.

The threshold wavelengths for the dissociation of H_2O resulting in the production of $O(^1S)$ and $O(^1D)$ are 1390 Å and 1770 Å, respectively. Till now, the photo-yield value for the production of $O(^1D)$ from H_2O have been measured in only two experiments. *Slanger and Black* [1982] measured the $O(^1D)$ yield in photodissociation of H_2O at 1216 Å, and found its value to be 10%. *McNesby et al.* [1962] reported a 25% yield for the production of $O(^1D)$ or $O(^1S)$ at 1236 Å for H_2O. *Huebner et al.* [1992] calculated photoproduction rates for different excited species produced from H_2O using absorption and ionization cross sections compiled from different experimental measurements. In our model the cross sections for the production of $O(^1D)$ in photodissociation of H_2O are taken from *Huebner et al.* [1992], which were determined based on experiments of *Slanger*

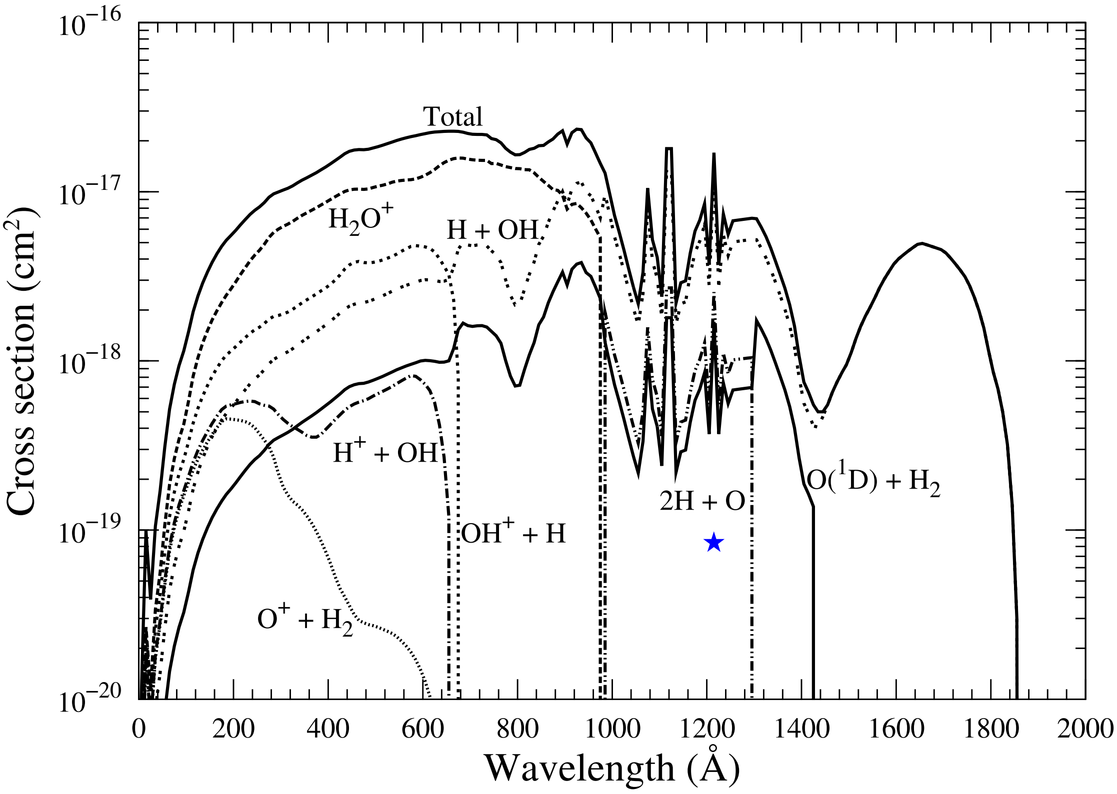

Figure 2.6: Photon cross sections of H_2O for different dissociation and ionization channels. These cross sections are taken from *Huebner et al.* [1992]. Big star represents the cross section value for the production of $O(^1S)$ from H_2O at 1216 Å assuming 1% yield.

and Black [1982] and *McNesby et al.* [1962]. *Huebner et al.* [1992] assumed that in the 1770 to 1300 Å wavelength region around 25% of H_2O molecules photodissociate into H_2 and $O(^1D)$, while between 1300 and 984 Å about 10% of H_2O dissociation produces $O(^1D)$. Below 984 Å, *Huebner et al.* [1992] assumed that 33% of dissociation of H_2O leads to the formation of $O(^1D)$. According to *Stief et al.* [1975] approximately 1% of H_2O molecules are dissociated into H_2 and $O(^1D)$ in 1357 to 1860 Å wavelength region. The calculated rates for the $O(^1D)$ production from photodissociative excitation of H_2O by *Huebner et al.* [1992] are 5.97×10^{-7} s^{-1} and 1.48×10^{-6} s^{-1} for solar quiet and active conditions, respectively. Using S2K solar flux on 1996 March 30 and cross sections from *Huebner et al.* [1992], our calculated value is 8×10^{-7} s^{-1}, which is a factor of ~1.5 higher than that of *Huebner et al.* [1992] for solar minimum condition at 1 AU. This difference in calculated values is mainly due to the higher (a factor of 1.24) value of solar flux at 1216 Å in S2K model than that used by *Huebner et al.* [1992].

No experimentally determined cross sections for the production of $O(^1S)$ in photodissociation of H_2O are available. The solar flux at H Lyman-α is more than an order of magnitude larger than the flux at wavelengths below 1390 Å, which is the threshold for the $O(^1S)$ production in dissociation of H_2O. To account for the production of $O(^1S)$

in photodissociation of H_2O, I assumed an yield of 0.5% at solar H Lyman-α (1216 Å). However, to assess the impact of this assumption on the green and red line emissions I varied the yield between 0 and 1%. The calculated photo-rate for the production of $O(^1S)$ from H_2O is 6.4×10^{-8} s^{-1} at 1 AU assuming 1% yield at 1216 Å.

The primary dissociative product of H_2O is OH. The important destruction mechanisms of OH molecule are pre-dissociation through fluorescence process and direct photodissociation. The solar radiation shortward of 928 Å can ionize OH molecule. The threshold wavelengths for the production of $O(^1D)$ and $O(^1S)$ in photodissociation of OH are 1940 and 1477 Å, respectively. The dissociation channels of OH have been discussed by *Budzien et al.* [1994] and *van Dishoeck and Dalgarno* [1984]. I have used the photo-rates given by *Huebner et al.* [1992] for the production of $O(^1D)$ and $O(^1S)$ from OH molecule whose values are 6.4×10^{-7} and 6.7×10^{-8} s^{-1}, respectively.

2.6.2 CO_2

The absorption, ionization, dissociation, dissociative excitation and dissociative ionization cross sections of CO_2 molecule which are averaged over 1 nm presented in Table A.4. The cross sections for different dissociation and ionization channels are graphically presented in Figure 2.7. The threshold wavelengths for dissociation of CO_2 molecule producing $O(^1D)$ and $O(^1S)$ are 1671 Å and 1286 Å, respectively. As noted by *Huestis and Slanger* [2006], the $O(^1D)$ yield in photodissociation of CO_2 has never been measured because of the problem of rapid quenching of this metastable state. However, experiment by *Kedzierski et al.* [1998] suggested that this dissociation channel can be studied in electron impact experiment using solid neon matrix as detector. *Huebner et al.* [1992] estimated the cross section for $O(^1D)$ production in photodissociative excitation of CO_2, and obtained photo-rate values of 9.24×10^{-7} and 1.86×10^{-6} s^{-1} for solar minimum and maximum conditions, respectively. Using S2K solar flux on 30 March 1996 our calculated rate for $O(^1D)$ production in photodissociation of CO_2 is 1.2×10^{-6} s^{-1} at 1 AU, which is higher than the solar minimum rate of *Huebner et al.* [1992] by a factor of 1.3. This variation is mainly due to the differences in the solar fluxes in the wavelength region 950 to 1100 Å where the photodissociative cross section for the production of $O(^1D)$ maximizes. *Jain* [2013] reviewed the measured the experimentally determined yields for different channels of photodissociative excitation of CO_2 molecule and recommended the yield for $O(^1D)$. Using this yield we calculated the cross section for photodissociation of CO_2 producing $O(^1D)$ which is shown in Figure 2.7.

Lawrence [1972a] measured the $O(^1S)$ yield in photodissociative excitation of CO_2 from threshold (1286 Å) to 800 Å. The yield of *Lawrence* [1972a] is different from that measured by *Slanger et al.* [1977] in the 1060 to 1175 Å region. However, the yield from both experimental measurements closely matches in the 1110–1140 Å wavelength region, where the yield is unity. *Huestis et al.* [2010] reviewed the experimental results

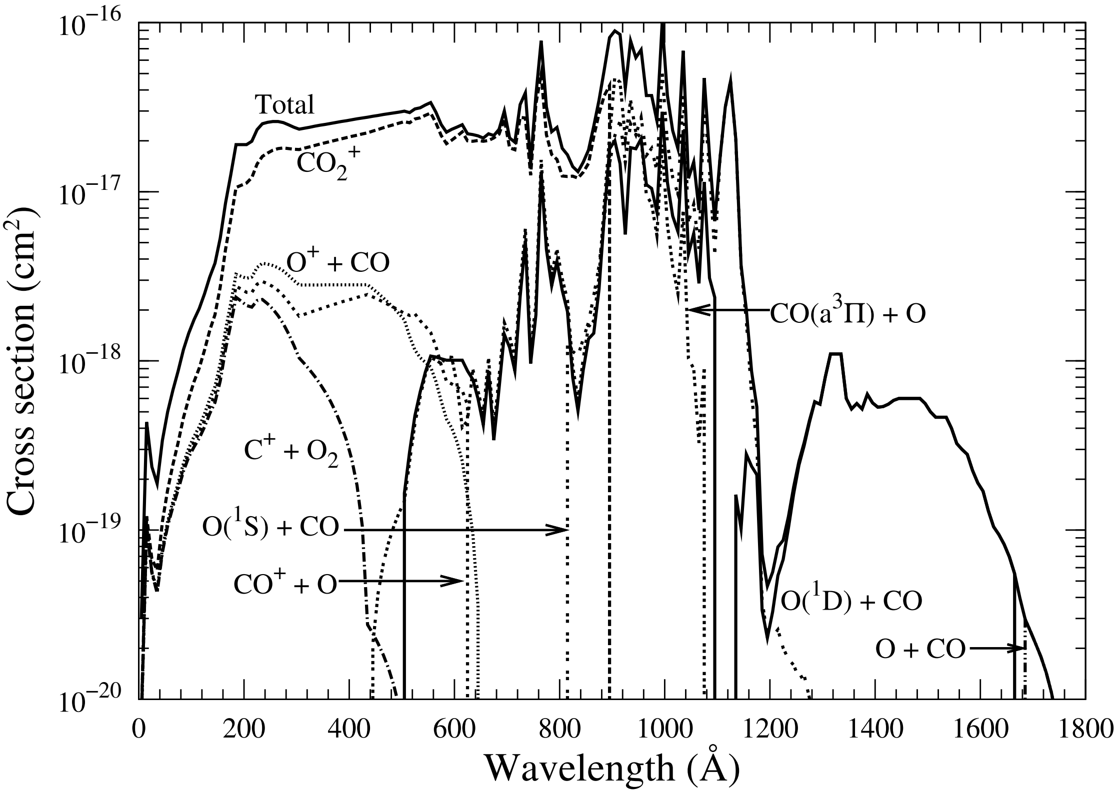

Figure 2.7: Photon cross sections of CO_2 for different dissociation and ionization channels. These cross sections are taken from *Huebner et al.* [1992]. The cross sections for production of O(^{1}S) and O(^{1}D) are calculated by using yields from *Huestis et al.* [2010] and *Jain* [2013], respectively.

and suggested the yield for O(^{1}S) in photodissociation of CO_2. The cross section for the O(^{1}S) production in photodissociative excitation of CO_2 is calculated by multiplying the yield recommended by *Huestis et al.* [2010] with total absorption cross section of CO_2. Using this cross section and S2K solar flux, the rate for O(^{1}S) production is 7.2×10^{-7} s^{-1} at 1 AU.

2.6.3 CO

The absorption, ionization, dissociation, dissociative excitation and dissociative ionization cross sections of CO molecule are averaged over 1 nm and presented in Table A.5. The cross sections for different dissociation and ionization channels are graphically presented in Figure 2.8. The threshold wavelength for the dissociation of CO molecule into neutral products in the ground state is 1117.8 Å and in the metastable O(^{1}D) and C(^{1}D) states is 863.4 Å. Among the O-bearing species discussed in this paper, CO has the highest dissociation energy of 11.1 eV, while its ionization potential is 14 eV. *Huebner et al.* [1992] calculated cross sections for the photodissociative excitation of CO producing O(^{1}D) using branching ratios from *McElroy and McConnell* [1971]. *Huebner et al.* [1992] calculated CO photodissociation rates producing O(^{1}D) for solar minimum and maximum conditions as 3.47 × 10^{-8} and 7.87 × 10^{-8} s^{-1}, respectively. Using the cross section of *Huebner et al.* [1992] and S2K model solar flux, our calculated rate for the O(^{1}D) production from CO is 5.1 × 10^{-8} s^{-1} at 1 AU, which is 1.5 times higher than the solar minimum rate of *Huebner et al.* [1992]. This difference in the calculated value is due to variation in the solar fluxes used in the two studies in wavelength region 600 to 800 Å.

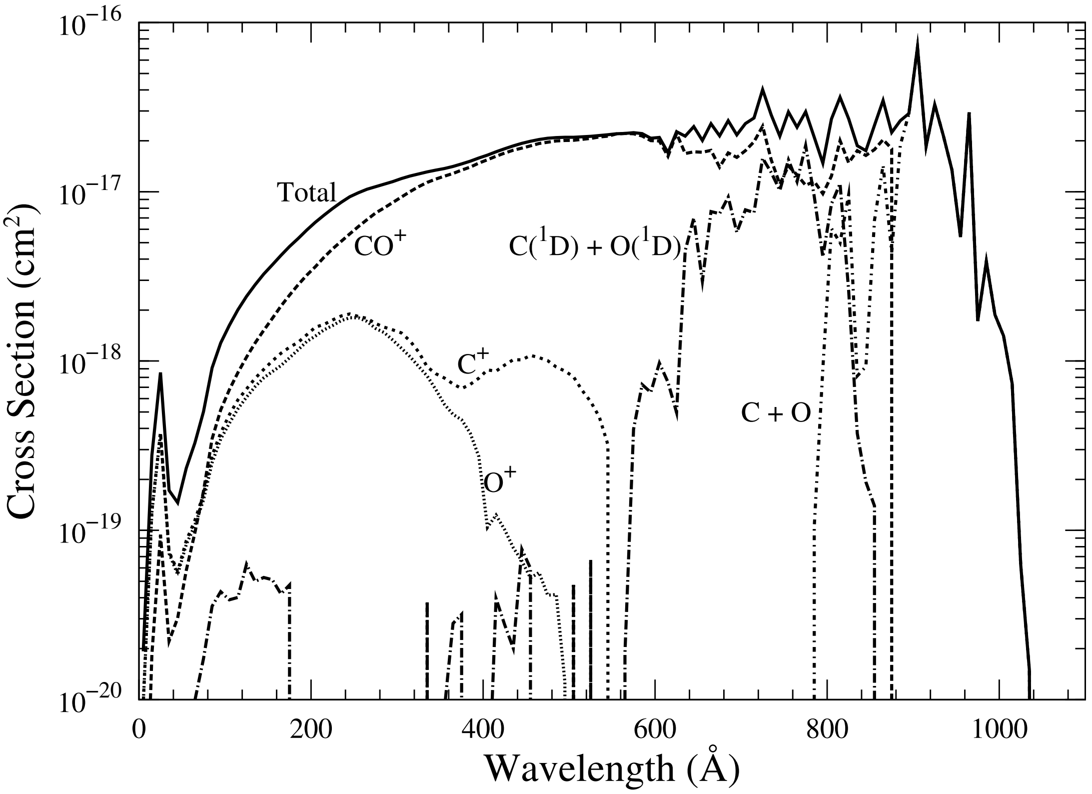

Figure 2.8: Photon cross sections of CO for different dissociation and ionization channels. These cross sections are taken from *Huebner et al.* [1992]

I did not find any reports on the cross section for the production of O(^{1}S) in photodissociation of the CO molecule. According to *Huebner and Carpenter* [1979] the rate for this reaction can not be more than 4 × 10^{-8} s^{-1}. I have used this value in our model calculations. This process can be an important source of O(^{1}S) since the comet Hyakutake has a higher CO abundance (∼20%).

2.7 Electron impact cross sections

The total inelastic electron impact cross sections for water are taken from *Rao et al.* [1995], and those for CO_2 and CO are taken from *Jackman et al.* [1977]. *Jackman et al.* [1977] have assembled the experimental and theoretical cross sections for electron impact on important atmospheric gases in a workable analytical form. The electron impact different excitation and ionization state cross sections for CO_2 and CO are calculated using the analytically fitted cross sections of *Jackman et al.* [1977].

Discrete excited states:

The following analytical expression has been used to calculate the electron impact cross section value $\sigma_j(E)$ at energy E for jth state of the species.

$$\sigma_j(E) = \frac{q_0 F}{W^2}\left[1 - \left(\frac{W}{E}\right)^{\alpha}\right]^{\beta}\left[\frac{W}{E}\right]^{\Omega} \tag{2.16}$$

where $q_0 = 4\pi a_0 R^2$ and has the value 6.512×10^{-14} eV^2 cm^2, a_0 being the Bohr radius and R the Rydberg energy. W is the low energy parameter determines the low energy shape of the cross section. F is the optical oscillator strength of the species. α, β, and Ω are the fitting parameters.

Ionized states:

To calculate cross sections for the different excited states of ionized species following analytical expression given by *Jackman et al.* [1977] is used in our model.

$$\sigma(E) = A(E)\ \Gamma(E)\left[arctan\frac{(T_M - T_0)}{\Gamma} + arctan\left(\frac{T_0}{\Gamma}\right)\right], \tag{2.17}$$

where

$$A(E) = \left[\frac{K}{E + K_B}\right]\ln\left[\frac{E}{J} + J_B + \frac{J_C}{E}\right];\ \Gamma(E) = \Gamma_S\left[\frac{E}{E + \Gamma_B}\right];$$

$$T_0 = T_S - \left[\frac{T_A}{E + T_B}\right];\ T_M = \frac{E - I}{2}.$$

Here E is the incident energy in eV, I is the fitting ionization potential in the eV, which is generally close to the threshold potential (W$_{th}$), and σ is in units of 10^{-16} cm^2. The parameters used for calculation of electron impact cross sections of different excited and ionized states of the species viz., H_2O, CO_2, and CO are tabulated in Tables A.6, A.7, and A.8.

2.7.1 H_2O

The total inelastic cross section for water, is taken from *Rao et al.* [1995] and ionization and dissociative ionization cross sections are taken from *Itikawa and Mason* [2005]. *Kedzierski et al.* [1998] measured the cross section for electron impact dissociative excitation of H_2O producing O(^{1}S), with overall uncertainty of 30%. In our literature survey I could not find any reported cross section for the production of O(^{1}D) due to the electron impact dissociation of H_2O. The cross sections used in our model is presented in Figure 2.9.

2.7.2 CO_2 and CO

The total inelastic cross section for CO and CO_2 are calculated by adding the different excitation state cross sections and ionization cross sections using the analytical

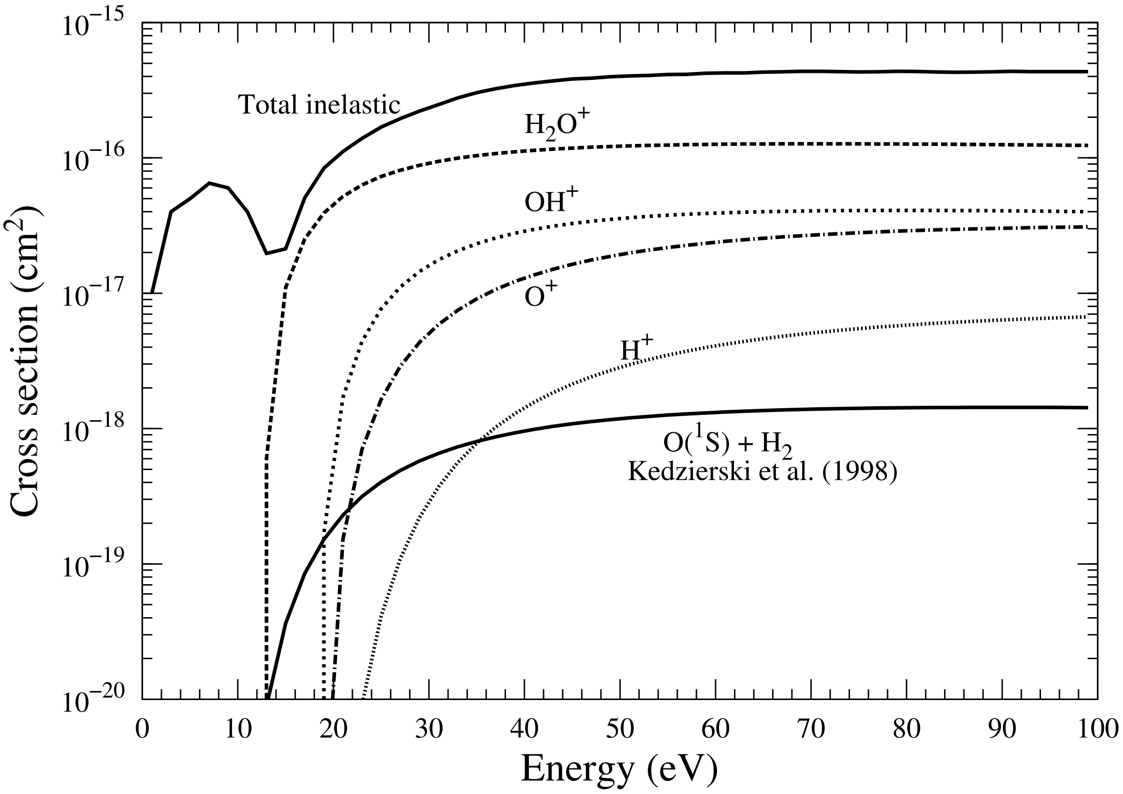

Figure 2.9: The electron impact collision cross sections of H_2O. The cross section for the production of $O(^1S)$ by electron impact of H_2O is also plotted in this figure.

expressions given by *Jackman et al.* [1977]. *LeClair and McConkey* [1994] measured cross section for the production of $O(^1S)$ in dissociation of CO_2 by electron impact; they claimed an uncertainty of 12% in their experimental cross section measurements. The cross section for fragmentation of CO into metastable $O(^1S)$ atom by electron impact is measured by *LeClair et al.* [1994]. These electron impact cross sections are also recommended by *McConkey et al.* [2008], and are used in our model for calculating the production rate of $O(^1S)$ from H_2O, CO_2, and CO. The total inelastic, ionization and dissociative ionization of CO_2 and CO are presented in Figures 2.10 and 2.11, respectively.

2.8 Dissociative recombination of ions

The ions produced in the cometary coma recombine with the thermal electrons and produce a variety of excited and ground state species. The important recombination reactions and their dissociative branching channels are considered in our model. The ions considered in our model are H_3O^+, H_2O^+, OH^+, H^+, CO_2^+, CO^+, O^+, C^+, O_2^+, and HCO^+.

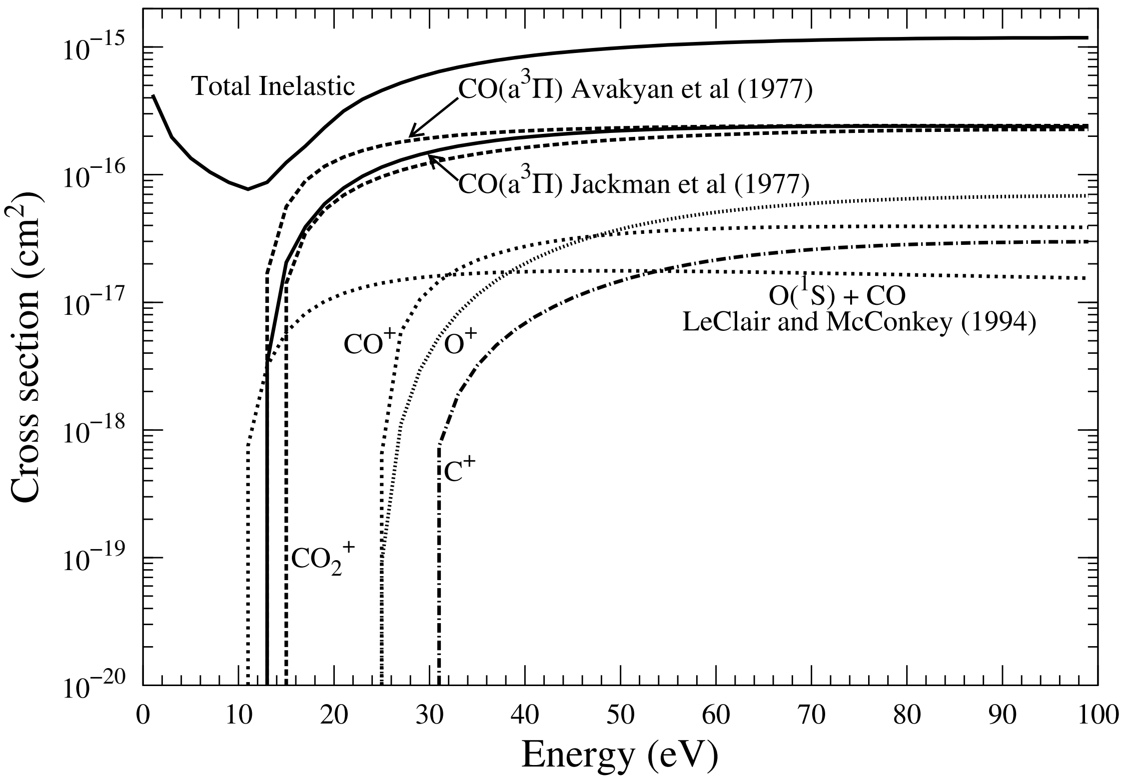

Figure 2.10: The electron impact collision cross sections of CO_2. The cross sections for the production of $CO(a^3\Pi)$ and $O(^1S)$ by electron impact of CO_2 are also presented in this figure.

2.8.1 H_3O^+ and H_2O^+

The collisional reaction of H_2O with H_2O^+ produces H_3O^+ which is the dominant ion in the inner cometary coma. The thermal recombination of this ion results in different neutral dissociative products. The recombination channels of H_3O^+ and excess energy (ΔE) and branching ratios (α) are

$$H_3O^+ + e^- \rightarrow \begin{cases} H_2O + H, & \Delta E = 6.4\ eV,\ \alpha = 0.33\ (a) \\ OH + H_2, & \Delta E = 5.7\ eV,\ \alpha = 0.18\ (b) \\ OH + H + H, & \Delta E = 1.3\ eV,\ \alpha = 0.48\ (c) \\ O + H_2 + H, & \Delta E = 1.4\ eV,\ \alpha = 0.01\ (d) \end{cases} \tag{2.18}$$

Vejby-Christensen et al. [1997] measured the branching fractions for different products in the dissociative recombination of H_3O^+ ion. The possible dissociation channels and their branching ratios are presented in the equation 2.18. Assuming the dissociated products are in ground state the calculated excess energy released in the recombination is also presented in the same equation. It is found that the production of OH along with two H atoms is most probable recombination channel for the H_3O^+.

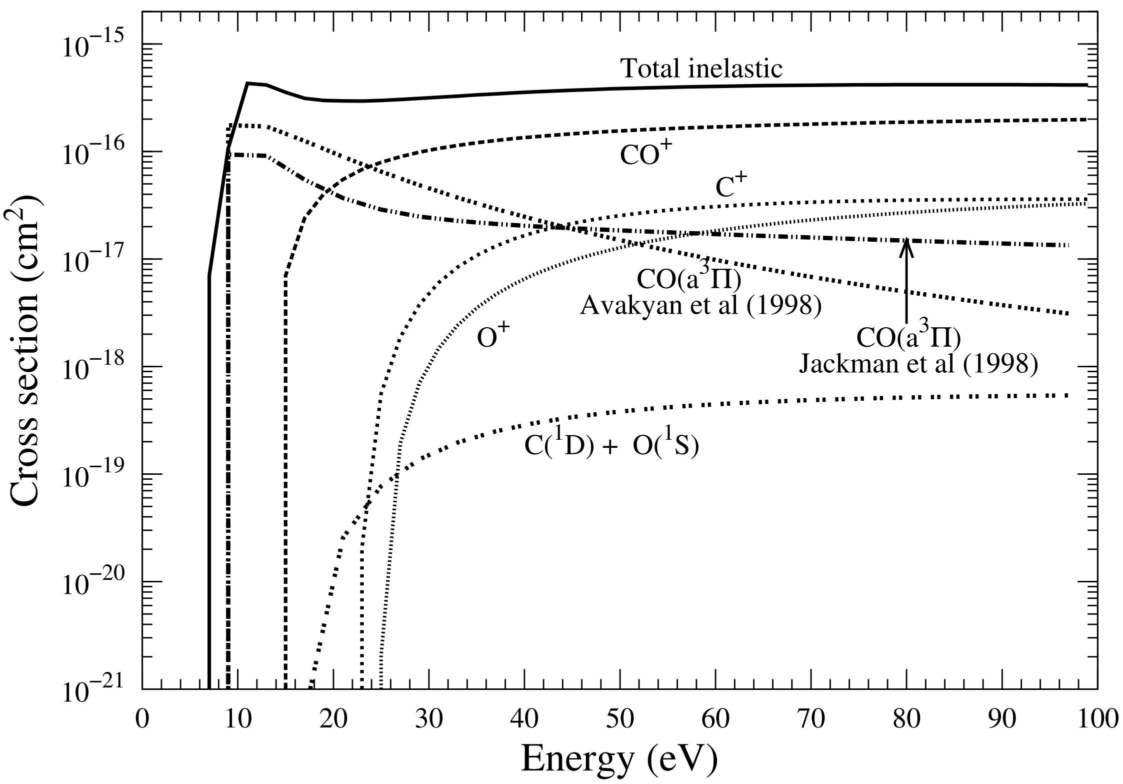

Figure 2.11: The electron impact collision cross sections of CO. The cross sections for the production of CO($a^3\Pi$), C(^1D) and O(^1S) by electron impact of CO_2 are also presented in this figure.

The major formation of H_2O^+ ion in the inner cometary coma is via photoionization of H_2O. The dissociation recombination of this ion produces different products. *Rosen et al.* [2000] measured the branching ratio for the dissociative recombination of H_2O^+ ion and it was found that the most probable recombination channel is the production of atomic oxygen along with two hydrogen atoms. The branching ratios of these dissociative recombination channels and maximum excess energies released is presented in the equation 2.19. The dissociative recombination channels for H_2O^+ are

$$\mathrm{H_2O^+ + e^-} \rightarrow \begin{cases} \mathrm{OH + H}, & \Delta E = 7.5\ eV,\ \alpha = 0.20\ (a) \\ \mathrm{O + H_2}, & \Delta E = 7.6\ eV,\ \alpha = 0.09\ (b) \\ \mathrm{O + H + H}, & \Delta E = 3.1\ eV,\ \alpha = 0.71\ (c) \end{cases} \tag{2.19}$$

The total dissociative recombination rate for H_2O^+ reported by *Rosen et al.* [2000] is 4.3×10^{-7} cm^{-3} s^{-1} at 300 K. The channels of dissociative recombination have also been studied by this group. It was found that the dissociation process is dominated by three-body breakup (H + H + O) that occurs with a branching ratio of 0.71, while the fraction of two-body breakup (O + H_2) is 0.09, and the branching ratio for the formation of OH + H is 0.2. The maximum kinetic energy of the dissociative products forming atomic oxygen produced in ground state are 3.1 eV and 7.6 eV for the three-and two-body dissociation, respectively. Since the excitation energy required for the formation of metastable O(^{1}S) is 4.19 eV, the three-body dissociation can not produce oxygen atoms in ^{1}S state. However, the O(^{1}D) atom can be produced in both, the three-body and the two-body, breakup dissociation processes. To incorporate the contribution of H_2O^+ dissociative recombination in the production of O(^{1}D) and O(^{1}S), I assumed that 50% of branching fraction of the total recombination in three-body and two-body breakups lead to the formation of O(^{1}D) and O(^{1}S) atoms, respectively.

2.8.2 CO_2^+ and CO^+

The dissociative recombination channels of CO_2^+ and CO^+ ions are presented in the equations 2.20 and 2.21.

$$\mathrm{CO_2^+} + \mathrm{e^-} \rightarrow \begin{cases} \mathrm{CO_2}, & \Delta E = 13.8\ eV,\ \alpha = 0.04\ (a) \\ \mathrm{C} + \mathrm{O_2}, & \Delta E = 2.3\ eV,\ \ \alpha = 0.09\ \ (b) \\ \mathrm{CO} + \mathrm{O}, & \Delta E = 8.3\ eV,\ \ \alpha = 0.87\ \ (c) \end{cases} \tag{2.20}$$

$$\mathrm{CO^+} + \mathrm{e^-} \rightarrow \begin{cases} \mathrm{O(^3P)} + \mathrm{C(^3P)}, & \Delta E = 2.92\ eV,\ \alpha = 0.39\ (a) \\ \mathrm{O(^3P)} + \mathrm{C(^1D)}, & \Delta E = 1.66\ eV,\ \alpha = 0.35\ (b) \\ \mathrm{O(^1D)} + \mathrm{C(^3P)}, & \Delta E = 0.96\ eV,\ \alpha = 0.15\ (c) \\ \mathrm{O(^3P)} + \mathrm{C(^1S)}, & \Delta E = 0.24\ eV,\ \alpha = 0.05\ (d) \\ \mathrm{O(^1D)} + \mathrm{C(^1D)}, & \Delta E = -0.33\ eV,\ \alpha = 0.06\ (e) \end{cases} \tag{2.21}$$

For dissociative recombination of CO_2^+, CO^+ and OH^+ ions I assumed that the recombination rates are same for the production of both O(^{1}D) and O(^{1}S). I will show that these assumptions can affect the calculated O(^{1}S) and O(^{1}D) densities only at larger ($\geq 10^4$ km) cometocentric distances, but not in the inner coma.

2.9 Summary

A model is developed to understand the photochemistry of CO Cameron and atomic oxygen visible emissions in comets. These emissions are governed by various production and loss mechanisms of the excited species CO(a$^3\Pi$), O(^{1}S), and O(^{1}D) in the cometary coma. We accounted for the important physical processes that govern the photochemistry of these excited species. Our model calculations are applied on several comets having different gas production rates and different chemical abundances. The results of model calculations on different comets and comparison with the observations are discussed in the following chapters.

Chapter 3

CO Cameron band emission

Contents

3.1 Introduction **43**
3.2 Model **45**
3.3 Calculations on comet 103P/Hartley 2 . . . . **47**
3.4 Results for 103P/Hartley 2 . . . . **48**
3.4.1 Production and loss of CO(a$^3\Pi$) 48
3.4.2 Intensity of Cameron band of CO molecule 49
3.5 Calculations on comet 1P/Halley **52**
3.6 Results for comet 1P/Halley **54**
3.6.1 Production and loss of CO(a$^3\Pi$) 54
3.6.2 Intensity of CO Cameron bands 55
3.7 Discussion **61**
3.7.1 Effect of model parameters on the calculations 62
3.7.1.1 Electron impact cross sections 62
3.7.1.2 Solar EUV-UV flux 63
3.8 Summary **64**

3.1 Introduction

Since CO_2 does not emit visible and ultraviolet photons it is difficult to detect this molecule in cometary ultraviolet and visible spectra. Hence the relative abundances of CO_2 in cometary coma have been derived using UV-emissions from its dissociative products which are produced in metastable states. Assuming that photodissociative excitation is the main production mechanism in populating the a$^3\Pi$ metastable state of CO, the Cameron band (a$^3\Pi \rightarrow$ X$^1\Sigma^+$) emission has been used to estimate the CO_2 abundance in comets [*Weaver et al.*, 1994; *Weaver et al.*, 1997; *Feldman et al.*, 1997].

This band emissions lies in the ultraviolet region (1800–2600 Å). Various electronic transitions of CO molecule is shown in the following Figure 3.1.

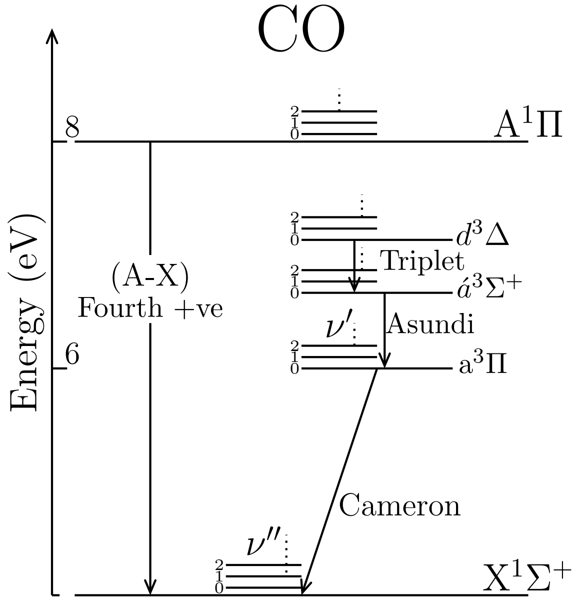

Figure 3.1: Schematic energy level diagram of carbon monoxide molecule showing different electronic different transitions.

The CO Cameron band emission is due to electronic transition ($a^3\Pi$–$X^1\Sigma^+$) which is spin forbidden for dipole transitions hence resonance fluorescence by solar photons is not an effective excitation mechanism to populate CO($a^3\Pi$) state. Since the excited upper state ($a^3\Pi$) of Cameron band emission is metastable and its lifetime is very small [3 ms at 1 AU, *Gilijamse et al.*, 2007] compared to lifetime of CO_2 molecule [$\sim$135 hours at 1 AU, *Huebner et al.*, 1992], the CO($a^3\Pi$) molecule can travel a distance of only a few meters in the cometary coma before de-exciting into ground state ($X^1\Sigma^+$) by emitting photons. Hence, the Cameron band emission can be used to probe CO_2 distribution, and thus its abundance in the coma, provided it is produced mainly through dissociative excitation CO_2. Thus, Cameron band emissions are treated as “prompt emissions”. The photodissociative excitation of CO_2 is considered as the major production mechanism of CO Cameron band and has been used to trace the distribution and abundance of CO_2 on comets [*Feldman et al.*, 1997; *Weaver et al.*, 1994]. The cascading of higher metastable states also can produce CO($a^3\Pi$) (see Figure 3.1) and eventually leads to Cameron band emission [*Kalogerakis et al.*, 2012].

The first clear detection of the Cameron band ($a^3\Pi$–$X^1\Sigma$) of CO was reported by *Weaver et al.* [1994] using Field Object Spectrograph on HST in comets 103P/Hartley 2 and C/1992 T2 Shoemaker-Levy. The observation of CO Cameron band in the coma of comet 103P/Hartley 2 [*Weaver et al.*, 1994] by HST gave an incitement to re-examine the data of several comets observed by the IUE satellite. Cameron band (1-0) emission at 1993 Å is observed in 4 comets viz., C/1979 Y1 (Bradfield), C/1989 X1 (Austin), C/1990 K1 (Levy), and 1P/Halley, in the IUE spectra [*Feldman et al.*, 1997]. The Cameron band (0-0) and (0-1) emissions at 2063 and 2155 Å, respectively, could not be observed since they fall in the low sensitivity end of the IUE long-wavelength camera. Reanalysis of the IUE data on comet 1P/Halley showed 5 observations of the Cameron 1-0 band emission, which span over a 10-days period in March 1986; the intensity of 1-0 emission varied by a factor of about 4 from lowest value of 20±6 to highest value of 65±9 Rayleigh [*Feldman et al.*, 1997].

Besides photodissociative excitation of CO_2, there are other channels of excitation of CO molecule in the $a^3\Pi$ state. It has been shown that photoelectrons generated by solar EUV radiation can also play an important role in excitation, dissociation, and ionization processes leading to different emissions and chemistry in the cometary comae [e.g., *Ip*, 1985; *Boice et al.*, 1986; *Körösmezey et al.*, 1987; *Bhardwaj et al.*, 1990, 1996; *Bhardwaj*, 1999, 2003; *Weaver et al.*, 1994; *Haider and Bhardwaj*, 2005; *Capria et al.*, 2008]. Recently, *Campbell and Brunger* [2009] demonstrated the importance of photoelectron impact excitation in comets, and showed that electron impact on CO gives 40% contribution to the total CO Fourth positive emission. The presence of photoelectron excitation in the cometary coma is clearly publicized by detection of OI 1356 Å emission in comets [e.g., *Sahnow et al.*, 1993; *McPhate et al.*, 1999], since this emission being a spin-forbidden transition cannot be produced by solar fluorescence. There are other significant evidences for an important role of photoelectron excitation in cometary coma [e.g., *Tozzi et al.*, 1998; *Bhardwaj*, 1999; *Feldman et al.*, 2009]. In addition to photon and electron impact reactions, dissociative electron recombination reactions of CO-bearing ions can also produce CO in the $a^3\Pi$ excited state.

3.2 Model

We have modelled the photochemistry for the Cameron band emission on comets 103P/Hartley 2 and 1P/Halley using the basic coupled chemistry model described in Chapter 2. Various sources for production and loss of $CO(a^3\Pi)$ accounted in the model are summarized in Table 3.1. The aim of this work is to study the chemistry of $CO(a^3\Pi)$ and to estimate the contribution of photoelectron impact excitation of CO and CO_2 in the production of CO Cameron band for different relative abundances of CO_2 and CO in comets 103P/Hartley 2 and 1P/Halley. Since model calculations depend on input solar flux, we have estimated its sensitivity on the calculated intensity of Cameron band emission.

The cross section for electron impact excitation of CO in the $a^3\Pi$ state is taken from *Jackman et al.* [1977] and for dissociative excitation of CO_2 producing $CO(a^3\Pi)$ is taken from *Bhardwaj and Jain* [2009]. These cross sections are presented in Figure 3.2. To estimate the effect of electron impact cross sections on emissions, we have used the electron impact cross sections recommended by *Avakyan et al.* [1998] for the above two

Table 3.1: Reactions for the production and loss of CO($a^3\Pi$).

Reaction	Rate(cm^3 s^{-1} or s^{-1})	Reference
$CO_2 + h\nu \rightarrow CO(a^3\Pi) + O(^3P)$	Model	*Present work*
$CO + h\nu \rightarrow CO(a^3\Pi)$	1.69×10^{-9}	*Weaver et al.* [1994]
$CO_2 + e^-_{ph} \rightarrow CO(a^3\Pi) + O + e^-$	Model	*Present work*
$CO + e^-_{ph} \rightarrow CO(a^3\Pi) + e^-$	Model	*Present work*
$CO_2^+ + e^-_{th} \rightarrow CO(a^3\Pi) + O$	$K_a{}^*$	*Seiersen et al.* [2003], *Rosati et al.* [2003]
$HCO^+ + e^- \rightarrow CO(a^3\Pi) + H$	$K_b{}^\dagger$	*Rosati et al.* [2007], *Schmidt et al.* [1988]
$CO(a^3\Pi) + h\nu \rightarrow C + O$	7.2×10^{-5}	*Huebner et al.* [1992]
$CO(a^3\Pi) + h\nu \rightarrow CO^+ + e^-$	8.58×10^{-6}	*Huebner et al.* [1992]
$CO(a^3\Pi) + h\nu \rightarrow O+C^+ + e^-$	2.45×10^{-8}	*Huebner et al.* [1992]
$CO(a^3\Pi) + h\nu \rightarrow C + O^+ + e^-$	2.06×10^{-8}	*Huebner et al.* [1992]
$CO(a^3\Pi) + H_2O \rightarrow CO + H_2O$	3.3×10^{-10}	*Wysong* [2000]
$CO(a^3\Pi) + CO_2 \rightarrow CO + CO_2$	1.0×10^{-11}	*Skrzypkowski et al.* [1998]
$CO(a^3\Pi) + CO \rightarrow CO + CO$	5.7×10^{-11}	*Wysong* [2000]
$CO(a^3\Pi) + e^-_{ph} \rightarrow CO^+ + 2e^-$	Model	*Present work*
$CO(a^3\Pi) \longrightarrow CO + h\nu$	1.26×10^2	*Lawrence* [1972b]

$^*K_a = 6.5 \times 10^{-7}\ (300/Te)^{0.8} \times 0.87 \times 0.29$ cm^3 s^{-1}; here 0.87 is yield of dissociative recombination of CO_2^+ producing CO, and 0.29 is yield of $CO(a^3\Pi)$ produced from CO.
$^\dagger K_b = 2.4 \times 10^{-7}\ (300/Te)^{0.7} \times 0.23$ cm^3 s^{-1}; here 0.23 is yield of dissociative recombination of HCO^+ producing $CO(a^3\Pi)$; e^-_{ph} = photoelectron, and e^-_{th} = thermal electron.

processes, which are also shown in Figure 3.2. The electron impact volume production rates of different ions and volume excitation rates of $CO(a^3\Pi)$ state produced from CO_2 and CO are calculated using photoelectron flux $\phi_p(E,r)$ which is described in Chapter 2 (see eq. 2.11) and electron impact excitation cross section σ_{ik} of ith species and kth state as

$$V(r) = n_i(r) \int_w^{100} \phi_p(E,r)\ \sigma_{ik}(E) dE \tag{3.1}$$

Where w is the threshold energy for the corresponding kth excitation or ionization state.

The solar UV flux is known to vary considerably both with the 27-day solar rotation period and with the 11-year solar activity cycle. Since the continuous measurements of solar EUV fluxes are not available for different cometary observations, one has to depend on the empirical solar EUV models. To assess the impact of solar EUV flux on the calculated brightness of Cameron band emission we have taken two most commonly used solar EUV flux models, namely EUVAC model of *Richards et al.* [1994] and S2K SOLAR2000 v.2.3.6 model of *Tobiska* [2004]. The solar EUV fluxes from these two models for 13 March 1986 are shown in Figure 3.3. The calculated photoelectron fluxes for the two solar EUV flux models at 1000 km are shown in Figure 3.2. *Huebner et al.* [1992] calculated the cross section for photodissociative excitation of CO_2 producing

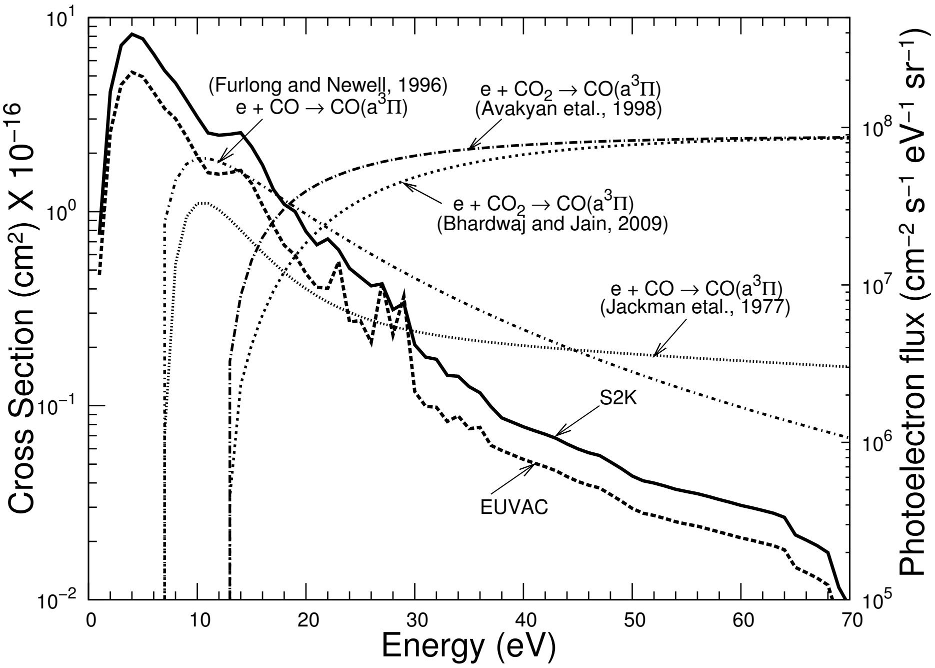

Figure 3.2: Cross sections for the formation of CO(a$^3\Pi$) by electron impact excitation of CO and CO$_2$. The Calculated photoelectron flux on Halley, which is having gas production rate of 6.9×10^{29} s^{-1} with 80% H$_2$O, 4.3% CO$_2$, and 7% CO, when comet is at heliocentric distance of 1 AU, at cometocentric distance of 1000 km is also shown for both SOLAR2000 (S2K) and EUVAC model solar fluxes with magnitude on right side y-axis.

CO in a$^3\Pi$ state using total absorption cross section and *Lawrence* [1972b] measured yield. We averaged these cross section values over 50 Å bin intervals to calculate photodissociative excitation rate using solar flux from EUVAC and S2K models; this cross section is shown in Figure 2.7.

3.3 Calculations on comet 103P/Hartley 2

The total water production rate is taken as 6.3×10^{28} s^{-1} for comet 103P/Hartley 2 [*Weaver et al.*, 1994]. The electron temperature profile required for dissociative recombination reactions is taken from *Körösmezey et al.* [1987] and is assumed to be same as on comet Halley. Calculations are made for comet 103P/Hartley 2 at heliocentric distance of 0.96 AU. Comet 103P/Hartley 2 is CO depleted (relative abundance $\leq$1%) and the contribution to Cameron band emission through dissociative excitation of CO$_2$ by EUV-generated photoelectrons can be more important.

The photodissociation of CO$_2$ producing CO in a$^3\Pi$ state is determined by solar flux mainly in the wavelength region 550 to 1050 Å (see figure 3.3). Table 3.1 presents the calculated photon production frequencies of CO(a$^3\Pi$) for two different solar flux models. The CO(a$^3\Pi$) production frequencies calculated for photoelectron impact on

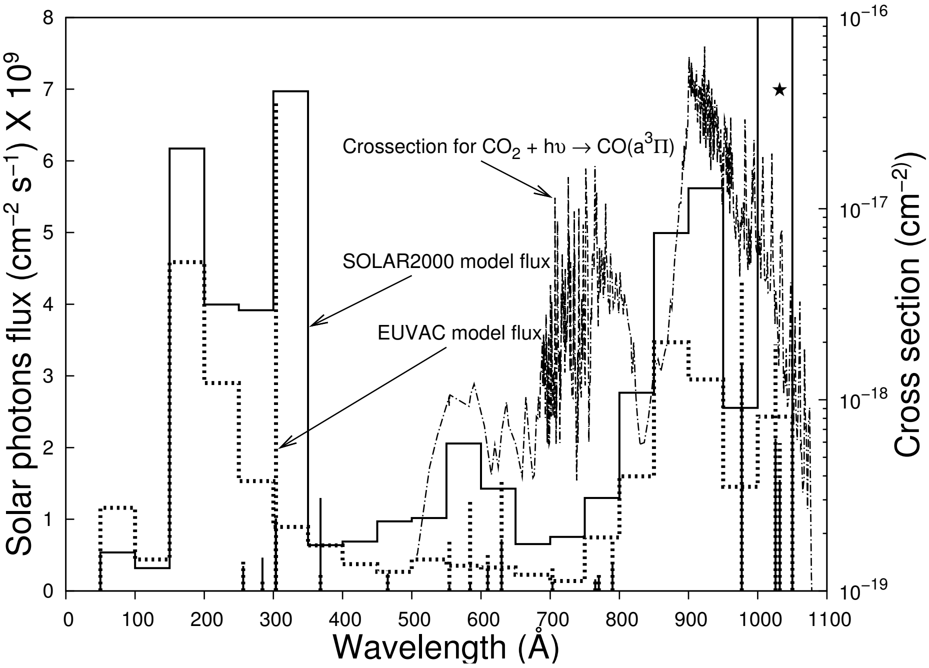

Figure 3.3: Solar EUV fluxes from EUVAC model [*Richards et al.*, 1994] and SOLAR2000 (S2K) model [*Tobiska*, 2004] for the day 13 March 1986. Significant differences in the two model solar EUV fluxes can be noticed. (★) The value of solar flux in SOLAR2000 (S2K) model in the bin 1000–1050 Å is 30 × 10^9 cm^{-2} s^{-1}. The photodissociation cross section of CO_2 producing CO($a^3\Pi$) is plotted on the right y-axis.

CO_2 and CO are also shown in the same table for the corresponding solar flux models. Our calculated photodissociation frequencies are about 50% to a factor of 2 lower than those reported by *Huebner et al.* [1992] which is mainly due to the difference in the solar fluxes used for calculation.

3.4 Results for 103P/Hartley 2

3.4.1 Production and loss of CO($a^3\Pi$)

Using EUVAC solar flux, the calculated radial profile of volume production rate for the various sources of CO($a^3\Pi$) at the relative abundance of 4% CO_2 and 0.5% CO are shown in Figure 3.4. At 100 km cometocentric distance, the dominant source of production of CO($a^3\Pi$) is electron impact on CO_2 (∼50%) followed by electron impact on CO (∼25%), and photodissociation of CO_2 (∼15%). The contributions from dissociative recombination reactions are quite small ($\leq$5%) at lower cometocentric distances, but the recombination of CO_2^+ is a significant (∼30%) source at 1000 km and beyond. Figure 3.5 shows radial profile of various loss frequencies of CO($a^3\Pi$) for the same relative composition of CO_2 and CO. Since the chemical lifetime of CO in excited state ($a^3\Pi$) is very short [∼3 ms; *Gilijamse et al.*, 2007], the radiative decay is the dominant loss

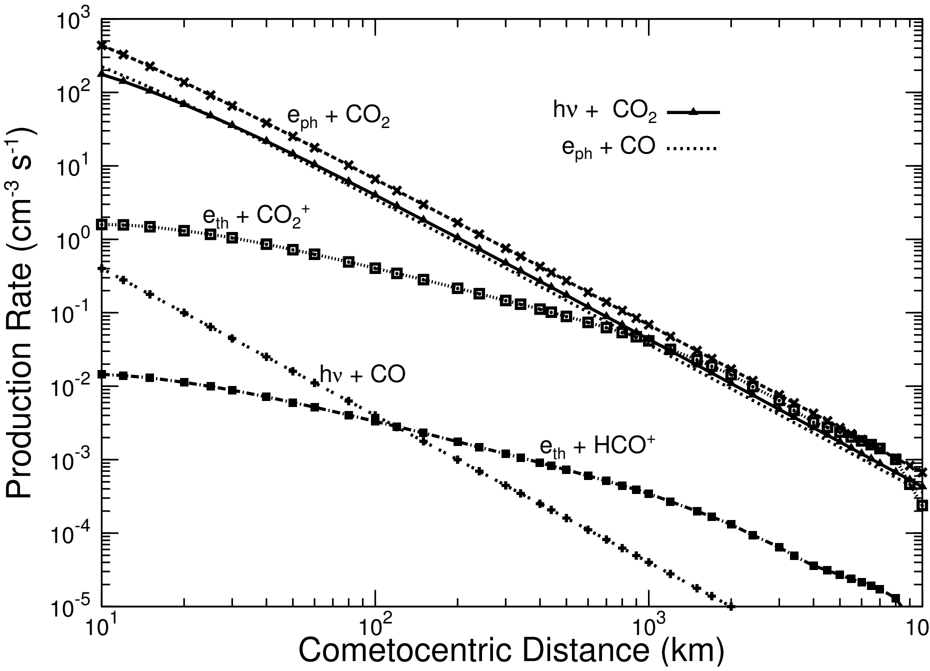

Figure 3.4: Calculated radial profiles of the production rate profiles of CO(a$^3\Pi$) in comet 103P/Hartley 2 for 0.5% CO and 4% CO_2 relative to H_2O production rate of 6.3 × 10^{28} s^{-1} using EUVAC solar flux on 18-19 September 1991.

process. Collisional quenching of CO(a$^3\Pi$) by cometary neutral species is negligible due to low gas production rate comet of 103P/Hartley 2. But in the case of large production rate comets, like Hale-Bopp, quenching by water would be a dominant loss process in the innermost part of the coma.

3.4.2 Intensity of Cameron band of CO molecule

The line of sight intensity is calculated at a given projected distance z from the cometary nucleus using production rates of different excitation processes of CO(a$^3\Pi$) as

$$I(z) = 2\int_z^R V(s)\, ds \tag{3.2}$$

where s is abscissa along the line of sight and V(s) is the corresponding emission rate. The maximum limit of integration R is taken as 10^5 km.

Figure 3.6 shows the modelled surface brightness profiles of Cameron band emission for different production processes of CO(a$^3\Pi$). The cometary coma is assumed to be spherically symmetric. The production rates are integrated up to 10^5 km along the line of sight at a given projected distances from the cometary nucleus, and converted into brightness. The brightness profiles are averaged over the projected area of slit (2870 × 954 km) corresponding to the HST observation [*Weaver et al.*, 1994]. The volume emission rate for 3 transitions (0-0, 1-0, and 0-1) of Cameron band emission are

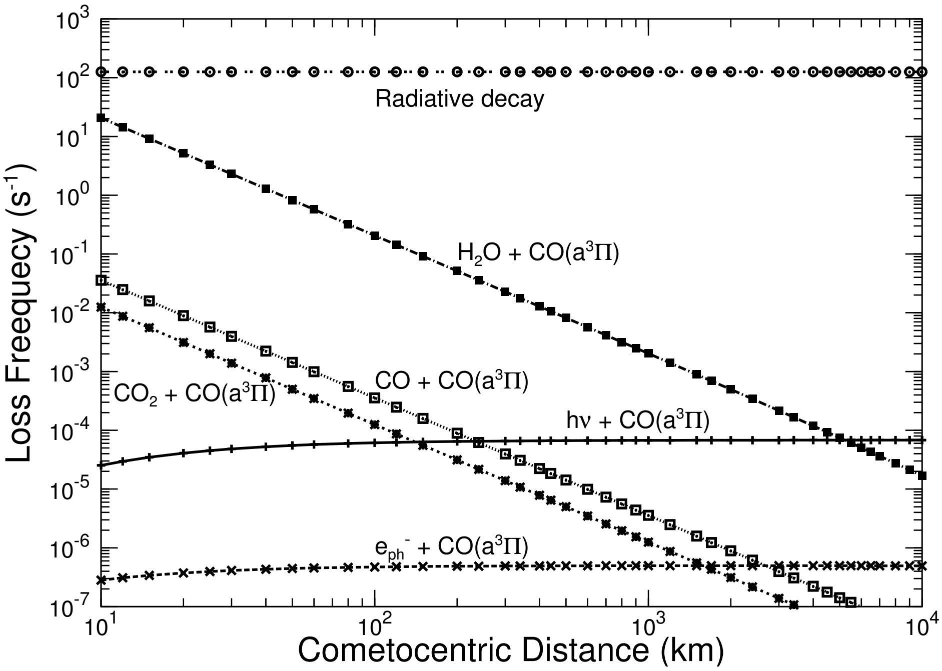

Figure 3.5: Calculated radial profiles of the loss frequencies of CO($a^3\Pi$) in comet 103P/Hartley 2 using EUVAC solar flux on 18-19 September 1991 for 0.5% CO and 4% CO_2 relative to H_2O production rate of 6.3 × 10^{28} s^{-1}.

calculated using the following formula

$$V_{\nu'\nu''}(r) = q_{o\nu'}(A_{\nu'\nu''}/\sum_{\nu''} A_{\nu'\nu''})\ V(r)\ exp(-\tau) \tag{3.3}$$

where V(r) is the total volume excitation rate of CO($a^3\Pi$) at cometocentric distance r, $q_{o\nu'}$ is the Franck-Condon factor for transition, $A_{\nu'\nu''}$ is Einstein transition probability from upper state ν' to lower state ν'', and τ is optical depth. Since resonance fluorescence is not an effective excitation mechanism for the Cameron band and the total gas production rate is only 6.3 × 10^{28} s^{-1}, the cometary coma can be safely assumed to be optically thin. The Franck-Condon factors are taken from *Nicholls* [1962] and branching ratios from *Conway* [1981]. The relative contributions of (1-0), (0-0), (0-1) transitions to the total Cameron band are 13.9%, 10.4%, and 14.7%, respectively.

Table 3.3 presents the model calculated slit-averaged brightness of (1-0), (0-0), (0-1) transitions of Cameron band, as well as total Cameron band brightness and height-integrated column brightness for different relative abundances of CO and CO_2 corresponding to the HST observation of comet 103P/Hartley 2 on September 18-19, 1991. Due to the absence of CO Fourth positive emission in this comet [*Weaver et al.*, 1994], the abundance of CO is constrained to 0.5%. However, a case of 1% of CO is considered to evaluate its implications on the results. This table also depicts fractional contribution of photodissociation of CO_2, photoelectron impact on CO and CO_2, and dissociative recombination of CO_2^+ to the total calculated brightness at 3 projected distances (10^2,

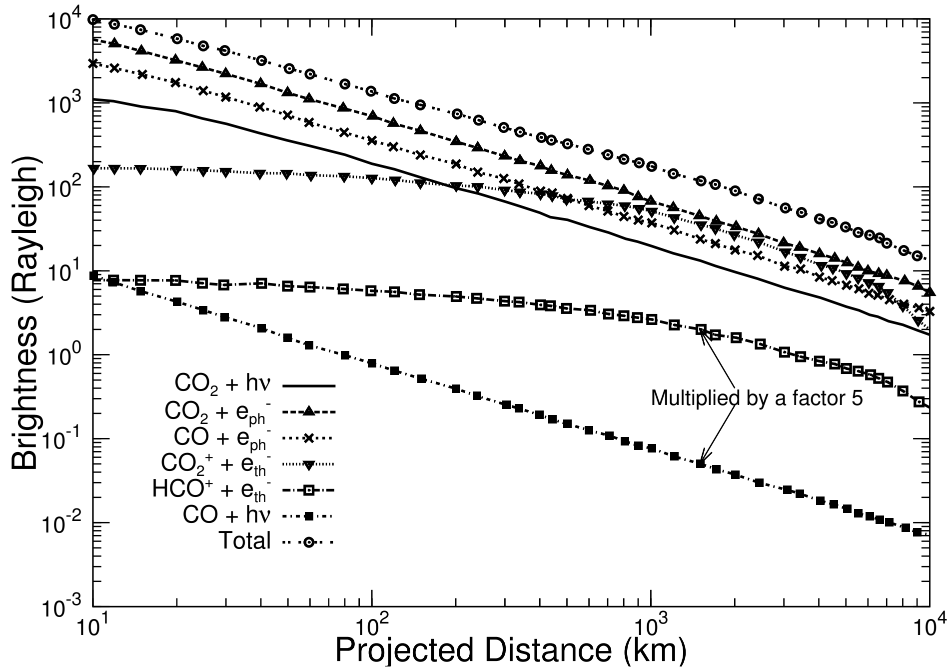

Figure 3.6: Brightness profile of Cameron band on comet 103P/Hartley 2 as a function of projected distance from nucleus for 4% CO_2 and 0.5% of CO using EUVAC solar flux on 18-19 sept 1991. Resonance fluorescence values and dissociative recombination of HCO^+ profiles are plotted after multiplication by a factor 5.

10^3, and 10^4 km) from the nucleus. Since the production rates of photodissociative excitation of CO_2, and photoelectron impact on CO and CO_2 depends on input solar flux model, results are presented for the EUVAC and S2K solar fluxes relevant to the date of comet observation which was in solar maximum condition.

The HST observation of 0-0 transition of Cameron band is 35 Rayleigh [*Weaver et al.*, 1994], which is consistent with model calculated brightness for the relative abundance of 4 to 5% of CO_2 and 0.5% CO when EUVAC solar flux is used. In this case, at 100 km, the photoelectron impact on CO_2 (50%) and CO (25%) contribute around 75%, while the contribution of photodissociative excitation of CO_2 is <15%. At 1000 km and beyond, the contribution due to electron impact on CO_2 and CO is about 60–70% while that of dissociative recombination of CO_2^+ is ∼15–30% and of photodissociative excitation of CO_2 is ∼10%. On an average, the photoelectron impact on CO_2 and CO contributes about 60-75% to the production of Cameron band emission, while photodissociative excitation of CO_2 contribute about 10-15% only. In the case of S2K solar flux model, the CO_2 abundance of 3 to 4% is required to match HST-observed Cameron band 0-0 transition brightness. In this case the contribution of photodissociative excitation of CO_2 is ∼20%, while the electron impact on CO_2 and CO together contribute ∼65%, to the total Cameron band emission. When the CO abundance is doubled to 1% of water, the relative contribution due to electron impact on

CO increases, resulting in the reduction (by ∼1%) in the requirement for CO_2 abundance to match the HST-observation brightness. However, there is no major change in the percentage contributions of photodissociation and photoelectron impact excitation of CO and CO_2.

Table 3.2: The calculated $CO(a^3\Pi)$ production frequency (s^{-1}) for three different processes at 1 AU.

Solar flux	$h\nu + CO_2$		$e_{ph} + CO_2$		e_{ph} + CO	
model	Solar min*	Solar max†	Solar min	Solar max	Solar min	Solar max
S2K	1.1×10^{-7}	5.6×10^{-7}	3.4×10^{-7}	9.7×10^{-7}	1.5×10^{-6}	4.3×10^{-6}
EUVAC	1.7×10^{-7}	2.6×10^{-7}	3.5×10^{-7}	8.9×10^{-7}	1.5×10^{-6}	3.7×10^{-6}

*Solar min: Solar minimum condition on 1 September 2010; †Solar max: Solar maximum condition on 18 September 1991; $h\nu$: solar photon, e_{ph} : photoelectron, and e_{th} : thermal electron

3.5 Calculations on comet 1P/Halley

The total gas production rate on comet 1P/Halley is taken as 6.9×10^{29} s^{-1}, which has been observed by Giotto mission [*Krankowsky et al.*, 1986]. Since cometary coma is dominated by water, 80% of total production rate is assumed to be H_2O. The in-situ gas measurements at comet 1P/Halley made by Giotto Neutral Mass Spectrometer (NMS) on the encounter date 13 March 1986 showed that CO_2 abundance is 3.5% of water [*Krankowsky et al.*, 1986]. On the same day, based on IUE observation, *Feldman et al.* [1997] derived CO_2 abundance of 4.3%. *Eberhardt et al.* [1987] suggested that below 1000 km radial distance, nuclear CO production rate can be 7% of water. The radial profile of CO calculated by *Eberhardt et al.* [1987] showed almost a constant value of CO relative abundance ($\leq$15%) above 15000 km. This increase in CO abundance is attributed to the presence of CO extended sources in the cometary coma. The IUE-derived average production rate of CO is 4.7% [*Feldman et al.*, 1997]. In the model I have taken 4% CO_2 and 7% CO in the cometary coma as the standard input for the model. A case study for the extended CO density profile is taken directly from Giotto NMS observation [*Eberhardt et al.*, 1987] is also conducted. Further, the relative abundances of CO_2 and CO are varied to assess the effect on the intensity of Cameron band emission and different production channels of $CO(a^3\Pi)$. The electron temperature profile, required for dissociative recombination reactions, is taken from *Körösmezey et al.* [1987].

Table 3.3: The Calculated CO Cameron band brightness of comet 103P/Hartley 2 for different conditions

Relative abundance		HST-slit averaged brightness (R)			Percentage contribution to total Cameron band for different processes at three different projected radial distances (km)												Total Cameron band brightness (R)	
CO_2 (%)	CO (%)				Photodissociation of CO_2			Photoelectron impact on CO_2			Photoelectron impact on CO			Recombination of CO_2^+			HST-Slit Average	Height integrated nadir view
		(1-0)	(0-0)	(0-1)	10^2	10^3	10^4	10^2	10^3	10^4	10^2	10^3	10^4	10^2	10^3	10^4		
EUVAC*																		
7	0.5	68	51	72	15	12	15	57	42	51	17	12	15	10	32	17	489	4769
5	0.5	51	39	54	14	11	14	53	40	48	22	17	21	9	30	16	369	3710
4	0.5	43	32	45	13	11	13	50	38	45	26	20	25	9	29	15	309	3172
3	0.5	34	26	36	12	10	12	46	36	42	32	26	30	8	26	13	250	2628
2	0.5	26	20	28	11	9	10	39	32	36	42	34	40	7	23	12	190	2078
4	1	51	38	54	11	9	11	40	32	36	41	33	38	7	24	12	311	3948
3	1	43	32	46	10	8	10	35	29	32	48	40	45	6	21	11	311	3420
S2K*																		
7	0.5	86	64	91	26	21	25	48	36	44	15	11	14	10	31	16	622	5928
5	0.5	65	48	68	25	20	24	45	35	42	20	15	19	9	29	15	467	4586
4	0.5	54	40	57	23	19	22	43	33	40	24	19	22	8	28	14	390	3903
3	0.5	43	32	46	22	18	21	40	31	37	30	23	28	8	26	13	313	3210
2	0.5	33	25	35	19	16	18	35	28	32	39	32	37	8	23	11	236	2508
3	1	53	40	56	17	15	17	31	25	29	45	37	42	6	21	10	384	4093
2	1	43	32	45	14	12	14	25	21	23	55	47	52	5	18	8	308	3411

*Solar flux on 18 September 1991; †Relative contribution of band in total nadir view intensity.

3.6 Results for comet 1P/Halley

3.6.1 Production and loss of CO($a^3\Pi$)

The calculated production rate profiles of CO($a^3\Pi$) using solar EUVAC and S2K models for relative abundance of 4% CO_2 and 7% CO are shown in Figure 3.7. For both solar EUV flux models, the peak production rate occurs at cometocentric distance ~20 km. The major production mechanism of CO($a^3\Pi$) is the photoelectron impact on CO, whose contribution is ~70% to the total CO($a^3\Pi$) production. On using the S2K solar flux, the calculated total production rate is 1.5 times larger than that obtained using the EUVAC flux. This variation is mainly due to the difference in the input solar EUV flux (cf. Figure 3.3) and subsequently EUV-generated photoelectron flux (cf. Figure 3.2). In the wavelength region 700–1050 Å, the S2K model solar flux is a factor of ~2.5 larger than the EUVAC model (cf. Figure 3.3). As shown in Figure 2.7, the photodissociative excitation cross section of CO_2 producing CO($a^3\Pi$) maximizes around 880–1000 Å. Further, the S2K solar flux in the 1000–1050 Å wavelength bin is around 20 times higher than the EUVAC flux.

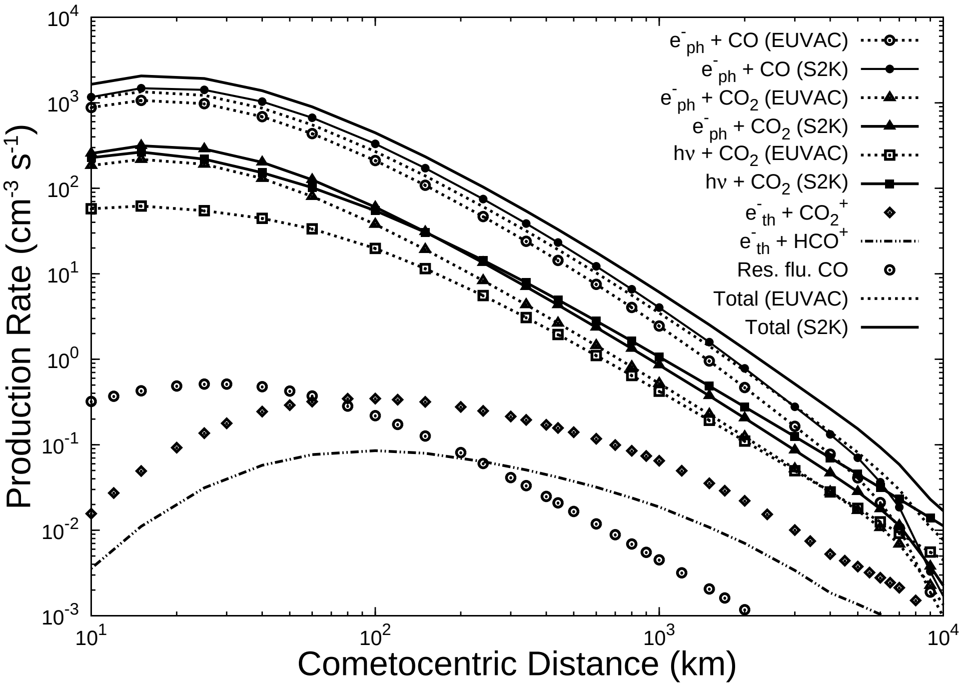

Figure 3.7: Calculated radial profiles of various production mechanisms of CO($a^3\Pi$) in comet 1P/Halley on 13 March 1986 for relative abundance of 4% CO_2 and 7% CO. The calculated profiles for dissociative recombination of CO_2^+ and HCO^+, and resonance fluorescence of CO are shown for EUVAC solar flux only. Res. flu. = resonance fluorescence of CO molecule, e^-_{ph} = photoelectron, hν = solar photon, and e^- = thermal electron.

Moreover, in the inner cometary coma, below cometocentric distance of 50 km, the optical depth for solar flux at wavelengths below 200 Å and above 1000 Å is smaller compared to other wavelengths because of smaller absorption cross sections of neutral species (mainly water). The rate of photodissociative excitation of CO_2 molecule into $CO(a^3\Pi)$ mainly depends on the degradation of solar flux in the wavelength region 850–1050 Å. Hence, in the innermost coma ($\leq$50 km), for a given relative abundance of CO_2, the production rate of $CO(a^3\Pi)$ via photodissociation of CO_2 is determined by the solar flux in the wavelength bin 1000–1050 Å and at wavelengths 1025.7 Å (H I) and 1031.9 Å (O VI). The calculated photodissociation rates of CO_2 producing $CO(a^3\Pi)$ at 0.9 AU are 1.66×10^{-7} s^{-1} and 5.28×10^{-7} s^{-1} using EUVAC and S2K solar fluxes, respectively, on 13 March 1986.

From Figure 3.2 it is seen that the calculated steady state photoelectron flux using two solar flux models differ in magnitude by a factor of 2. Since the cross section for electron impact on CO producing $CO(a^3\Pi)$ peaks at lower energies ($\sim$10 eV) where the photoelectron flux is also high ($\sim 10^8$ cm^{-2} s^{-1} eV^{-1} sr^{-1}; cf. Figure 3.2), the electron impact excitation of CO is the major production source of Cameron band emission. At larger (>5000 km) cometocentric distances, due to decrease in photoelectron flux, the photodissociative excitation of CO_2 starts becoming an increasingly important process (cf. Figure 3.7). Contributions from dissociative recombination reactions and resonance fluorescence of CO are more than two orders of magnitude lower compared to major production processes.

Since the lifetime of $CO(a^3\Pi)$ is about $\sim$3 ms, the quenching of the excited $a^3\Pi$ metastable state by various cometary species is not very efficient. The calculated loss rate profiles of $CO(a^3\Pi)$ for various processes are shown in Figure 3.8. The radiative de-excitation is the main loss process. Very close to the nucleus, the loss due to quenching of $CO(a^3\Pi)$ by water is comparable to the radiative de-excitation. Quenching by water molecule would be a more significant loss process of $CO(a^3\Pi)$ in a high water production rate comets like Hale-Bopp. The calculated number density profile of $CO(a^3\Pi)$ is shown in Figure 3.9. Above 100 km, the density profile of $CO(a^3\Pi)$ mostly following the number density profiles of the parent species CO_2 and CO. Since peak absorption of solar photons is around 50 km the which results in maximum formation of $CO(a^3\Pi)$ is below 100 km.

3.6.2 Intensity of CO Cameron bands

The calculated total production rate is integrated up to 10^5 km to obtain the height-integrated column intensity of Cameron band emission which is presented in Table 3.4. These brightness profiles are then averaged over the projected area 6600 × 11000 km^2 corresponding to the IUE slit dimension $9.07'' \times 15.1''$ centered on nucleus of comet 1P/Halley at geocentric distance 0.96 AU on 13 March 1986. The volume emission rate

Table 3.4: The Calculated brightness of the CO Cameron band at comet 1P/Halley for different conditions on 13 March 1986.

Relative abundance		IUE-slit averaged brightness (R)			Percentage contribution to total Cameron band for different processes at three different projected radial distances (km)												Total Cameron band brightness (R)	
CO_2 (%)	CO (%)				hν + CO_2			e^-_{ph} + CO_2			e^-_{ph} + CO			e^-_{th} + CO_2^+			IUE-slit averaged	Height integrated column
		(1-0)*	(0-0)	(0-1)	10^2	10^3	10^4	10^2	10^3	10^4	10^2	10^3	10^4	10^2	10^3	10^4		
EUVAC																		
4	Ext†	59	44	63	9	14	52	15	15	11	74	66	25	0.5	2	5	430	10946
4	7	51	38	54	9	15	65	14	16	13	75	64	12	0.5	3	5	308	8836
3	7	46	34	48	7	12	63	11	13	12	80	70	15	0.5	2	5	331	10626
4.3	4.7	45	34	48	11	19	69	20	21	13	68	55	9	0.5	3	6	329	9582
S2K																		
4	Ext	87	66	96	14	19	61	13	13	9	71	62	20	0.5	3	4	638	15612
4	7	77	58	82	14	21	73	13	14	10	71	60	10	0.5	2	5	559	15841
3	7	68	51	72	11	17	71	10	12	9	77	66	11	0.5	2	5	490	14991
4.3	4.7	67	50	70	16	24	76	17	18	10	65	52	6	0.5	3	5	472	13582

*The intensity of Cameron (1-0) band observed by IUE is 37 ± 6 Raleigh on 13 March 1986.;

†Ext: Extended CO distribution.;

hν is photon, e^-_{ph} is photoelectron and e^-_{th} is thermal electron.;

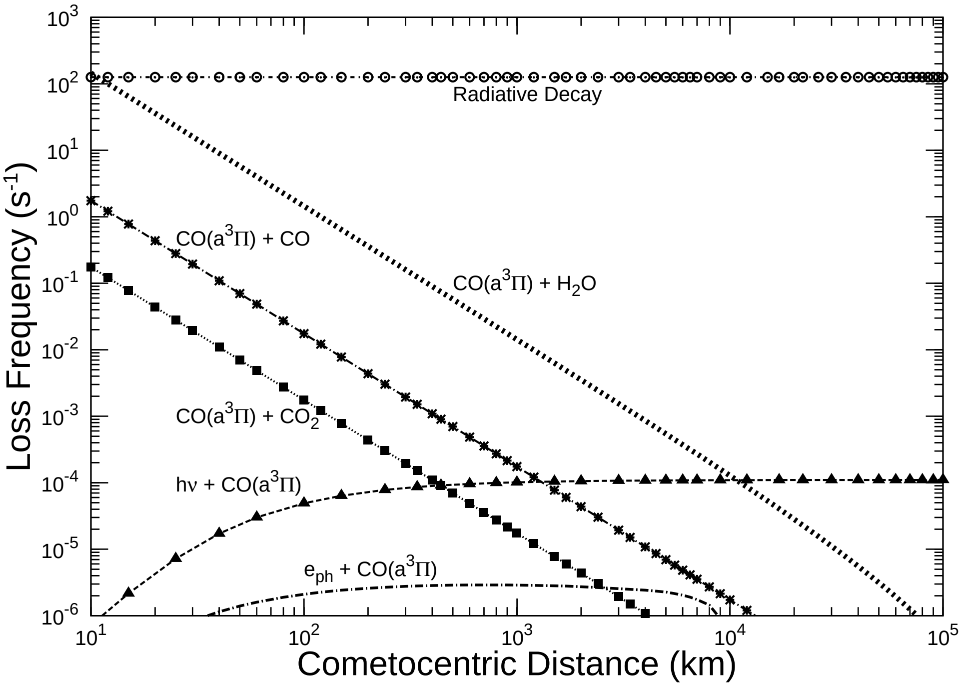

Figure 3.8: Radial profiles of various loss mechanisms of CO(a$^3\Pi$) in comet 1P/Halley for 4% CO_2 and 7% CO relative abundances using EUVAC solar flux. Photoelectron impact ionization of CO(a$^3\Pi$) is plotted after multiplying by a factor 20.

for 3 transitions (0-0, 1-0, and 0-1) of the Cameron band are calculated as described in Section 3.4.2. The IUE projected field of view is calculated for IUE slit dimension used in observation, which vary according to the geocentric distance of the comet in March 1986.

The calculated brightness profiles for each of the production processes as a function of projected distances from nucleus are shown in Figure 3.10. At 100 km projected distance, the contribution due to photoelectron impact excitation of CO to the total Cameron band intensity is about a factor 4 higher than the dissociative excitation processes of CO_2, while contributions of other production processes are around two orders of magnitude smaller. Around 1000 km projected distance, both photodissociative excitation and electron impact dissociative excitation of CO_2 are contributing equally to the total Cameron band intensity. The photodissociative excitation of CO_2 dominates the electron impact excitation processes above 5000 km.

The calculated relative contributions of (1-0), (0-0), and (0-1) bands to the total Cameron band are 13.9%, 10.4%, and 14.5%, respectively. The intensities of (1-0), (0-0) and (0-1) Cameron bands of CO molecule are calculated as a function of relative abundances of CO_2 and CO. The calculated percentage contributions of different production processes of Cameron band at three projected distances for two different solar flux models are presented in Table 3.4.

The IUE-observed 1-0 Cameron band emission on 13 March 1986 is 37±6 Rayleighs.

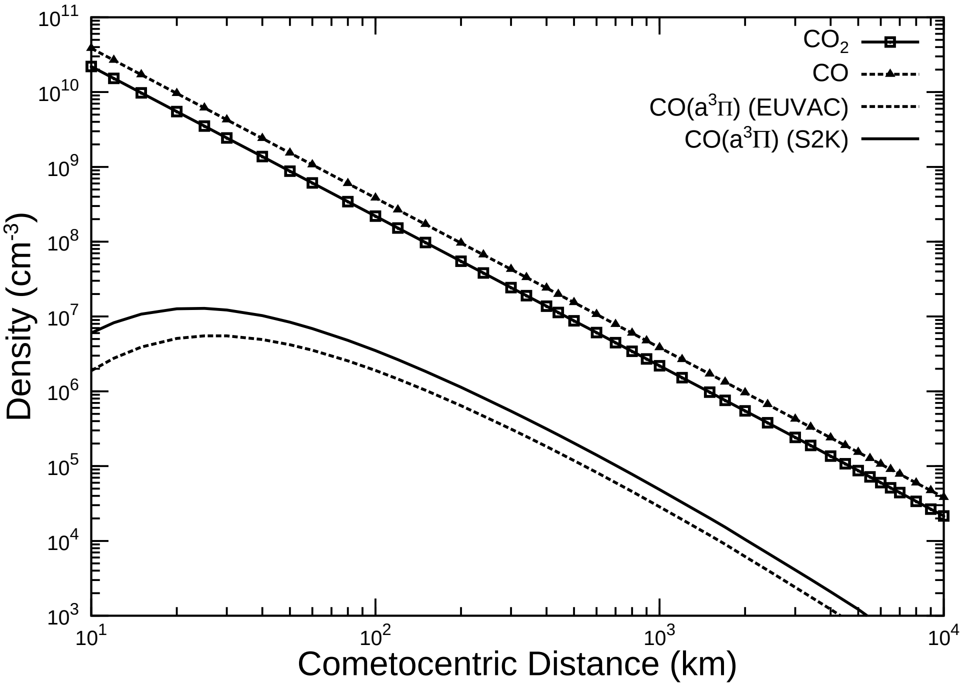

Figure 3.9: The calculated radial profiles of number density $CO(a^3\Pi)$ for SOLAR2000 (S2K) and EUVAC solar flux models in comet 1P/Halley. The density of $CO(a^3\Pi)$ is plotted after multiplying by a factor 10^6. The number density profiles of CO_2 and CO are also shown for 4% and 7% relative abundances, respectively.

Using EUVAC solar flux as input, our model calculated 1-0 Cameron band emission intensity for the relative abundance 4% CO_2 and extended distribution of CO is 59 Rayleigh which is higher than IUE observed intensity by a factor 1.3 to 2. Taking CO_2 abundance as 4% and CO abundance as 7% from nucleus, the calculated 1-0 intensity is 51 Rayleigh, which is higher than the IUE-observed value by a factor 1.2 to 1.6. The calculated intensity for 3% CO_2 and 7% CO is 46 Rayleighs, which is consistent only with the upper limit of IUE-observed intensity. In all the above cases, below 1000 km projected distances, the contribution of photodissociation of CO_2 to the Cameron band emission is <15%, while the electron impact on CO contributes 65 to 80%. We have also calculated the intensity of Cameron band taking the *Feldman et al.* [1997] derived abundances of 4.3% CO_2 and 4.7% CO. The calculated intensity of 1-0 Cameron band emission in this case is 40 R, which is consistent with the observed value of 37 ± 6 R on 13 March 1986 (cf. Table 3.5). The calculated 1-0 Cameron band emission intensity at various projected distances in the IUE-slit field of view is presented in Figure 3.11; the circular contours and gray scale provide information on brightness variation.

The calculated results using S2K solar flux model for the above discussed relative compositions of CO_2 and CO are also presented in Table 3.4. The calculated intensities are higher by a factor of ~1.5, which is mainly due to higher solar flux in S2K model and subsequently EUV-produced photoelectron flux (cf. Figs. 3.3 and 3.2).

Table 3.5: The Calculated CO Cameron band brightness of comet 1P/Halley on different days of IUE observation.

Date in March 1986	r (AU)	Δ (AU)	Q_{H_2O} (10^{29} s^{-1})†	Relative abundance (%)†		Ratio Q_{CO_2} /Q_{CO}	IUE-slit averaged brightness (R)			Percentage contribution to the IUE-slit averaged total Cameron band emission for different excitation processes (%)				IUE-slit averaged total brightness (R)
				CO_2	CO		(1-0)	(0-0)	(0-1)	hν+CO_2	e^-_{ph}+CO_2	e^-_{ph}+CO	e^-_{th}+CO_2^+	
EUVAC														
9	0.84	1.07	7.50	6.0	6.5	0.92	75 [64 ± 9]*	57	80	22	22	51	3	550
11	0.87	1.02	5.84	5.1	4.3	1.2	43 [43 ± 8]	32	45	25	24	44	4	310
13	0.90	0.96	5.98	4.3	4.7	0.9	40 [37 ± 6]	30	43	22	21	51	4	293
16	0.95	0.89	4.90	6.3	8.2	0.77	42 [44 ± 9]	32	45	23	20	51	4	307
18	0.97	0.84	4.92	2.8	4.1	0.68	24 [20 ± 6]	18	26	20	19	57	3	177
S2K														
9	0.84	1.07	7.50	6.0	6.5	0.92	116 [64 ± 9]	87	123	31	19	44	4	837
11	0.87	1.02	5.84	5.1	4.3	1.2	66 [43 ± 8]	49	69	33	21	39	4	475
13	0.90	0.96	5.98	4.3	4.7	0.9	62 [37 ± 6]	46	65	30	19	45	4	446
16	0.95	0.89	4.90	6.3	8.2	0.77	64 [44 ± 9]	48	68	30	18	45	4	456
18	0.97	0.84	4.92	2.8	4.1	0.68	37 [20 ± 6]	28	39	25	16	53	3	262

*The value in square brackets is IUE-observed (1-0) Cameron band intensity; hν is photon, e^-_{ph} is photoelectron and e^-_{th} is thermal electron.

†The production rates of H_2O and abundances of CO_2 & CO are taken from *Feldman et al.* [1997].

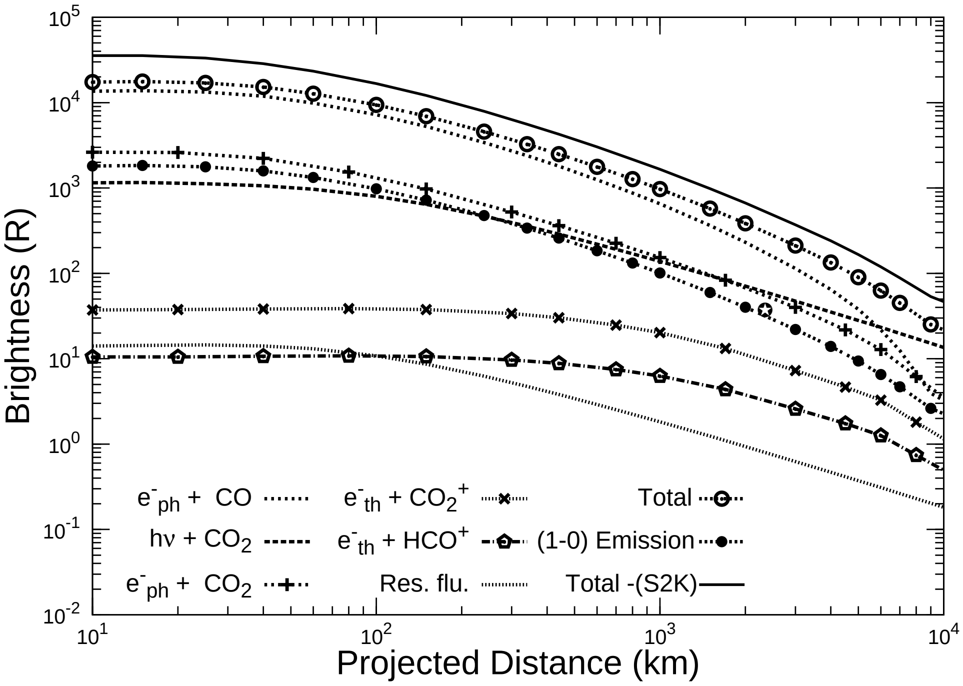

Figure 3.10: The integrated Cameron band brightness profiles as a function of projected distance from nucleus for different production processes of the Cameron band, using EUVAC solar flux model and relative contribution of 4% CO_2 and 7% CO in comet 1P/Halley. The calculated brightness profiles for Cameron (1-0) band for EUVAC solar flux and total brightness for S2K solar flux are also shown.

The intensity of Cameron band for different days of IUE observations have been calculated taking the same H_2O, CO_2, and CO production rates as quoted in *Feldman et al.* [1997]. The calculated intensity of 1-0 emission is consistent with the IUE-observation for the EUVAC solar flux model, while it is higher by a factor of 1.5 on using the S2K solar flux. The calculations presented in Table 3.5 show that for a change in the CO_2/CO abundance ratio by a factor of 2, the total photoelectron impact excitation contribution changes by only ∼10%; it varies from 68 to 76% (60 to 69%) of the total IUE-observed intensity for EUVAC (S2K) solar flux model. The photoelectron impact excitation of CO alone contribute around 45 to 55% (40 to 60%) to the Cameron band intensity when EUVAC (S2K) solar flux is used. The contribution of photodissociation of CO_2 to the IUE-observed Cameron band brightness is around 20% (30%) for EUVAC (S2K) solar flux model when the abundances of CO and CO_2 in the comet are almost equal. These computations show that in the IUE field of view the photoelectrons are the major production source (60-75% contribution) for the Cameron band emission, whereas the contribution due to photons is small (20-35%).

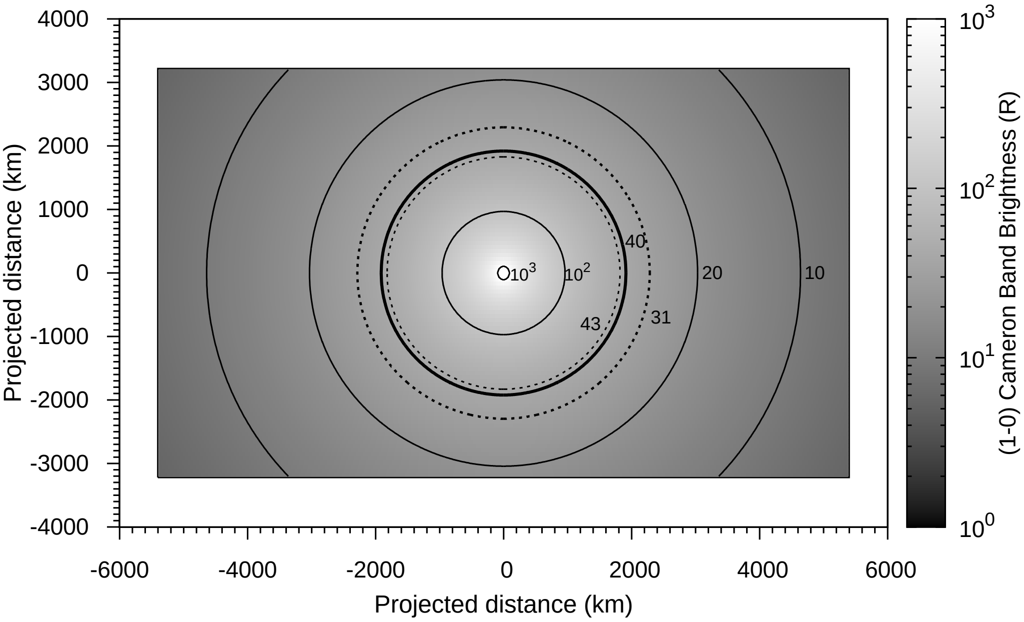

Figure 3.11: The calculated (1-0) Cameron band emission brightness in the IUE projected field of view on 13 March 1986, assuming spherical symmetry, using EUVAC solar flux model, for relative contribution of 4.3% CO_2 and 4.7% CO in comet 1P/Halley. The rectangle represent the projected field of view corresponding to IUE slit dimension of 9.07″ × 15.1″ centered on the nucleus of comet 1P/Halley, which is 11000 × 6600 km. The gray scale represent the calculated brightness with contours (solid lines) for 10^3, 10^2, 20, and 10 R marked in the figure. The calculated brightness averaged over IUE slit projected area (40 R) is shown by thick black contour between two dotted line contours which represent the upper and lower limits of IUE observed intensity value (37 ± 6 R).

3.7 Discussion

To explain the Cameron band emission in comet 103P/Hartley 2, *Weaver et al.* [1994] considered five possible production mechanisms of CO($a^3\Pi$). The modelled CO Cameron band emission by *Weaver et al.* [1994] suggested that 60% of total CO($a^3\Pi$) production can be through photodissociative excitation of CO_2; the remaining was attributed to other excitation processes. However the present study (cf., Table 3.3) suggest that whatever be the relative abundances of CO_2 and CO, and the solar input flux, the photodissociation contribution is in the range of 5–20%, while photoelectron impact excitation contribution is about 50–80%. We conclude that photoelectron impact excitation of Cameron band in comets is much more important than that was thought previously. Further, the contribution due to photoelectron impact excitation of CO is significant and vary between 20-50%. We have also shown that dissociative recombination of CO_2^+ ion is also a significant source of Cameron band at cometocentric distances $\geq$1000 km with contribution becoming as high as 30%. Hence, the derivation of CO_2 abundances based on the assumption that photodissociation of CO_2 is major production mechanism of $CO(a^3\Pi)$ should be revisited. The results presented in Section 3.4 suggest that Cameron band emission may not be used to probe cometary CO_2 abundance uniquely.

Feldman et al. [1997] assumed that photodissociative excitation of CO_2 is the only source of Cameron band emissions in comet 1P/Halley and derived CO_2 relative abundances in this comet. But the calculations of CO Cameron band in comet 103P/Hartley 2, have demonstrated that 60 to 90% of $CO(a^3\Pi)$ production is through the photoelectron impact on CO_2 and CO and that the contribution of photodissociation of CO_2 is quite small (20–30%). Comet 103P/Hartley 2 is depleted in CO (relative abundance <1%). But in the case of comet 1P/Halley the CO abundance is relatively higher compared to that on the 103P/Hartley 2, and hence the contribution due to direct excitation of CO by electron impact is much larger. The calculations presented in Tables 3.4 and 3.5 renders that in case of comets where CO_2/CO abundance ratio is closer to one or larger than one, the emission intensity of Cameron band is mainly controlled by the abundance of CO in the inner cometary coma. The photoelectron impact excitation of CO is the main production mechanism for the production of Cameron band emission, but not the photodissociative excitation of CO_2 as suggested or assumed in earlier studies [*Weaver et al.*, 1994; *Weaver et al.*, 1997; *Feldman et al.*, 1997]. Thus, in comets that have significant CO abundance the electron impact excitation of CO producing $CO(a^3\Pi)$ can be an efficient excitation mechanism for Cameron band emission. Since CO Cameron band emission is mainly governed by electron impact excitation reactions, this emission can be used to track the photoelectron density mainly in the energy range 10 to 15 eV near the nucleus.

In the case of comet 103P/Hartley 2, which has an order of magnitude lower gas production rate and much lower CO (abundance $< 1\%$) than comet 1P/Halley, the dissociative recombination of CO_2^+ becomes a competing production mechanism at larger ($>10^4$ km) cometocentric distances [*Bhardwaj and Raghuram*, 2011]. However, in comparison, on comet 1P/Halley the production rates of H_2O, CO_2, and CO are so high that the photon and photoelectron impact reactions are dominant throughout the inner cometary coma.

3.7.1 Effect of model parameters on the calculations

3.7.1.1 Electron impact cross sections

In this section I will discuss on the electron impact of cross sections of CO_2 and CO producing $CO(a^3\Pi)$. The threshold for exciting CO molecule in the metastable $a^3\Pi$ state is 6 eV and the peak value of cross section occurs around 10 eV (cf. Figure 3.2). The cross section for electron impact excitation of CO producing $CO(a^3\Pi)$ reported by *Jackman et al.* [1977] is theoretically fitted based on Born approximation and experimental measurements of *Ajello* [1971]. The uncertainty associated with measurement is about 75%. However, the uncertainty in the cross section at energies less than 15 eV is 35% [*Ajello*, 1971], where the contribution of electron impact excitation plays a major role (cf. Fig 3.2). The measured electron impact on CO producing CO($a^3\Pi$) by *Furlong and Newell* [1996] differ at the peak by a factor of 2 with the *Jackman et al.* [1977] value. (cf. Figure 3.2). The threshold for dissociation of CO_2 molecule into CO($a^3\Pi$) state is 11.45 eV. *Ajello* [1971] measured Cameron band emission cross sections in the wavelength region 1950–2500 Å by exciting CO_2 molecule through electron impact. *Erdman and Zipf* [1983] measured the excitation cross section value of CO($a^3\Pi$) due to electron impact on CO_2 at 80 eV as 2.4×10^{-16} cm^{-2}. *Bhardwaj and Jain* [2009] modified the fitting parameters given by *Jackman et al.* [1977] for the excited states of 12.6 eV and 13.6 eV of CO_2 molecule to match the cross section value measured by *Erdman and Zipf* [1983] at 80 eV [for more discussion on these cross sections see *Ajello*, 1971; *Sawada et al.*, 1972; *Bhardwaj and Jain*, 2009]. *Avakyan et al.* [1998] corrected *Ajello* [1971] reported cross sections based on measurements of *Erdman and Zipf* [1983]. The difference in the CO($a^3\Pi$) cross sections given by *Avakyan et al.* [1998] and *Bhardwaj and Jain* [2009] below 30 eV is about a factor of 2 (cf. Fig 3.2).

Using electron impact CO($a^3\Pi$) excitation cross sections from *Furlong and Newell* [1996] for CO and from *Avakyan et al.* [1998] for CO_2, and using EUVAC solar flux, the calculated emission intensity of 1-0 Cameron band on comet Halley, for a given relative abundance of CO and CO_2, is larger by a factor 2. In these calculations the contribution of electron impact excitation of CO is increased from 70% to 85% at cometocentric distances below 10^3 km and 40% to 60% at distances above 10^3 km. On using these cross sections, the percentage contribution of photoelectron impact excitation of CO to the total Cameron emission in the IUE-slit-averaged intensity is found to increase by 10%. However, no significant change is found due to change in the electron impact excitation cross section of CO_2. In this case the contribution from photodissociative excitation of CO_2 is decreased by 10%.

3.7.1.2 Solar EUV-UV flux

In the present study the solar EUV fluxes on each day of observation was obtained by using EUVAC and S2K solar flux models at 1 AU and scaled them according to the heliocentric distance of comet. The solar EUV fluxes given by two different model for the same day differs by few factors in magnitude in various bins which can be seen in Figure 3.3. The solar flux between wavelengths ∼600 and 1100 Å mainly governs the photodissociation of CO_2 in producing CO($a^3\Pi$). The solar fluxes given by two models in the former wavelength region significantly varies. However, the photorates calculated using different S2K and EUVAC solar fluxes, which are presented in Table 3.1 differ by 1.5 to 2. The calculations presented in Tables 3.3, 3.4 and 3.5 shows that by using solar flux from S2K model the calculated intensities of different CO Cameron transition are higher than the intensities calculated by EUVAC model fluxes by 1.5 to ∼2. The continuous measurements of solar flux with high resolution is very much important to predict the intensities of cometary emissions.

3.8 Summary

We developed a model to study the production and loss process of CO($a^3\Pi$) in comets 103P/Hartley 2 and 1P/Halley which had different CO and CO_2 abundances quantitatively. Based on the model calculations we conclude that in comets the photodissociative excitation of CO_2 is not the dominant source of CO($a^3\Pi$) and thus the Cameron band emission can not be used to derive the CO_2 abundances in comets. This work demonstrated that in comets the photoelectron impact excitation of CO plays a major role in determining the brightness of Cameron band and not the photodissociation of CO_2. Since the Cameron band emission is a forbidden transition and electron impact is the major excitation mechanism, this emission is suitable to track photoelectron density in the inner cometary coma rather than the CO_2 abundance.

Chapter 4

Red and Green emissions of atomic oxygen at heliocentric distance of 1 AU

Contents

4.1 Introduction 66

4.2 Model 69

4.3 Calculations on comet C/1996 B2 Hyakutake 72

4.4 Results for comet C/1996 B2 Hyakutake 72

4.4.1 Production and loss of O(^{1}S) 72

4.4.2 Production and loss of O(^{1}D) 74

4.4.3 Green and red-doublet emission intensities 77

4.5 Calculations on comet C/1995 O1 Hale-Bopp 84

4.6 Results for comet C/1995 O1 Hale-Bopp 86

4.6.1 Production and loss of O(^{1}S) 86

4.6.2 Production and loss of O(^{1}D) 87

4.6.3 Green and Red-doublet emission intensities 92

4.6.4 Radiative efficiencies of O(^{1}S) and O(^{1}D) atoms 96

4.6.5 Excess velocities of O(^{1}S) and O(^{1}D) 98

4.7 Discussion 100

4.7.1 Comparison of model calculations with observations 102

4.7.1.1 Atomic oxygen emission lines on comet C/1996 B2 Hyakutake 102

4.7.1.2 Atomic oxygen [OI] 6300 Å emission line on comet Hale-Bopp 105

4.7.1.3 Width of green and red-doublet emission lines . . . 108

4.7.2 Effect of model parameters on the calculated intensities . . . 109

4.7.2.1 Expansion velocity of neutrals 109
4.7.2.2 Relative abundances of neutral species 110
4.7.2.3 Effect of slit dimension on the derived O(^{1}D) production rate 112
4.8 Summary and Conclusions 112

4.1 Introduction

It is a known fact that at smaller (<2 AU) heliocentric distances, the inner cometary coma is dominantly composed of H_2O. The infrared emissions of H_2O molecule are not easily accessible from ground because of strong attenuation by the terrestrial atmosphere. Since H_2O does not show any spectroscopic transitions in ultraviolet or visible regions of solar spectrum, one can estimate it's abundance indirectly based on the emissions from daughter products, like OH (3080 Å), O (6300, 6364 Å) and H (Ly-α). Thus, tracking these emissions of the dissociative products of H_2O has became an important diagnostic tool in estimating the production rate as well as in understanding the spatial distribution of H_2O in comets [*Delsemme and Combi*, 1976; *Delsemme and Combi*, 1979; *Fink and Johnson*, 1984; *Schultz et al.*, 1992; *Morgenthaler et al.*, 2001; *Furusho et al.*, 2006]. For estimating the density distribution of H_2O from the emissions of daughter species, one has to account for photochemistry and associated emission processes.

The major dissociative channel of H_2O is the formation of H and OH, but a small fraction is also possible in O(^{3}P, ^{1}S, ^{1}D) and H_2 production. The radiative decay of metastable ^{1}D and ^{1}S states of atomic oxygen leads to emissions at wavelengths 6300, 6364 Å (red doublet), 2972 Å and 5577 Å (green line), respectively. The energy levels of atomic oxygen and these forbidden transitions are shown in Figure 4.1. Even though these emissions are accessible from ground-based observatories, most of the times they are contaminated by telluric night sky emissions as well as emissions from other cometary species. Doppler shift of these lines, which is a function of the relative velocity of comet with respect to the Earth, offers a separation from telluric emissions provided a high resolution cometary spectrum is obtained. In most of the cometary observations it is very difficult to separate the green line in optical spectrum because of the contamination from cometary C_2 (1-2) P-branch band emission. The red line 6300 Å emission is also mildly contaminated by the Q-branch emission of NH_2 molecule, but in high resolution spectrum this can be easily resolved.

Since these atomic oxygen emissions are dipole forbidden electronic transitions solar radiation cannot populate atoms in these excited states via resonance fluorescence. The photodissociative excitation and electron impact dissociative excitation of neutral species containing atomic oxygen, and ion-electron dissociative recombination of O-bearing ion species, can produce these metastable states [*Bhardwaj and Haider*, 2002]. If O(^{1}D) is

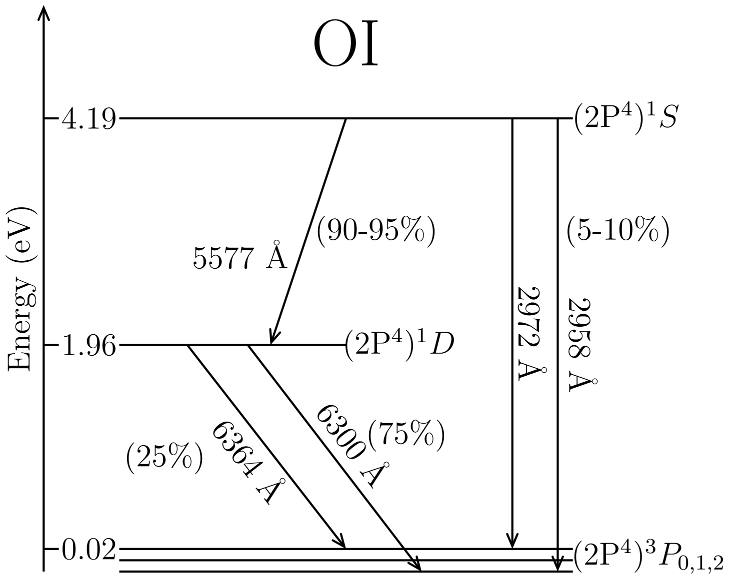

Figure 4.1: Schematic energy level diagram of atomic oxygen showing different spectroscopic transitions related to ^{1}S and ^{1}D metastable states.

not quenched by ambient cometary species, then photons at wavelengths 6300 and 6364 Å will be emitted in radiative decay to the ground ^{3}P state. Only about 5-10% of O(^{1}S) atoms result in 2972 and 2958 Å emissions via direct radiative transition to the ground ^{3}P state and around 90-95% of O(^{1}S) atoms decays to the ground state via O(^{1}D) state by emitting green line [*Slanger et al.*, 2006]. This implies that if the green line emission is present in cometary coma, the red doublet emission will also be present, but the opposite is not always true. The average lifetime of O(^{1}D) is relatively small (∼110 s) compared to the lifetime of H_2O molecule (∼8 × 10^4 s) at 1 AU. The O(^{1}S) also has a very short average lifetime of about 0.1 s. Due to the short lifetime of these metastable species, they cannot travel larger distances in cometary coma before de-exciting via radiative transitions. Hence, these emissions have been used as diagnostic tools to estimate the abundance and distribution of H_2O in comets [*Fink and Johnson*, 1984; *Magee-Sauer et al.*, 1990; *Morgenthaler et al.*, 2001]. The intensity of [OI] emissions, in Rayleigh, can be calculated using the following equation [*Festou and Feldman*, 1981]

$$I = 10^{-6}\tau_p^{-1}\alpha\beta N \tag{4.1}$$

where τ_p is the photodissociative lifetime of parent species in seconds, α is the yield of photodissociation, β is the branching ratio, and N is the column density of cometary species in cm^{-2}.

In the case of red doublet (6300 and 6364 Å), since both emissions arise due to transition from the same excited state (2P^4 ^{1}D) to the ground triplet state (2P^4 ^{3}P), the intensity ratio of these two lines should be the same as that of branching ratio of corresponding transitions. Using Einstein transition probabilities, *Storey and Zeippen*

[2000] calculated the intensity ratio of red doublet and suggested that the intensity of 6300 Å emission would be 3 times stronger than that of 6364 Å emission, and this has been observed in several comets also [*Spinrad*, 1982; *Fink and Johnson*, 1984; *Morrison et al.*, 1997; *Cochran and Cochran*, 2001; *Capria et al.*, 2005; *Furusho et al.*, 2006; *Capria et al.*, 2008; *Cochran*, 2008].

The ratio of intensity of green line to the sum of intensities of red doublet can be calculated as

$$\frac{I_{5577}}{I_{6300}+I_{6364}} = \frac{\tau_{green}^{-1}\alpha_{green}N_{green}\beta_{green}}{\tau_{red}^{-1}\alpha_{red}N_{red}(\beta_{6300+6364})} \tag{4.2}$$

If the emission intensities of oxygen lines are completely attributed to only photodissociative excitation of H_2O and column densities are assumed almost same for both emissions, then the ratio of intensities of green line to red doublet is directly proportional to the ratio of $\tau^{-1}\alpha\beta$. *Festou and Feldman* [1981] reviewed these atomic oxygen emissions in comets. Based on the observation of [OI] 2972 Å emission in the IUE spectrograph of comet Bradfield (1979X), *Festou and Feldman* [1981] calculated the brightness profiles of red and green emissions. *Festou and Feldman* [1981] also calculated a theoretical value for the ratio of the intensity of green line to red doublet (hereafter refer to as the G/R ratio), which has a value of around 0.1 if H_2O is the source for these [OI] emissions in cometary comae, and it is nearly 1 if the source is CO_2 or CO. Observations of green and red line emissions in several comets have shown that the G/R ratio is around 0.1, suggesting that H_2O is the main source of these [OI] lines. However, since no experimental cross section or yield for the production of $O(^1S)$ from H_2O is available in literature, the G/R ratio has been questioned by *Huestis and Slanger* [2006].

Generally, the red line is more intense than the green line because the production of $O(^1D)$ via dissociative excitation of H_2O is larger compared to the radiative decay of $O(^1S)$. Since the lifetime of $O(^1D)$ is larger, quenching is also a significant loss process for $O(^1D)$ near the nucleus. So far, the observed G/R ratio in comets is found to vary from 0.022 to 0.3 [*Cochran*, 1984; *Cochran*, 2008; *Morrison et al.*, 1997; *Zhang et al.*, 2001; *Cochran and Cochran*, 2001; *Furusho et al.*, 2006; *Capria et al.*, 2005; *Capria et al.*, 2008; *Capria et al.*, 2010].

There are several reactions not involving H_2O which can also produce these forbidden oxygen lines [*Bhardwaj and Haider*, 2002]. Among the O-bearing species, CO_2 and CO also have dissociative channels producing $O(^1D)$ and $O(^1S)$. However, complex O-bearing molecules (e.g., H_2CO, CH_3OH, HCOOH) do not produce atomic oxygen as a first dissociative product. Based on the brightness of 6300 Å emission intensity, *Delsemme and Combi* [1976] derived the production rate of $O(^1D)$ in comet Bennett 1970 II and suggested that the abundance of CO_2 is more than that of H_2O. *Delsemme and Combi* [1979] estimated the production of $O(^1D)$ in dissociation of H_2O and CO_2; about 12% of H_2O is dissociated into H_2 and $O(^1D)$, while 67% of CO_2 is dissociated into CO and $O(^1D)$. They suggested that a small amount of CO_2 can contribute much more than H_2O to the red doublet emission. The model calculations of *Bhardwaj and Haider* [2002] showed that the production of $O(^1D)$ is largely through photodissociative excitation of H_2O while the major loss mechanism in the innermost coma is quenching by H_2O. *Cochran and Cochran* [2001], based on the observation of width of red and green lines, argued that there must be another potential source of atomic oxygen in addition to H_2O, which can produce $O(^1S)$ and $O(^1D)$. Observations of the green and red lines in nine comets showed that the green line is wider than the red line [*Cochran*, 2008], which could be due to the involvement of various parent sources in the production of $O(^1S)$.

The model of *Glinski et al.* [2004] showed that the chemistry in the inner coma can produce 1% O_2, which can also be a source of red and green lines. *Manfroid et al.* [2007] also argued, based on lightcurves, that forbidden [OI] emissions are probably contributed through dissociation sequence of CO_2. Recent observation of comet 17P/Holmes showed that the G/R ratio can be even 0.3, which is the highest reported value so far: suggesting that CO_2 and CO abundances might be higher at the time of observation [*Capria et al.*, 2010].

Considering various arguments based on different observations as well as theoretical works, we have developed a coupled chemistry-emission model to quantify various mechanisms involved in the production of red and green line emissions of atomic oxygen. This model is applied to comets C/1996 B2 Hyakutake and Hale-Bopp in which the forbidden atomic oxygen emission lines have been observed when these comets are at around 1 AU from the Sun. The main aim of this study is also to understand the factors that determine the magnitude of G/R ratio. Comet Hale-Bopp is chosen since H_2O production rates in this comet is higher by an order of magnitude than that on comet Hyakutake. Hence the photo-attenuation in a comet having high H_2O production rates and its implications on the photochemistry of metastable $O(^1S)$ and $O(^1D)$ atoms can be studied. We have calculated the production and loss rates, and density profiles, of metastable $O(^1D)$ and $O(^1S)$ atoms from the O-bearing species, like H_2O, CO_2, and CO, and also from the dissociated products OH and O in both these comets.

4.2 Model

The neutral parent species considered in this model are H_2O, CO_2, and CO. We do not consider other significant O-bearing species, like H_2CO, CH_3OH, since their first dissociation does not lead to the formation of atomic oxygen atom; the O atom appears in subsequent photodissociation of daughter products, like OH, CO, HCO. The parent species density distribution in the cometary coma is calculated using Haser's formula which is discussed in Chapter 2.5.1.

The total photoabsorption and photoionization cross sections of H_2O, CO_2, and CO are taken from the compilation of *Huebner et al.* [1992] (`http://amop.space.swri.`

`edu`), and interpolated at 10 Å bins to make them compatible with the S2K solar flux wavelength bins for use in the model calculations. The photochemical production rates for ionization and excitation of various species are calculated using degraded solar flux and cross sections of corresponding processes (discussed in Section 2.6) at different cometocentric distances.

Using AYS approach, which is based on the Monte Carlo method, the primary photoelectrons are degraded to calculate steady state photoelectron flux. The electron impact excitation rates for various ionized and excited states are calculated using the steady state photoelectron spectrum and the corresponding electron impact cross section.

The total inelastic electron impact cross sections for H_2O are taken from *Jackman et al.* [1977] and *Seng and Linder* [1976], and those for CO_2 and CO are taken from *Jackman et al.* [1977]. The electron impact cross sections for different dissociative ionization states of H_2O are taken from *Itikawa and Mason* [2005], for CO_2 from *Bhardwaj and Jain* [2009], and for CO from *McConkey et al.* [2008].

Since the ^{1}D and ^{1}S are metastable states, the direct excitation of atomic oxygen by solar radiation is not an effective excitation mechanism. However the electron impact excitation of atomic oxygen can populate these excited metastable states, which is a major source of airglow emissions in the upper atmospheres of Venus, Earth, and Mars [*Fox and Dalgarno*, 1981, 1979; *Fox*, 2004; *Torr and Torr*, 1982; *Witasse et al.*, 1999; *Singh et al.*, 2010, 1996]. We calculated the excitation rates for these processes using electron impact cross sections from *Jackman et al.* [1977]. In calculating the photoelectron impact ionization rates of metastable oxygen states, we calculated the cross sections by changing the threshold energy parameter for ionization of neutral atomic oxygen in the analytical expression given by *Jackman et al.* [1977]. The above mentioned electron impact cross sections for the production of O(^{1}S) from H_2O, CO_2, CO, and O, used in the model, are discussed in Chapter 2 in Section 2.7.

In our literature survey we could not find any reported cross section for the production of O(^{1}D) due to electron impact dissociation of H_2O. *Jackman et al.* [1977] have assembled the experimental and theoretical cross sections for electron impact on important atmospheric gases in a workable analytical form. The cross sections for electron impact on atomic oxygen producing metastable (^{1}D) state given by *Jackman et al.* [1977] have been used in the model. The obtained ratios of 85% in ground and 15% in metastable state are used for the atomic states of C and O produced in electron impact dissociation of H_2O, CO_2, and CO. It may be noted that the ground state to metastable state production ratio of 89:11 is observed for atomic carbon and atomic oxygen produced in the photodissociation of CO [*Singh et al.*, 1991]. However, as shown later, the contribution of these electron impact processes to the total production of O(^{1}D) is very small (<5%).

The detailed description of coupled chemistry-transport model has been given in

Table 4.1: Reactions accounted for the production and loss of $O(^1S)$ in the model.

Reaction	Rate ($cm^3\ s^{-1}$ or s^{-1})	Reference
$H_2O + h\nu \rightarrow O(^1S) + H_2$	$6.4 \times 10^{-8*}$	This work
$OH + h\nu \rightarrow O(^1S) + H$	6.7×10^{-8}	*Huebner et al.* [1992]
$CO_2 + h\nu \rightarrow O(^1S) + CO$	7.2×10^{-7}	This work
$CO + h\nu \rightarrow O(^1S) + C$	4.0×10^{-8}	*Huebner and Carpenter* [1979]
$H_2O + e_{ph} \rightarrow O(^1S)$ + others	9.0×10^{-10}	This work
$OH + e_{ph} \rightarrow O(^1S)$ + others	2.2×10^{-10}	This work
$CO_2 + e_{ph} \rightarrow O(^1S)$ + others	4.4×10^{-8}	This work
$CO + e_{ph} \rightarrow O(^1S)$ + others	2.2×10^{-10}	This work
$O + e_{ph} \rightarrow O(^1S)$	3.0×10^{-8}	This work
$H_2O^+ + e_{th} \rightarrow O(^1S)$ + others	$4.3 \times 10^{-7} \times (300/T_e)^{0.5} \times 0.045^\dagger$	*Rosen et al.* [2000]
$OH^+ + e_{th} \rightarrow O(^1S)$ + others	$6.3 \times 10^{-9} \times (300/T_e)^{0.5}$	*Guberman* [1995]
$CO_2^+ + e_{th} \rightarrow O(^1S)$ + others	$2.9 \times 10^{-7} \times (300/T_e)^{0.5}$	*Mitchell* [1990]
$CO^+ + e_{th} \rightarrow O(^1S)$ + others	$5.0 \times 10^{-8} \times (300/T_e)^{0.46}$	*Mitchell* [1990]
$O(^1S) + h\nu \rightarrow O^+ + e$	1.9×10^{-7}	*Huebner et al.* [1992]
$O(^1S) + e_{ph} \rightarrow O^+ + 2e$	2.7×10^{-7}	This work
$O(^1S) \longrightarrow O(^3P) + h\nu_{2972}$	0.075	*Wiese et al.* [1996]
$O(^1S) \longrightarrow O(^1D) + h\nu_{5577}$	1.26	*Wiese et al.* [1996]
$O(^1S) + H_2O \rightarrow 2\ OH$	3×10^{-10}	*Zipf* [1969]
$\rightarrow O(^1D) + H_2O$	$3 \times 10^{-10} \times 0.01^\ddagger$	*Zipf* [1969]
$O(^1S) + CO_2 \rightarrow O(^3P) + CO_2$	3.1×10^{-11} exp(-1330/T)	*Atkinson and Welge* [1972]
$\rightarrow O(^1D) + CO_2$	2.0×10^{-11} exp(-1327/T)	*Capetanakis et al.* [1993]
$O(^1S) + CO \rightarrow CO + O$	3.2×10^{-12} exp(-1327/T)	*Capetanakis et al.* [1993]
$\rightarrow O(^1D) + CO$	7.4×10^{-14} exp(-961/T)	*Capetanakis et al.* [1993]
$O(^1S) + e_{th} \rightarrow O(^1D) + e$	8.5×10^{-9}	*Berrington and Burke* [1981]
$\rightarrow O(^3P) + e$	$1.5 \times 10^{-9}\ (T_e/300)^{0.94}$	*Berrington and Burke* [1981]
$O(^1S) + O \rightarrow 2\ O(^1D)$	2.0×10^{-14}	*Krauss and Neumann* [1975]

The calculated photorates and photoelectron impact rates are at 1 AU on 30 March 1996. *This rate is calculated assuming 1% yield for the production of $O(^1S)$ at 1216 Å wavelength. †0.045 is the assumed branching ratio for the formation of $O(^1S)$ via dissociative recombination of H_2O^+ ion. ‡0.01 is the assumed yield for the formation of $O(^1D)$ via quenching of H_2O. e_{ph} = photoelectron, e_{th} = thermal electron, $h\nu$ = solar photon, T_e = electron temperature, T = neutral temperature.

Chapter 2 and in our earlier papers [*Bhardwaj et al.*, 1995, 1996; *Bhardwaj*, 1999; *Bhardwaj and Haider*, 2002; *Haider and Bhardwaj*, 2005; *Bhardwaj and Raghuram*, 2011]. Various reactions involved in the production and loss of metastable $O(^1S)$ and $O(^1D)$ atoms considered in the model are listed in Tables 4.1 and 4.2, respectively.

4.3 Calculations on comet C/1996 B2 Hyakutake

On 24 March 1996, the H_2O production rate for comet C/1996 B2 Hyakutake measured by *Mumma et al.* [1996] was 1.7×10^{29} s^{-1}. Based on H Ly-α emission observation, *Combi et al.* [1998] measured H_2O production rate as 2.6×10^{29} s^{-1} on 4 April 1996. Using molecular radio line emissions, *Biver et al.* [1999] derived the production rates of different species at various heliocentric distances from 1.6 to 0.3 AU. They found that around 1 AU the relative abundance of CO with respect to H_2O is high (~22%) in comet C/1996 B2 Hyakutake.

In the model calculations the H_2O production rate on 30 March 1996 is taken as 2.2×10^{29} s^{-1}. The abundance of CO relative to H_2O is taken as 22%. Since there is no report on the observation of CO_2 in comet Hyakutake, we assumed its abundance as 1% relative to H_2O. However, we vary CO_2 abundance to evaluate its effect on the green and red-doublet emissions. The calculations are made when comet C/1996 B2 Hyakutake was at a heliocentric distance of 0.94 AU and a geocentric distance of 0.19 AU on 30 March 1996. The calculated G/R ratio on other days of the observation is also reported. The radius of cometary nucleus is taken as 10 km. The electron temperature required for ion-electron dissociative recombination reactions is taken from *Körösmezey et al.* [1987]. The solar UV-EUV flux is taken from SOLAR2000 v.2.3.6 (S2K) model of *Tobiska et al.* [2000] for the day 30 March 1996.

4.4 Results for comet C/1996 B2 Hyakutake

4.4.1 Production and loss of O(^{1}S)

The calculated O(^{1}S) production rate profiles for different processes in comet C/1996 B2 Hyakutake are presented in Figure 4.2. These calculations are made under the assuming 0.5% yield of O(^{1}S) from H_2O at 1216 Å solar H Lyman-α line and 1% CO_2 relative abundance. The major production source of O(^{1}S) is the photodissociative excitation of H_2O throughout the cometary coma. However, very close to the nucleus, the photodissociative excitation of CO_2 is also an equally important process for the O(^{1}S) production. Above 100 km, the photodissociative excitation of CO_2 and CO makes an equal contribution in the production of O(^{1}S). Since the cross section for electron impact dissociative excitation of H_2O, CO_2, and CO are small (see Figures 2.9, 2.10 and 2.11), the contributions from electron impact dissociation to O(^{1}S) production are smaller by an order of magnitude or more than that due to photodissociative excitation. At larger cometocentric distances (>2×10^3 km), the dissociative recombination of H_2O^+ ion is a significant production mechanism for O(^{1}S), whose contribution is higher than those

Table 4.2: Reactions accounted for the production and loss of $O(^1D)$ in the model.

Reaction	Rate ($cm^3\ s^{-1}$ or s^{-1})	Reference
$H_2O + h\nu \rightarrow O(^1D) + H_2$	8.0×10^{-7}	This work
$OH + h\nu \rightarrow O(^1D) + H$	6.4×10^{-7}	*Huebner et al.* [1992]
$CO_2 + h\nu \rightarrow O(^1D) + CO$	1.2×10^{-6}	This work
$CO + h\nu \rightarrow O(^1D) + C$	5.1×10^{-8}	This work
$O(^1S) \rightarrow O(^1D) + h\nu_{557nm}$	1.26	*Wiese et al.* [1996]
$H_2O + e_{ph} \rightarrow O(^1D) + H_2 + e$	2.1×10^{-10}	This work
$OH + e_{ph} \rightarrow O(^1D) + H + e$	7×10^{-11}	This work
$CO_2 + e_{ph} \rightarrow O(^1D) + CO + e$	8.5×10^{-9}	This work
$CO + e_{ph} \rightarrow O(^1D) + C(^1D) + e$	7×10^{-11}	This work
$O + e_{ph} \rightarrow O(^1D)$	3.7×10^{-7}	This work
$H_2O^+ + e_{th} \rightarrow O(^1D) + H_2$	$4.3 \times 10^{-7} \times (300/T_e)^{0.5} \times 0.35$[*]	*Rosen et al.* [2000]
$OH^+ + e_{th} \rightarrow O(^1D) + H$	$6.3 \times 10^{-9} \times (300/T_e)^{0.48}$	*Guberman* [1995]
$CO_2^+ + e_{th} \rightarrow O(^1D) + CO$	$2.9 \times 10^{-7}\ (300/T_e)^{0.5}$	*Mitchell* [1990]
$CO^+ + e_{th} \rightarrow O(^1D) + C(^1D)$	$5 \times 10^{-8}\ (300/T_e)^{0.46}$	*Mitchell* [1990]
$O(^1S) + e_{th} \rightarrow O(^1D) + e$	$1.5 \times 10^{-10}\ (T_e/300)^{0.94}$	*Berrington and Burke* [1981]
$O(^1S) + H_2O \rightarrow O(^1D) + H_2O$	$3 \times 10^{-10} \times 0.01$[†]	*Zipf* [1969]
$O(^1S) + CO_2 \rightarrow O(^1D) + CO_2$	2.0×10^{-11} exp(-1327/T)	*Capetanakis et al.* [1993]
$O(^1S) + CO \rightarrow O(^1D) + CO$	7.4×10^{-14} exp(-961/T)	*Capetanakis et al.* [1993]
$O(^1D) + h\nu \rightarrow O^+ + e$	1.82×10^{-7}	*Huebner et al.* [1992]
$O(^1D) \longrightarrow O(^3P) + h\nu_{6300}$	6.44×10^{-3}	*Storey and Zeippen* [2000]
$O(^1D) \longrightarrow O(^3P) + h\nu_{6364}$	2.15×10^{-3}	*Storey and Zeippen* [2000]
$O(^1D) + e_{ph} \rightarrow O^+ + 2e$	1.75×10^{-7}	This work
$O(^1D) + e_{th} \rightarrow O(^3P) + e$	$8.1 \times 10^{-10}\ (T_e/300)^{0.5}$	*Link* [1982]
$O(^1D) + H_2O \rightarrow OH + OH$	2.1×10^{-10}	*Atkinson et al.* [1997]
$\rightarrow O(^3P) + H_2O$	9.0×10^{-12}	*Atkinson et al.* [1997]
$\rightarrow H_2 + O_2$	2.2×10^{-12}	*Atkinson et al.* [1997]
$O(^1D) + CO_2 \rightarrow O + CO_2$	7.4×10^{-11} exp(-120/T)	*Atkinson et al.* [1997]
$\rightarrow CO + O_2$	2.0×10^{-10}	*Atkinson et al.* [1997]
$O(^1D) + CO \rightarrow O + CO$	5.5×10^{-10} exp(-625/T)	*Schmidt et al.* [1988]
$\rightarrow CO_2$	8.0×10^{-11}	*DeMore et al.* [1997]

The calculated photorates and photoelectron impact rates are at 1 AU on 30 March 1996. [*]0.35 is the assumed branching ratio for the formation of $O(^1D)$ via dissociative recombination of H_2O^+ ion. [†]0.01 is the assumed branching ratio for the formation of $O(^1D)$ via quenching of H_2O. e_{ph} = photoelectron, e_{th} = thermal electron, $h\nu$ = solar photon, T_e = electron temperature, T = neutral temperature.

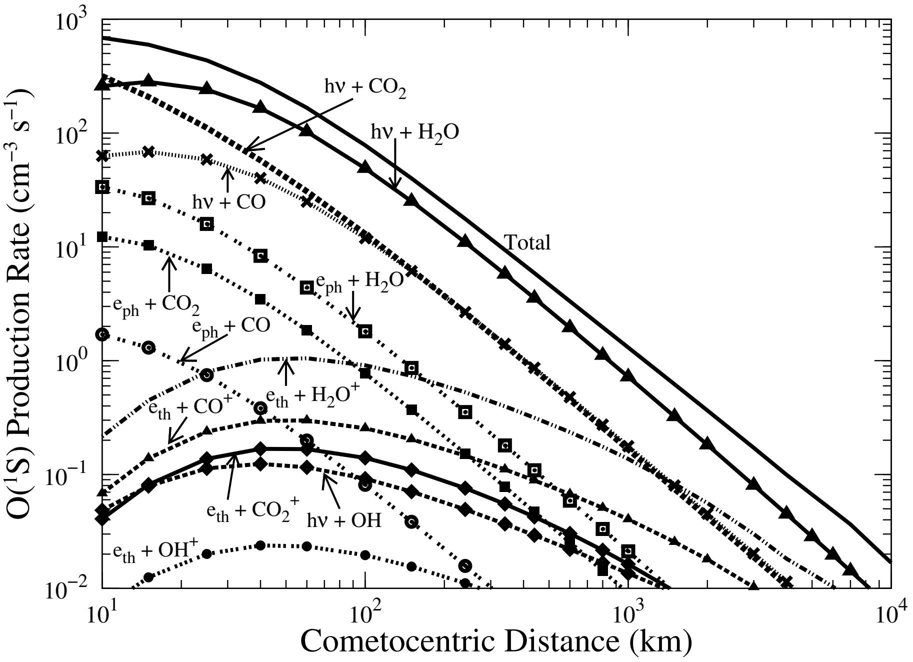

Figure 4.2: Calculated radial profiles on comet C/1996 B2 Hyakutake for major production mechanisms of O(^{1}S) along with the total production profile for the abundances of 1% CO_2 and 22% CO to H_2O production rate of 2.2 × 10^{29} s^{-1}. hν = solar photon, e_{ph} = photoelectron, and e_{th} = thermal electron.

from photodissociative excitation of CO_2 and CO. The dissociative recombination of other ions do not make any significant contribution to the production of O(^{1}S).

In the inner coma, the calculated production rates of O(^{1}S) via photodissociative excitation is CO_2 at various wavelengths are presented in Figure 4.3. The major production of O(^{1}S) occurs in the wavelength region 955–1165 Å where the average cross section is $\sim$2 × 10^{-17} cm^{-2} (cf. Figure 2.10) and the average solar flux is $\sim$1 × 10^9 photons cm^{-2} s^{-1}.

The calculated loss rate profiles of O(^{1}S) for major processes are presented in Figure 4.4. Close to the nucleus (<50 km), quenching by H_2O is the main loss mechanism for metastable O(^{1}S). Above 100 km, the radiative decay of O(^{1}S) becomes the dominant loss process. The contributions from other loss processes are orders of magnitude smaller and hence are not shown in Figure 4.4.

4.4.2 Production and loss of O(^{1}D)

The production rates as a function of cometocentric distance for various excitation mechanisms of the O(^{1}D) are shown in Figure 4.5. The major source of O(^{1}D) production in the inner coma is photodissociation of H_2O. The wavelength dependent production rates of O(^{1}D) from H_2O are presented in Figure 4.6. The O(^{1}D) production in photodissociation of H_2O is governed by solar radiation at H Lyman-α (1216 Å) wavelength.

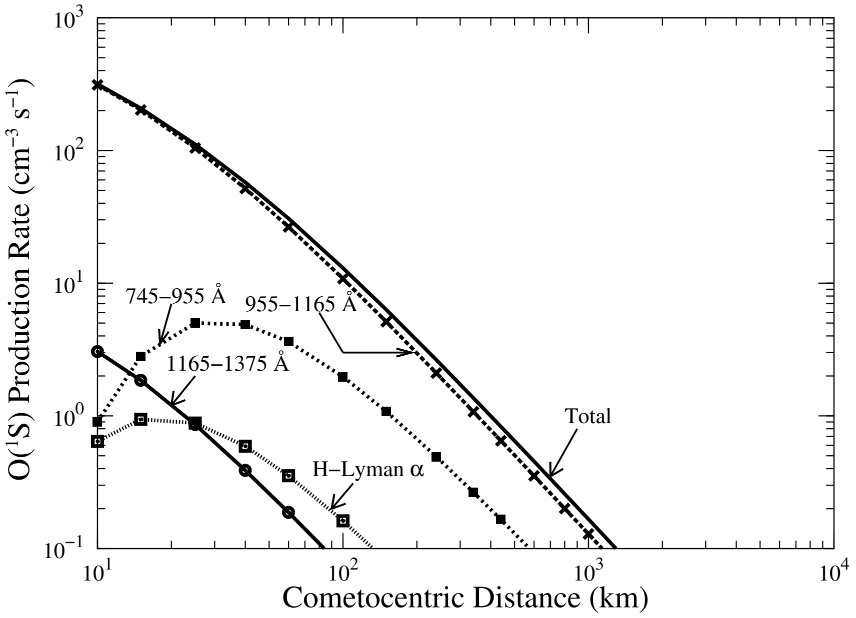

Figure 4.3: Calculated radial profiles on comet C/1996 B2 Hyakutake for the photodissociation of CO_2 producing O(^{1}S) at different wavelength bands for the abundances of 1% CO_2 and 22% CO to H_2O production rate of 2.2 × 10^{29} s^{-1}.

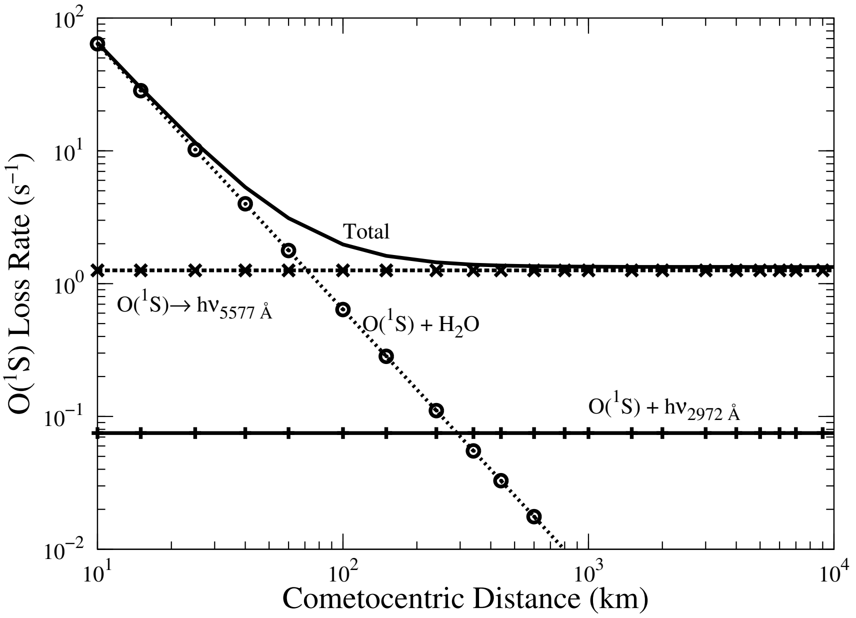

Figure 4.4: Calculated radial profiles on comet C/1996 B2 Hyakutake for the major loss mechanisms of O(^{1}S) atom for the abundances of 1% CO_2 and 22% CO to H_2O production rate of 2.2 × 10^{29} s^{-1}.

However, very close to the nucleus, the production of O(^{1}D) is largely due to photons in the wavelength region 1165–1375 Å. Since the average absorption cross section of H_2O decreases in this wavelength region by an order of magnitude, the optical depth at wavelengths greater than 1165 Å is quite small. Hence, these photons are able to

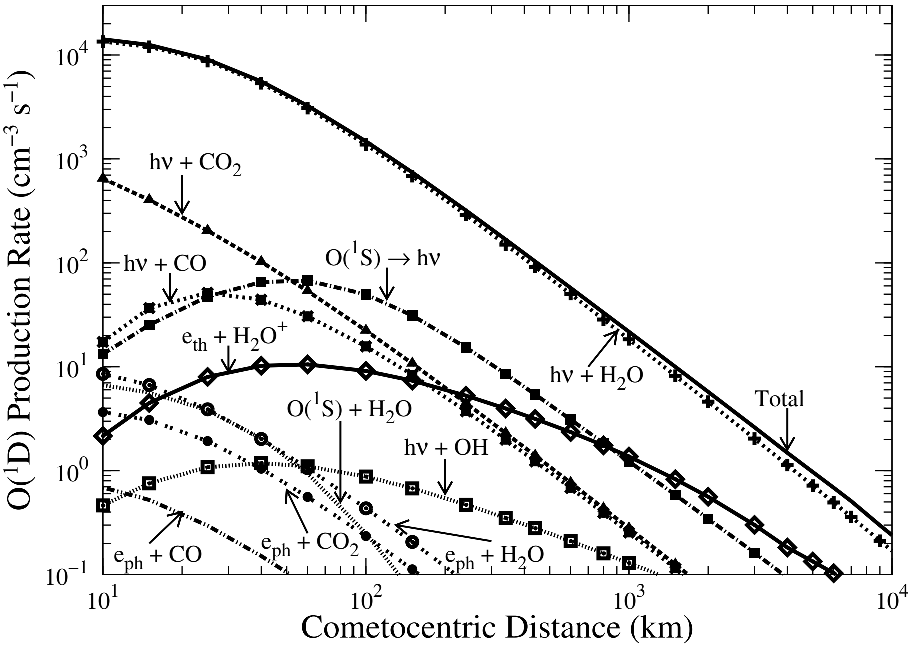

Figure 4.5: Calculated radial profiles on comet C/1996 B2 Hyakutake for the major production mechanisms of O(^{1}D) along with total O(^{1}D) production rate profile for the abundances of 1% CO_2 and 22% CO to H_2O production rate of 2.2 × 10^{29} s^{-1}. hν = solar photon, e_{ph} = photoelectron, and e_{th} = thermal electron.

travel deeper into the coma unattenuated, thereby reaching close to the nucleus where they dissociate H_2O producing O(^{1}D). Thus, at the surface of cometary nucleus the production of O(^{1}D) is controlled by the solar radiation in this wavelength band. The production of O(^{1}D) from H_2O by solar photons from other wavelength regions is smaller by more than an order of magnitude.

After photodissociative excitation of H_2O, the next significant O(^{1}D) production process at radial distances below 50 km is the photodissociative excitation of CO_2. Above 50 km to about 1000 km, the radiative decay of O(^{1}S), and at radial distances above 1000 km the dissociative recombination of H_2O^+, are the next potential sources of the O(^{1}D) (see Figure 4.5). The calculated wavelength dependent production rates of O(^{1}D) for photodissociation of CO_2 are shown in Figure 4.7. Solar radiation in the wavelength region 1165–955 Å dominates the O(^{1}D) production. Since the cross section for the production of O(^{1}D) due to photodissociation of CO_2 is more than an order of magnitude higher in this wavelength region compared to cross section at other wavelengths (see Figure 2.7), the solar radiation in this wavelength band mainly controls the formation of O(^{1}D) from CO_2. Other potential contributions are made by solar photons in the wavelength band 1585–1375 Å at distances <50 km, and 955–745 Å at radial distances >100 km. Since the CO_2 absorption cross section at around 1216 Å is smaller by more than two orders of magnitude compared to its maximum value, the

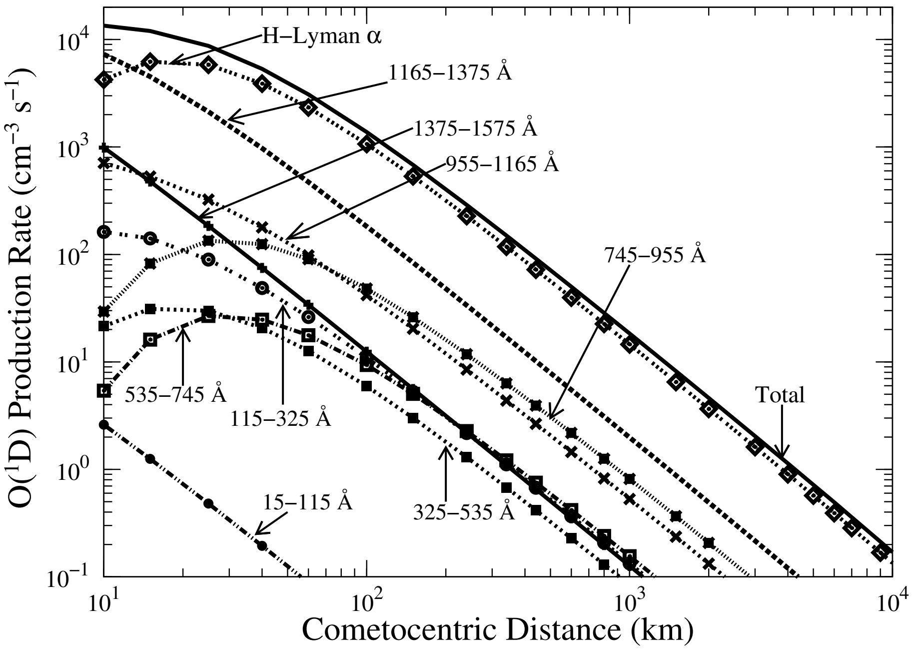

Figure 4.6: Calculated radial profiles on comet C/1996 B2 Hyakutake for the photodissociation of H_2O producing $O(^1D)$ at different wavelength bands for the abundances of 1% CO_2 and 22% CO to H_2O production rate of 2.2×10^{29} s^{-1}.

solar radiation at H Ly-α is not an efficient source of $O(^1D)$ atoms.

Zipf [1969] measured the total $O(^1S)$ quenching rate coefficient by H_2O as 3×10^{-10} cm^3 s^{-1}. The primary loss channel in this quenching mechanism is the production of two OH atoms. The production of $O(^1D)$ is also a possible channel whose rate coefficient is not reported in the literature. Hence, we assumed that 1% of total rate coefficient can lead to the formation of $O(^1D)$ in this quenching mechanism. However, this assumption has no implications on the $O(^1D)$ production since the total contribution due to $O(^1S)$ quenching is about three orders of magnitude smaller than the major production process of $O(^1D)$.

The calculated loss rate profiles of $O(^1D)$ are presented in Figure 4.8. Below 1000 km, the $O(^1D)$ can get be quenched by various cometary species. The quenching by H_2O is the major loss mechanism for $O(^1D)$ below 1000 km. Above 2×10^3 km radiative decay is the dominant loss process for $O(^1D)$.

4.4.3 Green and red-doublet emission intensities

Using the calculated production and loss rates and assuming photochemical equilibrium, we computed the number density of $O(^1S)$ and $O(^1D)$ metastable atoms. The calculated number densities are presented in Figure 4.9. The $O(^1D)$ density profile shows a broad peak around 200–600 km. But, in the case of $O(^1S)$, the density peaks at much lower radial distances of ~60 km. The number densities of $O(^1D)$ and $O(^1S)$

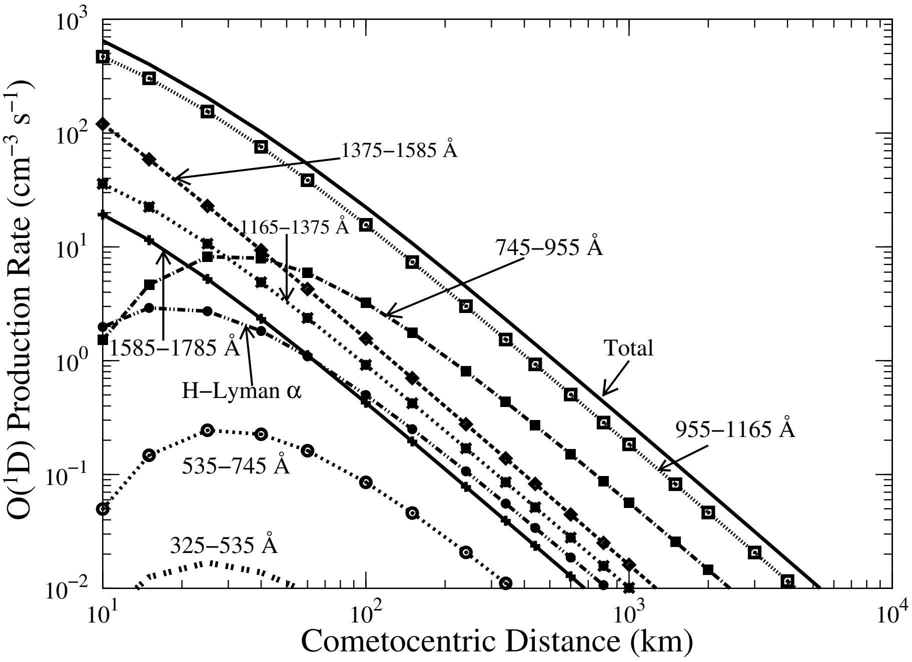

Figure 4.7: Calculated radial profiles on comet C/1996 B2 Hyakutake for the photodissociation of CO_2 producing $O(^1D)$ at different wavelength bands for the abundances of 1% CO_2 and 22% CO to H_2O production rate of 2.2×10^{29} s^{-1}.

are converted into emission rate profiles for the red-doublet and green line emissions, respectively, by multiplying with Einstein transition probabilities as

$$V_{(6300+6364)}(r) = A_{(6300+6364)} \times [O^1D(r)] = A_{(6300+6364)} \frac{\sum_{i=1}^{k} P_i(r)}{\sum_{i=1}^{k} L_i(r) + A(^1D)} \tag{4.3}$$

and

$$V_{(5577)}(r) = A_{(5577)} \times [O^1S(r)] = A_{(5577)} \frac{\sum_{i=1}^{k} P_i(r)}{\sum_{i=1}^{k} L_i(r) + A(^1S)} \tag{4.4}$$

Where $[O^1S(r)]$ and $[O^1D(r)]$ are the calculated number density for the corresponding production rates $P_i(r)$ and loss frequencies $L_i(r)$ for $O(^1S)$ and $O(^1D)$ at radial distance r due to ith process, respectively. $A(^1D)$ and $A(^1S)$ are the total Einstein spontaneous emission coefficients for red-doublet and green line emissions. Using the emission rate profiles, the line of sight intensity of green and red-doublet emissions along the projected distance z is calculated as

$$I(z) = 2 \int_{z}^{R} V_{(5577,\ 6300+6364)}(s) ds \tag{4.5}$$

where s is the abscissa along the line of sight, and $V_{(5577,\ 6300+6364)}(s)$ is the emission rate for the green or red-doublet emission. The multiplication of 2 is due to assumed spherical symmetry of the cometary coma. The maximum limit of integration R is taken as 10^5 km. The calculated brightness profiles of 5577 and 6300 Å emissions are presented in Figure 4.10. These brightness profiles are then averaged over the projected

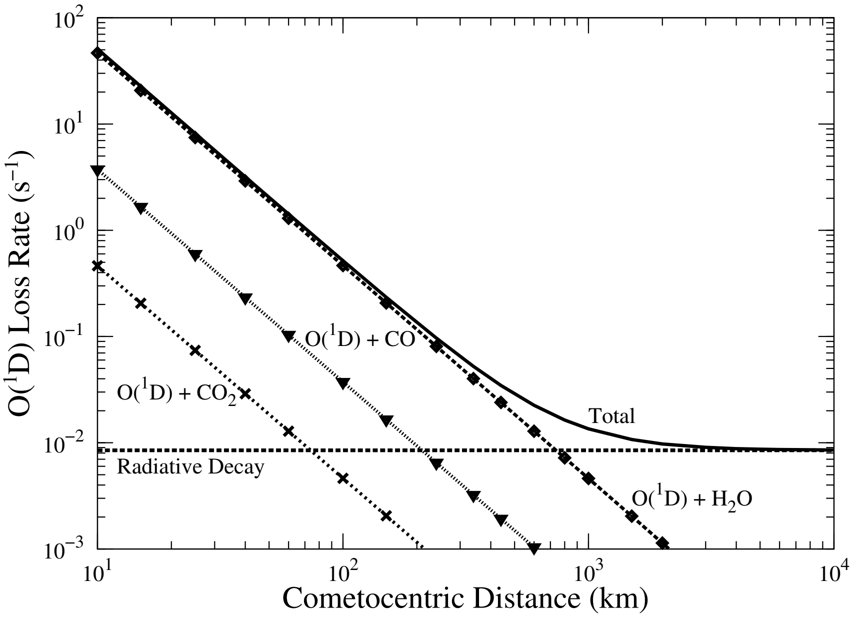

Figure 4.8: Calculated radial profiles on comet C/1996 B2 Hyakutake for major loss mechanisms of $O(^1D)$ atom for the abundances of 1% CO_2 and 22% CO to H_2O production rate of 2.2 × 10^{29} s^{-1}.

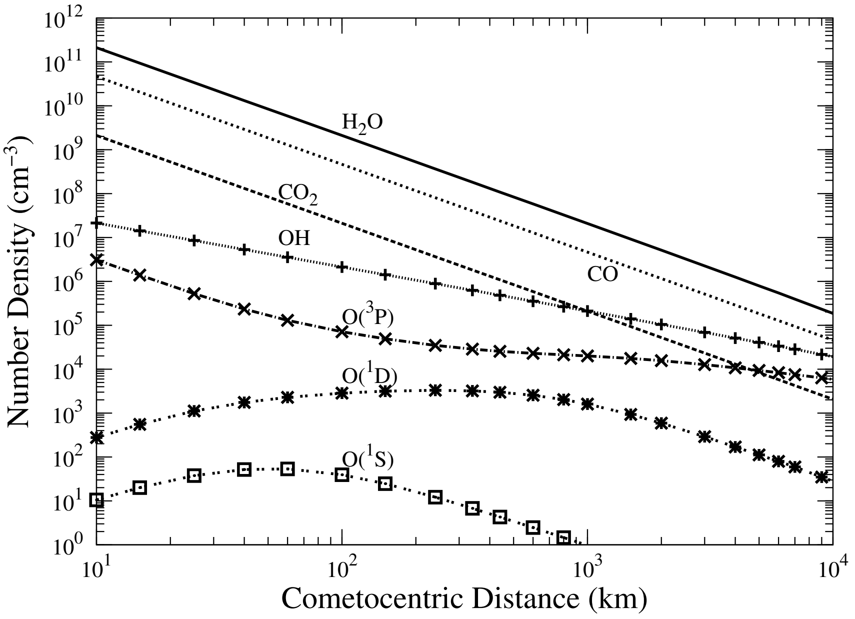

Figure 4.9: Calculated number density profiles of $O(^1S)$, $O(^1D)$, $O(^3P)$, and OH, along with those of H_2O, CO, and CO_2 on comet C/1996 B2 Hyakutake for the abundances of 1% CO_2 and 22% CO to H_2O production rate of 2.2 × 10^{29} s^{-1}.

area corresponding to the slit dimension 1.2″ × 8.2″ centred on the nucleus of comet C/1996 B2 Hyakutake for the observation on 30 March 1996 [*Cochran*, 2008]. The G/R ratio averaged over the slit is also calculated.

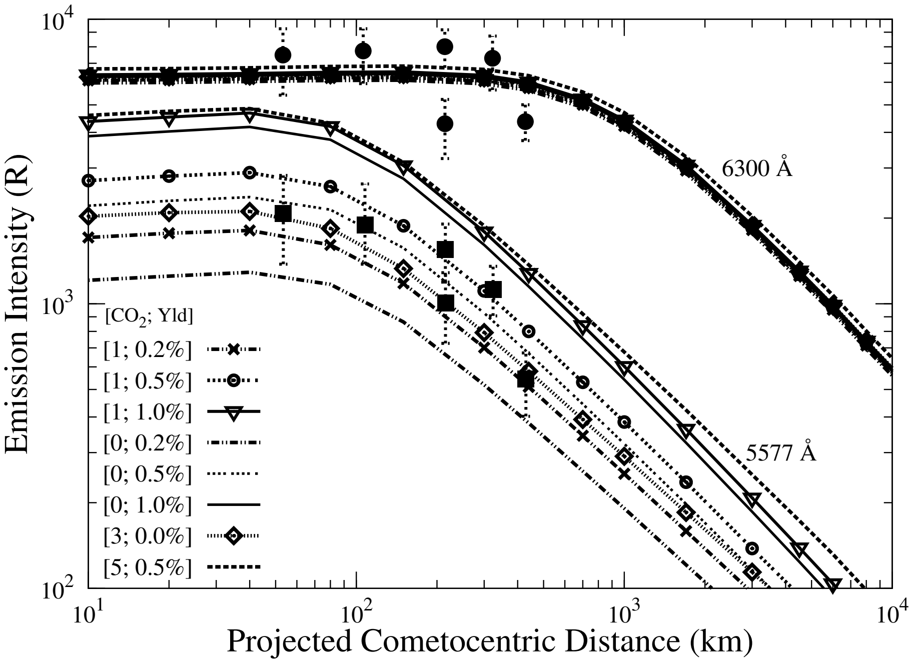

Figure 4.10: Calculated emission brightness profiles on comet Hyakutake along projected distances for 5577 Å (green) and 6300 Å (red) line emissions for different CO_2 relative abundance [CO_2] and yield [Yld] for $O(^1S)$ production in photodissociation of H_2O. The green and red emission intensities at different projected distances observed on 30 March 1996 taken from *Cochran* [2008] are also shown (filled symbols with error bars) for comparison with the calculated values.

Morrison et al. [1997] observed the green and red-doublet emissions on comet C/1996 B2 Hyakutake in the high resolution optical spectra obtained on 23 and 27 March 1996 and found the G/R ratio in the range 0.12–0.16. *Cochran* [2008] observed the 5577 and 6300 Å line emissions on this comet on 9 and 30 March 1996, with the G/R ratio as 0.09 for 9 March observation. We calculated the G/R ratio by varying the yield for $O(^1S)$ production in photodissociation of H_2O at 1216 Å (henceforth refer to as $O(^1S)$ yield). Since CO_2 is not observed in this comet, we assumed that a minimum 1% CO_2 is present in the coma. However, we also carried out calculations for 0%, 3% and 5% CO_2 abundances in the comet. We calculated the contributions of different production processes in the formation of $O(^1S)$ and $O(^1D)$ at three different projected distances of 10^2, 10^3, and 10^4 km from the nucleus for the above mentioned CO_2 abundances and the $O(^1S)$ yield values varying from 0% to 1%. These calculations are presented in Table 4.3.

The percentage contribution of major production processes in the projected field of view for the green and red-doublet emissions are also calculated. The G/R ratio is calculated after averaging the intensity over the projected area of 165 × 1129 km which corresponds to the dimension of slit used in the observation made by *Cochran* [2008] on 30 March 1996. These calculated values are presented in Table 4.4.

Table 4.3: Calculated percentage contribution for major production processes of O(^{1}S) and O(^{1}D) atoms in comet C/1996 B2 Hyakutake with varying relative abundance of CO_2 and O(^{1}S) yield.

O(^{1}S)	Production processes of O(^{1}S) and O(^{1}D) at three cometocentric projected distances (km)																	
Yield	hν + H_2O			hν + OH			hν + CO_2			e + H_2O^+			O(^{1}S) → O(^{1}D)			hν + CO		
(%)*	10^2	10^3	10^4	10^2	10^3	10^4	10^2	10^3	10^4	10^2	10^3	10^4	10^2	10^3	10^4	10^2	10^3	10^4
1% CO_2																		
0.0	0	0	0	1	5	19	39	23	14	10	28	27				37	24	16
	[92]†	[82]	[61]	[0.5]	[1]	[8]	[1]	[1]	[1]	[2]	[9]	[12]	[1]	[3]	[4]	[1]	[1]	[1]
0.2	38	28	17	1	4	15	24	17	12	6	20	22				23	17	13
	[91]	[81]	[60]	[0.5]	[1]	[8]	[1]	[1]	[1]	[2]	[9]	[12]	[3]	(4)	[5]	[1]	[1]	[1]
0.5	62	50	34	0.5	3	12	15	11	10	4	14	17				15	12	10
	[90]	[80]	[60]	[0.5]	[1]	[8]	[1]	[1]	[1]	[2]	[9]	[12]	[4]	[6]	[6]	[1]	[1]	[1]
1.0	75	66	51	0.5	2	10	9	8	7	2	10	13				9	8	7
	[88]	[77]	[58]	[0.5]	[1]	[7]	[1]	[1]	[1]	[2]	[9]	[12]	[7]	[9]	[9]	[1]	[1]	[1]
0% CO_2																		
0.0	0	0	0	2	7	23	0	0	0	17	39	34				65	34	20
	[95]	[84]	[62]	[0.5]	[2]	[8]	[0]	[0]	[0]	[2]	[9]	[12]	[1]	[2]	[3]	[1]	[1]	[1]
0.2	51	35	21	1	5	18	0	0	0	8	25	27				31	22	16
	[94]	[83]	[62]	[0.5]	[1]	[8]	[0]	[0]	[0]	[2]	[9]	[12]	[2]	[3]	[4]	[1]	[1]	[1]
0.5	72	57	40	0.5	3	14	0	0	0	5	16	20				17	14	12
	[92]	[81]	[61]	[0.5]	[1]	[8]	[0]	[0]	[0]	[2]	[9]	[12]	[4]	[5]	[5]	[1]	[1]	[1]
1.0	84	73	57	0.5	2	10	0	0	0	2	10	14				10	9	8
	[90]	[79]	[60]	[0.5]	[2]	[8]	[0]	[0]	[0]	[2]	[9]	[12]	[6]	[8]	[8]	[1]	[1]	[1]
3% CO_2																		
0.0	0	0	0	1	3	13	62	44	30	5	18	19				20	15	11
	[89]	[79]	[58]	[0.5]	[1]	[7]	[4]	[4]	[3]	[2]	[9]	[12]	[3]	[4]	[5]	[1]	[1]	[1]
5% CO_2																		
0.5	36	31	22	0.5	2	7	45	37	30	2	10	12				9	8	7
	[83]	[72]	[54]	[0.5]	[2]	[8]	[1]	[1]	[1]	[2]	[10]	[12]	[7]	[8]	[9]	[1]	[1]	[1]

*Yield for the production of O(^{1}S) from photodissociation of H_2O at solar Lyman-α (1216 Å) line.

†The values in square brackets are for the O(^{1}D). Calculations are made for 30 March 1996, when r = 0.94 AU and Δ = 0.19 AU.

Table 4.4: Calculated percentage contribution for the major production processes of the green (red-doublet) emission in the slit projected field of view on comet C/1996 B2 Hyakutake.

O(^{1}S) Yield (%)	hν + H_2O	hν + OH	hν + CO_2	e^- + H_2O^+	O(^{1}S) → O(^{1}D)	hν + CO	G/R ratio[†]
1% CO_2							
0.0	0 [91]*	2 [0.5]	36 [1]	13 [3]	[1]	35 [1]	0.07
0.2	36 [91]	1 [0.5]	23 [1]	8 [3]	[3]	22 [1]	0.11
0.5	59 [89]	1 [0.5]	14 [1]	5 [3]	[4]	14 [1]	0.17
1.0	76 [87]	0.5 [0.5]	10 [1]	0.5 [3]	[6]	10 [1]	0.27
0% CO_2							
0.0	0 [94]	4 [0.5]	0 [0]	21 [3]	[1]	59 [1]	0.04
0.2	49 [93]	2 [0.5]	0 [0]	11 [3]	[2]	30 [1]	0.08
0.5	70 [91]	1 [0.5]	0 [0]	6 [3]	[4]	17 [1]	0.15
1.0	82 [89]	0.5 [0.5]	0 [0]	3 [3]	[6]	10 [1]	0.25
3% CO_2							
0.0	0 [87]	1 [0.5]	60 [4]	7 [3]	[3]	20 [1]	0.13
5% CO_2							
0.5	35 [82]	0.5 [0.5]	45 [6]	3 [3]	[7]	7 [1]	0.27

*The values in square brackets are the calculated percentage contribution for the red-doublet emission. [†]The calculated values are averaged over the projected area of 165 × 1130 km corresponding to slit size of $1.2'' \times 8.2''$ at $\Delta = 0.19$ AU centered on the nucleus of comet C/1996 B2 Hyakutake on 30 March 1996 [*Cochran*, 2008].

Taking 1% CO_2 abundance and 0% O(^{1}S) yield, the calculated percentage contributions of major production processes of O(^{1}S) and O(^{1}D) atoms are presented in Table 4.3. Around 60 to 90% of the O(^{1}D) is produced from photodissociation of H_2O. Contributions of photodissociative excitation of CO_2 and CO in the production of O(^{1}S) and O(^{1}D) are 15 to 40% and 1%, respectively. Around 10^4 km projected distance, the photodissociative excitation of OH (∼20%) and the dissociative recombination of H_2O^+ (∼30%) are also significant production processes for O(^{1}S) atoms. But, the contributions from these processes in O(^{1}D) production is around 10% only.

For CO_2 abundance of 1% and O(^{1}S) yield of 0.2%, the calculations presented in Table 4.3 show that the photodissociation of H_2O contribute around 20 to 40% in the production of O(^{1}S) and 60 to 90% in the production of O(^{1}D) atom. The next major source of O(^{1}S) production is the photodissociation of CO_2 and CO with each contributing ∼10 to 25%. The relative contributions from photodissociation of parent species H_2O, CO_2, and CO to O(^{1}S) and O(^{1}D) production decreases with increase in projected distance from the nucleus. At 10^4 km projected distance, the photodissociation of OH contribute 15% and 8% to the production of O(^{1}S) and O(^{1}D) atoms, respectively. Above 1000 km projected distance, the contribution of H_2O^+ dissociative recombination to O(^{1}S) production is around 20%. The production of O(^{1}D) atom is mainly via photodissociation of H_2O, but around 10^4 km the dissociative recombination of H_2O^+ ion is also a significant production process contributing around 12%. At 10^4 km, dissociative recombination of OH^+ also contribute around 10% to the total O(^{1}D) production, which is not shown in Table 4.3, and this value is independent of O(^{1}S) yield or CO_2 abundance. Radiative decay of O(^{1}S) is a minor ($\leq$5%) production process in the formation of O(^{1}D).

We also calculated the relative contributions of different processes in the formation of green and red line emissions in the slit projected field of view, which are presented in Table 4.4. For this case, the photodissociation of H_2O contribute around 35%, while the photodissociation of CO_2 and CO contribute 23% and 22%, respectively, to the production of green line emission. The contribution of dissociative recombination of H_2O^+ ions is around 10%. The major production process of red lines is photodissociation of H_2O (90%); the dissociative recombination of H_2O^+ and radiative decay of O(^{1}S) atom are minor ($\leq$5%) production processes. With the O(^{1}S) yield of 0.2% and 1% CO_2 abundance, the slit-averaged G/R ratio is found to be 0.11.

When the O(^{1}S) yield is increased to 0.5% with 1% CO_2 abundance (see Table 4.3), the contribution from photodissociative excitation of H_2O to the O(^{1}S) production is increased, with value varying from 35 to 60%, while the contribution to O(^{1}D) production is not changed. In this case, the contribution from photodissociation of CO_2 and CO to the O(^{1}S) production is reduced (values between 10 to 15%). The contributions from other processes are not changed significantly. Table 4.4 shows that in this case around 60% of green line in the slit projected field of view is produced via photodissociation of H_2O, while the contributions from photodissociation of CO_2 and CO are around 15% each. The main (90%) production of red-doublet emission is through photodissociation of H_2O. In this case the slit-averaged G/R ratio for the observed slit dimension is 0.17.

On further increasing the O(^{1}S) yield to 1% with CO_2 abundances of 1%, the contribution of photodissociation of H_2O to O(^{1}S) atom production is further increased (values between 50 to 75%) while the contribution from photodissociation of CO_2 and CO is decreased to around 10% each (cf. Table 4.3). The contributions from other processes are not affected compared to the previous case. As seen from Table 4.4, in this case the contribution of photodissociation of H_2O to green line is around 75% in the slit projected field of view, while contributions from photodissociation of CO_2 and CO are decreased to 10% each. The calculated G/R ratio is 0.27 (Table 4.4).

We also evaluated the effect of CO_2 on the red-doublet and green line emissions by varying its abundance to 0%, 3% and 5%. The calculated percentage contribution of major processes along the projected distances and in the slit projected field of view are presented in Tables 4.3 and 4.4, respectively. In the absence of CO_2, the contributions from H_2O, H_2O^+ and CO in O(^{1}S) production are increased by $\sim$10% (cf. Tables 4.3 and 4.4). Taking 0% O(^{1}S) yield and by increasing CO_2 relative abundance from 1 to 3%, the percentage contributions for O(^{1}S) from photodissociative excitation of CO_2 (CO) is increased (decreased) by 50%. The contribution from H_2O to O(^{1}D) production is not changed.

The calculations presented in Tables 4.3 and 4.4 depict that the contribution of various processes are significant in the production of O(^{1}S) atom, whereas photodissociative excitation of H_2O is the main production process for O(^{1}D) atom. Since comet C/1996 B2 Hyakutake is rich in CO (abundance ∼22%) compared to other comets, the contribution from CO photodissociation to O(^{1}S) production is significant (10–25%). In the case of a comet having CO abundance less than 20%, the major production source of metastable O(^{1}S) atom would be photodissociation of H_2O and CO_2.

4.5 Calculations on comet C/1995 O1 Hale-Bopp

Owing to its very high H_2O production rate, C/1995 O1 Hale-Bopp was a great comet in the night sky of the year 1997. The visible emissions of atomic oxygen ([OI] 6300, 6364, and 5577 Å), which are accessible to the ground-based optical instruments, have been observed by *Morgenthaler et al.* [2001] and *Zhang et al.* [2001] in the coma of Hale-Bopp.

The details of the model and the chemistry are presented in our previous section. Here we present the input parameters that have been used in the model for the observed condition of comet Hale-Bopp on 10 March 1997 (solar radio flux F10.7 = 74.7×10^{-22} J s^{-1} m^{-2} Hz^{-1}) when it was at a geocentric distance (Δ) of 1.32 AU and a heliocentric distance (r_h) of 0.93 AU.

The radius of the cometary nucleus is taken as 25 km [*Weaver et al.*, 1997; *Combi et al.*, 1999]. Though a variety of O-bearing minor species [with relative abundances ≤1%, *Bockelée-Morvan et al.*, 2000] have been found in comet Hale-Bopp, the dominant species H_2O, CO_2, and CO are only considered in the model calculations. The neutral density profiles of these parent species are calculated using Haser's formula.

Using ground-based observations of H_2O infrared emissions during January to May 1997, *Dello Russo et al.* [2000] derived water production rates at different heliocentric distances and fitted as a function of r_h as $Q_{H_2O} = 8.35 \pm 0.13 \times 10^{30}\ [r_h^{(-1.88\pm0.13)}]$ molecules s^{-1}. We used this expression as a standard input in calculating H_2O density profiles on different days. The H_2O production rates in Hale-Bopp are also derived by observing the emissions from its dissociative products, like OH 18-cm emission, OH (0-0) 3080 Å emission, [OI] 6300 Å emission, and H Lyman-α, over large projected distances [*Weaver et al.*, 1997; *Colom et al.*, 1999; *Schleicher et al.*, 1997; *Combi et al.*, 2000; *Woods et al.*, 2000; *Morgenthaler et al.*, 2001; *Harris et al.*, 2002; *Fink*, 2009]. These derived H_2O production rates depend on the observational condition and also on the assumed model parameters. We have discussed the effect of H_2O production rate on the calculated green and red-doublet emission intensities of atomic oxygen in Section 4.7.2.2.

High resolution ground-based infrared spectroscopic observations are used to study the CO production rate in comet Hale-Bopp from June 1996 to September 1997 [*DiSanti* *et al.*, 2001]. The spatial distribution of CO in the coma of Hale-Bopp is assumed to have two distinct sources: nucleus-originated, and extensively distributed in the cometary coma. During this observation period, the relative abundance of CO is found to be ~25% of H_2O. *DiSanti et al.* [2001] fitted the observed CO production rate as a function of heliocentric distance near the perihelion as $Q_{CO} = 2.07 \times 10^{30}\ r_h^{-1.66\pm0.22}$ molecules s^{-1}, and above 1.5 AU as $Q_{CO} = 1.06 \times 10^{30}\ r_h^{-1.76\pm0.26}$ molecules s^{-1}. Since observations of [OI] 6300 Å emission are done when comet was at around 1 AU, we have used the former formulation to calculate the neutral CO density in the model. *DiSanti et al.* [2001] suggested that the increase in CO production rate below 1.5 AU is due to distributed sources prevailing in the cometary coma. Recent study of *Bockelée-Morvan et al.* [2010] showed that the infrared CO (1-0) rotational vibrational emission lines are optical thick in the cometary coma of Hale-Bopp. Based on the modelling studies of these emission lines they rejected the idea of extended source distribution of CO in comet Hale-Bopp. However, the model calculations show that the role of CO in determining green and red-doublet emission intensities is very small compared to other species, and hence the impact of distributed CO source is insignificant on these forbidden emission lines.

The CO_2 has been detected in Hale-Bopp by *Crovisier et al.* [1997] in April 1996, when the comet was at heliocentric distance of 2.9 AU. Based on the infrared emissions between 2.5 to 5 μm, the derived CO_2 production rate at 2.9 AU was 1.3×10^{28} molecules s^{-1}, which corresponds to a relative abundance of ~20% of H_2O. Assuming that the photodissociative excitation is the main production mechanism in populating the $CO(a^3\Pi)$ metastable state, the observed CO Cameron band ($a^3\Pi \rightarrow X^1\Sigma^+$) emission intensity has been used to estimate the abundance of CO_2 in this comet by *Weaver et al.* [1997]. The estimated CO_2 abundance is more than 10% when the comet was beyond 2.7 AU. However, the model calculations on comets 103P/Hartley 2 and 1P/Halley presented in Chapter 3 have shown that photoelectron impact excitation is the main production mechanism of CO Cameron band emission and not the photodissociation of CO_2. Assuming that the CO_2/CO abundance ratio did not vary with heliocentric distance in this comet, *Bockelée-Morvan et al.* [2004] suggested 6% relative abundance of CO_2 when the comet was at 1 AU. We have taken 6% CO_2 relative abundance with respect to H_2O in the model. However, we discuss the impact of CO_2 abundance by varying its relative abundance on the calculated intensities of green and red-doublet emissions. The OH neutral density profile in comet Hale-Bopp is calculated by fitting *Harris et al.* [2002] observed OH (0-0) 3080 Å resonant scattering emission along the projected distance with the Haser's two step formulation. The photodissociative excitation rates of OH producing $O(^1S)$ and $O(^1D)$ are taken from *Huebner et al.* [1992] which were determined using theoretical [*van Dishoeck and Dalgarno*, 1984] and experimental [*Nee and Lee*, 1984] photoabsorption cross sections, respectively.

There is a clear evidence that in comet Hale-Bopp the expansion velocity of neutrals increases with increasing cometocentric distance [*Colom et al.*, 1999; *Biver et al.*, 1997; *Harris et al.*, 2002]. The sources involved in accelerating the neutral species across the cometary coma is discussed in several works [*Colom et al.*, 1999; *Combi et al.*, 1999; *Harris et al.*, 2002; *Combi*, 2002]. To incorporate the acceleration of these neutrals in the model we have taken the velocity profile calculated by *Combi et al.* [1999] at 1 AU and used as a input in the Haser's density distribution. We also verified the effect of expansion velocity on the calculated intensity of green and red-doublet emissions by varying its static value between 0.7 to 2.2 km s^{-1}, which is discussed in Section 4.7.2.1.

The electron temperature profile required to calculate dissociative recombination rates is taken from *Lovell et al.* [2004]. *Bhardwaj and Raghuram* [2012] have found that the yield of $O(^1S)$ in the photodissociation of H_2O at solar H Ly-α can not be more than 1%. In the present study we have taken this yield value as 0.5%. The impact of this assumption is discussed in Section 4.7 and in our previous work [*Bhardwaj and Raghuram*, 2012]. The photodissociative excitation cross section for CO_2 producing $O(^1D)$ is taken from *Jain* [2013].

4.6 Results for comet C/1995 O1 Hale-Bopp

4.6.1 Production and loss of $O(^1S)$

The calculated $O(^1S)$ production rate profiles for major production processes are presented in Figure 4.11. The photodissociation of CO_2 is the major production process of $O(^1S)$. Above cometocentric distance of 1000 km, the photodissociative excitation of H_2O is also an equally important production source of $O(^1S)$. Photodissociative excitation of CO is the next significant production mechanism of $O(^1S)$. Since no cross section is reported in the literature for photodissociation of CO producing $O(^1S)$, we have taken the photo-rate for this process from *Huebner and Carpenter* [1979] and assumed that the formation of $O(^1S)$ is similar to $O(^1D)$. This assumption results in the calculated $O(^1S)$ profile below 100 km similar to that of $O(^1D)$. However, this assumption does not make any significant impact on the calculated green line intensity, since photodissociation of CO_2 and H_2O can produce $O(^1S)$ an order of magnitude higher than that of CO in the inner coma. Above 10^4 km, the contribution from dissociative recombination reactions of H_2O^+ and CO^+ to the total $O(^1S)$ production is significant. The photodissociation of OH is a minor source of $O(^1S)$ below 10^5 km radial distance.

The calculated $O(^1S)$ production rate profiles for photodissociation of CO_2 in the different wavelength bands are shown in Figure 4.12. The cross section for photodissociation of CO_2 in the wavelength band 955–1165 Å is higher by a few orders of magnitude compared to that at other wavelength regions (cf. Figure 2.6). Moreover, in this wavelength band, the yield of $O(^1S)$ in photodissociation of CO_2 tends to unity [*Slanger et al.*, 1977; *Lawrence*, 1972b], while the total absorption cross section of H_2O

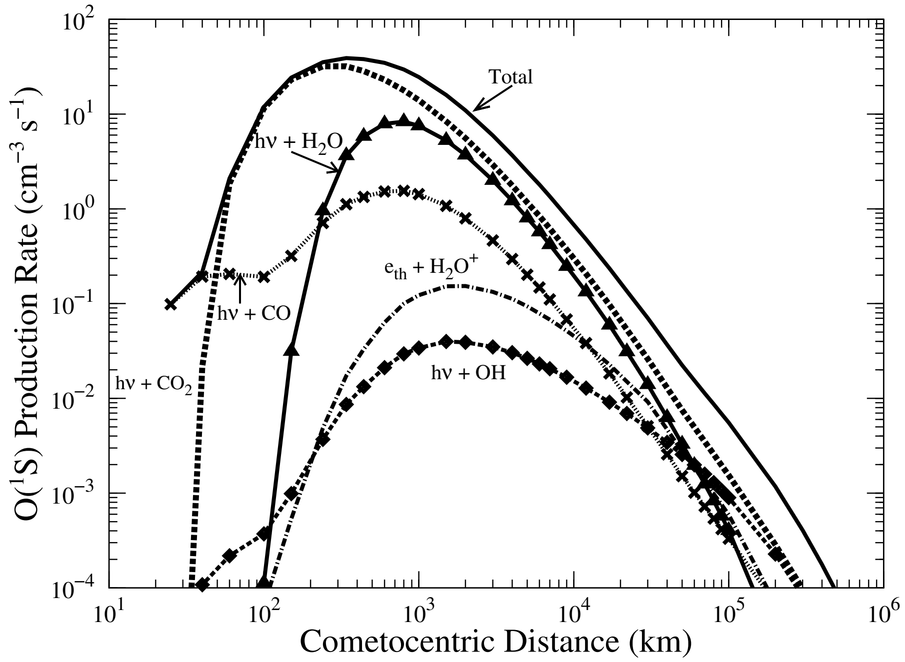

Figure 4.11: Calculated radial profiles on comet C/1995 O1 Hale-Bopp for major production mechanisms of O(^{1}S) along with the total production profile for the abundances of 6% CO$_2$ and 24% CO relative to H$_2$O production rate of 8.3 × 10^{30} s^{-1}. hν : solar photon and e$_{th}$: thermal electron

has a strong dip (cf. Figure 2.6). Thus, solar photons in this wavelength band can dissociate CO$_2$ and produce O(^{1}S) very efficiently. The photons in the wavelength bands 1165-1375 and 745-955 Å make a smaller (<10%) contribution to the total O(^{1}S) production. The contribution of 1216 Å solar photons to the O(^{1}S) formation is two orders of magnitude low because of the small ($\sim$8 × 10^{-20} cm^2) absorption cross section of CO$_2$.

The calculated destruction rate profiles of O(^{1}S) are presented in Figure 4.13. The collisional quenching of O(^{1}S) by H$_2$O is the dominant loss process at cometocentric distances shorter than 300 km. Above 1000 km the radiative decay via [OI] 5577 Å line emission is the main loss process for the O(^{1}S) atom. The radiative decay via [OI] 2972 Å emission is a minor loss process of O(^{1}S).

4.6.2 Production and loss of O(^{1}D)

The calculated production rate profiles of metastable O(^{1}D) for different formation mechanisms are shown in Figure 4.14. Between 100 and $\sim$2 × 10^4 km, most (>90%) of the O(^{1}D) is produced via photodissociation of H$_2$O. However, below 100 km, the photodissociation of CO$_2$ is also an important source of O(^{1}D). Between 200 and 2000 km, the radiative decay of O(^{1}S) makes a minor contribution in the formation of O(^{1}D). Above 10^4 km, the photodissociation of OH plays a significant role in the formation of

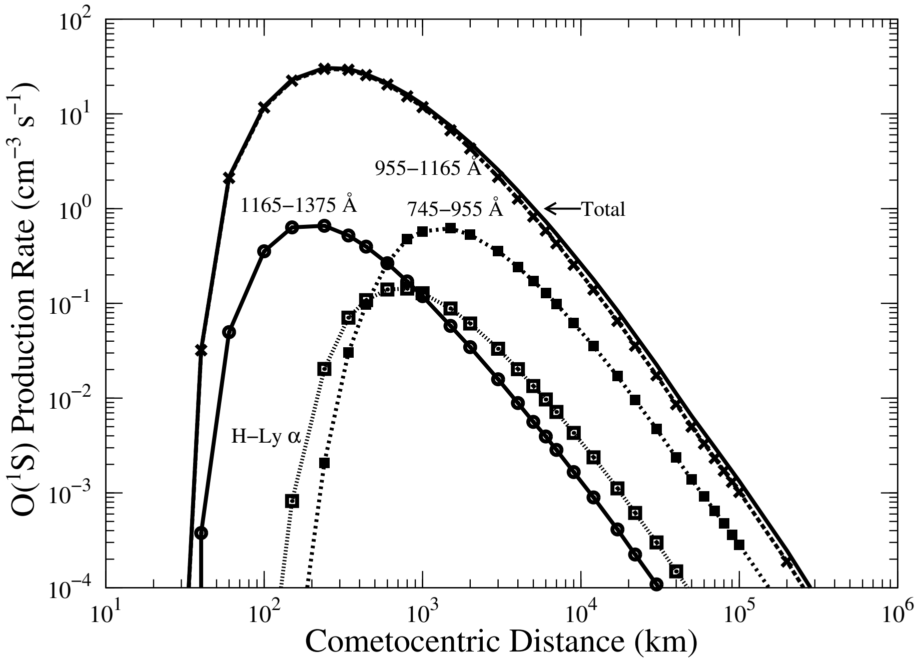

Figure 4.12: Calculated radial profiles on comet C/1995 O1 Hale-Bopp for the photodissociation of CO_2 producing O(^{1}S) at different wavelength bands for the abundances of 6% CO_2 and 24% CO relative to H_2O production rate of 8.3 × 10^{30} s^{-1}.

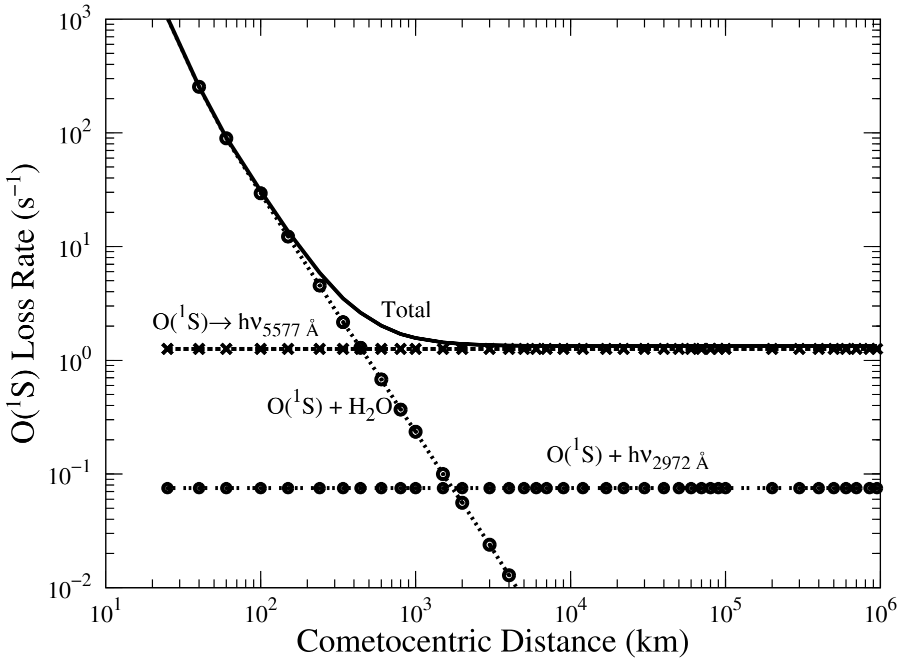

Figure 4.13: Calculated radial profiles on comet C/1995 O1 Hale-Bopp for the major loss mechanisms of the O(^{1}S) atom for the abundances of 6% CO_2 and 24% CO relative to H_2O production rate of 8.3 × 10^{30} s^{-1}.

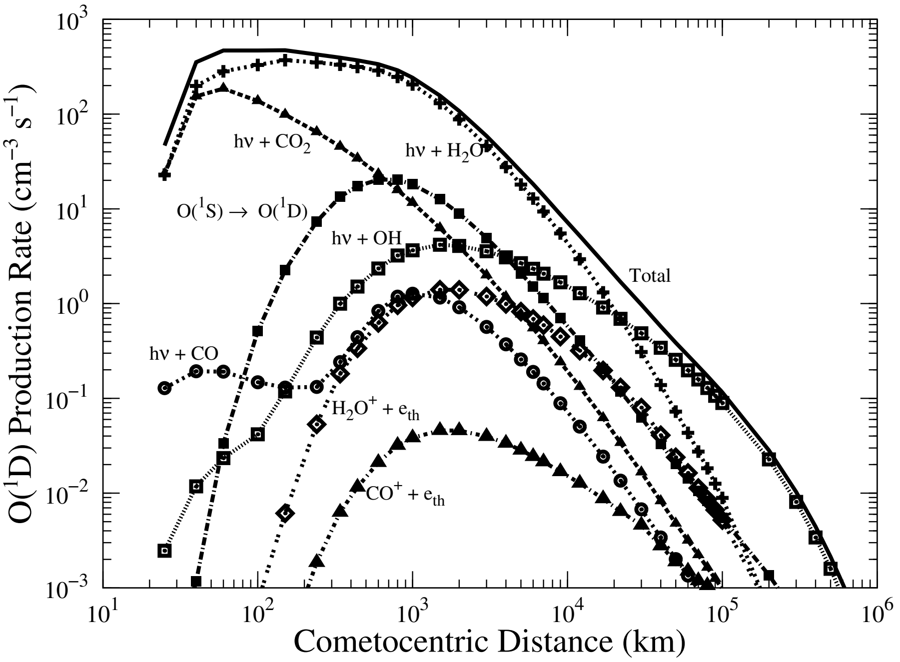

Figure 4.14: Calculated radial profiles on comet C/1995 O1 Hale-Bopp for the major production mechanisms of $O(^1D)$ along with the total $O(^1D)$ production rate profile for the abundances of 6% CO_2 and 24% CO relative to H_2O production rate of 8.3 × 10^{30} s^{-1}. hν : solar photon.

$O(^1D)$. Even though the relative abundance of CO in Hale-Bopp is high (∼25%), the photodissociation of CO is not a potential source mechanism of $O(^1D)$. The calculated $O(^1D)$ photodissociation rate profile for photodissociation of CO shows a double peak structure, which is explained later.

The wavelength-dependent production rates of $O(^1D)$ in the photodissociation of H_2O are shown in Figure 4.15. The most intense line of solar UV spectrum, H Ly-α at 1216 Å, produces maximum $O(^1D)$ around 1000 km, while solar photons in the wavelength regions 1165–1375 and 1375–1575 Å are responsible for producing maximum $O(^1D)$ at shorter radial distances of 200 and 50 km, respectively. Since the total absorption cross section of H_2O in the 1165–1575 Å wavelength region is small (cf. Figure 2.6), these solar photons are able to penetrate deeper in the coma and mostly get attenuated at shorter cometocentric distances by dissociating H_2O. The $O(^1D)$ formation rate by solar photons at other wavelengths is smaller by more than an order of magnitude.

Similarly, the production rate of $O(^1D)$ due to photodissociation of CO_2 calculated at different wavelength bands is shown in Figure 4.17. At radial distances <100 km, solar photons in 1375–1585 Å wavelength region is the main source for $O(^1D)$ formation. This is because the absorption cross section of H_2O has a strong dip around 1400 Å (cf. Figure 2.6) and the average absorption cross section values of H_2O and CO_2 are nearly same in this wavelength region. Thus, solar photons in this wavelength band

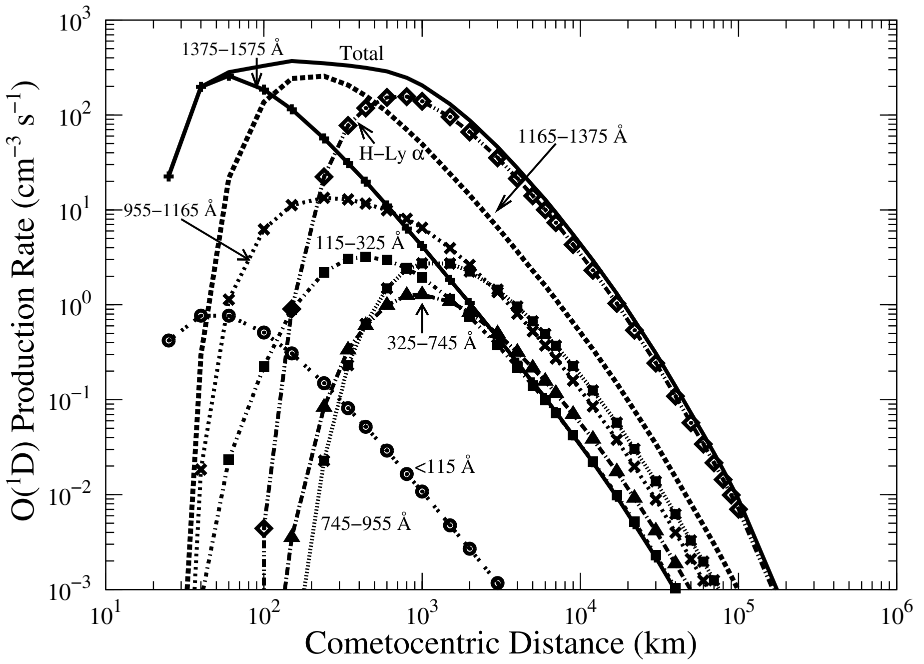

Figure 4.15: Calculated radial profiles on comet C/1995 O1 Hale-Bopp for the photodissociation of H_2O producing O(^{1}D) at different wavelength bands for the abundances of 6% CO_2 and 24% CO relative to H_2O production rate of 8.3 × 10^{30} s^{-1}.

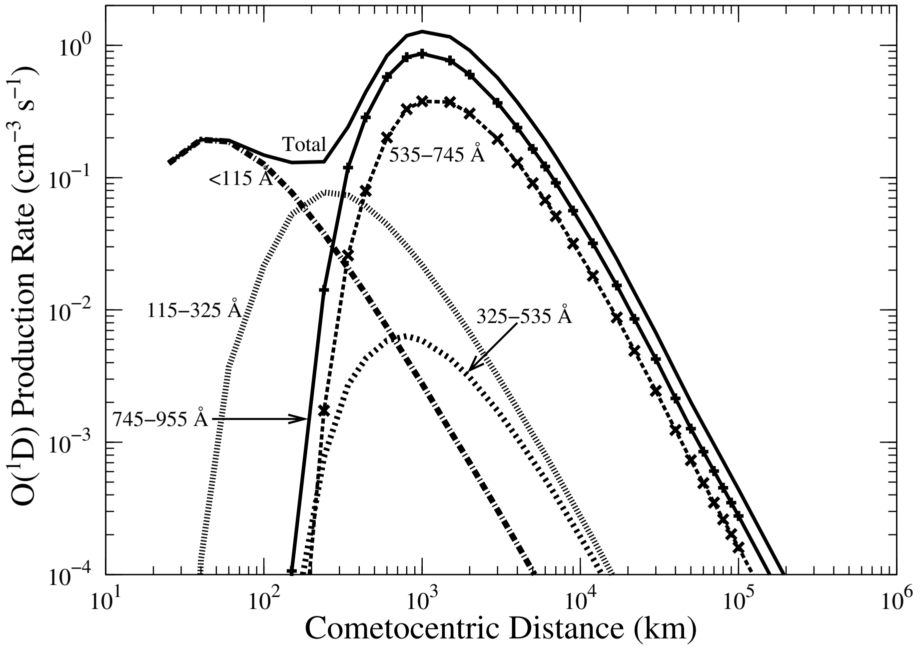

Figure 4.16: Calculated radial profiles on comet C/1995 O1 Hale-Bopp for the photodissociation of CO producing O(^{1}D) at different wavelength bands for the abundances of 6% CO_2 and 24% CO relative to H_2O production rate of 8.3 × 10^{30} s^{-1}.

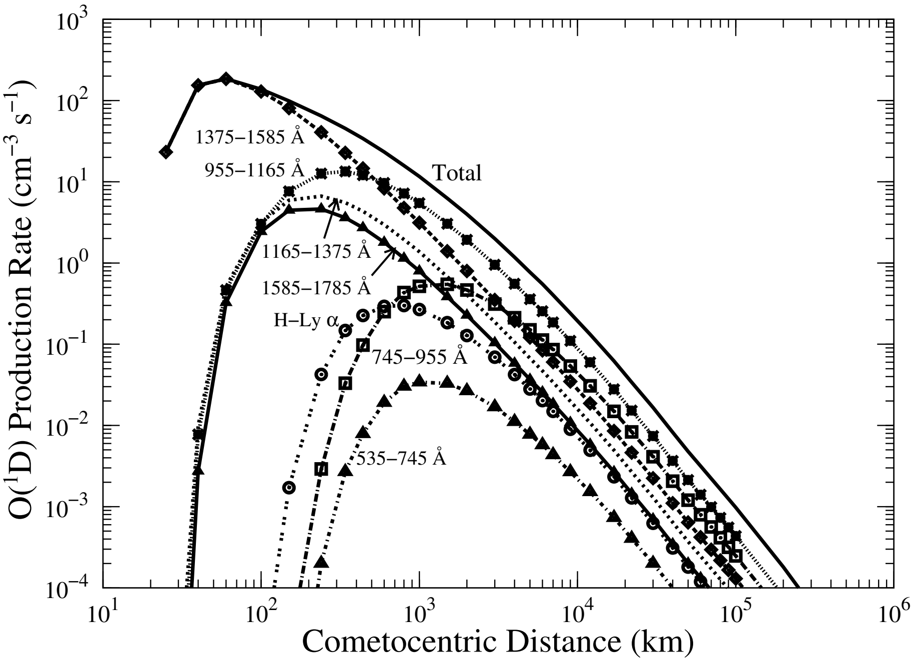

Figure 4.17: Calculated radial profiles on comet C/1995 O1 Hale-Bopp for the photodissociation of CO_2 producing $O(^1D)$ at different wavelength bands for the abundances of 6% CO_2 and 24% CO relative to H_2O production rate of 8.3×10^{30} s^{-1}.

are able to reach the innermost coma and produce $O(^1D)$ by dissociating CO_2. Since the cross section for production of $O(^1D)$ in photodissociation of CO_2 peaks in the wavelength band 955–1165 Å, the solar photons of this region leads the production of $O(^1D)$ above 500 km.

The production rates of $O(^1D)$ via photodissociation of CO in different wavelength bands are presented in Figure 4.16. The total absorption cross section of H_2O is around two orders of magnitude smaller below 115 Å than at other wavelengths, so these high energy photons can travel deeper into the cometary coma (even below 100 km) almost unattenuated. Since the CO molecule offers a cross section (average $\sim 2 \times 10^{-20}$ cm^2) to these photons it leads to the formation of $O(^1D)$ and $C(^1D)$ via photodissociation closer to the cometary nucleus. Between 100 and 500 km, the solar photons in the wavelength region 115–325 Å produce maximum $O(^1D)$ atoms via photodissociation of CO. The dissociative excitation cross section of CO is maximum in the wavelength region 535–955 Å (cf. Figure 2.6), which results in the peak production of $O(^1D)$ via photodissociation of CO at 1000 km. More details on the attenuation of solar flux in high water production rate comets are given in *Bhardwaj* [2003].

The model calculated loss rate profiles of $O(^1D)$ are presented in Figure 4.18. This figure depicts that the predominant destruction channel of $O(^1D)$ in the inner coma (below 3000 km) of comet Hale-Bopp is quenching by H_2O, which results in the formation

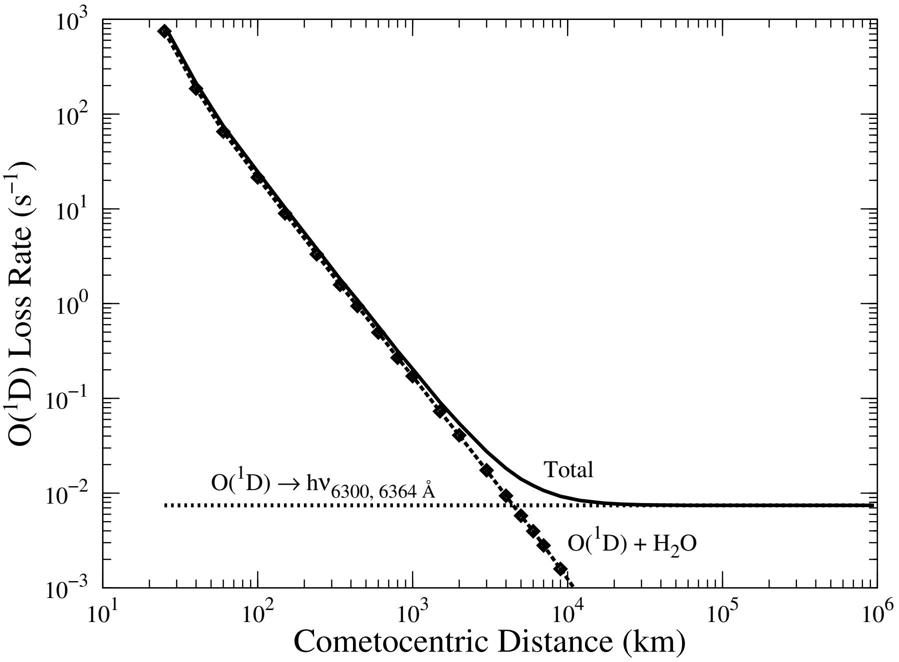

Figure 4.18: Calculated radial profiles on comet C/1995 O1 Hale-Bopp for major loss mechanisms of the $O(^1D)$ atom for the abundances of 6% CO_2 and 24% CO relative to H_2O production rate of 8.3×10^{30} s^{-1}.

of two OH molecules. Above radial distance of 10^4 km, the radiative decay leading to the red-doublet emissions is the major loss for $O(^1D)$ atoms. Quenching by CO_2 and CO are minor loss processes, about one order of magnitude smaller and hence is not shown.

The calculated density profiles of $O(^1S)$, $O(^1D)$, and $O(^3P)$ in comet Hale-Bopp along with parent species considered in the model are shown in Figure 4.19. The density of $O(^1S)$ peaks around 500 km, while the density profile of $O(^1D)$ shows a broad peak between 2000 and 5000 km. The calculated number density profiles of $O(^1D)$ and $O(^1S)$ without collisional quenching processes are also presented in this figure (with dashed lines). This calculation clearly shows that collisional quenching can significantly reduce the $O(^1S)$ and $O(^1D)$ densities in the inner coma. The formation of $O(^3P)$ below 200 km is due to collisions between OH molecules.

4.6.3 Green and Red-doublet emission intensities

The emission rates of [OI] 5577, 2972, 6300, and 6364 Å are calculated by multiplying Einstein transition probabilities ($A_{5577} = 1.26$ s^{-1}, $A_{2972} = 0.134$ s^{-1}, $A_{6300} = 6.44 \times 10^{-3}$ s^{-1}, and $A_{6364} = 2.17 \times 10^{-3}$ s^{-1}) with the densities of $O(^1S)$ and $O(^1D)$. The intensity of these line emissions along the line of sight is calculated by integrating the emission rates. The model calculated brightness profiles as a function of projected distance for these forbidden emissions along with the [OI] 6300 Å observations of *Morgenthaler et al.* [2001] made on 2 and 5 March 1997 using Hydra and WHAM instruments, respectively,

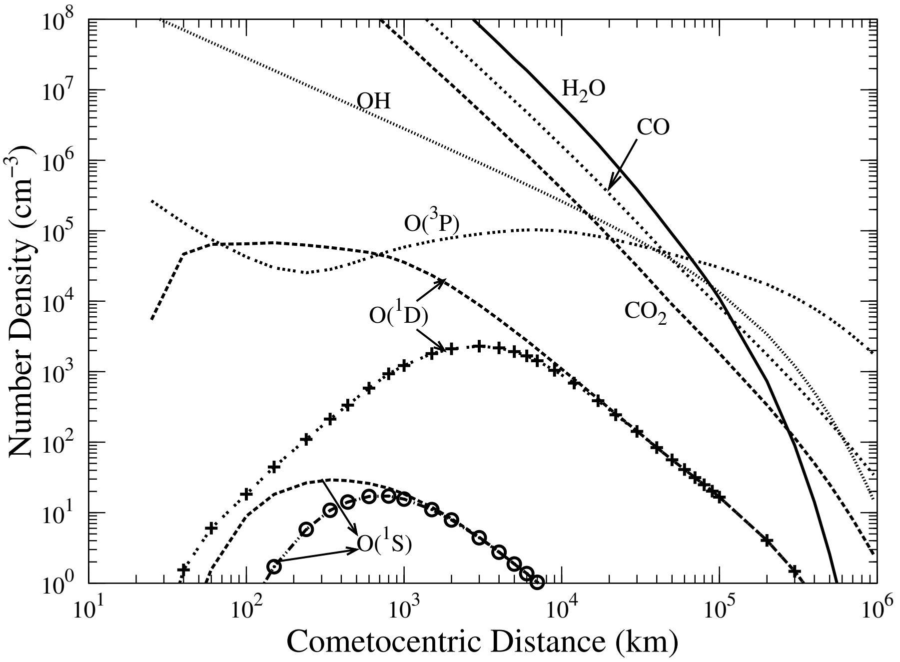

Figure 4.19: Calculated number density profiles of O(^{1}S), O(^{1}D), O(^{3}P), and OH, along with those of H_2O, CO, and CO_2 on comet C/1995 O1 Hale-Bopp. The calculations are done for the abundances of 6% CO_2 and 24% CO relative to H_2O production rate of 8.3 × 10^{30} s^{-1}. The dashed lines of O(^{1}S) and O(^{1}D) are the calculated densities without accounting the collisional quenching processes.

are presented in Figure 4.20. To show the collisional quenching effect, we also presented the calculated forbidden emission line intensities (with dotted lines) in Figure 4.20, by considering only radiative decay as the loss process of O(^{1}S) and O(^{1}D).

The calculated percentage contributions of various processes involved in the production of metastable O(^{1}S) and O(^{1}D) at different projected distances are presented in Table 5.2. For 6% relative abundance of CO_2, photodissociation of CO_2 is the major source of O(^{1}S) production rather than photodissociation of H_2O (cf. Figure 4.11). So we varied the CO_2 relative abundance to study the change in the contribution of CO_2 to the O(^{1}S) and O(^{1}D) production. Calculations presented in Table 5.2 depict that, for a 6% relative abundance of CO_2, below 10^4 km projected distances, around 25 to 30% of O(^{1}S) production is via photodissociation of H_2O, while 40 to 60% production is through photodissociation of CO_2. Though the relative abundance of CO in comet Hale-Bopp is high (∼25%), the photodissociation of CO could contribute a maximum of 10% to the O(^{1}S) production. The dissociative recombination of H_2O^+ and CO^+ together can contribute 10% to the production of O(^{1}S), whereas photodissociative excitation of OH is a minor (<5%) source. At 10^5 km projected distance, the photon reactions together contributing 60% of O(^{1}S) and remaining is contributed by dissociative recombination of O-bearing ions. When the abundance of CO_2 is reduced to 3%, below 10^4 km projected

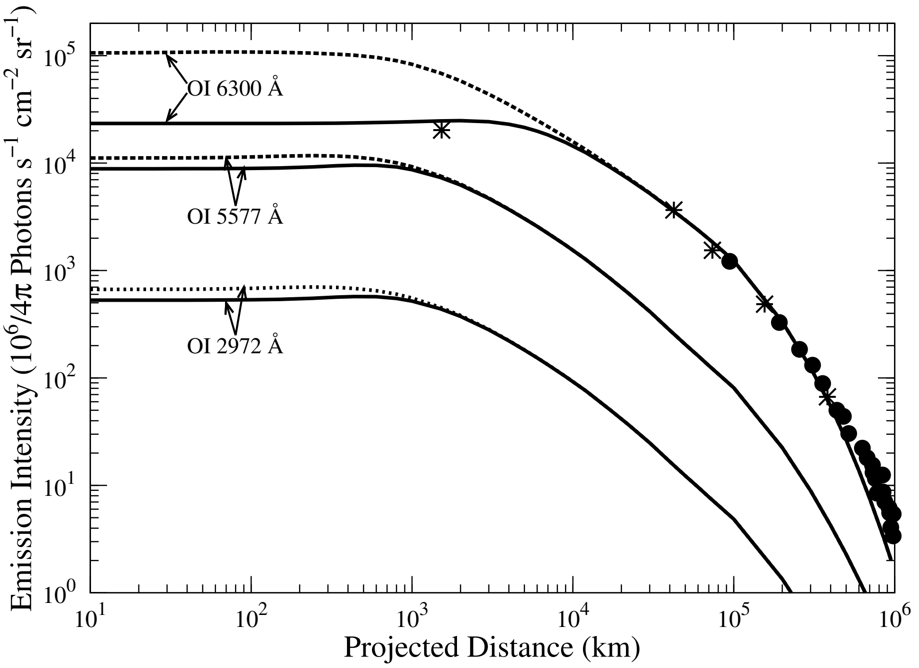

Figure 4.20: Calculated [OI] 6300, 5577, and 2972 Å emission lines brightness profiles on comet C/1995 O1 Hale-Bopp as a function of the projected distance for the abundances of 6% CO_2 and 24% CO relative to H_2O production rate of 8.3 × 10^{30} s^{-1}. For comparison the observed intensities of 6300 Å line emission by *Morgenthaler et al.* [2001] using Hydra (stars) and WHAM (filled circles) instruments on 2 March (r_h = 1.05 AU and Δ = 1.46 AU) and 5 March, 1997 (r_h = 1.03 AU and Δ = 1.42 AU), respectively, are also shown. During the observation the field of view of Hydra and WHAM instruments are 1° and 45′, respectively [*Morgenthaler et al.*, 2001]. Dotted lines are the calculated intensities when collisional quenching is not considered.

distance, photodissociation of H_2O (35 to 40%) and CO_2 (30 to 50%) contribute almost equally to the production of $O(^1S)$.

Below 10^4 km projected distance, the major production process of $O(^1D)$ is the photodissociation of H_2O, whose contribution is 60 to 80% (cf. Table 5.2). Around 10^4 km the photodissociation of OH is also a significant (around 20%) production source of $O(^1D)$; but, in the inner coma the contribution of this process is small (<10%). Radiative decay of $O(^1S)$ and electron recombination of H_2O^+ contribute less than 10% each. At 10^5 km projected distance, most (75%) of $O(^1D)$ is produced by photodissociation of OH and remaining is contributed by other reactions. The change in the relative abundance of CO_2 by a factor of 2, from 6% to 3%, does not affect the relative contributions of various sources of $O(^1D)$ below 10^4 km projected distance.

Table 4.5: Calculated percentage contributions for the major production processes of O(^{1}S) and O(^{1}D) in comet C/1995 O1 Hale-Bopp with varying relative abundance of CO$_2$ for 0.5 % O(^{1}S) yield.

CO$_2$ (%)	Production processes of O(^{1}S) and O(^{1}D) at three cometocentric projected distances (km) (%)																							
	hν + H$_2$O				hν + OH				hν + CO$_2$				hν + CO				O(^{1}S) → O(^{1}D)				e + H$_2$O$^+$			
	10^2	10^3	10^4	10^5	10^2	10^3	10^4	10^5	10^2	10^3	10^4	10^5	10^2	10^3	10^4	10^5	10^2	10^3	10^4	10^5	10^2	10^3	10^4	10^5
6	25	31	24	6	0.5	1	4	14	58	50	40	23	6	7	8	5					2	3	9	7
	(77)†	(76)	(49)	(7)	(6)	(8)	(33)	(75)	(7)	(4)	(2)	(1)	(0.5)	(0.5)	(1)	(0.5)	(6)	(8)	(8)	(5)	(2)	(2)	(8)	(5)
3	33	42	33	8	1	1	5	18	47	36	26	15	8	9	10	7					2	3	11	11
	(82)	(80)	(49)	(8)	(7)	(9)	(34)	(77)	(4)	(2)	(1)	(0.5)	(0.5)	(1)	(1)	(0.5)	(5)	(6)	(6)	(4)	(2)	(2)	(8)	(5)
1	49	57	42	10	1	2	7	24	27	17	11	7	12	13	13	9					4	5	15	14
	(85)	(82)	(51)	(8)	(7)	(9)	(35)	(78)	(1)	(0.5)	(0.5)	(0.5)	(1)	(1)	(1)	(0.5)	(4)	(5)	(5)	(3)	(2)	(3)	(7)	(5)

†The values in parenthesis are for the O(^{1}D).

Table 4.6: Calculated percentage contributions for the major production processes of green and red-doublet emissions in the total observed projected field of view (2.4 × 10^5 km) on comet C/1995 O1 Hale-Bopp with varying relative abundance of CO_2.

CO_2 (%)	hν + H_2O	hν + OH	hν + CO_2	e^- + CO_2^+	e^- + H_2O^+	$O(^1S) \rightarrow O(^1D)$	hν + CO
6	23 (48)[‡]	4 (35)	41 (3)	8 (0.5)	7 (5)	(7)	7 (1)
3	32 (50)	6 (36)	30 (2)	5 (0.5)	10 (8)	(7)	10 (1)
1	42 (50)	8 (37)	13 (0.5)	2 (0.5)	13 (8)	(5)	13 (1)

[‡] The values in parenthesis are the calculated percentage contributions for red-doublet emission.

For a 4′ circular aperture projected field of view (∼2.4 × 10^5 km) on comet Hale-Bopp, which is similar to the 50 mm Fabry-Pérot spectrometer observations of *Morgenthaler et al.* [2001], the calculated percentage contribution of major production processes for the green and red-doublet emissions, for different relative abundances of CO_2, are presented in Table 5.3. These calculations clearly suggest that in a comet which has been observed over a large projected area, the photodissociation of H_2O and OH mainly (∼ 80%) controls the [OI] 6300 Å emission, while the radiative decay of $O(^1S)$ contributes a maximum value of 10% to the total red-doublet intensity. With 6% relative abundance of CO_2, the [OI] 5577 Å line emission observed in the coma is largely (∼40%) contributed by photodissociation of CO_2, and photodissociation of H_2O is the next significant (∼25%) production process. The other production processes, like dissociative recombination of ions, photodissociation of CO, OH, etc, together contribute less than 30% to the [OI] 5577 Å intensity. When the CO_2 abundance is reduced to 3%, both photodissociation of H_2O and CO_2 are contributing equally (∼30%) to the green line emission intensity. In all these cases, in spite of CO relative abundance being high (∼25%) in comet Hale-Bopp, the photodissociation of CO could contribute a maximum value of 10%.

We calculated the G/R ratio profiles on comet Hale-Bopp on 26 March 1997 by varying CO_2 relative abundance from 6 to 3 to 1% which are presented in Figure 4.21. For comparison, the G/R ratio profile calculated on comet Hyakutake is also plotted in Figure 4.21. In comet Hyakutake the G/R ratio is constant up to 100 km projected distance, while in the case of comet Hale-Bopp it is constant even up to 1000 km. The flatness of the G/R ratio depends on the quenching rate of metastable $O(^1S)$ and $O(^1D)$ by H_2O which is a function of water production rate of the comet. Thus, in comets where H_2O production rate is still larger than that of Hale-Bopp, the G/R ratio would be constant up to projected distances larger than 10^3 km.

4.6.4 Radiative efficiencies of $O(^1S)$ and $O(^1D)$ atoms

The number density of $O(^1S)$ and $O(^1D)$ in the cometary coma is controlled by various production and loss processes at that radial distance. To understand the region of maximum emission of green and red-doublet lines in the coma we calculated the

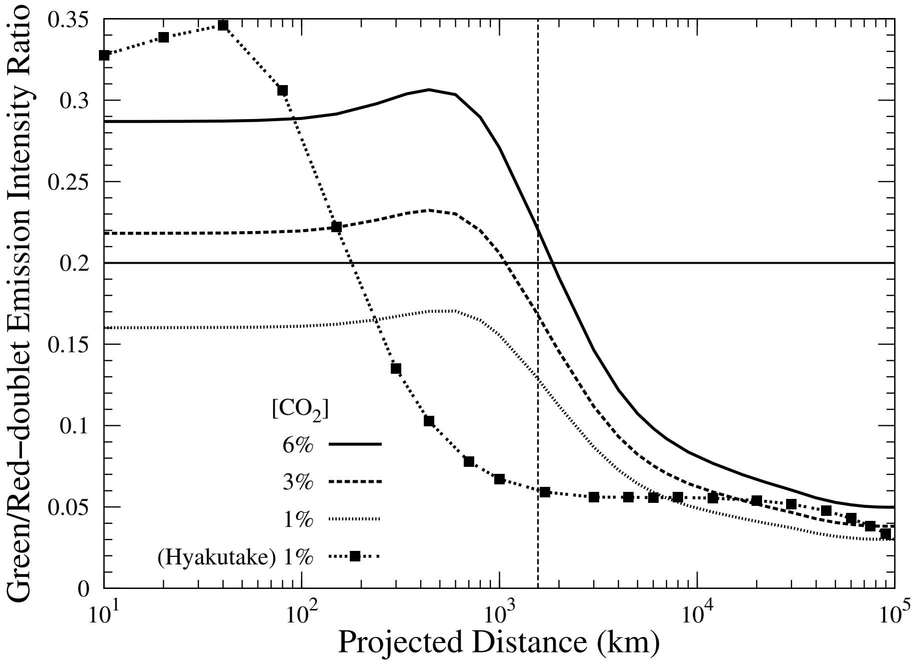

Figure 4.21: Calculated green to red-doublet intensity ratio along projected distances in comet C/1995 O1 Hale-Bopp for different CO_2 relative abundances [CO_2] and with 0.5% yield for O(^{1}S) production in the photodissociation of H_2O. *Zhang et al.* [2001] observed average green to red-doublet intensity ratio was 0.2 for the slit projected size of 522 × 1566 km over comet Hale-Bopp on 28 March 1997, which is shown with a horizontal line. The vertical dotted line represents 1566 km projected distance on the cometary coma. For comparison the calculated G/R ratio profile with 1% CO_2 and 0.5% yield in comet C/1996 B2 Hyakutake is also shown.

radiative efficiency profiles of O(^{1}S) and O(^{1}D) in comets Hale-Bopp and Hyakutake by calculating the ratio of emission rate to total production rate of respective species. The calculated radiative efficiency profiles of O(^{1}S) and O(^{1}D) are presented in Figure 4.22 with solid and dotted lines for comets Hale-Bopp and Hyakutake, respectively. This figure depicts that in comet Hale-Bopp all the O(^{1}S) atoms produced above 1000 km radial distance emit 5577 Å (or 2972 Å) photons, while for O(^{1}D) the radiative efficiency is unity above 10^4 km. Since the lifetime of O(^{1}D) is higher by two orders of magnitude than that of O(^{1}S), most of the produced O(^{1}D) in the inner coma get quenched by other cometary species (mainly by H_2O) without emitting photons at wavelengths 6300 and 6364 Å. But in case of comet Hyakutake the radiative efficiency of O(^{1}S) and O(^{1}D) is unity above 100 and 1000 km, respectively. This calculation shows that in comets most of the green and red-doublet emissions are produced above the collisional-dominated region where the radiative decay is the dominant loss process for O(^{1}S) and O(^{1}D) atoms.

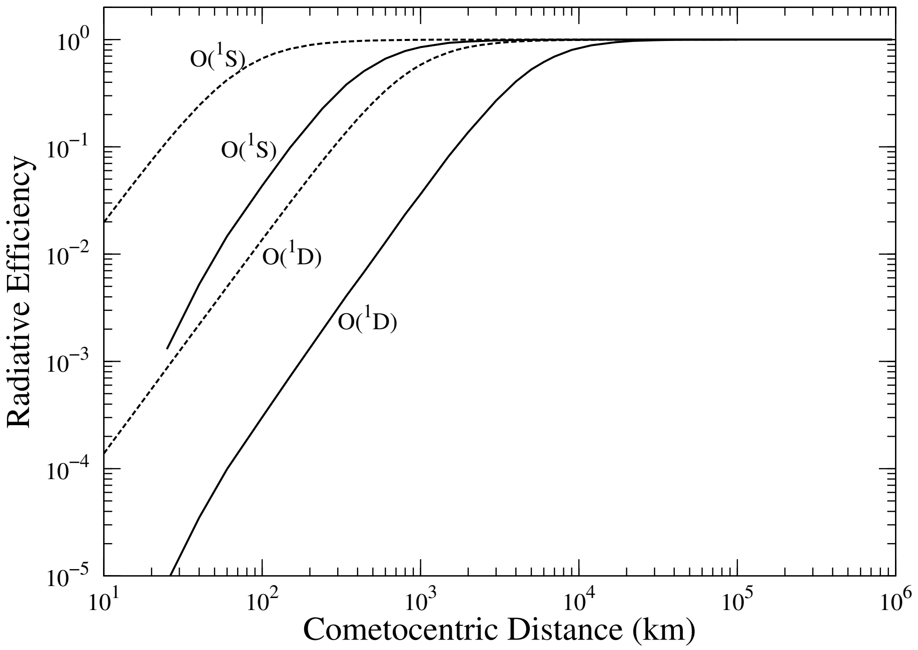

Figure 4.22: Calculated radiative efficiency profiles of O(^{1}S) and O(^{1}D) on comets C/1995 O1 Hale-Bopp (solid lines) and C/1996 B2 Hyakutake (dashed lines). Radiative efficiency is the ratio of emission rate to the production rate.

4.6.5 Excess velocities of O(^{1}S) and O(^{1}D)

Solar photons having energy more than the dissociation threshold of cometary species impart the additional energy to the kinetic motions of daughter products. The mean excess energy released in the ith dissociation process at a radial distance r can be determined as

$$E_i(r) = \frac{\int_0^{\lambda_{th}} hc\left(\frac{1}{\lambda} - \frac{1}{\lambda_{th}}\right)\sigma(\lambda)\phi(\lambda, r)e^{-\tau(\lambda,r)}d\lambda}{\int_0^{\lambda_{th}} \sigma(\lambda)\phi(\lambda, r)e^{-\tau(\lambda,r)}d\lambda} \tag{4.6}$$

where λ is the wavelength of solar photon, λ_{th} is the threshold wavelength for the dissociation process, h is Planck's constant, and c is the velocity of light. $\sigma(\lambda)$ is the dissociation cross section of the cometary species at wavelength λ. $\phi(\lambda, r)$ and $\tau(\lambda, r)$ are the solar flux and the optical depth of the medium for the photon of the wavelength λ at a radial distance r, respectively.

The model calculated mean excess energy profiles for the photodissociation of H_2O, CO_2, and CO forming O(^{1}S) and O(^{1}D) are presented in Figure 4.23 with solid and dotted lines for comets Hale-Bopp and Hyakutake, respectively. Above 3000 km radial distance, the calculated excess energies in different photodissociation processes in both comets show a constant profile, because the optical depth in this region for photons of different wavelengths is very small. These values are in agreement with the calculations of *Huebner et al.* [1992]. However, at shorter radial distances the neutral density is

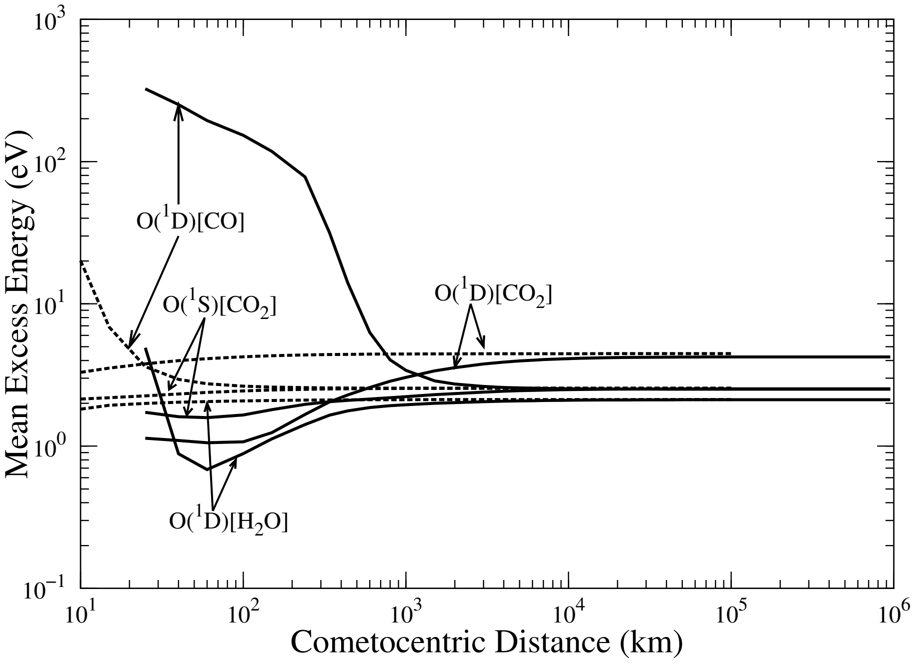

Figure 4.23: Calculated excess energy profiles of O(^{1}D) in photodissociation of H_2O, CO, and CO_2 and that of O(^{1}S) in photodissociation of CO_2 on comets Hale-Bopp (solid lines) and Hyakutake (dashed lines).

higher and hence the wavelength dependent photodissociation is significant which causes different excess energy values.

In comet Hale-Bopp the calculated mean excess energy in photodissociation of H_2O producing O(^{1}D) shows a highest value of 5.6 eV at the surface of the nucleus and decreases to a minimum value of 0.7 eV at 50 km. Above 50 km the mean excess energy increases and becomes constant (2.12 eV) above 3000 km. This is because of the formation of O(^{1}D) via the photodissociation of H_2O is associated with the photons of different energies and it also varies with radial distance as shown in Figure 4.15. At a given radial distance the mean excess energy released in the photodissociation process is determined by the mean of energies of different solar photons involved. The threshold energy for production of O(^{1}D) by dissociating H_2O is 7 eV. Very close to the cometary nucleus (<50 km), photons of wavelength smaller than 115 Å and in the wavelength band 1375–1575 Å determines the formation of O(^{1}D) (cf. Figure 4.15). At this distance, most of O(^{1}D) is produced by the photons of low energy (7–9 eV) in the wavelength band 1375–1575 Å, and a small amount of O(^{1}D) is produced by very high energy (>100 eV) photons which results in the mean excess energy of about 2–5 eV. But around 50 km, the majority of O(^{1}D) production is determined by the photons of low energy 7 to 12 eV (955–1575 Å wavelength band) and the contribution from photons of wavelength below 115 Å is very small. This causes the minimum value of mean excess energy 0.7 eV at this radial distance.

Between 50 and 300 km, the increase in the excess energy is due to the production of O(^{1}D) atoms by photons of wavelength bands 115–325, 955–1575 Å, and solar H Ly-α. Though high energy photons (115–325 Å) are also involved in this region, the intense solar photon flux at H Ly-α (1216 Å) governs the majority of O(^{1}D) production and subsequently determines the mean excess energy. The solar H Ly-α photons can provide the maximum excess energy of 3 eV in the photodissociation of H_2O. Above 1000 km more than 90% of the O(^{1}D) production is controlled by photons at 1216 Å wavelength and the remaining from other wavelength bands (cf. Figure 4.15), which results a constant value of mean excess energy of 2.12 eV.

Similarly, the mean excess energy calculated in the photodissociation of CO_2 producing O(^{1}D) can be explained based on the wavelength dependent photon attenuated profiles presented in Figure 4.17. The threshold energy for the O(^{1}D) production in photodissociation of CO_2 is 7 eV and for O(^{1}S) it is 9 eV. At radial distances less than 100 km, the production of O(^{1}D) in photodissociation of CO_2 is determined by the photons of low energy (average 8 eV) in the wavelength bands 1375-1785 Å and 955-1165 Å, which results in low mean excess energy of $\sim$1 eV. Above 100 km, photons of different energies ranging from 7 to 16 eV (cf. Figure 4.17) causes the mean excess energy of $\sim$4 eV. The calculated mean excess energy profiles in the photodissociation of CO_2 producing O(^{1}S) and O(^{1}D) are not similar. This is because the O(^{1}S) production occurs via photodissociation of CO_2 in the wavelength band of 800 to 1300 Å (photons of 10-15 eV), whereas O(^{1}D) is produced by photons of wavelength less than 800 Å (>15 eV) (cf. Figure 2.6).

The threshold energy for the dissociation of CO producing O(^{1}D) is 14.3 eV. Below 200 km the calculated maximum mean excess energy in the photodissociation of CO producing O(^{1}D) is more than 100 eV. This is because the formation of O(^{1}D) at these distances (cf. Figure 4.16) is mainly determined by photons of wavelength less than 115 Å (>110 eV) with some contribution from the wavelength band 115–325 Å (40–110 eV). Above 500 km, the formation of O(^{1}D) is mainly due to solar photons in the wavelength band 535–955 Å (23–13 eV) which results in the maximum excess energy of 2.5 eV.

4.7 Discussion

The major difference between comets Hale-Bopp and Hyakutake is the H_2O production rate, which is larger by a factor of 30 in the former. This difference in the H_2O production rates result in a change in the photochemistry of O(^{1}S) and O(^{1}D) in the cometary coma. Due to the dense coma of comet Hale-Bopp, the attenuation of solar UV-EUV photons on Hale-Bopp differs significantly from that in Hyakutake. Moreover, the CO_2 abundance in comet Hyakutake is smaller (<3% relative abundance) compared to that in Hale-Bopp ($\sim$6% relative abundance). The high H_2O production rate in comet Hale-Bopp results in a larger collisional coma (radius few $\times$ 10^5 km) which is comparable to the scale length ($\sim 8 \times 10^4$ km) of H_2O molecule. In the low production rate comets the collisional zone is smaller and photochemistry significantly differs.

The photodissociation rate of H_2O producing $O(^1S)$ is smaller than that of CO_2 is smaller by a factor of 20 (cf. Table 4.1). Hence, the major source of $O(^1S)$ in the inner coma of comet Hale-Bopp is photodissociation of CO_2 rather than photodissociation of H_2O. Since the relative abundance of CO_2 in comet Hyakutake is 1%, the photodissociation of CO_2 becomes an important source only near the surface of the nucleus (cf., Figure 4.2). The production peak of $O(^1S)$ in comet Hyakutake is closer to the nucleus (<20 km), whereas in comet Hale-Bopp it is between 100 and 1000 km. Even when we reduced the CO_2 abundance by 50% in Hale-Bopp, the peak production of $O(^1S)$ in the inner coma is mainly controlled by photodissociation of CO_2 and not by photodissociation of H_2O. Hence, in a high water production rate comet a small relative abundance (~5%) of CO_2, makes CO_2 as a potentially important source of $O(^1S)$ compared to H_2O.

In comet Hyakutake, below 10^5 km, the photodissociation of H_2O is the major (more than 90%) production process of $O(^1D)$ formation and the contributions from other processes are very small. Since H_2O and CO_2 production rates are higher in comet Hale-Bopp, the solar photons of wavelength band 955–1165 Å, which are less attenuated by H_2O, can travel deeper into the cometary coma and dissociate the CO_2 to form $O(^1D)$, which is not the case in comet Hyakutake.

With a high H_2O production rate, comet Hale-Bopp provided a large gaseous environment, which has not been seen in previous comets. Since the apparition was at small geocentric distances, the giant cometary coma has provided a laboratory for investigating several collisional-driven effects. These collision driven processes are very important in determining the distribution of cometary excited species in the coma, which manifests into the emissions of the cometary coma. The radius of collisional coma, which is a function of total gas production rate, differs by an order of magnitude in comets Hyakutake and Hale-Bopp. In comet Hyakutake quenching of $O(^1S)$ by H_2O is the main destruction mechanism only close to the nucleus (<50 km) and radiative decay dominates at distances larger than 100 km. However, in comet Hale-Bopp collisional quenching is significant up to 500 km and above this radial distance radiative decay is the major loss mechanism of $O(^1S)$. Similarly, the collisional quenching radii of $O(^1D)$ in comets Hyakutake ($\sim 10^3$ km) and Hale-Bopp ($\sim 10^4$ km) also differs by an order of magnitude.

The $O(^1D)$ density peak in comet Hale-Bopp is broader (2000 to 5000 km) than that in comet Hyakutake (200 to 600 km). This change in the peak distribution of $O(^1D)$ in the two comets is due to different H_2O production rates and wavelength dependent photo-attenuation in the cometary comae.

4.7.1 Comparison of model calculations with observations

4.7.1.1 Atomic oxygen emission lines on comet C/1996 B2 Hyakutake

In March 1996, the green and red-doublet emissions were observed in comet C/1996 B2 Hyakutake from two ground-based observatories [*Morrison et al.*, 1997; *Cochran*, 2008]. Each observatory determined the G/R ratio using different slit size. Using a circular slit, the projected radial distance over the comet for *Morrison et al.* [1997] observation on 23 March and 27 March 1996 varied from 640 to 653 km, while for *Cochran* [2008] observation, using a rectangular slit, the projected area was 480 × 3720 km on 9 March and 165 × 1129 km on 30 March. The clear detection of both green and red-doublet emissions and determination of the G/R ratio could be done for 9 March and 23 March observations only [*Cochran*, 2008; *Morrison et al.*, 1997]. The observed G/R ratio was 0.09 and 0.12 to 0.16 for the observation on 9 March and 23 March, respectively.

Making a very high resolution (R = 200,000) observation of comet C/1996 B2 Hyakutake on 30 March 1996, *Cochran* [2008] obtained radial profiles of 5577 and 6300 Å lines. In Figure 4.10 we have compared the model calculated intensity profiles of 6300 and 5577 Å lines at different projected cometocentric distances with the observation of *Cochran* [2008]. The 6300 Å emission shows a flat profile upto ∼500 km, whereas the 5577 Å green line starts falling off beyond 100 km. This is because of the quenching of O(^{1}S) and O(^{1}D) by H_2O in the inner most coma (cf. Figures 4.4 and 4.8), thereby making both the production and loss mechanisms being controlled by H_2O. Above these distances, the emissions are mainly controlled by the radiative decay of ^{1}S and ^{1}D states of oxygen atoms. The calculated G/R ratio along projected distance is shown in Figure 4.24.

Similar to the calculations presented in Tables 4.3 and 4.4 we present the calculated red and green line intensity profiles and the G/R ratios along projected distance in Figures 4.10 and 4.24, respectively, for different contributions of O(^{1}S) yield and CO_2 abundances. Since photodissociative excitation of H_2O is the main production process for O(^{1}D) atom, the red line intensity is almost independent of the variation in O(^{1}S) yield and CO_2 abundance. In the case of 0% CO_2 abundance, the best fit to the observed green line profile is obtained when the O(^{1}S) yield is ∼0.5% (± 0.1%), where the G/R ratio varied from 0.06 to 0.26 (cf. Figure 4.24) and the slit-averaged G/R ratio for 30 March 1996 observation is 0.15 (cf. Table 4.4). The shape of green line profile cannot be explained with 1% or 0% O(^{1}S) yield, while the case for 0.2% O(^{1}S) yield can be considered as somewhat consistent with the observation. For this case, the value of G/R ratio shown in Figure 4.24 is found to vary over a large range of 0.54 to 0.02.

When we consider 1% CO_2 in the comet, the best-fit green profile is obtained when the O(^{1}S) yield is ∼0.2%. The case for 0.5% O(^{1}S) yield also provides the green line

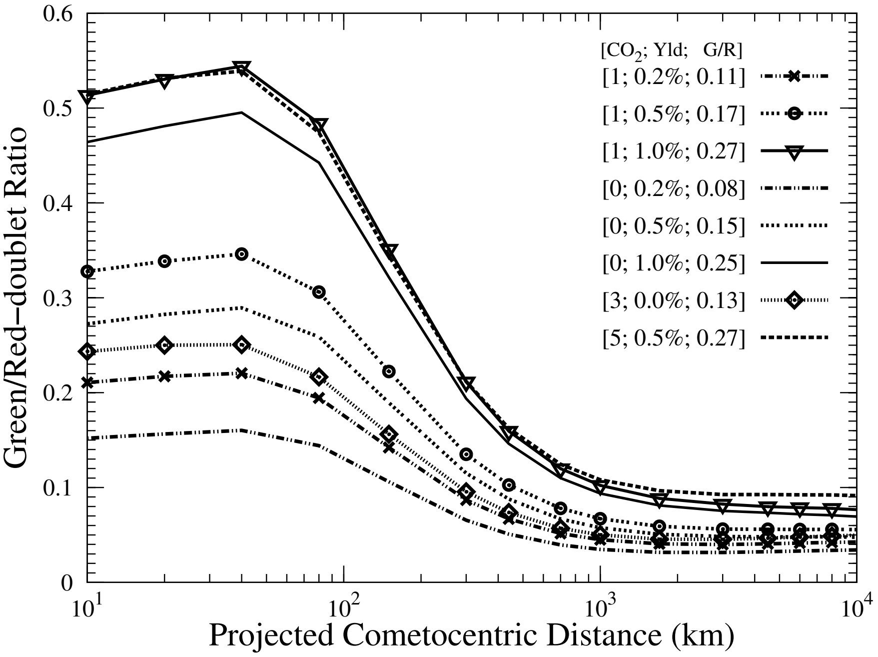

Figure 4.24: Calculated green to red-doublet intensity ratio along projected distance in comet C/1996 B2 Hyakutake for different CO_2 relative abundance [CO_2] and yield [Yld] for O(^{1}S) production in photodissociation of H_2O. G/R = calculated green to red-doublet intensity ratio averaged over slit projected size 165 × 1130 km for C/1996 B2 Hyakutake on 30 March 1996.

profile consistent with the observation. In both these cases the G/R ratio varies between 0.32 and 0.04 over the cometocentric projected distances of 10 to 10^4 km. The calculated 5577 Å profiles for O(^{1}S) yield of 0% and 1% are inconsistent with the observed profile.

In Figure 4.10 we also show a calculated profile for a case when the CO_2 abundance is 3% while the O(^{1}S) yield is 0% (i.e., no O(^{1}S) is produced in photodissociation of H_2O). The calculated 5577 Å green line profile shows a good fit to the observed profile: suggesting that even a small abundance of CO_2 is enough to produce the required O(^{1}S). This is because the CO_2 is about an order of magnitude more efficient in producing O(^{1}S) atom than H_2O in the photodissociation process (see Table 4.1). However, since O(^{1}S) would definitely be produced in the photodissociation of H_2O, and that the CO_2 would surely be present in comet (though in smaller abundance), the most consistent value for the O(^{1}S) yield would be around 0.5%. Assuming 5% CO_2 and 0.5% O(^{1}S) yield, the calculated green line emission profile is inconsistent with the observation (cf. Figure 4.24). In this case, the calculated G/R ratio shown in Figure 4.24 is found to vary between 0.24 and 0.05.

From the above calculations it is clear that the slit projected area on to the comet also plays an important role in deciding the G/R ratio. This point can be better understood from Table 4.7 where the G/R ratio is presented for a projected square slit on the comet at different geocentric distances. It is clear from this table that for a given physical condition of a comet and at a given heliocentric distance, the observed G/R ratio for a given slit size can vary according to the geocentric distance of the comet. For example, for a $O(^1S)$ yield of 0.2% (0.5%) and CO_2 abundance of 1%, the G/R ratio can be 0.17 (0.26) if the comet is very close to the Earth (0.1 AU), whereas the G/R ratio can be 0.07 (0.1), 0.06 (0.08), or 0.06 (0.07), if the comet, at the time of observation, is at a larger distance of 0.5, 1, and 2 AU from the Earth, respectively. Further, a G/R ratio of ∼0.1 can be obtained even for the $O(^1S)$ yield of 0%. This suggests that the value of 0.1 for the G/R ratio is in no way a definitive benchmark value to conclude that H_2O is the parent of atomic oxygen atom in the comet, since smaller (∼5% relative to H_2O) amounts of CO_2 and CO itself can produce enough $O(^1S)$ compared to that from H_2O. This table also shows that for observations made around a geocentric distance of 1 AU, the G/R ratio would be generally closer to 0.1. The G/R ratio observed in different comets ranges from 0.02 to 0.3 [e.g., *Cochran*, 2008; *Capria et al.*, 2010].

Table 4.7: Calculated green to red-doublet emission brightness ratio averaged over 5″ × 5″ slit, at different geocentric distances of comet C/1996 B2 Hyakutake and by varying CO_2 abundance.

Yield*	Geocentric distance (AU)					
(%)	0.1	0.2	0.5	1	1.5	2
1% CO_2						
0.0	0.11	0.07	0.05	0.04	0.04	0.04
0.2	0.17	0.11	0.07	0.06	0.05	0.05
0.5	0.26	0.17	0.10	0.08	0.07	0.07
1.0	0.40	0.26	0.15	0.12	0.10	0.10
0% CO_2						
0.0	0.07	0.05	0.03	0.03	0.03	0.03
0.2	0.13	0.09	0.05	0.05	0.04	0.04
0.5	0.23	0.15	0.09	0.07	0.06	0.06
1.0	0.37	0.24	0.14	0.11	0.01	0.01
3% CO_2						
0.0	0.19	0.13	0.08	0.06	0.06	0.06
0.5	0.33	0.21	0.13	0.10	0.09	0.09

*$O(^1S)$ yield from photodissociation of H_2O. Calculations are made for 30 March 1996, where r=0.94 AU.

Thus, we can conclude that the G/R ratio not only depends on the production and loss mechanisms of $O(^1S)$ atom, but also depends on the nucleocentric slit projected area over the comet. Moreover, the CO_2 plays an important role in the production of $O(^1S)$, and thus the green line emission, in comets. With the present model calculations and based on the literature survey of dissociation channels of H_2O, we suggest that the $O(^1S)$

yield from photodissociation of H_2O cannot be more than 1% of the total absorption cross section of H_2O at solar Ly-α radiation. The best fit value of O(^{1}S) yield derived from Figure 4.10 for a smaller (1%) CO_2 abundance in comet C/1996 B2 Hyakutake is 0.4 (±0.1)%. As per Tables 4.1 and 4.2, this means that the ratio of production rates of O(^{1}S) to O(^{1}D) in the H_2O photodissociation should be 0.03 (±0.01), which is much smaller than the value of 0.1 generally used in literature based on *Festou and Feldman* [1981]. Further, if the source of red and green lines is CO_2 (CO), the ratio of photorates for O(^{1}S) to O(^{1}D) would be around 0.6 (0.8) (see Tables 4.1 and 4.2).

Table 4.8: Calculated intensities of green and red-doublet emissions and the G/R ratio in comet C/1996 B2 Hyakutake on different days of observation in March 1996.

DoB.[§]	r (AU)	Δ (AU)	Q_{H_2O} (s^{-1})	Projected distance (km)	Green (kR)	Red-doublet (kR)	G/R ratio Cal.	G/R ratio Obs.
9*	1.37	0.55	0.5×10^{29}	470 × 3720	0.06	0.62	0.09	0.09*
23[†]	1.08	0.12	1.8×10^{29}	640	0.69	5.88	0.12	0.12 - 0.16[†]
27[†]	1.00	0.11	2.0×10^{29}	653	0.89	7.12	0.12	–
30*	0.94	0.19	2.2×10^{29}	165 × 1129	0.90	7.97	0.17	–

[§]DoB.=Date of observation (March 1996); *Cochran [2008] used a square slit of dimension 1.2″ × 8.2″; [†]*Morrison et al.* [1997] used cirular slit of diameter 7.5″ ; Calculations are made for O(^{1}S) yield of 0.5%, and CO_2 and CO relative abundances of 1% and 22%, respectively.

To verify the derived O(^{1}S) 0.5% O(^{1}S) yield (for the CO_2 abundance of 1%) is consistent with observations we also calculated G/R values for other days of observation. The calculated G/R ratio values for the observations made on 9, 23, 27, and 30 March 1996 along with the observed value of G/R ratio from *Morrison et al.* [1997] and *Cochran* [2008] are presented in Table 4.8 The calculated G/R ratio on 9 March, when geocentric distance was 0.55 AU and H_2O production rate 5×10^{28} s^{-1}, is 0.09 (see Table 4.8) which is same as the observed ratio obtained by *Cochran* [2008]. On 23 and 27 March 1996 the comet is closer to both Sun and Earth (geocentric distance ∼0.1 AU) and its H_2O production rate was 4 times higher than the value on 9 March 1996. The calculated G/R ratio on 23 March 1996 is 0.12, which is in agreement with the observed ratio obtained by *Morrison et al.* [1997].

4.7.1.2 Atomic oxygen [OI] 6300 Å emission line on comet Hale-Bopp

Morgenthaler et al. [2001] observed [OI] 6300 Å emission on comet Hale-Bopp on several days during February to April 1997 using 4 different ground based instruments. Large aperture observations of 6300 Å emission using WHAM and Hydra spectrometers are made for the field of view 1° and 45′, which covers projected distances of 1.5×10^6 and 2.4×10^5 km on the comet, respectively. The model calculated brightness profile of [OI] 6300 Å emission shown in Figure 4.20 is consistent with these observations. The brightness profile of [OI] 5577 Å starts falling off beyond 1000 km, while the [OI]

6300 Å profile remains constant up to 5000 km. The flatness in the calculated surface brightness profiles mainly depends on the collisional quenching of metastable species which is a function of H_2O production rate. The calculated green and red-doublet emission intensities (dotted lines in Figure 4.20) when radiative decay is considered as the only loss mechanism shows the role of collisional quenching. The $O(^1D)$ is substantially quenched by H_2O due to its larger lifetime (∼110 s) in the inner coma. Hence, below 1000 km, the calculated [OI] 6300 Å emission intensities differ by a factor of 5.

Table 4.9: The model calculated intensities of forbidden atomic oxygen emission lines on comet Hale-Bopp and the comparison of [OI] 6300 Å line with the observation of *Morgenthaler et al.* [2001] with 3% CO_2 and 24% CO.

Date on	r	Δ	Intensity (R)				
1997	(AU)	(AU)	2972 Å	5577 Å	6364 Å	6300 Å	
						Calculated‡	Observed§
Mar 9	0.999	1.383	34	330	1162	3637	2580–2922
Mar 10	0.992	1.373	36	339	1192	3730	2300–2649
Apr 7	0.920	1.408	45	423	1422	4450	2915–4964
Apr 8	0.923	1.420	43	416	1400	4379	3057–3496
Apr 9	0.925	1.431	43	411	1380	4323	2920–3197
Apr 10	0.928	1.444	43	403	1358	4248	1579–1669
Apr 13	0.939	1.484	39	372	1271	3296	1451–1960
Apr 14	0.943	1.497	37	361	1240	3878	1575–2360
Apr 16	0.952	1.526	36	339	1179	3688	2335–2974

‡The calculated average surface brightness over the observed projected distance of 2.5 × 10^5 km. §The upper and lower limits of [OI] 6300 Å intensity observed by *Morgenthaler et al.* [2001].

We also calculated the [OI] 6300 Å emission intensity for a circular aperture of 4′ diameter on different days of March and April 1997 similar to the observation conditions of *Morgenthaler et al.* [2001]. The calculated intensities of different atomic oxygen emissions are presented in Table 4.9 along with the [OI] 6300 Å emission intensities observed by *Morgenthaler et al.* [2001]. Our calculated intensities are higher by a factor of 1.5 to 2.5 compared to the observation and also vary for different days due to change in solar flux, H_2O production rate, and heliocentric and geocentric distances. The observed [OI] 6300 Å intensity on comet Hale-Bopp on 7 April 1997 is found to vary by a factor of 1.6 in a span of less than 20 minutes, which is difficult to explain with the variation of heliocentric dependent water production rate. Similarly, the observed intensity values on the other days of observation also show large variation. The brightness during April 10 to 14 is consistently lower than during April 7 to 9. The variation in the observed intensity might be associated with spectral extraction process because of non uniform sensitivity of

Fabry-Pérot spectrometer [*Morgenthaler et al.*, 2001], rather than the intrinsic variation in the comet.

Zhang et al. [2001] observed comet Hale-Bopp on 26 March 1997 using a rectangular slit ($1.06'' \times 3.18''$) when the comet was at a geocentric distance of 1.32 AU and heliocentric distance of 0.92 AU. For this observation, the projected field of view on the comet was 522 × 1566 km. Our calculated G/R ratio with 3% relative abundance of CO_2 and 0.5% yield of $O(^1S)$ is 0.21, which is consistent with the observed G/R ratio range (0.18–0.22) of *Zhang et al.* [2001]. The calculated average G/R ratio, for a $4'$ circular aperture field of view with 3% relative abundance of CO_2 for the different days of observation presented in Table 4.9, is around 0.1. This shows that in a high water production rate comet the observed G/R ratio over a large projected distances ($\sim 10^4$ km) can be around 0.1 (cf. Figure 4.21). However, the calculated contributions of different production processes for $O(^1S)$ suggest that photodissociation of CO_2 is more important source rather than the photodissociation of H_2O. Hence, in comets with sufficient CO_2 abundances ($\geq$5%), the green line emission is largely controlled by photodissociation of CO_2 and the derived G/R ratio over large cometocentric distances could be around 0.1.

Table 4.10: The model calculated green and red-doublet emission intensities on comet Hale-Bopp and the derived $O(^1D)$ and H_2O production rates for different slit dimensions. The calculations are done for comet Hale-Bopp taking $Q(H_2O) = 8.3 \times 10^{30}$ s^{-1} for the relative abundances of 6% CO_2 and 24% CO at r_h = 1 AU and Δ = 1 AU using solar flux on 10 April 1997 (solar minimum period : solar radio flux F10.7 = 74.7×10^{-22} J s^{-1} m^{-2} Hz^{-1}).

Slit dimension (Projected distance in km)	Average intensity (R)†		Production rate (s^{-1})		G/R**
	[OI] 6300 Å	[OI] 5577 Å	$Q[O(^1D)]$	$Q[H_2O]^\ddagger$	
$2'' \times 2''$ (725)	18895 [83188]*	7584 [9245]	1.3×10^{26}	3.7×10^{26}	0.30 (0.08)††
$5'' \times 5''$ (1.8×10^3)	18909 [68301]	6723 [7584]	8.1×10^{26}	23×10^{26}	0.21 (0.08)
$10'' \times 10''$ (3.6×10^3)	19021 [52977]	5369 [5825]	3.3×10^{27}	9.3×10^{27}	0.21 (0.08)
$30'' \times 30''$ (1.1×10^4)	15668 [29341]	2963 [3118]	2.5×10^{28}	7.1×10^{28}	0.14 (0.08)
$1' \times 1'$ (2.2×10^4)	11785 [18793]	1846 [1924]	7.6×10^{28}	2.1×10^{29}	0.10 (0.08)
$4' \times 4'$ (8.7×10^4)	5005 [6767]	605 [624]	5.0×10^{29}	1.4×10^{30}	0.09 (0.07)
$10' \times 10'$ (2.1×10^5)	2351 [3056]	263 [271]	1.4×10^{30}	3.9×10^{30}	0.08 (0.07)

*The values in the square brackets are the calculated intensities without accounting for collisional quenching of $O(^1S)$ and $O(^1D)$. †Intensity is averaged over the projected field of view, 1 R = $\frac{10^6}{4\pi}$ Photons s^{-1} cm^{-2} sr^{-1}; ‡The branching ratio for the production of $O(^1D)$ in the photodissociation of OH is taken as 0.357 [see *Morgenthaler et al.*, 2001], while for the photodissociation of H_2O producing $O(^1D)$ it is 0.064 (This work). The branching ratio (0.81) for the production of OH in photodissociation of H_2O is taken from *Huebner et al.* [1992]. **Green to red-doublet emission intensity ratio determined over the projected field of view. ††The calculated G/R ratio without collisional quenching.

To evaluate the role of slit dimension in determining the G/R ratio we calculated green and red line intensities for various slit sizes by keeping H_2O, CO and CO_2 production rates as a constant. These calculations are presented in Table 4.10. By varying the slit dimension from $2'' \times 2''$ to $10' \times 10'$ the calculated G/R ratio over the projected cometary coma changed from 0.3 to 0.08. This result clearly shows that the G/R ratio depends not only on the photo-chemistry in the coma but also on the projected area observed for the comet. The calculated G/R ratio is a constant value (0.08) throughout the cometary coma when collisional quenching is neglected in the model. By doubling the CO_2 relative abundance in the coma, the G/R ratio increases by 30% whereas the collisional quenching of $O(^1D)$ and $O(^1S)$ can change its value even by an order of magnitude.

Besides the dimension of the slit used for observation, the projected area observed on the comet depends on geocentric distance of the comet. Hence in a comet, where the collisional coma is resolvable in the observation, the derived G/R ratio depends on the projected area and also on the collisional quenching of $O(^1S)$ and $O(^1D)$ in the cometary coma. Thus, we conclude that the observed G/R ratio of 0.1 is not a definitive benchmark value to verify H_2O or CO_2/CO as the parent sources of atomic oxygen visible emissions in comets.

4.7.1.3 Width of green and red-doublet emission lines

Cochran [2008] has found that the width of green line is larger than either of the red-doublet lines in the spectra of 8 comets. The wider green line implies the higher mean velocity of metastable $O(^1S)$, which could be associated with different production processes. Besides collisions with different cometary species, the mean velocity of $O(^1S)$ in the cometary coma is determined by various production processes, and/or could be due to the involvement of photons of various energies in dissociating O-bearing species [*Cochran*, 2008].

The observed width of forbidden line emission depends on the velocity distribution of radiating metastable oxygen atoms. We found that the excess velocity released in photodissociation H_2O in the unity radiative efficiency region is 2.1 eV (cf. Figure 4.23). If we assume that most of this excess energy is transfered to kinetic motion of atomic oxygen then the maximum mean velocity that can be acquired by the $O(^1D)$ atom would be 1.6 km s^{-1}. This velocity is consistent with values of 0.5 to 1.8 km s^{-1} derived by *Cochran* [2008] in 8 comets. This supports the idea that most of the red-doublet emission in cometary coma is governed by the photodissociation of H_2O. The excess energy profiles shown in Figure 4.23 suggest that the $O(^1D)$ produced in photodissociation of CO and CO_2 will have higher velocity than that produced in photodissociation of H_2O. The excess energy released in the photodissociation of CO and CO_2 in the unity radiative efficiency region is 2.5 eV and 4.1 eV, which corresponds to $O(^1D)$ excess velocity of

~3.7 km s^{-1} and 4 km s^{-1}, respectively. However, our calculations suggest that CO and CO_2 together can contribute to a maximum of 10% to the red-doublet emission. The contributions of CO and CO_2 in the wings of red-doublet lines are probable.

In the case of green line emission, since there is no experimentally determined cross section or yield for the photodissociation of H_2O producing O(^{1}S), it is difficult to determine the mean velocity acquired by an O(^{1}S) atom in the the photolysis of H_2O. The maximum excess energy that can be released in photolysis of H_2O producing O(^{1}S) at solar H Ly-α is 1.27 eV. Again, if we assume all the excess energy is transferred as kinetic energy of atomic oxygen in ^{1}S state then the maximum excess velocity of O(^{1}S) would be 1.3 km s^{-1}. But in the case of photodissociation of CO_2, the excess energy is 2.5 eV, which corresponds to a maximum O(^{1}S) velocity of 4.3 km s^{-1}. The dissociative recombination of ions H_2O^+, CO_2^+, and CO^+ can contribute a maximum of 30% in the production of green line emission. But the excess energy released in these recombination reactions is very small [*Rosen et al.*, 2000; *Rosén et al.*, 1998; *Seiersen et al.*, 2003]. By assuming that the maximum mean velocity that can be acquired by O(^{1}S) via the dissociative recombination processes is about 1 km s^{-1}, we found that the mean velocity of O(^{1}S) from all production processes is ~2 km s^{-1}. This value is consistent with the derived velocity range of 1.9 to 3.1 km s^{-1} for O(^{1}S) in 8 comets by *Cochran* [2008].

Before coming to a broad conclusion, we suggest that one has to calculate the exact mean excess velocities of O(^{1}S) and O(^{1}D) over the observed cometary coma, by accounting for all collisional processes and the mean excess velocity profiles of various species. Due to non availability of photon cross sections for some of the photodissociation processes, and uncertainties involved in the excess energy calculations for dissociative recombination reactions, the model is limited in determining the exact line widths of green and red-doublet emissions. However, based on the model calculations on comets Hale-Bopp and Hyakutake, we suggest that involvement of multiple sources in the formation O(^{1}S) could be a potential reason for the higher line width of green emission compared to that of red-doublet emission observed in several comets.

4.7.2 Effect of model parameters on the calculated intensities

4.7.2.1 Expansion velocity of neutrals

As we mentioned earlier in Section 4.5, we have used the velocity profile from the work of *Combi et al.* [1999] for calculating the number densities of parent species H_2O, CO_2, and CO in comet Hale-Bopp. *Combi et al.* [1999] have shown that in comet Hale-Bopp there is an acceleration of neutrals in the inner coma due to the photolytic heating [*Combi et al.*, 1999; *Colom et al.*, 1999; *Biver et al.*, 1997; *Combi*, 2002] and other processes [*Harris et al.*, 2002]. To evaluate the impact of this acceleration on the model results we carried out calculations by taking a constant gas expansion velocity profile with the values 0.7 and 2.2 km s^{-1}. By using a constant velocity profile of 0.7 km s^{-1} in the coma, rather than a radially varying velocity of *Combi et al.* [1999], the calculated intensities of green and red-doublet emissions are increased by 30% and 25%, respectively, which are still higher than the observation. By changing the constant gas expansion velocity from 0.7 to 2.2 km s^{-1}, the calculated intensities of atomic oxygen emission lines in comet Hale-Bopp are decreased by ∼50%. However using the *Combi et al.* [1999] velocity profile, our calculated [OI] 6300 Å emission intensities over 4′ circular aperture field of view are closer to the observation (cf. Table 4.9). Hence, the velocity profile of neutral species is an important input in the model that should be accounted in calculating the intensities of these forbidden emissions.

4.7.2.2 Relative abundances of neutral species

The water production rate in comet Hale-Bopp has been derived using emissions of direct and daughter products of H_2O by different observers [*Weaver et al.*, 1997; *Colom et al.*, 1999; *Schleicher et al.*, 1997; *Combi et al.*, 2000; *Dello Russo et al.*, 2000; *Woods et al.*, 2000; *Morgenthaler et al.*, 2001; *Harris et al.*, 2002; *Fink*, 2009]. During the observation period of these green and red-doublet emissions (r_h of the comet was around 0.9 AU), *Dello Russo et al.* [2000] measured the H_2O production rates using infrared emissions of water molecules for different days. In this period, *Combi et al.* [2000] derived the H_2O production rate in this comet using H Ly-α emission. The difference between these two derived production rates is less than 20%. These observations found that around 1 AU the water production rate in comet Hale-Bopp was about $\sim 1 \times 10^{31}$ s^{-1}. Similarly, the derived water production rates of *Fink* [2009] on 3 March 1997 was 6.1×10^{30} s^{-1} which is smaller than the *Combi et al.* [2000] derived rate by a factor of 1.5. Using visible emission of atomic oxygen *Morgenthaler et al.* [2001] derived the H_2O production rates by applying standard branching ratios of OH and H_2O. These derived H_2O production rates are higher by factor of 3 to 6 compared to values determined from other observations. To assess the impact of H_2O production rate on the calculated green and red-doublet emissions we increased its value by a factor of 5. With increase in H_2O production rate the model calculated surface brightness of green and red-doublet emissions over 4′ circular field of view is increased by a factor of 3.

As demonstrated earlier, the role of CO_2 is very significant in determining the green line emission intensity and subsequently the G/R ratio. During the observation period of these forbidden emission lines the CO_2 is not observed in comet Hale-Bopp. To evaluate the impact of CO_2 we varied its relative abundance from 3 to 6%. We found an increase (25%) in the calculated green line emission intensity over the 4′ circular aperture field of view whereas it is small (<5%) for red-doublet emission intensity.

Based on infrared observations made near perihelion on comet Hale-Bopp, *DiSanti* *et al.* [2001] suggested that 50% of CO abundance present in the cometary coma is contributed by distributed sources. *Bockelée-Morvan et al.* [2010] investigated the extended distribution of CO by probing Hale-Bopp between ∼800 to ∼20,000 km region using CO rotational line emissions (viz, CO J(1-0) and CO J(2-1)). Based on the observation and radiative transfer modelling studies, *Bockelée-Morvan et al.* [2010] rejected the idea of an extended distribution of CO in Hale-Bopp. Since the contribution of photodissociation of CO to formation of O(^{1}S) and O(^{1}D) is less than 10%, no significant variation in the calculated intensity of green and red-doublet emissions is found by reducing the CO relative abundance by half. Hence, the involvement of CO in these oxygen forbidden line emissions is almost insignificant.

Though OH column densities are determined using 3080 Å surface brightness profile, there are large uncertainties in photo-cross sections of OH in producing O(^{1}D) and O(^{1}S) [*Huebner et al.*, 1992; *Morgenthaler et al.*, 2001]. The calculated photo-rates for the production of O(^{1}D) via photodissociation of OH, using theoretical and experimental cross sections differ by about an order of magnitude [*Huebner et al.*, 1992]. *Morgenthaler et al.* [2001] studied the effect of these cross sections in deriving the H_2O production rates using 6300 Å surface brightness profile and found that on using the theoretical OH photodissociative branching ratios of O(^{1}D), the derived H_2O production rates are higher by a factor of 3–6, than those determined based on experimental branching ratios of *Nee and Lee* [1984]. The photodissociation of OH influences the calculated green and red-doublet emission intensities significantly above 10^4 km (cf. Figures 4.11 and 4.14, and Table 5.2). By changing photorates determined by *Nee and Lee* [1984] experimental cross sections (which are used in the model) with the rates derived based on theoretically calculated cross sections of *van Dishoeck and Dalgarno* [1984], we found a 40% decrease in the calculated slit-averaged brightness over the 4′ circular aperture field of view for both green and red-doublet emissions. But the calculated O(^{1}S) and O(^{1}D) production rates along the radial distances are decreased by an order of magnitude above 10^4 km. Since OH is the dominant O-bearing species in the outer coma, the cross sections can affect the calculated the surface brightness of [OI] 6300 Å at larger projected distances ($>10^5$ km). To fit the observed [OI] 6300 Å emission in the outer coma *Glinski et al.* [2004] found it necessary to increase theoretical determined OH to O(^{1}D) photorate by a factor of around 3.

The chemistry model developed by *Glinski et al.* [2004] suggested that the collisions of O(^{3}P) with OH leads to the formation of O_2. These calculations also showed that the O_2 densities can be as high as 1% of H_2O. We evaluated the change in green and red-doublet emission intensities by incorporating O_2 in the model in comet Hale-Bopp by taking its density profiles from *Glinski et al.* [2004]. No significant change (<5%) is found in the green and red-doublet emission intensities by including O_2 in the model. This is because the other O-bearing species are several orders of magnitude higher in the inner coma compared to that of O_2.

4.7.2.3 Effect of slit dimension on the derived $O(^1D)$ production rate

In comet the derivation of H_2O based on the observed [OI] 6300 Å emission intensity. We have evaluated the role of slit dimension in deriving $O(^1D)$ production rate. As a case study, for a fixed H_2O production rate and CO and CO_2 relative abundances, we calculated [OI] 6300 Å emission intensity over a projected field of view for different slit dimensions. We then derived the $O(^1D)$ production rate based on the calculated average [OI] 6300 emission intensity over the projected field view. These calculations are presented in Table 4.10. Since the model calculations are limited up to the projected distances of 10^5 km we present the calculated intensities of [OI] 6300 and 5577 Å emissions for the slit dimension up to $10' \times 10'$. Though $O(^1D)$ is substantially produced in the inner coma via photodissociation, the collisional quenching by cometary species results in a very few [OI] 6300 Å photons. The role of quenching in determining the [OI] 6300 Å flux can be understood from the calculated values presented in Table 4.10. A large aperture observation is required, which covers the entire [OI] 6300 Å emission region, to derive the H_2O production rate. The calculations presented in Table 4.10 suggest that by using large aperture slit the derived water production rate is closer to the actual production rate of H_2O. Hence, to derive the water production rate using [OI] 6300 Å, the slit dimension which covers a projected distance more than the scale length of H_2O should be used.

4.8 Summary and Conclusions

The Green ([OI] 5577 Å) and red-doublet ([OI] 6300 and 6364 Å) atomic oxygen emissions are observed in comet C/1996 B2 Hyakutake on 30 March 1996 when it was passing quite close to the Earth ($\Delta = 0.1$ to 0.55 AU) [*Cochran*, 2008]. These forbidden oxygen emissions are also observed in comet C/1995 O1 Hale-Bopp, which had an order of magnitude higher water production rate compared to that on Hyakutake, when comet was at around 1.42 AU from the Earth [*Morgenthaler et al.*, 2001; *Zhang et al.*, 2001]. A coupled chemistry-emission model has been developed to study the production of green and red-doublet emissions in comets. This model has been applied to comets C/1996 B2 Hyakutake and C/1995 O1 Hale-Bopp when they are at around 1 AU heliocentric distance and the results are compared with the observed radial profiles of 5577 and 6300 Å line emissions and the green to red-doublet intensity ratio. The important results from the present model calculations can be summarized as following.

1. In these comets the photodissociation of H_2O is the dominant production process for the formation of $O(^1D)$ throughout the inner cometary coma. The solar H Ly-α (1216 Å) flux mainly governs the production of $O(^1D)$ in the photodissociative

excitation of H_2O, but near the nucleus solar radiation in the wavelength band 1375–1165 Å can control the formation of O(^{1}D) from H_2O.

2. In comet Hale-Bopp, below 10^5 km, the main production mechanism of O(^{1}D) is photodissociation of H_2O; but, in the innermost part of the coma (<100 km) the photodissociation of CO_2 is also a significant source.
3. Other than the photodissociation of H_2O molecule, above cometocentric distance of 100 km the radiative decay of O(^{1}S) to O(^{1}D) (via 5577 Å line emission), while above 1000 km the dissociative recombination of H_2O^+ ions, are also significant source mechanisms for the formation of O(^{1}D) and O(^{1}S) atoms.
4. The collisional quenching of O(^{1}D) atoms by H_2O is significant up to radial distance of ∼1000 km; above this distance the radiative decay is the main loss mechanism of O(^{1}D) atoms. The collisional quenching of O(^{1}D) by other neutral species is an order of magnitude smaller.
5. In Hale-Bopp, the photodissociation of H_2O production produces peak O(^{1}D) via H Ly-α (1216 Å), 1165–1375 Å and 1375–1575 Å wavelength bands at cometocentric distances of 1000, 200, and 50 km, respectively. Solar photons at all other wavelengths produce O(^{1}D) with one or more orders of magnitude smaller efficiency.
6. In comet Hale-Bopp, below 100 km, solar photons in the wavelength band 1375–1585 Å mainly produce O(^{1}D) by photodissociation of CO_2. The contribution from other wavelength bands is significant above cometocentric distances of 200 km.
7. The major destruction mechanism of O(^{1}D) up to 3000 km cometocentric distance is quenching by H_2O; above 5000 km radiative decay takes over.
8. In comet Hale-Bopp the O(^{1}D) density peaks occurs between 10^3 and 10^4 km, while for O(^{1}S) the peak is around 500–1000 km.
9. In both comets the photodissociation of H_2O is the major O(^{1}S) production process, but near the nucleus the photodissociation of CO_2 can be the dominant source. The solar H Ly-α (1216 Å) flux controls the production of O(^{1}S) via photodissociative excitation of H_2O.
10. In Hale-Bopp, below cometocentric distance of 10^3 km, photodissociation of CO_2 is the major production mechanism of O(^{1}S). Between 10^3 and 10^4 km, the contributions from the photodissociation of CO_2 and H_2O are nearly equal. Above 2×10^4 km several other processes are also significant to the O(^{1}S) production.
11. In both comets at small cometocentric distances (<100 km), the main loss process for O(^{1}S) is quenching by H_2O molecule, while above 100 km the radiative decay is the dominant loss process.

12. Quenching by H_2O is the main loss mechanism for O(^{1}S) at radial distances below 300 km; above 10^3 km radiative decay via 5577 Å emission is the dominant destruction mechanism.

13. Since the photoabsorption cross section of CO_2 molecule is quite small at 1216 Å, the contribution of CO_2 in the production of O(^{1}S) and O(^{1}D) at the solar H Ly-α is insignificant.

14. Because the CO_2 absorption cross section in the 1165–955 Å wavelength range is higher by an order of magnitude compared to that at other wavelengths, the solar radiation in this wavelength region mainly controls the production of O(^{1}D) and O(^{1}S) in the photodissociative excitation of CO_2. Moreover, the CO_2 absorption cross section in this band is also the largest compared to those of H_2O and CO.

15. Since the cross section of photodissociation of CO_2 for the production of O(^{1}S) is more than two orders of magnitude larger than that of H_2O, even a small amount (few percent relative abundance) of CO_2 can make it an important source of the O(^{1}S).

16. The cross section for the photodissociation of H_2O producing O(^{1}S) at the solar H Ly-α wavelength (with 1% O(^{1}S) yield) is smaller by more than two orders of magnitude than the cross section for the photodissociation of CO_2 producing O(^{1}S) in the wavelength region 1165–955 Å . Though the solar flux at 1216 Å is higher compared to that in the 1165–955 Å wavelength region by two orders of magnitude, the larger value of CO_2 cross section in this wavelength band enables CO_2 to be an important source for the production of metastable O(^{1}S) atom.

17. In the case of CO, the dissociation and ionization thresholds are close to each other. Hence, most of the solar radiation ionizes CO molecule rather than producing the O(^{1}S) and O(^{1}D) atoms.

18. Though the CO abundance is relatively high (∼22%) in comet C/1996 B2 Hyakutake, the contribution of CO photodissociation in the O(^{1}D) production is small (∼1%), while for the production of O(^{1}S) its contribution is 10 to 25%.

19. The photoelectron impact dissociative excitation of H_2O, CO_2, and CO makes only a minor contribution (<1%) in the formation of metastable O(^{1}S) and O(^{1}D) atoms in the inner coma.

20. The O(^{1}S) density peaks at shorter radial distances than the O(^{1}D) density. The peak value of O(^{1}S) density is found around 60 km from the nucleus, while for the O(^{1}D) a broad peak around 200-600 km is observed.

21. In a H_2O-dominated comet, the green line emission is mainly generated in the photodissociative excitation of H_2O with contribution of 40 to 60% (varying according to the radial distance) to the total intensity, while the photodissociation of CO_2 is the next potential source contributing 10 to 40%.

22. For the red line emission the major source is photodissociative excitation of H_2O, with contribution varying from 60 to 90% depending on the radial distance from the nucleus.

23. The G/R ratio depends not only on the production and loss processes of the $O(^1S)$ and $O(^1D)$ atoms, but also on the size of observing slit and the geocentric distance of comet at the time of observation.

24. For a fixed slit size, the calculated value of the G/R ratio is found to vary between 0.03 and 0.5 depending on the geocentric distance of the comet. In the inner ($<$300 km) most part of the coma, the G/R ratio is always larger than 0.1, with values as high as 0.5. On the other hand, at cometocentric distances larger than 1000 km the G/R ratio is always less than 0.1.

25. The model calculated radial profiles of 6300 and 5577 Å lines are consistent with the observed profiles on comet C/1996 B2 Hyakutake for $O(^1S)$ yield of 0.4 ($\pm$0.1) and CO_2 abundances of 1%.

26. The model calculated G/R ratio on comet Hyakutake is in good agreement with the G/R ratio observed on two days in March 1996 by two observatories using different slit sizes.

27. To accurately measure the H_2O production rate in cometary coma, a slit dimension which covers a projected distance more than the scale length of H_2O is preferred to cover the entire [OI] 6300 Å emission region.

28. Collisional quenching can change the G/R ratio by an order of magnitude, whereas doubling the relative abundance of CO_2 increases its value by maximum of 30%.

29. The radiative efficiency of $O(^1S)$ and $O(^1D)$ atoms in comet Hale-Bopp are unity above 10^3 and 10^4 km, respectively. In comet Hyakutake these distances are 10^2 and 10^3 km, respectively.

30. The model calculated green to red-doublet emission intensity ratio on comet Hale-Bopp is consistent with the observation of *Zhang et al.* [2001].

31. The model calculated [OI] 6300 Å emission intensity profile as a function of projected distance is in agreement with the observation of *Morgenthaler et al.*

[2001]. The model calculated surface brightness averaged over a $4'$ circular aperture field of view is higher by a factor of 1.5 to 2 compared to the observation.

32. The calculated mean excess velocity of O(^{1}D) and O(^{1}S) atoms in the region of unity radiative efficiency is $\sim$1.6 and $\sim$2 km s^{-1}, respectively, which is consistent with the range of velocities observed by *Cochran* [2008] in several comets.

33. Based on the model calculations for comets Hyakutake and Hale-Bopp, we conclude that [OI] 6300 Å emission is mainly controlled by the photodissociation of H_2O, while the [OI] 5577 Å emission line is contributed by both H_2O and CO_2. Since O(^{1}S) production is associated with different molecules, whereas the O(^{1}D) production is mainly from H_2O, the width of the green line would be higher than that of the red-doublet lines.

Chapter 5

Red and Green emissions of atomic oxygen at large heliocentric distances

Contents

5.1 Introduction **117**

5.2 Model **118**

5.3 Results **122**

5.3.1 Production processes of O(^{1}S) and O(^{1}D) 122

5.3.2 Loss processes of O(^{1}S) and O(^{1}D) 122

5.3.3 [OI] green to red-doublet emission intensity ratio and line widths 123

5.4 Discussion **131**

5.4.1 Impact of CO on the G/R ratio 133

5.4.2 Impact of CO$_2$ on the G/R ratio 134

5.4.3 Impact of collisional quenching of O(^{1}S) and O(^{1}D) on the G/R ratio 135

5.4.4 Green and red-doublet emission line widths 136

5.5 Summary and conclusion **137**

5.1 Introduction

In the previous Chapter I have developed a coupled chemistry-emission model for the production of green and red-doublet emissions by accounting for important production and loss mechanisms of O(^{1}S) and O(^{1}D) atoms. The model has been applied to comets Hyakutake and Hale-Bopp. Our model calculations showed that in a H$_2$O-dominated cometary coma more than 90% of the O(^{1}D) is populated via photodissociative excitation of H$_2$O and the rest is through photodissociation of CO$_2$ and CO. We also demonstrated that the G/R ratio depends not only on the photochemistry involved in the formation of O(^{1}D) and O(^{1}S) but also on the projected area observed on the comet, which is a function of slit dimension and geocentric distance of the comet. The model calculations on comets Hyakutake and Hale-Bopp showed that the intensity of [OI] 6300 Å line is largely governed by photodissociation of H_2O, whereas [OI] 5577 Å emission line is mainly controlled by the photodissociation of both H_2O and CO_2. It also suggested that CO_2 can produce $O(^1S)$ more efficiently than H_2O. The calculated mean excess energy profiles in various photodissociation processes showed that the photodissociation of CO_2 can produce $O(^1S)$ with higher excess velocity compared to the photodissociation of H_2O. All these calculations are carried out at ∼1 AU.

At larger heliocentric distances the cometary coma is composed of larger proportions of CO and CO_2 than at 1 AU [*Meech and Svoreň*, 2004; *Crovisier et al.*, 1999; *Biver et al.*, 1997, 1999; *Bockelée-Morvan et al.*, 2004; *Bockelée-Morvan et al.*, 2010]. At heliocentric distances of more than 2 AU the prompt emissions of atomic oxygen are observed in several comets, viz., C/2007 Q3 Siding Spring, C/2006 W3 Christensen, C/2009 P1 (Garradd), C/2001 Q4 (NEAT), 116P/Wild 4, and C/2002 K4 (LINEAR) [*Furusho et al.*, 2006; *McKay et al.*, 2012; *Decock et al.*, 2012]. Assuming that CO_2 and CO are the main sources of green and red-doublet emissions, the observed G/R ratio in comets at large heliocentric distances ($>$ 2 AU) has been used to estimate the CO_2 abundance in comets [*Decock et al.*, 2012; *McKay et al.*, 2012].

The present study is aimed at studying the photochemistry of $O(^1S)$ and $O(^1D)$ atoms and associated green and red-doublet emission production mechanisms in the above mentioned six comets at larger heliocentric distance ($>$ 2 AU) where gas production rate of CO can be equal to that of H_2O. One of the objectives of the study is to verify whether the G/R ratio value can be used to infer the CO_2 relative abundance, with respect to H_2O, in the comets that are observed at larger heliocentric distances. In this study we have shown that even at large heliocentric distances, the photodissociation of CO is only a minor source of $O(^1S)$ and $O(^1D)$ atoms, and its impact on the G/R ratio is negligible. The red-doublet emission intensity is mainly governed by H_2O, while the green line emission intensity is controlled by CO_2. We also demonstrated that collisional quenching can significantly change the observed G/R ratio and that its impact on the G/R ratio is much more than due to variation in the CO_2 and H_2O abundances.

5.2 Model

The details of model and the photochemical reactions considered in the model are presented in Chapter 4. Here we present the input parameters that have been used in the model for the calculation of green and red-doublet emission intensities for the observed conditions of six comets (viz., 116P/Wild 4, C/2002 K4 (LINEAR), C/2007 Q3 Siding Spring, C/2006 W3 Christensen, C/2009 P1 (Garradd), C/2001 Q4 (NEAT)). The photochemical reaction network and cross sections of photon and electron impact processes that have been considered in our previous work are retained same for the present calculation. The photoelectron impact excitation reactions are accounted by degrading solar EUV-generated photoelectrons and electron impact cross sections in the cometary coma using the Analytical Yield Spectrum (AYS) technique which is based on the Monte-Carlo method. Details of the AYS approach and the method to calculate photoelectron flux and excitation rates are given in Chapter 2. Only the dominant O-bearing neutral species H_2O, CO_2, and CO are considered in the model.

The neutral gas production rates used in the model calculations for different comets during observation period of oxygen emission lines are tabulated in Table 5.1. Since in some comets these gas production rates are not measured, we have made a reasonable approximation to incorporate CO_2 and CO in the model. However, we vary the CO_2 and CO relative abundances on these comets to assess the impact on the green and red-doublet emission intensities and subsequently on the G/R ratio.

Table 5.1: Observational conditions (slit dimension, heliocentric (r) and geocentric (Δ) distances) of various comets along with corresponding H_2O production rates and CO_2 and CO relative abundances relative to H_2O and comparison of calculated green to red-doublet emission intensity ratios (G/R ratio) with the observations.

Comet	r	Δ	Slit dimension	$Q(H_2O)$	CO_2[¶]	CO[¶]	G/R ratio		Reference
	(AU)	(AU)	($'' \times ''$)	(s^{-1})	(%)	(%)	cal.	obs.	
116P/Wild 4	2.40	1.4	8×1	$1 \times 10^{27*}$	10	20	0.09	0.15	*Furusho et al.* [2006]
C/2002 K4 (LINEAR)	2.60	2.36	0.80×11	$1 \times 10^{29\P}$	$10^{\|}$	$25^{\|}$	0.09	0.09	*Decock et al.* [2012]
C/2007 Q3 Siding Spring	2.96	2.48	3.20×1.6	$4 \times 10^{27*}$	17	10	0.12	0.20	*McKay et al.* [2012]
C/2006 W3 Christensen	3.13	2.35	3.20×1.6	$2.0 \times 10^{28*}$	42	98	0.18	0.24	*McKay et al.* [2012]
C/2009 P1 (Garradd)	3.25	3.50	0.44×12	$2.3 \times 10^{27\ddagger}$	25	$100^{\|}$	0.14	0.21	*Decock et al.* [2012]
C/2001 Q4 (NEAT)	3.70	3.40	0.45×11	$3.8 \times 10^{27\dagger}$	$75^{\|}$	$100^{\|}$	0.23	0.33	*Decock et al.* [2012]
comet X**	3.70	3.40	0.45×11	4×10^{27}	100	100	0.25	–	–

[*] *Ootsubo et al.* [2012]; [†] *Combi et al.* [2009]; [‡] *Bodewits et al.* [2012]; [‖] Assumed; [¶] See text; [**] comet X is a hypothetical comet similar to the observational condition of comet NEAT but having equal gas production rate of H_2O, CO_2, and CO; cal. = Calculated, obs. = Observation.

Furusho et al. [2006] observed the forbidden oxygen lines in comet 116P/Wild 4 when it was at 2.4 AU from the Sun. Using infrared satellite AKARI, *Ootsubo et al.* [2012] measured the H_2O production rate in this comet as $\sim 1 \times 10^{27}$ s^{-1} and abundance of CO_2 was found to be 10% relative to the water at heliocentric distance of 2.22 AU. *Ootsubo et al.* [2012] also determined the upper limit for CO abundance in this comet as 20% relative to water. In our model we have used these measured gas production rates and relative abundances as input assuming that these values did not vary significantly in this comet from 2.2 to 2.4 AU.

Using SPITZER space telescope, *Woodward et al.* [2007] measured the H_2O production rate in comet C/2002 K4 (LINEAR) as 2.43×10^{29} s^{-1} when comet was at 1.76 AU from the Sun during pre-perihelion. *Decock et al.* [2012] observed atomic oxygen forbidden lines in this comet when it was at 2.6 AU heliocentric distance. Since H_2O production rate is not measured at 2.6 AU we scaled *Woodward et al.*'s measured H_2O production rate to heliocentric distance of 2.6 AU assuming that it varies as inverse square of heliocentric distance. However, we evaluate the impact of estimated H_2O production rate on the calculated G/R by decreasing its value by a factor of 2. Since CO_2 and CO are not observed in this comet we have assumed their abundances as 10 and 25% relative to the H_2O, respectively. We show that CO does not play a significant role in determining green and red-doublet emission line intensities, whereas the CO_2 abundance is important in determining the G/R ratio.

In comet C/2007 Q3 Siding Spring, only [OI] 6300 Å emission line was observed and the intensity of [OI] 5577 Å was estimated with 3σ upper limit when it was at heliocentric distance of 2.96 AU [*McKay et al.*, 2012]. AKARI satellite detected both H_2O and CO_2 in comet C/2007 Q3 Siding Spring during its pre-perihelion period and measured the CO_2 relative abundance as 17% relative to H_2O production rate when the comet was at a heliocentric distance of 3.3 AU [*Ootsubo et al.*, 2012]. Assuming that the photodissociation of H_2O is the major source for the observed [OI] 6300 Å emission, *McKay et al.* [2012] inferred the H_2O production rate in comet C/2007 Q3 Siding Spring as 1.8×10^{27} s^{-1} which is smaller by a factor of 2 than the *Ootsubo et al.* [2012] measurement. Since *Ootsubo et al.* [2012] observation covers larger ($43'' \times 43''$) projected area on the coma compared to that of *McKay et al.* [2012] observation ($3.2'' \times 1.62''$), it can account for most of H_2O in the coma. Hence we have used *Ootsubo et al.* [2012] measured gas production rates in the model. We have taken the H_2O production rate on comet C/2007 Q3 Siding Spring as 4×10^{27} s^{-1} with 17% and 10% relative abundances of CO_2 and CO with respect to water, respectively, in our model.

By making radio observations on comet C/2006 W3 Christensen, *Bockelée-Morvan et al.* [2010] derived H_2O and CO production rates as 4.2×10^{28} and 3.9×10^{28} s^{-1}, respectively. During this measurement the comet was at heliocentric distance of 3.2 AU. These values are higher by a factor of 2 compared to the infrared satellite observed values reported by *Ootsubo et al.* [2012] which were derived when comet was nearly at the same heliocentric distance. *Ootsubo et al.* [2012] reported 42% and 98% of CO_2 and CO abundances relative to H_2O, respectively, in this comet when it was at 3.13 AU. During the green and red-doublet emission observation, comet C/2006 W3 Christensen was at a heliocentric distance of 3.13 AU [*McKay et al.*, 2012]. We have used *Bockelée-Morvan et al.* [2010] and *Ootsubo et al.* [2012] measured H_2O, CO_2, and CO gas production rates as inputs in our model.

The H_2O production rate in comet C/2009 P1 (Garradd) beyond 2 AU has been reported by various workers [*Paganini et al.*, 2012; *Villanueva et al.*, 2012; *Bodewits et al.*, 2012; *Combi et al.*, 2013; *Farnham et al.*, 2012; *Feaga et al.*, 2012]. Using SWIFT satellite, *Bodewits et al.* [2012] observed OH 3080 Å emission line in comet C/2009 P1 (Garradd) and derived the H_2O production rate when it was between 2 and 4 AU heliocentric distances. We have taken H_2O production at 3.25 AU from the Sun as 2.3 $\times\ 10^{27}$ s^{-1} by linearly interpolating *Bodewits et al.*'s derived production rates between 3 and 3.5 AU heliocentric distances. *Decock et al.* [2012] used the observed G/R ratio at 3.25 AU and estimated that around 25% CO_2 abundance relative to H_2O was present in this comet. Since CO is highly volatile and the comet is at large heliocentric distance we assumed that the gas production rates H_2O and CO are equal in this comet.

In comet C/2001 Q4 (NEAT), the H_2O production rate is measured by *Biver et al.* [2009] and *Combi et al.* [2009] at different heliocentric distances using hydrogen Ly-α (1216 Å) and radio (557 GHz) emissions, respectively. *Combi et al.* [2009] fitted the observed H_2O production rate as a function of heliocentric distance (r_h) as $3.5 \times 10^{29} \times r_h^{-1.7}$ s^{-1}. We used this expression to calculate H_2O production rate in this comet at 3.7 AU where the green and red-doublet emissions were observed [*Decock et al.*, 2012]. Since the comet is at large heliocentric distance we assumed that the CO and H_2O abundances are equal. Based on the observed G/R ratio on this comet, *Decock et al.* [2012] suggested that CO_2 relative abundance in this comet could be between 60 and 80% with respect to H_2O. In our model we have taken CO_2 relative abundance at 3.7 AU heliocentric distance as 75%.

To evaluate the individual contributions of major O-bearing species in producing green and red-doublet emissions and their affect on the G/R ratio we have made a case study for a hypothetical comet X in which we assumed equal gas production of H_2O, CO_2, and CO in the comet. This is similar to the observation of *Ootsubo et al.* [2012] on comet C/2006 W3 Christensen in which it is found that CO_2 and H_2O gas production rates are equal ($\sim 8 \times 10^{27}$ s^{-1}); however the CO production rate is around 3 times higher when comet was at 3.7 AU from the Sun.

The solar flux, which is required to calculate photorates of different species, is taken from SOLAR2000 (S2K) v.2.36 model of *Tobiska* [2004] at 1 AU and scaled accordingly to the observed heliocentric distance of different comets. The electron temperature which determines the dissociative recombination rates of ions is taken as constant 300 K in the cometary coma. The effect of this constant temperature profile on the model calculation is discussed later. The yield of $O(^1S)$ at solar H Ly-α in the photodissociation of H_2O is taken as 0.5%. The impact of this assumption was discussed in Chapter 4. The photodissociative excitation cross section for CO_2 producing $O(^1D)$ is taken from *Jain* [2013]. The photorate for the production of $O(^1S)$ from the photodissociation of CO has been taken from the theoretically estimated value of *Festou and Feldman* [1981] and scaled to the observed heliocentric distance.

5.3 Results

Since these comets have different water production rates (varying from 10^{27} to 10^{29} s^{-1}) as well as different CO_2 and CO relative abundances with respect to H_2O, we present calculations in comet C/2006 W3 Christensen which is followed by discussion on the calculated results at other comets.

5.3.1 Production processes of O(^{1}S) and O(^{1}D)

The calculated production rates for the O(^{1}S) from different processes in comet C/2006 W3 Christensen are presented in Figure 5.1. The major production source of oxygen atoms in ^{1}S metastable state is photodissociation of CO_2 followed by photodissociation of CO and H_2O. The contribution from the photoelectron impact excitation reactions is smaller compared to photodissociative excitation processes. Above 10^3 km dissociative recombination of CO_2^+ also contributes significantly. The solar flux in wavelength bin 955–1165 Å is the main source that dissociates CO_2 and produce atomic oxygen in ^{1}S state. Since the yield for photodissociation of CO_2 in this wavelength bin is almost unity the absorption of solar photons of this wavelength bin by CO_2 leads to the formation of O(^{1}S) and CO [*Raghuram and Bhardwaj*, 2013; *Bhardwaj and Raghuram*, 2012].

The calculated O(^{1}D) production rate profiles for different mechanisms are shown in Figure 5.2. The major production of O(^{1}D) is via photodissociation of H_2O. But close to the nucleus (<30 km) photodissociation of CO_2 is also a significant O(^{1}D) production process, and above 30 km the radiative decay of O(^{1}S) became an important source of O(^{1}D) than the former. The photodissociation of CO and OH are minor production sources of O(^{1}D). Most of the O(^{1}D) production (>95%) is due to photodissociation of H_2O by solar H Ly-α photon flux.

5.3.2 Loss processes of O(^{1}S) and O(^{1}D)

The calculated O(^{1}S) and O(^{1}D) destruction rate profiles in comet C/2006 W3 Christensen are presented in Figure 5.3. Since this comet has a low neutral gas production rate, the collisional quenching is a dominant O(^{1}S) destructive mechanism only close to the nucleus (<30 km). The radiative decay which produces photons at wavelengths 5577 and 2972 Å is the major loss process for O(^{1}S) throughout the coma. The calculated loss rate profiles of O(^{1}D) by various processes are also presented in the same figure. Below 300 km, quenching by H_2O and CO_2 are the dominant loss mechanisms of the O(^{1}D). Above 300 km, the radiative decay, which results in the emission of photons at wavelengths 6300 and 6364 Å, is major loss process for O(^{1}D). Quenching by CO is a minor loss process for O(^{1}D) which is not shown in the figure.

The calculated number density profiles of O(^{1}S) and O(^{1}D) in comet C/2006 W3

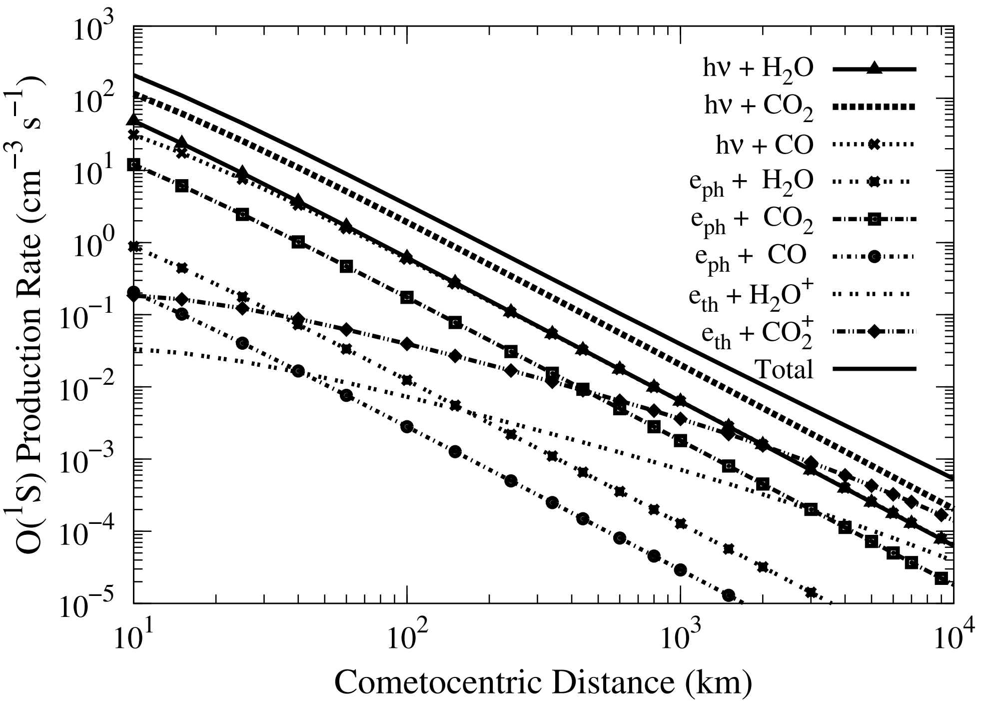

Figure 5.1: Calculated radial O(^{1}S) production rate profiles for major production mechanisms in comet C/2006 W3 Christensen having H_2O production rate of 2 × 10^{28} s^{-1} and 42% CO_2 and 98% CO abundances relative to H_2O in the cometary coma at 3.13 AU heliocentric distance. hν: solar photon; e_{ph}: photoelectron; and e_{th}: thermal electron.

Christensen along with parent species H_2O, CO_2, and CO are presented in Figure 5.4. Close to the cometary nucleus the flatness in the calculated O(^{1}S) and O(^{1}D) number density profiles is due to collisional quenching by cometary species (mainly by H_2O) and depends on neutral gas production rate of the comet.

5.3.3 [OI] green to red-doublet emission intensity ratio and line widths

The calculated number density profiles shown in Figure 5.4 are multiplied with Einstein emission transition probabilities to obtain emission rates. By integrating these emission rates along the line of sight we calculated the emission intensities of green and red-doublet lines as a function of projected distance. The calculated surface brightness profiles for [OI] 5577 Å and red-doublet (6300 + 6364 Å) emissions are shown in Figure 5.5 with solid curves. It can be noticed in this figure that close to nucleus (below 40 km projected distance) the green line emission is more intense than the red-doublet emission, which is mainly due to O(^{1}S) emission rate (1.26 s^{-1}) being higher by about two orders of magnitude compared to that of O(^{1}D) (8.59 × 10^{-3} s^{-1}). The calculated G/R ratio in comet C/2006 W3 Christensen, which is shown with a dashed

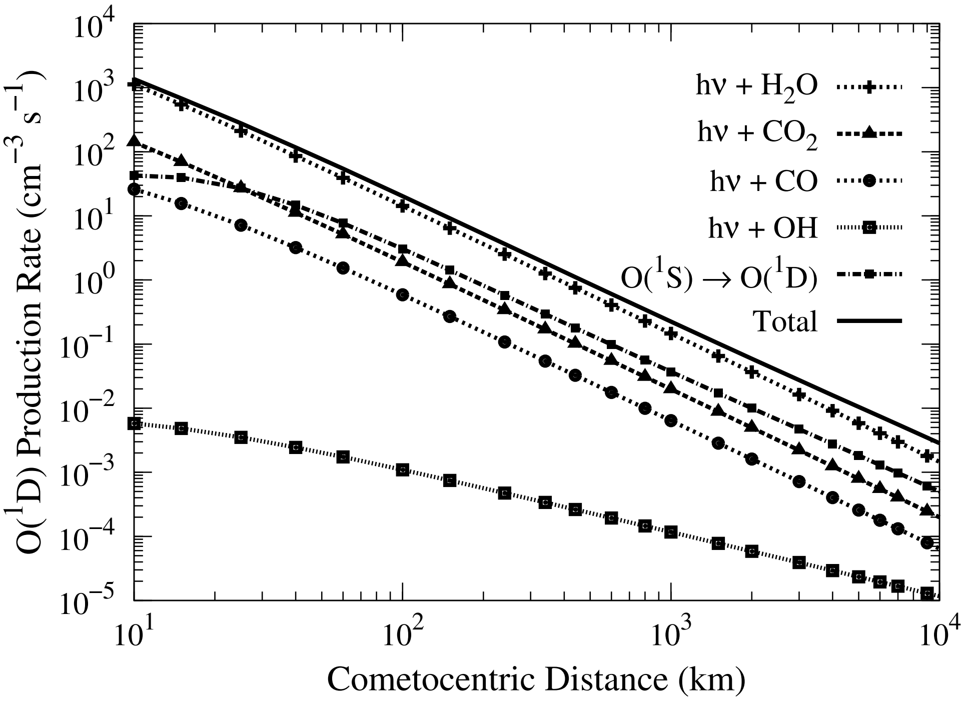

Figure 5.2: Calculated radial $O(^1D)$ production rate profiles for major production mechanisms in comet C/2006 W3 Christensen having H_2O production rate of 2×10^{28} s^{-1} and 42% CO_2 and 98% CO relative abundances with respect to H_2O in the cometary coma when comet was at 3.13 AU from the Sun. hν: solar photon.

curve ('with CO') in Figure 5.5, is varying between 1.8 and ~0.2. In the same figure the calculated G/R ratio profiles for different cases are also presented. Since there is an uncertainty in the photo-rate of CO in producing $O(^1S)$, which is discussed later, we also did calculations for the G/R ratio neglecting this source mechanism which is shown in Figure 5.5 with dotted curve ('without CO'). In this case the calculated G/R ratio varies between 1.6 and 0.18. Since comet C/2006 W3 Christensen had very low gas production rate the collisional quenching may be less important. To assess the effect of collisional quenching on the green and red-doublet emissions, we calculated G/R ratio without considering collisional destruction mechanisms of $O(^1S)$ and $O(^1D)$. In this case the calculated G/R ratio is a constant value of 0.18 throughout the coma which is represented with dash-dotted line in Figure 5.5.

Similarly, all these calculations have been carried out on other comets. Considering both collisional quenching and photodissociation of CO the calculated G/R ratio profiles as a function of projected distance in six comets are presented in Figure 5.6. This figure depicts that in comets C/2006 W3 Christensen and C/2001 Q4 (NEAT), close to the nucleus, the calculated G/R ratio value is more than one which is due to higher CO_2 relative abundances and strong collisional quenching of $O(^1D)$ by cometary species whereas in other comets this value is always less than one throughout the coma. In

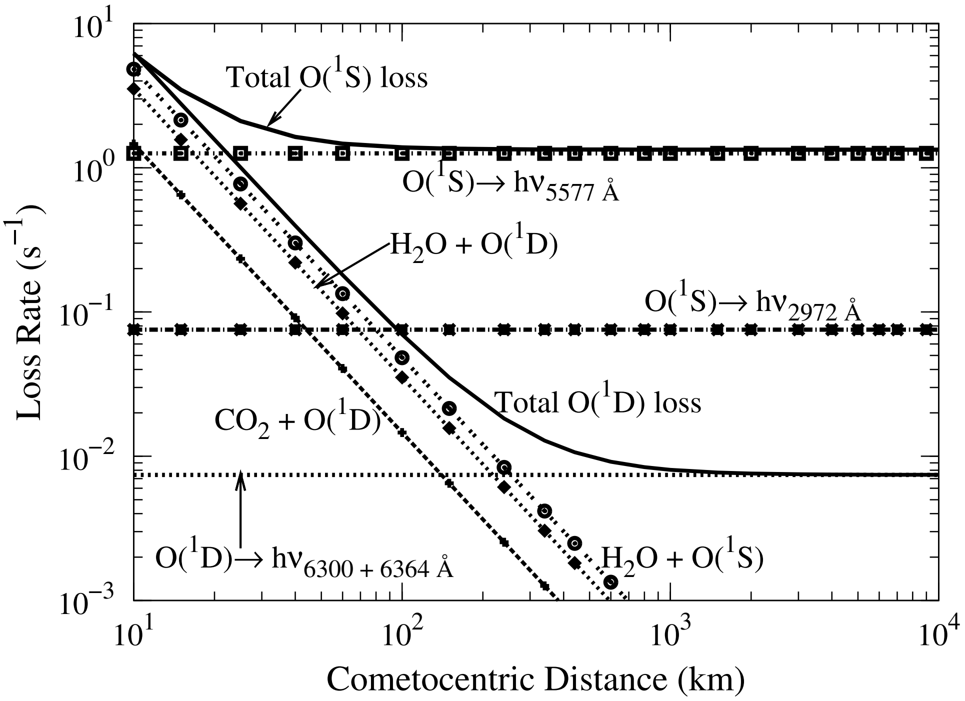

Figure 5.3: Calculated radial loss rate profiles for major loss mechanisms of the O(^{1}D) and O(^{1}S) in comet C/2006 W3 Christensen having H_2O production rate of 2 × 10^{28} s^{-1} and 42% CO_2 and 98% CO abundances relative to H_2O in the cometary coma when comet was at 3.13 AU from the Sun.

comets C/2006 W3 Christensen and C/2001 Q4 (NEAT) the CO_2 abundances are very large (cf. Table 5.1) and no significant collisional quenching of O(^{1}S). Thus the green line intensity throughout the coma is determined by CO_2 and subsequently G/R ratio governed by quenching of O(^{1}D) depending on H_2O production rate. In other comets G/R ratio is small because of less CO_2 abundances compared to former comets.

We calculated the average G/R ratio over the observed projected area on each comet. The projected area on a comet changes with the dimension of slit used for observation and the geocentric distance of comet. The calculated averaged G/R ratio on different comets are tabulated in Table 5.1 along with the values derived from observations. Our calculated G/R ratio values are consistent with the observations on different comets observed at different heliocentric and geocentric distances.

The percentage contributions for various production processes involved in the formation of O(^{1}S) and O(^{1}D) in these comets at three different projected distances are given in Table 5.2. These calculations suggest that in all these comets, the photodissociation of H_2O and CO_2 together produce 50–80% of O(^{1}S), whereas, irrespective of CO_2 and CO relative abundances, the major (∼50 to 80%) source for the formation of O(^{1}D) is photodissociation of H_2O followed by radiative decay of O(^{1}S) (10–15%). At larger

Table 5.2: Calculated percentage contributions for major production processes of O(^{1}S) and O(^{1}D) in six different comets.

Comet	Production processes of O(^{1}S) and O(^{1}D) at three cometocentric projected distances (km) (%)																	
	hν + H_2O			hν + CO_2			hν + CO			O(^{1}S) → O(^{1}D)			e^-_{th} + H_2O^+			e^-_{th} + CO_2^+		
	10^2	10^3	10^4	10^2	10^3	10^4	10^2	10^3	10^4	10^2	10^3	10^4	10^2	10^3	10^4	10^2	10^3	10^4
116P/Wild 4	43	33	25	33	25	20	9	7	5				5	15	22	5	15	17
	(83)*	(71)	(59)	(3)	(2)	(2)	(0.5)	(0.5)	(0.5)	(8)	(9)	(9)	(4)	(14)	(22)	(0.1)	(0.7)	(2)
C/2002 K4	46	42	32	35	32	25	11	11	9				1	4	13	1	5	14
(LINEAR)	(88)	(83)	(71)	(3)	(3)	(2)	(1)	(1)	(1)	(7)	(8)	(9)	(0.5)	(3)	(13)	(0.5)	(0.5)	(1)
C/2007 Q3	35	29	21	46	37	28	4	3	2				2	18	17	4	15	23
Siding Spring	(82)	(73)	(60)	(4)	(4)	(3)	(0.5)	(0.5)	(0.5)	(9)	(10)	(11)	(2)	(9)	(20)	(0.5)	(2)	(3)
C/2006 W3	18	15	11	55	47	37	17	15	11				0.5	3	8	3	15	28
Christensen	(69)	(61)	(48)	(9)	(8)	(7)	(3)	(2)	(2)	(15)	(16)	(17)	(1)	(6)	(15)	(0.5)	(3)	(5)
C/2009 P1	22	17	14	41	32	28	22	17	15				3	9	13	8	20	23
(Garradd)	(71)	(58)	(47)	(6)	(5)	(4)	(3)	(3)	(2)	(13)	(14)	(13)	(4)	(14)	(19)	(1)	(3)	(3)
C/2001 Q4	11	9	7	63	50	40	11	9	7				1	4	6	7	23	34
(NEAT)	(57)	(47)	(37)	(13)	(11)	(9)	(2)	(2)	(2)	(21)	(22)	(22)	(2)	(8)	(14)	(1)	(5)	(8)
comet X†	8	6	5	63	47	41	8	6	5				1	3	5	12	30	37
	(48)	(38)	(31)	(15)	(12)	(10)	(2)	(1)	(1)	(23)	(25)	(24)	(3)	(10)	(13)	(3)	(8)	(10)

*The values in parenthesis are for O(^{1}D); †comet X is a hypothetical comet similar to the observational condition of comet NEAT and having equal gas production rates of H_2O, CO_2, and CO; hν = photon; e^-_{th} = thermal electron.

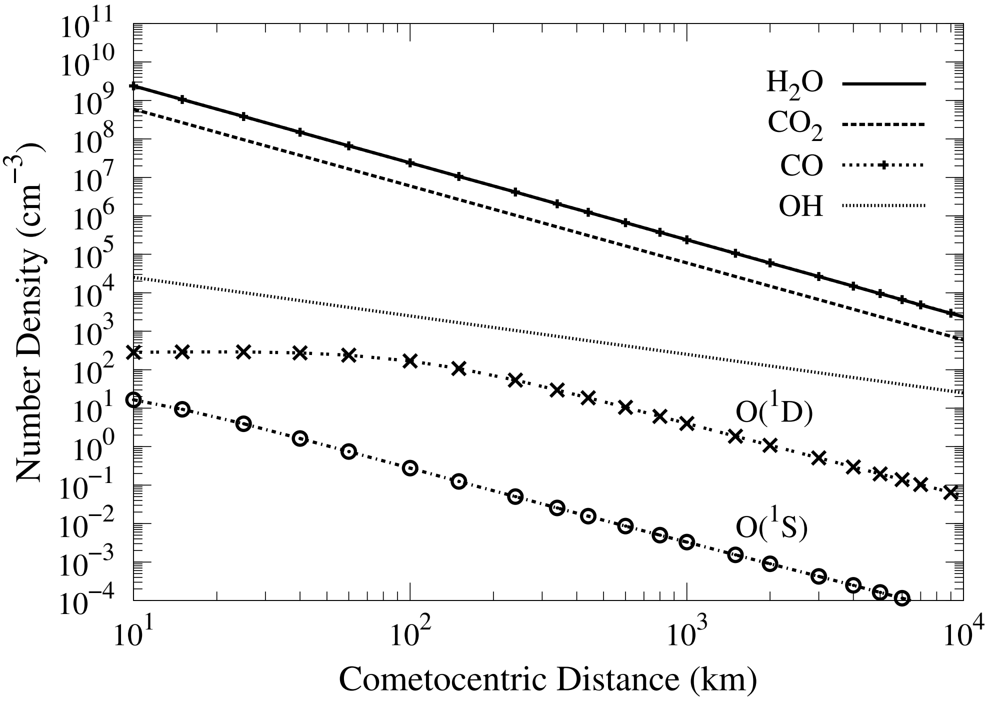

Figure 5.4: Calculated number density profiles of $O(^1S)$, $O(^1D)$, and OH, along with those of H_2O, CO, and CO_2 in comet C/2006 W3 Christensen which is having H_2O production rate of 2×10^{28} s^{-1} and 42% CO_2 and 98% CO relative abundances with respect to H_2O in the cometary coma when comet was at 3.13 AU from the Sun.

projected distances (>10^3 km), dissociative recombination processes of H_2O^+ and CO_2^+ ions are also important production sources of $O(^1S)$ (30–40%) and $O(^1D)$ (~20%).

The calculated percentage contributions of different production processes in the total intensity of [OI] emissions over the observed coma on these comets are tabulated in Table 5.3. These calculations suggest that photodissociation of CO_2 and H_2O together contribute 50–70% to the green line emission and the remaining contribution is through dissociative recombination of H_2O^+ and CO_2^+ ions. In the case of red-doublet emission, photodissociation of H_2O and radiative decay of $O(^1S)$ together produces 70–90% and contributions from other sources are very small.

In the case of hypothetical comet X which is having equal H_2O, CO_2, and CO, gas production rates, ~80% of green line emission intensity is governed by CO_2 (via photodissociation of CO_2 and dissociative recombination of CO_2^+) whereas photodissociation of H_2O and CO together contribute around 10%. Dissociative recombination of CO_2^+ is second important source which contribute around 30% to the total green line emission. In this case around 35% of red-doublet emission is produced via H_2O photodissociation. The production of $O(^1D)$ via CO_2 photodissociation is around 10% to the total while it is ~25% via radiative decay of $O(^1S)$ which is also essentially produced from CO_2. In this case both CO_2 and H_2O are playing equally important roles in producing red-doublet

Table 5.3: Calculated percentage contributions for major production processes of green and red-doublet emissions in the slit projected field of view on different comets and the comparison of the calculated and observed line widths.

Comet	hν + H_2O	hν + CO_2	hν + CO	$O(^1S) \rightarrow O(^1D)$	e^-_{th} + H_2O^+	e^-_{th} + CO_2^+	5577 Line width		6300 Line width	
							Cal[‡]	Obs[†]	Cal[‡]	Obs[†]
116P/Wild 4	34 (72)[*]	26 (2)	7 (0.5)	(9)	14 (13)	14 (1)	1.70	–	1.32	–
C/2002 K4 (LINEAR)	40 (81)	31 (3)	10 (1)	(8)	6 (5)	7 (0.5)	2.05	2.38–2.76	1.87	1.81–2.12
C/2007 Q3 Siding Spring	28 (72)	37 (4)	3 (0.5)	(10)	9 (10)	15 (1)	2.04	–	1.44	–
C/2006 W3 Christensen	14 (61)	47 (8)	14 (3)	(16)	3 (6)	15 (3)	2.48	–	1.58	–
C/2009 P1 (Garradd)	16 (55)	31 (4)	17 (3)	(13)	10 (15)	21 (3)	1.85	2.16–2.54	1.25	1.25–1.67
C/2001 Q4 (NEAT)	8 (44)	47(11)	8 (2)	(22)	4 (9)	26 (6)	2.30	2.31–2.55	1.65	2.39–2.75
comet X[§]	6 (36)	46(11)	6 (1)	(25)	4 (10)	31 (8)	2.35	–	1.65	–

[*] The values in parenthesis are calculated percentage contributions for red-doublet emission;

[†] Obs: observed line widths are taken from *Decock et al.* [2012];

[‡] Cal: model calculated line widths; [§] comet X is a hypothetical comet similar to the observational condition of comet NEAT and having equal gas production rates of H_2O, CO_2, and CO; hν = photon; e^-_{th} = thermal electron.

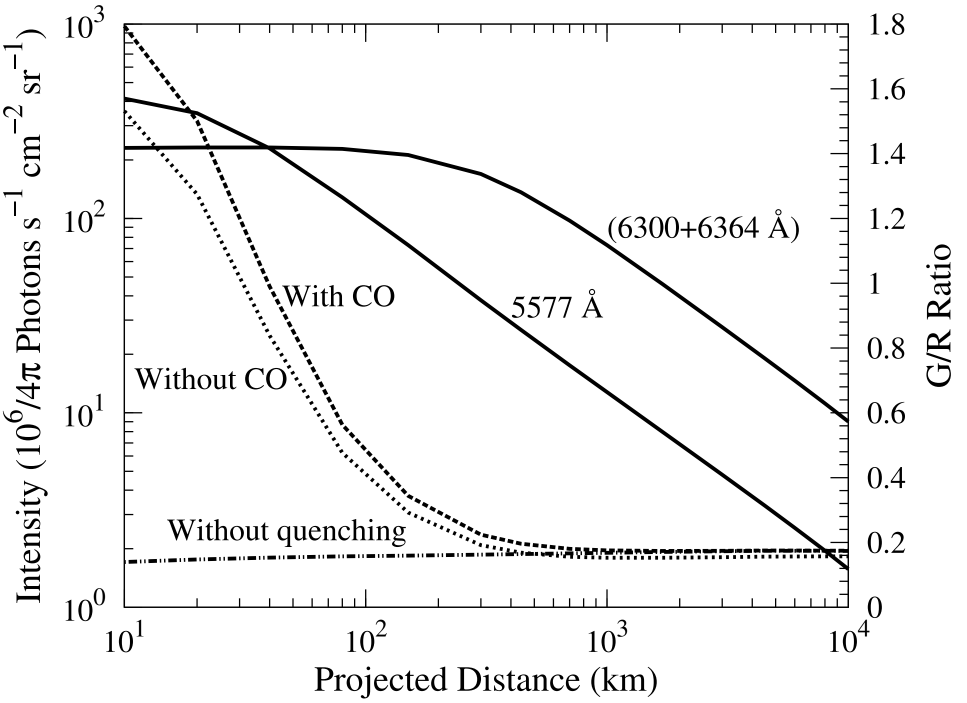

Figure 5.5: Calculated [OI] red-doublet (6300+6364 Å) and 5577 Å line brightness profiles (with solid curves) along the cometocentric projected distances on comet C/2006 W3 Christensen which is having H_2O production rate of 2 × 10^{28} s^{-1} and 42% CO_2 and 98% CO relative abundances with respect to H_2O in the cometary coma when comet was at 3.13 AU from the Sun. The calculated G/R ratio by considering CO, without considering CO, and without quenching cases are plotted with dashed, dotted, and dash-dotted curves, respectively, on the right y-axis.

emission.

We also calculated the mean excess energy released in these photodissociative excitation reactions. The maximum excess energy in photodissociation of H_2O producing O(^{1}S) by solar Ly-α photons is 1.27 eV whereas the mean excess energy in the photodissociation of CO_2 forming O(^{1}S) is 2.55 eV. Mean excess energies in photodissociative excitation of H_2O, CO_2, and CO producing O(^{1}D) are 2.12, 4.46, and 2.54 eV, respectively. We assumed that most of these excess energies will result in kinetic motion of daughter products. Thus, the excess velocities of O(^{1}S) in photodissociative excitation of H_2O and CO_2 are 1.3 and 4.4 km s^{-1}, respectively. Similarly, the calculated excess velocities of O(^{1}D) in photodissociation of H_2O, CO_2, and CO are 1.6, 5.8, and 3.6 km s^{-1}, respectively.

Considering only photoreactions and using the calculated contributions of each process over the cometary coma (cf., Table 5.3) we calculated the mean excess energies of O(^{1}S) and O(^{1}D). Our calculated mean velocities of O(^{1}S) and O(^{1}D) atoms on these comets are tabulated in Table 5.3 along with the derived velocities based on the observed

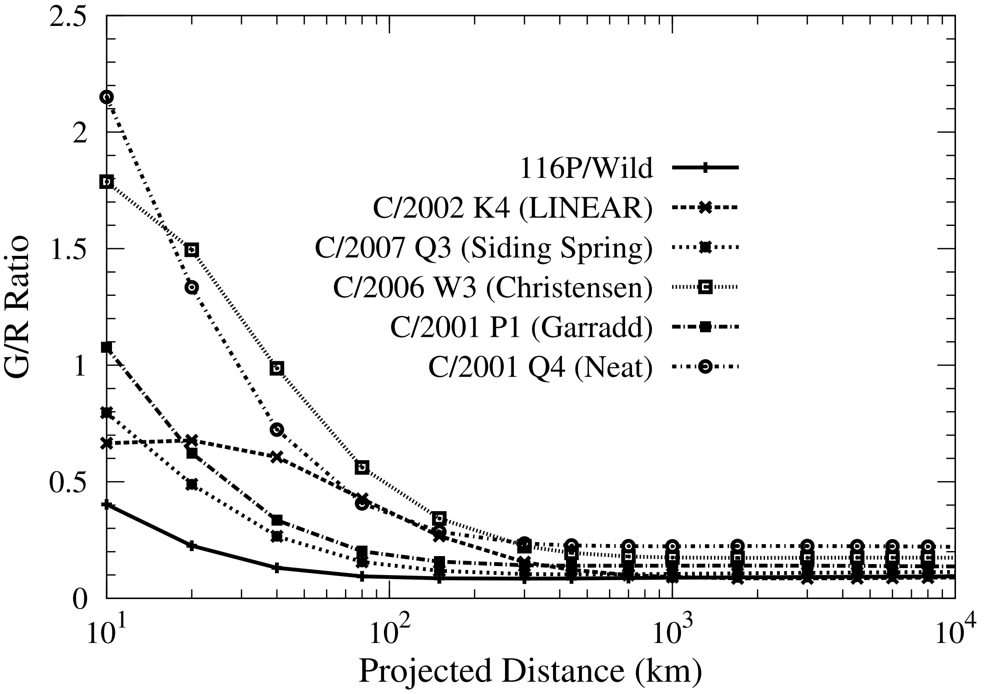

Figure 5.6: The calculated G/R ratio profiles along the projected distance in six different comets. The input parameters used to calculate the G/R ratio are tabulated in Table 5.1. It can be noticed that in comets C/2006 W3 Christensen and C/2001 Q4 (NEAT) due to substantial collisional quenching of O(^{1}S) and O(^{1}D) with other cometary species the calculated G/R ratio is more than 1 closer to the nucleus whereas above 400 km projected distances it is a constant.

line widths. In comets having large CO_2 relative abundances the width of green line, which is a function of mean O(^{1}S) velocity, is mainly determined by photodissociation of CO_2. Since the mean excess energy released in photodissociation of CO_2 is higher, the width of the green line would be larger compared to the red-doublet emission line width (which is mainly determined by photodissociation of H_2O). Our calculated green line widths in different comets, which are presented in Table 5.3, are higher than the calculated red-doublet emission line widths, which is consistent with the observations.

Depending on the composition and activity of the nucleus, comets have different gas production rates at different heliocentric distances. In order to appraise the collisional quenching of O(^{1}S) and O(^{1}D) with increase in H_2O production rate we calculated the radiative efficiencies of O(^{1}S) and O(^{1}D) for different water production rates. The calculated radiative efficiency profiles are shown in Figure 5.7. This calculation shows that for a given water production rate the O(^{1}D) is always much more get quenched than that of O(^{1}S). This is mainly because the lifetime of O(^{1}D) ($\sim$120 s) is larger by two orders of magnitude than that of O(^{1}S) ($\sim$0.8 s).

Since CO_2 is a potentially important source of O(^{1}S) we have also carried out

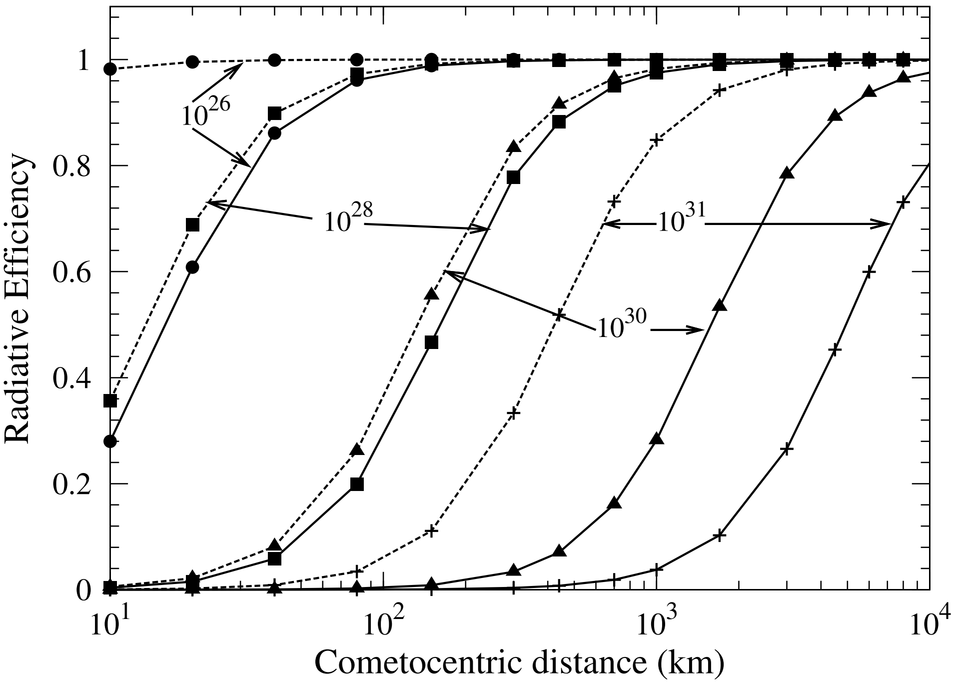

Figure 5.7: The calculated radiative efficiency profiles of O(^{1}S) (green lines) and O(^{1}D) (red lines) in comets for different gas production rates with 5% CO_2 and 10% CO relative abundances with respect to H_2O. The circles, squares, triangles, and cross symbols represent the calculated radiative efficiencies for the water production rates of 10^{26}, 10^{28}, 10^{30}, and 10^{31}, respectively.

model calculations of the G/R ratio on different water production rates by varying its relative abundance from 0% to 100% with respect to H_2O. The calculations presented in Figure 5.8 suggests that by increasing CO_2 relative abundance in a comet the G/R ratio increases almost monotonically.

5.4 Discussion

For comets close to 1 AU from the Sun the dominant species in the cometary coma is H_2O. Due to lower ice-sublimation temperatures of CO and CO_2, at large heliocentric distances the cometary coma is dominantly composed of CO_2 and CO [*Meech and Svoreň*, 2004; *Crovisier et al.*, 1999; *Biver et al.*, 1997, 1999; *Bockelée-Morvan et al.*, 2004; *Bockelée-Morvan et al.*, 2010]. Due to strong absorption of cometary H_2O infrared emission lines by terrestrial water molecules, it is difficult to detect H_2O in the coma for ground-based observations. But the spatial profiles of water can be easily derived in comets from ground-based observatories by observing infrared H_2O non-resonance fluorescence emissions [*Mumma et al.*, 1995, 1996; *Dello Russo et al.*, 2000]. Since H_2O does not have any transitions in the visible region the emissions of its daughter products have been used as tracers to understand the spatial distribution of water in the cometary

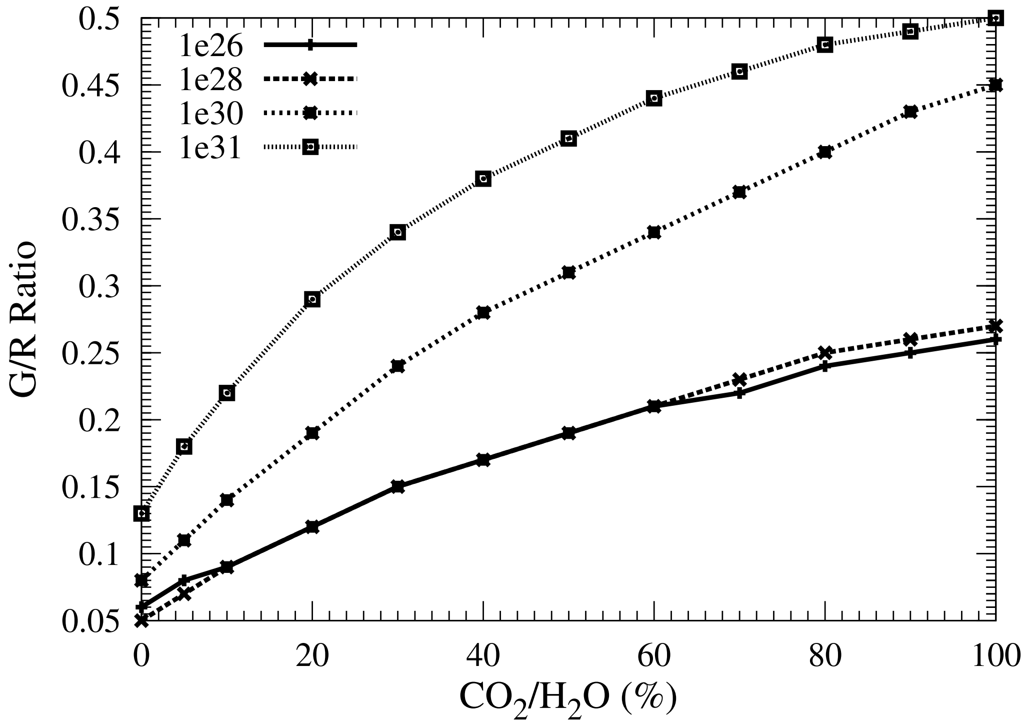

Figure 5.8: The calculated G/R ratio as a function CO_2 abundance for different water production rates, with 10% CO abundance relative to H_2O in the coma. These calculations are done at heliocentric and geocentric distances of 1 AU using a square slit of side 5″.

coma. The observed atomic oxygen visible emissions (viz., O[I] 5577, 6300, and 6364 Å) have been used to quantify the H_2O production rate in several comets around 1 AU [*Delsemme and Combi*, 1976; *Delsemme and Combi*, 1979; *Fink and Johnson*, 1984; *Schultz et al.*, 1992; *Morgenthaler et al.*, 2001]. Since CO_2 and CO can also produce these metastable oxygen atoms, based on the theoretical work of *Festou and Feldman* [1981], the G/R ratio of 0.1 has been used as the benchmark to confirm H_2O as the parent species for these oxygen emission lines. The available theoretical and experimental cross sections for the production of O(^{1}S) and O(^{1}D) from different O-bearing species have been reviewed in Chapter 4. Our coupled chemistry-emission model, which has been applied to comets Hyakutake and Hale-Bopp, suggested that the observed G/R ratio not only depends on the relative abundances of CO_2 and CO but also on the projected area observed on the comet.

Since CO_2 does not emit ultraviolet or visible photons we can not detect this molecule directly in the cometary ultraviolet or visible spectra. Moreover, CO_2 is a symmetric molecule with no permanent dipole moment and hence it is difficult to observe this molecule even in radio range from the ground [*Ootsubo et al.*, 2012]. Thus this molecule is probed using indirect methods using the emissions of its dissociative products, like CO Cameron band ($a^3\Pi$–$X^1\Sigma^+$) in ultraviolet [*Weaver et al.*, 1994; *Feldman et al.*, 1997] and visible atomic oxygen green and red-doublet emissions [*Furusho et al.*, 2006; *McKay et al.*, 2012; *Decock et al.*, 2012]. Our earlier works [*Bhardwaj and Raghuram*, 2011; *Raghuram and Bhardwaj*, 2012] have shown that CO Cameron band emission is not suitable to measure CO_2 abundances in comets since this emission is mainly governed by photoelectron impact excitation of CO rather than the photodissociation of CO_2.

Assuming that the green line emission is governed by photodissociation of CO_2 while the red-doublet emission is controlled by photodissociation of H_2O, the observed G/R ratio has been used to quantify CO_2 relative abundance in the comets [*McKay et al.*, 2012; *Decock et al.*, 2012]. At larger heliocentric distances CO_2 and CO are the dominant O-bearing species in the coma which can produce green and red-doublet emissions. In several comets the observed G/R ratio at large (>2 AU) heliocentric distances is more than 0.1 [*Decock et al.*, 2012; *McKay et al.*, 2012; *Furusho et al.*, 2006].

5.4.1 Impact of CO on the G/R ratio

At larger heliocentric distances, though CO abundance is substantial in the cometary comae, the photodissociation of CO is not a potential source of $O(^1S)$ and $O(^1D)$ atoms. This is mainly due to the proximity in the threshold energies of photodissociative excitation and photoionization of CO molecule. The threshold energies for dissociation of CO into $O(^1D)$ and $O(^1S)$ states are 14.35 and 16.58 eV, respectively, whereas it is 14 eV for ionization. Moreover, branching ratio of ionization for the photons having energy more than 14 eV is ∼0.98 [*Huebner et al.*, 1992]. Since the ionization energy is smaller than energy required in the formation of $O(^1S)$ and $O(^1D)$, most of the photons (>90%) having energy >14 eV ionize the CO molecule rather than causing photodissociative excitation. Based on *Huebner and Carpenter* [1979] compiled cross sections, *Festou and Feldman* [1981] estimated that the photodissociation of CO produces $O(^1S)$ and $O(^1D)$ with nearly equal rate. To evaluate the role of CO we also did calculations in comet C/2006 W3 Christensen by discarding photodissociation of CO as a source mechanism of both $O(^1S)$ and $O(^1D)$ (cf., Figure 5.5). Though CO production rate is equal to that of H_2O in this comet (cf. Table 5.1), by removing CO contribution the calculated G/R ratio decreased by a maximum of about 10%. Similarly, our calculated percentage contribution over the observed coma on different comets, which is presented in Table 5.3, also suggests that the role of CO is very small (<20%) in producing $O(^1S)$ and $O(^1D)$ atoms and subsequently in determining the red-doublet emission intensity. Even without considering photodissociation of CO in the model the calculated G/R ratio values are in agreement with the observations. Based on these calculations we can suggest that the photodissociation of CO is an insignificant source of $O(^1S)$ and $O(^1D)$. Hence, the photodissociation of CO has almost no impact on the G/R ratio.

5.4.2 Impact of CO_2 on the G/R ratio

The relative abundance of CO_2, with respect to H_2O, is very important in determining the G/R ratio. This can be understood from the calculated G/R ratio profiles on comets 116P/Wild 4, C/2007 Q3 Siding Spring, and C/2001 Q4 (NEAT), which have nearly same H_2O production rates (1–4 $\times$ 10^{28} s^{-1}) but different relative abundances of CO_2 and CO, and observed at different heliocentric distances. As discussed in Section 5.4.1, the CO abundance does not have any appreciable impact on the G/R ratio. Hence, the change in the calculated G/R ratio on these comets can be ascribed mainly to the difference in CO_2 relative abundances. The calculated G/R ratio profiles on these comets are shown in Figure 5.6, which depicts that by increasing CO_2 the G/R ratio increases. In comet C/2001 Q4 (NEAT), due to higher (75%) CO_2 relative abundance, the calculated G/R ratio value is more than one close to the cometary nucleus. Similar behavior is seen for comet C/2006 W3 Christensen which is due to larger ($\sim$40%) CO_2 relative abundance with respect to H_2O, and also due to significant collisional quenching of O(^{1}D) (cf. Figure 5.5). We found that by doubling CO_2 relative abundance the G/R ratio changes by $\sim$25%, whereas collisional quenching alone can vary its value by an order of magnitude. The model calculated G/R ratio values in comets 116P/Wild 4, C/2007 Q3 Siding Spring, and C/2009 P1 (Garradd) are smaller by a factor of around 1.5 compared to the observations.

The detection of CO_2 molecules in the coma has been carried out using several infrared satellites by observing its fundamental vibrational band emission (ν_3) at 4.26 μm [*Crovisier et al.*, 1996; *Crovisier et al.*, 1997, 1999; *Colangeli et al.*, 1999; *Reach et al.*, 2010; *Ootsubo et al.*, 2012]. The quantification of CO_2 abundance based on the observed infrared emission intensity is subjected to opacity of cometary coma. Since the fluorescence efficiency factor ($g-$factor) is larger compared to that of H_2O and CO [cf. Table 2 of *Ootsubo et al.*, 2012], these emission lines are optically thick in the inner coma, which can result in underestimation of CO_2 abundance if proper treatment of radiative transfer is not accounted in the analysis. The optical depth effects in the inner coma may cause the surface brightness profile of these emissions to be much flatter and resembling the presence of extended source in the coma. In comet Hale-Bopp, *Bockelée-Morvan et al.* [2010] have shown that that the observed broad extent of infrared CO brightness is due to optical depth effects of the emitted radiation and not because of extended sources. Since these comets are observed at larger heliocentric distances and have low gas production rates, and the collision dominated coma size is a few hundreds of kilometers only. Thus the opacity effects of these IR emissions can be significant close to the nucleus and can influence the derivation CO_2 production rate based on the observed flux over the field of view. The discrepancies between *Ootsubo et al.* [2012] derived production rates and other observations might be due to opacity of the cometary comae. Though *Ootsubo et al.* [2012] assumed optically thin conditions in the analysis, their derived gas production rates differ from that of other observations by a factor of 2. Considering these observational facts we varied CO_2 abundances in the model to assess our model calculated G/R ratio with the observations. By increasing CO_2 abundances in these comets by a factor of 3 we could achieve better agreement with the observed G/R ratio.

Similarly, the calculations presented in Figure 5.8 demonstrate that for a constant H_2O production rate, the G/R ratio increases with increasing CO_2 relative abundance. This figure suggests that for a constant CO_2 relative abundance, by increasing H_2O production rate, the collisional quenching of $O(^1S)$ and $O(^1D)$ can increase the G/R ratio. Thus, the observation of a larger G/R ratio value need not be always due to higher CO_2 abundances.

In case of hypothetical comet X, which has CO_2 abundance equal to that of H_2O, the calculated percentage contributions of different processes to red-doublet emissions presented in Table 5.3 suggest that the red-doublet emission intensity is equally controlled by CO_2 and H_2O. If a comet possess equal abundances of CO_2 and H_2O, which is the case for comet C/2006 W3 Christensen observed by *Ootsubo et al.* [2012] at 3.7 AU from the Sun, deriving the water production rates based on the observed red-doublet emission intensity may result in over estimation of H_2O. In this case the derivation of CO_2 abundances using the observed G/R ratio also leads to improper estimation. This calculation suggest that in a comet having high CO_2 abundance the red-doublet emission intensity is not suitable to measure H_2O rates. Similarly, our model calculations for comet C/2001 Q4 (NEAT), which is having 75% CO_2, also suggest that around 30% of red-doublet emission are governed by both photodissociation of CO_2 and radiative decay of $O(^1S)$ which is comparable to the contribution from H_2O ($\sim$45%).

5.4.3 Impact of collisional quenching of $O(^1S)$ and $O(^1D)$ on the G/R ratio

The G/R ratio at a given projected distance mainly depends on the formation and destruction processes of excited oxygen atoms in the cometary coma along the line of sight. The abundances of O-bearing species and solar flux governs the formation rate of these metastable species while the chemical lifetime and collisional quenching by other cometary species, determines the destruction rate. In a comet having moderate H_2O production rate of 4×10^{28} s^{-1}, the radius of H_2O collisional zone is around 1000 km [*Whipple and Huebner*, 1976]. When the comet is at larger heliocentric distance lower gas evaporation rate results in a smaller collisional coma. Discarding collisional quenching effect the observed G/R ratio has been used to infer CO_2 production rate in comets observed at large heliocentric distance [*McKay et al.*, 2012; *Decock et al.*, 2012]. Our calculated G/R ratio values as a function of projected distance on different comets (cf., Figures 5.5 and 5.6) have shown that the collisional quenching of O(^{1}S) and O(^{1}D) can result in larger (even >1) G/R ratio values. Since the G/R ratio is averaged over the observed large projected distances, the collisional quenching may not influence the average value. In this case the observed G/R ratio is mainly determined by photochemical reactions of H_2O and CO_2 in producing red and green emissions, respectively. Hence, the observed G/R ratio value can be used to estimate upper limit of CO_2 abundance relative to H_2O production rate. But in the case of observations over smaller projected distances the collisional zone predominantly can affect the observed G/R ratio value which eventually can lead to estimation of higher CO_2 abundances. Since the comets considered in this study are observed over large projected distance the effect of collisional quenching is small on the averaged G/R ratio. In such cases the observed G/R ratio value can be effective in constraining the upper limit of CO_2 relative abundance.

5.4.4 Green and red-doublet emission line widths

Cochran [2008] made high resolution observations on different comets and found that the green line width is higher than both red-doublet emission lines. The observation of these forbidden lines made on 12 comets also have shown the same feature [*Decock et al.*, 2012]. The wider green line implies higher mean velocity distribution of O(^{1}S) atoms in the cometary coma. The high velocity of O(^{1}S) atoms in the cometary coma could be due to a parent source other than H_2O or could be due to involvement of high energy photons in H_2O dissociation. Our model calculations on comet Hale-Bopp showed that CO_2 photodissociation is potentially more important source than that of H_2O in producing O(^{1}S) atoms with high excess velocity [*Raghuram and Bhardwaj*, 2013].

From the calculations presented in Table 5.3, it can be understood that both CO_2 and H_2O are the important sources of O(^{1}S), whereas O(^{1}D) is mainly sourced from H_2O. Since high energy photons (955–1165 Å) mainly dissociate CO_2 and produce O(^{1}S), the mean excess energy released in this reaction is larger (~2.5 eV) compared to that of H_2O (~1.2 eV). This results in the production of O(^{1}S) atoms with large velocities (4.3 km s^{-1}) in cometary coma. The calculations presented in Table 5.3 show that above 10^4 km projected distances, the thermal recombination of H_2O^+ and CO_2^+ ions together results in the production of 15–40% of O(^{1}S) and around 20% of O(^{1}D). *Rosen et al.* [2000] and *Seiersen et al.* [2003] experimentally determined the excess energies and branching ratios for the dissociative products in dissociative recombination of H_2O^+ and CO_2^+ ions, respectively. Based on these measured branching fractions and by theoretical estimation, we calculated the excess velocities of O(^{1}S) and O(^{1}D) and green and red line widths by incorporating the dissociative recombination reactions. We found an increase in our calculated green and red line widths by a factor of 1.2–1.7 and 1.1–2.2, respectively. However, without accounting for dissociative recombination reactions in our model, the calculated G/R ratio values (cf. Table 5.1) and line widths (cf. Table 5.3) are consistent with the observations. In comet C/2001 Q4 (NEAT) our calculated red line width is smaller than the observed value. It can be noticed that in this comet both green and red-doublet line widths are nearly same and the red line widths are higher compared to that on other comets, which is difficult to explain based on the model calculations.

Our calculations show that the dissociative recombination of H_2O^+ and CO_2^+ ions are important source of O(^{1}S) in the outer coma. In the model calculations we assumed a constant electron-ion recombination temperature of 300 K. Since comets are observed at large heliocentric distances the temperature values can be less than 300 K. To study the effect of electron temperature on the calculated G/R ratio and line widths we decreased the temperature to 200 K. We did not find any noticeable change in the calculated G/R ratio values or line widths. Since most of the green and red-doublet emission intensities are determined by photodissociation reactions in the inner coma the contribution of thermal recombination of ions on the averaged G/R ratio is rather small.

Several observations at beyond 2 AU have shown that the H_2O production rate in comets does not vary as a function of inverse square of heliocentric distance [*Biver et al.*, 1997, 1999, 2007; *Bodewits et al.*, 2012]. Hence, extrapolation of H_2O production rate based on approximation of inverse square of heliocentric distance may be inappropriate. We evaluated the implication on this extrapolation in comet C/2002 K4 (LINEAR) by decreasing the H_2O production rate by a factor of 2. No significant change (decrease by $\leq 5\%$) is observed in the model calculated G/R ratio and the calculated line widths.

5.5 Summary and conclusion

The observation of green and red-doublet emission lines in comets at larger (> 2 AU) heliocentric distances suggest that the G/R ratio value is larger than 0.1. Moreover, the high resolution observation reports that the green line is wider than the red-doublet lines which is difficult to explain based on the single parent source for these oxygen emission lines [*Decock et al.*, 2012]. We have developed a coupled chemistry-emission model for atomic oxygen visible prompt emissions and applied it on six comets, (viz., 116P/Wild 4, C/2002 K4 (LINEAR), C/2007 Q3 Siding Spring, C/2006 W3 Christensen, C/2009 P1 (Garradd), C/2001 Q4 (NEAT)) which are observed at heliocentric distances greater than 2 AU. By accounting for important chemical reactions in the model we calculated the G/R ratio values and widths of green and red-doublet emission lines on these comets. It is found that CO_2 is potentially more important than H_2O in O(^{1}S) production while O(^{1}D) is mainly controlled by H_2O. The photodissociation of CO is insignificant source of metastable oxygen atoms. The observed large green line width in several comets is due to higher velocity of O(^{1}S) atoms that are essentially produced via photodissociation of CO_2 by higher energy (955-1165 Å) photons. We have shown that the collisional quenching of O(^{1}S) and O(^{1}D) by H_2O can lead to a larger G/R ratio value and that its impact on the G/R ratio is larger than the change in CO_2 relative abundance. Hence, the larger G/R ratio value need not always be linked to larger CO_2 abundances. In a comet having large (>50%) CO_2 abundances, the photodissociation of CO_2 plays a significant role in producing both green and red-doublet emissions; thus, this process also should be accounted while deriving H_2O production rate based on the red-doublet emission intensity. When a comet is observed over a larger projected distance where the collisional zone is less resolvable, the collisional quenching does not affect the observed G/R ratio. At larger heliocentric distances, due to smaller gas production rates, the radius of collisional coma is smaller; hence, the G/R ratio observed over larger projected distances can be used to constrain the CO_2 relative abundance. However, if the slit-projected area on the comet is smaller (with respect to collisional zone), the derived CO_2 abundance based on the G/R ratio would be overestimated. Our model calculated G/R ratio and line widths of green and red-doublet emission are in agreement with the observation.

Chapter 6

Summary, Limitations, and Future scope

Summary

Comets are small bodies of the solar system orbiting around the Sun in highly elliptical orbits. The solid body of comet is nucleus with a size of one to a few kilometers. Cometary nucleus is a conglomerated mixture of water ice, dust and some organic compounds. During their orbital motion, due to solar radiation heating, the ices in the nucleus sublimates and produce a transient gaseous envelope around the nucleus called cometary coma. In a active comet, at around 1 AU, the gases and dust in the cometary coma radially expands typically to a million kilometer distance. The solar radiation exert pressure on the dust grains drives them radially away from the Sun and forms a dust tail whereas the interaction of solar wind with the cometary ions produces ion tail. The solar radiation interact with the cometary coma produce various emissions in the cometary coma. Several space and ground based optical instruments have been used to study these emissions and to determine the composition and spatial distribution of cometary species. The observed intensities of various emissions have been used to quantify the abundances of different cometary species. At 1 AU the cometary coma comprises H_2O as the main constituent in the inner cometary coma whereas at larger heliocentric distances CO_2 and CO are the important species.

The interaction of solar UV-radiation turn molecular cometary coma into atomic coma by dissociating the molecular species. The EUV-UV photons can ionize and excite various atomic and molecular species in the coma. During ionization process most of the excess energy is transferred to ejecting electrons. The electrons created in the cometary coma by UV ionization are called photoelectrons. Photoelectrons having sufficient energy can interact with ambient cometary species and can drive several chemical reactions. The species which are produced via different excitation processes can be in electronically excited state and produce various emissions in the cometary coma provided they are not quenched by collisions with other cometary species. We can not study the emission mechanisms quantitatively by any observational technique. To understand these emission processes we have to model by accounting for all possible production sources and various destruction channels of these excited species. Based on the observed emission intensity over the cometary coma the abundances of various species have been derived. Since several photochemical reactions are involved in driving the observed emission it is essential to understand these processes quantitatively before estimate the abundances in the comets.

H_2O and CO_2 are important parent molecules that have been observed in several comets. These molecules do not have ultraviolet or visible electronic transitions hence direct detection of these molecules is possible in infrared cometary spectrum. The quantification of these molecular abundances has been done using the emissions of their dissociative products. If the dissociated products are metastable states they can not travel to large distances from the source region without decaying to ground state. Hence these emissions can be used as tracers to quantify and to study spatial distribution of parent molecules. CO Cameron band emission has been used to quantify the CO_2 abundance in comets assuming photodissociation of CO_2 is the major production mechanism in producing this emission. Similarly the estimation of H_2O production rate in comets has been done using atomic oxygen forbidden emission (6300, 6364 ,5577 Å). Since CO_2 and CO also can produce these emissions the confirmation of these emissions as H_2O parent source has been done by studying the green to red-doublet emission ratio.

In the present thesis I have studied CO Cameron band and atomic oxygen visible emission in the cometary coma by developing models. I have accounted for major production and destruction mechanisms of $CO(a^3\Pi)$ and metastable states of atomic oxygen atom (^1D and ^1S) in the cometary coma which are excited states of Cameron band and forbidden visible emissions of atomic oxygen. These modelled emissions are applied to different observations made on comets which are having different relative abundances. Calculation of CO Cameron band emission is applied to comets 1P/Halley and 103P/Hartley 2. Model calculations suggest that photoelectron impact excitation is more important process in producing $CO(a^3\Pi)$ in the cometary coma than via photodissociation of CO_2. Since this emission is controlled mainly by electron impact reactions model calculations suggest that the observed CO Cameron band emission intensity can be used to calculated the photoelectron density rather than the CO_2 relative abundance in comets.

A coupled chemistry-emission model is developed to study the forbidden atomic oxygen green (5577 Å) and red-doublet (6300 & 6364 Å) emissions in comets. In several comets, the observations made near heliocentric distance of 1 AU have observed the G/R ratio of 0.1 which has been used as an indicator to confirm H_2O as the parent source for these emissions by referring to the theoretical calculations. The higher (>0.1) observed value of the G/R ratio is ascribed to larger relative abundances of CO_2 and CO. The model developed in this thesis applied to two different comets viz., C/1996 B2 Hyakutake and C/1995 O1 Hale-Bopp which are having different H_2O production rates and observed nearly at 1 AU. It is found that besides CO_2 relative abundance the G/R ratio depends on the observed projected area on the comet which depends on slit-dimension used for the observation and geocentric distance of the comet. The model calculations suggest that the G/R ratio value of 0.1 can not be used as a benchmark to confirm H_2O as the parent source for forbidden atomic oxygen visible emissions.

At larger heliocentric distances (>2 AU), due to low sublimation temperatures the relative abundances of CO_2 and CO are dominant species in the cometary coma. The forbidden atomic oxygen emission lines are observed on several comets at larger (2 to 5 AU) heliocentric distances. I have applied the coupled chemistry-emission model on six comets (viz., C/2006 W3 Christensen, C/2007 Q3 Siding Spring, C/2002 K4 (LINEAR), 116P/Wild 4, C/2009 P1 (Garradd), C/2001 Q4 (NEAT)) where the G/R ratio, and green and red-doublet emission line widths are observed at heliocentric distances of 2 to 4 AU. This study suggests that the photodissociation of CO does not have any role in producing green and red-doublet emission and hence the G/R ratio. The photodissociation of CO_2 produces the $O(^1S)$ atoms with larger kinetic energy which manifests in the green line being wider than the red-doublet emissions. Using the model we have shown that the collisional quenching can alter the G/R ratio value by an order of magnitude whereas the effect of change in the CO_2 relative abundance is relatively smaller. The model calculations suggest that the observed G/R ratio can be used to probe CO_2 relative abundances provided the cometary coma is observed over a large projected distances where the collisional coma does not affect the G/R ratio. If comet has equal abundances of CO_2 and H_2O, then the red-doublet emission is significantly ($\sim$50%) controlled by CO_2 photodissociation and thus in this case the G/R ratio is not suitable to estimate CO_2 relative abundance.

Limitations of the model

The density of the species produced in the inner coma (radial distances less than 10^5 km) is mainly controlled by photochemical reactions. Above these distances the transport of species starts becoming significant in determining the number density of the calculated species. Our model calculations are based on photochemical equilibrium condition and is for a collisional coma. Hence, model results presented at distances beyond 5×10^5 km are not as reliable as the values in the inner coma. Moreover, above these radial distances the chemical lifetimes of neutral species are significantly altered by the solar wind interaction through charge exchange and impact ionization processes. Also, we could not incorporate altitude distribution of dust density in our model calculations which can affect the calculated optical depth. Since our model is time independent and one dimensional it is difficult to explain the asymmetry in the observed [OI] 6300Å emission intensity over the cometary coma. For determining the spectral width of green and red-doublet lines elaborated calculations are required along with laboratory measured photodissociation cross sections.

Future scope of this work

The work presented in this study is useful to understand the underlying processes that governing the ultraviolet and visible emissions in the comets quantitatively. The contribution of this work is useful to estimate the molecular abundances in the coma and subsequently to understand the composition of cometary nuclei. This study can be useful to predict the intensities of CO Cameron band emission and atomic oxygen forbidden cometary emissions for future observations from ground and space based and space-borne optical instruments.

Appendix A

Additional Tables

Table A.1: List of gas-phase ion-chemistry reactions accounted for the coupled chemistry model.

Reaction	**Rate coefficient (cm^3 s^{-1} or s^{-1})**	**Reference**
	H^+	
$H_2O + h\nu \rightarrow H^+ + OH$	calculated	This work
$H_2O + e^-_{ph} \rightarrow H^+ + OH$	calculated	This work
$C^+ + OH \rightarrow H^+ + CO$	1.5×10^{-7} $(300/T_e)^{0.42}$	*Schmidt et al.* [1988]
$O^+ + H \rightarrow H^+ + O$	6.0×10^{-10}	*Anicich* [1993a]
$CO^+ + H \rightarrow H^+ + CO$	7.5×10^{-10}	*Anicich* [1993a]
$CO_2^+ + H \rightarrow H^+ + CO_2$	2.4×10^{-10}	*Anicich* [1993b]
$H^+ + H_2O \rightarrow H_2^+O + H$	8.2×10^{-9}	*Anicich* [1993a]
$H^+ + CO_2 \rightarrow CO_2^+ + H$	4.2×10^{-9}	*Anicich* [1993a]
$H^+ + OH \rightarrow OH^+ + H$	1.0×10^{-9}	*Schmidt et al.* [1988]
$H^+ + e^-_{th} \rightarrow H$	3.5×10^{-12} $(300/T_e)^{0.7}$	*Schmidt et al.* [1988]
$O^+ + OH \rightarrow H^+ + O_2$	7.2×10^{-10}	*Woodall et al.* [2007]
	C^+	
$CO + h\nu \rightarrow C^+$	calculated	This work
$CO_2 + h\nu \rightarrow C^+ + O_2$	calculated	This work
$CO + e^-_{ph} \rightarrow C^+ + O$	calculated	This work
$CO_2 + e^-_{ph} \rightarrow C^+ + O_2$	calculated	This work
$C^+ + H_2O \rightarrow HCO^+ + H$	3.6×10^{-10}	*Anicich* [1993a]
$C^+ + H_2O \rightarrow HOC^+ + H$	1.9×10^{-9}	*Anicich* [1993a]
$C^+ + CO_2 \rightarrow CO^+ + CO$	9.9×10^{-10}	*Anicich* [1993a]
$C^+ + CO_2 \rightarrow CO_2^+ + C$	1.1×10^{-10}	*Anicich* [1993a]
$C^+ + OH \rightarrow CO^+ + H$	1.0×10^{-9}	*Schmidt et al.* [1988]

Continued on next page

Table A.1 – *Continued from previous page*

Reaction	**Rate coefficient** **(cm^3 s^{-1} or s^{-1})**	**Reference**
$C^+ + OH \rightarrow H + CO^+$	1.0×10^{-9}	*Schmidt et al.* [1988]
$C^+ + e^-_{th} \rightarrow C$	3.5×10^{-12} $(300/T_e)^{0.7}$	*Schmidt et al.* [1988]
	O^+	
$H_2O + h\nu \rightarrow O^+ + H_2$	calculated	This work
$CO_2 + h\nu \rightarrow O^+ + CO$	calculated	This work
$CO + h\nu \rightarrow O^+ + C$	calculated	This work
$H_2O + e^-_{ph} \rightarrow O^+ + H_2$	calculated	This work
$CO_2 + e^-_{ph} \rightarrow O^+ + CO$	calculated	This work
$CO + e^-_{ph} \rightarrow O^+ + C$	calculated	This work
$H^+ + O \rightarrow O^+ + H$	3.75×10^{-10}	*Stancil et al.* [1999]
$CO^+ + O \rightarrow O^+ + CO$	1.4×10^{-10}	*Fehsenfeld and Ferguson* [1972]
$CO_2^+ + O \rightarrow O^+ + CO_2$	9.6×10^{-11}	*Fehsenfeld et al.* [1970]
$O^+ + H \rightarrow O + H^+$	6.0×10^{-10}	*Anicich* [1993a]
$O^+ + H_2O \rightarrow H_2O^+ + O$	2.5×10^{-9}	*Anicich* [1993a]
$O^+ + CO_2 \rightarrow O_2^+ + CO$	9.4×10^{-10}	*Anicich* [1993a]
$O^+ + OH \rightarrow H^+ + O_2$	7.2×10^{-10}	*Woodall et al.* [2007]
$O^+ + e^-_{th} \rightarrow O$	3.5×10^{-12} $(300/T_e)^{0.7}$	*Schmidt et al.* [1988]
	OH^+	
$H_2O + h\nu \rightarrow OH^+ + H$	calculated	This work
$H_2O + e^-_{ph} \rightarrow OH^+ + H$	calculated	This work
$H^+ + OH \rightarrow OH^+ + H$	1.0×10^{-9}	*Schmidt et al.* [1988]
$O^+ + OH \rightarrow OH^+ + O$	3.6×10^{-10}	*Woodall et al.* [2007]
$CO^+ + OH \rightarrow OH^+ + CO$	3.2×10^{-10}	*Woodall et al.* [2007]
$OH^+ + H_2O \rightarrow H_2O^+ + OH$	1.6×10^{-9}	*Anicich* [1993a]
$OH^+ + H_2O \rightarrow H_3O^+ + O$	1.3×10^{-9}	*Anicich* [1993a]
$OH^+ + CO \rightarrow HCO^+ + O$	7.1×10^{-10}	*Anicich* [1993a]
$OH^+ + CO_2 \rightarrow HCO_2^+ + O$	1.1×10^{-9}	*Anicich* [1993a]
$OH^+ + OH \rightarrow H_2O^+ + O$	7.0×10^{-10}	*Woodall et al.* [2007]
$OH^+ + e^-_{th} \rightarrow O + H$	3.7×10^{-8} $(300/T_e)^{0.5}$	*Guberman* [1995]
$OH^+ + C \rightarrow CO^+ + H$	1×10^{-9}	*Schmidt et al.* [1988]
$OH^+ + C \rightarrow CH^+ + O$	1×10^{-9}	*Schmidt et al.* [1988]
$OH^+ + O \rightarrow O_2^+ + H$	1.0×10^{-9}	*Woodall et al.* [2007]

Continued on next page

Table A.1 – *Continued from previous page*

Reaction	**Rate coefficient (cm^3 s^{-1} or s^{-1})**	**Reference**
	CO^+	
$CO + h\nu \rightarrow CO^+$	calculated	This work
$CO + e^-_{th} \rightarrow CO^+$	calculated	This work
$C + OH^+ \rightarrow CO^+ + H$	1.0×10^{-9}	*Schmidt et al.* [1988]
$C^+ + CO_2 \rightarrow CO^+ + CO$	9.9×10^{-10}	*Schmidt et al.* [1988]
$C^+ + OH \rightarrow CO^+ + H$	1.0×10^{-9}	*Schmidt et al.* [1988]
$CO^+ + H \rightarrow H^+ + CO$	7.5×10^{-10}	*Federer et al.* [1984]
$CO^+ + O \rightarrow CO + O^+$	1.4×10^{-10}	*Fehsenfeld and Ferguson* [1972]
$CO^+ + H_2O \rightarrow CHO^+ + OH$	1.8×10^{-9}	*Anicich* [1993a]
$CO^+ + CO_2 \rightarrow CO_2^+ + CO$	9.6×10^{-10}	*Woodall et al.* [2007]
$CO^+ + OH \rightarrow HCO^+ + O$	6.5×10^{-10}	*Woodall et al.* [2007]
$CO^+ + e^-_{th} \rightarrow$	1.0×10^{-7} $(300/T_e)^{0.46}$	*Rosén et al.* [1998]
	O_2^+	
$OH^+ + O \rightarrow O_2^+ + H$	1.0×10^{-9}	
$O^+ + CO_2 \rightarrow O_2^+ + CO$	9.4×10^{-10}	*Anicich* [1993a]
$O^+ + OH \rightarrow O_2^+ + H$	3.6×10^{-10}	*Woodall et al.* [2007]
$CO_2^+ + O \rightarrow O_2^+$	1.6×10^{-10}	*Schmidt et al.* [1988]
$O_2^+ + e^-_{th} \rightarrow O + O$	1.9×10^{-7} $(300/T_e)^{0.7}$	*Schmidt et al.* [1988]
	H_2O^+	
$H_2O + h\nu \rightarrow H_2O^+$	calculated	This work
$H_2O + e^-_{ph} \rightarrow H_2O^+$	calculated	This work
$H^+ + H_2O \rightarrow H_2O^+$	8.2×10^{-9}	*Anicich* [1993b]
$O^+ + H_2O \rightarrow H_2O^+$	2.5×10^{-9}	*Anicich* [1993b]
$OH^+ + H_2O \rightarrow H_2O^+$	1.6×10^{-9}	*Anicich* [1993b]
$OH^+ + OH \rightarrow H_2O^+$	7.0×10^{-10}	*Woodall et al.* [2007]
$CO^+ + H_2O \rightarrow H_2O^+ + CO$	1.7×10^{-9}	*Schmidt et al.* [1988]
$CO_2^+ + H_2O \rightarrow H_2O^+$	1.7×10^{-9}	*Schmidt et al.* [1988]
$H_2O^+ + H_2O \rightarrow H_3O^+ + OH$	2.0×10^{-9}	*Schmidt et al.* [1988]
$H_2O^+ + CO \rightarrow HCO^+ + OH$	3.6×10^{-10}	*Anicich* [1993a]
$H_2O^+ + OH \rightarrow H_3O^+ + O$	6.9×10^{-10}	*Woodall et al.* [2007]
$H_2O^+ + e^-_{th} \rightarrow 2H + O$	3.1×10^{-7} $(300/T_e)^{0.5}$	*Rosen et al.* [2000]

Continued on next page

Table A.1 – *Continued from previous page*

Reaction	Rate coefficient (cm^3 s^{-1} or s^{-1})	Reference
$H_2O^+ + C \rightarrow CH^+ + OH$	1.0×10^{-9}	*Schmidt et al.* [1988]
	H_3O^+	
$OH^+ + H_2O \rightarrow H_3O^+ + O$	1.3×10^{-9}	*Schmidt et al.* [1988]
$H_2O^+ + H_2O \rightarrow H_3O^+ + OH$	2.05×10^{-9}	*Schmidt et al.* [1988]
$H_2O^+ + OH \rightarrow H_3O^+ + O$	6.9×10^{-10}	*Woodall et al.* [2007]
$H_3O^+ + e^-_{th} \rightarrow 2H + OH$	$3.1 \times 10^{-7}\ (300/T_e)^{0.5}$	*Jensen et al.* [2000]
$H_3O^+ + C \rightarrow CHO^+ + H_2$	2.0×10^{-9}	*Schmidt et al.* [1988]
	CO_2^+	
$CO_2 + h\nu \rightarrow CO_2^+$	calculated	This work
$CO_2 + e^-_{ph} \rightarrow CO_2^+$	calculated	This work
$C^+ + CO_2 \rightarrow CO_2^+$	1.1×10^{-10}	*Anicich* [1993a]
$CO^+ + CO_2 \rightarrow CO_2^+ + CO$	9.6×10^{-10}	*Woodall et al.* [2007]
$CO_2^+ + H \rightarrow CHO^+ + O$	6.2×10^{-11}	*Schmidt et al.* [1988]
$CO_2^+ + O \rightarrow O_2^+ + CO$	1.6×10^{-10}	*Schmidt et al.* [1988]
$CO_2^+ + O \rightarrow CO_2 + O$	9.6×10^{-11}	*Fehsenfeld et al.* [1970]
$CO_2^+ + H_2O \rightarrow CO_2H^+ + OH$	2×10^{-9}	*Karpas and Huntress* [1978]
$CO_2^+ + e^-_{th} \rightarrow CO + O$	$6.5 \times 10^{-7}\ (300/T_e)^{0.8}$	*Seiersen et al.* [2003]
$CO_2^+ + C \rightarrow CO^+ + CO$	2.3×10^{-10}	*Schmidt et al.* [1988]
	HCO^+	
$C + H_2O^+ \rightarrow HCO^+ + H$	2.0×10^{-9}	*Woodall et al.* [2007]
$CO^+ + OH \rightarrow HCO^+ + O$	3.2×10^{-10}	*Woodall et al.* [2007]
$H^+ + CO_2 \rightarrow HCO^+ + O$	4.2×10^{-9}	*Anicich* [1993a]
$C^+ + H_2O \rightarrow HCO^+ + H$	3.6×10^{-10}	*Anicich* [1993a]
$OH^+ + CO \rightarrow HCO^+ + O$	7.1×10^{-10}	*Anicich* [1993a]
$H_2O^+ + CO \rightarrow HCO^+ + OH$	3.6×10^{-10}	*Anicich* [1993a]
$CO^+ + H_2O \rightarrow HCO^+ + H$	9.1×10^{-10}	*Anicich* [1993a]
$CO_2^+ + H \rightarrow HCO^+ + O$	6.0×10^{-11}	*Schmidt et al.* [1988]
$CO_2^+ + H_2O \rightarrow HCO^+ + OH + O$	5.1×10^{-10}	*Karpas and Huntress* [1978]
$HCO^+ + H_2O \rightarrow H_3O^+ + CO$	3.2×10^{-9}	*Schmidt et al.* [1988]
$HCO^+ + OH \rightarrow H_2O^+ + CO$	2.0×10^{-9}	*Schmidt et al.* [1988]
$HCO^+ + e^-_{th} \rightarrow H + CO$	$2.4 \times 10^{-7}\ (300/T_e)^{0.69}$	*Schmidt et al.* [1988]

e^-_{th} = thermal electron; e^-_{ph} = photoelectron; T_e = electron temperature; hν = photon; T_n = neutral temperature.

Table A.2: Parameters for the EUVAC solar flux model.

bin	λ **Å**	**F74113**	**Ai**
1*	50–100	1.200	1.0017E-02
2	100–150	0.450	7.1250E-03
3*	150–200	4.800	1.3375E-02
4*	200–250	3.100	1.9450E-02
5	256.32	0.460	2.7750E-03
6*	284.15	0.210	1.3768E-01
7*	250–300	1.679	2.6467E-02
8*	303.31	0.800	2.5000E-02
9	303.78	6.900	3.3333E-03
10*	300–350	0.965	2.2450E-02
11*	368.07	0.650	6.5917E-03
12*	350–400	0.314	3.6542E-02
13*	400–450	0.383	7.4083E-03
14*	465.22	0.290	7.4917E-03
15*	450–500	0.285	2.0225E-02
16	500–550	0.452	8.7583E-03
17	554.37	0.720	3.2667E-03
18	584.33	1.270	5.1583E-03
19	550–600	0.357	3.6583E-03
20*	609.76	0.530	1.6175E-02
21	629.73	1.590	3.3250E-03
22	600–650	0.342	1.1800E-02
23	650–700	0.230	4.2667E-03
24	703.36	0.360	3.0417E-03
25	700–750	0.141	4.7500E-03
26	765.15	0.170	3.8500E-03
27*	770.41	0.260	1.2808E-02
28	789.36	0.702	3.2750E-03
29	750–800	0.758	4.7667E-03
30	800–850	1.625	4.8167E-03
31	850–900	3.537	5.6750E-03
32	900–950	3.000	4.9833E-03
33	977.02	4.400	3.9417E-03
34	950–1000	1.475	4.4167E-03
35	1025.72	3.500	5.1833E-03
36	1031.91	2.100	5.2833E-03

Continued on next page

Table A.2 – *Continued from previous page*

bin	**λ Å**	**F74113**	**Ai**
37	1000–1050	2.467	4.3750E-03

*Bin dominated by coronal fluxes. F74113 reference flux unit is 10^9 photon cm^{-2} s^{-1}. Read 1.0017E-02 as 1.0017×10^{-2}.

Table A.3: Photon cross section of H_2O for different dissociation and ionization channels (cm^{-2})

Wavelength bin (Å)	**Total absorption**	**Total ionization**	**H_2O^+**	**OH^+**	**O^+**	**H^+**
0-10	1.00E-20	8.99E-21	2.56E-21	2.49E-21	1.97E-21	1.97E-21
10-20	9.90E-20	8.89E-20	2.67E-20	2.44E-20	1.88E-20	1.90E-20
20-30	3.89E-20	3.50E-20	1.14E-20	9.53E-21	6.95E-21	7.11E-21
30-40	1.05E-19	9.53E-20	3.38E-20	2.57E-20	1.74E-20	1.82E-20
40-50	1.71E-19	1.55E-19	5.63E-20	4.19E-20	2.78E-20	2.93E-20
50-60	3.09E-19	2.77E-19	1.07E-19	7.35E-20	4.71E-20	5.00E-20
60-70	5.18E-19	4.62E-19	1.85E-19	1.20E-19	7.53E-20	8.02E-20
70-80	7.27E-19	6.46E-19	2.64E-19	1.67E-19	1.03E-19	1.10E-19
80-90	9.36E-19	8.30E-19	3.43E-19	2.14E-19	1.31E-19	1.40E-19
90-100	1.14E-18	1.01E-18	4.22E-19	2.61E-19	1.59E-19	1.70E-19
100-110	1.48E-18	1.31E-18	5.78E-19	3.32E-19	1.91E-19	2.07E-19
110-120	1.95E-18	1.71E-18	8.12E-19	4.28E-19	2.26E-19	2.51E-19
120-130	2.42E-18	2.12E-18	1.04E-18	5.24E-19	2.62E-19	2.95E-19
130-140	2.89E-18	2.53E-18	1.27E-18	6.19E-19	2.97E-19	3.39E-19
140-150	3.35E-18	2.94E-18	1.51E-18	7.15E-19	3.32E-19	3.83E-19
150-160	3.82E-18	3.35E-18	1.74E-18	8.10E-19	3.67E-19	4.27E-19
160-170	4.29E-18	3.76E-18	1.97E-18	9.06E-19	4.03E-19	4.71E-19
170-180	4.76E-18	4.16E-18	2.21E-18	1.00E-18	4.38E-19	5.15E-19
180-190	5.17E-18	4.52E-18	2.44E-18	1.08E-18	4.54E-19	5.41E-19
190-200	5.52E-18	4.82E-18	2.67E-18	1.14E-18	4.52E-19	5.49E-19
200-210	5.92E-18	5.16E-18	2.94E-18	1.21E-18	4.49E-19	5.58E-19
210-220	6.37E-18	5.54E-18	3.24E-18	1.29E-18	4.45E-19	5.68E-19
220-230	6.85E-18	5.94E-18	3.56E-18	1.37E-18	4.36E-19	5.75E-19
230-240	7.35E-18	6.36E-18	3.90E-18	1.45E-18	4.24E-19	5.79E-19
240-250	7.77E-18	6.72E-18	4.22E-18	1.52E-18	4.02E-19	5.74E-19
250-260	8.12E-18	7.01E-18	4.50E-18	1.58E-18	3.71E-19	5.58E-19
260-270	8.62E-18	7.44E-18	4.89E-18	1.66E-18	3.41E-19	5.47E-19

Continued on next page

Table A.3 – *Continued from previous page*

Wavelength bin (Å)	**Total absorption**	**Total ionization**	**H_2O^+**	**OH^+**	**O^+**	**H^+**
270-280	9.27E-18	7.98E-18	5.37E-18	1.76E-18	3.11E-19	5.41E-19
280-290	9.72E-18	8.36E-18	5.74E-18	1.83E-18	2.69E-19	5.19E-19
290-300	9.97E-18	8.56E-18	6.01E-18	1.85E-18	2.15E-19	4.81E-19
300-310	1.02E-17	8.77E-18	6.24E-18	1.89E-18	1.79E-19	4.50E-19
310-320	1.04E-17	8.96E-18	6.43E-18	1.94E-18	1.61E-19	4.27E-19
320-330	1.08E-17	9.25E-18	6.67E-18	2.01E-18	1.48E-19	4.08E-19
330-340	1.12E-17	9.62E-18	6.97E-18	2.11E-18	1.40E-19	3.94E-19
340-350	1.17E-17	9.96E-18	7.25E-18	2.20E-18	1.31E-19	3.78E-19
350-360	1.21E-17	1.02E-17	7.51E-18	2.29E-18	1.21E-19	3.62E-19
360-370	1.25E-17	1.06E-17	7.77E-18	2.39E-18	1.10E-19	3.54E-19
370-380	1.29E-17	1.09E-17	8.05E-18	2.49E-18	9.80E-20	3.54E-19
380-390	1.34E-17	1.13E-17	8.35E-18	2.59E-18	8.62E-20	3.67E-19
390-400	1.40E-17	1.18E-17	8.67E-18	2.70E-18	7.44E-20	3.93E-19
400-410	1.46E-17	1.23E-17	9.00E-18	2.84E-18	6.33E-20	4.21E-19
410-420	1.52E-17	1.28E-17	9.34E-18	3.00E-18	5.29E-20	4.50E-19
420-430	1.60E-17	1.34E-17	9.69E-18	3.22E-18	4.52E-20	4.80E-19
430-440	1.68E-17	1.40E-17	1.00E-17	3.48E-18	4.02E-20	5.10E-19
440-450	1.73E-17	1.45E-17	1.02E-17	3.69E-18	3.57E-20	5.36E-19
450-460	1.76E-17	1.47E-17	1.03E-17	3.83E-18	3.17E-20	5.56E-19
460-470	1.77E-17	1.48E-17	1.03E-17	3.87E-18	2.92E-20	5.71E-19
470-480	1.77E-17	1.47E-17	1.03E-17	3.81E-18	2.83E-20	5.81E-19
480-490	1.78E-17	1.48E-17	1.04E-17	3.80E-18	2.76E-20	5.98E-19
490-500	1.81E-17	1.50E-17	1.06E-17	3.82E-18	2.72E-20	6.20E-19
500-510	1.84E-17	1.53E-17	1.07E-17	3.87E-18	2.66E-20	6.40E-19
510-520	1.88E-17	1.55E-17	1.09E-17	3.95E-18	2.59E-20	6.59E-19
520-530	1.92E-17	1.58E-17	1.11E-17	4.04E-18	2.52E-20	6.81E-19
530-540	1.96E-17	1.62E-17	1.13E-17	4.14E-18	2.44E-20	7.06E-19
540-550	2.01E-17	1.65E-17	1.15E-17	4.28E-18	2.34E-20	7.33E-19
550-560	2.05E-17	1.68E-17	1.16E-17	4.44E-18	2.20E-20	7.63E-19
560-570	2.08E-17	1.71E-17	1.17E-17	4.60E-18	2.06E-20	7.91E-19
570-580	2.11E-17	1.73E-17	1.17E-17	4.74E-18	1.90E-20	8.17E-19
580-590	2.14E-17	1.75E-17	1.19E-17	4.80E-18	1.71E-20	8.12E-19
590-600	2.17E-17	1.77E-17	1.21E-17	4.77E-18	1.49E-20	7.74E-19
600-610	2.20E-17	1.79E-17	1.25E-17	4.71E-18	1.27E-20	7.26E-19

Continued on next page

Table A.3 – *Continued from previous page*

Wavelength bin (Å)	**Total absorption**	**Total ionization**	**H_2O^+**	**OH^+**	**O^+**	**H^+**
610-620	2.23E-17	1.82E-17	1.29E-17	4.63E-18	1.03E-20	6.68E-19
620-630	2.25E-17	1.85E-17	1.35E-17	4.40E-18	8.19E-21	5.65E-19
630-640	2.26E-17	1.86E-17	1.42E-17	4.02E-18	6.17E-21	4.18E-19
640-650	2.27E-17	1.87E-17	1.48E-17	3.63E-18	4.13E-21	2.70E-19
650-660	2.27E-17	1.87E-17	1.53E-17	3.23E-18	2.07E-21	1.20E-19
660-670	2.27E-17	1.80E-17	1.56E-17	2.29E-18	0.00E+00	0.00E+00
670-680	2.27E-17	1.66E-17	1.58E-17	7.97E-19	0.00E+00	0.00E+00
680-690	2.25E-17	1.58E-17	1.58E-17	0.00E+00	0.00E+00	0.00E+00
690-700	2.21E-17	1.56E-17	1.56E-17	0.00E+00	0.00E+00	0.00E+00
700-710	2.18E-17	1.54E-17	1.54E-17	0.00E+00	0.00E+00	0.00E+00
710-720	2.18E-17	1.53E-17	1.53E-17	0.00E+00	0.00E+00	0.00E+00
720-730	2.18E-17	1.53E-17	1.53E-17	0.00E+00	0.00E+00	0.00E+00
730-740	2.16E-17	1.53E-17	1.53E-17	0.00E+00	0.00E+00	0.00E+00
740-750	2.06E-17	1.46E-17	1.46E-17	0.00E+00	0.00E+00	0.00E+00
750-760	2.03E-17	1.46E-17	1.46E-17	0.00E+00	0.00E+00	0.00E+00
760-770	1.94E-17	1.44E-17	1.44E-17	0.00E+00	0.00E+00	0.00E+00
770-780	1.80E-17	1.40E-17	1.40E-17	0.00E+00	0.00E+00	0.00E+00
780-790	1.71E-17	1.38E-17	1.38E-17	0.00E+00	0.00E+00	0.00E+00
790-800	1.65E-17	1.37E-17	1.37E-17	0.00E+00	0.00E+00	0.00E+00
800-810	1.65E-17	1.37E-17	1.37E-17	0.00E+00	0.00E+00	0.00E+00
810-820	1.70E-17	1.35E-17	1.35E-17	0.00E+00	0.00E+00	0.00E+00
820-830	1.78E-17	1.34E-17	1.34E-17	0.00E+00	0.00E+00	0.00E+00
830-840	1.80E-17	1.29E-17	1.29E-17	0.00E+00	0.00E+00	0.00E+00
840-850	1.87E-17	1.21E-17	1.21E-17	0.00E+00	0.00E+00	0.00E+00
850-860	1.87E-17	1.15E-17	1.15E-17	0.00E+00	0.00E+00	0.00E+00
860-870	1.97E-17	1.09E-17	1.09E-17	0.00E+00	0.00E+00	0.00E+00
870-880	2.05E-17	1.03E-17	1.03E-17	0.00E+00	0.00E+00	0.00E+00
880-890	2.19E-17	1.02E-17	1.02E-17	0.00E+00	0.00E+00	0.00E+00
890-900	2.29E-17	9.55E-18	9.55E-18	0.00E+00	0.00E+00	0.00E+00
900-910	1.91E-17	7.89E-18	7.89E-18	0.00E+00	0.00E+00	0.00E+00
910-920	2.23E-17	8.42E-18	8.42E-18	0.00E+00	0.00E+00	0.00E+00
920-930	2.34E-17	8.52E-18	8.52E-18	0.00E+00	0.00E+00	0.00E+00
930-940	2.33E-17	8.04E-18	8.04E-18	0.00E+00	0.00E+00	0.00E+00
940-950	2.07E-17	7.47E-18	7.47E-18	0.00E+00	0.00E+00	0.00E+00

Continued on next page

Table A.3 – *Continued from previous page*

Wavelength bin (Å)	**Total absorption**	**Total ionization**	**H_2O^+**	**OH^+**	**O^+**	**H^+**
950-960	1.94E-17	6.80E-18	6.80E-18	0.00E+00	0.00E+00	0.00E+00
960-970	1.69E-17	6.00E-18	6.00E-18	0.00E+00	0.00E+00	0.00E+00
970-980	1.47E-17	5.36E-18	5.36E-18	0.00E+00	0.00E+00	0.00E+00
980-990	1.28E-17	0.00E+00	0.00E+00	0.00E+00	0.00E+00	0.00E+00
990-1000	9.62E-18	0.00E+00	0.00E+00	0.00E+00	0.00E+00	0.00E+00
1000-1010	7.25E-18	0.00E+00	0.00E+00	0.00E+00	0.00E+00	0.00E+00
1010-1020	5.75E-18	0.00E+00	0.00E+00	0.00E+00	0.00E+00	0.00E+00
1020-1030	4.50E-18	0.00E+00	0.00E+00	0.00E+00	0.00E+00	0.00E+00
1030-1040	3.50E-18	0.00E+00	0.00E+00	0.00E+00	0.00E+00	0.00E+00
1040-1050	2.72E-18	0.00E+00	0.00E+00	0.00E+00	0.00E+00	0.00E+00
1050-1060	2.17E-18	0.00E+00	0.00E+00	0.00E+00	0.00E+00	0.00E+00
1060-1070	3.35E-18	0.00E+00	0.00E+00	0.00E+00	0.00E+00	0.00E+00
1070-1080	1.05E-17	0.00E+00	0.00E+00	0.00E+00	0.00E+00	0.00E+00
1080-1090	5.20E-18	0.00E+00	0.00E+00	0.00E+00	0.00E+00	0.00E+00
1090-1100	4.10E-18	0.00E+00	0.00E+00	0.00E+00	0.00E+00	0.00E+00
1100-1110	2.40E-18	0.00E+00	0.00E+00	0.00E+00	0.00E+00	0.00E+00
1110-1120	1.80E-17	0.00E+00	0.00E+00	0.00E+00	0.00E+00	0.00E+00
1120-1130	1.80E-17	0.00E+00	0.00E+00	0.00E+00	0.00E+00	0.00E+00
1130-1140	2.20E-18	0.00E+00	0.00E+00	0.00E+00	0.00E+00	0.00E+00
1140-1150	2.90E-18	0.00E+00	0.00E+00	0.00E+00	0.00E+00	0.00E+00
1150-1160	2.97E-18	0.00E+00	0.00E+00	0.00E+00	0.00E+00	0.00E+00
1160-1170	4.32E-18	0.00E+00	0.00E+00	0.00E+00	0.00E+00	0.00E+00
1170-1180	5.85E-18	0.00E+00	0.00E+00	0.00E+00	0.00E+00	0.00E+00
1180-1190	6.80E-18	0.00E+00	0.00E+00	0.00E+00	0.00E+00	0.00E+00
1190-1200	8.50E-18	0.00E+00	0.00E+00	0.00E+00	0.00E+00	0.00E+00
1200-1210	3.70E-18	0.00E+00	0.00E+00	0.00E+00	0.00E+00	0.00E+00
1210-1220	1.70E-17	0.00E+00	0.00E+00	0.00E+00	0.00E+00	0.00E+00
1220-1230	3.70E-18	0.00E+00	0.00E+00	0.00E+00	0.00E+00	0.00E+00
1230-1240	7.40E-18	0.00E+00	0.00E+00	0.00E+00	0.00E+00	0.00E+00
1240-1250	5.60E-18	0.00E+00	0.00E+00	0.00E+00	0.00E+00	0.00E+00
1250-1260	6.73E-18	0.00E+00	0.00E+00	0.00E+00	0.00E+00	0.00E+00
1260-1270	6.79E-18	0.00E+00	0.00E+00	0.00E+00	0.00E+00	0.00E+00
1270-1280	6.85E-18	0.00E+00	0.00E+00	0.00E+00	0.00E+00	0.00E+00
1280-1290	6.91E-18	0.00E+00	0.00E+00	0.00E+00	0.00E+00	0.00E+00

Continued on next page

Table A.3 – *Continued from previous page*

Wavelength bin (Å)	**Total absorption**	**Total ionization**	**H_2O^+**	**OH^+**	**O^+**	**H^+**
1290-1300	6.97E-18	0.00E+00	0.00E+00	0.00E+00	0.00E+00	0.00E+00
1300-1310	6.93E-18	0.00E+00	0.00E+00	0.00E+00	0.00E+00	0.00E+00
1310-1320	6.16E-18	0.00E+00	0.00E+00	0.00E+00	0.00E+00	0.00E+00
1320-1330	5.40E-18	0.00E+00	0.00E+00	0.00E+00	0.00E+00	0.00E+00
1330-1340	4.64E-18	0.00E+00	0.00E+00	0.00E+00	0.00E+00	0.00E+00
1340-1350	3.88E-18	0.00E+00	0.00E+00	0.00E+00	0.00E+00	0.00E+00
1350-1360	3.23E-18	0.00E+00	0.00E+00	0.00E+00	0.00E+00	0.00E+00
1360-1370	2.69E-18	0.00E+00	0.00E+00	0.00E+00	0.00E+00	0.00E+00
1370-1380	2.15E-18	0.00E+00	0.00E+00	0.00E+00	0.00E+00	0.00E+00
1380-1390	1.61E-18	0.00E+00	0.00E+00	0.00E+00	0.00E+00	0.00E+00
1390-1400	1.07E-18	0.00E+00	0.00E+00	0.00E+00	0.00E+00	0.00E+00
1400-1410	7.50E-19	0.00E+00	0.00E+00	0.00E+00	0.00E+00	0.00E+00
1410-1420	6.50E-19	0.00E+00	0.00E+00	0.00E+00	0.00E+00	0.00E+00
1420-1430	5.50E-19	0.00E+00	0.00E+00	0.00E+00	0.00E+00	0.00E+00
1430-1440	5.00E-19	0.00E+00	0.00E+00	0.00E+00	0.00E+00	0.00E+00
1440-1450	5.00E-19	0.00E+00	0.00E+00	0.00E+00	0.00E+00	0.00E+00
1450-1460	5.50E-19	0.00E+00	0.00E+00	0.00E+00	0.00E+00	0.00E+00
1460-1470	6.50E-19	0.00E+00	0.00E+00	0.00E+00	0.00E+00	0.00E+00
1470-1480	7.50E-19	0.00E+00	0.00E+00	0.00E+00	0.00E+00	0.00E+00
1480-1490	8.50E-19	0.00E+00	0.00E+00	0.00E+00	0.00E+00	0.00E+00
1490-1500	9.50E-19	0.00E+00	0.00E+00	0.00E+00	0.00E+00	0.00E+00
1500-1510	1.12E-18	0.00E+00	0.00E+00	0.00E+00	0.00E+00	0.00E+00
1510-1520	1.36E-18	0.00E+00	0.00E+00	0.00E+00	0.00E+00	0.00E+00
1520-1530	1.60E-18	0.00E+00	0.00E+00	0.00E+00	0.00E+00	0.00E+00
1530-1540	1.84E-18	0.00E+00	0.00E+00	0.00E+00	0.00E+00	0.00E+00
1540-1550	2.08E-18	0.00E+00	0.00E+00	0.00E+00	0.00E+00	0.00E+00
1550-1560	2.37E-18	0.00E+00	0.00E+00	0.00E+00	0.00E+00	0.00E+00
1560-1570	2.71E-18	0.00E+00	0.00E+00	0.00E+00	0.00E+00	0.00E+00
1570-1580	3.05E-18	0.00E+00	0.00E+00	0.00E+00	0.00E+00	0.00E+00
1580-1590	3.39E-18	0.00E+00	0.00E+00	0.00E+00	0.00E+00	0.00E+00
1590-1600	3.73E-18	0.00E+00	0.00E+00	0.00E+00	0.00E+00	0.00E+00
1600-1610	4.01E-18	0.00E+00	0.00E+00	0.00E+00	0.00E+00	0.00E+00
1610-1620	4.23E-18	0.00E+00	0.00E+00	0.00E+00	0.00E+00	0.00E+00
1620-1630	4.45E-18	0.00E+00	0.00E+00	0.00E+00	0.00E+00	0.00E+00

Continued on next page

Table A.3 – *Continued from previous page*

Wavelength bin (Å)	**Total absorption**	**Total ionization**	**H_2O^+**	**OH^+**	**O^+**	**H^+**
1630-1640	4.67E-18	0.00E+00	0.00E+00	0.00E+00	0.00E+00	0.00E+00
1640-1650	4.89E-18	0.00E+00	0.00E+00	0.00E+00	0.00E+00	0.00E+00
1650-1660	4.95E-18	0.00E+00	0.00E+00	0.00E+00	0.00E+00	0.00E+00
1660-1670	4.85E-18	0.00E+00	0.00E+00	0.00E+00	0.00E+00	0.00E+00
1670-1680	4.75E-18	0.00E+00	0.00E+00	0.00E+00	0.00E+00	0.00E+00
1680-1690	4.65E-18	0.00E+00	0.00E+00	0.00E+00	0.00E+00	0.00E+00
1690-1700	4.55E-18	0.00E+00	0.00E+00	0.00E+00	0.00E+00	0.00E+00
1700-1710	4.35E-18	0.00E+00	0.00E+00	0.00E+00	0.00E+00	0.00E+00
1710-1720	4.05E-18	0.00E+00	0.00E+00	0.00E+00	0.00E+00	0.00E+00
1720-1730	3.75E-18	0.00E+00	0.00E+00	0.00E+00	0.00E+00	0.00E+00
1730-1740	3.45E-18	0.00E+00	0.00E+00	0.00E+00	0.00E+00	0.00E+00
1740-1750	3.15E-18	0.00E+00	0.00E+00	0.00E+00	0.00E+00	0.00E+00
1750-1760	2.79E-18	0.00E+00	0.00E+00	0.00E+00	0.00E+00	0.00E+00
1760-1770	2.38E-18	0.00E+00	0.00E+00	0.00E+00	0.00E+00	0.00E+00
1770-1780	1.97E-18	0.00E+00	0.00E+00	0.00E+00	0.00E+00	0.00E+00
1780-1790	1.56E-18	0.00E+00	0.00E+00	0.00E+00	0.00E+00	0.00E+00
1790-1800	1.15E-18	0.00E+00	0.00E+00	0.00E+00	0.00E+00	0.00E+00
1800-1810	8.60E-19	0.00E+00	0.00E+00	0.00E+00	0.00E+00	0.00E+00
1810-1820	6.80E-19	0.00E+00	0.00E+00	0.00E+00	0.00E+00	0.00E+00
1820-1830	5.00E-19	0.00E+00	0.00E+00	0.00E+00	0.00E+00	0.00E+00
1830-1840	3.20E-19	0.00E+00	0.00E+00	0.00E+00	0.00E+00	0.00E+00
1840-1850	1.40E-19	0.00E+00	0.00E+00	0.00E+00	0.00E+00	0.00E+00
1850-1860	3.00E-20	0.00E+00	0.00E+00	0.00E+00	0.00E+00	0.00E+00
1860-1870	1.00E-35	0.00E+00	0.00E+00	0.00E+00	0.00E+00	0.00E+00
1870-1880	1.00E-35	0.00E+00	0.00E+00	0.00E+00	0.00E+00	0.00E+00
1880-1890	1.00E-35	0.00E+00	0.00E+00	0.00E+00	0.00E+00	0.00E+00
1890-1900	1.00E-35	0.00E+00	0.00E+00	0.00E+00	0.00E+00	0.00E+00
1900-1910	1.00E-35	0.00E+00	0.00E+00	0.00E+00	0.00E+00	0.00E+00
1910-1920	1.00E-35	0.00E+00	0.00E+00	0.00E+00	0.00E+00	0.00E+00
1920-1930	1.00E-35	0.00E+00	0.00E+00	0.00E+00	0.00E+00	0.00E+00
1930-1940	1.00E-35	0.00E+00	0.00E+00	0.00E+00	0.00E+00	0.00E+00
1940-1950	1.00E-35	0.00E+00	0.00E+00	0.00E+00	0.00E+00	0.00E+00
1950-1960	1.00E-35	0.00E+00	0.00E+00	0.00E+00	0.00E+00	0.00E+00
1960-1970	1.00E-35	0.00E+00	0.00E+00	0.00E+00	0.00E+00	0.00E+00

Continued on next page

Table A.3 – *Continued from previous page*

Wavelength bin (Å)	**Total absorption**	**Total ionization**	**H_2O^+**	**OH^+**	**O^+**	**H^+**
1970-1980	1.00E-35	0.00E+00	0.00E+00	0.00E+00	0.00E+00	0.00E+00
1980-1990	1.00E-35	0.00E+00	0.00E+00	0.00E+00	0.00E+00	0.00E+00
1990-2000	1.00E-35	0.00E+00	0.00E+00	0.00E+00	0.00E+00	0.00E+00

Table A.4: Photon cross section of CO_2 for different dissociation and ionization channels (cm^{-2})

Wavelength bin (Å)	**Total absorption**	**Total ionization**	**CO_2^+**	**CO^+**	**O^+**	**C^+**
0-10	3.00E-20	3.00E-20	7.82E-21	7.37E-21	7.41E-21	7.37E-21
10-20	4.35E-19	4.35E-19	1.20E-19	1.04E-19	1.05E-19	1.03E-19
20-30	2.36E-19	2.36E-19	6.75E-20	5.61E-20	5.69E-20	5.57E-20
30-40	1.87E-19	1.87E-19	5.80E-20	4.31E-20	4.41E-20	4.24E-20
40-50	3.39E-19	3.39E-19	1.11E-19	7.56E-20	7.77E-20	7.39E-20
50-60	5.00E-19	4.99E-19	1.72E-19	1.08E-19	1.12E-19	1.05E-19
60-70	6.71E-19	6.71E-19	2.43E-19	1.42E-19	1.48E-19	1.37E-19
70-80	8.73E-19	8.73E-19	3.29E-19	1.80E-19	1.89E-19	1.73E-19
80-90	1.16E-18	1.16E-18	4.61E-19	2.33E-19	2.47E-19	2.22E-19
90-100	1.45E-18	1.45E-18	5.97E-19	2.85E-19	3.04E-19	2.69E-19
100-110	1.74E-18	1.74E-18	7.52E-19	3.30E-19	3.56E-19	3.09E-19
110-120	2.04E-18	2.03E-18	9.07E-19	3.75E-19	4.08E-19	3.49E-19
120-130	2.49E-18	2.49E-18	1.15E-18	4.42E-19	4.86E-19	4.07E-19
130-140	3.13E-18	3.13E-18	1.51E-18	5.35E-19	5.96E-19	4.87E-19
140-150	3.78E-18	3.77E-18	1.87E-18	6.29E-19	7.06E-19	5.68E-19
150-160	5.33E-18	5.33E-18	2.74E-18	8.55E-19	9.71E-19	7.62E-19
160-170	8.57E-18	8.57E-18	4.55E-18	1.32E-18	1.52E-18	1.16E-18
170-180	1.26E-17	1.26E-17	6.85E-18	1.89E-18	2.20E-18	1.65E-18
180-190	1.90E-17	1.89E-17	1.06E-17	2.76E-18	3.25E-18	2.38E-18
190-200	1.90E-17	1.89E-17	1.09E-17	2.65E-18	3.16E-18	2.25E-18
200-210	1.90E-17	1.90E-17	1.12E-17	2.54E-18	3.08E-18	2.12E-18
210-220	1.98E-17	1.98E-17	1.21E-17	2.53E-18	3.13E-18	2.07E-18
220-230	2.32E-17	2.32E-17	1.45E-17	2.83E-18	3.57E-18	2.27E-18

Continued on next page

Table A.4 – *Continued from previous page*

Wavelength bin (Å)	**Total absorption**	**Total ionization**	**CO_2^+**	**CO^+**	**O^+**	**C^+**
230-240	2.52E-17	2.52E-17	1.61E-17	2.94E-18	3.77E-18	2.30E-18
240-250	2.57E-17	2.57E-17	1.69E-17	2.86E-18	3.73E-18	2.17E-18
250-260	2.60E-17	2.60E-17	1.75E-17	2.74E-18	3.66E-18	2.02E-18
260-270	2.60E-17	2.60E-17	1.80E-17	2.60E-18	3.55E-18	1.84E-18
270-280	2.56E-17	2.56E-17	1.81E-17	2.42E-18	3.39E-18	1.65E-18
280-290	2.48E-17	2.48E-17	1.79E-17	2.21E-18	3.19E-18	1.44E-18
290-300	2.40E-17	2.40E-17	1.78E-17	2.01E-18	2.98E-18	1.23E-18
300-310	2.34E-17	2.34E-17	1.77E-17	1.83E-18	2.81E-18	1.04E-18
310-320	2.37E-17	2.37E-17	1.80E-17	1.88E-18	2.81E-18	9.62E-19
320-330	2.40E-17	2.40E-17	1.84E-17	1.93E-18	2.81E-18	8.84E-19
330-340	2.43E-17	2.43E-17	1.87E-17	1.98E-18	2.81E-18	8.06E-19
340-350	2.47E-17	2.47E-17	1.91E-17	2.03E-18	2.81E-18	7.28E-19
350-360	2.50E-17	2.50E-17	1.94E-17	2.07E-18	2.81E-18	6.51E-19
360-370	2.53E-17	2.53E-17	1.98E-17	2.12E-18	2.81E-18	5.73E-19
370-380	2.56E-17	2.56E-17	2.01E-17	2.17E-18	2.81E-18	4.95E-19
380-390	2.59E-17	2.60E-17	2.05E-17	2.22E-18	2.81E-18	4.17E-19
390-400	2.63E-17	2.63E-17	2.08E-17	2.27E-18	2.81E-18	3.39E-19
400-410	2.66E-17	2.66E-17	2.12E-17	2.32E-18	2.81E-18	2.61E-19
410-420	2.69E-17	2.69E-17	2.15E-17	2.37E-18	2.81E-18	1.83E-19
420-430	2.72E-17	2.72E-17	2.19E-17	2.42E-18	2.81E-18	1.05E-19
430-440	2.76E-17	2.76E-17	2.23E-17	2.47E-18	2.82E-18	2.76E-20
440-450	2.79E-17	2.79E-17	2.28E-17	2.38E-18	2.66E-18	2.44E-20
450-460	2.82E-17	2.81E-17	2.33E-17	2.30E-18	2.51E-18	2.13E-20
460-470	2.85E-17	2.84E-17	2.38E-17	2.22E-18	2.36E-18	1.82E-20
470-480	2.89E-17	2.87E-17	2.43E-17	2.14E-18	2.20E-18	1.51E-20
480-490	2.92E-17	2.90E-17	2.49E-17	2.06E-18	2.05E-18	1.20E-20
490-500	2.95E-17	2.93E-17	2.54E-17	1.98E-18	1.90E-18	8.94E-21
500-510	2.99E-17	2.96E-17	2.59E-17	1.90E-18	1.74E-18	5.83E-21
510-520	2.93E-17	2.87E-17	2.55E-17	1.85E-18	1.39E-18	4.01E-21
520-530	3.08E-17	2.99E-17	2.69E-17	1.89E-18	1.16E-18	2.90E-21
530-540	3.13E-17	3.01E-17	2.73E-17	1.72E-18	1.04E-18	1.60E-21
540-550	3.25E-17	3.09E-17	2.83E-17	1.60E-18	9.80E-19	0.00E+00
550-560	3.36E-17	3.15E-17	2.91E-17	1.47E-18	9.20E-19	0.00E+00
560-570	2.95E-17	2.74E-17	2.55E-17	1.21E-18	7.55E-19	0.00E+00

Continued on next page

Table A.4 – *Continued from previous page*

Wavelength bin (Å)	**Total absorption**	**Total ionization**	$\mathbf{CO_2^+}$	$\mathbf{CO^+}$	$\mathbf{O^+}$	$\mathbf{C^+}$
570-580	2.49E-17	2.30E-17	2.14E-17	9.45E-19	5.79E-19	0.00E+00
580-590	2.25E-17	2.04E-17	1.92E-17	7.59E-19	4.53E-19	0.00E+00
590-600	2.33E-17	2.13E-17	2.01E-17	7.31E-19	4.02E-19	0.00E+00
600-610	2.41E-17	2.23E-17	2.13E-17	7.01E-19	3.32E-19	0.00E+00
610-620	2.49E-17	2.35E-17	2.26E-17	6.68E-19	2.56E-19	0.00E+00
620-630	2.20E-17	2.07E-17	2.00E-17	5.50E-19	1.58E-19	0.00E+00
630-640	2.17E-17	2.01E-17	1.98E-17	0.00E+00	9.64E-20	0.00E+00
640-650	2.14E-17	2.01E-17	2.01E-17	0.00E+00	3.57E-20	0.00E+00
650-660	2.07E-17	1.98E-17	1.98E-17	0.00E+00	0.00E+00	0.00E+00
660-670	2.20E-17	2.01E-17	2.01E-17	0.00E+00	0.00E+00	0.00E+00
670-680	2.15E-17	2.08E-17	2.08E-17	0.00E+00	0.00E+00	0.00E+00
680-690	2.34E-17	2.19E-17	2.19E-17	0.00E+00	0.00E+00	0.00E+00
690-700	3.00E-17	2.68E-17	2.68E-17	0.00E+00	0.00E+00	0.00E+00
700-710	2.08E-17	1.82E-17	1.82E-17	0.00E+00	0.00E+00	0.00E+00
710-720	1.96E-17	1.77E-17	1.77E-17	0.00E+00	0.00E+00	0.00E+00
720-730	3.27E-17	2.75E-17	2.75E-17	0.00E+00	0.00E+00	0.00E+00
730-740	3.84E-17	2.73E-17	2.73E-17	0.00E+00	0.00E+00	0.00E+00
740-750	1.46E-17	1.25E-17	1.25E-17	0.00E+00	0.00E+00	0.00E+00
750-760	3.71E-17	3.30E-17	3.30E-17	0.00E+00	0.00E+00	0.00E+00
760-770	7.80E-17	4.95E-17	4.95E-17	0.00E+00	0.00E+00	0.00E+00
770-780	3.16E-17	2.17E-17	2.17E-17	0.00E+00	0.00E+00	0.00E+00
780-790	2.26E-17	1.65E-17	1.65E-17	0.00E+00	0.00E+00	0.00E+00
790-800	2.39E-17	1.55E-17	1.55E-17	0.00E+00	0.00E+00	0.00E+00
800-810	1.80E-17	1.23E-17	1.23E-17	0.00E+00	0.00E+00	0.00E+00
810-820	1.65E-17	1.23E-17	1.23E-17	0.00E+00	0.00E+00	0.00E+00
820-830	1.40E-17	1.23E-17	1.23E-17	0.00E+00	0.00E+00	0.00E+00
830-840	1.31E-17	1.20E-17	1.20E-17	0.00E+00	0.00E+00	0.00E+00
840-850	1.49E-17	1.30E-17	1.30E-17	0.00E+00	0.00E+00	0.00E+00
850-860	1.76E-17	1.47E-17	1.47E-17	0.00E+00	0.00E+00	0.00E+00
860-870	2.44E-17	2.12E-17	2.12E-17	0.00E+00	0.00E+00	0.00E+00
870-880	3.48E-17	2.90E-17	2.90E-17	0.00E+00	0.00E+00	0.00E+00
880-890	5.27E-17	3.70E-17	3.70E-17	0.00E+00	0.00E+00	0.00E+00
890-900	8.15E-17	4.24E-17	4.24E-17	0.00E+00	0.00E+00	0.00E+00
900-910	8.92E-17	0.00E+00	0.00E+00	0.00E+00	0.00E+00	0.00E+00

Continued on next page

Table A.4 – *Continued from previous page*

Wavelength bin (Å)	**Total absorption**	**Total ionization**	$\mathbf{CO_2^+}$	$\mathbf{CO^+}$	$\mathbf{O^+}$	$\mathbf{C^+}$
910-920	8.50E-17	0.00E+00	0.00E+00	0.00E+00	0.00E+00	0.00E+00
920-930	4.10E-17	0.00E+00	0.00E+00	0.00E+00	0.00E+00	0.00E+00
930-940	7.80E-17	0.00E+00	0.00E+00	0.00E+00	0.00E+00	0.00E+00
940-950	6.20E-17	0.00E+00	0.00E+00	0.00E+00	0.00E+00	0.00E+00
950-960	6.90E-17	0.00E+00	0.00E+00	0.00E+00	0.00E+00	0.00E+00
960-970	3.70E-17	0.00E+00	0.00E+00	0.00E+00	0.00E+00	0.00E+00
970-980	3.70E-17	0.00E+00	0.00E+00	0.00E+00	0.00E+00	0.00E+00
980-990	2.63E-17	0.00E+00	0.00E+00	0.00E+00	0.00E+00	0.00E+00
990-1000	9.96E-17	0.00E+00	0.00E+00	0.00E+00	0.00E+00	0.00E+00
1000-1010	3.70E-17	0.00E+00	0.00E+00	0.00E+00	0.00E+00	0.00E+00
1010-1020	2.30E-17	0.00E+00	0.00E+00	0.00E+00	0.00E+00	0.00E+00
1020-1030	1.80E-17	0.00E+00	0.00E+00	0.00E+00	0.00E+00	0.00E+00
1030-1040	6.81E-17	0.00E+00	0.00E+00	0.00E+00	0.00E+00	0.00E+00
1040-1050	1.20E-17	0.00E+00	0.00E+00	0.00E+00	0.00E+00	0.00E+00
1050-1060	1.50E-17	0.00E+00	0.00E+00	0.00E+00	0.00E+00	0.00E+00
1060-1070	7.80E-18	0.00E+00	0.00E+00	0.00E+00	0.00E+00	0.00E+00
1070-1080	4.70E-17	0.00E+00	0.00E+00	0.00E+00	0.00E+00	0.00E+00
1080-1090	1.64E-17	0.00E+00	0.00E+00	0.00E+00	0.00E+00	0.00E+00
1090-1100	6.70E-18	0.00E+00	0.00E+00	0.00E+00	0.00E+00	0.00E+00
1100-1110	1.58E-17	0.00E+00	0.00E+00	0.00E+00	0.00E+00	0.00E+00
1110-1120	3.16E-17	0.00E+00	0.00E+00	0.00E+00	0.00E+00	0.00E+00
1120-1130	4.50E-17	0.00E+00	0.00E+00	0.00E+00	0.00E+00	0.00E+00
1130-1140	2.05E-17	0.00E+00	0.00E+00	0.00E+00	0.00E+00	0.00E+00
1140-1150	3.70E-18	0.00E+00	0.00E+00	0.00E+00	0.00E+00	0.00E+00
1150-1160	2.01E-18	0.00E+00	0.00E+00	0.00E+00	0.00E+00	0.00E+00
1160-1170	8.66E-19	0.00E+00	0.00E+00	0.00E+00	0.00E+00	0.00E+00
1170-1180	5.33E-19	0.00E+00	0.00E+00	0.00E+00	0.00E+00	0.00E+00
1180-1190	7.20E-20	0.00E+00	0.00E+00	0.00E+00	0.00E+00	0.00E+00
1190-1200	4.66E-20	0.00E+00	0.00E+00	0.00E+00	0.00E+00	0.00E+00
1200-1210	5.65E-20	0.00E+00	0.00E+00	0.00E+00	0.00E+00	0.00E+00
1210-1220	7.95E-20	0.00E+00	0.00E+00	0.00E+00	0.00E+00	0.00E+00
1220-1230	8.70E-20	0.00E+00	0.00E+00	0.00E+00	0.00E+00	0.00E+00
1230-1240	1.20E-19	0.00E+00	0.00E+00	0.00E+00	0.00E+00	0.00E+00
1240-1250	1.80E-19	0.00E+00	0.00E+00	0.00E+00	0.00E+00	0.00E+00

Continued on next page

Table A.4 – *Continued from previous page*

Wavelength bin (Å)	**Total absorption**	**Total ionization**	**CO_2^+**	**CO^+**	**O^+**	**C^+**
1250-1260	2.55E-19	0.00E+00	0.00E+00	0.00E+00	0.00E+00	0.00E+00
1260-1270	3.30E-19	0.00E+00	0.00E+00	0.00E+00	0.00E+00	0.00E+00
1270-1280	4.45E-19	0.00E+00	0.00E+00	0.00E+00	0.00E+00	0.00E+00
1280-1290	5.75E-19	0.00E+00	0.00E+00	0.00E+00	0.00E+00	0.00E+00
1290-1300	5.55E-19	0.00E+00	0.00E+00	0.00E+00	0.00E+00	0.00E+00
1300-1310	8.00E-19	0.00E+00	0.00E+00	0.00E+00	0.00E+00	0.00E+00
1310-1320	1.10E-18	0.00E+00	0.00E+00	0.00E+00	0.00E+00	0.00E+00
1320-1330	1.10E-18	0.00E+00	0.00E+00	0.00E+00	0.00E+00	0.00E+00
1330-1340	1.10E-18	0.00E+00	0.00E+00	0.00E+00	0.00E+00	0.00E+00
1340-1350	6.00E-19	0.00E+00	0.00E+00	0.00E+00	0.00E+00	0.00E+00
1350-1360	5.20E-19	0.00E+00	0.00E+00	0.00E+00	0.00E+00	0.00E+00
1360-1370	5.60E-19	0.00E+00	0.00E+00	0.00E+00	0.00E+00	0.00E+00
1370-1380	5.20E-19	0.00E+00	0.00E+00	0.00E+00	0.00E+00	0.00E+00
1380-1390	6.35E-19	0.00E+00	0.00E+00	0.00E+00	0.00E+00	0.00E+00
1390-1400	5.65E-19	0.00E+00	0.00E+00	0.00E+00	0.00E+00	0.00E+00
1400-1410	5.32E-19	0.00E+00	0.00E+00	0.00E+00	0.00E+00	0.00E+00
1410-1420	5.37E-19	0.00E+00	0.00E+00	0.00E+00	0.00E+00	0.00E+00
1420-1430	5.55E-19	0.00E+00	0.00E+00	0.00E+00	0.00E+00	0.00E+00
1430-1440	5.85E-19	0.00E+00	0.00E+00	0.00E+00	0.00E+00	0.00E+00
1440-1450	6.00E-19	0.00E+00	0.00E+00	0.00E+00	0.00E+00	0.00E+00
1450-1460	6.00E-19	0.00E+00	0.00E+00	0.00E+00	0.00E+00	0.00E+00
1460-1470	6.00E-19	0.00E+00	0.00E+00	0.00E+00	0.00E+00	0.00E+00
1470-1480	6.00E-19	0.00E+00	0.00E+00	0.00E+00	0.00E+00	0.00E+00
1480-1490	6.00E-19	0.00E+00	0.00E+00	0.00E+00	0.00E+00	0.00E+00
1490-1500	5.60E-19	0.00E+00	0.00E+00	0.00E+00	0.00E+00	0.00E+00
1500-1510	5.00E-19	0.00E+00	0.00E+00	0.00E+00	0.00E+00	0.00E+00
1510-1520	4.65E-19	0.00E+00	0.00E+00	0.00E+00	0.00E+00	0.00E+00
1520-1530	4.65E-19	0.00E+00	0.00E+00	0.00E+00	0.00E+00	0.00E+00
1530-1540	4.65E-19	0.00E+00	0.00E+00	0.00E+00	0.00E+00	0.00E+00
1540-1550	4.00E-19	0.00E+00	0.00E+00	0.00E+00	0.00E+00	0.00E+00
1550-1560	3.25E-19	0.00E+00	0.00E+00	0.00E+00	0.00E+00	0.00E+00
1560-1570	3.00E-19	0.00E+00	0.00E+00	0.00E+00	0.00E+00	0.00E+00
1570-1580	2.80E-19	0.00E+00	0.00E+00	0.00E+00	0.00E+00	0.00E+00
1580-1590	2.25E-19	0.00E+00	0.00E+00	0.00E+00	0.00E+00	0.00E+00

Continued on next page

Table A.4 – *Continued from previous page*

Wavelength bin (Å)	**Total absorption**	**Total ionization**	**CO_2^+**	**CO^+**	**O^+**	**C^+**
1590-1600	1.90E-19	0.00E+00	0.00E+00	0.00E+00	0.00E+00	0.00E+00
1600-1610	1.70E-19	0.00E+00	0.00E+00	0.00E+00	0.00E+00	0.00E+00
1610-1620	1.30E-19	0.00E+00	0.00E+00	0.00E+00	0.00E+00	0.00E+00
1620-1630	1.04E-19	0.00E+00	0.00E+00	0.00E+00	0.00E+00	0.00E+00
1630-1640	9.42E-20	0.00E+00	0.00E+00	0.00E+00	0.00E+00	0.00E+00
1640-1650	8.25E-20	0.00E+00	0.00E+00	0.00E+00	0.00E+00	0.00E+00
1650-1660	6.95E-20	0.00E+00	0.00E+00	0.00E+00	0.00E+00	0.00E+00
1660-1670	5.52E-20	0.00E+00	0.00E+00	0.00E+00	0.00E+00	0.00E+00
1670-1680	3.97E-20	0.00E+00	0.00E+00	0.00E+00	0.00E+00	0.00E+00
1680-1690	2.97E-20	0.00E+00	0.00E+00	0.00E+00	0.00E+00	0.00E+00
1690-1700	2.52E-20	0.00E+00	0.00E+00	0.00E+00	0.00E+00	0.00E+00
1700-1710	2.12E-20	0.00E+00	0.00E+00	0.00E+00	0.00E+00	0.00E+00
1710-1720	1.78E-20	0.00E+00	0.00E+00	0.00E+00	0.00E+00	0.00E+00
1720-1730	1.44E-20	0.00E+00	0.00E+00	0.00E+00	0.00E+00	0.00E+00
1730-1740	1.09E-20	0.00E+00	0.00E+00	0.00E+00	0.00E+00	0.00E+00
1740-1750	7.52E-21	0.00E+00	0.00E+00	0.00E+00	0.00E+00	0.00E+00
1750-1760	5.40E-21	0.00E+00	0.00E+00	0.00E+00	0.00E+00	0.00E+00
1760-1770	4.60E-21	0.00E+00	0.00E+00	0.00E+00	0.00E+00	0.00E+00
1770-1780	3.80E-21	0.00E+00	0.00E+00	0.00E+00	0.00E+00	0.00E+00
1780-1790	3.00E-21	0.00E+00	0.00E+00	0.00E+00	0.00E+00	0.00E+00
1790-1800	2.20E-21	0.00E+00	0.00E+00	0.00E+00	0.00E+00	0.00E+00
1800-1810	1.67E-21	0.00E+00	0.00E+00	0.00E+00	0.00E+00	0.00E+00
1810-1820	1.41E-21	0.00E+00	0.00E+00	0.00E+00	0.00E+00	0.00E+00
1820-1830	1.15E-21	0.00E+00	0.00E+00	0.00E+00	0.00E+00	0.00E+00
1830-1840	8.90E-22	0.00E+00	0.00E+00	0.00E+00	0.00E+00	0.00E+00
1840-1850	6.30E-22	0.00E+00	0.00E+00	0.00E+00	0.00E+00	0.00E+00
1850-1860	4.62E-22	0.00E+00	0.00E+00	0.00E+00	0.00E+00	0.00E+00
1860-1870	3.86E-22	0.00E+00	0.00E+00	0.00E+00	0.00E+00	0.00E+00
1870-1880	3.10E-22	0.00E+00	0.00E+00	0.00E+00	0.00E+00	0.00E+00
1880-1890	2.34E-22	0.00E+00	0.00E+00	0.00E+00	0.00E+00	0.00E+00
1890-1900	1.58E-22	0.00E+00	0.00E+00	0.00E+00	0.00E+00	0.00E+00
1900-1910	1.09E-22	0.00E+00	0.00E+00	0.00E+00	0.00E+00	0.00E+00
1910-1920	8.70E-23	0.00E+00	0.00E+00	0.00E+00	0.00E+00	0.00E+00
1920-1930	6.50E-23	0.00E+00	0.00E+00	0.00E+00	0.00E+00	0.00E+00

Continued on next page

Table A.4 – *Continued from previous page*

Wavelength bin (Å)	**Total absorption**	**Total ionization**	**CO_2^+**	**CO^+**	**O^+**	**C^+**
1930-1940	4.30E-23	0.00E+00	0.00E+00	0.00E+00	0.00E+00	0.00E+00
1940-1950	2.10E-23	0.00E+00	0.00E+00	0.00E+00	0.00E+00	0.00E+00
1950-1960	9.84E-24	0.00E+00	0.00E+00	0.00E+00	0.00E+00	0.00E+00
1960-1970	9.54E-24	0.00E+00	0.00E+00	0.00E+00	0.00E+00	0.00E+00
1970-1980	9.23E-24	0.00E+00	0.00E+00	0.00E+00	0.00E+00	0.00E+00
1980-1990	8.93E-24	0.00E+00	0.00E+00	0.00E+00	0.00E+00	0.00E+00
1990-2000	8.62E-24	0.00E+00	0.00E+00	0.00E+00	0.00E+00	0.00E+00

Table A.5: Photon cross section of CO for different dissociation and ionization channels (cm^{-2})

Wavelength bin (Å)	**Total absorption**	**Total ionization**	**CO^+**	**C^+**	**O^+**
0-10	1.92E-20	1.92E-20	4.74E-22	9.40E-21	9.37E-21
10-20	2.76E-19	2.74E-19	1.84E-20	1.29E-19	1.27E-19
20-30	8.55E-19	8.46E-19	9.42E-20	3.79E-19	3.72E-19
30-40	1.72E-19	1.70E-19	2.21E-20	7.48E-20	7.30E-20
40-50	1.45E-19	1.42E-19	3.03E-20	5.71E-20	5.48E-20
50-60	2.33E-19	2.27E-19	5.80E-20	8.68E-20	8.25E-20
60-70	3.28E-19	3.18E-19	9.68E-20	1.14E-19	1.07E-19
70-80	5.02E-19	4.84E-19	1.70E-19	1.63E-19	1.51E-19
80-90	9.11E-19	8.76E-19	3.47E-19	2.77E-19	2.51E-19
90-100	1.28E-18	1.23E-18	5.14E-19	3.76E-19	3.45E-19
100-110	1.62E-18	1.58E-18	6.76E-19	4.81E-19	4.28E-19
110-120	2.00E-18	1.96E-18	8.54E-19	5.89E-19	5.21E-19
120-130	2.41E-18	2.34E-18	1.05E-18	6.83E-19	6.11E-19
130-140	2.82E-18	2.77E-18	1.27E-18	7.90E-19	7.05E-19
140-150	3.26E-18	3.20E-18	1.51E-18	8.92E-19	7.95E-19
150-160	3.70E-18	3.65E-18	1.78E-18	1.00E-18	8.65E-19
160-170	4.20E-18	4.16E-18	2.11E-18	1.11E-18	9.40E-19
170-180	4.75E-18	4.70E-18	2.45E-18	1.20E-18	1.04E-18
180-190	5.29E-18	5.27E-18	2.82E-18	1.29E-18	1.16E-18
190-200	5.94E-18	5.94E-18	3.21E-18	1.42E-18	1.30E-18

Continued on next page

Table A.5 – *Continued from previous page*

Wavelength bin (Å)	**Total absorption**	**Total ionization**	**CO^+**	**C^+**	**O^+**
200-210	6.60E-18	6.60E-18	3.60E-18	1.58E-18	1.40E-18
210-220	7.27E-18	7.27E-18	4.09E-18	1.64E-18	1.52E-18
220-230	7.96E-18	7.96E-18	4.59E-18	1.74E-18	1.61E-18
230-240	8.66E-18	8.66E-18	5.08E-18	1.84E-18	1.73E-18
240-250	9.33E-18	9.33E-18	5.64E-18	1.89E-18	1.80E-18
250-260	9.86E-18	9.86E-18	6.22E-18	1.83E-18	1.80E-18
260-270	1.03E-17	1.03E-17	6.84E-18	1.78E-18	1.71E-18
270-280	1.07E-17	1.07E-17	7.48E-18	1.66E-18	1.55E-18
280-290	1.10E-17	1.10E-17	8.03E-18	1.58E-18	1.47E-18
290-300	1.14E-17	1.15E-17	8.64E-18	1.52E-18	1.32E-18
300-310	1.19E-17	1.19E-17	9.31E-18	1.46E-18	1.19E-18
310-320	1.23E-17	1.23E-17	1.00E-17	1.31E-18	1.06E-18
320-330	1.27E-17	1.27E-17	1.07E-17	1.13E-18	9.29E-19
330-340	1.31E-17	1.31E-17	1.13E-17	9.23E-19	8.15E-19
340-350	1.34E-17	1.34E-17	1.18E-17	8.40E-19	6.78E-19
350-360	1.37E-17	1.37E-17	1.23E-17	7.93E-19	5.55E-19
360-370	1.41E-17	1.40E-17	1.28E-17	7.32E-19	4.83E-19
370-380	1.46E-17	1.45E-17	1.34E-17	6.87E-19	4.50E-19
380-390	1.51E-17	1.50E-17	1.39E-17	7.27E-19	3.74E-19
390-400	1.58E-17	1.58E-17	1.47E-17	7.91E-19	2.72E-19
400-410	1.64E-17	1.64E-17	1.54E-17	8.87E-19	1.04E-19
410-420	1.72E-17	1.72E-17	1.62E-17	8.70E-19	1.22E-19
420-430	1.79E-17	1.79E-17	1.69E-17	9.46E-19	1.00E-19
430-440	1.86E-17	1.86E-17	1.75E-17	1.01E-18	7.89E-20
440-450	1.93E-17	1.91E-17	1.81E-17	1.01E-18	6.59E-20
450-460	1.98E-17	1.98E-17	1.86E-17	1.08E-18	5.23E-20
460-470	2.03E-17	2.03E-17	1.92E-17	1.04E-18	5.63E-20
470-480	2.06E-17	2.06E-17	1.96E-17	1.00E-18	4.13E-20
480-490	2.08E-17	2.09E-17	1.99E-17	9.21E-19	4.17E-20
490-500	2.09E-17	2.09E-17	2.00E-17	8.72E-19	1.27E-20
500-510	2.10E-17	2.09E-17	2.01E-17	8.08E-19	0.00E+00
510-520	2.11E-17	2.10E-17	2.04E-17	6.71E-19	0.00E+00
520-530	2.12E-17	2.12E-17	2.06E-17	5.75E-19	0.00E+00
530-540	2.15E-17	2.15E-17	2.10E-17	4.67E-19	0.00E+00
540-550	2.17E-17	2.16E-17	2.13E-17	3.20E-19	0.00E+00

Continued on next page

Table A.5 – *Continued from previous page*

Wavelength bin (Å)	**Total absorption**	**Total ionization**	**CO^+**	**C^+**	**O^+**
550-560	2.19E-17	2.19E-17	2.19E-17	0.00E+00	0.00E+00
560-570	2.21E-17	2.20E-17	2.20E-17	0.00E+00	0.00E+00
570-580	2.23E-17	2.19E-17	2.19E-17	0.00E+00	0.00E+00
580-590	2.20E-17	2.13E-17	2.13E-17	0.00E+00	0.00E+00
590-600	2.06E-17	2.00E-17	2.00E-17	0.00E+00	0.00E+00
600-610	2.09E-17	1.99E-17	1.99E-17	0.00E+00	0.00E+00
610-620	1.70E-17	1.62E-17	1.62E-17	0.00E+00	0.00E+00
620-630	2.26E-17	2.21E-17	2.21E-17	0.00E+00	0.00E+00
630-640	2.13E-17	1.68E-17	1.68E-17	0.00E+00	0.00E+00
640-650	2.42E-17	1.72E-17	1.72E-17	0.00E+00	0.00E+00
650-660	2.01E-17	1.71E-17	1.71E-17	0.00E+00	0.00E+00
660-670	2.52E-17	1.75E-17	1.75E-17	0.00E+00	0.00E+00
670-680	2.14E-17	1.40E-17	1.40E-17	0.00E+00	0.00E+00
680-690	2.62E-17	1.69E-17	1.69E-17	0.00E+00	0.00E+00
690-700	2.17E-17	1.59E-17	1.59E-17	0.00E+00	0.00E+00
700-710	2.53E-17	1.75E-17	1.75E-17	0.00E+00	0.00E+00
710-720	2.73E-17	1.97E-17	1.97E-17	0.00E+00	0.00E+00
720-730	4.01E-17	2.43E-17	2.43E-17	0.00E+00	0.00E+00
730-740	2.84E-17	1.54E-17	1.54E-17	0.00E+00	0.00E+00
740-750	2.12E-17	1.10E-17	1.10E-17	0.00E+00	0.00E+00
750-760	2.96E-17	1.42E-17	1.42E-17	0.00E+00	0.00E+00
760-770	2.40E-17	1.25E-17	1.25E-17	0.00E+00	0.00E+00
770-780	2.96E-17	1.09E-17	1.09E-17	0.00E+00	0.00E+00
780-790	2.10E-17	1.15E-17	1.15E-17	0.00E+00	0.00E+00
790-800	1.47E-17	9.73E-18	9.73E-18	0.00E+00	0.00E+00
800-810	2.69E-17	1.24E-17	1.24E-17	0.00E+00	0.00E+00
810-820	3.62E-17	2.00E-17	2.00E-17	0.00E+00	0.00E+00
820-830	2.70E-17	1.48E-17	1.48E-17	0.00E+00	0.00E+00
830-840	1.87E-17	1.75E-17	1.75E-17	0.00E+00	0.00E+00
840-850	1.75E-17	1.64E-17	1.64E-17	0.00E+00	0.00E+00
850-860	2.46E-17	1.77E-17	1.77E-17	0.00E+00	0.00E+00
860-870	3.46E-17	2.03E-17	2.03E-17	0.00E+00	0.00E+00
870-880	2.24E-17	1.80E-17	1.80E-17	0.00E+00	0.00E+00
880-890	2.62E-17	0.00E+00	0.00E+00	0.00E+00	0.00E+00
890-900	2.90E-17	0.00E+00	0.00E+00	0.00E+00	0.00E+00

Continued on next page

Table A.5 – *Continued from previous page*

Wavelength bin (Å)	**Total absorption**	**Total ionization**	**CO^+**	**C^+**	**O^+**
900-910	7.15E-17	0.00E+00	0.00E+00	0.00E+00	0.00E+00
910-920	1.86E-17	0.00E+00	0.00E+00	0.00E+00	0.00E+00
920-930	3.27E-17	0.00E+00	0.00E+00	0.00E+00	0.00E+00
930-940	2.15E-17	0.00E+00	0.00E+00	0.00E+00	0.00E+00
940-950	1.34E-17	0.00E+00	0.00E+00	0.00E+00	0.00E+00
950-960	5.40E-18	0.00E+00	0.00E+00	0.00E+00	0.00E+00
960-970	2.94E-17	0.00E+00	0.00E+00	0.00E+00	0.00E+00
970-980	1.72E-18	0.00E+00	0.00E+00	0.00E+00	0.00E+00
980-990	3.87E-18	0.00E+00	0.00E+00	0.00E+00	0.00E+00
990-1000	1.87E-18	0.00E+00	0.00E+00	0.00E+00	0.00E+00
1000-1010	1.41E-18	0.00E+00	0.00E+00	0.00E+00	0.00E+00
1010-1020	7.36E-19	0.00E+00	0.00E+00	0.00E+00	0.00E+00
1020-1030	6.21E-20	0.00E+00	0.00E+00	0.00E+00	0.00E+00
1030-1040	1.50E-20	0.00E+00	0.00E+00	0.00E+00	0.00E+00
1040-1050	1.00E-35	0.00E+00	0.00E+00	0.00E+00	0.00E+00
1050-1060	1.00E-35	0.00E+00	0.00E+00	0.00E+00	0.00E+00
1060-1070	1.00E-35	0.00E+00	0.00E+00	0.00E+00	0.00E+00
1070-1080	1.00E-35	0.00E+00	0.00E+00	0.00E+00	0.00E+00
1080-1090	1.00E-35	0.00E+00	0.00E+00	0.00E+00	0.00E+00
1090-1100	1.00E-35	0.00E+00	0.00E+00	0.00E+00	0.00E+00
1100-1110	1.00E-35	0.00E+00	0.00E+00	0.00E+00	0.00E+00
1110-1120	1.00E-35	0.00E+00	0.00E+00	0.00E+00	0.00E+00

Table A.6: Jackman's analytical fitting parameters for electron impact cross sections of different excited states of H_2O.

S. No.	Excited states	W	α	β	$\bar{W}_j$	Ω	F_i	A.F
1	$(A_1)\ \nu_2$	0.198	1.000	3.000	0.198	6.000	0.001840	0.0
2	$(A_1)\ 2\nu_2$	0.391	1.000	3.000	0.391	6.000	0.000043	0.0
3	$(A_1)\ \nu_1$	0.453	1.000	3.000	0.453	6.000	0.006780	0.0
4	$(B_1)\ \nu_3$	0.466	1.000	3.000	0.466	6.000	0.007170	0.0
5	$(B_1)\ \nu_2 + \nu_3$	0.661	1.000	3.000	0.661	6.000	0.000948	0.0
6	$(B_1)\ \nu_1 + \nu_3$	0.899	1.000	3.000	0.899	6.000	0.001830	0.0
7	$(B_1)\ \nu_1 + \nu_2 + \nu_3$	1.092	1.000	3.000	1.092	6.000	0.000113	0.0
8	$(B_1)\ 2\nu_1 + \nu_3$	1.316	1.000	3.000	1.316	6.000	0.000082	0.0
9	Triplet	4.500	1.000	3.000	4.500	3.000	0.007000	0.0
10	Triplet	12.500	1.000	1.000	9.810	3.000	0.018000	0.0
11	Disso. cont.‡	7.400	1.000	3.000	7.400	0.750	0.063000	0.0
12	Disso. cont.‡	9.670	1.000	3.000	9.670	0.800	0.138000	0.0
13	Diffuse bands	13.320	1.000	3.000	13.320	0.750	0.626000	0.0
14	H* Lyman-α	28.500	0.300	1.000	17.000	1.000	3.490000	0.0
15	H* Hα	28.500	0.300	1.000	19.000	1.000	0.735000	0.0
16	H* Hβ	28.500	0.300	1.000	20.000	1.000	0.125000	0.0
17	H* Hγ	28.500	0.300	1.000	20.000	1.000	0.050000	0.0
18	H* Hδ	28.500	0.300	1.000	20.000	1.000	0.021000	0.0
19	O* 1304 Å	32.500	1.000	3.000	16.000	1.250	0.089000	0.0
20	O* 8447 Å	38.000	1.000	2.000	17.000	4.850	0.220000	0.0
21	O* 8447 Å	50.000	1.000	3.000	34.000	1.850	0.175000	0.0
22	O* 3064 Å	14.200	5.350	1.000	10.000	1.000	0.053700	0.0
23	O* 2800 Å	16.400	2.350	1.000	11.000	1.000	0.005800	0.0

‡Dissociative continuum.

	Rydberg	I_i	α	β	δ	Ω	F	A.F. -n	A.F. -n	A.F. -n
24	Series A	12.62	1.00	3.00	0.729	0.75	0.427	0.0 -3	0.0 -4	0.0 -5
25	Series B	12.62	1.00	3.00	0.700	0.75	0.438	0.0 -3	0.0 -4	0.0 -5
26	Series C	12.62	1.00	3.00	0.050	0.75	1.850	0.0 -3	0.0 -4	0.0 -5
27	Series D	12.62	1.00	3.00	0.050	0.75	1.850	0.0 -3	0.0 -4	0.0 -5

	Ionization	$I_i^\dagger$	K	K_B	J	J_B	J_C	Γ_S	Γ_B	T_S	T_A	T_B
28	H_2O^+	12.6	4.05	110.0	1.00	30.0	0.0	11.4	0.0	-2.37	0.0	0.0
29	OH^+	20.0	1.13	94.0	1.00	0.0	0.0	11.4	0.0	-2.37	0.0	0.0
30	H^+	20.0	1.55	147.0	1.00	-18.0	0.0	11.4	0.0	-2.37	0.0	0.0
31	O^+	20.0	0.12	90.5	1.00	-19.0	0.0	11.4	0.0	-2.37	0.0	0.0
32	O^{++}	60.0	0.00	78.0	2.86	-20.0	0.0	11.4	0.0	-2.37	0.0	0.0
33	H_2^+	23.0	0.00	29.4	1.00	0.0	0.0	11.4	0.0	-2.37	0.0	0.0

Table A.7: Jackman's analytical fitting parameters for electron impact cross sections of different excited states of CO_2.

S. No.	Excited States	W	α	β	$\bar{W}_j$	Ω	F	A.F.
1	Vibration, 010	0.080	2.750	1.000	0.080	0.750	0.000032	0.000
2	Vibration, 100	0.180	1.070	1.000	0.180	0.750	0.000046	0.000
3	Vibration, 001	0.300	2.210	1.000	0.300	0.750	0.000517	0.000
4	8.6 eV state	8.600	0.556	2.000	8.600	0.936	0.060600	0.000
5	9.3 eV state	9.300	0.603	2.000	9.300	0.909	0.064000	0.000
6	11.1 eV state	7.760	0.246	3.000	11.100	1.110	4.420000	0.000
7	12.4 eV state	9.610	0.458	3.000	12.400	1.020	3.560000	0.000
8	13.6 eV state	10.500	0.625	3.000	13.600	0.849	3.250000	0.000
9	15.5 eV state	15.500	0.739	2.000	15.500	0.793	0.139000	0.750
10	16.3 eV state	12.300	0.605	3.000	16.300	0.911	0.716000	0.750
11	17.0 eV state	13.000	0.649	3.000	17.000	0.878	0.114000	0.750
12	17.8 eV state	14.700	0.977	3.000	17.800	0.725	0.051100	0.750
13	OI (1304)	20.100	0.599	3.000	22.000	1.000	0.127000	0.750
14	OI (1356)	16.400	0.600	3.000	20.400	0.944	0.168000	0.500
15	CI (1279)	15.700	1.000	3.000	26.200	0.643	0.010400	0.500
16	CI (1329)	21.800	1.000	3.000	20.900	1.040	0.020200	0.500
17	CI (1561)	22.400	1.000	3.000	24.500	0.982	0.053800	0.500
18	CI (1657)	21.100	1.000	3.000	24.100	0.947	0.087200	0.500

	State[§]	I_i	K	K_B	J	J_B	J_C	Γ_S	Γ_B	T_S	T_A	T_B
19	$X^2\Pi_g^+$	13.76	3.430	0.0	4.099	-2.35	0.0	11.11	-13.26	-0.847	1000	27.52
20	$A^2\Pi_u$	17.80	9.425	0.0	90.75	1.014	0.0	11.02	-17.50	-0.876	1000	35.60
21	$B^2\Sigma_u^+$	18.10	6.632	0.0	89.36	1.034	0.0	11.02	-17.50	-0.878	1000	36.20
22	$C^2\Sigma_g$	19.40	0.580	0.0	21.19	1.270	0.0	10.98	-19.00	-0.887	1000	38.80
23	Diss.[‡]	22.00	3.799	6.3	2.737	-8.00	0.0	11.92	22.00	-1.600	621.8	44.00

[‡] Total dissociative ionization. [§] Electronic state of the ion.

Table A.8: Jackman's analytical fitting parameters for electron impact cross sections of different excited states of CO.

S.No	Excited states	W	α	β	$\bar{W_j}$	Ω	F$_i$	A.F
1	$A^1\Pi$	7.900	0.125	1.000	8.510	0.750	0.749000	0.000
2	$B^1\Sigma^+$ (n=3)	9.580	0.125	1.000	10.780	0.750	0.067100	0.000
3	$C^1\Sigma^+$ (n=3)	10.700	0.125	1.000	10.400	0.750	0.553000	0.000
4	$E^1\Pi$ (n=3)	10.800	0.125	1.000	11.520	0.750	0.325000	0.000
5	$F^1\Pi$ (n=3)	11.700	0.125	1.000	12.370	0.750	0.069500	0.000
6	$B^1\Sigma^+$ (n=4)	11.400	0.125	1.000	12.590	0.750	0.168000	0.000
7	$C^1\Sigma^+$ (n=4)	12.100	0.125	1.000	12.800	0.750	0.369000	0.000
8	$E^1\Pi$ (n=4)	12.100	0.125	1.000	12.820	0.750	0.217000	0.000
9	$F^1\Pi$ (n=4)	12.400	0.125	1.000	13.110	0.750	0.046400	0.000
10	13.5 ev state	12.700	0.125	1.000	13.500	0.750	1.630000	0.000
11	$a^3\Pi$ (1)	6.450	1.000	3.000	6.220	5.020	13.60000	0.000
12	$a^3\Pi$ (2)	6.220	1.000	3.000	6.220	0.750	0.076000	0.000
13	$b^3\Sigma^+$ (1)	10.400	1.000	3.000	10.400	6.950	6.010000	0.000
14	$b^3\Sigma^+$ (2)	10.400	1.000	3.000	10.400	0.750	0.013500	0.000
15	$a'^3\Sigma^+$	9.350	10.300	1.870	6.910	2.600	0.874000	0.000
16	$c^3\Pi$	18.600	14.700	1.550	11.400	2.590	0.116000	0.000
17	$d^3\Delta$	2.320	2.550	111.00	7.500	1.860	0.010600	0.000
18	$j^3\Sigma^+$	8.000	10.000	17.700	11.270	2.630	0.026400	0.000
19	$D^1\Delta$	5.150	0.714	3.000	8.070	1.000	0.032500	0.000
20	CO^-	9.400	3.000	1.000	9.620	17.400	0.004760	0.000
21	CO^-	21.300	2.000	1.000	22.000	0.955	0.003440	0.000
22	OI (1304)	32.400	0.384	1.000	20.630	0.750	0.023900	0.500
23	OI (8447)	36.000	0.400	1.000	22.000	0.886	0.087300	0.500
24	OI (1279)	21.400	0.114	1.000	21.000	0.687	0.084600	0.500

	Rydberg states	I$_i$	α	β	δ	Ω	F	A.F. -n	A.F. -n	A.F. -n
25	$B^1\Sigma^+$	14.01	0.125	1.0	0.90	0.75	0.621	0.0 -5	0.0 -6	
26	$C^1\Sigma^+$	14.01	0.125	1.0	0.65	0.75	7.180	0.0 -5	0.0 -6	
27	$E^1\Pi$	14.01	0.125	1.0	0.62	0.75	4.390	0.0 -5	0.0 -6	
28	$F^1\Pi$	14.01	0.125	1.0	0.11	0.75	1.680	0.0 -5	0.0 -6	
29	(L1)	16.54	0.125	1.0	1.04	0.75	6.940	0.5 -3	0.5 -4	0.5 -5
30	Tanaka α	16.54	0.125	1.0	0.68	0.75	3.470	0.5 -3	0.5 -4	0.5 -5
31	(L2)	16.54	0.125	1.0	0.15	0.75	3.470	0.5 -3	0.5 -4	0.5 -5
32	Ogawa 3	19.68	0.125	1.0	0.94	0.75	0.694	0.5 -3	0.5 -4	0.5 -5
33	Tanaka sharp β	19.68	0.125	1.0	0.68	0.75	2.770	0.5 -3	0.5 -4	0.5 -5
34	Tanaka diffuse β	19.68	0.125	1.0	0.58	0.75	2.770	0.5 -3	0.5 -4	0.5 -5
35	Ogawa 4	19.68	0.125	1.0	0.20	0.75	0.694	0.5 -3	0.5 -4	0.5 -5

	Ion. states	I$_i$	K	K$_B$	J	J$_B$	J$_C$	Γ_S	Γ_B	T$_S$	T$_A$	T$_B$
36	$X^2\Sigma^+$	14.01	3.530	0.0	12.6	0.0	0.0	12.1	-13.5	2.09	1000.0	28.0
37	$A^2\Pi_u$	16.54	3.370	0.0	12.6	0.0	0.0	12.1	-13.5	2.09	1000.0	28.0
38	$B^2\Sigma^+$	19.68	1.640	0.0	12.6	0.0	0.0	12.1	-13.5	2.09	1000.0	28.0
39	Diss. Ion.*	22.00	0.866	0.0	0.01	0.0	0.0	13.6	44.00	2.04	1000.0	44.0

‡Dissociative Ionization.

Appendix B

Publications

Monthly Notices of the ROYAL ASTRONOMICAL SOCIETY LETTERS

Mon. Not. R. Astron. Soc. (2011) doi:10.1111/j.1745-3933.2010.00998.x

Model for Cameron-band emission in comets: a case for the *EPOXI* mission target comet 103P/Hartley 2

Anil Bhardwaj★ and Susarla Raghuram★

Space Physics Laboratory, Vikram Sarabhai Space Center, Trivandrum 695022, India

Accepted 2010 November 26. Received 2010 November 3

ABSTRACT

The CO_2 production rate has been derived in comets using Cameron-band ($a^3\Pi \rightarrow X^1\Sigma$) emission of CO molecules, assuming that photodissociative excitation of CO_2 is the main production mechanism of CO in the $a^3\Pi$ metastable state. We have developed a model for the production and loss of CO($a^3\Pi$), which has been applied to comet 103P/Hartley 2: the target of the *EPOXI* mission. Our model calculations show that photoelectron impact excitation of CO and dissociative excitation of CO_2 can together contribute about 60–90 per cent to Cameron-band emission. The modelled brightness of (0–0) Cameron-band emission on comet Hartley 2 is consistent with *Hubble Space Telescope* observations for 3–5 per cent CO_2 (depending on the model input solar flux) and 0.5 per cent CO relative to water, where the photoelectron impact contribution is about 50–75 per cent. We suggest that estimation of CO_2 abundances on comets using Cameron-band emission may be reconsidered. We predict a height-integrated column brightness of the Cameron band of ∼1300 Rayleigh during the *EPOXI* mission encounter period.

Key words: astrochemistry – molecular processes – comets: general – comets: individual: 103P/Hartley 2 – ultraviolet: general.

1 INTRODUCTION

In the exploration of the Solar system, comets have been targeted by various space missions. After a successful encounter with comet 9P/Temple 1 on 2005 July 4, NASA's *Deep Impact* mission, also called the *EPOXI* mission, under its extended investigation programme DIXI, will encounter comet 103P/Hartley 2 on 2010 November 4, with the closest approach around 700 km from the nucleus. This comet has been observed by several space telescopes in different spectral regions (Weaver, Feldman & McPhate 1994; Colangeli et al. 1999; Crovisier et al. 1999; Groussin et al. 2004; Snodgrass, Lowry & Fitzsimmons 2008; Lisse et al. 2009; Snodgrass, Meech & Hainaut 2010).

The first clear detection of the Cameron band ($a^3\Pi \rightarrow X^1\Sigma$) of CO was reported by Weaver et al. (1994) in the *Hubble Space Telescope* (*HST*)/FOS spectrum of comet 103P/Hartley 2. Since Cameron-band emission is a forbidden transition, resonance fluorescence is not an effective excitation mechanism. The upper state of this emission ($a^3\Pi$) is a metastable state with lifetime of 3 ms (Gilijamse et al. 2007), which is quite small. Thus, Cameron-band emissions are treated as 'prompt emissions' and can be used to probe the distribution of parent species if this emission is produced in dissociative excitation of a molecular species. Photodissociative excitation of CO_2 is considered as the major production mechanism of the CO Cameron band and has been used to trace the distribution and abundance of CO_2 on comets (Weaver et al. 1994; Feldman et al. 1997).

Besides photodissociative excitation of CO_2, there are other channels of excitation of CO molecules in the $a^3\Pi$ state. It has been shown that photoelectrons generated by solar extreme-ultraviolet (EUV) radiation also play an important role in excitation, dissociation and ionization processes leading to emission and chemistry in cometary comae (e.g. Boice et al. 1986; Ip 1986; Körösmezey et al. 1987; Bhardwaj, Haider & Singhal 1990; Bhardwaj, Haider & Singhal 1996; Weaver et al. 1994; Bhardwaj 1999, 2003; Haider & Bhardwaj 2005; Capria et al. 2008). Recently, Campbell & Brunger (2009) demonstrated the importance of photoelectron impact excitation in comets and showed that electron impact on CO gives 40 per cent contribution to the total CO Fourth positive emission. The presence of photoelectron excitation in a cometary coma is clearly demonstrated by detection of O I 1356 Å emission in comets (e.g. Sahnow et al. 1993; McPhate et al. 1999), since this emission, being a spin-forbidden transition, cannot be produced by solar fluorescence. There is other significant evidence for an important role of photoelectron excitation in cometary comae (e.g. Tozzi, Feldman & Festou 1998; Bhardwaj 1999; Feldman et al. 2009). In addition to

---

★E-mail: anil_bhardwaj@vssc.gov.in, bhardwaj_spl@yahoo.com (AB); raghuramsusarla@gmail.com (SR) photon and electron impact reactions, dissociative electron recombination reactions of CO^+-bearing ions can also produce CO in the $a^3\Pi$ excited state.

Our aim in this Letter is to study various production and loss mechanisms of $CO(a^3\Pi)$ and to estimate the contribution of photoelectron impact excitation of CO and CO_2 in the production of the Cameron band for different relative abundances of CO_2 on comet 103P/Hartley 2: the target of the *EPOXI* mission. Since model calculations depend on input solar flux, we have estimated its sensitivity on the calculated intensity of Cameron-band emission. We show that photoelectron impact on CO and CO_2 is a dominant process (∼60–90 per cent contribution) in producing CO molecules in the $(a^3\Pi)$ state. Around the *EPOXI* encounter epoch, predictions are made for the brightness of the Cameron band for comet 103P/Hartley 2, which will be observed by several space-based telescopes, including the *HST*.

2 MODEL

We have developed a model for the production of Cameron-band emission on comets, which uses the basic coupled chemistry model described in detail in our earlier papers (Bhardwaj et al. 1996; Bhardwaj 1999; Haider & Bhardwaj 2005). Various sources of production and loss of $CO(a^3\Pi)$ are summarized in Table 1. The total water production rate is taken as $6.3 \times 10^{28}\ s^{-1}$ for comet 103P/Hartley 2 (Weaver et al. 1994).

To evaluate the effect of solar EUV flux on model calculations, we have considered two solar flux models: the EUVAC model of Richards, Fennelly & Torr (1994) and the SOLAR 2000 (S2K) model of Tobiska et al. (2000). The degradation of the solar UV–EUV radiation and solar EUV-generated photoelectrons in the coma is modelled using the method of Bhardwaj et al. (1990, 1996), further developed by Bhardwaj (1999, 2003). The electron impact production rates are calculated using the Analytical Yield Spectrum (AYS) approach, which is based on the Monte Carlo method. Details of the AYS approach are given in many of the previous papers (Bhardwaj et al. 1990, 1996; Bhardwaj 1999; Bhardwaj & Michael 1999a,b; Bhardwaj & Jain 2009). The present model takes into account the most recently published cross-sections for the photon impact and electron impact dissociation, ionization and excitation processes for the gases in the coma. The cross-section for photodissociative excitation of CO_2 producing CO in the $a^3\Pi$ state is calculated using absorption cross-sections of CO_2 and the yield of the Cameron band measured by Lawrence (1972). The cross-section for electron impact excitation of $CO(a^3\Pi)$ from CO is taken from Jackman, Garvey & Green (1977), and for dissociative excitation of CO_2 it is taken from Bhardwaj & Jain (2009). The electron temperature profile required for dissociative recombination reactions is taken from Körösmezey et al. (1987) and is assumed to be the same as on comet Halley. Calculations are made for comet 103P/Hartley 2 at a heliocentric distance of 0.96 au.

3 RESULTS AND DISCUSSION

The photodissociation of CO_2 producing CO in the $a^3\Pi$ state is determined by solar flux mainly in the wavelength region 550–1050 Å. Table 2 presents the calculated photon-production frequencies of $CO(a^3\Pi)$ for two different solar flux models. The $CO(a^3\Pi)$ production frequencies calculated for photoelectron impact on CO_2 and CO are also shown in the same table for the corresponding solar flux models. Our calculated photodissociation frequencies are approximately 15 to 50 per cent lower than those reported by Huebner, Keady & Lyon (1992).

Using the EUVAC solar flux, the calculated radial profile of the volume production rate for the various sources of $CO(a^3\Pi)$ at the relative abundance of 4 per cent CO_2 and 0.5 per cent CO is shown in Fig. 1. At 100 km cometocentric distance, the dominant source of production of $CO(a^3\Pi)$ is electron impact of CO_2 (∼50 per cent) followed by electron impact of CO (∼25 per cent) and photodissociation of CO_2 (∼15 per cent). The contributions from dissociative recombination reactions are quite small (≤5 per cent) at lower cometocentric distances, but the recombination of CO_2^+ is a significant (<30 per cent) source at 1000 km and beyond. Fig. 2 shows the radial profiles of various loss processes of $CO(a^3\Pi)$ for the same relative composition of CO_2 and CO. Since the lifetime of CO in the excited state $(a^3\Pi)$ is very short (∼3 ms; Gilijamse et al. 2007), the radiative decay is the dominant loss process. Collisional quenching of $CO(a^3\Pi)$ by cometary neutral species is negligible since comet

Table 1. Reactions for the production and loss of $CO(a^3\Pi)$.

Reaction	Rate ($cm^{-3}\ s^{-1}$ or s^{-1})	Reference
$CO_2 + h\nu \rightarrow CO(a^3\Pi) + O(^3P)$	Model	Shunk & Nagy (2009); Lawrence (1972)
$CO + h\nu \rightarrow CO(a^3\Pi)$	1.69×10^{-9}	Weaver et al. (1994)
$CO_2 + e^-_{ph} \rightarrow CO(a^3\Pi) + O + e^-$	Model	Present work
$CO + e^-_{ph} \rightarrow CO(a^3\Pi) + e^-$	Model	Present work
$CO_2^+ + e^- \rightarrow CO(a^3\Pi) + O$	$6.5 \times 10^{-7}\ (300/T_e)^{0.8} \times 0.87^a \times 0.29^b$	Seiersen et al. (2003); Rosati, Johnsen & Golde (2003)
$HCO^+ + e^- \rightarrow CO(a^3\Pi) + H$	$0.23^c \times 2.4 \times 10^{-7}\ (300/T_e)^{0.7}$	Rosati et al. (2007), Schmidt et al. (1988)
$CO(a^3\Pi) + h\nu \rightarrow C + O$	7.2×10^{-5}	Huebner et al. (1992)
$CO(a^3\Pi) + h\nu \rightarrow CO^+ + e^-$	8.58×10^{-6}	Huebner et al. (1992)
$CO(a^3\Pi) + h\nu \rightarrow O + C^+ + e^-$	2.45×10^{-8}	Huebner et al. (1992)
$CO(a^3\Pi) + h\nu \rightarrow C + O^+ + e^-$	2.06×10^{-8}	Huebner et al. (1992)
$CO(a^3\Pi) + H_2O \rightarrow CO + H_2O$	3.3×10^{-10}	Wysong (2000)
$CO(a^3\Pi) + CO_2 \rightarrow CO + CO_2$	1.0×10^{-11}	Skrzypkowski et al. (1998)
$CO(a^3\Pi) + CO \rightarrow CO + CO$	5.7×10^{-11}	Wysong (2000)
$CO(a^3\Pi) + e^-_{ph} \rightarrow CO^+ + 2e^-$	Model	Present work
$CO(a^3\Pi) \longrightarrow CO + h\nu$	1.26×10^2	Weaver et al. (1994)

[a] 0.87 is the yield of dissociative recombination of CO_2^+ that produces CO.
[b] 0.29 is the yield of $CO(a^3\Pi)$ produced from CO.
[c] 0.23 is the yield of dissociative recombination of HCO^+ that produces $CO(a^3\Pi)$; e^-_{ph} = photoelectron.

Table 2. Production frequency (s^{-1}) of CO($a^3\Pi$) for three different processes at 1 au.

Solar flux	Photodissociation of CO_2		Photoelectron impact of CO_2		Photoelectron impact of CO	
	Solar min (2010 September 1)	Solar max (1991 September 18)	Solar min (2010 September 1)	Solar max (1991 September 18)	Solar min (2010 September 1)	Solar max (1991 September 18)
S2K	1.1×10^{-7}	5.6×10^{-7}	3.4×10^{-7}	9.7×10^{-7}	1.5×10^{-6}	4.3×10^{-6}
EUVAC	1.7×10^{-7}	2.6×10^{-7}	3.5×10^{-7}	8.9×10^{-7}	1.5×10^{-6}	3.7×10^{-6}

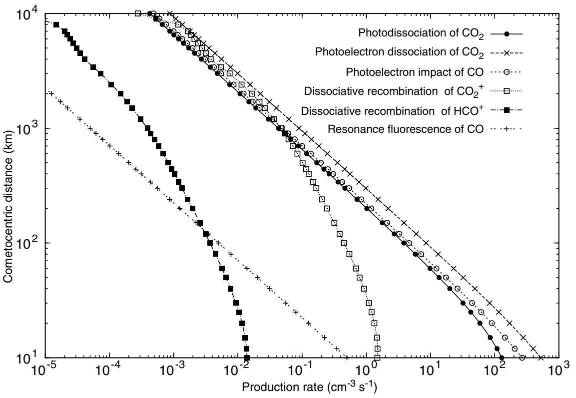

Figure 1. Radial profiles of the production processes of CO($a^3\Pi$) in comet 103P/Hartley 2 for 0.5 per cent CO and 4 per cent CO_2 using the EUVAC solar flux on 1991 September 18 and 19.

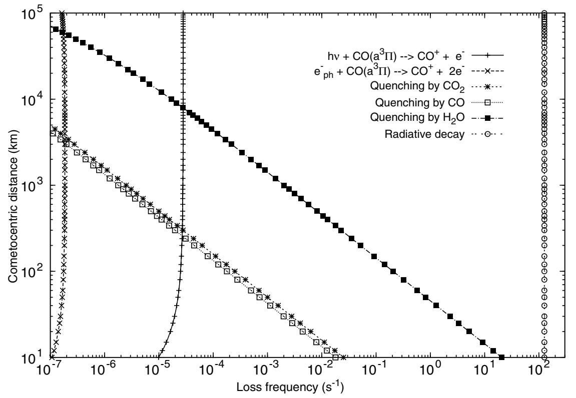

Figure 2. Radial profiles of the loss frequencies of CO($a^3\Pi$) in comet 103P/Hartley 2 for 0.5 per cent CO and 4 per cent CO_2 using the EUVAC solar flux on 1991 September 18 and 19.

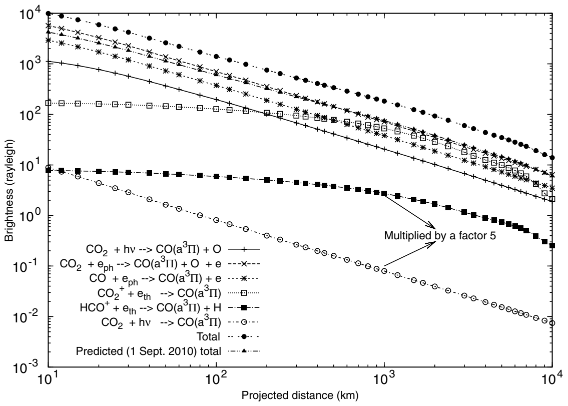

Figure 3. Brightness profile of the Cameron band on comet 103P/Hartley 2 as a function of the projected distance from the nucleus for 4 per cent of CO_2 and 0.5 per cent of CO using the EUVAC solar flux on 1991 September 18 and 19. Resonance fluorescence values and dissociative recombination profiles are plotted after multiplication by a factor of 5. The total brightness predicted profile for the *EPOXI* mission period is also shown.

103P/Hartley 2 is a low production rate comet. In the case of large production rate comets, like Hale–Bopp, however, quenching by water would be a dominant loss process in the innermost part of the coma.

Fig. 3 shows the modelled limb brightness profiles of Cameron-band emission for different production processes of CO($a^3\Pi$). The cometary coma is assumed to be spherically symmetric. The production rates are integrated up to 10^5 km along the line of sight at a given projected distance from the cometary nucleus and converted into brightness. The brightness profiles are averaged over the projected area of the slit (2870 × 954 km) corresponding to the *HST* observation (Weaver et al. 1994). The volume emission rates for three transitions (0–0, 1–0, 0–1) of Cameron-band emission are calculated using the following formula:

$$V_{v'v''}(r) = q_{ov'} \left(A_{v'v''} \bigg/ \sum_{v''} A_{v'v''} \right) V(r) \exp(-\tau), \qquad (1)$$

where $V(r)$ is the total volume excitation rate of CO($a^3\Pi$) at the cometocentric distance r, $q_{ov'}$ is the Franck–Condon factor for the transition, $A_{v'v''}$ is the Einstein transition probability from the upper state v' to the lower state v'', and τ is the optical depth. Since resonance fluorescence is not an effective excitation mechanism for the Cameron band and the total gas production rate is only $6.3 \times 10^{28}\,s^{-1}$, the cometary coma can be safely assumed to be optically thin. The Franck–Condon factors are taken from Nicholls (1962) and branching ratios are taken from Conway (1981). The relative contributions of (1–0), (0–0) and (0–1) transitions to the total Cameron band are 13.9, 10.4 and 14.7 per cent, respectively.

Table 3 presents the model-calculated slit-averaged brightness of (1–0), (0–0) and (0–1) transitions of the Cameron band, as well as the total Cameron-band brightness and height-integrated column brightness for different relative abundances of CO and CO_2 corresponding to the *HST* observation of comet 103P/Hartley 2 on 1991 September 18 and 19. Due to the absence of CO Fourth positive emission in this comet (Weaver et al. 1994), the abundance of CO is constrained to 0.5 per cent. However, we do consider a case of 1 per cent of CO to evaluate its implications on the results. This table also depicts the fractional contribution of photodissociation of CO_2, photoelectron impact of CO and CO_2, and dissociative recombination of CO_2^+ to the total calculated brightness at three projected distances (10^2, 10^3 and 10^4 km) from the nucleus. Since the production rates of photodissociative excitation of CO_2, and photoelectron impact of CO and CO_2 are dependent on the input solar flux model, results are

Table 3. Calculated brightness of the Cameron band on comet 103P/Hartley 2 for different conditions.

Relative abundance		*HST*/slit averaged brightness (Rayleigh)			Percentage contribution to the total Cameron band for different processes at three different projected radial distances (km)												Total Cameron-band brightness (Rayleigh)	
CO_2 (per cent)	CO (per cent)				Photodissociation of CO_2			Photoelectron impact of CO_2			Photoelectron impact of CO			Recombination of CO_2^+			*HST*/slit averaged	Height-integrated nadir view
		(1–0)	(0–0)	(0–1)	10^2	10^3	10^4	10^2	10^3	10^4	10^2	10^3	10^4	10^2	10^3	10^4		
EUVAC[a]																		
7	0.5	68	51	72	15	12	15	57	42	51	17	12	15	10	32	17	489	4769
5	0.5	51	39	54	14	11	14	53	40	48	22	17	21	9	30	16	369	3710
4	0.5	43	32	45	13	11	13	50	38	45	26	20	25	9	29	15	309	3172
3	0.5	34	26	36	12	10	12	46	36	42	32	26	30	8	26	13	250	2628
2	0.5	26	20	28	11	9	10	39	32	36	42	34	40	7	23	12	190	2078
4	1	51	38	54	11	9	11	40	32	36	41	33	38	7	24	12	311	3948
3	1	43	32	46	10	8	10	35	29	32	48	40	45	6	21	11	311	3420
S2K[a]																		
7	0.5	86	64	91	26	21	25	48	36	44	15	11	14	10	31	16	622	5928
5	0.5	65	48	68	25	20	24	45	35	42	20	15	19	9	29	15	467	4586
4	0.5	54	40	57	23	19	22	43	33	40	24	19	22	8	28	14	390	3903
3	0.5	43	32	46	22	18	21	40	31	37	30	23	28	8	26	13	313	3210
2	0.5	33	25	35	19	16	18	35	28	32	39	32	37	8	23	11	236	2508
3	1	53	40	56	17	15	17	31	25	29	45	37	42	6	21	10	384	4093
2	1	43	32	45	14	12	14	25	21	23	55	47	52	5	18	8	308	3411
Prediction EUVAC[b]																		
4	0.5	189[c]	142[c]	200[c]	21	18	20	46	37	42	25	20	23	7	23	12	–	1365
S2K[b]																		
4	0.5	175[c]	130[c]	185[c]	16	14	16	50	41	46	28	23	25	7	23	13	–	1258

[a] Solar flux for 1991 September 18.

[b] Solar flux for 2010 September 1.

[c] Relative contribution of the band in the total height-integrated nadir view intensity.

presented for the EUVAC and S2K solar fluxes relevant to the date of comet observation, which was in the solar maximum condition.

The intensity of the 0–0 transition of the Cameron band observed by the *HST* is 35 Rayleigh (Weaver et al. 1994), which is consistent with the model-calculated brightness for the relative abundance of 4–5 per cent of CO_2 and 0.5 per cent of CO when the EUVAC solar flux is used. In this case, at 100 km, the photoelectron impact of CO_2 (50 per cent) and CO (25 per cent) contributes around 75 per cent, while photodissociative excitation of CO_2 contributes <15 per cent. At 1000 km and beyond, the contribution due to electron impact of CO_2 and CO is about 60–70 per cent, while that of dissociative recombination of CO_2^+ is $\sim$15–30 per cent and that of photodissociative excitation of CO_2 is $\sim$10 per cent only. On average, photoelectron impact of CO_2 and CO contributes about 60–75 per cent to the production of Cameron-band emission, while photodissociative excitation of CO_2 contributes about 10–15 per cent only. In the case of the S2K solar flux model, a CO_2 abundance of 3–4 per cent is required to match the *HST*-observed Cameron-band 0–0 transition brightness. Here the contribution of photodissociative excitation of CO_2 is $\sim$20 per cent, while electron impact of CO_2 and CO together contributes $\sim$65 per cent to the total Cameron-band emission. When the CO abundance is doubled to 1 per cent of water, the relative contribution due to electron impact on CO increases, resulting in the reduction (by $\sim$1 per cent) of the requirement for CO_2 abundance to match the *HST*-observed brightness. However, there is no major change in percentage contribution due to photodissociation and photoelectron impact excitation of CO and CO_2. Hence, we conclude that photodissociative excitation of CO_2 is not the dominant source for the production of the Cameron band in comets.

4 SUMMARY

The summary of Table 3 and the above results is that whatever are the relative abundances of CO_2 and CO, and the solar input flux, the photodissociation contribution is in the range of 5–20 per cent, while the photoelectron impact excitation contribution is about 50–80 per cent. We conclude that photoelectron impact excitation of the Cameron band in comets is much more important than was thought previously. Further, the contribution due to photoelectron impact excitation of CO is significant and varies between 20 and 50 per cent. We have also shown that dissociative recombination of the CO_2^+ ion is a significant source of the Cameron band at cometocentric distances $\geq$1000 km with a contribution of as high as 30 per cent. Hence, the derivation of CO_2 abundances based on the assumption that photodissociation of CO_2 is a major mechanism should be revisited. The results presented in this Letter suggest that Cameron-band emission may not be used to probe the cometary CO_2 abundance uniquely.

5 PREDICTION

The *EPOXI* mission will encounter comet 103P/Hartley 2 on 2010 November 4 when the comet will be at a heliocentric distance of 1.06 au and geocentric distance of 0.15 au. In the present solar minimum period, using our model, we have estimated the intensity of the Cameron band around the mission-encounter date by taking the solar flux on 2010 September 1 for both the EUVAC and the S2K solar flux models. The calculated Cameron-band intensity is tabulated in Table 3 for the relative abundance of 4 per cent of CO_2 and 0.5 per cent of CO. For the EUVAC solar flux, the predicted height-integrated column intensity of the Cameron band is 1365 Rayleigh, in which 1–0, 0–0 and 0–1 band transitions contribute 189, 142 and 200 Rayleigh, respectively. Fig. 3 presents the total Cameron-band predicted brightness profile as a function of projected distances from the nucleus. For the same relative abundances of CO_2 and CO and the solar S2K flux, the predicted intensity is 1258 Rayleigh. The results presented in this Letter will help in understanding and interpreting the extensive data to be obtained during the *EPOXI* encounter period.

ACKNOWLEDGMENTS

SR was supported by an ISRO Research Fellowship.

REFERENCES

Bhardwaj A., 1999, J. Geophys. Res., 104, 1929

Bhardwaj A., 2003, Geophys. Res. Lett., 30, 2244

Bhardwaj A., Jain S. K., 2009, J. Geophys. Res., 114, A11309

Bhardwaj A., Haider S. A., Singhal R. P., 1990, Icarus, 85, 216

Bhardwaj A., Haider S. A., Singhal R. P., 1996, Icarus, 120, 412

Bhardwaj A., Michael M., 1999a, J. Geophys. Res., 104, 713

Bhardwaj A., Michael M., 1999b, Geophys. Res. Lett., 26, 393

Boice D. C. et al., 1986, Geophys. Res. Lett., 13, 381

Campbell L., Brunger M. J., 2009, Geophys. Res. Lett., 36, L03101

Capria M. T. et al., 2008, A&A, 479, 257

Colangeli L. et al., 1999, A&A, 343, L87

Conway R. R., 1981, J. Geophys. Res., 86, 4767

Crovisier J. et al., 1999, in Cox P., Kessler M. F., eds, ESA-SP 427, The Universe as Seen by ISO. ESA, Noordwijk, p. 161

Feldman P. D. et al., 1997, ApJ, 475, 829

Feldman P. D., Lupu R. E., McCandliss S. R., Weaver H. A., 2009, ApJ, 699, 1104

Gilijamse J. J. et al., 2007, J. Chem. Phys., 127, 221102

Groussin O., Lamy P., Jorda L., Toth I., 2004, A&A, 413, 1163

Haider S. A., Bhardwaj A., 2005, Icarus, 177, 196

Huebner W. F., Keady J. J., Lyon S. P., 1992, Ap&SS, 195, 1

Ip W. H., 1986, Adv. Space Res., 5, 47

Jackman C. H., Garvey R. H., Green A. E. S., 1977, J. Geophys. Res., 82, 5081

Körösmezey A. et al., 1987, J. Geophys. Res., 92, 7331

Lawrence G. M., 1972, J. Chem. Phys., 56, 3435

Lisse C. et al., 2009, PASP, 121, 968

McPhate J. B., Feldman P. D., McCandliss S. R., Burgh E. B., 1999, ApJ, 521, 920

Nicholls R. W., 1962, J. Quant. Spectrosc. Radiat. Transfer, 2, 433

Richards P. G., Fennelly J. A., Torr D. G., 1994, J. Geophys. Res., 99, 8981

Rosati R. E., Johnsen R., Golde M. F., 2003, J. Chem. Phys., 119, 11630

Rosati R. E., Skrzypkowski M. P., Johnsen R., Golde M. F., 2007, J. Chem. Phys., 126, 154302

Sahnow D. J., Feldman P. D., McCandliss S. R., Marinez M. E., 1993, Icarus, 101, 71

Schmidt H. U., Wegmann R., Huebner W. F., Boice D. C., 1988, Comput. Phys. Commun., 49, 17

Seiersen K. et al., 2003, Phys. Rev. A, 68, 022708

Shunk R. W., Nagy A. F., 2009, Ionospheres – Physics, Plasma Physics, and Chemistry. Cambridge Univ. Press, Cambridge

Skrzypkowski M. P., Gougousi T., Johnsen R., Golde M. F., 1998, J. Chem. Phys., 108, 8400

Snodgrass C., Lowry S. C., Fitzsimmons A., 2008, MNRAS, 385, 737

Snodgrass C., Meech K., Hainaut O., 2010, A&A, 516, L9

Tobiska W. K. et al., 2000, J. Atmos. Sol.-Terr. Phys., 62, 1233

Tozzi G. P., Feldman P. D., Festou M. C., 1998, A&A, 330, 753

Weaver H. A., Feldman P. D., McPhate J. B., 1994, ApJ, 422, 374

Wysong I. J., 2000, Chem. Phys. Lett., 42, 329

This paper has been typeset from a TEX/LATEX file prepared by the author.

Planetary and Space Science 63–64 (2012) 139–149

Contents lists available at SciVerse ScienceDirect

Planetary and Space Science

journal homepage: www.elsevier.com/locate/pss

Model for the production of CO Cameron band emission in Comet 1P/Halley

Susarla Raghuram, Anil Bhardwaj *

Space Physics Laboratory, Vikram Sarabhai Space Centre, Trivandrum 695022, India

ARTICLE INFO

Article history:
Received 26 April 2011
Received in revised form
21 October 2011
Accepted 16 November 2011
Available online 3 December 2011

Keywords:
CO molecule
Comet 1P/Halley
Cameron band emission
UV emission
Photochemistry

ABSTRACT

The abundance of CO_2 in comets has been derived using CO Cameron band ($a^3\Pi \rightarrow X^1\Sigma^+$) emission assuming that photodissociative excitation of CO_2 is the main production process of CO($a^3\Pi$). On comet 1P/Halley the Cameron (1-0) band has been observed by International Ultraviolet Explorer (IUE) on several days in March 1986. A coupled chemistry–emission model is developed for comet 1P/Halley to assess the importance of various production and loss mechanisms of CO($a^3\Pi$) and to calculate the intensity of Cameron band emission on different days of IUE observation. Two different solar EUV flux models, EUVAC of Richards et al. (1994) and SOLAR2000 of Tobiska (2004), and different relative abundances of CO and CO_2, are used to evaluate the role of photon and photoelectron in producing CO molecule in $a^3\Pi$ state in the cometary coma. It is found that in comet 1P/Halley 60–70% of the total intensity of the Cameron band emission is contributed by electron impact excitation of CO and CO_2, while the contribution from photodissociative excitation of CO_2 is small (20–30%). Thus, in the comets where CO and CO_2 relative abundances are comparable, the Cameron band emission is largely governed by electron impact excitation of CO, and not by the photodissociative excitation of CO_2 as assumed earlier. Model calculated Cameron band 1-0 emission intensity (40 R) is consistent with the observed IUE slit-averaged brightness (37 ± 6 R) using EUVAC model solar flux on 13 March 1986, and also on other days of observations. Since electron impact excitation is the major production mechanism, the Cameron emission can be used to derive photoelectron density in the inner coma rather than the CO_2 abundance.

1. Introduction

Ejecting neutral gas and dust into space, comets create extensive and unique atmospheres in the interplanetary space. Interaction of solar extreme ultraviolet (EUV) radiation with cometary species causes spectrum of different emissions. Spectroscopic observations of comets in the UV region by space-based telescopes give information about composition, abundance, and spatial distribution of neutral species in the cometary coma (e.g., Feldman et al., 2004). The number densities of CO_2 and CO in cometary coma have been derived using emissions from the dissociative products which can be produced in metastable states. Assuming photodissociative excitation is the main production mechanism in populating the $a^3\Pi$ metastable state of CO, the Cameron band ($a^3\Pi \rightarrow X^1\Sigma^+$) emission has been used to estimate the abundance of CO_2 in comets (Weaver et al., 1994, 1997; Feldman et al., 1997).

The observation of Cameron band of CO molecule in the coma of comet 103P/Hartley 2 (Weaver et al., 1994) by Hubble Space Telescope (HST) gave an incitement to re-examine the data of several comets observed by the International Ultraviolet Explorer (IUE) satellite. Cameron band (1-0) emission at 1993 Å is observed in four comets, including comet 1P/Halley, in the IUE spectra (Feldman et al., 1997). The Cameron band (0-0) and (0-1) emissions at 2063 and 2155 Å, respectively, could not be observed since they fall in the low sensitivity end of the IUE long-wavelength camera. Since the excited upper state ($a^3\Pi$) of Cameron band emission is metastable and its lifetime is very small (~ 3 ms, Gilijamse et al., 2007) compared to lifetime of CO_2 molecule (~ 135 h at 1 AU, Huebner et al., 1992), the CO($a^3\Pi$) molecule can travel a distance of few meters only in the cometary coma before de-exciting into ground state ($X^1\Sigma^+$) via emitting photons. Hence, the Cameron band emission can be used to probe CO_2 distribution, and thus its abundance in the coma, provided it is produced only through photodissociation of CO_2.

Besides photons, the solar EUV-generated photoelectrons also play a significant role in driving the chemistry of cometary species in the coma. The importance of photoelectrons in excitation, dissociation, and ionization of various cometary species and subsequent effects on emissions in the inner coma are discussed

---

* Corresponding author. Tel.: +91 471 2562330; fax: +91 471 2706535.
E-mail addresses: anil_bhardwaj@vssc.gov.in, bhardwaj_spl@yahoo.com (A. Bhardwaj).

0032-0633/$ - see front matter © 2011 Elsevier Ltd. All rights reserved.
doi:10.1016/j.pss.2011.11.011

in several works (e.g., Cravens and Green, 1978; Ip, 1985; Boice et al., 1986; Körösmezey et al., 1987; Bhardwaj et al., 1990, 1996; Haider et al., 1993; Häberli et al., 1996; Bhardwaj, 1999, 2003; Haider and Bhardwaj, 2005; Campbell and Brunger, 2009; Feldman et al., 2009; Bhardwaj and Raghuram, 2011a,b). To explain the Cameron band emission in comet 103P/Hartley 2, Weaver et al. (1994) considered five possible production mechanisms of CO($a^3\Pi$) molecule. The modelled Cameron band emission of CO molecule by Weaver et al. (1994) suggested that 60% of total CO($a^3\Pi$) production can be through photodissociative excitation of CO_2; the remaining was attributed to other excitation processes. Feldman et al. (1997) assumed that photodissociative excitation of CO_2 is the only source of Cameron band emission in comet 1P/Halley. Recent calculations of Bhardwaj and Raghuram (2011a) have demonstrated that in the comet 103P/Hartley 2, 60–90% of CO($a^3\Pi$) production is through the photoelectron impact of CO_2 and CO and that the contribution of photodissociation of CO_2 is quite small. The derived rates of electron impact dissociation of CO_2 producing CO($a^3\Pi$) by Feldman et al. (2009) show that the photodissociation can be comparable with the electron impact excitation in producing Cameron band emission. However, the comet 103P/Hartley 2 is depleted in CO (relative abundance $<1\%$). But in the case of comet 1P/Halley the CO abundance is relatively higher compared to that on the 103P/Hartley 2, and hence the contribution due to direct excitation of CO by electron impact would be much larger.

There are several observations of CO in comet 1P/Halley, as well as in other comets, which suggest that CO is produced directly from the nucleus as well as having prevailed distributed sources in the cometary coma (Eberhardt et al., 1987; Eberhardt, 1999; DiSanti et al., 2003; Cottin and Fray, 2008). The measured number density of CO by neutral mass spectrometer on Giotto spacecraft, which flew through the coma of 1P/Halley, is $\leq 7\%$ relative to water at 1000 km cometocentric distance. This relative abundance is higher ($\leq 15\%$) at larger distances (2×10^4 km) in the coma (Eberhardt et al., 1987; Eberhardt, 1999; Festou, 1999). This increase in abundance can be explained by dissociation of CO-bounded species and also through heating of several refractory grains by sunlight. Other cometary species like H_2CO, C_3O_2, POM (polyoxymethylene, or polyformaldehyde), CH_3OH, and CO_2 can also produce CO molecules in photodissociation process (see Greenberg and Li, 1998; Cottin and Fray, 2008, and references therein). However, there are no literature reports on the production of CO($a^3\Pi$) from CO-bearing species, like H_2CO, CH_3OH, and C_3O_2, via photodissociation or electron impact dissociative excitation.

Reanalysis of the IUE data on comet 1P/Halley showed five observations of the Cameron 1-0 band emission, which span over a 10-day period on March 1986; the intensity of 1-0 emission varied by a factor of about 4 from lowest value of 20 ± 6 to highest value of 65 ± 9 Rayleighs (Feldman et al., 1997). Assuming that the production of Cameron band emission is only through photodissociation of CO_2, Feldman et al. (1997) derived the CO_2 abundances of ~2–6%, and also the CO_2/CO abundance ratio.

The production of CO($a^3\Pi$) is mainly associated with spatial distribution of CO_2 and CO molecules in the coma. We have recently developed a model for the chemistry of CO($a^3\Pi$) on comet 103P/Hartley 2 (Bhardwaj and Raghuram, 2011a). In the present paper this coupled chemistry model has been employed to study the production of Cameron band emissions on comet 1P/Halley. The contributions of major production and loss processes of CO($a^3\Pi$) in comet 1P/Halley are evaluated for different relative abundances of CO and CO_2.

The photochemistry in the cometary coma is driven by solar UV–EUV radiation. The solar UV flux is known to vary considerably both with the 27-day solar rotation period and with the 11-year solar activity cycle. Since the continuous measurements of solar EUV fluxes are not available for different cometary observations, one has to depend on the empirical solar EUV models. To assess the impact of solar EUV flux on the calculated brightness of Cameron band emission we have taken two most commonly used solar EUV flux models, namely EUVAC model of Richards et al. (1994) and SOLAR2000 v.2.3.6 (S2K) model of Tobiska (2004). The solar EUV fluxes from these two models on 13 March 1986 are shown in Fig. 1.

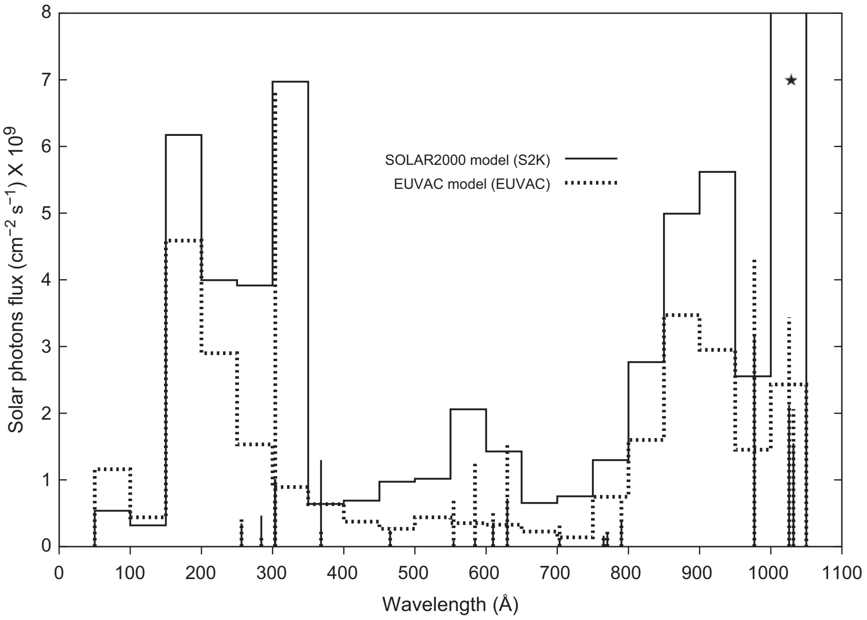

Fig. 1. Solar EUV fluxes from EUVAC model (Richards et al., 1994) and SOLAR2000 (S2K) model (Tobiska, 2004) for the day 13 March 1986. Significant differences in the two model solar EUV fluxes can be noticed. (★) The value of solar flux in SOLAR2000 model for the bin 1000–1050 Å is 30×10^9 cm^{-2} s^{-1}.

This paper will demonstrate that in comets where CO_2 and CO relative abundances are comparable, the photoelectron impact excitation of CO plays a major role in controlling the brightness of Cameron band, and not the photodissociation of CO_2 as assumed previously. Since the Cameron band emission is forbidden and electron impact is the major excitation mechanism, this emission is suitable to track photoelectron flux in the inner cometary coma rather than the CO_2 abundance. We have also studied the sensitivity of calculations associated with the variation in input solar flux and electron impact excitation cross-sections of CO_2 and CO in estimating the intensity of Cameron band emission.

2. Model

The neutral parent species considered in the model are H_2O, CO_2, and CO. The density of neutral parent species in the coma is calculated using Haser's formula, which assumes spherical distribution of gaseous environment around the nucleus. The number density $n_i(r)$ of ith species in the coma at a cometocentric distance r is given by

$$n_i(r) = \frac{f_i Q_p}{4\pi v_i r^2}(e^{-\beta_i/r}) \tag{1}$$

Here Q_p is the total gas production rate of the comet, v_i is the average velocity of neutral species taken as 1 km s^{-1}, β_i is the scale length ($\beta_{H_2O} = 8.2 \times 10^4$ km, $\beta_{CO_2} = 5.0 \times 10^5$ km, and $\beta_{CO} = 1.4 \times 10^6$ km) and f_i is the fractional abundance of ith species. Calculations are made for comet 1P/Halley taking the total gas production rate as 6.9×10^{29} s^{-1}, which has been observed by Krankowsky et al. (1986). Since the cometary coma is dominated by water, 80% of total production rate is assumed to be H_2O.

The in situ gas measurements at comet 1P/Halley made by Giotto Neutral Mass Spectrometer (NMS) on the encounter date 13 March 1986 showed that CO_2 abundance is 3.5% of water (Krankowsky et al., 1986). On the same day, based on IUE observation, Feldman et al. (1997) derived CO_2 abundance of 4.3%. Eberhardt et al. (1987) suggested that below 1000 km, nuclear rate of CO production can be 7% of water. The radial profile of CO calculated by Eberhardt et al. (1987) showed almost a constant value of CO relative abundance ($\leq 15\%$) above 15,000 km. This increase in CO abundance is attributed to the presence of an extended source for CO in the cometary coma. The IUE-derived average production rate of CO is 4.7% (Feldman et al., 1997). We have taken 4% CO_2 and 7% CO directly coming from nucleus as the standard input for the model. We have also considered extended CO density profile directly from Giotto NMS observation (Eberhardt et al., 1987). Further, the relative abundances of CO_2 and CO are varied to assess the effect on the intensity of Cameron band emission and different production channels of CO($a^3\Pi$).

The primary photoelectron energy spectrum $Q(E,r,\theta)$, at energy E, cometocentric distance r, and solar zenith angle θ, is calculated by degrading the solar UV–EUV radiation in the cometary coma using the following equation

$$Q(E,r,\theta) = \sum_i \int_\lambda n_i(r)\sigma_i^I(\lambda) I_\infty(\lambda) \exp[-\tau(r,\theta,\lambda)]\, d\lambda \tag{2}$$

where,

$$\tau(r,\theta,\lambda) = \sum_i \sigma_i^A(\lambda) \sec\theta \int_r^\infty n_i(r')\, dr' \tag{3}$$

Here $\sigma_i^A(\lambda)$ and $\sigma_i^I(\lambda)$ are the photoabsorption and photoionization cross-sections, respectively, of the ith species at wavelength λ, $n_i(r)$ is its neutral gas density calculated using Eq. (1), and $\tau(r,\theta,\lambda)$ is the optical depth of the medium. $I_\infty(\lambda)$ is the unattenuated solar flux at the top of atmosphere at wavelength λ. All calculations are made at the solar zenith angle 0^0. The photoabsorption and photoionization cross-sections of H_2O, CO_2, and CO are taken from Shunk and Nagy (2009).

The steady state photoelectron fluxes are calculated using the Analytical Yield Spectrum (AYS) approach, which is based on the Monte Carlo method. Details of the AYS approach are given in several of the previous papers (Singhal and Haider, 1984;

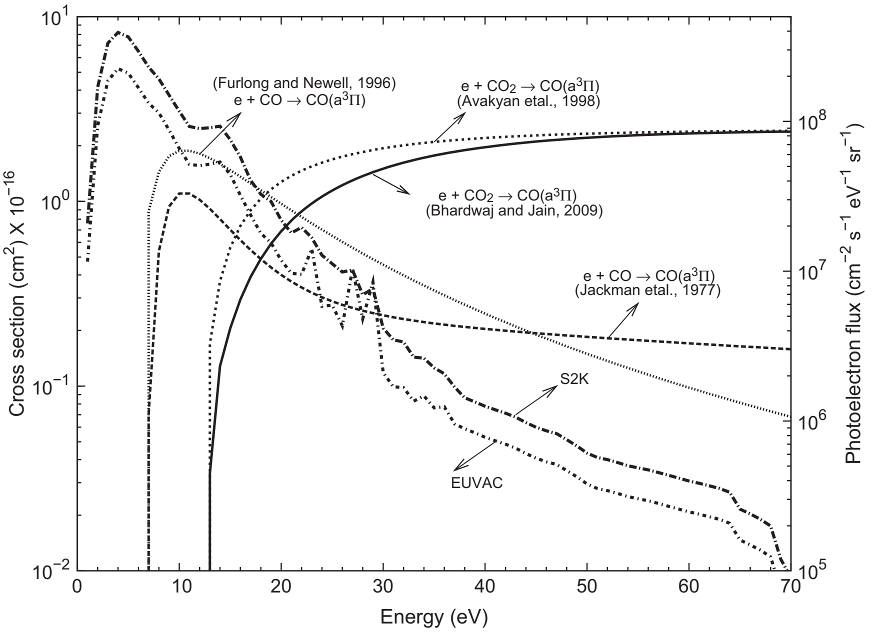

Fig. 2. Cross-sections for electron impact excitation of CO($a^3\Pi$) from CO and CO_2. Calculated photoelectron flux at cometocentric distance of 1000 km is also shown for both SOLAR2000 (S2K) and EUVAC model solar fluxes with magnitude on right side y-axis.

Bhardwaj et al., 1990, 1996; Singhal and Bhardwaj, 1991; Bhardwaj and Singhal, 1993; Bhardwaj, 1999, 2003; Bhardwaj and Michael, 1999a,b; Haider and Bhardwaj, 2005; Bhardwaj and Jain, 2009). We have used the two dimensional yield spectra to calculate the photoelectron flux $f_p(E,r)$ as a function of energy E and cometocentric distance r

$$f_p(E,r) = \int_w^{\infty} \frac{Q(E,r,\theta)U^c(E,E_o)}{\sum n_i(r)\sigma_{iT}(E)} \tag{4}$$

where $Q(E,r,\theta)$ is the primary photoelectron production rate calculated using Eq. (2). $\sigma_{iT}(E)$ is the total inelastic electron impact cross-section at energy E for the ith species whose number density is $n_i(r)$. The lower limit of integration w is minimum excitation energy and $U^c(E,E_0)$ is the two dimensional composite yield spectra (Singhal and Haider, 1984; Bhardwaj et al., 1990). The total inelastic electron impact cross-sections for water are taken from Rao et al. (1995), and those for CO_2 and CO are taken from Jackman et al. (1977).

The loss process of photoelectrons through collisions with thermal electrons is considered using the following formula

$$n_e \sigma_{e-e}^{eff} = \frac{n_e \beta(E,n_e,T)}{E\overline{W}} \tag{5}$$

where n_e is the thermal electron density, E is the energy of photoelectron, and $\overline{W}$ is the average energy lost per collision between photoelectron and the thermal electron. The expression β is given by McCormick et al. (1976). More details are provided in Bhardwaj et al. (1990). The calculated photoelectron fluxes for the two solar EUV flux models at 1000 km are shown in Fig. 2.

The electron impact volume production rates of different ions from neutral species and volume excitation rates for $CO(a^3\Pi)$ state from CO_2 and CO are calculated using photoelectron flux $f_p(E,r)$ and electron impact excitation cross-section σ_{ik} of ith species and kth state as

$$V(r) = n_i(r) \int_w^{100} f_p(E,r)\sigma_{ik}(E)\, dE \tag{6}$$

The cross-sections for electron impact dissociative ionization of water are taken from Itikawa and Mason (2005), for CO_2 from Bhardwaj and Jain (2009), and for CO from McConkey et al. (2008).

Table 1 presents the reactions involved in the production and loss of $CO(a^3\Pi)$. Huebner et al. (1992) calculated the cross-section for photodissociative excitation of CO_2 producing CO in $a^3\Pi$ state using total absorption cross-section and the yield measured by Lawrence (1972). We averaged these cross-section values over 50 Å bin intervals to calculate the photodissociative excitation rate using solar flux from EUVAC and S2K models; this cross-section is shown in Fig. 3. The cross-section for electron impact excitation of CO in the $a^3\Pi$ state is taken from Jackman et al. (1977) and for dissociative excitation of CO_2 producing $CO(a^3\Pi)$ is taken from Bhardwaj and Jain (2009). These cross-sections are presented in Fig. 2. To estimate the effect of electron impact cross-sections on emissions, we have used the electron impact cross-sections recommended by Avakyan et al. (1998) for the above two processes, which are also shown in Fig. 2. The electron temperature profile, required for dissociative recombination reactions, is taken from Körösmezey et al. (1987).

3. Results and discussions

3.1. Cameron band emission

The first clear observation of Cameron band emission of CO molecule is made in comets 103P/Hartley 2 and C/1992 T2 Shoemaker-Levy by HST (Weaver et al., 1994), which was followed by detection in several other comets, including 1P/Halley, in the IUE reprocessed data (Feldman et al., 1997). Assuming that the photodissociative excitation of CO_2 is the major production mechanism of Cameron band emission, Weaver et al. (1994) derived the abundance of CO_2 in comet 103P/Hartley 2. Recently, Bhardwaj and Raghuram (2011a) have demonstrated that on comet 103P/Hartley 2 the photoelectron impact dissociative excitation of CO_2 followed by photoelectron impact of CO are the major production processes of Cameron band, and not the photodissociative excitation of CO_2 as suggested by Weaver et al. (1994).

Since comet 103P/Hartley 2 is CO depleted (relative abundance $\leq 1\%$), the contribution to Cameron band emission through dissociative excitation of CO_2 by EUV-generated photoelectrons is more important. However, in case of comets where CO abundance is larger, like 1P/Halley, the contribution of CO to the Cameron band emission would be significant. The derived CO_2/CO abundance ratios for several IUE observations of comet

Table 1
Reactions for the production and loss of $CO(a^3\Pi)$.

Reaction	Rate ($cm^3\ s^{-1}$ or s^{-1})	Reference
$CO_2 + h\nu \rightarrow CO(a^3\Pi) + O(^3P)$	Model	*Present work*
$CO + h\nu \rightarrow CO(a^3\Pi)$	1.69×10^{-9}	Weaver et al. (1994)
$CO_2 + e^-_{ph} \rightarrow CO(a^3\Pi) + O + e^-$	Model	*Present work*
$CO + e^-_{ph} \rightarrow CO(a^3\Pi) + e^-$	Model	*Present work*
$CO_2^+ + e^- \rightarrow CO(a^3\Pi) + O$	K_a[a]	Seiersen et al. (2003) and Rosati et al. (2003)
$HCO^+ + e^- \rightarrow CO(a^3\Pi) + H$	K_b[b]	Rosati et al. (2007) and Schmidt et al. (1988)
$CO(a^3\Pi) + h\nu \rightarrow C + O$	7.2×10^{-5}	Huebner et al. (1992)
$CO(a^3\Pi) + h\nu \rightarrow CO^+ + e^-$	8.58×10^{-6}	Huebner et al. (1992)
$CO(a^3\Pi) + h\nu \rightarrow O + C^+ + e^-$	2.45×10^{-8}	Huebner et al. (1992)
$CO(a^3\Pi) + h\nu \rightarrow C + O^+ + e^-$	2.06×10^{-8}	Huebner et al. (1992)
$CO(a^3\Pi) + H_2O \rightarrow CO + H_2O$	3.3×10^{-10}	Wysong (2000)
$CO(a^3\Pi) + CO_2 \rightarrow CO + CO_2$	1.0×10^{-11}	Skrzypkowski et al. (1998)
$CO(a^3\Pi) + CO \rightarrow CO + CO$	5.7×10^{-11}	Wysong (2000)
$CO(a^3\Pi) + e^-_{ph} \rightarrow CO^+ + 2e^-$	Model	*Present work*
$CO(a^3\Pi) \longrightarrow CO + h\nu$	1.26×10^2	Lawrence (1972)

[a] $K_a = 6.5 \times 10^{-7}\ (300/Te)^{0.8} \times 0.87 \times 0.29\ cm^3\ s^{-1}$; here 0.87 is yield of dissociative recombination of CO_2^+ producing CO, and 0.29 is yield of $CO(a^3\Pi)$ produced from CO.

[b] $K_b = 2.4 \times 10^{-7}\ (300/Te)^{0.7} \times 0.23\ cm^3\ s^{-1}$; here 0.23 is yield of dissociative recombination of HCO^+ producing $CO(a^3\Pi)$, e^-_{ph} = photoelectron.

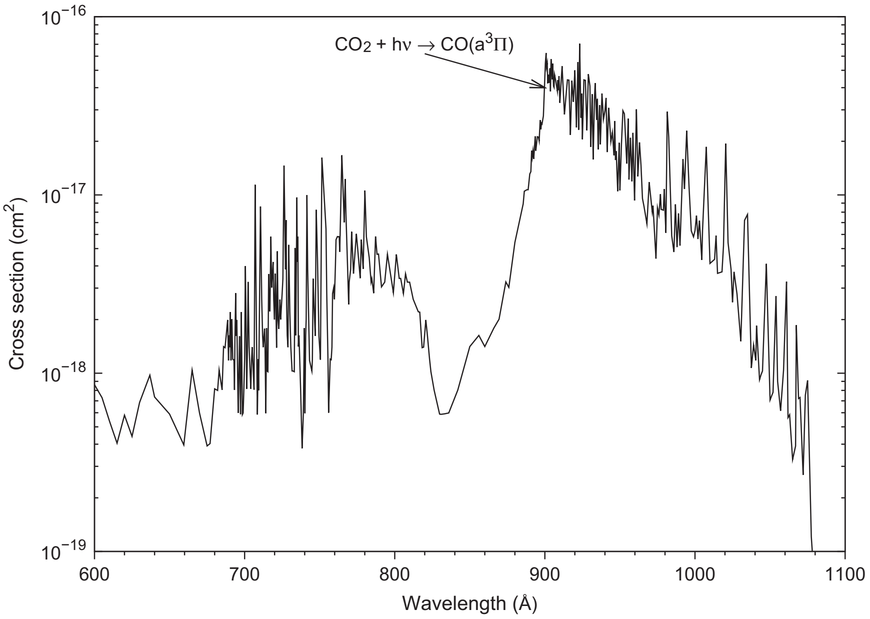

Fig. 3. Photodissociative excitation cross-section of CO_2 producing $CO(a^3\Pi)$, taken from Huebner et al. (1992).

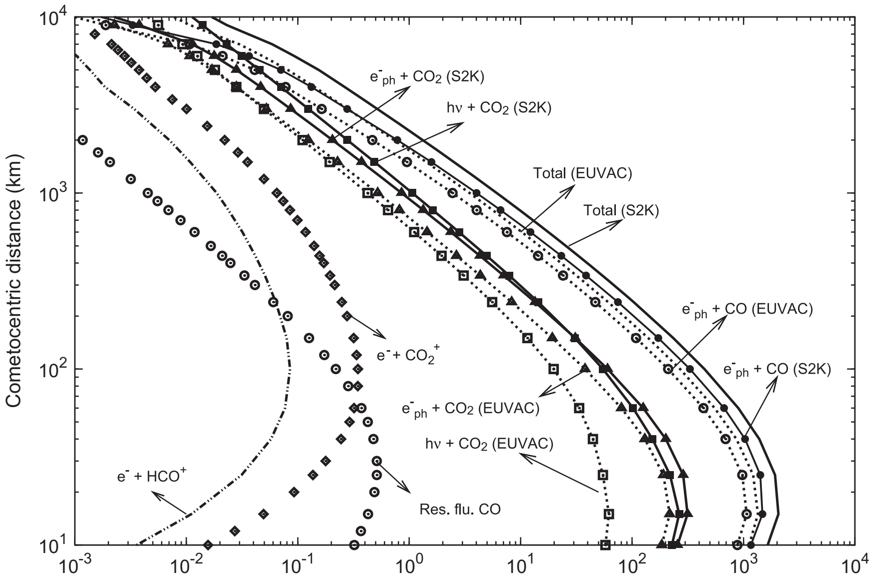

Fig. 4. Radial profiles of various production mechanisms of $CO(a^3\Pi)$ in comet 1P/Halley on 13 March 1986 for relative abundance of 4% CO_2 and 7% CO. The calculated profiles for dissociative recombination of CO_2^+ and HCO^+, and resonance fluorescence of CO are shown for EUVAC solar flux only. Res. flu. = resonance fluorescence of CO molecule. e^-_{ph} = photoelectron, $h\nu$ = solar photon, and e^- = thermal electron.

1P/Halley showed that the abundance of CO can be even double that of CO_2 (Feldman et al., 1997).

The calculated production rate profiles of $CO(a^3\Pi)$ using solar EUVAC and S2K models for relative abundance of 4% CO_2 and 7% CO are shown in Fig. 4. For both solar EUV flux models, the peak production rate occurs at cometocentric distance ~20 km. The major production mechanism of $CO(a^3\Pi)$ is the photoelectron impact of CO, whose contribution is ~70% to the total $CO(a^3\Pi)$ production. On using the S2K solar flux, the calculated total production rate is 1.5 times larger than that obtained using the EUVAC flux. This variation is mainly due to the difference in the input solar EUV flux (cf. Fig. 1) and subsequently EUV-generated photoelectron flux (cf. Fig. 2). In the wavelength region 700–1050 Å, the S2K model solar flux is a factor of ~2.5 larger than the EUVAC model (cf. Fig. 1). As shown in Fig. 3, the photodissociative excitation cross-section of CO_2 producing $CO(a^3\Pi)$

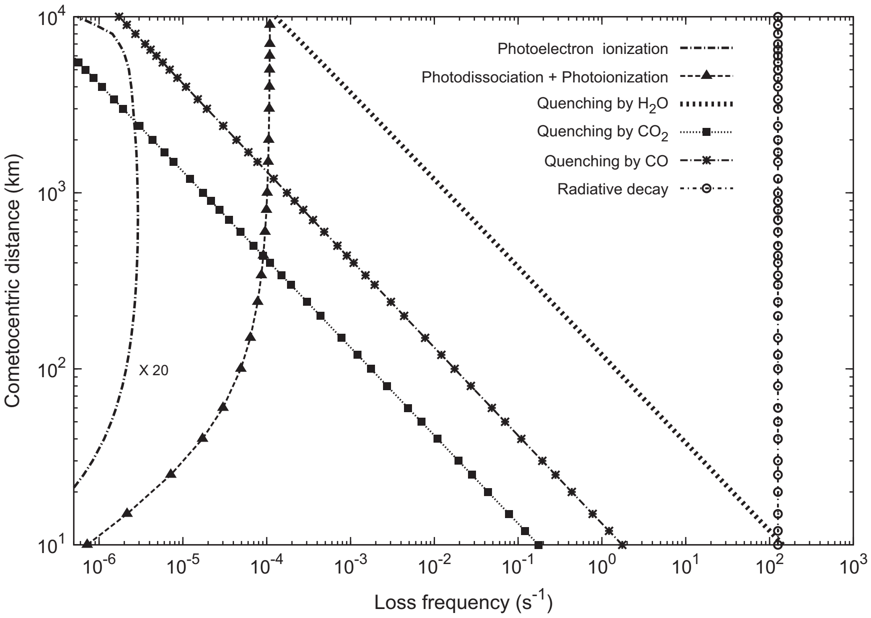

Fig. 5. Radial profiles of various loss mechanisms of CO($a^3\Pi$) for 4% CO_2 and 7% CO relative abundances using EUVAC solar flux. Photoelectron impact ionization of CO($a^3\Pi$) is plotted after multiplying by a factor 20.

maximizes around 880–1000 Å. Further, the S2K solar flux in the 1000–1050 Å wavelength bin is around 20 times higher than the EUVAC flux. The average cross-section value for photodissociation of CO_2 producing CO($a^3\Pi$) in the wavelength region 1000–1050 Å is comparable with the peak value around 900 Å (cf. Fig. 3).

Moreover, in the inner cometary coma, below cometocentric distance of 50 km, the optical depth for solar flux at wavelengths below 200 Å and above 1000 Å is smaller compared to other wavelengths because of smaller absorption cross-sections of neutral species (mainly water). The rate of photodissociative excitation of CO_2 molecule into CO($a^3\Pi$) mainly depends on the degradation of solar flux in the wavelength region 850–1050 Å. Hence, in the innermost coma (≤ 50 km), for a given relative abundance of CO_2, the production rate of CO($a^3\Pi$) via photodissociation of CO_2 is determined by the solar flux in the wavelength bin 1000–1050 Å and at wavelengths 1025.7 Å (H I) and 1031.9 Å (O VI). The calculated photodissociation rates of CO_2 producing CO($a^3\Pi$) at 0.9 AU are 1.66×10^{-7} s^{-1} and 5.28×10^{-7} s^{-1} using EUVAC and S2K solar fluxes, respectively, on 13 March 1986.

From Fig. 2 it is seen that the calculated steady state photoelectron flux using two solar flux models differ in magnitude by a factor of 2. Since the cross-section for electron impact of CO producing CO($a^3\Pi$) peaks at lower energies (~ 10 eV) where the photoelectron flux is also high ($\sim 10^8$ cm^{-2} s^{-1} eV^{-1} sr^{-1}; cf. Fig. 2), the electron impact excitation of CO is a major production source of Cameron band emission. At larger (> 5000 km) cometocentric distances, due to decrease in photoelectron flux, the photodissociative excitation of CO_2 starts becoming an increasingly important process (cf. Fig. 4). Contributions from dissociative recombination reactions and resonance fluorescence of CO are more than two orders of magnitude lower compared to major production processes.

Since the lifetime of CO($a^3\Pi$) is about ~ 3 ms, the quenching of the excited $a^3\Pi$ metastable state by various cometary species is not very efficient. The calculated loss rate profiles of CO($a^3\Pi$) for various processes are shown in Fig. 5. The radiative de-excitation is the main loss process. Very close to the nucleus, the loss due to quenching of CO($a^3\Pi$) by water is comparable to the radiative de-excitation. Quenching by water molecule would be a more significant loss process of CO($a^3\Pi$) in the higher water production rate comets, like Hale–Bopp or when the comet is much closer to the Sun than 1 AU. The calculated number density profile of CO($a^3\Pi$) is shown in Fig. 6. Above 100 km, the density profile of CO($a^3\Pi$) mostly following the number density profiles of the parent species CO_2 and CO.

The above calculated total production rate is integrated up to 10^5 km to obtain the height-integrated column intensity of Cameron band emission which is presented in Table 2. We also calculated the line of sight intensity at a given projected distance z from the cometary nucleus using production rates of different excitation processes of CO($a^3\Pi$) as

$$I(z) = 2\int_z^R V(s)\,ds \tag{7}$$

where s is the abscissa along the line of sight and $V(s)$ is the corresponding emission rate. The maximum limit of integration R is taken as 10^5 km. These brightness profiles are then averaged over the projected area $6600 \times 11{,}000$ km^2 corresponding to the IUE slit dimension $9.07'' \times 15.1''$ centred on nucleus of comet 1P/Halley on 13 March 1986 at geocentric distance 0.96 AU. The volume emission rate for three transitions (0-0, 1-0, and 0-1) of the Cameron band are calculated using the following formula

$$V_{v'v''}(r) = q_{ov'}\left(A_{v'v''}\Big/\sum_{v''} A_{v'v''}\right)V(r)\exp(-\tau) \tag{8}$$

where $V(r)$ is the total volume excitation rate of CO($a^3\Pi$) at a given cometocentric distance r, given by Eq. (6), $q_{ov'}$ is the Franck–Condon factor for transition, $A_{v'v''}$ is the Einstein transition probability from upper state v' to lower state v'', and τ is the optical depth. Since resonance fluorescence is not an effective excitation mechanism for the Cameron band, the cometary coma can be safely assumed to be optically thin. The Franck–Condon factors are taken from Nicholls (1962) and the branching ratios from Conway (1981).

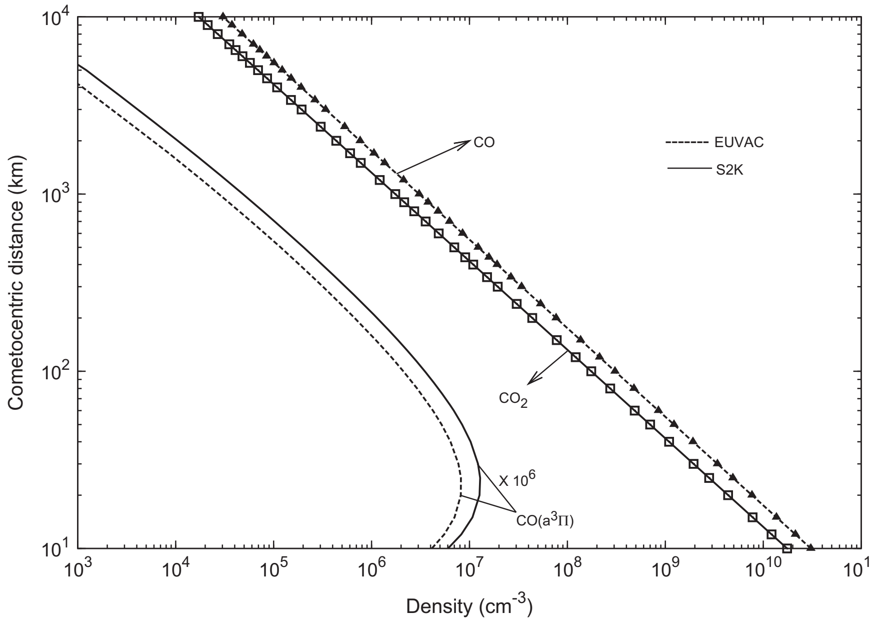

Fig. 6. The calculated radial profiles of number density CO($a^3\Pi$) for SOLAR2000 (S2K) and EUVAC solar flux models. The density of CO($a^3\Pi$) is plotted after multiplying by a factor 10^6. The number density profiles of CO_2 and CO are also shown for 4% and 7% relative abundances, respectively.

Table 2
Calculated brightness of the Cameron band at comet 1P/Halley for different conditions on 13 March 1986.

Relative abundance		IUE-slit averaged brightness (R)			Percentage contribution to total Cameron band for different processes at three different projected radial distances (km)												Total Cameron band brightness (R)	
CO_2 (%)	CO (%)				$h\nu+CO_2$			$e^-_{ph}+CO_2$			$e^-_{ph}+CO$			$e^-+CO_2^+$			IUE-slit averaged	Height integrated column
		(1-0)[a]	(0-0)	(0-1)	10^2	10^3	10^4	10^2	10^3	10^4	10^2	10^3	10^4	10^2	10^3	10^4		
EUVAC																		
4	Ext[b]	59	44	63	9	14	52	15	15	11	74	66	25	0.5	2	5	430	10 946
4	7	51	38	54	9	15	65	14	16	13	75	64	12	0.5	3	5	308	8836
3	7	46	34	48	7	12	63	11	13	12	80	70	15	0.5	2	5	331	10 626
4.3	4.7	45	34	48	11	19	69	20	21	13	68	55	9	0.5	3	6	329	9582
S2K																		
4	Ext	87	66	96	14	19	61	13	13	9	71	62	20	0.5	3	4	638	15 612
4	7	77	58	82	14	21	73	13	14	10	71	60	10	0.5	2	5	559	15 841
3	7	68	51	72	11	17	71	10	12	9	77	66	11	0.5	2	5	490	14 991
4.3	4.7	67	50	70	16	24	76	17	18	10	65	52	6	0.5	3	5	472	13 582

[a] The intensity of Cameron (1-0) band observed by IUE is 37 ± 6 Rayleighs on 13 March 1986.

[b] Ext: extended CO distribution; e^-_{ph} is photoelectron and e^- is thermal electron.

The calculated brightness profiles for each of the production processes along projected distances from nucleus are shown in Fig. 7. At 100 km projected distance, the contribution due to photoelectron impact excitation of CO to the total Cameron band intensity is about a factor 4 higher than the dissociative excitation processes of CO_2, while contributions of other production processes are around 2 orders of magnitude smaller. Around 1000 km projected distance, both photodissociative excitation and electron impact dissociative excitation of CO_2 are contributing equally to the total Cameron band intensity. The photodissociative excitation of CO_2 dominates the electron impact excitation processes above 5000 km.

The calculated relative contributions of (1-0), (0-0), and (0-1) bands to the total Cameron band are 13.9%, 10.4%, and 14.5%, respectively. The intensities of (1-0), (0-0) and (0-1) Cameron bands of CO molecule are calculated as a function of relative abundances of CO_2 and CO. The calculated percentage contributions of different production processes of Cameron band at three projected distances for two different solar flux models are presented in Table 2. The IUE-observed 1-0 Cameron band emission on 13 March 1986 is 37 ± 6 Rayleighs.

Using EUVAC solar flux as input, our model calculated 1-0 Cameron band emission intensity for the relative abundance 4% CO_2 and extended distribution of CO is 59 Rayleighs which is higher than IUE observed intensity by a factor 1.3–2. Taking CO_2 abundance as 4% and CO abundance as 7% from nucleus, the calculated 1-0 intensity is 51 Rayleighs, which is higher than the IUE-observed value by a factor 1.2–1.6. The calculated intensity for 3% CO_2 and 7% CO is 46 Rayleighs, which is consistent only with the upper limit of IUE-observed intensity. In all the above cases, below 1000 km projected distances, the contribution of photodissociation of CO_2 to the Cameron band emission is $< 15\%$, while electron impact of CO contribute 65–80%. We have also calculated the intensity of Cameron band taking the Feldman

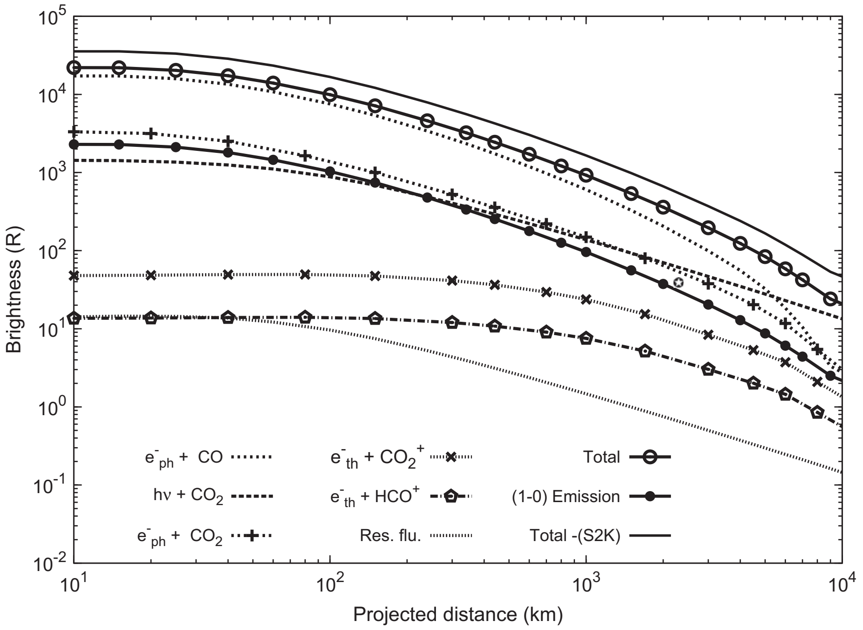

Fig. 7. The integrated Cameron band brightness profiles as a function of projected distance from nucleus for different production processes of the Cameron band, using EUVAC solar flux model and relative contribution of 4% CO_2 and 7% CO. The calculated brightness profiles for Cameron (1-0) band for EUVAC solar flux and total brightness for S2K solar flux are also shown.

Table 3
Calculated brightness of the Cameron band at comet 1P/Halley on different days of IUE observations.

Date in March 1986	r (AU)	Δ (AU)	Q_{H_2O} (10^{29} s^{-1})[a]	Derived abundances (%)[b]		Ratio Q_{CO_2}/Q_{CO}	IUE-slit averaged brightness (R)			Percentage contribution to the IUE-slit averaged total Cameron band emission for different excitation processes (%)				IUE-slit averaged total brightness (R)
				CO_2	CO		(1-0)	(0-0)	(0-1)	$h\nu+CO_2$	$e^-_{ph}+CO_2$	$e^-_{ph}+CO$	$e^-+CO_2^+$	
EUVAC														
9	0.84	1.07	7.50	6.0	6.5	0.92	75 [64 ± 9][a]	57	80	22	22	51	3	550
11	0.87	1.02	5.84	5.1	4.3	1.2	43 [43 ± 8]	32	45	25	24	44	4	310
13	0.90	0.96	5.98	4.3	4.7	0.9	40 [37 ± 6]	30	43	22	21	51	4	293
16	0.95	0.89	4.90	6.3	8.2	0.77	42 [44 ± 9]	32	45	23	20	51	4	307
18	0.97	0.84	4.92	2.8	4.1	0.68	24 [20 ± 6]	18	26	20	19	57	3	177
S2K														
9	0.84	1.07	7.50	6.0	6.5	0.92	116 [64 ± 9]	87	123	31	19	44	4	837
11	0.87	1.02	5.84	5.1	4.3	1.2	66 [43 ± 8]	49	69	33	21	39	4	475
13	0.90	0.96	5.98	4.3	4.7	0.9	62 [37 ± 6]	46	65	30	19	45	4	446
16	0.95	0.89	4.90	6.3	8.2	0.77	64 [44 ± 9]	48	68	30	18	45	4	456
18	0.97	0.84	4.92	2.8	4.1	0.68	37 [20 ± 6]	28	39	25	16	53	3	262

[a] The value in square brackets is IUE-observed (1-0) Cameron band intensity; e^-_{ph} = photoelectron, e^- = thermal electron.
[b] The production rates of H_2O and abundances of CO_2 and CO are taken from Feldman et al. (1997).

et al. (1997) derived abundances of 4.3% CO_2 and 4.7% CO. The calculated intensity of 1-0 Cameron band emission in this case is 40 R, which is consistent with the observed value of 37 ± 6 R on 13 March 1986 (cf. Table 3). The calculated 1-0 Cameron band emission intensity at various projected distances in the IUE-slit field of view is presented in Fig. 8; The circular contours and grayscale provide information on brightness variation. The calculated results using S2K solar flux model for the above discussed relative compositions of CO_2 and CO are also presented in Table 2. The calculated intensities are higher by a factor of ~1.5, which is mainly due to higher input solar flux and subsequently EUV-produced photoelectron's flux (cf. Figs. 1, 2).

Using OH 3085 Å emission observation by IUE, Tozzi et al. (1998) derived water production rates for different days of IUE observations (1986 March 9, 11, 13, 16, 18) around Giotto encounter period. The water production rate derived on 13 March 1986, the closest approach day of Giotto spacecraft, was $5.9\times10^{29}\ s^{-1}$. Feldman et al. (1997) have considered these derived production rates of H_2O to estimate relative abundances of CO_2 and CO for corresponding days of observation. We have calculated the intensity of Cameron band for different days of IUE observations taking the same H_2O, CO_2, and CO production rates as quoted in Feldman et al. (1997). The solar EUV fluxes on each day of observation were obtained by using EUVAC and S2K solar

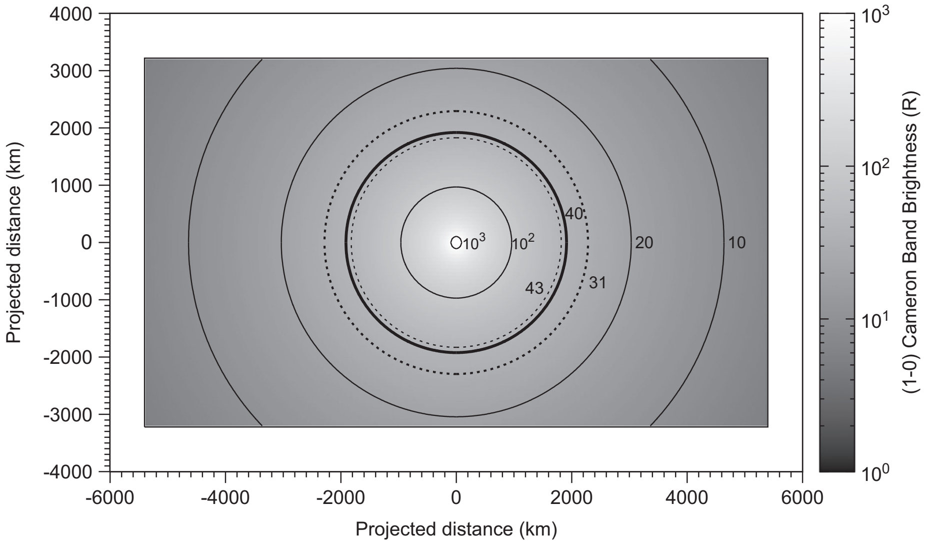

Fig. 8. The calculated (1-0) Cameron band emission brightness in the IUE projected field of view on 13 March 1986, assuming spherical symmetry, using EUVAC solar flux model, for relative contribution of 4.3% CO_2 and 4.7% CO. The rectangle represent the projected field of view corresponding to IUE slit dimension of 9.07″ × 15.1″ centred on the nucleus of comet 1P/Halley, which is 11,000 × 6600 km. The grayscale represent the calculated brightness with contours (solid lines) for 10^3, 10^2, 20, and 10 R marked in the figure. The calculated brightness averaged over IUE slit projected area (40 R) is shown by thick black contour between two dotted line contours which represent the upper and lower limit of IUE observed intensity value (37 ± 6 R).

flux models and scaling them according to the heliocentric distance of comet. The IUE projected field of view is calculated for IUE slit dimension used in observation, which vary according to the geocentric distance of the comet in March 1986. The calculated intensities of Cameron 1-0, 0-0, 0-1 bands and percentage contributions from different production process to the IUE slit-averaged brightness are presented in Table 3. The calculated intensity of 1-0 emission is consistent with the IUE-observation for the EUVAC solar flux model, while it is higher by a factor of 1.5 on using S2K solar flux. The calculations presented in Table 3 show that for a change in the CO_2/CO abundance ratio by a factor of 2, the total photoelectron impact excitation contribution changes by only $\sim 10\%$; it varies from 68% to 76% (60–69%) of the total IUE-observed intensity for EUVAC (S2K) solar flux model. The photoelectron impact excitation of CO alone contribute around 45–55% (40–60%) to the total Cameron band intensity when EUVAC (S2K) solar flux is used. The contribution of photodissociation of CO_2 to the IUE-observed Cameron band brightness is around 20% (30%) for EUVAC (S2K) solar flux model when the abundances of CO and CO_2 in the comet are almost equal. These computation show that in the IUE field of view the photoelectron is a major production source (60–75% contribution) for the Cameron band emission, whereas the contribution due to photons is small (20–35%).

The calculations presented in Tables 2 and 3 renders that in case of comets where CO_2/CO abundance ratio is closer to 1 or larger than 1, the emission intensity of Cameron band is mainly controlled by the abundance of CO in the inner cometary coma. The photoelectron impact excitation of CO is the main production mechanism for the production of Cameron band emission, but not the photodissociative excitation of CO_2 as suggested or assumed in earlier studies (Weaver et al., 1994, 1997; Feldman et al., 1997). Thus, in comets that have sufficient CO abundance the electron impact excitation of CO producing CO($a^3\Pi$) can be an efficient excitation mechanism for Cameron band emission. Since Cameron emission is mainly governed by electron impact excitation reactions, this emission can be used to track the photoelectron density mainly in the energy range 10–15 eV near the nucleus.

In the case of comet 103P/Hartley 2, which has an order of magnitude lower gas production rate and much lower CO (abundance $< 1\%$) than comet 1P/Halley, the dissociative recombination of CO_2^+ becomes a competing production mechanism at larger ($> 10^4$ km) cometocentric distances (Bhardwaj and Raghuram, 2011a). However, in comparison, on comet 1P/Halley the production rates of H_2O, CO_2, and CO are so high that the photon and photoelectron impact reactions are dominant throughout the inner cometary coma.

3.2. *Effect of electron impact cross-section*

In this section we will discuss the impact of cross-sections for electron impact excitation of CO($a^3\Pi$) from CO_2 and CO. The threshold for exciting CO molecule in the metastable $a^3\Pi$ state is 6 eV and the peak value of cross-section occurs around 10 eV (cf. Fig. 2). The cross-section for electron impact excitation of CO producing CO($a^3\Pi$) reported by Jackman et al. (1977) is theoretically fitted based on Born approximation and experimental measurements of Ajello (1971). The uncertainty associated with the measurement is about 75%. However, the uncertainty in the cross-section at energies less than 15 eV is 35% (Ajello, 1971), where the contribution of electron impact excitation plays a major role (cf. Fig. 2). The cross-section measurements of Furlong and Newell (1996) differ at the peak value of cross-section by a factor 2 (cf. Fig. 2). The threshold for dissociation of CO_2 molecule into CO($a^3\Pi$) state is 11.45 eV. Ajello (1971) measured Cameron band emission cross-sections in the wavelength region 1950–2500 Å by exciting CO_2 molecule through electron impact. Sawada et al. (1972) concluded that these cross-sections are comparable with cross-sections of 12.6 eV and 13.6 eV states. The cross-section value for CO($a^3\Pi$) production due to electron impact of CO_2 measured at 80 eV by Erdman and Zipf (1983) is 2.4×10^{-16} cm^{-2}. Bhardwaj and Jain (2009) modified the fitting parameters given by Jackman et al. (1977) for the excited states 12.6 eV and 13.6 eV of CO_2 molecule to match cross-section value measured by Erdman and Zipf (1983) at 80 eV (for more discussion on these cross-sections see Ajello, 1971; Sawada et al., 1972; Bhardwaj and Jain, 2009). Avakyan et al. (1998) corrected Ajello (1971) reported cross-sections based on measurements of Erdman and Zipf (1983). The difference in the cross-section of Avakyan et al. (1998) and Bhardwaj and Jain (2009) below 30 eV is about a factor of 2 (cf. Fig. 2).

Using electron impact CO(a$^3\Pi$) excitation cross-sections from Furlong and Newell (1996) for CO and from Avakyan et al. (1998) for CO_2, and using EUVAC solar flux, the calculated emission intensity of 1-0 Cameron band, for a given relative abundances of CO and CO_2, is larger by a factor 2. In these calculations the contribution of electron impact excitation of CO is increased from 70% to 85% at cometocentric distances below 10^3 km and 40–60% at distances above 10^3 km. On using these cross-sections, the percentage contribution of photoelectron impact excitation of CO to the total Cameron emission in the IUE slit-averaged intensity is found to increase by 10%, but there is no significant change in electron impact excitation of CO_2. In this case the contribution from photodissociative excitation of CO_2 is decreased by 10%.

4. Summary

Using the coupled chemistry–emission model a detailed study of Cameron band (a$^3\Pi \rightarrow$X$^1\Sigma^+$) emission has been carried out on the comet 1P/Halley around the Giotto encounter period. The effects of change in solar flux on the production of CO(a$^3\Pi$) and thus the Cameron band intensity have been evaluated by considering two different solar EUV flux models, viz. EUVAC model (Richards et al., 1994) and S2K (SOLAR2000) model (Tobiska, 2004). Calculations are made for different days of IUE-observation of comet 1P/Halley. The important results from the present model calculations can be summarized as follows:

- For the same day, the solar fluxes from the two models (EUVAC and S2K) are different, and the difference between them varies with wavelength.
- The production rates obtained by using S2K solar flux model are higher than that of EUVAC model. The photodissociation of CO_2 is larger by a factor of 2.5, while the photoelectron impact excitation is larger by a factor of ~ 1.5.
- The total production rate of CO(a$^3\Pi$) peaks around cometocentric distance of 20 km for both solar flux models.
- Throughout the inner coma the main loss mechanism of CO(a$^3\Pi$) is radiative decay. Very close to the nucleus (<20 km) quenching by water is also significant.
- In the inner (≤ 5000 km) coma the major production mechanism of CO(a$^3\Pi$) is photoelectron impact excitation of CO.
- On using EUVAC solar flux, and abundances of CO and CO_2 as derived from IUE-observation, the model calculated Cameron band 1-0 emission intensity (40 R) is consistent with the IUE-observed brightness (37 ± 6 R) on 13 March 1986, and also on other days of observations. However, the calculated intensities are larger by a factor 1.5 when the S2K solar EUV flux is used.
- For EUVAC (S2K) solar flux model, around 70% (65%) of the total intensity of Cameron band observed by the IUE is contributed by electron impact excitation of CO and CO_2 molecules, while the contribution from photodissociative excitation of CO_2 is about 20–30% only.
- In comets having comparable CO and CO_2 relative abundances, the intensity of Cameron band is largely determined by the photoelectron impact excitation of CO, and not the photodissociative excitation of CO_2 as suggested by earlier studies.
- Since the emission intensity of Cameron band is mainly governed by electron impact reactions, this emission may be more useful to track the photoelectron density in 10–15 eV energy region in the inner coma, rather than the CO_2 abundance.

Acknowledgements

One of the authors (SR) was supported by ISRO research fellowship during the period of this study.

References

Ajello, J.M., 1971. Emission cross sections of CO_2 by electron impact in the interval 1260–4500 Å, II. Journal of Chemical Physics 55, 3169–3177. doi:10.1063/1.1676564.

Avakyan, S.V., Il'in, R.N., Lavrov, V.M., Ogurtsov, G.N. (Eds.), 1998. Collision Processes and Excitation of UV Emission from Planetary Atmospheric Gases: A Handbook of Cross Sections. Gordon and Breach Science Publishers.

Bhardwaj, A., 1999. On the role of solar EUV, photoelectrons, and auroral electrons in the chemistry of C(^{1}D) and the production of C I 1931 Å in the inner cometary coma: a case for comet P/Halley. Journal of Geophysical Research 104, 1929–1942. doi:10.1029/1998JE900004.

Bhardwaj, A., 2003. On the solar EUV deposition in the inner coma of comets with large gas production rates. Geophysical Research Letters 30 (24). doi:10.1029/2003GL018495.

Bhardwaj, A., Singhal, R.P., 1993. Optical thin H Lyman alpha production on outer planets: low energy proton acceleration in parallel electric fields and neutral H atom precipitation from ring current. Journal of Geophysical Research 9473–9481 (98). doi:10.1029/92JA02400.

Bhardwaj, A., Haider, S.A., Singhal, R.P., 1990. Auroral and photoelectron fluxes in cometary ionospheres. Icarus 85, 216–228. doi:10.1016/0019-1035(90)90112-M.

Bhardwaj, A., Haider, S.A., Singhal, R.P., 1996. Production and emissions of atomic carbon and oxygen in the inner coma of comet 1P/Halley: role of electron impact. Icarus 120, 412–430. doi:10.1006/icar.1996.0061.

Bhardwaj, A., Jain, S.K., 2009. Monte Carlo model of electron energy degradation in a CO_2 atmosphere. Journal of Geophysical Research 114, 11309. doi:10.1029/2009JA014298.

Bhardwaj, A., Michael, M., 1999a. Monte Carlo model for electron degradation in SO_2 gas: cross sections, yield spectra and efficiencies. Journal of Geophysical Research 104 (10), 24713–24728. doi:10.1029/1999JA900283.

Bhardwaj, A., Michael, M., 1999b. On the excitation of Io's atmosphere by the photoelectrons: application of the analytical yield spectrum of SO_2. Geophysical Research Letters 26, 393–396. doi:10.1029/1998GL900320.

Bhardwaj, A., Raghuram, S., 2011a. Model for Cameron-band emission in comets: a case for the EPOXI mission target comet 103P/Hartley 2. Monthly Notices of the Royal Astronomical Society 412, L25–L29. doi:10.1111/j.1745-3933.2010.00998.x.

Bhardwaj, A., Raghuram, S., 2011. Coupled chemistry–emission model for atomic oxygen green and red-doublet emissions in comet C/1996 B2 Hyakutake. The Astrophysical Journal, in press.

Boice, D.C., Huebner, W.F., Keady, J.J., Schmidt, H.U., Wegmann, R., 1986. A model of comet P/Giacobini-Zinner. Geophysical Research Letters 13, 381–384. doi:10.1029/GL013i004p00381.

Campbell, L., Brunger, M.J., 2009. Electron impact excitation of the carbon monoxide in comet Hale–Bopp. Geophysical Research Letters 36. doi:10.1029/2008GL036641.

Cravens, T.E., Green, A.E.S., 1978. Airglow from the inner comas of comets. Icarus 33, 612–623. doi:10.1016/0019-1035(78)90193-8.

Conway, R.R., 1981. Spectroscopy of the Cameron bands in the Mars airglow. Journal of Geophysical Research 86, 4767–4775. doi:10.1029/JA086iA06p04767.

Cottin, H., Fray, N., 2008. Distributed sources in comets. Space Science Reviews. doi:10.1007/s11214-008-9399-z.

DiSanti, M., Mumma, M., Russo, N.D., Magee-Sauer, K., Griep, D., 2003. Evidence for a dominant native source of carbon monoxide in comet C/1996 B2 (Hyakutake). Journal of Geophysical Research—Planets 108f, 11–15. doi:10.1007/s11214-008-9399-z.

Eberhardt, P., 1999. Distributed sources in comets. Space Science Reviews 90, 45–52. doi:10.1023/A:1005221309219.

Eberhardt, P., Krankowsky, D., Schulte, W., Dolder, U., Lammerzahl, P., Berthelier, J.J., Woweries, J., Stubbemann, U., Hodges, R.R., Hoffman, J.H., Illiano, J.M., 1987. The CO and N_2 abundance in comet 1P/Halley. Astronomy and Astrophysics 187, 414–481.

Erdman, P.W., Zipf, E.C., 1983. Electron-impact excitation of the Cameron system ($a^3\Pi \rightarrow X^1\Sigma$) of CO. Planetary and Space Science 31, 317–321. doi:10.1016/0032-0633(83)90082-X.

Feldman, P.D., Cochran, A.L., Combi, M.R., 2004. In: Festou, M.C., Weaver, H.A., Keller, H.U. (Eds.), Spectroscopic Investigations of Fragment Species in the Coma. , University of Arizona, Tucson.

Feldman, P.D., Festou, M.C., Tozzi, G.P., Feldman, P.D., Weaver, H.A., 1997. The CO_2/CO abundance ratio in 1P/Halley and several other comets observed by IUE and HST. The Astrophysical Journal 475, 829–834. doi:10.1086/303553.

Feldman, P.D., Lupu, R.E., McCandliss, S.R., Weaver, H.A., 2009. The far ultraviolet spectral signatures of formaldehyde and carbon dioxide in comets. The Astrophysical Journal 699 (2), 1104–1112. doi:10.1088/0004-637X/699/2/1104.

Festou, M.C., 1999. Distributed sources in comets. Space Science Reviews 90, 53–67. doi:10.1023/A:1005225426057.

Furlong, J.M., Newell, W.R., 1996. Total cross section measurement for the metastable ($a^3\Pi$) state in CO. Journal of Physics B: Atomic, Molecular and Optical Physics 29, 331–338. doi:10.1088/0953-4075/29/2/020.

Gilijamse, J.J., Hoekstra, S., Meek, S.A., Metsälä, M., van de Meerakker, S.Y.T., Meijer, G., Groenenboom, G.C., 2007. The radiative lifetime of metastable CO ($a^3\Pi, v=0$). Journal of Chemical Physics 127, 221102–221104. doi:10.1063/1.2813888.

Greenberg, J.M., Li, A., 1998. From interstellar dust to comets: the extended CO source in Halley. Astronomy and Astrophysics 332, 374–384.

Häberli, R.M., Altwegg, K., Balsiger, H., Geiss, J., 1996. Heating of the thermal electrons in the coma of comet P/Halley. Journal of Geophysical Research 101 (A7), 15579–15589.

Haider, S.A., Bhardwaj, A., 2005. Radial distribution of production rates, loss rates and densities corresponding to ion masses ≤ 40 amu in the inner coma of comet Halley: composition and chemistry. Icarus 177, 196–216. doi:10.1016/j.icarus.2005.02.019.

Haider, S.A., Bhardwaj, A., Singhal, R.P., 1993. Role of auroral and photoelectrons on the abundances of methane and ammonia in the coma of comet Halley. Icarus 101, 234–243. doi:10.1006/icar.1993.1021.

Huebner, W.F., Keady, J.J., Lyon, S.P., 1992. Solar photorates for planetary atmospheres and atmospheric pollutants. Astrophysics and Space Science 195 (1), 1–294. doi:10.1007/BF00644558.

Ip, W., 1985. A preliminary consideration of the electron impact ionization effect in cometary comas. Advances in Space Research 5, 47–51. doi:10.1016/0273-1177(85)90066-3.

Itikawa, Y., Mason, N., 2005. Cross sections for electron collisions with water molecules. Journal of Physical and Chemical Reference Data 34 (1), 1–22. doi:10.1063/1.1799251.

Jackman, C.H., Garvey, R.H., Green, A.E.S., 1977. Electron impact on atmospheric gases, I, updated cross sections. Journal of Geophysical Research 82, 5081–5090. doi:10.1029/JA082i032p05081.

Körösmezey, A., Cravens, T.E., Gombosi, T.I., Nagy, A.F., Mendis, D.A., Szegö, K., Gribov, B.E., Sagdeev, R.Z., Shapiro, V.D., Shevchenko, V.I., 1987. A new model of cometary ionosphere. Journal of Geophysical Research 92 (A7), 7331–7340. doi:10.1029/JA092iA07p07331.

Krankowsky, D., Lammerzahl, P., Herrwerth, I., Woweries, J., Eberhardt, P., Dolder, U., Herrmann, U., Schulte, W., Berthelier, J.J., Illiano, J.M., Hodges, R.R., Hoffman, J.H., 1986. In situ gas and ion measurements at comet Halley. Nature 321, 326–329. doi:10.1038/321326a0.

Lawrence, G.M., 1972. Photodissociation of CO_2 to produce CO($a^3\pi$). Journal of Chemical Physics 56 (7), 3435–3442. doi:10.1063/1.1677717.

McConkey, J.W., Malone, C.P., Johnson, P.V., Winstead, C., McKoy, V., Kanik, I., 2008. Electron impact dissociation of oxygen-containing molecules a critical review. Physics Reports 466, 1–103. doi:10.1016/j.physrep.2008.05.001.

McCormick, P.T., Michelson, P.F., Pettibone, D.W., Whitten, R.C., 1976. On the energy deposition of photoelectrons in the atmosphere of Venus. Journal of Geophysical Research 81, 5196–5200. doi:10.1029/JA081i028p05196.

Nicholls, R.W., 1962. Laboratory astrophysics. Journal of Quantitative Spectroscopy and Radiative Transfer 2, 433–449. doi:10.1016/0022-4073(62)90030-4.

Rao, M.V.V.S., Iga, I., Srivastava, S.K., 1995. Ionization cross-sections for the production of positive ions from H_2O by electron impact. Journal of Geophysical Research 100, 26421–26425. doi:10.1029/95JE02314.

Richards, P.G., Fennelly, J.A., Torr, D.G., 1994. EUVAC: a solar EUV flux model of aeronomic calculations. Journal of Geophysical Research 99 (A5), 8981–8992. doi:10.1029/94JA00518.

Rosati, R.E., Johnsen, R., Golde, M.F., 2003. Absolute yields of CO($a'^3\Sigma^+$, $d^3\Delta_i$, $e^3\Sigma^-$)+O from the dissociative recombination of CO_2^+ ions with electrons. Journal of Chemical Physics 119 (22), 11630–11635. doi:10.1063/1.1623480.

Rosati, R.E., Skrzypkowski, M.P., Johnsen, R., Golde, M.F., 2007. Yield of excited CO molecules from dissociative recombination of HCO^+ and HOC^+ ions with electrons. Journal of Chemical Physics 126, 154302. doi:10.1063/1.2715943.

Sawada, T., Strickland, D.J., Green, A.E.S., 1972. Electron energy deposition in CO_2. Journal of Geophysical Research 77, 4812–4818. doi:10.1029/JA077-i025p04812.

Schmidt, H.U., Wegmann, R., Huebner, W.F., Boice, D.C., 1988. Cometary gas and plasma flow and with detailed chemistry. Computer Physics Communications 49, 17–59. doi:10.1016/0010-4655(88)90214-7.

Seiersen, K., Al-Khalili, A., Heber, O., Jensen, M.J., Nielsen, I.B., Pedersen, H.B., Safvan, C.P., Andersen, L.H., 2003. Dissociative recombination of the cation and dication of CO_2. Physical Review A 68. doi:10.1103/PhysRevA.68.022708.

Shunk, R.W., Nagy, A.F., 2009. Ionospheres—Physics, Plasma Physics, and Chemistry. Cambridge University Press.

Singhal, R.P., Bhardwaj, A., 1991. Monte Carlo simulation of photoelectron energization in parallel electric fields: electroglow on Uranus. Journal of Geophysical Research 96, 15963–15972.

Singhal, R.P., Haider, S.A., 1984. Analytical yield spectrum approach to photoelectron fluxes in the Earth's atmosphere. Journal of Geophysical Research 89, 6847–6852. doi:10.1029/JA089iA08p06847.

Skrzypkowski, M.P., Gougousi, T., Johnsen, R., Golde, M.F., 1998. Measurement of the absolute yield of CO($a^3\pi$)+O products in the dissociative recombination of CO_2^+ ions with electrons. Journal of Chemical Physics 108 (20), 8400–8407. doi:10.1063/1.476267.

Tobiska, W.K., 2004. SOLAR2000 irradiances for climate change, aeronomy and space system engineering. Advances in Space Research 34, 1736–1746. doi:10.1016/j.asr.2003.06.032.

Tozzi, G.P., Feldman, P.D., Festou, M.C., 1998. Origin and production of C(^{1}D) atoms in cometary comae. Astronomy and Astrophysics 330, 753–763.

Weaver, H.A., Feldman, P.D., A'Hearn, M.F., Arpigny, C., Brandt, J.C., Festou, M.C., Haken, M., McPhate, J.B., Stern, S.A., Tozzi, G.P., 1997. The activity and size of the nucleus of comet Hale–Bopp (C/1995 O1). Science 275, 1900–1904.

Weaver, H.A., Feldman, P.D., McPhate, J.B., A'Hearn, M.F., Arpigny, C., Smith, T.E., 1994. Detection of CO Cameron band emission in comet P/Hartley-2 (1991 XV) with the hubble space telescope. The Astrophysical Journal 422, 374–380. doi:10.1086/173732.

Wysong, I.J., 2000. Measurement of quenching rates of CO($a^3\Pi$) using laser pump and probe technique. Chemical Physics Letters 1–2, 42–46. doi:10.1016/S0009-2614(00)00967-2.

The Astrophysical Journal, 748:13 (18pp), 2012 March 20 doi:10.1088/0004-637X/748/1/13

A COUPLED CHEMISTRY-EMISSION MODEL FOR ATOMIC OXYGEN GREEN AND RED-DOUBLET EMISSIONS IN THE COMET C/1996 B2 HYAKUTAKE

Anil Bhardwaj[1] and Susarla Raghuram
Space Physics Laboratory, Vikram Sarabhai Space Centre, Trivandrum 695022, India;
bhardwaj_spl@yahoo.com, anil_bhardwaj@vssc.gov.in, raghuramsusarla@gmail.com

Received 2011 September 1; accepted 2011 December 9; published 2012 February 29

ABSTRACT

The green (5577 Å) and red-doublet (6300, 6364 Å) lines are prompt emissions of metastable oxygen atoms in the ^1S and ^1D states, respectively, that have been observed in several comets. The value of the intensity ratio of green to red-doublet (G/R ratio) of 0.1 has been used as a benchmark to identify the parent molecule of oxygen lines as H_2O. A coupled chemistry-emission model is developed to study the production and loss mechanisms of the $O(^1S)$ and $O(^1D)$ atoms and the generation of red and green lines in the coma of C/1996 B2 Hyakutake. The G/R ratio depends not only on photochemistry, but also on the projected area observed for cometary coma, which is a function of the dimension of the slit used and the geocentric distance of the comet. Calculations show that the contribution of photodissociation of H_2O to the green (red) line emission is 30%–70% (60%–90%), while CO_2 and CO are the next potential sources contributing 25%–50% (<5%). The ratio of the photoproduction rate of $O(^1S)$ to $O(^1D)$ would be around 0.03 (±0.01) if H_2O is the main source of oxygen lines, whereas it is ∼0.6 if the parent is CO_2. Our calculations suggest that the yield of $O(^1S)$ production in the photodissociation of H_2O cannot be larger than 1%. The model-calculated radial brightness profiles of the red and green lines and G/R ratios are in good agreement with the observations made on the comet Hyakutake in 1996 March.

Key words: comets: general – comets: individual (C/1996 B2 Hyakutake) – molecular processes

1. INTRODUCTION

The spectroscopic emissions from dissociative products in cometary coma are often used in estimating production rates of respective cometary parent species that are sublimating directly from the nucleus (Feldman et al. 2004; Combi et al. 2004). It is a known fact that at smaller (<2 AU) heliocentric distances the inner cometary coma is dominantly composed of H_2O. The infrared emissions of H_2O molecule are inaccessible from the ground because of strong attenuation by the terrestrial atmosphere. Since H_2O does not show any spectroscopic transitions in ultraviolet or visible regions of solar spectrum, one can estimate its abundance indirectly based on the emissions from daughter products, such as OH, O, and H. Thus, tracking emissions of the dissociative products of H_2O has become an important diagnostic tool in estimating the production rate as well as in understanding the spatial distribution of H_2O in comets (Delsemme & Combi 1976, 1979; Fink & Johnson 1984; Schultz et al. 1992; Morgenthaler et al. 2001; Furusho et al. 2006). For estimating the density distribution of H_2O from the emissions of daughter species, one has to account for photochemistry and associated emission processes.

The major dissociative channel of H_2O is the formation of H and OH, but a small fraction is also possible in $O(^3P, {}^1S, {}^1D)$ and H_2. The radiative decay of metastable ^1D and ^1S states of atomic oxygen leads to emissions at wavelengths 6300, 6364 Å (red doublet) and 5577 Å (green line), respectively. The energy levels of atomic oxygen and these forbidden transitions are shown in Figure 1. Even though these emissions are accessible from ground-based observatories, most of the time they are contaminated by telluric night sky emissions as well as emissions from other cometary species. Doppler shift of these lines, which is a function of the relative velocity of comet with respect to the Earth, offers a separation from telluric emissions provided a high-resolution cometary spectrum is obtained. In most of the cometary observations it is very difficult to separate the green line in optical spectrum because of the contamination from cometary C_2 (1–2) P-branch band emission. The red line 6300 Å emission is also mildly contaminated by the Q-branch emission of NH_2 molecule, but in a high-resolution spectrum this can be easily resolved.

Since these atomic oxygen emissions result due to electronic transitions that are forbidden by selection rules, solar radiation cannot populate these excited states directly from the ground state via resonance fluorescence. The photodissociative excitation and electron impact excitation of neutral species containing atomic oxygen, and ion–electron dissociative recombination of O-bearing ion species, can produce these metastable states (Bhardwaj & Haider 2002). If $O(^1D)$ is not quenched by ambient cometary species, then photons at wavelengths 6300 and 6364 Å will be emitted in radiative decay to the ground ^3P state. Only about 5% of $O(^1S)$ atoms result in 2972 and 2958 Å emissions via direct radiative transition to the ground ^3P state of atomic oxygen. Around 95% of $O(^1S)$ decays to the ground state through $O(^1D)$ by emitting green line (cf. Figure 1). This implies that if the green line emission is present in cometary coma, the red-doublet emission will also be present, but the opposite is not always true. The average lifetime of $O(^1D)$ is relatively small (∼110 s) compared to the lifetime of H_2O molecule (∼8×10^4 s) at 1 AU. The $O(^1S)$ also has a very short average lifetime of about 0.1 s. Due to the short lifetime of these metastable species, they cannot travel larger distances in cometary coma before de-exciting via radiative transitions. Hence, these emissions have been used as diagnostic tools to estimate the abundance of H_2O in comets (Fink & Johnson 1984; Magee-Sauer et al. 1990; Morgenthaler et al. 2001). The intensity of O[I] emissions, in Rayleigh, can be calculated using the following equation (Festou & Feldman 1981):

$$I = 10^{-6}\tau_p^{-1}\alpha\beta N, \tag{1}$$

---

[1] Author to whom any correspondence should be addressed.

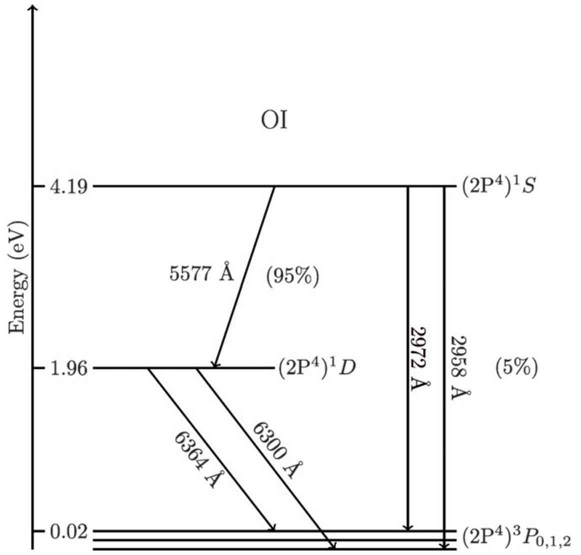

Figure 1. Energy level diagram of atomic oxygen showing different spectroscopic transitions related to the ^1S and ^1D states.

where τ_p is the lifetime of excited species in seconds, α is the yield of photodissociation, β is the branching ratio, and N is the column density of cometary species in cm^{-2}.

In the case of the red doublet (6300 and 6364 Å), since both emissions arise due to transition from the same excited state ($2P^4\ ^1D$) to the ground triplet state ($2P^4\ ^3P$), the intensity ratio of these two lines should be the same as that of the branching ratio of the corresponding transitions. Using Einstein transition probabilities, Storey & Zeippen (2000) calculated the intensity ratio of the red doublet and suggested that the intensity of 6300 Å emission would be three times stronger than that of 6364 Å emission, and this has been observed in several comets as well (Spinrad 1982; Fink & Johnson 1984; Morrison et al. 1997; Cochran & Cochran 2001; Capria et al. 2005, 2008; Furusho et al. 2006; Cochran 2008).

The ratio of the intensity of the green line to the sum of intensities of the red doublet can be calculated as

$$\frac{I_{5577}}{I_{6300} + I_{6364}} = \frac{\tau_{\text{green}}^{-1} \alpha_{\text{green}} N_{\text{green}} \beta_{\text{green}}}{\tau_{\text{red}}^{-1} \alpha_{\text{red}} N_{\text{red}} (\beta_{6300+6364})}. \qquad (2)$$

If the emission intensities of the oxygen lines are completely attributed only to photodissociative excitation of H_2O and column densities are assumed to be almost the same for both emissions, then the ratio of intensities of the green line to the red doublet is directly proportional to the ratio of $\tau^{-1}\alpha\beta$. Festou & Feldman (1981) reviewed these atomic oxygen emissions in comets. Based on the observation of the O[I] 2972 Å emission in the *International Ultraviolet Explorer* spectrograph of comet Bradfield (1979X), Festou & Feldman (1981) calculated the brightness profiles of red and green emissions. Festou & Feldman (1981) also calculated a theoretical value for the ratio of the intensity of the green line to the red doublet (hereafter referred to as the G/R ratio), which has a value of around 0.1 if H_2O is the source for these O[I] emissions in cometary comae, and it is nearly 1 if the source is CO_2 or CO. Observations of green and red line emissions in several comets have shown that the G/R ratio is around 0.1, suggesting that H_2O is the main source of these O[I] lines. However, since no experimental cross section or yield for the production of O(^1S) from H_2O is available in the literature, the G/R ratio has been questioned by Huestis & Slanger (2006).

Generally, the red line is more intense than the green line because the production of O(^1D) via dissociative excitation of H_2O is larger compared to the radiative decay of O(^1S). Since the lifetime of O(^1D) is larger, quenching is also a significant loss process near the nucleus. So far, the observed G/R ratio in comets is found to vary from 0.022 to 0.3 (Cochran 1984, 2008; Morrison et al. 1997; Zhang et al. 2001; Cochran & Cochran 2001; Furusho et al. 2006; Capria et al. 2005, 2008, 2010).

There are several reactions not involving H_2O which can also produce these forbidden oxygen lines (Bhardwaj & Haider 2002). Among the O-bearing species, CO_2 and CO also have dissociative channels producing O(^1D) and O(^1S). However, complex O-bearing molecules (e.g., H_2CO, CH_3OH, HCOOH) do not produce atomic oxygen as a first dissociative product. Based on the brightness of 6300 Å emission intensity, Delsemme & Combi (1976) derived the production rate of O(^1D) in comet Bennett 1970 II and suggested that the abundance of CO_2 is more than that of H_2O. Delsemme & Combi (1979) estimated the production of O(^1D) in the dissociation of H_2O and CO_2; about 12% of H_2O is dissociated into H_2 and O(^1D), while 67% of CO_2 is dissociated into CO and O(^1D). They suggested that a small amount of CO_2 can contribute much more than H_2O to the red-doublet emission. The model calculations of Bhardwaj & Haider (2002) showed that the production of O(^1D) is largely through the photodissociative excitation of H_2O, while the major loss mechanism in the innermost coma is quenching by H_2O. Cochran & Cochran (2001), based on the observation of the width of the red and green lines, argued that there must be another potential source of atomic oxygen in addition to H_2O, which can produce O(^1S) and O(^1D). Observations of the green and red lines in nine comets showed that the green line is wider than the red line (Cochran 2008), which could be because various parent sources are involved in the production of O(^1S).

The model of Glinski et al. (2004) showed that the chemistry in the inner coma can produce 1% O_2, which can also be a source of red and green lines. Manfroid et al. (2007) also argued, based on light curves, that forbidden O[I] emissions are probably contributed through a dissociation sequence of CO_2. A recent observation of comet 17P/Holmes showed that the G/R ratio can be even 0.3, which is the highest reported value so far: suggesting that CO_2 and CO abundances might be higher at the time of observation (Capria et al. 2010).

Considering various arguments based on different observations and theoretical works, we have developed a coupled chemistry-emission model to quantify various mechanisms involved in the production of red and green line emissions of atomic oxygen. We have calculated the production and loss rates, and the density profiles, of metastable O(^1D) and O(^1S) atoms from the O-bearing species, such as H_2O, CO_2, and CO, and also from the dissociated products OH and O. This model is applied to the comet C/1996 B2 Hyakutake, which was studied through several observations in 1996 March (Biver et al. 1999; Morrison et al. 1997; Cochran & Cochran 2001; Morgenthaler et al. 2001; Combi et al. 2005; Cochran 2008). The line-of-sight-integrated brightness profiles along cometocentric distances are calculated for 5577 and 6300 Å emissions and compared with the observed profiles of Cochran (2008). We have also evaluated the role of slit dimension, used in the observation, in determining the G/R ratio. The aim of this study is to understand the processes that determine the value of the G/R ratio.

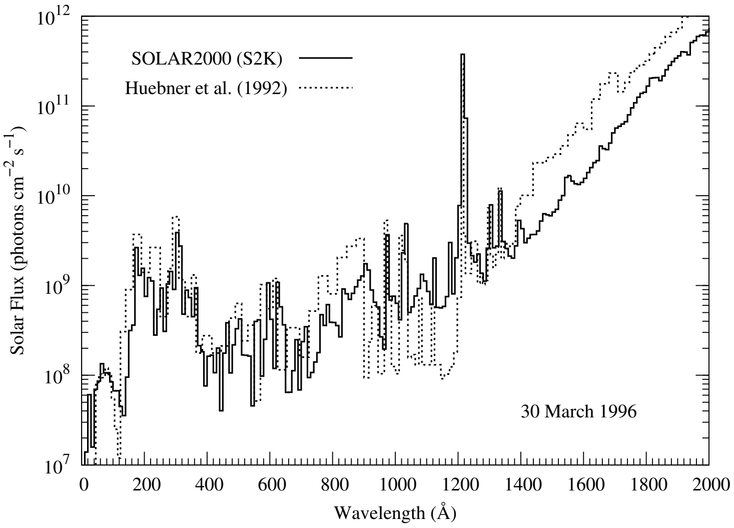

Figure 2. Solar EUV–UV flux from the SOLAR2000 (S2K) model of Tobiska (2004) for the day 1996 March 30 at a heliocentric distance of 1 AU. For comparison the solar flux used by Huebner et al. (1992) is also shown. At H Lyα (1216 Å) the solar flux given by the S2K model is higher than that of Huebner et al. (1992) by a factor of 1.24. Significant differences in the two solar fluxes can be noticed in the wavelength ranges 800–1200 Å, while above 1400 Å the solar flux of the S2K model is smaller than that of Huebner et al. (1992).

2. MODEL

The neutral parent species considered in this model are H_2O, CO_2, and CO. We do not consider other significant O-bearing species, such as H_2CO and CH_3OH, since their first dissociation does not lead to the formation of atomic oxygen atom; the O atom appears in the subsequent photodissociation of daughter products, such as OH, CO, and HCO. On 1996 March 24, the H_2O production rate for the comet C/1996 B2 Hyakutake measured by Mumma et al. (1996) was 1.7×10^{29} s^{-1}. Based on H Lyα emission observation, Combi et al. (1998) measured H_2O production rate as 2.6×10^{29} s^{-1} on 1996 April 4. Using molecular radio line emissions, Biver et al. (1999) derived the production rates of different species at various heliocentric distances from 1.6 to 0.3 AU. They found that around 1 AU the relative abundance of CO with respect to H_2O is high (∼22%) in the comet C/1996 B2 Hyakutake.

The number density $n_i(r)$ of the ith parent species at a cometocentric distance r in the coma is calculated using the following Haser's formula:

$$n_i(r) = \frac{Q_p}{4\pi v_i r^2}(e^{-\beta_i/r}). \tag{3}$$

Here, Q_p is the total gas production rate of the comet and v_i and β_i are the gas expansion velocity (taken as 0.8 km s^{-1}; Biver et al. 1999) and the scale length ($\beta_{H_2O} = 8.2 \times 10^4$ km, $\beta_{CO_2} = 5.0 \times 10^5$ km, and $\beta_{CO} = 1.4 \times 10^6$ km) of the ith species, respectively. The Haser model's neutral density distribution has been used in several previous studies for deriving the production rate of H_2O in comets based on the intensity of 6300 Å emission (Delsemme & Combi 1976, 1979; Fink & Johnson 1984; Morgenthaler et al. 2001). In our model calculations, the H_2O production rate on 1996 March 30 is taken to be 2.2×10^{29} s^{-1}. The abundance of CO relative to H_2O is taken to be 22%. Since there is no report on the observation of CO_2 in the comet Hyakutake, we assumed its abundance to be 1% relative to H_2O. However, we vary CO_2 abundance to evaluate its effect on the green and red-doublet emissions. The calculations are made when the comet C/1996 B2 Hyakutake was at a heliocentric distance of 0.94 AU and a geocentric distance of 0.19 AU on 1996 March 30. The calculated G/R ratio on other days of the observation is also reported.

The number density of OH produced in the dissociation of parent species H_2O at a given cometocentric distance r is calculated using Haser's two-parameter coma model:

$$n_{OH}(r) = \frac{Q_P}{4\pi v r^2}\frac{\beta_P}{\beta_R - \beta_P}(e^{-\beta_P r} - e^{-\beta_R r}). \tag{4}$$

Here, v is the average velocity of daughter species taken as 1 km s^{-1}, and β_P and β_R are the destruction scale lengths of the parent (H_2O, 8.2×10^4 km) and daughter (OH, 1.32×10^5 km) species, respectively (Huebner et al. 1992). The solar UV–EUV flux is taken from the SOLAR2000 version 2.3.6 (S2K) model of Tobiska et al. (2000) for the day 1996 March 30, which is shown in Figure 2. For comparison the solar flux used by Huebner et al. (1992) in calculating O(^1D) and O(^1S) production rates from various O-bearing species is also presented in the same figure.

The primary photoelectron energy spectrum $Q(E, r, \theta)$ is calculated by degrading solar radiation in the neutral atmosphere using

$$Q(E, r, \theta) = \sum_i \int_\lambda n_i(r)\, \sigma_i^I(\lambda)\, I_\infty(\lambda)\, \exp[-\tau(r, \theta, \lambda)]\, d\lambda, \tag{5}$$

where

$$\tau(r, \theta, \lambda) = \sum_i \sigma_i^A(\lambda)\, \sec\theta \int_r^\infty n_i(r')dr'. \tag{6}$$

Here, $\sigma_i^A(\lambda)$ and $\sigma_i^I(\lambda)$ are the absorption and ionization cross sections, respectively, of the ith species at the wavelength λ, $n_i(r)$ is its neutral gas density, and $\tau(r, \theta, \lambda)$ is the optical

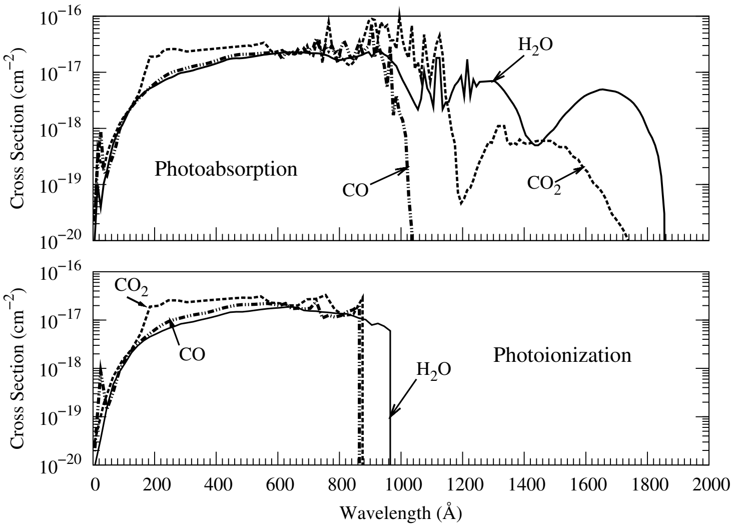

Figure 3. Total photoabsorption cross sections for H_2O, CO_2, and CO are shown in the top panel and total photoionization cross sections are shown in the bottom panel. The cross sections are taken from Huebner et al. (1992).

depth of the medium at the solar zenith angle θ. $I_\infty(\lambda)$ is the unattenuated solar flux at the top of atmosphere at wavelength λ. All calculations are made at solar zenith angle θ of 0°. The total photoabsorption and photoionization cross sections of H_2O, CO_2, and CO are taken from the compilation of Huebner et al. (1992; http://amop.space.swri.edu), and interpolated at 10 Å bins to make them compatible with the S2K solar flux wavelength bins for use in our model calculations. The total photoabsorption and photoionization cross sections for H_2O, CO_2, and CO are presented in Figure 3. The photochemical production rates for ionization and excitation of various species are calculated using degraded solar flux and cross sections of corresponding processes (discussed in Section 3) at different cometocentric distances.

The primary photoelectrons are degraded in cometary coma to calculate the steady state photoelectron flux using the analytical yield spectrum (AYS) approach, which is based on the Monte Carlo method (Singhal & Bhardwaj 1991; Bhardwaj & Singhal 1993; Bhardwaj & Michael 1999a; Bhardwaj & Jain 2009). The AYS method of degrading electrons in the neutral atmosphere can be explained briefly in the following manner. Monoenergetic electrons incident along the Z-axis in an infinite medium are degraded in a collision-by-collision manner using the Monte Carlo technique. The energy and position of the primary electron and its secondary or tertiary are recorded at the instant of an inelastic collision. The total number of inelastic events in the spatial and energy bins, after the incident electron and all its secondaries and tertiaries have been completely degraded, is used to generate numerical yield spectra. These yield spectra contain the yield information about the electron degradation process and can be employed to calculate the yield for any inelastic event. The numerical yield spectra generated in this way are in turn represented analytically, which contains the information about all possible collisional events based on the input electron impact cross sections, resulting in the AYS. This yield spectrum can be used to calculate the steady state photoelectron flux. More details of the AYS approach and the method of photoelectron computation are given in several previous papers (Singhal & Haider 1984; Bhardwaj et al. 1990, 1996; Singhal & Bhardwaj 1991; Bhardwaj 1999, 2003; Bhardwaj & Michael 1999b; Haider & Bhardwaj 2005; Bhardwaj & Jain 2009, 2012; Raghuram & Bhardwaj 2011). The total inelastic electron impact cross sections for H_2O are taken from Jackman et al. (1977) and Seng & Linder (1976), and those for CO_2 and CO are taken from Jackman et al. (1977). The electron impact cross sections for different dissociative ionization states of H_2O are taken from Itikawa & Mason (2005), for CO_2 from Bhardwaj & Jain (2009), and for CO from McConkey et al. (2008). The volume excitation rates for different processes are calculated using steady state photoelectron flux and electron impact cross sections. The electron temperature required for ion–electron dissociative recombination reactions is taken from Körösmezey et al. (1987). The detailed description of the coupled chemistry-transport model has been given in our earlier papers (Bhardwaj et al. 1995, 1996; Bhardwaj 1999; Bhardwaj & Haider 2002; Haider & Bhardwaj 2005; Bhardwaj & Raghuram 2011). Various reactions involved in the production and loss of metastable O(^1S) and O(^1D) atoms considered in our model are listed in Tables 1 and 2, respectively.

3. DISSOCIATION OF NEUTRAL SPECIES PRODUCING O(^1S) AND O(^1D)

3.1. Photodissociation

3.1.1. H_2O and OH

The dissociation of H_2O molecule starts at wavelengths less than 2424 Å and the primary products are H and OH. But the pre-dissociation process mainly starts from 1860 Å (Watanabe & Zelikoff 1953). The threshold wavelength for the photoionization of H_2O is 984 Å. Hence, solar UV photons in the wavelength region 1860–984 Å can dissociate H_2O and produce different daughter products. The threshold wavelengths for the dissociation of H_2O resulting in the production of O(^1S) and O(^1D) are 1390 Å and 1770 Å, respectively. Till now, the photoyield value for the production of O(^1D) from H_2O has been

Table 1
Reactions for the Production and Loss of O(^1S)

Reaction	Rate ($\mathrm{cm^3\ s^{-1}}$ or $\mathrm{s^{-1}}$)	Reference
$H_2O + h\nu \rightarrow O(^1S) + H_2$	6.4×10^{-8} [a]	This work
$OH + h\nu \rightarrow O(^1S) + H$	6.7×10^{-8}	Huebner et al. (1992)
$CO_2 + h\nu \rightarrow O(^1S) + CO$	7.2×10^{-7}	This work
$CO + h\nu \rightarrow O(^1S) + C$	4.0×10^{-8}	Huebner & Carpenter (1979)
$H_2O + e_{\mathrm{ph}} \rightarrow O(^1S)$ + others	9.0×10^{-10}	This work
$OH + e_{\mathrm{ph}} \rightarrow O(^1S)$ + others	2.2×10^{-10}	This work
$CO_2 + e_{\mathrm{ph}} \rightarrow O(^1S)$ + others	4.4×10^{-8}	This work
$CO + e_{\mathrm{ph}} \rightarrow O(^1S)$ + others	2.2×10^{-10}	This work
$O + e_{\mathrm{ph}} \rightarrow O(^1S)$	3.0×10^{-8}	This work
$H_2O^+ + e_{\mathrm{th}} \rightarrow O(^1S)$ + others	$4.3 \times 10^{-7}\ (300/T_e)^{0.5} \times 0.045$ [b]	Rosen et al. (2000)
$OH^+ + e_{\mathrm{th}} \rightarrow O(^1S)$ + others	$6.3 \times 10^{-9} \times (300/T_e)^{0.5}$	Guberman (1995)
$CO_2^+ + e_{\mathrm{th}} \rightarrow O(^1S)$ + others	$2.9 \times 10^{-7} \times (300/T_e)^{0.5}$	Mitchell (1990)
$CO^+ + e_{\mathrm{th}} \rightarrow O(^1S)$ + others	$5.0 \times 10^{-8} \times (300/T_e)^{0.46}$	Mitchell (1990)
$O(^1S) + h\nu \rightarrow O^+ + e$	1.9×10^{-7}	Huebner et al. (1992)
$O(^1S) + e_{\mathrm{ph}} \rightarrow O^+ + 2e$	2.7×10^{-7}	This work
$O(^1S) \longrightarrow O(^3P) + h\nu_{2972}$	0.075	Wiese et al. (1996)
$O(^1S) \longrightarrow O(^1D) + h\nu_{5577}$	1.26	Wiese et al. (1996)
$O(^1S) + H_2O \rightarrow 2\ OH$	3×10^{-10}	Zipf (1969)
$\rightarrow O(^1D) + H_2O$	$3 \times 10^{-10} \times 0.01$ [c]	Zipf (1969)
$O(^1S) + CO_2 \rightarrow O(^3P) + CO_2$	$3.1 \times 10^{-11}\ \exp(-1330/T)$	Atkinson & Welge (1972)
$\rightarrow O(^1D) + CO_2$	$2.0 \times 10^{-11}\ \exp(-1327/T)$	Capetanakis et al. (1993)
$O(^1S) + CO \rightarrow CO + O$	$3.21 \times 10^{-12}\ \exp(-1327/T)$	Capetanakis et al. (1993)
$\rightarrow O(^1D) + CO$	$7.4 \times 10^{-14}\ \exp(-961/T)$	Capetanakis et al. (1993)
$O(^1S) + e_{\mathrm{th}} \rightarrow O(^1D) + e$	8.56×10^{-9}	Berrington & Burke (1981)
$\rightarrow O(^3P) + e$	$1.56 \times 10^{-9}\ (T_e/300)^{0.94}$	Berrington & Burke (1981)
$O(^1S) + O \rightarrow 2\ O(^1D)$	2.0×10^{-14}	Krauss & Neumann (1975)

Notes. The photorates and photoelectron impact rates are at 1 AU on 1996 March 30; e_{ph}: photoelectron; e_{th}: thermal electron; $h\nu$: solar photon; T_e: electron temperature; T: neutral temperature.

[a] This rate is calculated assuming 1% yield for the production of O(^1S) at 1216 Å.

[b] 0.045 is the assumed branching ratio for the formation of O(^1S) via dissociative recombination of H_2O^+ ion.

[c] 0.01 is the assumed yield for the formation of O(^1D) via quenching of H_2O.

measured in only two experiments. Slanger & Black (1982) measured the O(^1D) yield in the photodissociation of H_2O at 1216 Å, and found its value to be 10%. McNesby et al. (1962) reported a 25% yield for the production of O(^1D) or O(^1S) at 1236 Å from H_2O.

Huebner et al. (1992) calculated photoproduction rates for different excited species produced from H_2O using absorption and ionization cross sections compiled from different experimental measurements. In our model the cross sections for the production of O(^1D) in the photodissociation of H_2O are taken from Huebner et al. (1992), which were determined based on experiments of Slanger & Black (1982) and McNesby et al. (1962). Huebner et al. (1992) assumed that in the 1770–1300 Å wavelength region around 25% of H_2O molecules photodissociate into H_2 and O(^1D), while between 1300 and 984 Å about 10% of H_2O dissociation produces O(^1D) (cf. Figure 4). Below 984 Å, Huebner et al. (1992) assumed that 33% of the dissociation of H_2O leads to the formation of O(^1D). Festou (1981) discussed various dissociation channels for H_2O in the wavelength region less than 1860 Å. Solar photons in the wavelength region 1357–1860 Å dissociates around 72% of H_2O molecules into ground states of H and OH. But, according to Stief et al. (1975) approximately 1% of H_2O molecules are dissociated into H_2 and O(^1D) in this wavelength region. The calculated rates for the O(^1D) production from the photodissociative excitation of H_2O by Huebner et al. (1992) are $5.97 \times 10^{-7}\ \mathrm{s^{-1}}$ and $1.48 \times 10^{-6}\ \mathrm{s^{-1}}$ for solar quiet and active conditions, respectively. Using the S2K solar EUV–UV flux on 1996 March 30 and cross sections from Huebner et al. (1992; see Figure 4), our calculated value is $8 \times 10^{-7}\ \mathrm{s^{-1}}$ (cf. Table 2), which is a factor of ~1.5 higher than that of Huebner et al. (1992) for solar minimum condition at 1 AU. This difference in calculated values is mainly due to the higher (a factor of 1.24) value of solar flux at 1216 Å in the S2K model than that used by Huebner et al. (1992; cf. Figure 2).

No experimentally determined cross sections for the production of O(^1S) in the photodissociation of H_2O are available. The solar flux at H Lyα (cf. Figure 2) is more than an order of magnitude larger than the flux at wavelengths below 1390 Å, which is the threshold for the O(^1S) production in the dissociation of H_2O. To account for the production of O(^1S) in the photodissociation of H_2O, we assumed a yield of 0.5% at solar H Lyα (1216 Å). However, to assess the impact of this assumption on the green and red line emissions we varied the yield between 0% and 1%. The calculated photorate for the production of O(^1S) from H_2O is $6.4 \times 10^{-8}\ \mathrm{s^{-1}}$ at 1 AU assuming 1% yield at 1216 Å (cf. Table 1).

The primary dissociative product of H_2O is OH. The important destruction mechanisms of OH molecule are predissociation through fluorescence process and direct photodissociation. The solar radiation shortward of 928 Å can ionize the OH molecule. The threshold wavelengths for the production of O(^1D) and O(^1S) in the photodissociation of OH are 1940 and 1477 Å, respectively. The dissociation channels of OH have been discussed by Budzien et al. (1994) and van Dishoeck & Dalgarno (1984). We have used the photorates given by

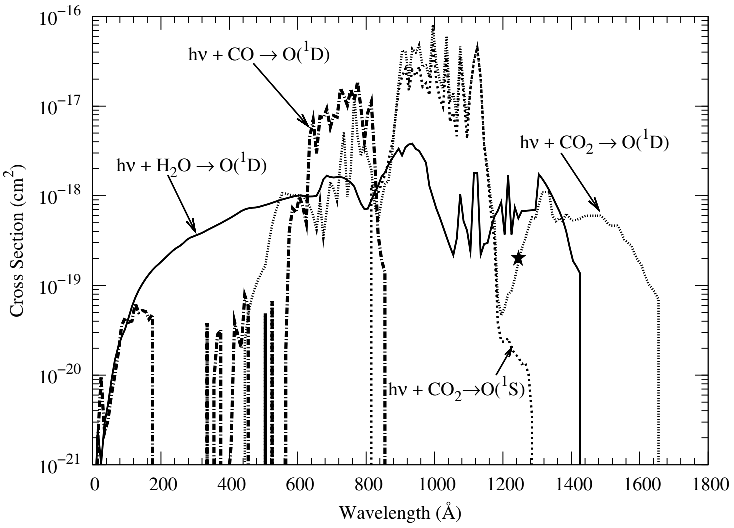

Figure 4. Photodissociative excitation cross sections for the production of O(^1D) from H_2O, CO_2, and CO. These cross sections are taken from Huebner et al. (1992). The "★" represents the cross section value for the production of O(^1S) from H_2O at 1216 Å assuming 1% yield.

Table 2
Reactions for the Production and Loss of O(^1D)

Reaction	Rate ($cm^3\ s^{-1}$ or s^{-1})	Reference
$H_2O + h\nu \to O(^1D) + H_2$	8.0×10^{-7}	This work
$OH + h\nu \to O(^1D) + H$	6.4×10^{-7}	Huebner et al. (1992)
$CO_2 + h\nu \to O(^1D) + CO$	1.2×10^{-6}	This work
$CO + h\nu \to O(^1D) + C$	5.1×10^{-8}	This work
$O(^1S) \to O(^1D) + h\nu_{557\,\mathrm{nm}}$	1.26	Wiese et al. (1996)
$H_2O + e_{\mathrm{ph}} \to O(^1D) + H_2 + e$	2.1×10^{-10}	This work
$OH + e_{\mathrm{ph}} \to O(^1D) + H + e$	7×10^{-11}	This work
$CO_2 + e_{\mathrm{ph}} \to O(^1D) + CO + e$	8.5×10^{-9}	This work
$CO + e_{\mathrm{ph}} \to O(^1D) + C(^1D) + e$	7×10^{-11}	This work
$O + e_{\mathrm{ph}} \to O(^1D)$	3.7×10^{-7}	This work
$H_2O^+ + e_{\mathrm{th}} \to O(^1D) + H_2$	$4.3 \times 10^{-7}\ (300/T_e)^{0.5} \times 0.35^{a}$	Rosen et al. (2000)
$OH^+ + e_{\mathrm{th}} \to O(^1D) + H$	$6.3 \times 10^{-9} \times (300/T_e)^{0.48}$	Guberman (1995)
$CO_2^+ + e_{\mathrm{th}} \to O(^1D) + CO$	$2.9 \times 10^{-7}\ (300/T_e)^{0.5}$	Mitchell (1990)
$CO^+ + e_{\mathrm{th}} \to O(^1D) + C(^1D)$	$5 \times 10^{-8}\ (300/T_e)^{0.46}$	Mitchell (1990)
$O(^1S) + e_{\mathrm{th}} \to O(^1D) + e$	$1.5 \times 10^{-10}\ (T_e/300)^{0.94}$	Berrington & Burke (1981)
$O(^1S) + H_2O \to O(^1D) + H_2O$	$3 \times 10^{-10} \times 0.01^{b}$	Zipf (1969)
$O(^1S) + CO_2 \to O(^1D) + CO_2$	$2.0 \times 10^{-11}\ \exp(-1327/T)$	Capetanakis et al. (1993)
$O(^1S) + CO \to O(^1D) + CO$	$7.4 \times 10^{-14}\ \exp(-961/T)$	Capetanakis et al. (1993)
$O(^1D) + h\nu \to O^+ + e$	1.82×10^{-7}	Huebner et al. (1992)
$O(^1D) \longrightarrow O(^3P) + h\nu_{6300}$	6.44×10^{-3}	Storey & Zeippen (2000)
$O(^1D) \longrightarrow O(^3P) + h\nu_{6364}$	2.15×10^{-3}	Storey & Zeippen (2000)
$O(^1D) + e_{\mathrm{ph}} \to O^+ + 2e$	1.75×10^{-7}	This work
$O(^1D) + e_{\mathrm{th}} \to O(^3P) + e$	$8.1 \times 10^{-10}\ (T_e/300)^{0.5}$	Link (1982)
$O(^1D) + H_2O \to OH + OH$	2.1×10^{-10}	Atkinson et al. (1997)
$\to O(^3P) + H_2O$	9.0×10^{-12}	Atkinson et al. (1997)
$\to H_2 + O_2$	2.2×10^{-12}	Atkinson et al. (1997)
$O(^1D) + CO_2 \to O + CO_2$	$7.4 \times 10^{-11}\ \exp(-120/T)$	Atkinson et al. (1997)
$\to CO + O_2$	2.0×10^{-10}	Atkinson et al. (1997)
$O(^1D) + CO \to O + CO$	$5.5 \times 10^{-10}\ \exp(-625/T)$	Schmidt et al. (1988)
$\to CO_2$	8.0×10^{-11}	Demore et al. (1997)

Notes. The photorates and photoelectron impact rates are at 1 AU on 1996 March 30; e_{ph}: photoelectron; e_{th}: thermal electron; $h\nu$: solar photon; T_e: electron temperature; T: neutral temperature.

[a] 0.35 is the assumed branching ratio for the formation of O(^1D) via dissociative recombination of H_2O^+ ion.

[b] 0.01 is the assumed branching ratio for the formation of O(^1D) via quenching of H_2O.

Huebner et al. (1992) for the production of O(^1D) and O(^1S) from an OH molecule whose values are 6.4 × 10^{-7} and 6.7 × 10^{-8} s^{-1}, respectively. These rates are based on the dissociation cross sections of van Dishoeck & Dalgarno (1984), which are consistent with the red line observation made by the wide-field spectrometer (Morgenthaler et al. 2007).

3.1.2. CO_2

The threshold wavelengths for the dissociation of CO_2 molecule producing O(^1D) and O(^1S) are 1671 Å and 1286 Å, respectively. As noted by Huestis & Slanger (2006), the O(^1D) yield in the photodissociation of CO_2 has never been measured because of the problem of rapid quenching of this metastable state. However, experiment by Kedzierski et al. (1998) suggested that this dissociation channel can be studied in electron impact experiment using solid neon matrix as detector. Huebner et al. (1992) estimated the cross section for O(^1D) production in the photodissociative excitation of CO_2 (see Figure 4), and obtained photorate values of 9.24 × 10^{-7} and 1.86 × 10^{-6} s^{-1} for solar minimum and maximum conditions, respectively. Using S2K solar flux on 1996 March 30 our calculated rate for O(^1D) production in the photodissociation of CO_2 is 1.2 × 10^{-6} s^{-1} at 1 AU, which is higher than the solar minimum rate of Huebner et al. (1992) by a factor of 1.3. This variation is mainly due to the differences in the solar fluxes (cf. Figure 2) in the wavelength region 950–1100 Å where the photodissociative cross section for the production of O(^1D) maximizes (cf. Figure 4).

Lawrence (1972) measured the O(^1S) yield in the photodissociative excitation of CO_2 from threshold (1286 Å) to 800 Å. The yield of Lawrence (1972) is different from that measured by Slanger et al. (1977) in the 1060–1175 Å region. However, the yield from both experimental measurements closely matches in the 1110–1140 Å wavelength region, where the yield is unity. In the experiment of Slanger et al. (1977), a dip in quantum yield is observed at 1089 Å. Huestis et al. (2010) reviewed the experimental results and suggested the yield for O(^1S) in the photodissociation of CO_2. We calculated the cross section for the O(^1S) production in the photodissociative excitation of CO_2 (see Figure 4) by multiplying the yield recommended by Huestis et al. (2010) with total absorption cross section of CO_2 (see Figure 3). Using this cross section and S2K solar flux, the rate for O(^1S) production is 7.2 × 10^{-7} s^{-1} at 1 AU.

3.1.3. CO

The threshold wavelength for the dissociation of the CO molecule into neutral products in the ground state is 1117.8 Å and in the metastable O(^1D) and C(^1D) is 863.4 Å. Among the O-bearing species discussed in this paper, CO has the highest dissociation energy of 11.1 eV, while its ionization potential is 14 eV. Huebner et al. (1992) calculated cross sections for the photodissociative excitation of CO producing O(^1D) using branching ratios from McElroy & McConnell (1971; cf. Figure 4). Rates for the production of O(^1D) from CO molecule calculated by Huebner et al. (1992) are 3.47 × 10^{-8} and 7.87 × 10^{-8} s^{-1} for solar minimum and maximum conditions, respectively. Using the cross section of Huebner et al. (1992) and the S2K model solar flux, our calculated rate for the O(^1D) production from CO is 5.1 × 10^{-8} s^{-1} at 1 AU, which is 1.5 times higher than the solar minimum rate of Huebner et al. (1992). This difference in the calculated value is due to variation in the solar fluxes used in the two studies in wavelength region 600–800 Å (cf. Figure 2).

We did not find any reports on the cross section for the production of O(^1S) in the photodissociation of the CO molecule. According to Huebner & Carpenter (1979) the rate for this reaction cannot be more than 4 × 10^{-8} s^{-1}. We have used this value in our model calculations. This process can be an important source of O(^1S) since the comet Hyakutake has a higher CO abundance (∼20%). Using this photorate and CO abundance, we will show that this reaction alone can contribute up to a maximum of 30% to the total O(^1S) production.

3.2. Electron Impact Dissociation

In our literature survey we could not find any reported cross section for the production of O(^1D) due to the electron impact dissociation of H_2O. Jackman et al. (1977) have assembled the experimental and theoretical cross sections for electron impact on important atmospheric gases in a workable analytical form. The cross sections for electron impact on atomic oxygen given by Jackman et al. (1977) have been used to estimate emissions which leave the O atom in the metastable (^1D) state. The obtained ratios of 85% in the ground state and 15% in the metastable state are used for the atomic states of C and O produced in the electron impact dissociation of H_2O, CO_2, and CO. It may be noted that the ground state to metastable state production ratio of 89:11 is observed for atomic carbon and atomic oxygen produced from the photodissociation of CO (Singh et al. 1991). However, as shown later, the contributions of these electron impact processes to the total production of O(^1D) are very small (<5%).

Kedzierski et al. (1998) measured the cross section for the electron impact dissociative excitation of H_2O producing O(^1S), with an overall uncertainty of 30%. LeClair & McConkey (1994) measured cross section for the production of O(^1S) in the dissociation of CO_2 by electron impact; they claimed an uncertainty of 12% in their experimental cross section measurements. The cross section for fragmentation of CO into the metastable O(^1S) atom by electron impact is measured by LeClair et al. (1994). These electron impact cross sections are also recommended by McConkey et al. (2008), and are used in our model for calculating the production rate of O(^1S) from H_2O, CO_2, and CO.

Since the ^1D and ^1S are metastable states, the direct excitation of atomic oxygen by solar radiation is not an effective excitation mechanism. However the electron impact excitation of atomic oxygen can populate these excited metastable states, which is a major source of airglow emissions in the upper atmospheres of Venus, Earth, and Mars. We calculated the excitation rates for these processes using electron impact cross sections from Jackman et al. (1977). In calculating the photoelectron impact ionization rates of metastable oxygen states, we calculated the cross sections by changing the threshold energy parameter for ionization of neutral atomic oxygen in the analytical expression given by Jackman et al. (1977). The above-mentioned electron impact cross sections for the production of O(^1S) from H_2O, CO_2, CO, and O, used in the current model, are presented in Figure 5 along with the calculated photoelectron flux energy spectrum at a cometocentric distance of 1000 km.

3.3. Dissociative Recombination

The total dissociative recombination rate for H_2O^+ reported by Rosen et al. (2000) is 4.3 × 10^{-7} cm^{-3} s^{-1} at 300 K. The channels of dissociative recombination have also been studied by this group. It was found that the dissociation process is

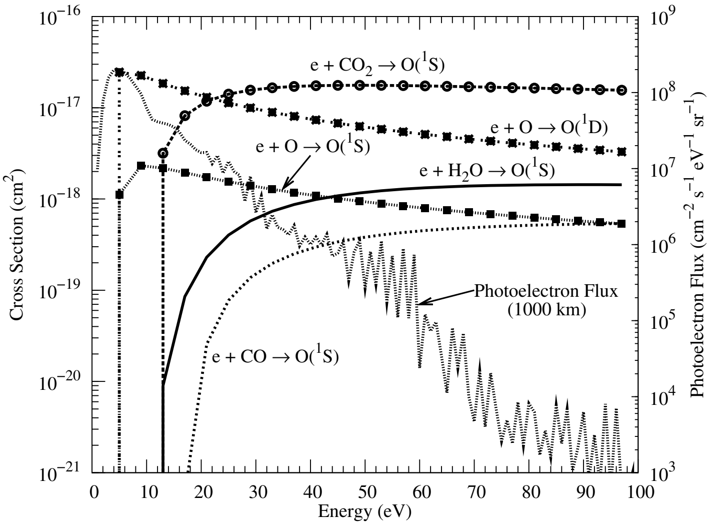

Figure 5. Cross sections for the production of metastable O(^1S) in the electron impact dissociative excitation of H_2O, CO_2, and CO. Cross sections for electron impact excitation of O to O(^1D) and O(^1S) are also plotted. Calculated steady state photoelectron flux at 1000 km cometocentric distance using the S2K model solar flux on 1996 March 30 is also shown with scale on the right-hand side y-axis.

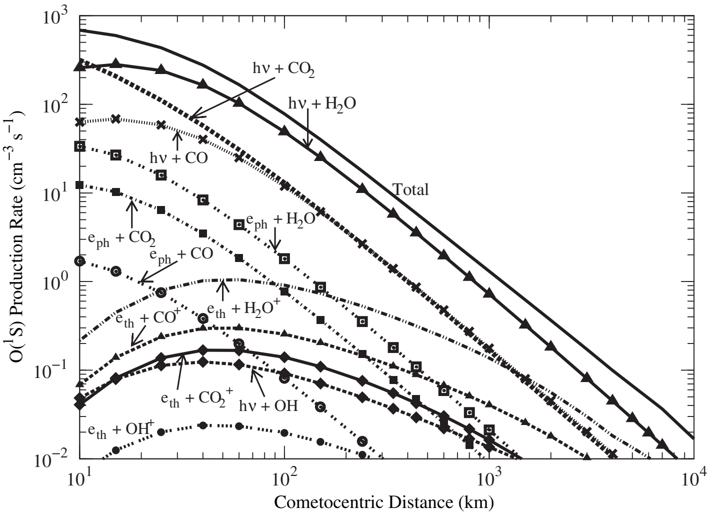

Figure 6. Calculated radial profiles for major production mechanisms of O(^1S) along with the total production profile. $h\nu$: solar photon; e_{ph}: photoelectron; and e_{th}: thermal electron.

dominated by three-body breakup (H + H + O) that occurs with a branching ratio of 0.71, while the fraction of two-body breakup (O + H_2) is 0.09, and the branching ratio for the formation of OH + H is 0.2. The maximum kinetic energy of the dissociative products forming atomic oxygen produced in ground state is 3.1 eV and 7.6 eV for the three- and two-body dissociation, respectively. Since the excitation energy required for the formation of metastable O(^1S) is 4.19 eV, the three-body dissociation cannot produce oxygen atoms in the ^1S state. However, the O(^1D) atom can be produced in both, the three-body and the two-body, breakup dissociation processes. To incorporate the contribution of H_2O^+ dissociative recombination in the production of O(^1D) and O(^1S), we assumed that 50% of branching fraction of the total recombination in three-body and two-body breakups lead to the formation of O(^1D) and O(^1S) atoms, respectively. For dissociative recombination of CO_2^+, CO^+, and OH^+ ions, we assumed that the recombination rates are the same for the production of both O(^1D) and O(^1S). We will show that these assumptions affect the calculated O(^1S) and O(^1D) densities only at larger ($\geqslant 10^4$ km) cometocentric distances, but not in the inner coma. Tables 1 and 2 list the rates, along with the source reference, for these recombination reactions.

4. RESULTS AND DISCUSSION

4.1. Production and Loss of O(^1S) Atom

The calculated O(^1S) production rate profiles for different processes in the comet C/1996 B2 Hyakutake are presented in Figure 6. These calculations are made under the assumption

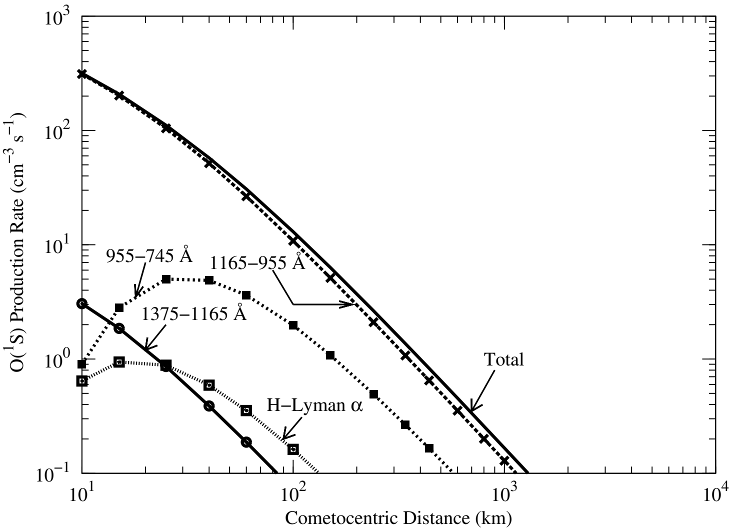

Figure 7. Calculated radial profiles for the photodissociation of CO_2 producing O(^1S) at different wavelength bands.

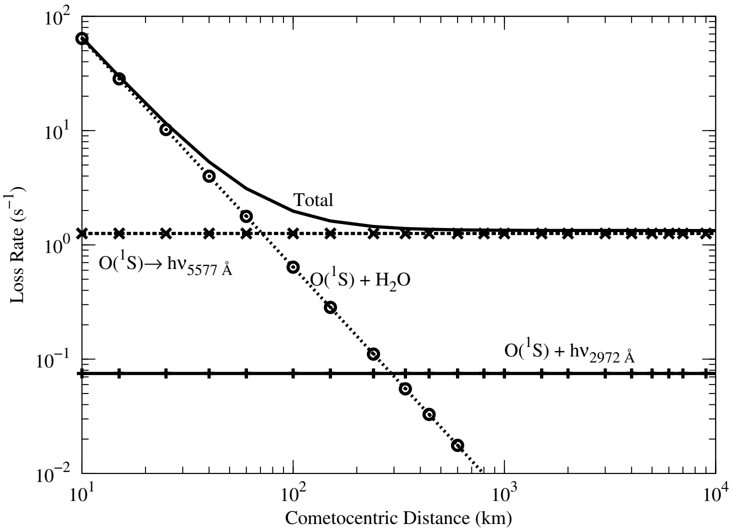

Figure 8. Calculated radial profiles for the major loss mechanisms of the O(^1S) atom.

of 0.5% yield of O(^1S) from H_2O at 1216 Å solar H Lyα line and 1% CO_2 relative abundance. The major production source of O(^1S) is the photodissociative excitation of H_2O throughout the cometary coma. However, very close to the nucleus, the photodissociative excitation of CO_2 is also an equally important process for the O(^1S) production. Above 100 km, the photodissociative excitation of CO_2 and CO makes an equal contribution in the production of O(^1S). Since the cross section for the electron impact dissociative excitation of H_2O, CO_2, and CO is small (see Figure 5), the contributions from electron impact dissociation to O(^1S) production are smaller by an order of magnitude or more than that due to photodissociative excitation. At larger cometocentric distances ($>2 \times 10^3$ km), the dissociative recombination of H_2O^+ ion is a significant production mechanism for O(^1S), whose contribution is higher than those from the photodissociative excitation of CO_2 and CO. The dissociative recombination of other ions do not make any significant contribution to the production of O(^1S).

In the inner coma, the calculated production rates of O(^1S) via photodissociative excitation is CO_2 at various wavelengths are presented in Figure 7. The major production of O(^1S) occurs in the wavelength region 955–1165 Å where the average cross section is $\sim 2 \times 10^{-17}$ cm^{-2} (cf. Figure 4) and the average solar flux is $\sim 1 \times 10^9$ photons cm^{-2} s^{-1} (cf. Figure 2). The calculated loss rate profiles of O(^1S) for major processes are presented in Figure 8. Close to the nucleus (<50 km), quenching by H_2O is the main loss mechanism for metastable O(^1S). Above 100 km, the radiative decay of O(^1S) becomes the dominant

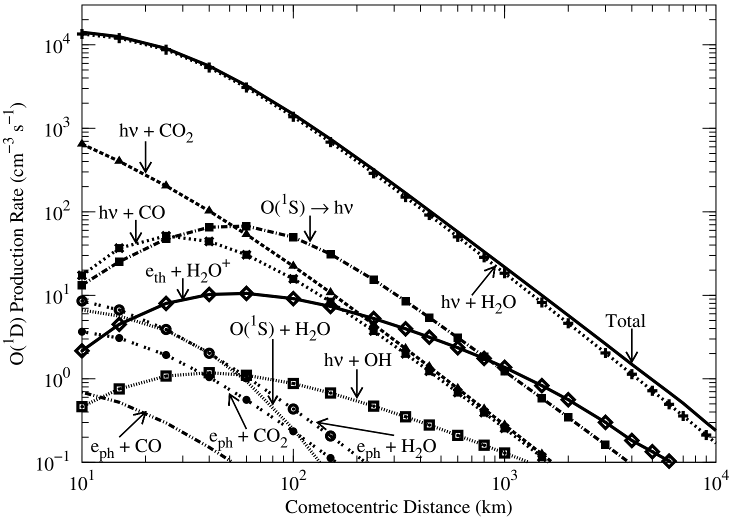

Figure 9. Calculated radial profiles for the major production mechanisms of O(^1D) along with the total O(^1D) production rate profile. $h\nu$: solar photon; $e_{\rm ph}$: photoelectron; and $e_{\rm th}$: thermal electron.

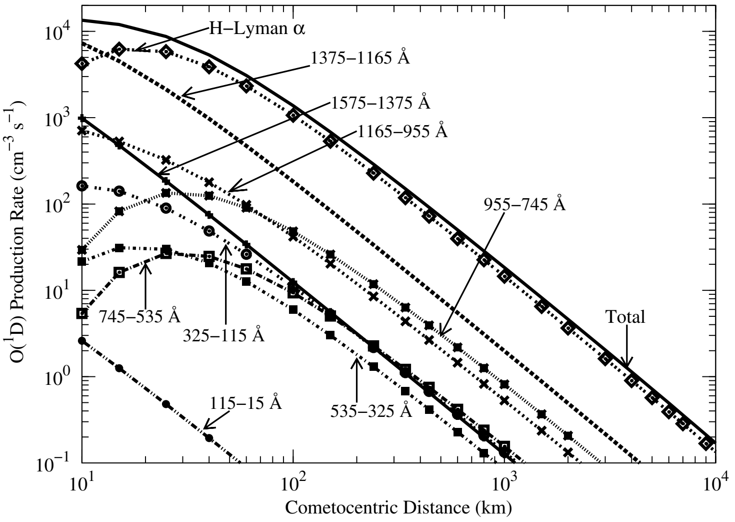

Figure 10. Calculated radial profiles for the photodissociation of H_2O producing O(^1D) at different wavelength bands.

loss process. The contributions from other loss processes are orders of magnitude smaller and hence are not shown in Figure 8.

4.2. Production and Loss of O(^1D) Atom

The production rates as a function of cometocentric distance for various excitation mechanisms of the O(^1D) are shown in Figure 9. The major source of O(^1D) production in the inner coma is the photodissociation of H_2O. The wavelength-dependent production rates of O(^1D) from H_2O are presented in Figure 10. The O(^1D) production in the photodissociation of H_2O is governed by solar radiation at H Lyα (1216 Å) wavelength. However, very close to the nucleus, the production of O(^1D) is largely due to photons in the wavelength region 1165–1375 Å. Since the average absorption cross section of H_2O decreases in this wavelength region by an order of magnitude, the optical depth at wavelengths greater than 1165 Å is quite small (see Figure 3). Hence, these photons are able to travel deeper into the coma unattenuated, thereby reaching close to the nucleus where they dissociate H_2O producing O(^1D). Thus, at the surface of cometary nucleus the production of O(^1D) is controlled by the solar radiation in this wavelength band. In high production rate comets, the production of O(^1D) near nucleus would be governed by solar photons in this wavelength region. The production of O(^1D) from H_2O by solar photons from other wavelength regions is smaller by more than an order of magnitude.

After the photodissociative excitation of H_2O, the next significant O(^1D) production process at radial distances below 50 km is the photodissociative excitation of CO_2. Above 50 km to about 1000 km, the radiative decay of O(^1S) and at radial

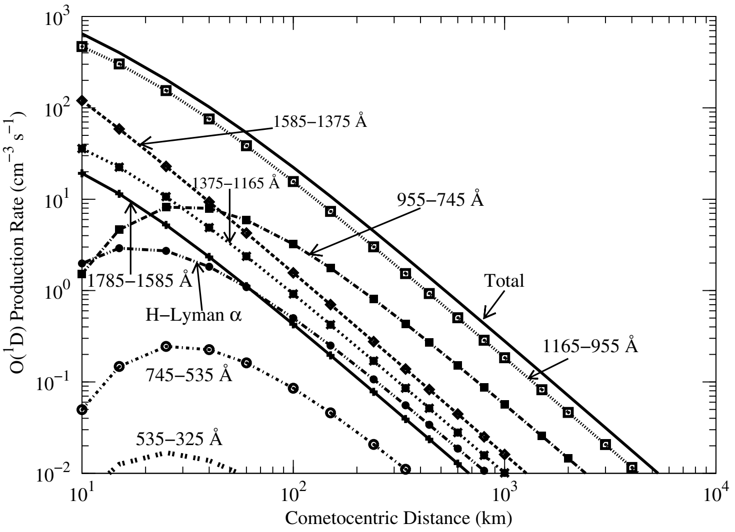

Figure 11. Calculated radial profiles for the photodissociation of CO_2 producing O(^1D) at different wavelength bands.

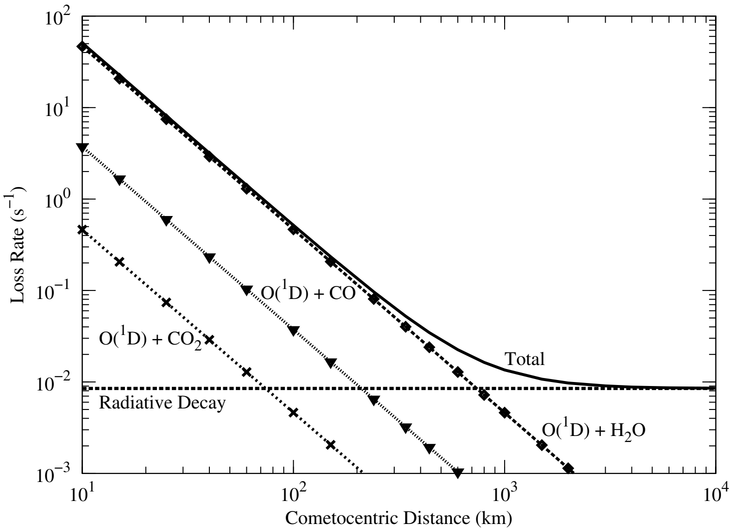

Figure 12. Calculated radial profiles for major loss mechanisms of the O(^1D) atom.

distances above 1000 km the dissociative recombination of H_2O^+ are the next potential sources of the O(^1D) (see Figure 9). The calculated wavelength-dependent production rates of O(^1D) for the photodissociation of CO_2 are shown in Figure 11. Solar radiation in the wavelength region 1165–955 Å dominates the O(^1D) production. Since the cross section for the production of O(^1D) due to the photodissociation of CO_2 is more than an order of magnitude higher in this wavelength region compared to the cross section at other wavelengths (see Figure 4), the solar radiation in this wavelength band mainly controls the formation of O(^1D) from CO_2. Other potential contributions are made by solar photons in the wavelength band 1585–1375 Å at distances <50 km, and 955–745 Å at radial distances >100 km. Since the CO_2 absorption cross section around 1216 Å is smaller by more than two orders of magnitude compared to its maximum value, the solar radiation at H Lyα is not an efficient source of O(^1D) atoms.

Zipf (1969) measured the total rate coefficient for the quenching of O(^1S) by H_2O as 3×10^{-10} cm^3 s^{-1}. The primary channel in quenching mechanism is the production of two OH atoms. The production of O(^1D) is also a possible channel whose rate coefficient is not reported in the literature. Hence, we assumed that 1% of the total rate coefficient can lead to the formation of O(^1D) in this quenching mechanism. However, this assumption has no implications on the O(^1D) production since the total contribution due to O(^1S) is about three orders of magnitude smaller than the major production process of O(^1D).

The calculated loss rate profiles of O(^1D) are presented in Figure 12. Below 1000 km, the O(^1D) can be quenched by

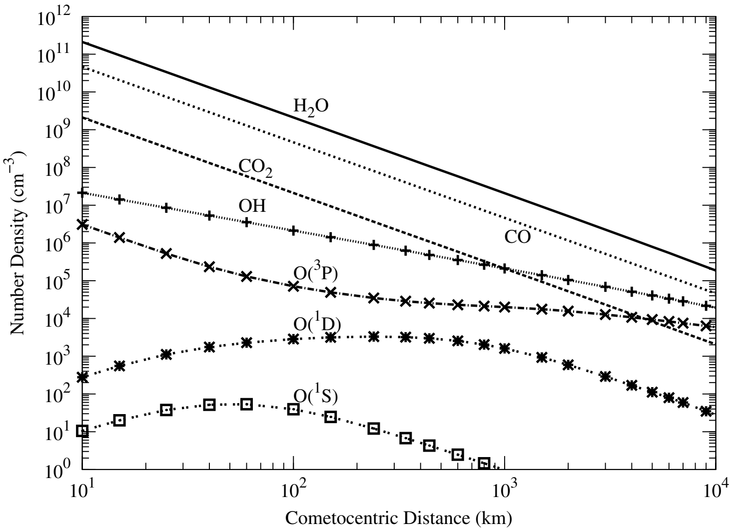

Figure 13. Calculated number density profiles of O(^1S), O(^1D), O(^3P), and OH, along with those of H_2O, CO, and CO_2.

various cometary species. The quenching by H_2O is the major loss mechanism for O(^1D) below 500 km. Above 2×10^3 km radiative decay is the dominant loss process for O(^1D).

4.3. Calculation of Green and Red-doublet Emission Intensity

Using the calculated production and loss rates due to various processes mentioned above, and assuming photochemical equilibrium, we computed the number density of O(^1S) and O(^1D) metastable atoms. The calculated number densities are presented in Figure 13. The O(^1D) density profile shows a broad peak around 200–600 km. But, in the case of O(^1S), the density peaks at much lower radial distances of ∼60 km. The number densities of O(^1D) and O(^1S) are converted into emission rate profiles for the red-doublet and green line emissions, respectively, by multiplying with Einstein transition probabilities as

$$V_{(6300+6364)}(r) = A_{(6300+6364)} \times [\mathrm{O}^1D(r)] = A_{(6300+6364)} \frac{\sum_{i=1}^{k} P_i(r)}{\sum_{i=1}^{k} L_i(r) + A(^1D)} \quad (7)$$

and

$$V_{(5577)}(r) = A_{(5577)} \times [\mathrm{O}^1S(r)] = A_{(5577)} \frac{\sum_{i=1}^{k} P_i(r)}{\sum_{i=1}^{k} L_i(r) + A(^1S)}, \quad (8)$$

where [O$^1S(r)$] and [O$^1D(r)$] are the calculated number density for the corresponding production rates $P_i(r)$ and loss frequencies $L_i(r)$ for O(^1S) and O(^1D), respectively. $A(^1D)$ and $A(^1S)$ are the total Einstein spontaneous emission coefficients for red-doublet and green line emissions. Using the emission rate profiles, the line-of-sight intensity of green and red-doublet emissions along the projected distance z is calculated as

$$I(z) = 2\int_{z}^{R} V_{(5577,\ 6300+6364)}(s)ds, \quad (9)$$

where s is the abscissa along the line of sight and $V_{(5577,\ 6300+6364)}(s)$ is the emission rate for the green or red-doublet emission. The maximum limit of integration R is taken as 10^5 km. The calculated brightness profiles of 5577 and 6300 Å emissions are presented in Figure 14. These brightness profiles are then averaged over the projected area corresponding to the slit dimension 1″.2 × 8″.2 centered on the nucleus of the comet C/1996 B2 Hyakutake for the observation on 1986 March 30 (Cochran 2008). The G/R ratio averaged over the slit is also calculated.

4.4. Model Results

Morrison et al. (1997) observed the green and red-doublet emissions on the comet C/1996 B2 Hyakutake in the high-resolution optical spectra obtained on 1996 March 23 and 27 and found the G/R ratio in the range 0.12–0.16. Cochran (2008) observed the 5577 and 6300 Å line emissions on this comet on 1996 March 9 and 30, with the G/R ratio as 0.09 for March 9 observation. We calculated the G/R ratio by varying the yield for O(^1S) production in the photodissociation of H_2O at 1216 Å (henceforth referred to as the O(^1S) yield). Since CO_2 is not observed in this comet, we assumed that a minimum of 1% CO_2 is present in the coma. However, we also carried out calculations for 0%, 3%, and 5% CO_2 abundances in the comet. We calculated the contributions of different production processes in the formation of O(^1S) and O(^1D) at three different projected distances of 10^2, 10^3, and 10^4 km from the nucleus for the above-mentioned CO_2 abundances and the O(^1S) yield values varying from 0% to 1%. These calculations are presented in Table 3. The percentage contribution of major production processes in the projected field of view for the green and red-doublet emissions is also calculated. The G/R ratio is calculated after averaging the intensity over the projected area 165 × 1129 km, which corresponds to the dimension of the slit used in the observation made by Cochran (2008) on 1996 March 30. These calculated values are presented in Table 4.

Taking 1% CO_2 abundance and 0% O(^1S) yield, the calculated percentage contributions of major production processes of the O(^1S) and O(^1D) atoms are presented in Table 3. Around 60%–90% of the O(^1D) is produced from the photodissociation of H_2O. Contributions of the photodissociative excitation of CO_2

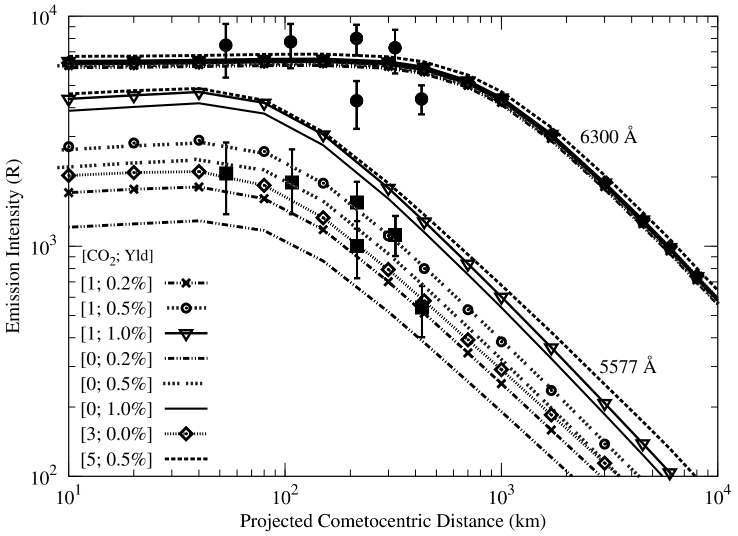

Figure 14. Calculated emission brightness profiles along projected distances for 5577 Å (green) and 6300 Å (red) line emissions for different CO_2 relative abundance [CO_2] and yield [Yld] for O(^1S) production in the photodissociation of H_2O. The green and red emission intensities at different projected distances observed on March 30 taken from Cochran (2008) are also shown (filled symbols with error bars) for comparison with the calculated values.

Table 3
Calculated Percentage Contribution for Major Production Processes of O(^1S) and O(^1D) Atoms in the Comet C/1996 B2 Hyakutake with Varying Relative Abundance of CO_2 and O(^1S) Yield

O(^1S)	Production Processes of O(^1S) and O(^1D) at Three Cometocentric Projected Distances (km)																	
Yield[a]	$h\nu$ + H_2O			$h\nu$ + OH			$h\nu$ + CO_2			e + H_2O^+			O(^1S) → O(^1D)			$h\nu$ + CO		
(%)	10^2	10^3	10^4	10^2	10^3	10^4	10^2	10^3	10^4	10^2	10^3	10^4	10^2	10^3	10^4	10^2	10^3	10^4
1% CO_2																		
0.0	0 [92][b]	0 [82]	0 [61]	1 [0.5]	5 [1]	19 [8]	39 [1]	23 [1]	14 [1]	10 [2]	28 [9]	27 [12]	[1]	[3]	[4]	37 [1]	24 [1]	16 [1]
0.2	38 [91]	28 [81]	17 [60]	1 [0.5]	4 [1]	15 [8]	24 [1]	17 [1]	12 [1]	6 [2]	20 [9]	22 [12]	[3]	[4)	[5]	23 [1]	17 [1]	13 [1]
0.5	62 [90]	50 [80]	34 [60]	0.5 [0.5]	3 [1]	12 [8]	15 [1]	11 [1]	10 [1]	4 [2]	14 [9]	17 [12]	[4]	[6]	[6]	15 [1]	12 [1]	10 [1]
1.0	75 [88]	66 [77]	51 [58]	0.5 [0.5]	2 [1]	10 [7]	9 [1]	8 [1]	7 [1]	2 [2]	10 [9]	13 [12]	[7]	[9]	[9]	9 [1]	8 [1]	7 [1]
0% CO_2																		
0.0	0 [95]	0 [84]	0 [62]	2 [0.5]	7 [2]	23 [8]	0 [0]	0 [0]	0 [0]	17 [2]	39 [9]	34 [12]	[1]	[2]	[3]	65 [1]	34 [1]	20 [1]
0.2	51 [94]	35 [83]	21 [62]	1 [0.5]	5 [1]	18 [8]	0 [0]	0 [0]	0 [0]	8 [2]	25 [9]	27 [12]	[2]	[3]	[4]	31 [1]	22 [1]	16 [1]
0.5	72 [92]	57 [81]	40 [61]	0.5 [0.5]	3 [1]	14 [8]	0 [0]	0 [0]	0 [0]	5 [2]	16 [9]	20 [12]	[4]	[5]	[5]	17 [1]	14 [1]	12 [1]
1.0	84 [90]	73 [79]	57 [60]	0.5 [0.5]	2 [2]	10 [8]	0 [0]	0 [0]	0 [0]	2 [2]	10 [9]	14 [12]	[6]	[8]	[8]	10 [1]	9 [1]	8 [1]
3% CO_2																		
0.0	0 [89]	0 [79]	0 [58]	1 [0.5]	3 [1]	13 [7]	62 [4]	44 [4]	30 [3]	5 [2]	18 [9]	19 [12]	[3]	[4]	[5]	20 [1]	15 [1]	11 [1]
5% CO_2																		
0.5	36 [83]	31 [72]	22 [54]	0.5 [0.5]	2 [2]	7 [8]	45 [1]	37 [1]	30 [1]	2 [2]	10 [10]	12 [12]	[7]	[8]	[9]	9 [1]	8 [1]	7 [1]

Notes. Calculations are made for 1996 March 30, when $r = 0.94$ AU and $\Delta = 0.19$ AU.

[a] Yield for the production of O(^1S) from the photodissociation of H_2O at solar Lyα (1216 Å) line.

[b] The values in square brackets are for the O(^1D).

and CO in the production of O(^1S) and O(^1D) are 15%–40% and 1%, respectively. Around 10^4 km projected distance, the photodissociative excitation of OH (∼20%) and the dissociative recombination of H_2O^+ (∼30%) are also significant production processes for the O(^1S) atoms. However, the contributions from these processes in O(^1D) production is only around 10%.

For CO_2 abundance of 1% and O(^1S) yield of 0.2%, the calculations presented in Table 3 show that the photodissociation of H_2O contributes around 20%–40% in the production of O(^1S) and 60%–90% in the production of O(^1D) atom. The next major source of O(^1S) production is the photodissociation of CO_2 and CO with each contributing ∼10%–25%. The relative contributions from the photodissociation of parent species H_2O, CO_2, and CO to O(^1S) and O(^1D) production decreases with an increase in projected distance from the nucleus. At 10^4 km projected distance, the photodissociation of OH contributes 15% and 8% to the production of O(^1S) and O(^1D) atoms, respectively. Above 1000 km projected distance, the contribution of H_2O^+ dissociative recombination to O(^1S) production is around 20%. The production of the O(^1D) atom is mainly via the photodissociation of H_2O, but around 10^4 km the dissociative recombination of H_2O^+ ion is also a significant production process contributing around 12%. At 10^4 km, the dissociative recombination of OH^+ also contributes around 10% to the total O(^1D) production, which is not shown in Table 3, and this value is independent of the O(^1S) yield or CO_2 abundance.

Table 4
Calculated Percentage Contribution for the Major Production Processes of the Green (Red-doublet) Emission in the Slit Projected Field of View on the Comet C/1996 B2 Hyakutake

$O(^1S)$ Yield (%)	$h\nu + H_2O$	$h\nu + OH$	$h\nu + CO_2$	$e^- + H_2O^+$	$O(^1S) \rightarrow O(^1D)$	$h\nu + CO$	G/R Ratio[b]
1% CO_2							
0.0	0 [91][a]	2 [0.5]	36 [1]	13 [3]	[1]	35 [1]	0.07
0.2	36 [91]	1 [0.5]	23 [1]	8 [3]	[3]	22 [1]	0.11
0.5	59 [89]	1 [0.5]	14 [1]	5 [3]	[4]	14 [1]	0.17
1.0	76 [87]	0.5 [0.5]	10 [1]	0.5 [3]	[6]	10 [1]	0.27
0% CO_2							
0.0	0 [94]	4 [0.5]	0 [0]	21 [3]	[1]	59 [1]	0.04
0.2	49 [93]	2 [0.5]	0 [0]	11 [3]	[2]	30 [1]	0.08
0.5	70 [91]	1 [0.5]	0 [0]	6 [3]	[4]	17 [1]	0.15
1.0	82 [89]	0.5 [0.5]	0 [0]	3 [3]	[6]	10 [1]	0.25
3% CO_2							
0.0	0 [87]	1 [0.5]	60 [4]	7 [3]	[3]	20 [1]	0.13
5% CO_2							
0.5	35 [82]	0.5 [0.5]	45 [6]	3 [3]	[7]	7 [1]	0.27

Notes.
[a] The values in square brackets are the calculated percentage contribution for the red-doublet emission.
[b] The calculated values are averaged over the projected area of 165 × 1130 km corresponding to the slit size of $1''.2 \times 8''.2$ at $\Delta = 0.19$ AU centered on the nucleus of the comet C/1996 B2 Hyakutake on 1996 March 30 (Cochran 2008).

Radiative decay of $O(^1S)$ is a minor ($\leqslant$5%) production process in the formation of $O(^1D)$.

We also calculated the relative contributions of different processes in the formation of green and red line emissions in the slit projected field of view, which are presented in Table 4. For the above case, the photodissociation of H_2O contributes around 35%, while the photodissociation of CO_2 and CO contributes 23% and 22%, respectively, to the production of green line emission. The contribution of dissociative recombination of H_2O^+ ions is around 10%. The major production process of red lines is the photodissociation of H_2O (90%); the dissociative recombination of H_2O^+ and radiative decay of the $O(^1S)$ atom are minor ($\leqslant$5%) production processes. With the $O(^1S)$ yield of 0.2% and 1% CO_2 abundance, the slit-averaged G/R ratio is found to be 0.11.

When the $O(^1S)$ yield is increased to 0.5% with 1% CO_2 abundance (see Table 3), the contribution from the photodissociative excitation of H_2O to the $O(^1S)$ production is increased, with values varying from 35% to 60%, while the contribution to $O(^1D)$ production is not changed. In this case, the contribution from the photodissociation of CO_2 and CO to the $O(^1S)$ production is reduced (values between 10% and 15%). The contributions from other processes are not changed significantly. Table 4 shows that in this case of around 60% of green line in the slit projected field of view is produced via the photodissociation of H_2O, while the contributions from the photodissociation of CO_2 and CO are around 15% each. The main (90%) production of red-doublet emission is through the photodissociation of H_2O. The slit-averaged G/R ratio is 0.17.

On further increasing the $O(^1S)$ yield to 1% with CO_2 abundances of 1%, the contribution of photodissociation of H_2O to $O(^1S)$ atom production is further increased (values between 50% and 75%), while the contribution from photodissociation of CO_2 and CO is decreased to around 10% each (cf. Table 3). The contributions from other processes are not affected compared to the previous case. As seen from Table 4, in this case the contribution of photodissociation of H_2O to green line is around 75% in the slit projected field of view, while contributions from the photodissociation of CO_2 and CO are decreased to 10% each. The calculated G/R ratio is 0.27 (Table 4).

We also evaluated the effect of CO_2 on the red-doublet and green line emissions by varying its abundance to 0%, 3%, and 5%. The calculated percentage contribution of major processes along the projected distances and in the slit projected field of view are presented in Tables 3 and 4, respectively. In the absence of CO_2, the contributions from H_2O, H_2O^+, and CO in $O(^1S)$ production are increased by ~10% (cf. Tables 3 and 4). Taking 0% $O(^1S)$ yield and by increasing CO_2 relative abundance from 1% to 3%, the percentage contributions for $O(^1S)$ from the photodissociative excitation of CO_2 (CO) are increased (decreased) by 50%. The contribution from H_2O to $O(^1D)$ production is not changed.

The calculations presented in Tables 3 and 4 depict that the contributions of various processes are significant in the production of $O(^1S)$ atom, whereas the photodissociative excitation of H_2O is the main production process for the $O(^1D)$ atom. Since the comet C/1996 B2 Hyakutake is rich in CO (abundance ~22%) compared to other comets, the contribution from CO photodissociation to $O(^1S)$ production is significant (10%–25%). In the case of a comet having CO abundance less than 20%, the major production source of the metastable $O(^1S)$ atom would be the photodissociation of H_2O and CO_2.

4.5. Comparison with Observations

In 1996 March, the green and red-doublet emissions were observed in the comet C/1996 B2 Hyakutake from two ground-based observatories (Morrison et al. 1997; Cochran 2008). Each observatory determined the G/R ratio using a different slit size. Using a circular slit, the projected radial distance over the comet for the Morrison et al. (1997) observation on March 23 and 27 varied from 640 to 653 km, while for the Cochran (2008) observation, using a rectangular slit, the projected area was 480 × 3720 km on March 9 and 165 × 1129 km on March 30. The clear detection of both green and red-doublet emissions and determination of the G/R ratio could be done for March 9 and 23 observations only (Cochran 2008; Morrison et al. 1997). The

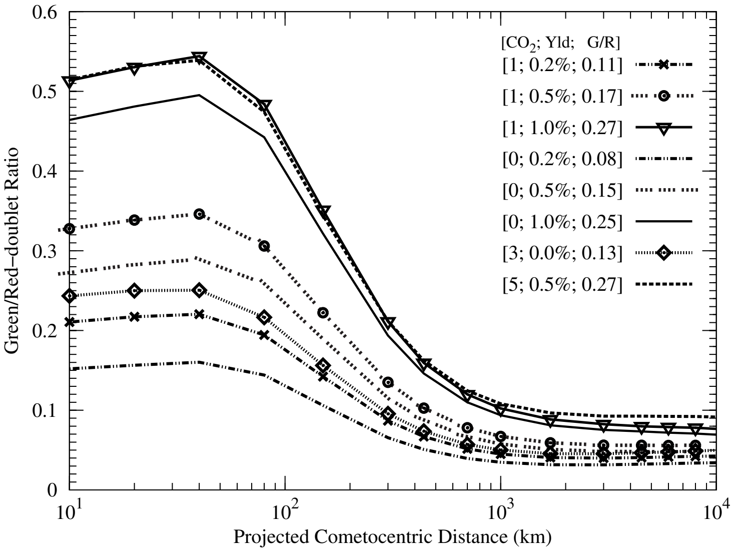

Figure 15. Calculated green to red-doublet intensity ratio along projected distances for different CO_2 relative abundance [CO_2] and yield [Yld] for O(^1S) production in the photodissociation of H_2O. G/R is the calculated green to red-doublet intensity ratio averaged over the slit projected size 165 × 1130 km for C/1996 B2 Hyakutake on 1996 March 30.

observed G/R ratio was 0.09 and 0.12–0.16 for the observation on March 9 and 23, respectively.

Performing a very high resolution ($R = 200{,}000$) observation of the comet C/1996 B2 Hyakutake on 1996 March 30, Cochran (2008) obtained radial profiles of 5577 and 6300 Å lines. In Figure 14, we have compared the model-calculated intensity profiles of 6300 and 5577 Å lines at different projected cometocentric distances with the observation of Cochran (2008). The calculated G/R ratio along the projected distance is shown in Figure 15. The 6300 Å emission shows a flat profile up to ∼500 km, whereas the 5577 Å green line starts falling off beyond 100 km. This is due to the quenching of O(^1S) and O(^1D) by H_2O in the innermost coma (cf. Figures 8 and 12), thereby making both the production and loss mechanisms controlled by H_2O. Above these distances, the emissions are mainly controlled by the radiative decay of ^1S and ^1D states of oxygen atoms.

Similar to the calculations presented in Tables 3 and 4, in Figures 14 and 15 we present the red and green line intensity profiles and the G/R ratios, respectively, for different contributions of O(^1S) yield and CO_2 abundances. Since the photodissociative excitation of H_2O is the main production process for the O(^1D) atom, the red line intensity is almost independent of the variation in O(^1S) yield and CO_2 abundance. In the case of 0% CO_2 abundance, the best fit to the observed green line profile is obtained when the O(^1S) yield is ∼0.5% (±0.1%), where the G/R ratio varies from 0.06 to 0.26 (cf. Figure 15) and the slit-averaged G/R ratio for March 30 observation is 0.15 (cf. Table 4). The shape of green line profile cannot be explained with 1% or 0% O(^1S) yield, while the case for 0.2% O(^1S) yield can be considered as somewhat consistent with the observation. For this case, the value of G/R ratio shown in Figure 15 is found to vary over a large range from 0.54 to 0.02.

When we consider 1% CO_2 in the comet, the best-fit green profile is obtained when the O(^1S) yield is ∼0.2%. The case for 0.5% O(^1S) yield also provides the green line profile consistent with the observation. In both these cases the G/R ratio varies between 0.32 and 0.04 over the cometocentric projected distances of 10 to 10^4 km. The calculated 5577 Å profiles for the O(^1S) yield of 0% and 1% are inconsistent with the observed profile.

Table 5
Calculated Green to Red-doublet Emission Brightness Ratio Averaged over the 5″ × 5″ Slit, at Different Geocentric Distances

Yield[a]	Geocentric Distance (AU)					
(%)	0.1	0.2	0.5	1	1.5	2
1% CO_2						
0.0	0.11	0.07	0.05	0.04	0.04	0.04
0.2	0.17	0.11	0.07	0.06	0.05	0.05
0.5	0.26	0.17	0.10	0.08	0.07	0.07
1.0	0.40	0.26	0.15	0.12	0.10	0.10
0% CO_2						
0.0	0.07	0.05	0.03	0.03	0.03	0.03
0.2	0.13	0.09	0.05	0.05	0.04	0.04
0.5	0.23	0.15	0.09	0.07	0.06	0.06
1.0	0.37	0.24	0.14	0.11	0.01	0.01
3% CO_2						
0.0	0.19	0.13	0.08	0.06	0.06	0.06
0.5	0.33	0.21	0.13	0.10	0.09	0.09

Notes. Calculations are made for 1996 March 30, where $r = 0.94$ AU.
[a] O(^1S) yield from the photodissociation of H_2O.

In Figure 14 we also show a calculated profile for a case when the CO_2 abundance is 3% while the O(^1S) yield is 0% (i.e., no O(^1S) is produced in the photodissociation of H_2O). The calculated 5577 Å green line profile shows a good fit to the observed profile: suggesting that even a small abundance of CO_2 is enough to produce the required O(^1S). This is because the CO_2 is about an order of magnitude more efficient in producing the O(^1S) atom than H_2O in the photodissociation process (see Table 1). However, since O(^1S) would definitely be produced in the photodissociation of H_2O, and that the CO_2 would surely be

Table 6
Calculated Intensities of Green and Red-doublet Emissions and the G/R Ratio in the Comet C/1996 B2 Hyakutake on Different Days of Observation in 1996 March

Date of Observation (1996 March)	r (AU)	Δ (AU)	Q_{H_2O} (s^{-1})	Slit Dimension (arcsec)	Projected Distance (km)	Calculated 5577 Å Intensity (kR)	Calculated (6300 + 6364 Å) Intensity (kR)	G/R Ratio Calculated	G/R Ratio Observed
9[a]	1.37	0.55	5×10^{28}	1″.2 × 8″.2	470 × 3720	0.06	0.62	0.09	0.09[a]
23[b]	1.08	0.12	1.8×10^{29}	7″.5 (circular)[c]	640	0.69	5.88	0.12	0.12–0.16[b]
27[b]	1.00	0.11	2×10^{29}	7″.5 (circular)	653	0.89	7.12	0.12	...
30[a]	0.94	0.19	2.2×10^{29}	1″.2 × 8″.2	165 × 1129	0.90	7.97	0.17	...

Notes. Calculations are made for O(^1S) yield of 0.5%, and CO_2 and CO relative abundances of 1% and 22%, respectively.
[a] Cochran (2008).
[b] Morrison et al. (1997).
[c] 7″.5 is the diameter of the circular slit.

present in the comet (though in smaller abundance), the most consistent value for the O(^1S) yield would be around 0.5%. Assuming 5% CO_2 and 0.5% O(^1S) yield, the calculated green line emission profile is inconsistent with the observation (cf. Figure 15). In this case, the calculated G/R ratio shown in Figure 15 is found to vary between 0.24 and 0.05.

From the above calculations, it is clear that the slit projected area on to the comet also plays an important role in deciding the G/R ratio. This point can be better understood from Table 5 where the G/R ratio is presented for a projected square slit on the comet at different geocentric distances. It is clear from this table that for a given physical condition of a comet and at a given heliocentric distance, the observed G/R ratio for a given slit size can vary according to the geocentric distance of the comet. For example, for an O(^1S) yield of 0.2% (0.5%) and CO_2 abundance of 1%, the G/R ratio can be 0.17 (0.26) if the comet is very close to the Earth (0.1 AU), whereas the G/R ratio can be 0.07 (0.1), 0.06 (0.08), or 0.06 (0.07), if the comet, at the time of observation, is at a larger distance of 0.5, 1, and 2 AU from the Earth, respectively. Furthermore, a G/R ratio of ∼0.1 can be obtained even for the O(^1S) yield of 0%. This suggests that the value of 0.1 for the G/R ratio is in no way a definitive benchmark value to conclude that H_2O is the parent of atomic oxygen atom in the comet, since smaller (∼5% relative to H_2O) amounts of CO_2 and CO itself can produce enough O(^1S) compared to that from H_2O. This table also shows that for observations made around a geocentric distance of 1 AU, the G/R ratio would be generally closer to 0.1. The G/R ratio observed in different comets ranges from 0.02 to 0.3 (e.g., Cochran 2008; Capria et al. 2010).

Thus, we can conclude that the G/R ratio not only depends on the production and loss mechanisms of the O(^1S) atom, but also depends on the nucleocentric slit projected area over the comet. Moreover, the CO_2 plays an important role in the production of O(^1S), and thus the green line emission, in comets. With the present model calculations and based on the literature survey of dissociation channels of H_2O, we suggest that the O(^1S) yield from the photodissociation of H_2O cannot be more than 1% of the total absorption cross section of H_2O at solar Lyα radiation. The best-fit value of the O(^1S) yield derived from Figure 14 for a smaller (1%) CO_2 abundance in the comet C/1996 B2 Hyakutake is 0.4% (±0.1)%. As per Tables 1 and 2, this means that the ratio of rates of O(^1S) to O(^1D) production in the H_2O photodissociation should be 0.03 (±0.01), which is much smaller than the value of 0.1 generally used in the literature based on Festou & Feldman (1981). Furthermore, if the source of red and green lines is CO_2 (CO), the ratio of photorates for O(^1S) to O(^1D) would be around 0.6 (0.8) (see Tables 1 and 2).

To verify whether the O(^1S) yield of 0.5% (for the CO_2 abundance of 1%) derived from Figure 14, based on the comparison between model and observed red and green line radial profiles in the comet Hyakutake on 1996 March 30, is consistent with the G/R ratio observed on other days on this comet, we present in Table 6 the G/R ratio calculated for observations made on 1996 March 9, 23, 27, and 30, along with the observed value of G/R ratio from Morrison et al. (1997) and Cochran (2008). These calculations are made by taking the solar flux on the day of observation using the Tobiska (2004) SOLAR2000 model and scaled according to the heliocentric distance of the comet on that date. The CO abundance is 22%, the same as in all the calculations presented in the paper.

The calculated G/R ratio on March 9, when the geocentric distance was 0.55 AU and the H_2O production rate was 5×10^{28} s^{-1}, is 0.09 (see Table 6) which is the same as the observed ratio obtained by Cochran (2008). On March 23 and 27, the comet is closer to both the Sun and Earth (geocentric distance ∼0.1 AU) and its H_2O production rate was four times higher than the value on March 9. The calculated G/R ratio on March 23 is 0.12, which is in agreement with the observed ratio obtained by Morrison et al. (1997).

5. CONCLUSIONS

The green and red-doublet atomic oxygen emissions are observed in the comet C/1996 B2 Hyakutake in 1996 March when it was passing quite close to the Earth ($\Delta = 0.1$–0.55 AU). A coupled chemistry-emission model has been developed to study the production of green (5577 Å) and red-doublet (6300 and 6364 Å) emissions in comets. This model has been applied to the comet Hyakutake and the results are compared with the observed radial profiles of 5577 and 6300 Å line emissions and the green to red-doublet intensity ratio. The important results from the present model calculations can be summarized as follows. It may be noted that some of these results enumerated below may vary for other comets having different gas production rate or heliocentric distance.

1. The photodissociation of H_2O is the dominant production process for the formation of O(^1D) throughout the inner cometary coma. The solar H Lyα (1216 Å) flux mainly governs the production of O(^1D) in the photodissociative

excitation of H_2O, but near the nucleus solar radiation in the wavelength band 1375–1165 Å can control the formation of $O(^1D)$ from H_2O.

2. Other than the photodissociation of H_2O molecule, above a cometocentric distance of 100 km the radiative decay of $O(^1S)$ to $O(^1D)$ (via 5577 Å line emission) and above 1000 km the dissociative recombination of H_2O^+ ions are also significant source mechanisms for the formation of $O(^1D)$ and $O(^1S)$ atoms.
3. The collisional quenching of $O(^1D)$ atoms by H_2O is significant up to a radial distance of ∼1000 km; above this distance, the radiative decay is the main loss mechanism of $O(^1D)$ atoms. The collisional quenching of $O(^1D)$ by other neutral species is an order of magnitude smaller.
4. The photodissociation of H_2O is the major process for the production of $O(^1S)$ atoms, but near the nucleus the photodissociation of CO_2 can be the dominant source. The solar H Lyα (1216 Å) flux controls the production of $O(^1S)$ via photodissociative excitation of H_2O.
5. At cometocentric distances of <100 km, the main loss process for $O(^1S)$ is quenching by H_2O molecule, while above 100 km the radiative decay is the dominant loss process.
6. Since the photoabsorption cross section of the CO_2 molecule is quite small at 1216 Å, the contribution of CO_2 in the production of $O(^1S)$ and $O(^1D)$ at the solar H Lyα is insignificant.
7. Because the CO_2 absorption cross section in the 1165–955 Å wavelength range is higher by an order of magnitude compared to that at other wavelengths, the solar radiation in this wavelength region mainly controls the production of $O(^1D)$ and $O(^1S)$ in the photodissociative excitation of CO_2. Moreover, the CO_2 absorption cross section in this band is also the largest compared to those of H_2O and CO.
8. The cross section for the photodissociation of H_2O producing $O(^1S)$ at the solar H Lyα wavelength (with 1% $O(^1S)$ yield) is smaller by more than two orders of magnitude than the cross section for the photodissociation of CO_2 producing $O(^1S)$ in the wavelength region 1165–955 Å. Though the solar flux at 1216 Å is higher compared to that in the 1165–955 Å wavelength region by two orders of magnitude, the larger value of the CO_2 cross section in this wavelength band enables CO_2 to be an important source for the production of metastable $O(^1S)$ atom.
9. In the case of CO, the dissociation and ionization thresholds are close to each other. Hence, most of the solar radiation ionizes the CO molecule rather than producing the $O(^1S)$ and $O(^1D)$ atoms.
10. Though the CO abundance is relatively high (∼22%) in the comet C/1996 B2 Hyakutake, the contribution of CO photodissociation in the $O(^1D)$ production is small (∼1%), while for the production of $O(^1S)$ its contribution is 10%–25%.
11. The photoelectron impact dissociative excitation of H_2O, CO_2, and CO makes only a minor contribution (<1%) in the formation of metastable $O(^1S)$ and $O(^1D)$ atoms in the inner coma.
12. The $O(^1S)$ density peaks at shorter radial distances than the $O(^1D)$ density. The peak value of $O(^1S)$ density is found around 60 km from the nucleus, while for the $O(^1D)$ a broad peak around 200–600 km is observed.
13. In an H_2O-dominated comet, the green line emission is mainly generated in the photodissociative excitation of H_2O with a contribution of 40%–60% (varying according to the radial distance) to the total intensity, while the photodissociation of CO_2 is the next potential source contributing 10%–40%.
14. For the red line emission the major source is the photodissociative excitation of H_2O, with contribution varying from 60% to 90% depending on the radial distance from the nucleus.
15. The G/R ratio depends not only on the production and loss processes of the $O(^1S)$ and $O(^1D)$ atoms, but also on the size of observing slit and the geocentric distance of comet at the time of observation.
16. For a fixed slit size, the calculated value of the G/R ratio is found to vary between 0.03 and 0.5 depending on the geocentric distance of the comet. In the innermost (<300 km) part of the coma, the G/R ratio is always larger than 0.1, with values as high as 0.5. On the other hand, at cometocentric distances larger than 1000 km the G/R ratio is always less than 0.1.
17. The model-calculated radial profiles of 6300 and 5577 Å lines are consistent with the observed profiles on the comet C/1996 B2 Hyakutake for the $O(^1S)$ yield of 0.4 (±0.1) and CO_2 abundances of 1%.
18. The model-calculated G/R ratio on the comet Hyakutake is in good agreement with the G/R ratio observed on two days in 1996 March by two observatories using different slit sizes.

S. Raghuram was supported by the ISRO Senior Research Fellowship during the period of this work.

REFERENCES

Atkinson, R., Baulch, D. L., Cox, R. A., et al. 1997, J. Phys. Chem. Ref. Data, 26, 1329

Atkinson, R., & Welge, K. H. 1972, J. Chem. Phys., 57, 3689

Berrington, K. A., & Burke, P. G. 1981, Planet. Space Sci., 29, 377

Bhardwaj, A. 1999, J. Geophys. Res., 104, 1929

Bhardwaj, A. 2003, Geophys. Res. Lett., 30, 2244

Bhardwaj, A., & Haider, S. A. 2002, Adv. Space Res., 29, 745

Bhardwaj, A., Haider, S. A., & Singhal, R. P. 1990, Icarus, 85, 216

Bhardwaj, A., Haider, S. A., & Singhal, R. P. 1995, Adv. Space Res., 16, 31

Bhardwaj, A., Haider, S. A., & Singhal, R. P. 1996, Icarus, 120, 412

Bhardwaj, A., & Jain, S. K. 2009, J. Geophys. Res., 114, 11309

Bhardwaj, A., & Jain, S. K. 2012, Icarus, 217, 752

Bhardwaj, A., & Michael, M. 1999a, J. Geophys. Res., 104, 24713

Bhardwaj, A., & Michael, M. 1999b, Geophys. Res. Lett., 26, 393

Bhardwaj, A., & Raghuram, S. 2011, MNRAS, 412, L25

Bhardwaj, A., & Singhal, R. P. 1993, J. Geophys. Res., 98, 9473

Biver, N., Bockelée-Morvan, D., Crovisier, J., et al. 1999, AJ, 118, 1850

Budzien, S. A., Festou, M. C., & Feldman, P. D. 1994, Icarus, 107, 164

Capetanakis, F. P., Sondermann, F., Höser, S., & Stuhl, F. 1993, J. Chem. Phys., 98, 7883

Capria, M. T., Cremonese, G., Bhardwaj, A., & Sanctis, M. C. D. 2005, A&A, 442, 1121

Capria, M. T., Cremonese, G., Bhardwaj, A., Sanctis, M. C. D., & Epifani, E. M. 2008, A&A, 479, 257

Capria, M. T., Cremonese, G., & Sanctis, M. C. D. 2010, A&A, 522, A82

Cochran, A. L. 2008, Icarus, 198, 181

Cochran, A. L., & Cochran, W. D. 2001, Icarus, 154, 381

Cochran, W. D. 1984, Icarus, 58, 440

Combi, M. R., Brown, M. E., Feldman, P. D., et al. 1998, ApJ, 494, 816

Combi, M. R., Harris, W. M., & Smyth, W. H. 2004, in Gas Dynamics and Kinetics in the Cometary Coma: Theory and Observations, ed. M. C. Festou, H. U. Keller, & H. A. Weaver (Tucson, AZ: Univ. Arizona Press), 523

Combi, M. R., Mäkinen, J. T. T., Bertaux, J.-L., & Quemérais, E. 2005, Icarus, 177, 228

Delsemme, A. H., & Combi, M. R. 1976, ApJ, 209, L149
Delsemme, A. H., & Combi, M. R. 1979, ApJ, 228, 330
Demore, W. B., Sander, S. P., Golden, D. M., et al. 1997, Chemical Kinetics and Photochemical Data for Use in Stratospheric Modeling, Technical Report Evaluation Number 12, JPL Publication 97-4
Feldman, P. D., Cochran, A. L., & Combi, M. R. 2004, in Spectroscopic Investigations of Fragment Species in the Coma, ed. M. C. Festou, H. U. Keller, & H. A. Weaver (Tucson, AZ: Univ. Arizona Press), 425
Festou, M. C. 1981, A&A, 96, 52
Festou, M. C., & Feldman, P. D. 1981, A&A, 103, 154
Fink, U., & Johnson, J. R. 1984, AJ, 89, 1565
Furusho, R., Kawakita, H., Fuse, T., & Watanabe, J. 2006, Adv. Space Res., 38, 1983
Glinski, R. J., Ford, B. J., Harris, W. M., Anderson, C. M., & Morgenthaler, J. P. 2004, ApJ, 608, 601
Guberman, S. L. 1995, J. Chem. Phys., 102, 1699
Haider, S. A., & Bhardwaj, A. 2005, Icarus, 177, 196
Huebner, W. F., & Carpenter, C. W. 1979, Los Alamos Report, 8085
Huebner, W. F., Keady, J. J., & Lyon, S. P. 1992, Adv. Space Sci., 195, 1
Huestis, D. L., & Slanger, T. G. 2006, BAAS, 38, 609
Huestis, D. L., Slanger, T. G., Sharpee, B. D., & Fox, J. L. 2010, Faraday Discuss., 147, 307
Itikawa, Y., & Mason, N. 2005, J. Phys. Chem. Ref. Data, 34, 1
Jackman, C. H., Garvey, R. H., & Green, A. E. S. 1977, J. Geophys. Res., 82, 5081
Kedzierski, W., Derbyshire, J., Malone, C., & McConkey, J. W. 1998, J. Phys. B: At. Mol. Opt. Phys., 31, 5361
Körösmezey, A., Cravens, T. E., Gombosi, T. I., et al. 1987, J. Geophys. Res., 92, 7331
Krauss, M., & Neumann, D. 1975, Chem. Phys. Lett., 36, 372
Lawrence, G. M. 1972, J. Chem. Phys., 57, 5616
LeClair, L. R., Brown, M. D., & McConkey, J. W. 1994, Chem. Phys., 189, 769
LeClair, L. R., & McConkey, J. W. 1994, J. Phys. B: At. Mol. Opt. Phys., 27, 4039
Link, R. 1982, PhD thesis, York Univ., Canada
Magee-Sauer, K., Scherb, F., Roesler, F. L., & Harlander, J. 1990, Icarus, 84, 154
Manfroid, J., Hutsemékers, D., Jehin, E., et al. 2007, Icarus, 187, 144
McConkey, J. W., Malone, C. P., Johnson, P. V., et al. 2008, Phys. Rep., 466, 1
McElroy, M. B., & McConnell, J. C. 1971, J. Geophys. Res., 76, 6674
McNesby, J. R., Tanaka, I., & Okabe, H. 1962, J. Chem. Phys., 36, 605
Mitchell, J. B. A. 1990, Phys. Rep., 186, 215
Morgenthaler, J. P., Harris, W. M., & Combi, M. R. 2007, ApJ, 657, 1162
Morgenthaler, J. P., Harris, W. M., Scherb, F., et al. 2001, ApJ, 563, 451
Morrison, N. D., Knauth, D. C., Mulliss, C. L., & Lee, W. 1997, PASP, 109, 676
Mumma, M. J., DiSanti, M. A., Russo, N. D., et al. 1996, Science, 272, 1310
Raghuram, S., & Bhardwaj, A. 2011, Planet. Space Sci., in press
Rosen, S., Derkatch, A., Semaniak, J., et al. 2000, Faraday Discuss., 407, 295
Schmidt, H. U., Wegmann, R., Huebner, W. F., & Boice, D. C. 1988, Comput. Phys. Commun., 49, 17
Schultz, D., Li, G. S. H., Scherb, F., & Roesler, F. L. 1992, Icarus, 96, 190
Seng, G., & Linder, F. 1976, J. Phys. B: At. Mol. Phys., 9, 2539
Singh, P. D., D'Ealmeida, A. A., & Huebner, W. F. 1991, Icarus, 90, 74
Singhal, R. P., & Bhardwaj, A. 1991, J. Geophys. Res., 96, 15963
Singhal, R. P., & Haider, S. A. 1984, J. Geophys. Res., 89, 6847
Slanger, T. G., & Black, G. 1982, J. Chem. Phys., 77, 2432
Slanger, T. G., Sharpless, R. L., & Black, G. 1977, J. Chem. Phys., 66, 5317
Spinrad, H. 1982, PASP, 94, 1008
Stief, L. J., Payne, W. A., & Klemm, R. B. 1975, J. Chem. Phys., 62, 4000
Storey, P. J., & Zeippen, C. J. 2000, MNRAS, 312, 813
Tobiska, W. K. 2004, Adv. Space Res., 34, 1736
Tobiska, W. K., Woods, T., Eparvier, F., et al. 2000, J. Atmos. Sol.-Terr. Phys., 62, 1233
van Dishoeck, E. F., & Dalgarno, A. 1984, ApJ, 277, 576
Watanabe, K., & Zelikoff, M. 1953, J. Opt. Soc. Am., 43, 753
Wiese, W. L., Fuhr, J. R., & Deters, T. M. (ed.) 1996, Atomic Transition Probabilities of Carbon, Nitrogen, and Oxygen: A Critical Data Compilation (Washington, DC: Am. Chem. Soc.)
Zhang, H. W., Zhao, G., & Hu, J. Y. 2001, A&A, 367, 1049
Zipf, E. C. 1969, Can. J. Chem., 47, 1863

Icarus 223 (2013) 91–104

Contents lists available at SciVerse ScienceDirect

Icarus

journal homepage: www.elsevier.com/locate/icarus

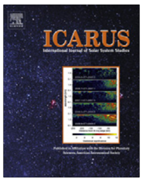

Model for atomic oxygen visible line emissions in Comet C/1995 O1 Hale-Bopp

Susarla Raghuram, Anil Bhardwaj *

Space Physics Laboratory, Vikram Sarabhai Space Centre, Trivandrum 695 022, India

ARTICLE INFO

Article history:
Received 27 April 2012
Revised 20 November 2012
Accepted 20 November 2012
Available online 12 December 2012

Keywords:
Comets
Comets, Coma
Comets, Composition
Comet Hale-Bopp
Photochemistry

ABSTRACT

We have recently developed a coupled chemistry-emission model for the green (5577 Å) and red-doublet (6300, 6364 Å) emissions of atomic oxygen on Comet C/1996 B2 Hyakutake. In the present work we applied our model to Comet C/1995 O1 Hale-Bopp, which had an order of magnitude higher H_2O production rate than Comet Hyakutake, to evaluate the photochemistry associated with the production and loss of $O(^1S)$ and $O(^1D)$ atoms and emission processes of green and red-doublet lines. We present the wavelength-dependent photo-attenuation rates for different photodissociation processes forming $O(^1S)$ and $O(^1D)$. The calculated radiative efficiency profiles of $O(^1S)$ and $O(^1D)$ atoms show that in Comet Hale-Bopp the green and red-doublet emissions are emitted mostly above radial distances of 10^3 and 10^4 km, respectively. The model calculated [OI] 6300 Å emission surface brightness and average intensity over the Fabry-Pérot spectrometer field of view are consistent with the observation of Morgenthaler et al. (Morgenthaler, J.P. et al. [2001]. Astrophys. J. 563, 451–461), while the intensity ratio of green to red-doublet emission is in agreement with the observation of Zhang et al. (Zhang, H.W., Zhao, G., Hu, J.Y. [2001]. Astron. Astophys. 367 (3), 1049–1055). In Comet Hale-Bopp, for cometocentric distances less than 10^5 km, the intensity of [OI] 6300 Å line is mainly governed by photodissociation of H_2O. Beyond 10^5 km, $O(^1D)$ production is dominated by photodissociation of the water photochemical daughter product OH. Whereas the [OI] 5577 Å emission line is controlled by photodissociation of both H_2O and CO_2. The calculated mean excess energy in various photodissociation processes show that the photodissociation of CO_2 can produce $O(^1S)$ atoms with higher excess velocity compared to the photodissociation of H_2O. Thus, our model calculations suggest that involvement of multiple sources in the formation of $O(^1S)$ could be a reason for the larger width of green line than that of red-doublet emission lines observed in several comets.

1. Introduction

Owing to its very high H_2O production rate, C/1995 O1 Hale-Bopp was a great comet in the night sky of the year 1997. The visible emissions of atomic oxygen ([OI] 6300, 6364, and 5577 Å), which are accessible to the ground-based optical instruments, have been observed by Morgenthaler et al. (2001) and Zhang et al. (2001) in the coma of Hale-Bopp. Since the lifetime of oxygen atom in the ^1D metastable state is relatively small (∼110 s) compared to the photochemical lifetime of H_2O ($\sim 8 \times 10^4$ s), it cannot travel larger distances in the coma without decaying to the ground ^3P state. Moreover, most of the production of oxygen in the ^1D state is through photodissociative excitation of H_2O (Bhardwaj and Haider, 2002). Thus, [OI] 6300 Å emission has been used to trace the spatial distribution as well as to quantify the production rate of H_2O in several comets (Delsemme et al., 1976; Delsemme and Combi, 1979; Fink and Johnson, 1984; Schultz et al., 1992; Morgenthaler et al., 2001; Furusho et al., 2006; Fink, 2009).

Based on the study of Festou and Feldman (1981) the intensity ratio of green (5577 Å) to red-doublet (6300 Å and 6364 Å) emissions (here after G/R ratio) of atomic oxygen has been used to determine whether the parent source of these lines is H_2O or CO_2/CO in the coma of comets (Cochran, 1984, 2008; Morrison et al., 1997; Zhang et al., 2001; Cochran et al., 2001; Furusho et al., 2006; Capria et al., 2005, 2008, 2010; McKay et al., 2012a,b). The modelling studies of these emissions in comets showed that photodissociative excitation of H_2O is the major production process of the [OI] 6300 Å emission (Festou and Feldman, 1981; Bhardwaj and Haider, 2002; Capria et al., 2005, 2008; Bhardwaj and Raghuram, 2012). Our recent theoretical study (Bhardwaj and Raghuram, 2012) for these prompt emissions of atomic oxygen in Comet C/1996 B2 Hyakutake showed that more than 90% of the $O(^1D)$ is populated via photodissociative excitation of H_2O and the rest through photodissociation of other oxygen bearing species, like CO_2 and CO. It also showed that quenching by H_2O is the major loss mechanism of $O(^1D)$ up to cometocentric distances of 1000 km, and above that distance radiative decay

---

* Corresponding author. Fax: +91 471 2706535.
E-mail addresses: raghuramsusarla@gmail.com (S. Raghuram), Anil_Bhardwaj@vssc.gov.in, bhardwaj_spl@yahoo.com (A. Bhardwaj).

0019-1035/$ - see front matter © 2012 Elsevier Inc. All rights reserved.
http://dx.doi.org/10.1016/j.icarus.2012.11.032

takes over. The study of Bhardwaj and Raghuram (2012) demonstrated that the G/R ratio depends not only on the photochemistry involved in populating O(^{1}S) and O(^{1}D) atoms in the cometary coma, but also on the projected area observed for the comet, which is a function of slit dimension used for observation and geocentric distance of the comet.

In the present study we applied our coupled chemistry-emission model (Bhardwaj and Raghuram, 2012) to Comet C/1995 O1 Hale-Bopp, which had an order of magnitude higher H_2O production rate compared to that of Comet Hyakutake, to evaluate the production and loss mechanisms of O(^{1}D) and O(^{1}S) and generation of green and red-doublet emissions. Our aim in this paper is to study the photo-attenuation in comets having high H_2O production rates and its implications on the photochemistry of metastable O(^{1}S) and O(^{1}D) atoms. We compared our model calculated [OI] 6300 Å emission surface brightness profile with the observation of Morgenthaler et al. (2001). We have shown that the photodissociation of H_2O mainly controls the formation of O(^{1}D) and subsequently determines the intensity of [OI] 6300 Å emission. However, in the case of [OI] 5577 Å emission, the photodissociation of both H_2O and CO_2 plays an important role in the formation of metastable O(^{1}S), with photodissociation of CO_2 being the major production source of O(^{1}S) in the inner cometary coma. We suggest that in comets with significant ($\geqslant 5\%$) CO_2 relative abundance, the photodissociation of CO_2 is more effective in populating O(^{1}S) than the photodissociation of H_2O. The model calculated G/R ratio is consistent with the observed value of Zhang et al. (2001). Based on the model results, we suggest that the involvement of multiple species in the formation O(^{1}S) could be a reason for the width of the green line emission to be larger than the red-doublet emission lines observed in several comets by Cochran (2008).

2. Model

The details of the model and the chemistry are presented in our previous work (Bhardwaj and Raghuram, 2012). Here we present the input parameters that have been used in the model for the observed condition of Comet Hale-Bopp on 10 March 1997 (solar radio flux F10.7 = 74.7×10^{-22} J s^{-1} m^{-2} Hz^{-1}) when it was at a geocentric distance (Δ) of 1.32 AU and a heliocentric distance (r_h) of 0.93 AU. The photochemical reaction network and cross sections for photon and electron impact processes are same as used in the previous work and any changes made are mentioned. The degradation of solar EUV-generated photoelectrons is accounted by using Analytical Yield Spectrum (AYS) technique which is based on the Monte-Carlo method (Singhal and Bhardwaj, 1991; Bhardwaj and Singhal, 1993; Bhardwaj and Michael, 1999a,b; Bhardwaj and Jain, 2009). Details of the AYS approach and the method to calculate photoelectron flux and excitation rates are given in our earlier papers (Bhardwaj et al., 1990, 1996; Bhardwaj, 1999, 2003; Haider and Bhardwaj, 2005; Bhardwaj and Raghuram, 2011; Raghuram and Bhardwaj, 2012; Bhardwaj and Jain, 2012).

In our previous work (Bhardwaj and Raghuram, 2012) it has been shown that the contribution of several processes to the production of O(^{1}S) and O(^{1}D) is small. Thus, only important production and destruction mechanisms of metastable O(^{1}S) and O(^{1}D) are presented in Table 1. The branching ratio of 0.81 is used for the production of OH in the photodissociation of H_2O (cf. Huebner et al., 1992; Nee and Lee, 1984). The radius of the cometary nucleus is taken as 25 km (Weaver et al., 1997; Combi et al., 1999). Though a variety of O-bearing minor species (with relative abundances $\leqslant 1\%$, Bockelée-Morvan et al. (2000)) have been found in Comet Hale-Bopp, the dominant species H_2O, CO_2, and CO are only considered in our model calculations. The neutral density profiles of these parent species are calculated using Haser's formula.

Using ground-based observations of direct H_2O infrared emissions during January to May 1997, Dello Russo et al. (2000) derived water production rates at different heliocentric distances and fitted as a function of r_h as $Q_{H_2O} = 8.35 \pm 0.13 \times 10^{30} \left[r_h^{(-1.88\pm0.13)}\right]$ molecules s^{-1}. We used this expression as a standard input in calculating H_2O density profiles on different days. The H_2O production rates in Hale-Bopp are also derived by observing the emissions from its dissociative products, like OH 18-cm emission, OH (0–0) 3080 Å emission, [OI] 6300 Å emission, and H Lyman-α, over large projected distances (Weaver et al., 1997; Colom et al., 1999; Schleicher et al., 1997; Combi et al., 2000; Woods et al., 2000; Morgenthaler et al., 2001; Harris et al., 2002; Fink, 2009). These derived H_2O production rates depend on the observational condition and also on the assumed model parameters. We have discussed the effect of H_2O production rate on the calculated green and red-doublet emission intensities of atomic oxygen in Section 4.2.2.

High resolution ground-based infrared spectroscopic observations are used to study the CO production rate in Comet Hale-Bopp from June 1996 to September 1997 (DiSanti et al., 2001). The spatial distribution of CO in the coma of Hale-Bopp is assumed to have two distinct sources: nucleus-originated, and extensively distributed in the cometary coma. During this observation period, the relative abundance of CO is found to be $\sim$25% of H_2O. DiSanti et al. (2001) fitted the observed CO production rate as a function of heliocentric distance near the perihelion as $Q_{CO} = 2.07 \times 10^{30}$ $r_h^{-1.66\pm0.22}$ molecules s^{-1}, and above 1.5 AU as $Q_{CO} = 1.06 \times 10^{30}$ $r_h^{-1.76\pm0.26}$ molecules s^{-1}. Since observations of [OI] 6300 Å emission are done when comet was at around 1 AU, we have used the former formulation to calculate the neutral CO density in our model. DiSanti et al. (2001) suggested that the increase in CO production rate below 1.5 AU is due to distributed sources prevailing in the cometary coma. Recent study of Bockelée-Morvan et al. (2010) showed that the infrared CO (1–0) rotational vibrational emission lines are optical thick in the cometary coma of Hale-Bopp. Based on the modelling studies of these emission lines they rejected the idea of extended source distribution of CO in Comet Hale-Bopp. However, our model calculations show that the role of CO in determining green and red-doublet emission intensities is very small compared to other species, and hence the impact of distributed CO source is insignificant on these forbidden emission lines.

The CO_2 has been detected in Hale-Bopp by Crovisier et al. (1997) in April 1996, when the comet was at heliocentric distance of 2.9 AU. Based on the infrared emissions between 2.5 and 5 μm, the derived CO_2 production rate at 2.9 AU was 1.3×10^{28} molecules s^{-1}, which corresponds to a relative abundance of $\sim$20% of H_2O. Assuming that the photodissociative excitation is the main production mechanism in populating the CO ($a^3\Pi$) metastable state, the observed CO Cameron band ($a^3\Pi \rightarrow X^1\Sigma^+$) emission intensity has been used to estimate the abundance of CO_2 in this comet by Weaver et al. (1997). The estimated CO_2 abundance is more than 10% when the comet was beyond 2.7 AU. However, our model calculations on Comets 103P/Hartley 2 (Bhardwaj and Raghuram, 2011) and 1P/Halley (Raghuram and Bhardwaj, 2012) have shown that photoelectron impact excitation is the main production mechanism of CO Cameron band emission and not the photodissociation of CO_2. Assuming that the CO_2/CO abundance ratio did not vary with heliocentric distance in this comet, Bockelée-Morvan et al. (2004) suggested 6% relative abundance of CO_2 when the comet was at 1 AU. We have taken 6% CO_2 relative abundance with respect to H_2O in the model. However, we discuss the impact of CO_2 abundance by varying its relative abundance on the calculated intensities of green and red-doublet emissions. The OH neutral density profile in Comet Hale-Bopp is calculated by fitting Harris et al. (2002) observed OH (0–0) 3080 Å resonant scattering emission along the projected distance with the Haser's two step formulation. The photodissociative excitation rates of OH producing O(^{1}S) and O(^{1}D) are taken from Huebner et al.

Table 1
Major production and destruction processes of the $O(^1S)$ and $O(^1D)$. Photorates are calculated using solar flux on 10 April 1997 (solar minimum period: solar radio flux F10.7 = 74.7 × 10^{-22} J s^{-1} m^{-2} Hz^{-1}) and scaled to 0.92 AU heliocentric distance.

Reaction	Rate (cm^{-3} s^{-1} or s^{-1})	Reference
$H_2O + h\nu \rightarrow O(^1S) + H_2$	3.78×10^{-8}	This work
$OH + h\nu \rightarrow O(^1S) + H$	6.71×10^{-8}	Huebner et al. (1992)[a]
$CO_2 + h\nu \rightarrow O(^1S) + CO$	8.5×10^{-7}	This work
$CO + h\nu \rightarrow O(^1S) + C$	4.0×10^{-8}	Huebner and Carpenter (1979)
$H_2O^+ + e_{th} \rightarrow O(^1S)$ + others	$4.3 \times 10^{-7}\ (300/T_e)^{0.5} \times 0.045$[b]	Rosén et al. (2000)
$O(^1S) + H_2O \rightarrow 2OH$	3×10^{-10}	Zipf (1969)
$O(^1S) \rightarrow O(^3P) + h\nu_{2972Å}$	0.134	Slanger et al. (2006)
$O(^1S) \rightarrow O(^1D) + h\nu_{5577Å}$	1.26	Wiese et al. (1996)
$H_2O + h\nu \rightarrow O(^1D) + H_2$	9.5×10^{-7}	This work
$OH + h\nu \rightarrow O(^1D) + H$	7.01×10^{-6}	Huebner et al. (1992)[c]
$CO_2 + h\nu \rightarrow O(^1D) + CO$	6.2×10^{-7}	This work
$CO + h\nu \rightarrow O(^1D) + C$	6.0×10^{-8}	This work
$H_2O^+ + e_{th} \rightarrow O(^1D)$ + others	$4.3 \times 10^{-7}\ (300/T_e)^{0.5} \times 0.045$[b]	Rosén et al. (2000)
$CO^+ + e_{th} \rightarrow O(^1D)$ + others	$5.0 \times 10^{-8} \times (300/T_e)^{0.46}$	Mitchell (1990)
$O(^1D) + H_2O \rightarrow 2OH$	2.1×10^{-10}	Atkinson et al. (1997)
$O(^1D) \rightarrow O(^3P) + h\nu_{6300Å}$	6.44×10^{-3}	Storey and Zeippen (2000)
$O(^1D) \rightarrow O(^3P) + h\nu_{6364Å}$	2.15×10^{-3}	Storey and Zeippen (2000)

$h\nu$: solar photon; e_{th}: thermal electron; T_e: electron temperature.

[a] Huebner et al. (1992) calculated this rate using theoretical OH absorption cross section of van Dishoeck and Dalgarno (1984).

[b] 0.045 is the assumed branching ratio for the formation of $O(^1S)$ and $O(^1D)$ via dissociative recombination of H_2O^+ ion (see Bhardwaj and Raghuram, 2012).

[c] Huebner et al. (1992) calculated this rate based on experimentally determined OH absorption cross section of Nee and Lee (1984).

(1992) which were determined using theoretical (van Dishoeck and Dalgarno, 1984) and experimental (Nee and Lee, 1984) photoabsorption cross sections, respectively.

There is a clear evidence that in Comet Hale-Bopp the expansion velocity of neutrals increases with increasing cometocentric distance (Colom et al., 1999; Biver et al., 1997; Harris et al., 2002). The sources involved in accelerating the neutral species across the cometary coma is discussed in several works (Colom et al., 1999; Combi et al., 1999; Harris et al., 2002; Combi, 2002). To incorporate the acceleration of these neutrals in our model we have taken the velocity profile calculated by Combi et al. (1999) at 1 AU and used as a input in the Haser's density distribution. We also verified the effect of expansion velocity on the calculated intensity of green and red-doublet emissions by varying its static value between 0.7 and 2.2 km s^{-1}, which is discussed in Section 4.2.1.

The input solar flux is taken from SOLAR2000 (S2K) v.2.36 model of Tobiska (2004) and scaled accordingly to the heliocentric distance of the comet at the time of observation. The electron temperature profile required to calculate dissociative recombination rates is taken from Lovell et al. (2004). Bhardwaj and Raghuram (2012) have found that the yield of $O(^1S)$ in the photodissociation of H_2O at solar H Ly-α cannot be more than 1%. In the present study we have taken this yield value as 0.5%. The impact of this assumption was discussed in our previous work (Bhardwaj and Raghuram, 2012). The photodissociative excitation cross section for CO_2 producing $O(^1D)$ is taken from Jain and Bhardwaj (2012, in preparation). The photodissociative excitation cross sections for the production of $O(^1D)$ and $O(^1S)$ from H_2O, CO_2, and CO used in the model are presented in Fig. 1. The attenuation of solar radiation and solar UV–EUV generated photoelectrons in the cometary coma are described in our previous works (Bhardwaj et al., 1990; Bhardwaj, 1999, 2003; Bhardwaj and Haider, 1999; Raghuram and Bhardwaj, 2012).

3. Results

3.1. Production and loss of $O(^1S)$

The calculated $O(^1S)$ volumetric production rate profiles for major production processes are presented in Fig. 2. The photodissociation of CO_2 is the major production process of $O(^1S)$. Above cometocentric distance of 1000 km, the photodissociative excitation of H_2O is also an equally important production source of $O(^1S)$. Photodissociative excitation of CO is the next significant production mechanism in producing $O(^1S)$. Since no cross section is reported in the literature for photodissociation of CO producing $O(^1S)$, we have taken the photo-rate for this process from Huebner and Carpenter (1979) and assumed that the formation of $O(^1S)$ is similar to $O(^1D)$. This assumption results in the calculated $O(^1S)$ profile below 100 km similar to that of $O(^1D)$. However, this assumption does not make any significant impact on the calculated green line intensity, since photodissociation of CO_2 and H_2O can produce $O(^1S)$ an order of magnitude higher than that of CO in the inner coma. Above 10^4 km, the contribution from dissociative recombination reactions of H_2O^+ and CO^+ to the total $O(^1S)$ production is significant. The photodissociation of OH is a minor source of $O(^1S)$ below 10^5 km radial distance.

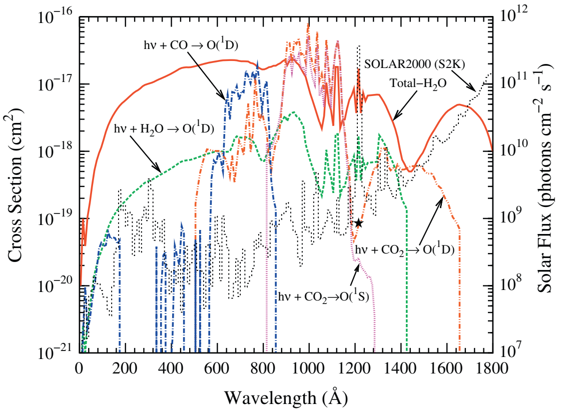

Fig. 1. Photodissociative excitation cross sections for the production of $O(^1D)$ from H_2O and CO are taken from Huebner et al. (1992). The photodissociation of CO_2 for the production of $O(^1D)$ are taken from Jain and Bhardwaj (2012, in preparation). The photodissociation cross section of CO_2 producing $O(^1S)$ is calculated using the yield suggested by Huestis et al. (2010) and total absorption cross section. ★Represents the cross section value for the production of $O(^1S)$ from H_2O at 1216 Å assuming 0.5% yield. For comparison the total photoabsorption cross section of H_2O taken from Huebner et al. (1992) is also shown. The solar flux taken from SOLAR2000 (S2K) model on 9 March 1997 (solar minimum condition; solar radio flux F10.7 = 74.7 × 10^{-22} J s^{-1} m^{-2} Hz^{-1}) is shown with scale on the right side *y*-axis.

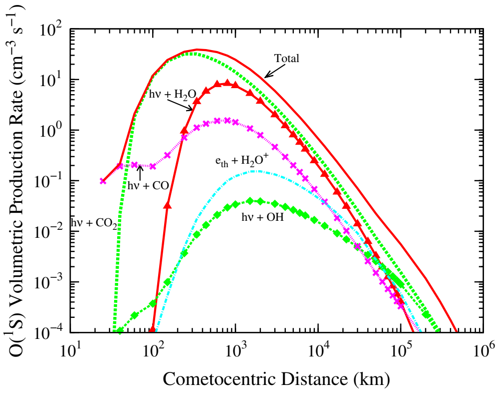

Fig. 2. Calculated radial profiles for major production mechanisms of $O(^1S)$ along with the total production profile for the abundances of 6% CO_2 and 24% CO relative to H_2O production rate of 8.3×10^{30} s^{-1}. *hν*: solar photon and e_{th}: thermal electron.

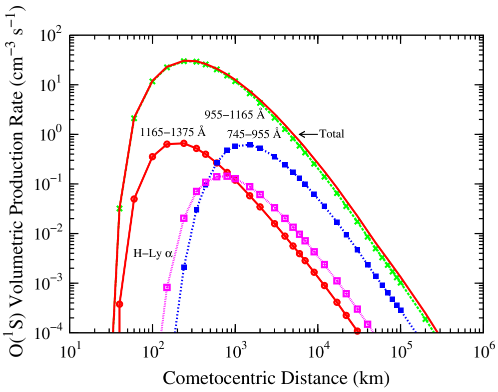

Fig. 3. Calculated radial profiles for the photodissociation of CO_2 producing $O(^1S)$ at different wavelength bands for the abundances of 6% CO_2 and 24% CO relative to H_2O production rate of 8.3×10^{30} s^{-1}.

The calculated $O(^1S)$ volumetric production rate profiles for photodissociation of CO_2 in the different wavelength bands are shown in Fig. 3. The cross section for photodissociation of CO_2 in the wavelength band 955–1165 Å is higher by a few orders of magnitude compared to that at other wavelength regions (cf. Fig. 1). Moreover, in this wavelength band, the yield of $O(^1S)$ in photodissociation of CO_2 tends to unity (Slanger et al., 1977; Lawrence, 1972), while the total absorption cross section of H_2O has a strong dip (cf. Fig. 1). Thus, solar photons in this wavelength band can dissociate CO_2 and produce $O(^1S)$ very efficiently. The photons in the wavelength bands 1165–1375 and 745–955 Å make a smaller (<10%) contribution to the total $O(^1S)$ production. The contribution of 1216 Å solar photons to the $O(^1S)$ formation is two orders of magnitude low because of the small absorption cross section of CO_2 ($\sim 8 \times 10^{-20}$ cm^2).

The calculated volumetric destruction rate profiles of $O(^1S)$ are presented in Fig. 4. The collisional quenching of $O(^1S)$ by H_2O is the dominant loss process at cometocentric distances shorter than 300 km. Above 1000 km the radiative decay via [OI] 5577 Å line emission is the main loss process for the $O(^1S)$ atom. The radiative decay via [OI] 2972 Å emission is a minor loss process of $O(^1S)$.

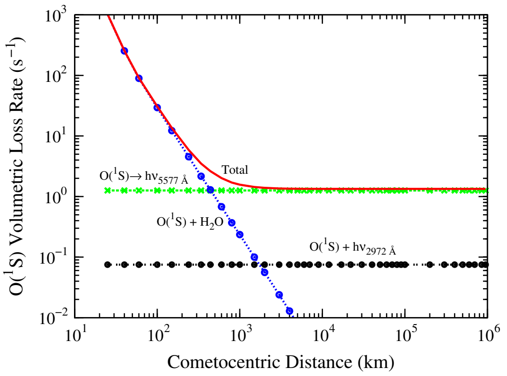

Fig. 4. Calculated radial profiles for the major loss mechanisms of the $O(^1S)$ atom for the abundances of 6% CO_2 and 24% CO relative to H_2O production rate of 8.3×10^{30} s^{-1}.

3.2. Production and loss of $O(^1D)$

The calculated volumetric production rate profiles of metastable $O(^1D)$ for different formation mechanisms are shown in Fig. 5. Between 100 and $\sim 2 \times 10^4$ km, most of the $O(^1D)$ (>90%) is produced via photodissociation of H_2O. However, below 100 km, the photodissociation of CO_2 is also an important source of $O(^1D)$. Between 200 and 2000 km, the radiative decay of $O(^1S)$ makes a minor contribution in the formation of $O(^1D)$. Above 10^4 km, the photodissociation of OH plays a significant role in the formation of $O(^1D)$. Even though the relative abundance of CO in Hale-Bopp is high (∼25%), the photodissociation of CO is not a potential source mechanism of $O(^1D)$. The calculated $O(^1D)$ photodissociation rate profile for photodissociation of CO shows a double peak structure, which is explained later.

The wavelength-dependent production rates of $O(^1D)$ in the photodissociation of H_2O are shown in Fig. 6. The most intense line of solar UV spectrum, H Ly-α at 1216 Å, produces maximum $O(^1D)$ around 1000 km, while solar photons in the wavelength regions 1165–1375 and 1375–1575 Å are responsible for producing maximum $O(^1D)$ at shorter radial distances of 200 and 50 km, respectively. Since the total absorption cross section of H_2O in the 1165–1575 Å wavelength region is small (cf. Fig. 1), these solar photons are able to penetrate deeper in the coma and mostly get attenuated at shorter cometocentric distances by dissociating H_2O. The $O(^1D)$ formation rate by solar photons at other wavelengths is smaller by more than an order of magnitude.

Similarly, the production rate of $O(^1D)$ due to photodissociation of CO_2 calculated at different wavelength bands is shown in Fig. 7. At radial distances <100 km, solar photons in 1375–1585 Å

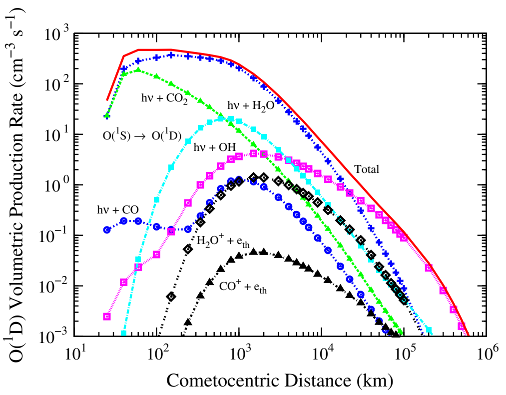

Fig. 5. Calculated radial profiles for the major production mechanisms of $O(^1D)$ along with the total $O(^1D)$ production rate profile for the abundances of 6% CO_2 and 24% CO relative to H_2O production rate of 8.3×10^{30} s^{-1}. *hν*: solar photon.

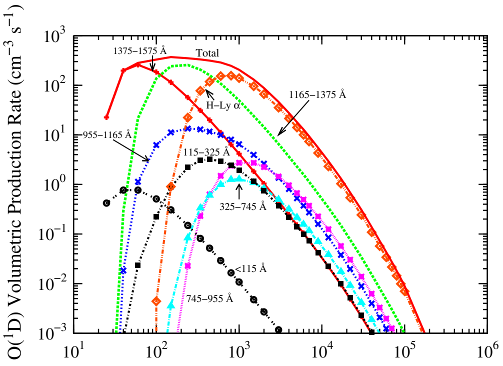

Fig. 6. Calculated radial profiles for the photodissociation of H_2O producing $O(^1D)$ at different wavelength bands for the abundances of 6% CO_2 and 24% CO relative to H_2O production rate of $8.3 \times 10^{30}\ s^{-1}$.

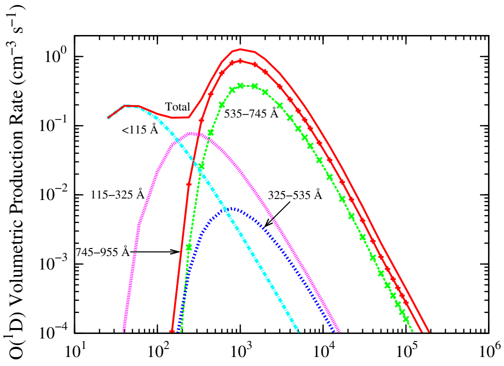

Fig. 8. Calculated radial profiles for the photodissociation of CO producing $O(^1D)$ at different wavelength bands for the abundances of 6% CO_2 and 24% CO relative to H_2O production rate of $8.3 \times 10^{30}\ s^{-1}$.

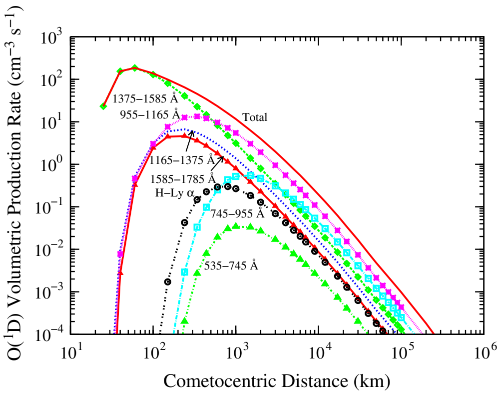

Fig. 7. Calculated radial profiles for the photodissociation of CO_2 producing $O(^1D)$ at different wavelength bands for the abundances of 6% CO_2 and 24% CO relative to H_2O production rate of $8.3 \times 10^{30}\ s^{-1}$.

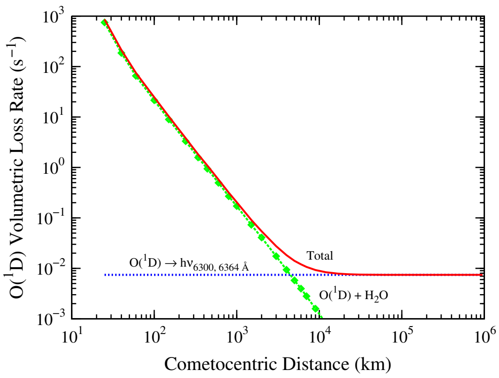

Fig. 9. Calculated radial profiles for major loss mechanisms of the $O(^1D)$ atom for the abundances of 6% CO_2 and 24% CO relative to H_2O production rate of $8.3 \times 10^{30}\ s^{-1}$.

wavelength region is the main source for $O(^1D)$ formation. This is because the absorption cross section of H_2O has a strong dip around 1400 Å (cf. Fig. 1) and the average absorption cross section values of H_2O and CO_2 are nearly same in this wavelength region. Thus, solar photons in this wavelength band are able to reach the innermost coma and produce $O(^1D)$ by dissociating CO_2. Since the cross section for production of $O(^1D)$ in photodissociation of CO_2 peaks in the wavelength band 955–1165 Å, the solar photons of this region leads the production of $O(^1D)$ above 500 km.

The production rates of $O(^1D)$ via photodissociation of CO in different wavelength bands are presented in Fig. 8. The total absorption cross section of H_2O is around two orders of magnitude smaller below 115 Å than at other wavelengths, so these high energy photons can travel deeper into the cometary coma (even below 100 km) almost unattenuated. Since the CO molecule offers a cross section (average $\sim 2 \times 10^{-20}\ cm^2$) to these photons it leads to the formation of $O(^1D)$ and $C(^1D)$ via photodissociation closer to the cometary nucleus. Between 100 and 500 km, the solar photons in the wavelength region 115–325 Å produce maximum $O(^1D)$ atoms via photodissociation of CO. The dissociative excitation cross section of CO is maximum in the wavelength region 535–955 Å (cf. Fig. 1), which results in the peak production of $O(^1D)$ via photodissociation of CO at 1000 km. More details on the attenuation of solar flux in high water production rate comets are given in Bhardwaj (2003).

The model calculated volumetric loss rate profiles of $O(^1D)$ are presented in Fig. 9. This figure depicts that the predominant destruction channel of $O(^1D)$ in the inner coma (below 3000 km) of Comet Hale-Bopp is quenching by H_2O, which results in the formation of two OH molecules. Above radial distance of 10^4 km, the radiative decay leading to the red-doublet emissions is the major loss for $O(^1D)$ atoms. Quenching by CO_2 and CO are minor loss processes, about one order of magnitude smaller and hence is not shown.

The calculated density profiles of $O(^1S)$, $O(^1D)$, and $O(^3P)$ in Comet Hale-Bopp along with parent species considered in our model are shown in Fig. 10. The density of $O(^1S)$ peaks around 500 km, while the density profile of $O(^1D)$ shows a broad peak between 2000 and 5000 km. The calculated number density profiles of $O(^1D)$ and $O(^1S)$ without collisional quenching processes are also presented in this figure (with dashed lines). This calculation clearly shows that collisional quenching can significantly reduce the $O(^1S)$ and $O(^1D)$ densities in the inner coma. The formation of $O(^3P)$ below 200 km is due to collisions between OH molecules.

3.3. Forbidden emissions of atomic oxygen: [OI] 5577, 2972, 6300, and 6364 Å

The emission rates of [OI] 5577, 2972, 6300, and 6364 Å are calculated by multiplying Einstein transition probabilities

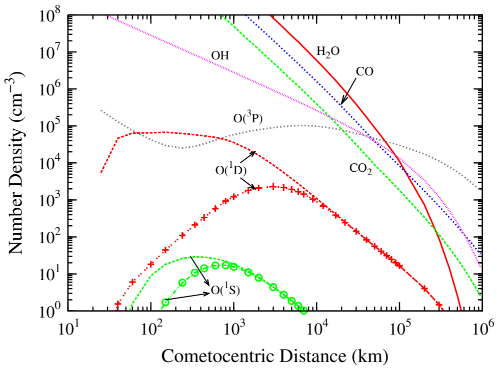

Fig. 10. Calculated number density profiles of O(^{1}S), O(^{1}D), O(^{3}P), and OH, along with those of H_2O, CO, and CO_2. The calculations are done for the abundances of 6% CO_2 and 24% CO relative to H_2O production rate of 8.3×10^{30} s^{-1}. The dashed lines of O(^{1}S) and O(^{1}D) are the calculated densities without accounting the collisional quenching processes.

($A_{5577} = 1.26$ s^{-1}, $A_{2972} = 0.134$ s^{-1}, $A_{6300} = 6.44 \times 10^{-3}$ s^{-1}, and $A_{6364} = 2.17 \times 10^{-3}$ s^{-1}) with the densities of O(^{1}S) and O(^{1}D) (see Bhardwaj and Raghuram (2012) for calculation details). The intensity of these line emissions along the line of sight is calculated by integrating the emission rates. The model calculated brightness profiles as a function of projected distance for these forbidden emissions along with the [OI] 6300 Å observations of Morgenthaler et al. (2001) made on 2 and 5 March 1997 using Hydra and WHAM instruments, respectively, are presented in Fig. 11. To show the collisional quenching effect, we also presented the calculated forbidden emission line intensities (with dotted lines) in Fig. 11, by considering only radiative decay as the loss process of O(^{1}S) and O(^{1}D). The [OI] 2972 Å emission profile is shown by taking branching ratio of 5577/2972 as 10 as suggested by Slanger et al. (2006). The NIST recommended value for this ratio is 16 (Wiese et al., 1996).

The calculated percentage contributions of various processes involved in the production of metastable O(^{1}S) and O(^{1}D) at different projected distances are presented in Table 2. For 6% relative abundance of CO_2, photodissociation of CO_2 is the major source of O(^{1}S) production rather than photodissociation of H_2O (cf. Fig. 2). So we varied the CO_2 relative abundance to study the change in the contribution of CO_2 to the O(^{1}S) and O(^{1}D) production. Calculations presented in Table 2 depict that, for a 6% relative abundance of CO_2, below 10^4 km projected distances, around 25 to 30% of O(^{1}S) production is via photodissociation of H_2O, while 40 to 60% production is through photodissociation of CO_2. Though the relative abundance of CO in Comet Hale-Bopp is high (~25%), the photodissociation of CO could contribute a maximum of 10% to the O(^{1}S) production. The dissociative recombination of H_2O^+ and CO^+ together can contribute 10% to the production of O(^{1}S), whereas photodissociative excitation of OH is a minor (<5%) source. At 10^5 km projected distance, the photochemical reactions mentioned in Table 2 all together contributing 60% of O(^{1}S) and remaining is contributed by dissociative recombination of O-bearing ions. When the abundance of CO_2 is reduced to 3%, below 10^4 km projected distance, photodissociation of H_2O (35–40%) and CO_2 (30 to 50%) contribute almost equally to the production of O(^{1}S).

The major production process of O(^{1}D) is the photodissociation of H_2O, whose contribution is 60–80% below 10^4 km projected distance (cf. Table 2). Around 10^4 km the photodissociation of OH is also a significant production source of O(^{1}D) and contributes around 20%; but, in the inner coma the contribution of this process is small (<10%). Radiative decay of O(^{1}S) and electron recombination of H_2O^+ contribute less than 10% each. At 10^5 km projected distance, most (75%) of O(^{1}D) is produced by photodissociation of OH and remaining is contributed by other reactions. The change in the relative abundance of CO_2 by a factor of 2, from 6% to 3%, does not affect the relative contributions of various sources of O(^{1}D) below 10^4 km projected distance.

For a 4′ circular aperture projected field of view (~2.4×10^5 km) on Comet Hale-Bopp, which is similar to the 50 mm Fabry-Pérot spectrometer observations of Morgenthaler et al. (2001), the calculated percentage contribution of major production processes for the green and red-doublet emissions, for different relative abundances of CO_2, are presented in Table 3. These calculations clearly suggest that in a comet which has been observed over a large projected area, the photodissociation of H_2O and OH mainly (~ 80%) controls the [OI] 6300 Å emission, while the radiative decay of O(^{1}S) contributes a maximum value of 10% to the total red-doublet intensity. With 6% relative abundance of CO_2, the [OI] 5577 Å line emission observed in the coma is largely (~40%) contributed by photodissociation of CO_2, and photodissociation of H_2O is the next significant (~25%) production process. The other production processes, like dissociative recombination of ions, photodissociation of CO, OH, etc., together contribute less than 30% to the [OI] 5577 Å intensity. When the CO_2 abundance is reduced to 3%, both photodissociation of H_2O and CO_2 are contributing equally (~30%) to the green line emission intensity. In all these cases, in spite of CO relative abundance being high (~25%) in Comet Hale-Bopp, the photodissociation of CO could contribute a maximum value of 10%.

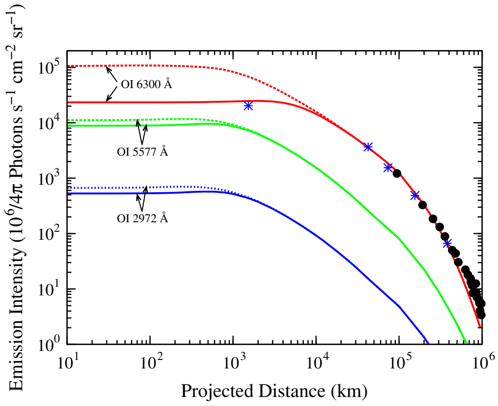

Fig. 11. Calculated [OI] 6300, 5577, and 2972 Å line brightness profiles as a function of the projected distances for the abundances of 6% CO_2 and 24% CO relative to H_2O production rate of 8.3×10^{30} s^{-1}. For comparison the observed intensities of 6300 Å line emission by Morgenthaler et al. (2001) using Hydra (stars) and WHAM (filled circles) instruments on 1997 March 2 (r_h = 1.05 AU and Δ = 1.46 AU) and 5 (r_h = 1.03 AU and Δ = 1.42 AU), respectively, are also shown. During the observation the field of view of Hydra and WHAM instruments are 1° and 45′, respectively (Morgenthaler et al., 2001). Dotted lines are the calculated intensities when collisional quenching is not accounted.

3.4. Green to red-doublet intensity ratio

In comets, the parent species of these atomic oxygen emission lines are assessed using the ratio of intensity of the green line to the sum of intensities of the red-doublet, which can calculated as

$$\frac{I_{5577}}{I_{6300} + I_{6364}} = \frac{\tau_{green}^{-1} \alpha_{green} N_{green} \beta_{green}}{\tau_{red}^{-1} \alpha_{red} N_{red} (\beta_{6300+6364})} \quad (1)$$

where τ is the lifetime of excited species in seconds (τ[O(^{1}D)] ≈ 110 s and τ[O(^{1}S)] ≈ 0.7 s), α is the yield of photodissociation (Huebner et al., 1992), β is the branching ratio

Table 2
Calculated percentage contributions for the major production processes of O(^{1}S) and O(^{1}D) in Comet Hale-Bopp with varying relative abundance of CO_2 for 0.5% O(^{1}S) yield.

CO_2	Production processes of O(^{1}S) and O(^{1}D) at four cometocentric projected distances (km) (%)																							
(%)	$h\nu + H_2O$				$h\nu$ + OH				$h\nu + CO_2$				$h\nu$ + CO				O(^{1}S) → O(^{1}D)				e + H_2O^+			
	10^2	10^3	10^4	10^5	10^2	10^3	10^4	10^5	10^2	10^3	10^4	10^5	10^2	10^3	10^4	10^5	10^2	10^3	10^4	10^5	10^2	10^3	10^4	10^5
6	25 (77)[a]	31 (76)	24 (49)	6 (7)	0.5 (6)	1 (8)	4 (33)	14 (75)	58 (7)	50 (4)	40 (2)	23(1)	6 (0.5)	7 (0.5)	8 (1)	5 (0.5)	(6)	(8)	(8)	(5)	2 (2)	3 (2)	9 (8)	7 (5)
3	33 (82)	42 (80)	33 (49)	8 (8)	1 (7)	1 (9)	5 (34)	18 (77)	47 (4)	36 (2)	26 (1)	15 (0.5)	8 (0.5)	9 (1)	10 (1)	7 (0.5)	(5)	(6)	(6)	(4)	2 (2)	3 (2)	11 (8)	11 (5)
1	49 (85)	57 (82)	42 (51)	10 (8)	1 (7)	2 (9)	7 (35)	24 (78)	27 (1)	17 (0.5)	11 (0.5)	7 (0.5)	12 (1)	13 (1)	13 (1)	9 (0.5)	(4)	(5)	(5)	(3)	4 (2)	5 (3)	15 (7)	14 (5)

[a] The values in parenthesis are for the O(^{1}D).

Table 3
Calculated percentage contributions for the major production processes of green and red-doublet emissions in the total observed projected field of view (2.4 × 10^5 km) on Comet C/1995 O1 Hale-Bopp with varying relative abundance of CO_2.

CO_2 (%)	$h\nu + H_2O$	$h\nu$ + OH	$h\nu + CO_2$	$e^- + CO_2^+$	$e^- + H_2O^+$	O(^{1}S) → O(^{1}D)	$h\nu$ + CO
6	23 (48)[a]	4 (35)	41 (3)	8 (0.5)	7 (5)	(7)	7 (1)
3	32 (50)	6 (36)	30 (2)	5 (0.5)	10 (8)	(7)	10 (1)
1	42 (50)	8 (37)	13 (0.5)	2 (0.5)	13 (8)	(5)	13 (1)

[a] The values in parenthesis are the calculated percentage contributions for red-doublet emission.

($\beta_{6300} = 0.75, \beta_{6364} = 0.25, \beta_{5577} = 0.90$, and $\beta_{2972} = 0.10$, Wiese et al., 1996; Slanger et al., 2011; Festou and Feldman, 1981) of the transition, and N is the column density of cometary species in cm^{-2}. Customarily, the observed G/R ratio of 0.1 has been used to confirm the parent species of these oxygen lines as H_2O in comets (Cochran, 1984, 2008; Morrison et al., 1997; Zhang et al., 2001; Cochran et al., 2001; Furusho et al., 2006; Capria et al., 2005, 2008, 2010). However, since no experimental cross section or yield for the production of O(^{1}S) from H_2O is available in the literature, this ratio has been questioned by Huestis and Slanger (2006). In our previous work (Bhardwaj and Raghuram, 2012), by fitting the observed green line emission intensity in Comet C/1996 B2 Hyakutake, we suggested that the yield for photo-production rate of O(^{1}S) from H_2O at solar H Ly-α cannot be more than 1%. Our previous model calculation also demonstrated that the determined G/R ratio depends on the projected area observed over the comet.

We calculated the G/R ratio profiles on Comet Hale-Bopp on 26 March 1997 by varying CO_2 relative abundance from 6 to 3 to 1% which are presented in Fig. 12. For comparison, the G/R ratio profile calculated on Comet Hyakutake (Bhardwaj and Raghuram, 2012) is also plotted in Fig. 12. In Comet Hyakutake the G/R ratio is constant up to 100 km projected distance, while in the case of Comet Hale-Bopp it is constant even up to 1000 km. The flatness of the G/R ratio depends on the quenching rate of metastable O(^{1}S) and O(^{1}D) by H_2O which is a function of water production rate of the comet. Thus, in comets where H_2O production rate is still larger than that of Hale-Bopp, the G/R ratio would be constant up to projected distances larger than 10^3 km.

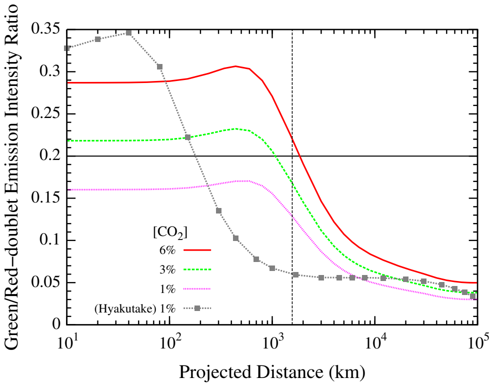

Fig. 12. Calculated green to red-doublet intensity ratio along projected distances for different CO_2 relative abundance [CO_2] and with 0.5% yield for O(^{1}S) production in the photodissociation of H_2O. Zhang et al. (2001) observed average green to red-doublet intensity ratio was 0.2 for the slit projected size of 522 × 1566 km over Comet Hale-Bopp on 28 March 1997, which is shown with a horizontal line. The vertical dotted line represents 1566 km projected distance on the cometary coma. For comparison the calculated G/R ratio profile with 1% CO_2 and 0.5% yield in Comet C/1996 B2 Hyakutake is also shown.

3.5. Radiative efficiencies of O(^{1}S) and O(^{1}D) atoms

The number density of O(^{1}S) and O(^{1}D) in the cometary coma is controlled by various production and loss processes at that radial distance. To understand the region of maximum emission of green and red-doublet lines in the coma we calculated the radiative efficiency profiles of O(^{1}S) and O(^{1}D) in Comets Hale-Bopp and Hyakutake by calculating the ratio of emission rate to total production rate of respective species. The calculated radiative efficiency profiles of O(^{1}S) and O(^{1}D) are presented in Fig. 13 with solid and dotted line for Comets Hale-Bopp and Hyakutake, respectively. This figure depicts that in Comet Hale-Bopp all the O(^{1}S) atoms produced above 1000 km radial distance emit 5577 Å (or 2972 Å) photons, while for O(^{1}D) the radiative efficiency is unity above 10^4 km. Since the lifetime of O(^{1}D) is higher by two orders of magnitude than that of O(^{1}S), most of the produced O(^{1}D) in the inner coma get quenched by other cometary species (mainly by H_2O) without emitting photons at wavelengths 6300 and 6364 Å. But in case of Comet Hyakutake the radiative efficiency of O(^{1}S) and O(^{1}D) is unity above 100 and 1000 km, respectively. This calculation shows that in comets most of the green and red-doublet emissions are produced above the collisional-dominated region where the radiative decay is the dominant loss process for O(^{1}S) and O(^{1}D) atoms.

3.6. Excess velocities of O(^{1}S) and O(^{1}D)

Solar photons having energy more than the dissociation threshold of cometary species impart the additional energy to the kinetic

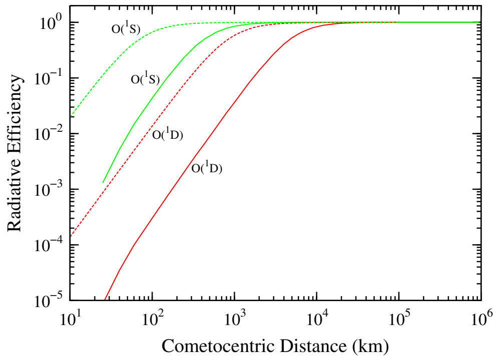

Fig. 13. The calculated radiative efficiency profiles of O(^{1}S) and O(^{1}D) on Comets Hale-Bopp (solid lines) and Hyakutake (dashed lines). Radiative efficiency is the ratio of emission rate to the production rate.

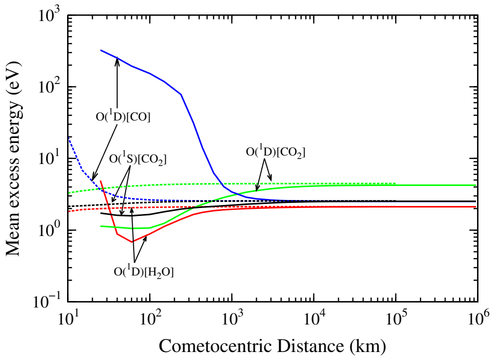

Fig. 14. Calculated excess energy profiles of O(^{1}D) in photodissociation of H_2O, CO, and CO_2 and that of O(^{1}S) in photodissociation of CO_2 on Comets Hale-Bopp (solid lines) and Hyakutake (dashed lines).

motions of daughter products. The mean excess energy released in the *i*th dissociation process at a radial distance *r* can be determined as

$$E_i(r) = \frac{\int_0^{\lambda_{th}} hc\left(\frac{1}{\lambda} - \frac{1}{\lambda_{th}}\right)\sigma(\lambda)\phi(\lambda, r)e^{-\tau(\lambda,r)}d\lambda}{\int_0^{\lambda_{th}} \sigma(\lambda)\phi(\lambda, r)e^{-\tau(\lambda,r)}d\lambda} \qquad (2)$$

where λ is the wavelength of solar photon, λ_{th} is the threshold wavelength for the dissociation process, *h* is Planck's constant, and *c* is the velocity of light. $\sigma(\lambda)$ is the dissociation cross section of the cometary species at wavelength λ. $\phi(\lambda, r)$ and $\tau(\lambda, r)$ are the solar flux and the optical depth of the medium for the photon of the wavelength λ at a radial distance *r*, respectively.

Our model calculated mean excess energy profiles for the photodissociation of H_2O, CO_2, and CO forming O(^{1}S) and O(^{1}D) are presented in Fig. 14 with solid and dotted lines for Comets Hale-Bopp and Hyakutake, respectively. Above 3000 km radial distance, the calculated excess energies in different photodissociation processes in both comets show a constant profile, because the optical depth in this region for photons of different wavelengths is very small. These values are in agreement with the calculations of Huebner et al. (1992). However, at shorter radial distances the neutral density is higher and hence the wavelength dependent photodissociation is significant which causes different excess energy values.

In Comet Hale-Bopp the calculated mean excess energy in photodissociation of H_2O producing O(^{1}D) shows a highest value of 5.6 eV at the surface of the nucleus and decreases to a minimum value of 0.7 eV at 50 km. Above 50 km the mean excess energy increases and becomes constant (2.12 eV) above 3000 km. This is because of the formation of O(^{1}D) via the photodissociation of H_2O is associated with the photons of different energies and it also varies with radial distance as shown in Fig. 6. At a given radial distance the mean excess energy released in the photodissociation process is determined by the mean of energies of different solar photons involved. The threshold energy for production of O(^{1}D) by dissociating H_2O is 7 eV. Very close to the cometary nucleus (<50 km), photons of wavelength smaller than 115 Å and in the wavelength band 1375–1575 Å determines the formation of O(^{1}D) (cf. Fig. 6). At this distance, most of O(^{1}D) is produced by the photons of low energy (7–9 eV) in the wavelength band 1375–1575 Å, and a small amount of O(^{1}D) is produced by very high energy (>100 eV) photons which results in the mean excess energy of about 2–5 eV. But around 50 km, the majority of O(^{1}D) production is determined by the photons of low energy 7–12 eV (955–1575 Å wavelength band) and the contribution from photons of wavelength below 115 Å is very small. This causes the minimum value of mean excess energy 0.7 eV at this radial distance.

Between 50 and 300 km, the increase in the excess energy is due to the production of O(^{1}D) atoms by photons of wavelength bands 115–325, 955–1575 Å, and solar H Ly-α. Though high energy photons (115–325 Å) are also involved in this region, the intense solar photon flux at H Ly-α (1216 Å) governs the majority of O(^{1}D) production and subsequently determines the mean excess energy. The solar H Ly-α photons can provide the maximum excess energy of 3 eV in the photodissociation of H_2O. Above 1000 km more than 90% of the O(^{1}D) production is controlled by photons at 1216 Å wavelength and the remaining from other wavelength bands (cf. Fig. 6), which results a constant value of mean excess energy of 2.12 eV.

Similarly, the mean excess energy calculated in the photodissociation of CO_2 producing O(^{1}D) can be explained based on the wavelength dependent photon attenuated profiles presented in Fig. 7. The threshold energy for the O(^{1}D) production in photodissociation of CO_2 is 7 eV and for O(^{1}S) it is 9 eV. At radial distances less than 100 km, the production of O(^{1}D) in photodissociation of CO_2 is determined by the photons of low energy (average 8 eV) in the wavelength bands 1375–1785 Å and 955–1165 Å, which results in low mean excess energy of ~1 eV. Above 100 km, photons of different energies ranging from 7 to 16 eV (cf. Fig. 7) causes the mean excess energy of ~4 eV. The calculated mean excess energy profiles in the photodissociation of CO_2 producing O(^{1}S) and O(^{1}D) are not similar. This is because the O(^{1}S) production occurs via photodissociation of CO_2 in the wavelength band of 800–1300 Å (photons of 10–15 eV), whereas O(^{1}D) can be produced by photons of wavelength less than 800 Å (>15 eV) (cf. Fig. 1).

The threshold energy for the dissociation of CO producing O(^{1}D) is 14.3 eV. Below 200 km the calculated maximum mean excess energy in the photodissociation of CO producing O(^{1}D) is more than 100 eV. This is because the formation of O(^{1}D) at these distances (cf. Fig. 8) is mainly determined by photons of wavelength less than 115 Å (>110 eV) with some contribution from the wavelength band 115–325 Å (40–110 eV). Above 500 km, the formation of O(^{1}D) is mainly due to solar photons in the wavelength band 535–955 Å (23–13 eV) which results in the maximum excess energy of 2.5 eV.

4. Discussion

The major difference between Comets Hale-Bopp and Hyakutake is the H_2O production rate, which is larger by a factor of 30 in the former. This difference in the H_2O production rates result in a change in the photochemistry of O(^{1}S) and O(^{1}D) in the cometary coma. Due to the dense coma of Comet Hale-Bopp, the attenuation of solar UV–EUV photons on Hale-Bopp differs significantly from that in Hyakutake. Moreover, the CO_2 abundance in Comet Hyakutake is smaller (<3% relative abundance) compared to that in Hale-Bopp (~6% relative abundance). The high H_2O production rate in Comet Hale-Bopp results in a larger collisional coma (radius few $\times 10^5$ km) which is comparable to the scale length ($\sim 8 \times 10^4$ km) of H_2O molecule. In the low production rate comets the collisional zone is smaller and photochemistry significantly differs.

The photodissociation rates of H_2O and CO_2 for O(^{1}S) production differ by a factor of 20 (cf. Table 1). Hence, the major source of O(^{1}S) in the inner coma of Comet Hale-Bopp is photodissociation of CO_2 rather than photodissociation of H_2O. Since the relative abundance of CO_2 in Comet Hyakutake is 1%, the photodissociation of CO_2 becomes an important source only near the surface of the nucleus (cf. Fig. 6 of Bhardwaj and Raghuram (2012)). The production peak of O(^{1}S) in Comet Hyakutake is closer to the nucleus (<20 km), whereas in Comet Hale-Bopp it is between 100 and 1000 km. Even when we reduced the CO_2 abundance by 50% in Hale-Bopp, the peak production of O(^{1}S) in the inner coma is mainly controlled by photodissociation of CO_2 and not by photodissociation of H_2O. Hence, in a high water production rate comet a small relative abundance (~5%) of CO_2, makes CO_2 as a potentially important source of O(^{1}S) compared to H_2O.

In Comet Hyakutake, inside 10^5 km, the photodissociation of H_2O is the major (more than 90%) production process of O(^{1}D) formation and the contributions from other processes are very small. But in Comet Hale-Bopp, since the H_2O production rate and CO_2 relative abundance are higher, the solar photons of wavelength 955–1165 Å, which are less attenuated by H_2O, can travel deeper into the cometary coma and dissociate the CO_2 to form O(^{1}D), which is not the case in Comet Hyakutake.

The radius of collisional coma, which is a function of total gas production rate, in Comets Hyakutake and Hale-Bopp differs by an order of magnitude. In Comet Hyakutake quenching of O(^{1}S) by H_2O is the main destruction mechanism only close to the nucleus (<50 km) and radiative decay dominates at distances larger than 100 km. However, in Comet Hale-Bopp collisional quenching is significant up to 500 km and only above that radiative decay is the major loss mechanism of O(^{1}S). Similarly, the collisional quenching radii of O(^{1}D) in Comets Hyakutake ($\sim 10^3$ km) and Hale-Bopp ($\sim 10^4$ km) also differs by an order of magnitude.

The O(^{1}D) density peak in Comet Hale-Bopp is broader (2000–5000 km) than that in Comet Hyakutake (200–600 km). This change in the peak distribution of O(^{1}D) in the two comets is due to different H_2O production rates and wavelength dependent photo-attenuation in the cometary comae.

4.1. Comparison of model calculations with observations

4.1.1. [OI] 6300 Å emission

Morgenthaler et al. (2001) observed [OI] 6300 Å emission on Comet Hale-Bopp on several days during February to April 1997 using four different ground based instruments. Large aperture observations of 6300 Å emission using WHAM and Hydra spectrometers are made for the field of view 1° and 45′, which covers projected distances of 1.5×10^6 and 2.4×10^5 km on the comet, respectively. Our model calculated brightness profile of [OI] 6300 Å emission shown in Fig. 11 is consistent with these observations. The brightness profile of [OI] 5577 Å starts falling off beyond 1000 km, while the [OI] 6300 Å profile remains constant up to 5000 km. The flatness in the calculated surface brightness profiles mainly depends on the collisional quenching of metastable species which is a function of H_2O production rate. The calculated green and red-doublet emission intensities (dotted lines in Fig. 11) when radiative decay is considered as the only loss mechanism shows the role of collisional quenching. Since the lifetime is relatively larger, the O(^{1}D) is substantially quenched by H_2O in the inner coma. Hence, below 1000 km, the calculated [OI] 6300 Å emission intensities differ by a factor of 5.

We also calculated the [OI] 6300 Å emission intensity for a circular aperture of 4′ diameter on different days of March and April 1997 similar to the observation conditions of Morgenthaler et al. (2001). The calculated intensities of different atomic oxygen emissions are presented in Table 4 along with the [OI] 6300 Å emission intensities observed by Morgenthaler et al. (2001). Our calculated intensities are higher by a factor of 1.5–2.5 compared to the observation and also vary for different days due to change in solar flux, H_2O production rate, and heliocentric and geocentric distances. The observed [OI] 6300 Å intensity on Comet Hale-Bopp on 7 April 1997 is found to vary by a factor of 1.6 in a span of less than 20 min, which is difficult to explain with the variation of heliocentric dependent water production rate. Similarly, the observed intensity values on the other days of observation also show large variation. The brightness during April 10–14 is consistently lower than during April 7–9. The variation in the observed intensity might be associated with spectral extraction process because of non uniform sensitivity of Fabry-Pérot spectrometer (Morgenthaler et al., 2001), rather than the intrinsic variation in the comet.

4.1.2. Green to red-doublet intensity ratio

Zhang et al. (2001) observed Comet Hale-Bopp on 26 March 1997 using a rectangular slit (1.06″ × 3.18″) when the comet was at a geocentric distance of 1.32 AU and heliocentric distance of 0.92 AU. For this observation, the projected field of view on the comet was 522 × 1566 km. Our calculated G/R ratio with 3% relative abundance of CO_2 and 0.5% yield of O(^{1}S) is 0.21, which is consistent with the observed G/R ratio range (0.18–0.22) of Zhang et al. (2001). The calculated average G/R ratio, for a 4′ circular aperture field of view with 3% relative abundance of CO_2 for the different days of observation presented in Table 4, is around 0.1. This shows that in a high water production rate comet the observed G/R ratio over a large projected distances ($\sim 10^4$ km) can be around 0.1 (cf. Fig. 12). However, the calculated contributions of different production processes for O(^{1}S) suggest that photodissociation of CO_2 is more important source rather than the photodissociation of H_2O. Hence, in comets with sufficient CO_2 abundances ($\geqslant$5%), the green line emission is largely controlled by photodissociation of CO_2 and the derived G/R ratio over large cometocentric distances could be around 0.1.

To evaluate the role of slit dimension in determining the G/R ratio we calculated green and red line intensities for various slit sizes by keeping H_2O, CO and CO_2 production rates as a constant. These calculations are presented in Table 5. By varying the slit dimension from 2″ × 2″ to 10′ × 10′ the calculated G/R ratio over the projected cometary coma changed from 0.3 to 0.08. This result clearly shows that the G/R ratio depends not only on the photo-chemistry in the coma but also on the projected area observed for the comet. The calculated G/R ratio is a constant value (0.08) throughout the cometary coma when collisional quenching is neglected in the model. By doubling the CO_2 relative abundance in the coma, the G/R ratio increases by 30% whereas the collisional quenching of O(^{1}D) and O(^{1}S) can change its value even by an order of magnitude.

Besides the dimension of the slit used for observation, the projected area observed on the comet depends on geocentric distance of the comet. Hence in a comet, where the collisional coma is resolvable in the observation, the derived G/R ratio depends on the projected area and also on the collisional quenching of O(^{1}S) and O(^{1}D) in the cometary coma. Thus, we conclude that the observed G/R ratio of 0.1 is not a definitive benchmark value to verify

Table 4
The model calculated intensities of forbidden atomic oxygen emission lines on Comet Hale-Bopp and the comparison of [OI] 6300 Å line with the observation of Morgenthaler et al. (2001) with 3% CO_2 and 24% CO.

Date on 1997	r (AU)	Δ (AU)	Intensity (R)				
			2972 Å	5577 Å	6364 Å	6300 Å	
						Calculated[a]	Observed[b]
March 9	0.999	1.383	34	330	1162	3637	2580–2922
March 10	0.992	1.373	36	339	1192	3730	2300–2649
April 7	0.920	1.408	45	423	1422	4450	2915–4964
April 8	0.923	1.420	43	416	1400	4379	3057–3496
April 9	0.925	1.431	43	411	1380	4323	2920–3197
April 10	0.928	1.444	43	403	1358	4248	1579–1669
April 13	0.939	1.484	39	372	1271	3296	1451–1960
April 14	0.943	1.497	37	361	1240	3878	1575–2360
April 16	0.952	1.526	36	339	1179	3688	2335–2974

[a] The calculated average surface brightness over the observed projected distance of 2.5×10^5 km.

[b] The upper and lower limits of [OI] 6300 Å intensity observed by Morgenthaler et al. (2001).

Table 5
The model calculated green and red-doublet emission intensities and the derived $O(^1D)$ and H_2O production rates for different slit dimensions. The calculations are done with $Q(H_2O) = 8.3 \times 10^{30}$ s^{-1} for the relative abundances of 6% CO_2 and 24% CO at r_h = 1 AU and Δ = 1 AU using solar flux on 10 April 1997 (solar minimum period: solar radio flux F10.7 = 74.7×10^{-22} J s^{-1} m^{-2} Hz^{-1}).

Slit dimension (projected distance in km)	Average intensity (R)[b]		Production rate (s^{-1})		G/R[d]
	[OI] 6300 Å	[OI] 5577 Å	$Q[O(^1D)]$	$Q[H_2O]$[c]	
2″ × 2″ (725)	18,895 [83,188][a]	7584 [9245]	1.3×10^{26}	3.7×10^{26}	0.30 (0.08)[e]
5″ × 5″ (1.8×10^3)	18,909 [68,301]	6723 [7584]	8.1×10^{26}	23×10^{26}	0.21 (0.08)
10″ × 10″ (3.6×10^3)	19,021 [52,977]	5369 [5825]	3.3×10^{27}	9.3×10^{27}	0.21 (0.08)
30″ × 30″ (1.1×10^4)	15,668 [29,341]	2963 [3118]	2.5×10^{28}	7.1×10^{28}	0.14 (0.08)
1′ × 1′ (2.2×10^4)	11,785 [18,793]	1846 [1924]	7.6×10^{28}	2.1×10^{29}	0.10 (0.08)
4′ × 4′ (8.7×10^4)	5005 [6767]	605 [624]	5.0×10^{29}	1.4×10^{30}	0.09 (0.07)
10′ × 10′ (2.1×10^5)	2351 [3056]	263 [271]	1.4×10^{30}	3.9×10^{30}	0.08 (0.07)

[a] The values in the square brackets are the calculated intensities without accounting for collisional quenching of $O(^1S)$ and $O(^1D)$.

[b] Intensity is averaged over the projected field of view, $1R = \frac{10^6}{4\pi}$ Photons s^{-1} cm^{-2} sr^{-1}.

[c] The branching ratio for the production of $O(^1D)$ in the photodissociation of OH is taken as 0.357 (see Morgenthaler et al., 2001), while for the photodissociation of H_2O producing $O(^1D)$ it is 0.064 (This work). The branching ratio (0.81) for the production of OH in photodissociation of H_2O is taken from Huebner et al. (1992).

[d] Green to red-doublet emission intensity ratio determined over the projected field of view.

[e] The calculated G/R ratio without collisional quenching.

H_2O or CO_2/CO as the parent sources of atomic oxygen visible emissions in comets.

4.1.3. Width of green and red-doublet emission lines

Cochran (2008) has found that the width of green line is higher than either of the red-doublet lines in the spectra of 8 comets. The wider green line implies the higher mean velocity of metastable $O(^1S)$, which could be associated with different production processes. Besides collisions with different cometary species, the mean velocity of $O(^1S)$ in the cometary coma is determined by various production processes, and/or could be due to the involvement of photons of various energies in dissociating O-bearing species (Cochran, 2008).

The observed width of forbidden line emission depends on the velocity distribution of radiating metastable oxygen atoms. We found that the excess velocity released in photodissociation H_2O in the unity radiative efficiency region is 2.1 eV (cf. Fig. 14). If we assume that most of this excess energy is transfered to kinetic motion of atomic oxygen then the maximum mean velocity that can be acquired by the $O(^1D)$ atom would be 1.6 km s^{-1}. This velocity is consistent with values of 0.5 to 1.8 km s^{-1} derived by Cochran (2008) in 8 comets. This supports the idea that most of the red-doublet emission in cometary coma is governed by the photodissociation of H_2O. The excess energy profiles shown in Fig. 14 suggest that the $O(^1D)$ produced in photodissociation of CO and CO_2 will have higher velocity than that produced in photodissociation of H_2O. The excess energy released in the photodissociation of CO and CO_2 in the unity radiative efficiency region is 2.5 eV and 4.1 eV, which corresponds to $O(^1D)$ excess velocity of ~3.7 km s^{-1} and 4 km s^{-1}, respectively. However, our calculations suggest that CO and CO_2 together can contribute to a maximum of 10% to the red-doublet emission. The contributions of CO and CO_2 in the wings of red-doublet lines are probable.

In the case of green line emission, since there is no experimentally determined cross section or yield for the photodissociation of H_2O producing $O(^1S)$, it is difficult to determine the mean velocity acquired by an $O(^1S)$ atom in the the photolysis of H_2O. The maximum excess energy that can be released in photolysis of H_2O producing $O(^1S)$ at solar H Ly-α is 1.27 eV. Again, if we assume all the excess energy is transferred as kinetic energy of atomic oxygen in ^1S state then the maximum excess velocity of $O(^1S)$ would be 1.3 km s^{-1}. But in the case of photodissociation of CO_2, the excess energy is 2.5 eV, which corresponds to a maximum $O(^1S)$ velocity of 4.3 km s^{-1}. The dissociative recombination of ions H_2O^+, CO_2^+, and CO^+ can contribute a maximum of 30% in the production of green line emission. But the excess energy released in these recombination reactions is very small (Rosén et al., 2000, 1998; Seiersen et al., 2003). By assuming that the maximum mean velocity that can be acquired by $O(^1S)$ via the dissociative recombination processes is about 1 km s^{-1}, we found that the mean velocity of $O(^1S)$ from all production processes is ~2 km s^{-1}. This value is consistent with the derived velocity range of 1.9–3.1 km s^{-1} for $O(^1S)$ in 8 comets by Cochran (2008).

Before coming to a broad conclusion, we suggest that one has to calculate the exact mean excess velocities of $O(^1S)$ and $O(^1D)$ over the observed cometary coma, by accounting for all collisional processes and the mean excess velocity profiles of various species. Due to nonavailability of photon cross sections for some of the photodissociation processes, and uncertainties involved in the excess energy calculations for dissociative recombination reactions, our model is limited in determining the exact line widths of green and red-doublet emissions. However, based on our model calculations on Comets Hale-Bopp and Hyakutake, we suggest that involvement of multiple sources in the formation $O(^1S)$ could be a potential reason for the higher line width of green emission compared to that of red-doublet emission observed in several comets.

4.2. Effect of model parameters on the calculated intensities

4.2.1. Expansion velocity of neutrals

As we mentioned earlier in Section 2, we have used the velocity profile from the work of Combi et al. (1999) for calculating the number densities of parent species H_2O, CO_2, and CO. Combi et al. (1999) have shown that there is an acceleration of neutrals in the inner coma due to the photolytic heating (Combi et al., 1999; Colom et al., 1999; Biver et al., 1997; Combi, 2002) and other processes (Harris et al., 2002). To evaluate the impact of this acceleration on our model results we carried out calculations by taking a constant gas expansion velocity profile with the values 0.7 and 2.2 km s^{-1}. By using a constant velocity profile of 0.7 km s^{-1} in the coma, rather than a radially varying velocity of Combi et al. (1999), the calculated intensities of green and red-doublet emissions are increased by 30% and 25%, respectively, which are still higher than the observation. By changing the constant gas expansion velocity from 0.7 to 2.2 km s^{-1}, the calculated intensities of atomic oxygen emission lines are decreased by ~50%. However using the Combi et al. (1999) velocity profile, our calculated [OI] 6300 Å emission intensities over 4′ circular aperture field of view are closer to the observation (cf. Table 4). Hence, the velocity profile of neutral species is an important input in the model that should be accounted in calculating the intensities of these forbidden emissions.

4.2.2. Relative abundances of neutral species

The water production rate in Comet Hale-Bopp has been derived using emissions of direct and daughter products of H_2O by different observers (Weaver et al., 1997; Colom et al., 1999; Schleicher et al., 1997; Combi et al., 2000; Dello Russo et al., 2000; Woods et al., 2000; Morgenthaler et al., 2001; Harris et al., 2002; Fink, 2009). During the observation period of these green and red-doublet emissions (r_h of the comet was around 0.9 AU), Dello Russo et al. (2000) measured the H_2O production rates using infrared emissions of water molecules for different days. In this period, Combi et al. (2000) derived the H_2O production rate in this comet using H Ly-α emission. The difference between these two derived production rates is less than 20%. These observations found that around 1 AU the water production rate in Comet Hale-Bopp was about $\sim 1 \times 10^{31}$ s^{-1}. Similarly, the derived water production rates of Fink (2009) on 1997 March 3 was 6.1×10^{30} s^{-1} which is smaller than the Combi et al. (2000) derived rate by a factor of 1.5. Using visible emission of atomic oxygen Morgenthaler et al. (2001) derived the H_2O production rates by applying standard branching ratios of OH and H_2O. These derived H_2O production rates are higher by factor of 3 to 6 compared to values determined from other observations. To assess the impact of H_2O production rate on the calculated green and red-doublet emissions we increased its value by a factor of 5. With increase in H_2O production rate the model calculated surface brightness of green and red-doublet emissions over 4′ circular field of view is increased by a factor of 3.

As demonstrated earlier in this paper, the role of CO_2 is very significant in determining the green line emission intensity and subsequently the G/R ratio. During the observation period of these forbidden emission lines the CO_2 is not observed in this comet. To evaluate the impact of CO_2 we varied its relative abundance from 3% to 6%. We found an increase (25%) in the calculated green line emission intensity over the 4′ circular aperture field of view whereas it is small (<5%) for red-doublet emission intensity.

Based on infrared observations made near perihelion on Comet Hale-Bopp, DiSanti et al. (2001) suggested that 50% of CO abundance present in the cometary coma is contributed by distributed sources. Bockelée-Morvan et al. (2010) investigated the extended distribution of CO by probing Hale-Bopp between ~800 to ~20,000 km region using CO rotational line emissions (viz, CO J (1–0) and CO J (2–1)). Based on the observation and radiative transfer modelling studies, Bockelée-Morvan et al. (2010) rejected the idea of an extended distribution of CO in Hale-Bopp. Since the contribution of photodissociation of CO to formation of $O(^1S)$ and $O(^1D)$ is less than 10%, no significant variation in the calculated intensity of green and red-doublet emissions is found by reducing the CO relative abundance by half. Hence, the involvement of CO in these oxygen forbidden line emissions is almost insignificant.

Though OH column densities are determined using 3080 Å surface brightness profile, there are large uncertainties in photo-cross sections of OH in producing $O(^1D)$ and $O(^1S)$ (Huebner et al., 1992; Morgenthaler et al., 2001). The calculated photo-rates for the production of $O(^1D)$ via photodissociation of OH, using theoretical and experimental cross sections differ by about an order of magnitude (Huebner et al., 1992). Morgenthaler et al. (2001) studied the effect of these cross sections in deriving the H_2O production rates using 6300 Å surface brightness profile and found that on using the theoretical OH photodissociative branching ratios of $O(^1D)$, the derived H_2O production rates are higher by a factor of 3–6, than those determined based on experimental branching ratios of Nee and Lee (1984). The photodissociation of OH influences the calculated green and red-doublet emission intensities significantly above 10^4 km (cf. Figs. 2 and 5, and Table 2). By changing photorates determined by Nee and Lee (1984) experimental cross sections (which are used in the model) with the rates derived based on theoretically calculated cross sections of van Dishoeck and Dalgarno (1984), we found a 40% decrease in the calculated slit-averaged brightness over the 4′ circular aperture field of view for both green and red-doublet emissions. But the calculated $O(^1S)$ and $O(^1D)$ production rates along the radial distances are decreased by an order of magnitude above 10^4 km. Since OH is the dominant O-bearing species in the outer coma, the cross sections can affect the calculated the surface brightness of [OI] 6300 Å at larger projected distances (>10^5 km). To fit the observed [OI] 6300 Å emission in the outer coma Glinski et al. (2004) found it necessary to increase theoretical determined OH to $O(^1D)$ photorate by a factor of around 3.

The chemistry model developed by Glinski et al. (2004) suggested that the collisions of $O(^3P)$ with OH leads to the formation of O_2. These calculations also showed that the O_2 densities can be as high as 1% of H_2O. We evaluated the change in green and red-doublet emission intensities by incorporating O_2 in the model by taking its density profiles from Glinski et al. (2004). No significant change (<5%) is found in the green and red-doublet emission intensities by including O_2 in the model. This is because the other O-bearing species are several orders of magnitude higher in the inner coma.

4.2.3. Effect of slit dimension on the derived $O(^1D)$ production rate

As a case study, for a fixed H_2O production rate and CO and CO_2 relative abundances, we calculated [OI] 6300 Å emission intensity over a projected field of view for different slit dimensions. We then derived the $O(^1D)$ production rate based on the calculated average [OI] 6300 emission intensity over the projected field view. These calculations are presented in Table 5. Since our model calculations are limited up to the projected distances of 10^5 km (which is discussed in Section 4.3) we present the calculated intensities of [OI] 6300 and 5577 Å emissions for the slit dimension up to $10' \times 10'$. Though O(^{1}D) is substantially produced in the inner coma via photodissociation, the collisional quenching by cometary species results in a very few [OI] 6300 Å photons. The role of quenching in determining the [OI] 6300 Å flux can be understood from the calculated values presented in Table 5. A large aperture observation is required, which covers the entire [OI] 6300 Å emission region, to derive the H_2O production rate. The calculations presented in Table 5 suggest that by using large aperture slit the derived water production rate is closer to the actual production rate of H_2O. Hence, to derive the water production rate using [OI] 6300 Å, the slit dimension which covers a projected distance more than the scale length of H_2O should be used.

4.3. Limitations and future scope of the model

The density of the species produced in the inner coma (radial distances less than 10^5 km) is mainly controlled by photochemical reactions. Above these distances the transport of species starts becoming significant in determining the number density of the calculated species. Our model calculations are based on photochemical equilibrium condition and is for a collisional coma. Hence, model results presented at distances beyond 5×10^5 km are not as reliable as the values in the inner coma. Moreover, above these radial distances the chemical lifetimes of neutral species are significantly altered by the solar wind interaction through charge exchange and impact ionization processes. Also, we could not incorporate altitude distribution of dust density in our model calculations which can affect the calculated optical depth. Since our model is time independent and one dimensional it is difficult to explain the asymmetry in the observed [OI] 6300 Å emission intensity over the cometary coma. For determining the spectral width of green and red-doublet lines elaborated calculations are required along with laboratory measured photodissociation cross sections.

5. Summary and conclusions

We have recently developed a coupled chemistry-emission model for the forbidden visible emissions 5577 and 6300 Å of atomic oxygen in Comet C/1996 B2 Hyakutake (Bhardwaj and Raghuram, 2012). In the present paper we applied our model to a high (~30 times more than on Hyakutake) gas production rate Comet C/1995 O1 Hale-Bopp in which these prompt emissions are observed in 1997 by Morgenthaler et al. (2001) and Zhang et al. (2001). The main results of our model calculations on Comet Hale-Bopp are summarized as follows:

1. Below cometocentric distance of 10^3 km, photodissociation of CO_2 is the major production mechanism of O(^{1}S). Between 10^3 and 10^4 km, the contributions from the photodissociation of CO_2 and H_2O are nearly equal. Above 2×10^4 km several other processes are also significant to the O(^{1}S) production.
2. Mainly the solar photons in 955–1165 Å wavelength band contribute to the production of O(^{1}S) in photodissociation of CO_2. This is because the yield of O(^{1}S) in CO_2 photodissociation reaches a maximum in this wavelength region.
3. Since the cross section of photodissociation of CO_2 for the production of O(^{1}S) is more than two orders of magnitude larger than that of H_2O, even a small amount (few percent relative abundance) of CO_2 can make it an important source of the O(^{1}S).
4. Quenching by H_2O is the main loss mechanism for O(^{1}S) at radial distances below 300 km; above 10^3 km radiative decay via 5577 Å emission is the dominant destruction mechanism.
5. Inside 10^5 km, the main production mechanism of O(^{1}D) is photodissociation of H_2O; but, in the innermost part of the coma (<100 km) the photodissociation of CO_2 is also a significant source.
6. For photodissociation of H_2O, the peak O(^{1}D) production occurs via H Ly-α (1216 Å), 1165–1375 Å and 1375–1575 Å wavelength bands at cometocentric distances of 1000, 200, and 50 km, respectively. Solar photons at all other wavelengths produce O(^{1}D) with one or more orders of magnitude smaller efficiency.
7. Below 100 km, solar photons in the wavelength band 1375–1585 Å mainly produce O(^{1}D) by photodissociation of CO_2. The contribution from other wavelength bands is significant above cometocentric distances of 200 km.
8. The major destruction mechanism of O(^{1}D) up to 3000 km cometocentric distance is quenching by H_2O; above 5000 km radiative decay takes over.
9. In Comet Hale-Bopp the O(^{1}D) density peaks occurs between 10^3 and 10^4 km, while for O(^{1}S) the peak is around 500–1000 km.
10. The radiative efficiency of O(^{1}S) and O(^{1}D) atoms in Comet Hale-Bopp are unity above 10^3 and 10^4 km, respectively. In Comet Hyakutake these distances are 10^2 and 10^3 km, respectively.
11. The model calculated green to red-doublet emission intensity ratio is consistent with the observation of Zhang et al. (2001).
12. Collisional quenching can change the G/R ratio by an order of magnitude, whereas doubling the relative abundance of CO_2 increases its value by maximum of 30%.
13. To accurately measure the H_2O production rate in cometary coma, a slit dimension which covers a projected distance more than the scale length of H_2O is preferred to cover the entire [OI] 6300 Å emission region.
14. The model calculated [OI] 6300 Å emission intensity profile as a function of projected distance is in agreement with the observation of Morgenthaler et al. (2001). The model calculated surface brightness averaged over a 4′ circular aperture field of view is higher by a factor of 1.5–2 compared to the observation.
15. The calculated mean excess velocity of O(^{1}D) and O(^{1}S) atoms in the region of unity radiative efficiency is ~1.6 and ~2 km s^{-1}, respectively, which is consistent with the range of velocities observed by Cochran (2008) in several comets.
16. Based on our model calculations for Comets Hyakutake and Hale-Bopp, we conclude that [OI] 6300 Å emission is mainly controlled by the photodissociation of H_2O, while the [OI] 5577 Å emission line is contributed by both H_2O and CO_2. Since O(^{1}S) production is associated with different molecules, whereas the O(^{1}D) production is mainly from H_2O, the width of the green line will be higher than that of the red-doublet lines.

With a high H_2O production rate, Comet Hale-Bopp provided a large gaseous environment, which has not been seen in previous comets. Since the apparition was at small geocentric distances, the giant cometary coma has provided a laboratory for investigating several collisional-driven effects. These collision driven processes are very important in determining the distribution of cometary excited species in the coma, which manifests into the emissions of the cometary coma.

Acknowledgments

S. Raghuram was supported by the ISRO Senior Research Fellowship during the period of this work. Solar Irradiance Platform historical irradiances are provided courtesy of W. Kent Tobiska and Space Environment Technologies. These historical irradiances have been developed with partial funding from the NASA UARS, TIMED, and SOHO missions. The authors thank the reviewers for their valuable comments and suggestions that has improved the paper significantly.

References

Atkinson, R. et al., 1997. Evaluated kinetic and photochemical data for atmospheric chemistry: Supplement VI. IUPAC subcommittee on gas kinetic data evaluation for atmospheric chemistry. J. Phys. Chem. Ref. Data 26 (November), 1329–1499. http://dx.doi.org/10.1063/1.556010.

Bhardwaj, A., 1999. On the role of solar EUV, photoelectrons, and auroral electrons in the chemistry of C(^{1}D) and the production of C I 1931 Å in the inner cometary coma: A case for Comet P/Halley. J. Geophys. Res. 104, 1929–1942. http://dx.doi.org/10.1029/1998JE900004.

Bhardwaj, A., 2003. On the solar EUV deposition in the inner coma of comets with large gas production rates. Geophys. Res. Lett. 30 (24). http://dx.doi.org/10.1029/2003GL018495.

Bhardwaj, A., Haider, S.A., 1999. Modeling of metastable carbon atoms in comets: Implications for ROSETTA. Adv. Space Res. 23 (7), 1325–1328.

Bhardwaj, A., Haider, S.A., 2002. Chemistry of O(^{1}D) atoms in the coma: Implications for cometary missions. Adv. Space Res. 29, 745–750. http://dx.doi.org/10.1016/S0273-1177(02)00006-6.

Bhardwaj, A., Haider, S.A., Singhal, R.P., 1990. Auroral and photoelectron fluxes in cometary ionospheres. Icarus 85, 216–228. http://dx.doi.org/10.1016/0019-1035(90)90112-M.

Bhardwaj, A., Haider, S.A., Singhal, R.P., 1996. Production and emissions of atomic carbon and oxygen in the inner coma of Comet 1P/Halley: Role of electron impact. Icarus 120, 412–430. http://dx.doi.org/10.1006/icar.1996.0061.

Bhardwaj, A., Jain, S.K., 2009. Monte Carlo model of electron energy degradation in a CO_2 atmosphere. J. Geophys. Res. 114 (A13), 11309. http://dx.doi.org/10.1029/2009JA014298.

Bhardwaj, A., Jain, S.K., 2012. Production of N_2 Vegard-Kaplan and other triplet band emissions in the dayglow of Titan. Icarus 218 (2), 989–1005. http://dx.doi.org/10.1016/j.icarus.2012.01.019.

Bhardwaj, A., Michael, M., 1999a. Monte Carlo model for electron degradation in SO_2 gas: Cross sections, yield spectra and efficiencies. J. Geophys. Res. 104 (10), 24713–24728. http://dx.doi.org/10.1029/1999JA900283.

Bhardwaj, A., Michael, M., 1999b. On the excitation of Io's atmosphere by the photoelectrons: Application of the Analytical Yield Spectrum of SO_2. Geophys. Res. Lett. 26, 393–396. http://dx.doi.org/10.1029/1998GL900320.

Bhardwaj, A., Raghuram, S., 2011. Model for Cameron-band emission in comets: A case for the EPOXI mission target Comet 103P/Hartley 2. Mon. Not. R. Astron. Soc. 412, L25–L29. http://dx.doi.org/10.1111/j.1745-3933.2010.00998.x.

Bhardwaj, A., Raghuram, S., 2012. A coupled chemistry-emission model for atomic oxygen green and red-doublet emissions in the Comet C/1996 B2 Hyakutake. Astrophys. J. 748, 13. http://dx.doi.org/10.1088/0004-637X/748/1/13.

Bhardwaj, A., Singhal, R.P., 1993. Optically thin H Lyman alpha production on outer planets: Low-energy proton acceleration in parallel electric fields and neutral H atom precipitation from ring current. J. Geophys. Res. 98 (A6), 9473–9481. http://dx.doi.org/10.1029/92JA02400.

Biver, N. et al., 1997. Evolution of the outgassing of Comet Hale-Bopp (C/1995 O1). Science 275, 1915–1918. http://dx.doi.org/10.1023/A:1006229818484.

Bockelée-Morvan, D., Crovisier, J., Mumma, M.J., Weaver, H.A., 2004. The composition of cometary volatiles: Comets II. pp. 391–423.

Bockelée-Morvan, D. et al., 2010. A study of the distant activity of Comet C/2006 W3 (Christensen) with Herschel and ground-based radio telescopes. Astron. Astrophys. 518 (L149). http://dx.doi.org/10.1051/0004-6361/201014655.

Bockelée-Morvan, D. et al., 2000. New molecules found in Comet C/1995 O1 (Hale-Bopp). Investigating the link between cometary and interstellar material. Astron. Astrophys. 353 (January), 1101–1114.

Capria, M.T., Cremonese, G., Bhardwaj, A., de Sanctis, M.C., 2005. O(^{1}S) and O(^{1}D) emission lines in the spectrum of 153P/2002 C1 (Ikeya-Zhang). Astron. Astophys. 442 (November), 1121–1126. http://dx.doi.org/10.1051/0004-6361:20053047.

Capria, M.T., Cremonese, G., Bhardwaj, A., Sanctis, M.C.D., Epifani, E.M., 2008. Oxygen emission lines in the high resolution spectra of 9P/Tempel 1 following the deep impact event. Astron. Astrophys. 479 (1), 257–263. http://dx.doi.org/10.1051/0004-6361:20077072.

Capria, M.T., Cremonese, G., de Sanctis, M.C., 2010. High resolution observation of 17P/Holmes during the outburst event in 2007. Astron. Astrophys. 522 (November), A82. http://dx.doi.org/10.1051/0004-6361/200913889.

Cochran, A.L., 2008. Atomic oxygen in the comae of comets. Icarus 198 (November), 181–188. http://dx.doi.org/10.1016/j.icarus.2008.06.007.

Cochran, A.L., Cochran, W.D., 2001. Observations of O(^{1}S) and O(^{1}D) in Spectra of C/1999 S4 (LINEAR). Icarus 154 (December), 381–390. http://dx.doi.org/10.1006/icar.2001.6718.

Cochran, W.D., 1984. Detection of [OI] ^{1}S–^{1}D in Comet IRAS-Araki-Alcock. Icarus 58 (3), 440–445. http://dx.doi.org/10.1016/0019-1035(84)90089-7.

Colom, P., Gérard, E., Crovisier, J., Bockelé-Morvan, D., Biver, N., Rauer, H., 1999. Observations of the OH Radical in Comet C/1995 O1 (Hale-Bopp) with the Nançay radio telescope. Earth Moon Planets 78 (July), 37–43. http://dx.doi.org/10.1023/A:1006206924786.

Combi, M., 2002. HaleBopp: What makes a big comet different? Coma dynamics: Observations and theory. Earth, Moon and Planets 89, 73–90.

Combi, M.R., Kabin, K., DeZeeuw, D.L., Gombosi, T.I., Powell, K.G., 1999. Dust gas interrelations in comets: Observations and theory. Earth Moon Planets 79 (1–3), 275–306. http://dx.doi.org/10.1023/A:1006257922294.

Combi, M.R., Reinard, A.A., Bertaux, J.-L., Quemerais, E., Mäkinen, T., 2000. SOHO/SWAN observations of the structure and evolution of the Hydrogen Lyman-α coma of Comet Hale-Bopp (1995 O1). Icarus 144, 191–202. http://dx.doi.org/10.1006/icar.1999.6335.

Crovisier, J., Leech, K., Bockelée-Morvan, D., Brooke, T.Y., Hanner, M.S., Altieri, B., Keller, H.U., Lellouch, E., 1997. The spectrum of Comet Hale-Bopp (C/1995 O1) observed with the infrared space observatory at 2.9 AU from the Sun. Science 275, 1904–1907. http://dx.doi.org/10.1126/science.275.5308.1904.

Dello Russo, N., Mumma, M.J., Disanti, M.A., Magee-Sauer, K., Novak, R., Rettig, T.W., 2000. Water production and release in Comet C/1995 O1 Hale-Bopp. Icarus 143 (February), 324–337.

Delsemme, A.H., Combi, M.R., 1976. The production rate and possible origin of O(^{1}D) in Comet Bennett 1970 II. Astrophys. J. Lett. 209, L149. http://dx.doi.org/10.1086/182286.

Delsemme, A.H., Combi, M.R., 1979. O(^{1}D) and H_2^+O in Comet Bennett 1970 II. Astrophys. J. 228, 330–337. http://dx.doi.org/10.1086/156850.

DiSanti, M.A., Mumma, M.J., Dello Russo, N., Magee-Sauer, K., 2001. Carbon monoxide production and excitation in Comet C/1995 O1 (Hale-Bopp): Isolation of native and distributed CO sources. Icarus 153, 361–390. http://dx.doi.org/10.1006/icar.2001.6695.

Festou, M.C., Feldman, P.D., 1981. The forbidden oxygen lines in comets. Astron. Astrophys. 103, 154–159.

Fink, U., 2009. A taxonomic survey of comet composition 1985–2004 using CCD spectroscopy. Icarus 201, 311–334. http://dx.doi.org/10.1016/j.icarus.2008.12.044.

Fink, U., Johnson, J.R., 1984. Luminosity and spatial distribution of the O[I] 6300 Å emission in comets. Astron. J. 89 (10), 1565–1572. http://dx.doi.org/10.1086/113660.

Furusho, R., Kawakitab, H., Fusec, T., Watanabe, J., 2006. Forbidden oxygen emission lines of Comet 116P/Wild 4 at 2.4 AU. Adv. Space Res. 9, 1983–1986. http://dx.doi.org/10.1016/j.asr.2006.06.003.

Glinski, R.J., Ford, B.J., Harris, W.M., Anderson, C.M., Morgenthaler, J.P., 2004. Oxygen/hydrogen chemistry in the inner comae of active comets. Astrophys. J. 608, 601–609.

Haider, S.A., Bhardwaj, A., 2005. Radial distribution of production rates, loss rates and densities corresponding to ion masses $\leqslant$40 amu in the inner coma of Comet Halley: Composition and chemistry. Icarus 177, 196–216. http://dx.doi.org/10.1016/j.icarus.2005.02.019.

Harris, W.M., Scherb, F., Mierkiewicz, E., Oliversen, R., Morgenthaler, J., 2002. Production, outflow velocity, and radial distribution of H_2O and OH in the Coma of Comet C/1995 O1 (Hale-Bopp) from wide-field imaging of OH. Astrophys. J. 578, 996–1008. http://dx.doi.org/10.1086/342648.

Huebner, W.F., Carpenter, C.W., 1979. Solar Photo Rate Coefficients. Los Alamos Report, 8085.

Huebner, W.F., Keady, J.J., Lyon, S.P., 1992. Solar photorates for planetary atmospheres and atmospheric pollutants. Astrophys. Space Sci. 195 (1), 1–294. http://dx.doi.org/10.1007/BF00644558.

Huestis, D.L., Slanger, T.G., 2006. DPS. American Astronomical Society 38, 62.20.

Huestis, D.L., Slanger, T.G., Sharpee, B.D., Fox, J.L., 2010. Chemical origins of the Mars ultraviolet dayglow. Faraday Discuss. 147, 307. http://dx.doi.org/10.1039/c003456h.

Lawrence, G.M., 1972. Photodissociation of CO_2 to produce CO($a^3\pi$). J. Chem. Phys. 56 (7), 3435–3442. http://dx.doi.org/10.1063/1.1677717.

Lovell, A.J., Kallivayalil, N., Schloerb, F.P., Combi, M.R., Hansen, K.C., Gombosi, T.I., 2004. On the effect of electron collisions in the excitation of cometary HCN. Astrophys. J. 613, 615–621.

McKay, A.J., Chanover, N.J., Morgenthaler, J.P., Cochran, A.L., Harris, W.M., Russo, N.D., 2012a. Forbidden oxygen lines in Comets C/2006 W3 Christensen and C/2007 Q3 siding spring at large heliocentric distance: Implications for the sublimation of volatile ice. Icarus, 277–285. http://dx.doi.org/10.1016/j.icarus.2012.04.030.

McKay, A.J., Chanover, N.J., Morgenthaler, J.P., Cochran, A.L., Harris, W.M., Russo, N.D., 2012b. Observations of the forbidden oxygen lines in DIXI target Comet 103P/Hartley. Icarus, http://dx.doi.org/10.1016/j.icarus.2012.06.020.

Mitchell, J.B.A., 1990. The dissociative recombination of molecular ions. Phys. Rept. 186, 215–248.

Morgenthaler, J.P. et al., 2001. Large-aperture O[I] 6300 Å photometry of Comet Hale-Bopp: Implications for the photochemistry of OH. Astrophys. J. 563, 451–461. http://dx.doi.org/10.1086/323773.

Morrison, N.D., Knauth, D.C., Mulliss, C.L., Lee, W., 1997. High resolution optical spectra of the head of the Comet C/1996 B2 (Hyakutake). Astron. Soc. Pac. 109, 676–681. http://dx.doi.org/10.1086/133931.

Nee, J.B., Lee, L.C., 1984. Photoabsorption cross sections of OH at 115–183 nm. J. Chem. Phys. 81, 31–36. http://dx.doi.org/10.1063/1.447387.

Raghuram, S., Bhardwaj, A., 2012. Model for the production of CO Cameron band emission in Comet 1P/Halley. Planet. Space Sci., 139–149. http://dx.doi.org/10.1016/j.pss.2011.11.011.

Rosén, S. et al., 2000. Recombination of simple molecular ions studied in storage ring: Dissociative recombination of H_2O^+. Faraday Discuss. 407 (115), 295–302. http://dx.doi.org/10.1039/a909314a.

Rosén, S. et al., 1998. Absolute cross sections and final-state distributions for dissociative recombination and excitation of $CO^+(v = 0)$ using an ion storage ring. Phys. Rev. A 57 (6), 4462–4471. http://dx.doi.org/10.1103/PhysRevA.57.4462.

Schleicher, D.G., Lederer, S.M., Millis, R.L., Farnham, T.L., 1997. Photometric behaviour of Comet Hale-Bopp (C/1995 O1) before perihelion. Science 275, 1913–1915. http://dx.doi.org/10.1126/science.275.5308.1913.

Schultz, D., Li, G.S.H., Scherb, F., Roesler, F.L., 1992. Comet Austin (1989c1) $O(^1D)$ and H_2O production rates. Icarus 96 (2), 190–197. http://dx.doi.org/10.1016/0019-1035(92)90072-F.

Seiersen, K. et al., 2003. Dissociative recombination of the cation and dication of CO_2. Phys. Rev. A, 68. http://dx.doi.org/10.1103/PhysRevA.68.022708.

Singhal, R.P., Bhardwaj, A., 1991. Monte Carlo simulation of photoelectron energization in parallel electric fields: Electroglow on Uranus. J. Geophys. Res. 96, 15963–15972. http://dx.doi.org/10.1029/90JA02749.

Slanger, T.G., Cosby, P.C., Sharpee, B.D., Minschwaner, K.R., Siskind, D.E., 2006. $O(^1S \rightarrow {}^1D, {}^3P)$ branching ratio as measured in the terrestrial nightglow. J. Geophys. Res. 111, 12318. http://dx.doi.org/10.1029/2006JA011972.

Slanger, T.G., 2011. Atomic oxygen emission intensity ratio: Observation and theory. Eos Trans. vol. 92, AGU 291–292.

Slanger, T.G., Sharpless, R.L., Black, G., 1977. CO_2 photodissociation, 1060–1175 Å. J. Chem. Phys. 66, 5317–5323. http://dx.doi.org/10.1063/1.434710.

Storey, P.J., Zeippen, C.J., 2000. Theoretical values for the [OIII] 50007/4959 line intensity ratio and homologous cases. Mon. Not. R. Astron. Soc. 312, 813–816. http://dx.doi.org/10.1046/j.1365-8711.2000.03184.x.

Tobiska, W.K., 2004. SOLAR2000 irradiances for climate change, aeronomy and space system engineering. Adv. Space Res. 34, 1736–1746. http://dx.doi.org/10.1016/j.asr.2003.06.032.

van Dishoeck, E.F., Dalgarno, A., 1984. The dissociation of OH and OD in comets by solar radiation. Icarus 5, 305–313. http://dx.doi.org/10.1016/0019-1035(84)90104-0.

Weaver, H.A. et al., 1997. The activity and size of the nucleus of Comet Hale-Bopp (C/1995 O1). Science 275, 1900–1904. http://dx.doi.org/10.1126/science.275.5308.1900.

Wiese, W.L., Fuhr, J.R., Deters, T.M., 1996. Atomic transition probabilities of carbon nitrogen, and oxygen: A critical data compilation. J. Phys. Chem. Ref. Data, Monograph 7, 364.

Woods, T.N., Feldman, P.D., Rottman, G.J., 2000. Ultraviolet observations of Comet Hale-Bopp (C/1995 O1) by the UARS SOLSTICE. Icarus 144, 182–186. http://dx.doi.org/10.1006/icar.1999.6262.

Zhang, H.W., Zhao, G., Hu, J.Y., 2001. A catalogue of emission lines in spectra of Comet C/1995 O1 (Hale-Bopp). Astron. Astophys. 367 (3), 1049–1055. http://dx.doi.org/10.1051/0004-6361:20010008.

Zipf, E.C., 1969. The collisional deactivation of metastable atoms and molecules in the upper atmosphere. Can. J. Chem. 47, 1863–1870. http://dx.doi.org/10.1139/v69-305.

References

Ajello, J. M. (1971), Emission cross sections of CO_2 by electron impact in the interval 1260-4500 Å, II, *J. Chem. Phys.*, *55*, 3169–3177, doi:10.1063/1.1676564.

Allen, M., M. Delitsky, W. Huntress, Y. Yung, and W.-H. Ip (1987), Evidence for methane and ammonia in the coma of comet P/Halley, *Astron. Astrophys.*, *187*, 502–512.

Anicich, V. G. (1993a), A survey of bimolecular ion-molecule reactions for use in modelling the chemistry of planetary atmospheres, cometary coma, and interstellar clouds: 1993 Supplement. Astrophys. J. Suppl., *Astrophys. J.*, *84*(3), 215 – 313.

Anicich, V. G. (1993b), Evaluated bimolecular ionmolecule gas phase kinetics of positive ions for use in modelling the chemistry of planetary atmospheres, cometary coma, and interstellar clouds., *J. Phys. Chem. Ref. Data*, *22*, 1469 – 1993.

Atkinson, R., and K. H. Welge (1972), Temperature Dependence of O(^{1}S) Deactivation by CO_2, O_2, N_2, and Ar, *J. Chem. Phys.*, *57*, 3689–3693, doi:10.1063/1.1678829.

Atkinson, R., D. L. Baulch, R. A. Cox, R. F. Hampson, Jr., J. A. Kerr, M. J. Rossi, and J. Troe (1997), Evaluated Kinetic and Photochemical Data for Atmospheric Chemistry: Supplement VI. IUPAC Subcommittee on Gas Kinetic Data Evaluation for Atmospheric Chemistry, *Journal of Physical and Chemical Reference Data*, *26*, 1329–1499, doi:10.1063/1.556010.

Avakyan, S. V., R. N. II'in, V. M. Lavrov, and G. N. Ogurtsov (Eds.) (1998), *Collision Processes and Excitation of UV Emission from Planetary Atmospheric Gases: A Handbook of Cross Sections*, Gordon and Breach Science Publishers.

Berrington, K. A., and P. G. Burke (1981), Effective collision strengths for forbidden transitions in e-N and e-O scattering, *Planetary and Space Science*, *29*(3), 377 – 381, doi:10.1016/0032-0633(81)90026-X.

Bhardwaj, A. (1999), On the role of solar EUV, photoelectrons, and auroral electrons in the chemistry of C(^{1}D) and the production of C I 1931 Å in the inner cometary coma: A case for comet P/Halley, *J. Geophys. Res.*, *104*, 1929 – 1942, doi:10.1029/1998JE900004.

Bhardwaj, A. (2003), On the solar EUV deposition in the inner coma of comets with large gas production rates., *Geophys. Res. Lett.*, *30*(24), 2244, doi:10.1029/2003GL018495.

Bhardwaj, A., and S. A. Haider (2002), Chemistry of O(^{1}D) atoms in the coma: implications for cometary missions, *Advances in Space Research*, *29*, 745–750, doi:10.1016/S0273-1177(02)00006-6.

Bhardwaj, A., and S. K. Jain (2009), Monte Carlo model of electron energy degradation in a CO_2 atmosphere, *J. Geophys. Res.*, *114*(A13), 11,309, doi:10.1029/2009JA014298.

Bhardwaj, A., and M. Michael (1999), On the excitation of Io's atmosphere by the photoelectrons: Application of the analytical yield spectrum of SO_2, *Geophys. Res. Lett.*, *26*, 393 – 396, doi:10.1029/1998GL900320.

Bhardwaj, A., and S. Raghuram (2011), Model for Cameron-band emission in comets: A case for the EPOXI mission target comet 103P/Hartley 2, *Mon. Not. R. Astron. Soc.*, *412*, L25 – L29, doi:10.1111/j.1745-3933.2010.00998.x.

Bhardwaj, A., and S. Raghuram (2012), A coupled chemistry-emission model for atomic oxygen green and red-doublet emissions in the comet C/1996 B2 Hyakutake, *Astrophys. J.*, *748*, 13, doi:10.1088/0004-637X/748/1/13.

Bhardwaj, A., S. A. Haider, and R. P. Singhal (1990), Auroral and photoelectron fluxes in cometary ionospheres, *Icarus*, *85*, 216 – 228, doi:10.1016/0019-1035(90)90112-M.

Bhardwaj, A., S. A. Haider, and R. P. Singhal (1995), Consequences of cometary aurora on the carbon chemistry at comet P/Halley., *Adv. Space Res.*, *16 (2)*, 31 – 36.

Bhardwaj, A., S. A. Haider, and R. P. Singhal (1996), Production and emissions of atomic carbon and oxygen in the inner coma of comet 1P/Halley: Role of electron impact, *Icarus*, *120*, 412 – 430, doi:10.1006/icar.1996.0061.

Bhardwaj, A., R. F. Elsner, G. R. Gladstone, T. E. Cravens, C. M. Lisse, K. Dennerl, G. Branduardi-Raymont, B. J. Wargelin, and J. H. W. Jr (2007), *Planetary and Space Science*, *57*, 1190 – 1196, doi:10.1016/j.pss.2006.11.009.

Biermann, L. (1951), Kometenschweife und solare Korpuskular- strahlung, *Z. Astrophys.*, *29*, 274 – 286.

Biermann, L., P. T. Giguere, and W. F. Huebner (1982), A model of a comet coma with interstellar molecules in the nucleus, *Astron. Astrophys.*, *108*, 221 – 226.

Biver, N., et al. (1997), Evolution of the outgassing of comet Hale-Bopp (C/1995 O1), *Science*, *275*, 1915–1918, doi:10.1023/A:1006229818484.

Biver, N., et al. (1999), Spectroscopic monitoring of comet C/1996 B2 (Hyakutake) with the JCMT and IRAM radio telescopes, *Astron. J.*, *118*, 1850–1872.

Biver, N., et al. (2007), Submillimetre observations of comets with Odin: 20012005, *Planetary and Space Science*, *55*, 1058–1068, doi:10.1016/j.pss.2006.11.010.

Biver, N., D. Bockelée-Morvan, P. Colom, J. Crovisier, A. Lecacheux, U. Frisk, Å. Hjalmarson, M. Olberg, and A. Sandqvist (2009), Periodic variation in the water production of comet C/2001 Q4 (NEAT) observed with the Odin satellite, *Astron. Astrophys.*, *501*, 359 – 366, doi:10.1051/0004-6361/200911790.

Bockelée-Morvan, D., et al. (2000), New molecules found in comet C/1995 O1 (Hale-Bopp). Investigating the link between cometary and interstellar material, *Astron. Astrophys.*, *353*, 1101–1114.

Bockelée-Morvan, D., J. Crovisier, M. J. Mumma, and H. A. Weaver (2004), *The composition of cometary volatiles: Comets II*, pp. 391–423.

Bockelée-Morvan, D., et al. (2010), A study of the distant activity of comet C/2006 W3 (Christensen) with Herschel and ground-based radio telescopes, *Astron. Astrophys.*, *518*(L149), doi:10.1051/0004-6361/201014655.

Bodewits, D., et al. (2008), Spectral Analysis of the Chandra Comet Survey, *Astron. and Astrophys.*, *469*, 1189.

Bodewits, D., T. L. Farnham, and M. F. A'Hearn (2012), SWIFT Observations of the Long Term Activity of Comet C/2009 P1 (Garradd), in *AAS/Division for Planetary Sciences Meeting Abstracts*, *AAS/Division for Planetary Sciences Meeting Abstracts*, vol. 44, p. 506.06.

Boice, D. C., W. F. Huebner, J. J. Keady, H. U. Schmidt, and R. Wegmann (1986), A model of comet P/Giacobini-Zinner, *Geophys. Res. Lett.*, *13*, 381–384, doi:10.1029/GL013i004p00381.

Boice, D. C., W. F. Huebner, M. J. Sablik, and I. Konno (1990), Distributed coma sources and the CH4/CO ratio in comet Halley, *Geophys. Res. Lett.*, *17*, 1813 – 1816.

Budzien, S. A., M. C. Festou, and P. D. Feldman (1994), Solar flux variability and the lifetimes of cometary H_2O and OH, *Icarus*, *107*, 164–188, doi:10.1006/icar.1994.1014.

Campbell, L., and M. J. Brunger (2009), Electron impact excitation of the carbon monoxide in comet Hale-Bopp, *Geophys. Res. Lett.*, *36*, L03101, doi:10.1029/2008GL036641.

Capetanakis, F. P., F. Sondermann, S. Höser, and F. Stuhl (1993), Temperature dependence of the quenching of $O(^1S)$ by simple inorganic molecules, *J. Chem. Phys.*, *98*, 7883, doi:10.1063/1.464596.

Capria, M. T., G. Cremonese, A. Bhardwaj, and M. C. de Sanctis (2005), $O(^1S)$ and $O(^1D)$ emission lines in the spectrum of 153P/2002 C1 (Ikeya-Zhang), *Astron. Astophys.*, *442*, 1121–1126, doi:10.1051/0004-6361:20053047.

Capria, M. T., G. Cremonese, A. Bhardwaj, M. C. D. Sanctis, and E. M. Epifani (2008), Oxygen emission lines in the high resolution spectra of 9P/Tempel 1 following the deep impact event, *Astron. Astrophys.*, *479*(1), 257–263, doi:10.1051/0004-6361:20077072.

Capria, M. T., G. Cremonese, and M. C. de Sanctis (2010), High resolution observation of 17P/Holmes during the outburst event in 2007, *Astron. Astrophys.*, *522*, A82, doi:10.1051/0004-6361/200913889.

Cochran, A. L. (2008), Atomic oxygen in the comae of comets, *Icarus*, *198*, 181–188, doi:10.1016/j.icarus.2008.06.007.

Cochran, A. L., and W. D. Cochran (2001), Observations of O (^{1}S) and O (^{1}D) in Spectra of C/1999 S4 (LINEAR), *Icarus*, *154*, 381–390, doi:10.1006/icar.2001.6718.

Cochran, A. L., and D. G. Schleicher (1993), Observational constraints on the lifetime of cometary H_2O, *Icarus*, *105*, 235 – 253.

Cochran, W. D. (1984), Detection of [OI] ^{1}S-^{1}D in comet IRAS-Araki-Alcock , *Icarus*, *58*(3), 440–445, doi:10.1016/0019-1035(84)90089-7.

Colangeli, L., et al. (1999), Infrared spectral observations of comet 103P/Hartley 2 by ISOPHOT, *Astron. Astrophys.*, *343*, L87-L90.

Colom, P., E. Gérard, J. Crovisier, D. Bockelé-Morvan, N. Biver, and H. Rauer (1999), Observations of the OH Radical in Comet C/1995 O1 (Hale-Bopp) with the Nançay Radio Telescope, *Earth Moon and Planets*, *78*, 37–43, doi:10.1023/A:1006206924786.

Combi, M. (2002), HaleBopp: What makes a big comet different? coma dynamics: Observations and theory, *Earth, Moon and Planets*, *89*, 73 – 90.

Combi, M. R. (1996), Time-dependent gas kinetics in tenuous plan- etary atmospheres: The cometary coma, *Icarus*, *123*, 207 – 226.

Combi, M. R., and A. H. Delsemme (1980), Neutral cometary atmospheres. I. Average random walk model for dissociation in comets, *Astrophys J.*, *237*, 633 – 641.

Combi, M. R., M. E. Brown, P. D. Feldman, H. U. Keller, R. R. Meier, and W. H. Smyth (1998), Hubble space telescope ultraviolet imaging and high-resolution spectroscopy of water photodissociation products in comet Hyakutake (c/1996 b2), *Astrophys. J.*, *494*, 816–821.

Combi, M. R., K. Kabin, D. L. DeZeeuw, T. I. Gombosi, and K. G. Powell (1999), Dust gas interrelations in comets: Observations and theory, *Earth, Moon, and Planets*, *79*(1 - 3), 275 – 306, doi:10.1023/A:1006257922294.

Combi, M. R., A. A. Reinard, J.-L. Bertaux, E. Quemerais, and T. Mäkinen (2000), SOHO/SWAN observations of the structure and evolution of the Hydrogen Lyman-α coma of comet Hale-Bopp (1995 O1), *Icarus*, *144*, 191 – 202, doi:10.1006/icar.1999.6335.

Combi, M. R., W. M. Harris, and W. H. Smyth (2004), *Gas dynamics and kinetics in the cometary coma: theory and observations*, pp. 523–552.

Combi, M. R., J. T. T. Mäkinen, J. L. Bertaux, Y. Lee, and E. Quémerais (2009), Water production in comets 2001 Q4 (NEAT) and 2002 T7 (LINEAR) determined from SOHO/SWAN observations, *Astron. J*, *137*, 4734 – 4743, doi:10.1088/0004-6256/137/6/4734.

Combi, M. R., J. T. T. Mäkinen, J.-L. Bertaux, E. Quémerais, S. Ferron, and N. Fougere (2013), Water production rate of Comet C/2009 P1 (Garradd) throughout the 20112012 apparition: Evidence for an icy grain halo, *Icarus*, *225*, 740 – 748, doi:10.1016/j.icarus.2013.04.030.

Conway, R. R. (1981), Spectroscopy of the Cameron bands in the Mars airglow, *J. Geophys. Res.*, *86*, 4767 – 4775, doi:10.1029/JA086iA06p04767.

Cottin, H., M. C. Gazeau, Y. Benilan, and F. Raulin (2001), Polyoxymethylene as parent molecule for the formaldehyde extended source in Comet Halley, *Astrophys J.*, *556*, 417 – 420.

Cravens, T. E., and A. E. S. Green (1978), Airglow from the inner comas of comets, *Icarus*, *33*(78), 612 – 623, doi:10.1016/0019-1035(78)90193-8.

Crovisier, J. (1989), The photodissociation of water in cometary atmospheres, *Astron. Astrophys.*, *213*, 459 – 464.

Crovisier, J., et al. (1996), The infrared spectrum of comet C/1995 O1 (Hale-Bopp) at 4.6 AU from the Sun., *Astron. Astophys.*, *315*, L385–L388.

Crovisier, J., K. Leech, D. Bockelée-Morvan, T. Y. Brooke, M. S. Hanner, B. Altieri, H. U. Keller, and E. Lellouch (1997), The spectrum of comet Hale-Bopp (C/1995 O1) observed with the Infrared Space Observatory at 2.9 AU from the Sun., *Science*, *275*, 1904 – 1907, doi:10.1126/science.275.5308.1904.

Crovisier, J., et al. (1999), ISO spectroscopic observations of short period comets , *Proceedings of the conferernce "The Universe as seen by ISO"*, *121*, 161–164.

Decock, A., E. Jehin, D. Hutsemékers, and J. Manfroid (2012), Forbidden oxygen lines in comets at various heliocentric distances, *Astron. Astrophys.*

Dello Russo, N., M. J. Mumma, M. A. Disanti, K. Magee-Sauer, R. Novak, and T. W. Rettig (2000), Water production and release in comet C/1995 O1 Hale-Bopp., *Icarus*, *143*, 324–337.

Delsemme, A. H., and M. R. Combi (1976), The production rate and possible origin of O (^{1}D) in comet Bennett 1970 II, *Astrophys. J. Lett.*, *209*, L149, doi:10.1086/182286.

Delsemme, A. H., and M. R. Combi (1979), O(^1D) and H_2^+O in comet Bennett 1970 II, *Astrophys. J.*, *228*, 330–337, doi:10.1086/156850.

DeMore, W. B., S.P., G. D. H. R.F., M. Kurylo, H. C.J., R. A.R., K. C.E., and M. M.J. (1997), Chemical Kinetics and Photochemical Data for Use in Stratospheric Modeling., *JPL Publ. 974*, (Evaluation Number 12), 1–266.

Dennerl, K., C. M. Lisse, A. Bhardwaj, D. J. Christian, S. J. Wolk, D. Bodewits, T. H. Zurbuchen, M. Combi, and S. Lepri (2012), Solar system X-rays from charge exchange processes, *Astron. Nachr.*, *333*(4), 324 – 334, doi:10.1002/asna.201211663.

DiSanti, M. A., M. J. Mumma, N. Dello Russo, and K. Magee-Sauer (2001), Carbon Monoxide Production and excitation in comet C/1995 O1 (Hale-Bopp): Isolation of native and distributed CO sources, *Icarus*, *153*, 361 – 390, doi:10.1006/icar.2001.6695.

Eberhardt, P., et al. (1987), The CO and N_2 Abundance in Comet 1P/Halley, *Astron. Astrophys.*, *187*, 481–414.

Erdman, P. W., and E. C. Zipf (1983), Electron-impact excitation of the Cameron system ($a^3\Pi \rightarrow X^1\Sigma$) of CO, *Planet. Spece. Sci.*, *31*, 317 – 321, doi:10.1016/0032-0633(83) 90082-X.

Farnham, T. L., D. Bodewits, M. F. A'Hearn, and L. M. Feaga (2012), Deep Impact MRI Observations of Comet Garradd (C/2009 P1, in *AAS/Division for Planetary Sciences Meeting Abstracts*, *AAS/Division for Planetary Sciences Meeting Abstracts*, vol. 44, p. 506.5.

Feaga, L. M., M. A'Hearn, T. Farnham, A. Gersch, D. Bodewits, and K. Klaasen (2012), A Study of C/2009 P1 Garradds Dominant Volatiles as Observed by the Deep Impact HRI-IR Spectrometer., in *AAS/Division for Planetary Sciences Meeting Abstracts*, *AAS/Division for Planetary Sciences Meeting Abstracts*, vol. 44, p. 313.08.

Federer, W., H. Villinger, F. Howorka, W. Lindinger, P. Tosis, D. Bassi, and E. Ferguson (1984), Reaction of O^+, CO^+, and CH^+ Ions with Atomic Hydrogen, *Physical Review Letters*, *52*, 2084–2086, doi:10.1103/PhysRevLett.52.2084.

Fehsenfeld, F. C., and E. E. Ferguson (1972), Thermal Energy Reaction Rate Constants for H^+ and CO^+ with O and NO, *J. Chem. Physics*, *56*, 3066–3070, doi:10.1063/1.1677642.

Fehsenfeld, F. C., D. B. Dunkin, and E. E. Ferguson (1970), Rate constants for the reaction of ${CO_2}^+$ with O, O_2 and NO; ${N_2}^+$ with O and NO; and ${O_2}^+$ with NO, *Planetary and Space Science*, *18*, 1267, doi:10.1016/0032-0633(70)90216-3.

Feldman, P. D., M. C. Festou, G. P. Tozzi, P. D. Feldman, and H. A. Weaver (1997), The CO_2/CO abundance ratio in 1P/Halley and several other comets observed by IUE and HST, *Astrophys. J.*, *475*, 829–834, doi:10.1086/303553.

Feldman, P. D., A. L. Cochran, and M. R. Combi (2004), *Spectroscopic investigations of fragment species in the coma: Comets II*, pp. 425–447, M. C. Festou, H. A. Weaver, & H. U. Keller (Ed.)(Tucson: Univ. of Arizona).

Feldman, P. D., R. E. Lupu, S. R. McCandliss, and H. A. Weaver (2009), The far ultraviolet spectral signatures of formaldehyde and carbon dioxide in comets , *Astrophys. J.*, *699*(2), 1104–1112, doi:10.1088/0004-637X/699/2/1104.

Festou, M. C. (1981), The density of Neutral compounds in cometary atmospheres, *Astron. Astrophys.*, *96*, 52 – 57.

Festou, M. C., and P. D. Feldman (1981), The forbidden oxygen lines in comets, *Astron. Astrophys.*, *103*, 154 – 159.

Fink, U. (2009), A taxonomic survey of comet composition 19852004 using CCD spectroscopy, *Icarus*, *201*, 311 – 334, doi:10.1016/j.icarus.2008.12.044.

Fink, U., and J. R. Johnson (1984), Luminosity and spatial distribution of the O[I] 6300 Å emission in comets, *Astron. J.*, *89*(10), 1565–1572, doi:10.1086/113660.

Fox, J. L. (2004), Advances in the aeronomy of Venus and Mars, *Adv. Space Res.*, *33*, 132 – 139, doi:10.1016/j.asr.2003.08.014.

Fox, J. L., and A. Dalgarno (1979), Ionization, luminosity, and heating of the upper atmosphere of Mars, *J. Geophys. Res.*, *84*, 7315 – 7333, doi:10.1029/JA084iA12p07315.

Fox, J. L., and A. Dalgarno (1981), Ionization, Luminosity and Heating of Upper atmosphere of Venus, *J. Geophys. Res.*, *86*, 629 – 639, doi:10.1029/JA086iA02p00629.

Furlong, J. M., and W. R. Newell (1996), Total cross section measurement for the metastable ($a^3\Pi$) state in CO, *J. Phys. B: At. Mol. Phys.*, *29*, 331 – 338, doi: 10.1088/0953-4075/29/2/020.

Furusho, R., H. Kawakitab, T. Fusec, and J. Watanabe (2006), Forbidden oxygen emission lines of comet 116P/Wild 4 at 2.4 AU , *Adv. Space Res.*, *9*, 1983–1986, doi:10.1016/j.asr.2006.06.003.

Giguere, P. T., and W. F. Huebner (1978), A model of comet comae. I. Gas-phase chemistry in one dimension, *Astrophys J.*, *223*, 638 – 654.

Gilijamse, J. J., S. Hoekstra, S. A. Meek, M. Metsälä, S. Y. T. van de Meerakker, S. Y. T, G. Meijer, G. C. Groenenboom, and G. C. (2007), The radiative lifetime of metastable CO ($a^3\Pi, \nu$=0), *J. Chem. Phys.*, *127*, 221,102–4, doi:10.1063/1.2813888.

Glinski, R. J., B. J. Ford, W. M. Harris, C. M. Anderson, and J. P. Morgenthaler (2004), Oxygen/Hydrogen chemistry in the inner comae of active comets, *Astrophys. J.*, *608*, 601–609.

Gombosi, T. I., A. F. Nagy, and T. E. Cravens (1986), Dust and neutral gas modelling of the inner atmospheres of comets, *Rew. of Geophys.*, *24*(3), 667–700.

Green, A. E. S., and J. D. Martin (1966), *A generalized Chapman function, in the Middle Ultraviolet: Its Science and Technology*, 140 pp., Wiley, New York.

Green, A. E. S., Dayashankar, and P. F. Schippnick (1985), Yield and concentration microplumes for electron impact on water, *Radiat. Res.*, *104*, 1 – 14.

Gringauz, K. I., et al. (1986), First in situ plasma and neutral gas measurements at comet Halley., *Nature*, *321*, 282 – 285.

Guberman, S. L. (1995), The dissociative recombination of OH^+, *J. Chem. Phys.*, *102*(4), 22.

Häberli, R. M., K. Altwegg, H. Balsiger, and J. Geiss (1996), Heating of the thermal electrons in the coma of comet P/Halley, *J. Geophys. Res.*, *101*(A7), 15,579–15,589.

Haider, S. A., and A. Bhardwaj (1997), Chemistry of the ions 40 amu in the inner coma of comet Halley, *Adv. Space Res.*, *20*(2), 291 – 294.

Haider, S. A., and A. Bhardwaj (2005), Radial distribution of production rates, loss rates and densities corresponding to ion masses $\leq$40 amu in the inner coma of comet Halley: Composition and chemistry., *Icarus*, *177*, 196 – 216, doi:10.1016/j.icarus.2005.02.019.

Haider, S. A., A. Bhardwaj, and R. P. Singhal (1993), Role of auroral and photoelectrons on the abundances of Methane and Ammonia in the coma of comet Halley, *Icarus*, *101*, 234 – 243, doi:10.1006/icar.1993.1021.

Harris, W. M., F. Scherb, E. Mierkiewicz, R. Oliversen, and J. Morgenthaler (2002), Production, outflow velocity, and radial distribution of H_2O and OH in the coma of comet C/1995 O1 (Hale-Bopp) from wide-field imaging of OH, *Astrophys. J.*, *578*, 996 – 1008, doi:10.1086/342648.

Haser, L. (1957), Distribution d'intensite dans la tete d'une comete, *Bull. Acad. R Sci Liege*, *43*, 740 – 750.

Heroux, L., and J. E. Higgins (1977), Summary of full disk solar fluxes between 250 and 1940 Å, *J. Geophys. Res.*, *82*, 3307.

Hodges, R. R. (1990), Monte Carlo simulation of nonadiabatic expansion in cometary atmospheres: Halley, *Icarus*, *83*, 410 – 433.

Huebner, W. F. (1985), *Cometary comae. In Molecular Astrophysics: State of the Art and Future Directions*, 311 - 330 pp., Reidel, Dordrecht.

Huebner, W. F., and D. C. Boice (1997), *Polymers and other macro- molecules in comets. In Comets and the Origin and Evolution of Life*, 111 - 129 pp., Springer-Verlag, New York.

Huebner, W. F., and C. W. Carpenter (1979), Solar photorate coefficients, *Los Alamos Report*, p. 8085.

Huebner, W. F., and P. T. Giguere (1980), A model of comet comae. II. Effects of solar photodissociative ionization, *Astrophys J.*, *238*, 753 – 762.

Huebner, W. F., J. J. Keady, and S. P. Lyon (1992), Solar photorates for planetary atmospheres and atmospheric pollutants, *Astrophys. Space Sci.*, *195*(1), 1–294, doi: 10.1007/BF00644558.

Huestis, D. L., and T. G. Slanger (2006), DPS, *American Astronomical Society*, *38*, 62.20.

Huestis, D. L., T. G. Slanger, B. D. Sharpee, and J. L. Fox (2010), Chemical origins of the Mars ultraviolet dayglow, *Faraday Discuss.*, *147*, 307, doi:10.1039/c003456h.

Ip, W. (1985), A preliminary consideration of the electron impact ionization effect in cometary comas, *Adv. Space Res.*, *5*, 47–51, doi:10.1016/0273-1177(85)90066-3.

Ip, W.-H. (1983), On photochemical heating of cometary comae - The cases of H2O and CO-rich comets, *Astrophys J.*, *264*, 726–732, doi:10.1086/160645.

Ip, W. H. (2004), *Global Solar Wind Interaction and Ionospheric Dynamics: Comets II*, pp. 605–629, M. C. Festou, H. A. Weaver, & H. U. Keller (Ed.)(Tucson: Univ. of Arizona).

Itikawa, Y., and N. Mason (2005), Cross sections for electron collisions with water molecules, *J. Phys. Chem. Ref. Data*, *34*(1), 1–22, doi:10.1063/1.1799251.

Jackman, C. H., R. H. Garvey, and A. E. S. Green (1977), Electron impact on atomospheric gases, I, updated cross sections, *J. Geophys. Res.*, *82*, 5081–5090, doi: 10.1029/JA082i032p05081.

Jain, S. K. (2013), Dayglow emission on Mars and Venus.

Jensen, M. J., R. C. Bilodeau, C. P. Safvan, K. Seiersen, L. H. Andersen, H. B. Pedersen, and O. Heber (2000), Dissociative Recombination of H_3O^+, HD_2O^+, and D_3O^+, *Astrophys. J.*, *543*, 764–774, doi:10.1086/317137.

Jewitt, D. C., and J. X. Luu (1993), The discovery of the candidate Kuiper Belt object 1992QB$_1$, *Nature*, *362*, 730 – 732.

Kalogerakis, K. S., C. Romanescu, M. Ahmed, K. R. Wilson, and T. G. Slanger (2012), CO prompt emission as a CO_2 marker in comets and planetary atmospheres, *Icarus*, *220*, 205 – 210, doi:10.1016/j.icarus.2012.04.028.

Karpas, Z., and W. T. Huntress, Jr. (1978), Reactions of OH^+ and H_2O^+ ions with some diatomic and simple polyatomic molecules, *Chemical Physics Letters*, *59*, 87–89, doi:10.1016/0009-2614(78)85621-8.

Kedzierski, W., J. Derbyshire, C. Malone, and J. W. McConkey (1998), Isotope effects in the electron impact break-up of water, *Journal of Physics B Atomic Molecular Physics*, *31*, 5361–5368, doi:10.1088/0953-4075/31/24/017.

Kissel, J., , and 18 colleagues (1986), Composition of comet Halley dust particles from Giotto observations, *Nature*, *321*, 336 – 337.

Körösmezey, A., et al. (1987), A new model of cometary ionosphere, *J. Geophys. Res*, *92*(A7), 7331 – 7340, doi:10.1029/JA092iA07p07331.

Krankowsky, D., et al. (1986), In situ gas and ion measurements at comet Halley, *Nature*, *321*, 326–329, doi:10.1038/321326a0.

Krasnopolsky, V. A., J. B. Greenwood, and P. C. Stancil (2004), *X-ray and extreme ultraviolet emission from comets*, vol. 0, 1 - 104 pp.

Krauss, M., and D. Neumann (1975), On the interaction of O(^{1}S) with O(^{3}P), *Chem. Phys. Lett.*, *36*(3), 372 – 374, doi:10.1016/0009-2614(75)80259-4.

Kuiper, G. P. (1951), *Astrophysics: ATopical Symposium*, 357 - 424 pp., McGraw Hill, New York.

Lamy, P. L., I. Toth, Y. R. Fernández, and H. A. Weaver (2004), *The sizes, shapes, albedos, and colors of cometary nuclei*, pp. 223–264, M. C. Festou, H. A. Weaver, & H. U. Keller (Ed.)(Tucson: Univ. of Arizona).

Lawrence, G. M. (1972a), Production of O(^{1}S) from the photodissociation of CO_2, *J. Chem. Phys.*, *57*(12), 5616 – 5617.

Lawrence, G. M. (1972b), Photodissociation of CO_2 to produce CO($a^3\pi$), *J. Chem. Phys.*, *56*(7), 3435 – 3442, doi:10.1063/1.1677717.

LeClair, L. R., and J. W. McConkey (1994), On O(^{1}S) and CO(a$^3\pi$) production from electron impact dissociation of CO_2, *J. Phys. B*, *27*, 4039–4055, doi:10.1088/0953-4075/27/17/026.

LeClair, L. R., M. D. Brown, and J. W. McConkey (1994), Selective detection of O(^{1}S) and CO(a$^3\pi$) following electron impact on CO using solid xenon, *Chem. Phys.*, *189*, 769 – 777.

Link, R. (1982), Dayside magnetospheric cleft auroral processes, *York Univ., Toronto, Canada.*

Lisse, C., et al. (1996), Discovery of X-ray and Extreme ultraviolet emissions in comet C/Hyakutake 1996 B2, *Science*, *274*, 205–208.

Lisse, C. M., T. E. Cravens, and K. Dennerl (2004), *X-Ray and Extreme Ultraviolet Emission from Comets*, pp. 631–643, M. C. Festou, H. A. Weaver, & H. U. Keller (Ed.)(Tucson: Univ. of Arizona).

Lovell, A. J., N. Kallivayalil, F. P. Schloerb, M. R. Combi, K. C. Hansen, and T. I. Gombosi (2004), On the effect of electron collisions in the excitation of cometary HCN, *Astrophys. J.*, *613*, 615 – 621.

Magee-Sauer, K., F. Scherb, F. L. Roesler, and J. Harlander (1990), Comet Halley O(^{1}D) and H_2O production rates , *Icarus*, *84*(1), 154–165.

Manfroid, J., D. Hutsemékers, E. Jehin, A. L. Cochran, C. Arpigny, W. M. Jackson, K. J. Meech, R. Schulz, and J. Zucconi (2007), The impact and rotational light curves of Comet 9P/Tempel 1, *Icarus*, *187*, 144–155, doi:10.1016/j.icarus.2006.08.003.

Marconi, M. L., and D. A. Mendis (1983), The atmosphere of a dirty-clathrate cometary nucleus – A two-phase, multifluid model, *Astrophys J.*, *273*, 381 – 396.

McConkey, J. W., C. P. Malone, P. V. Johnson, C. Winstead, V. McKoy, and I. Kanik (2008), Electron impact dissociation of oxygen-containing molecules A critical review, *Phys. Rept.*, *466*, 1–103, doi:10.1016/j.physrep.2008.05.001.

McElroy, M. B., and J. C. McConnell (1971), Atomic carbon in the atmospheres of Mars and Venus, *J. Geophys. Res.*, *76*, 6674 – 6690, doi:10.1029/JA076i028p06674.

McKay, A. J., N. J. Chanover, J. P. Morgenthaler, A. L. Cochran, W. M. Harris, and N. D. Russo (2012), Forbidden Oxygen Lines in Comets C/2006 W3 Christensen and C/2007 Q3 Siding Spring at Large Heliocentric Distance: Implications for the Sublimation of Volatile Ice, *Icarus*, doi:10.1016/j.icarus.2012.04.030.

McNesby, J. R., I. Tanaka, and H. Okabe (1962), Vacuum Ultraviolet Photochemistry. III. Primary Processes in the Vacuum Ultraviolet Photolysis of Water and Ammonia, *J. Chem. Phys.*, *36*, 605–607, doi:10.1063/1.1732579.

McPhate, J. B., P. D. Feldman, S. R. McCandliss, and E. B. Burgh (1999), Rocket bourne long slit ultraviolet spectroscopy of comet Hale-Bopp, *Astrophys. J.*, *521*, 920–927, doi:10.1086/307561.

Meech, K. J., and J. Svoreň (2004), *Using Cometary Activity to Trace the Physical and Chemical Evolution of Cometary Nuclei*, pp. 317–335, M. C. Festou, H. A. Weaver, & H. U. Keller (Ed.)(Tucson: Univ. of Arizona).

Mendis, D. A. (1987), A cometary aurora., *Earth Moon Planets*, *39*, 17 – 20.

Mitchell, G. F., S. S. Prasad, and W. T. Huntress (1981), Chemical model calculations of C_2, C_3, CH, CN, OH, and NH_2 abundances in cometary comae, *Astrophys J.*, *244*, 1087 – 1093.

Mitchell, J. B. A. (1990), The dissociative recombination of molecular ions., *Phys. Rept.*, *186*, 215 – 248.

Morgenthaler, J. P., W. M. Harris, F. Scherb, C. M. Anderson, R. J. Oliversen, N. E. Doane, M. R. Combi, M. L. Marconi, and W. H. Smyth (2001), Large-aperture O[I] 6300 Å photometry of comet Hale-Bopp: Implications for the photochemistry of OH, *Astrophys. J,*, *563*, 451 – 461, doi:10.1086/323773.

Morrison, N. D., D. C. Knauth, C. L. Mulliss, and W. Lee (1997), High resolution optical spectra of the head of the comet C/1996 B2 (Hyakutake), *Astro. Soc. Pac.*, *109*, 676–681, doi:10.1086/133931.

Mumma, M. J., M. A. DiSanti, A. Tokunaga, and E. E. Roettger (1995), Ground- based detection of water in Comet ShoemakerLevy 1992 XIX: Probing cometary parent molecules by hot-band fluorescence.], *Bull. Am. Astron. Soc.*, *27*, 1144.

Mumma, M. J., M. A. DiSanti, N. Dello Russo, M. Fomenkova, K. Magee-Sauer, C. D. Kaminski, and D. X. Xie (1996), Detection of abundant Ethane and Methane, Along with Carbon Monoxide and Water, in Comet C/1996 B2 Hyakutake: Evidence for Interstellar Origin, *Science*, *272*(5266), 1310 – 1314, doi:10.1126/science.272.5266.1310.

Nee, J. B., and L. C. Lee (1984), Photoabsorption cross sections of OH at 115-183 nm, *J. Chem. Phys.*, *81*, 31–36, doi:10.1063/1.447387.

Nicholls, R. W. (1962), Laboratory astrophysics, *J. Quant. Spectry. Radiat. Transfer*, *2*, 433 – 449, doi:10.1016/0022-4073(62)90030-4.

Oort, J. H. (1950), The structure of the cloud of comets surrounding the Solar System and a hypothesis concerning its origin, *Bull. Astron. Inst. Neth.*, *11*, 91 – 110.

Ootsubo, T., et al. (2012), Akari near-infrared spectroscopic survey for CO_2 in 18 comets, *Astrophys. J.*, *752*(15), 1–12, doi:10.1088/0004-637X/752/1/15.

Oppenheimer, M. (1975), Gas phase chemistry in comets, *Astrophys J.*, *196*, 251 – 259.

Oppenheimer, M., and C. J. Downey (1980), The effect of solar- cycle ultraviolet flux variations on cometary gas, *Astrophys J.*, *241*, L123 – L127.

Paganini, L., M. J. Mumma, G. L. Villanueva, M. A. DiSanti, B. P. Bonev, M. Lippi, and H. Boehnhardt (2012), The chemical composition of co-rich comet C/2009 P1 (GARRADD) at rH = 2.4 and 2.0 AU before perihelion, *Astrophys. J. Lett.*, *748*(L13), doi:10.1088/2041-8205/748/1/L13.

Raghuram, S., and A. Bhardwaj (2012), Model for the production of CO Cameron band emission in comet 1P/Halley, *Planetary and Space Science*, *6364*, 139149, doi:10.1016/j.pss.2011.11.011.

Raghuram, S., and A. Bhardwaj (2013), Model for Atomic Oxygen Visible Line Emissions in Comet C/1995 O1 Hale-Bopp, *Icarus*, *223*, 91–104, doi:10.1016/j.icarus.2012.11.032.

Rao, M. V. V. S., I. Iga, and S. K. Srivastava (1995), Ionization cross-sections for the production of positive ions from H_2O by electron impact, *J. Geophys. Res.*, *100*, 26,421–26,425, doi:10.1029/95JE02314.

Reach, W. T., J. Vaubaillon, C. M. Lisse, M. Holloway, and J. Rho (2010), Explosion of Comet 17P/Holmes as revealed by the Spitzer Space Telescope, *Icarus*, *208*, 276 – 292.

Richards, P. G., J. A. Fennelly, and D. G. Torr (1994), EUVAC: A solar EUV flux model of aeronomic calculations, *J. Geophys. Res.*, *99*(A5), 8981–8992, doi:10.1029/94JA00518.

Rodgers, S. D., and S. B. Charnley (2002), A model of the chemistry in cometary comae: Deuterated molecules, *Mon. Not. R. Astron. Soc.*, *330*, 660 – 674.

Rodgers, S. D., S. B. Charnley, W. F. Huebner, and D. C. Boice (2004), *Physical processes and chemical reactions in cometary comae*, pp. 505–522.

Rosati, R. E., R. Johnsen, and M. F. Golde (2003), Absolute yields of CO($a'^3\Sigma^+$, $d^3\Delta_i$, $e^3\Sigma^-$)+O from the dissociative recombination of CO_2^+ ions with electrons, *J. Chem. Phys.*, *119*(22), 11,630–11,635, doi:10.1063/1.1623480.

Rosati, R. E., M. P. Skrzypkowski, R. Johnsen, and M. F. Golde (2007), Yield of excited CO molecules from dissociative recombination of HCO^+ and HOC^+ ions with electrons, *J. Chem. Phys.*, *126*, 154,302, doi:10.1063/1.2715943.

Rosén, S., et al. (1998), Absolute cross sections and final-state distributions for dissociative recombination and excitation of CO^+(v=0) using an ion storage ring, *Phys. Rev. A*, *57*(6), 4462–4471, doi:10.1103/PhysRevA.57.4462.

Rosen, S., et al. (2000), Recombination of simple molecular ions studied in storage ring : Dissociative recombination of H_2O^+, *Faraday Discuss.*, *407*(115), 295–302, doi:10.1039/a909314a.

Safronov, V. S. (1987), *Evolution of the Small Bodies of the Solar System*, 217 - 226 pp., North-Holland, Amsterdam.

Sahnow, D. J., P. D. Feldman, S. R. McCandliss, and M. E. Marinez (1993), Long-slit ultraviolet spectroscopy of comet Austin (1990V), *Icarus*, *101*(1), 71–83.

Sawada, T., D. J. Strickland, and A. E. S. Green (1972), Electron energy deposition in CO_2, *J. Geophys. Res.*, *77*, 4812 – 4818, doi:10.1029/JA077i025p04812.

Schleicher, D. G., and T. L. Farnham (2004), *Photometry and imaging of the coma with narrowband filters*, pp. 449–469, M. C. Festou, H. A. Weaver, & H. U. Keller (Ed.)(Tucson: Univ. of Arizona).

Schleicher, D. G., S. M. Lederer, R. L. Millis, and T. L. Farnham (1997), Photometric behaviour of Comet Hale-Bopp (C/1995 O1) before perihelion, *Science*, *275*, 1913–1915, doi:10.1126/science.275.5308.1913.

Schmidt, H. U., R. Wegmann, W. F. Huebner, and D. C. Boice (1988), Cometary gas and plasma flow and with detailed chemistry, *Comp. Phy. Comm.*, *49*, 17 – 59, doi:10.1016/0010-4655(88)90214-7.

Schultz, D., G. S. H. Li, F. Scherb, and F. L. Roesler (1992), Comet Austin (1989c1) O(^{1}D) and H_2O production rates, *Icarus*, *96*(2), 190–197, doi:10.1016/0019-1035(92)90072-F.

Seiersen, K., A. Al-Khalili, O. Heber, M. J. Jensen, I. B. Nielsen, H. B. Pedersen, C. P. Safvan, and L. H. Andersen (2003), Dissociative recombination of the cation and dication of CO_2, *Phys. Rev. A*, *68*, 022708, doi:10.1103/PhysRevA.68.022708.

Seng, G., and F. Linder (1976), Vibrational excitation of polar molecules by electron impact. II. Direct resonant excitation in H_20, *J. Phys.*, *B 9*, 2539 – 2551.

Singh, P. D., A. A. D'Ealmeida, and W. F. Huebner (1991), The states of carbon and nitrogen atoms after photodissociation of CN, CH, CH^+, C2, C3, and CO in comets, *Icarus*, *90*, 74–78, doi:10.1016/0019-1035(91)90069-6.

Singh, V., I. C. Mcdade, G. G. Shepherd, B. H. Solheim, and W. E. Ward (1996), The $O(^1S)$ dayglow emissions as observed by the WIND imaging interferometer on the UARS, *Ann. Geophysicae*, *14*, 637.

Singh, V., A. K. Upadhayaya, and M. V. S. Krishna (2010), Modeling of redline dayglow emission, *Quarterly Journal of the Hungarian Meteorological Service*, *114*(3), 217 – 227.

Singhal, R. P., and A. Bhardwaj (1991), Monte Carlo Simulation of Photoelectron Energization in Parallel Electric Fields: Electroglow on Uranus, *J. Geophys. Res.*, *96*, 15,963 – 15,972, doi:10.1029/90JA02749.

Singhal, R. P., and S. A. Haider (1984), Analytical yield spectrum approach to photoelectron fluxes in the earth's atmosphere, *J. Geophys. Res.*, *89*, 6847–6852, doi: 10.1029/JA089iA08p06847.

Skrzypkowski, M. P., T. Gougousi, R. Johnsen, and M. F. Golde (1998), Measurement of the absolute yield of $CO(a^3\pi)$ + O products in the dissociative recombination of CO_2^+ ions with electrons, *J. Chem. Phys.*, *108*(20), 8400 – 8407, doi:10.1063/1.476267.

Slanger, T. G., and G. Black (1982), Photodissociative channels at 1216 Å for H_2O, NH_3, and CH_4, *J. Chem. Phys.*, *77*, 2432–2437, doi:10.1063/1.444111.

Slanger, T. G., R. L. Sharpless, and G. Black (1977), CO_2 photodissociation, 1060 - 1175 Å, *J. Chem. Phys.*, *66*, 5317 – 5323, doi:10.1063/1.434710.

Slanger, T. G., P. C. Cosby, B. D. Sharpee, K. R. Minschwaner, and D. E. Siskind (2006), $O(^1S \rightarrow {}^1D, {}^3P)$ branching ratio as measured in the terrestrial nightglow, *Journal of Geophysical Research (Space Physics)*, *111*(A10), A12318, doi:10.1029/2006JA011972.

Spinrad, H. (1982), Observations of the red auroral oxygen lines in nine comets, *Publ. Astron. Soc. Pac.*, *94*, 1008–1016.

Stancil, P. C., D. R. Schultz, M. Kimura, J.-P. Gu, G. Hirsch, and R. J. Buenker (1999), Charge transfer in collisions of O^+ with H and H^+ with O, *Astron. Astrophys. Supp.*, *140*, 225–234, doi:10.1051/aas:1999419.

Stern, S. A. (2003), The evolution of comets in the Oort cloud and Kuiper belt, *Nature*, *424*, 639 – 642.

Stief, L. J., W. A. Payne, and R. B. Klemm (1975), A flash photolysis-resonance fluorescence study of the formation of $O(^1D)$ in the photolysis of water and the reaction of $O(^1D)$ with H_2, Ar, and He , *J. Chem. Phys.*, *62*, 4000–4008, doi:10.1063/1.430323.

Storey, P. J., and C. J. Zeippen (2000), Theoretical values for the [OIII] 50007/4959 line intensity ratio and homologous cases, *Mon. Not. R. Astron. Soc.*, *312*, 813–816, doi:10.1046/j.1365-8711.2000.03184.x.

Tobiska, W. K. (2004), SOLAR2000 irradiances for climate change, aeronomy and space system engineering, *Adv. Space Res.*, *34*, 1736 – 1746, doi:10.1016/j.asr.2003.06.032.

Tobiska, W. K., T. Woods, F. Eparvier, R. Viereck, L. Floyd, D. Bouwer, G. Rottman, and O. R. White (2000), The SOLAR 2000 empirical solar irradiance model forecast tool, *J. Atmos. Solar-Terres. Phys.*, *62*(14), 1233–1250.

Torr, M. R., D. G. T. Torr, and H. E. Hinteregger (1979), Ionization freequencies for major thermospheric constituents as a function of solar cycle 21, *Geophys. Res. Lett.*, *6*, 771.

Torr, R., and D. G. Torr (1982), The role of metastable speciesin the thermosphere, *Reviews of geophysics and space physics*, *20*(1), 91 – 144.

Tozzi, G. P., P. D. Feldman, and M. C. Festou (1998), Origin and production of C(^{1}D) atoms in cometary comae, *Astron. Astrophys.*, *330*, 753–763.

van Dishoeck, E. F., and A. Dalgarno (1984), Photodissociation of OH in Interstellar Clouds, *Astrophys. J.*, *277*, 576–580, doi:10.1086/161729.

Vejby-Christensen, L., L. H. Andersen, O. Heber, D. Kella, H. B. Pedersen, H. T. Schmidt, and D. Zajfman (1997), Complete branching ratios for the dissociative recombination of H_2O^+, H_3O^+, and CH_3^+, *ApJ*, *483*, 531–540.

Villanueva, G. L., M. J. Mumma, M. A. DiSanti, B. P. Bonev, L. Paganini, and G. A. Blake (2012), A multi-instrument study of comet C/2009 P1 (Garradd) at 2.1 AU (pre-perihelion) from the Sun, *Icarus*, *220*, 291 – 295, doi:10.1016/j.icarus.2012.03.027.

Watanabe, K., and M. Zelikoff (1953), Absorption coefficients of water vapor in the vacuum ultraviolet, *Journal of the Optical Society of America (1917-1983)*, *43*, 753–.

Weaver, H. A., and F. D. Feldman (1992), Probing the Nature of Comets with the Hubble Space Telescope, in *European Southern Observatory Conference and Workshop Proceedings*, *European Southern Observatory Conference and Workshop Proceedings*, vol. 44, edited by P. Benvenuti and E. Schreier, p. 475.

Weaver, H. A., P. D. Feldman, J. B. McPhate, M. F. A'Hearn, C. Arpigny, and T. E. Smith (1994), Detection of CO Cameron band emission in comet P/Hartley-2 (1991 XV) with the Hubble Space Telescope, *Astrophys. J.*, *422*, 374 – 380, doi:10.1086/173732.

Weaver, H. A., et al. (1997), The activity and size of the nucleus of comet Hale-Bopp (C/1995 O1), *Science*, *275*, 1900–1904, doi:10.1126/science.275.5308.1900.

Wegmann, R., H. U. Schmidt, W. F. Huebner, and D. C. Boice (1987), Cometary MHD and chemistry., *Astron. Astrophys.*, *187*, 339 – 350.

Whipple, F. L. (1950), A comet model I. The acceleration of Comet Encke, *Astrophys J.*, *111*, 375 – 394.

Whipple, F. L., and W. F. Huebner (1976), Physical processes in comets, *Ann. rev. Astron. Astrophys.*, *14*, 143–172, doi:10.1146/annurev.aa.14.090176.001043.

Wiese, W. L., J. R. Fuhr, and T. M. D. (Eds.) (1996), *Atomic transition probabilities of carbon, nitrogen, and oxygen: A critical data compilation*, Am. Chem. Soc., Washington, D. C.

Witasse, O., J. Lilensten, C. L. re, and P.-L. Blelly (1999), Modelling the OI 630.0 And 557.7 nm thermospheric dayglow during EISCAT-WINDII coordinated measurements, *J. Geophys. Res.*, *104*, 24,639 – 24,656.

Woodall, J., M. Agúndez, A. J. Markwick-Kemper, and T. J. Millar (2007), The UMIST database for astrochemistry 2006, *Astron. Astrophs.*, *466*, 1197 – 1204, doi:10.1051/0004-6361:20064981.

Woods, T. N., P. D. Feldman, and G. J. Rottman (2000), Ultraviolet Observations of Comet Hale-Bopp (C/1995 O1) by the UARS SOLSTICE, *Icarus*, *144*, 182–186, doi: 10.1006/icar.1999.6262.

Woodward, C. E., M. S. Kelley, D. Bockelée-Morvan, and R. D. Gehrz (2007), Water in comet C/2003 K4 (LINEAR) with Spitzer, *Astrophys.*, *671*, 1065–1074, doi:10.1086/ 522366.

Wu, C. Y. R., and F. Z. Chen (1993), Velocity distributions of hydrogen atoms and hydroxyl radicals produced through solar photodissociation of water, *J. Geophys. Res.*, *98*, 7415 – 7435.

Wysong, I. J. (2000), Measurement of quenching rates of CO($a^3\Pi$) using laser pump and probe technique, *Chem. Phys. Lett.*, *1 - 2*, 42 – 46, doi:10.1016/S0009-2614(00) 00967-2.

Zhang, H. W., G. Zhao, and J. Y. Hu (2001), A catalogue of emission lines in spectra of comet C/1995 O1 (Hale-Bopp), *Astron. Astophys.*, *367*(3), 1049–1055, doi:10.1051/ 0004-6361:20010008.

Zipf, E. C. (1969), The collisional deactivation of metastable atoms and molecules in the upper atmosphere, *Can. J. Chem.*, *47*, 1863–1870, doi:10.1139/v69-305.